Transactions of the ASME

The Journal of Engineering for Gas Turbines and Power (ISSN 0022-0825) is published quarterly for $100 per year by The American Society of Mechanical Engineers, 345 East 47th Street, New York, NY 10017. Second class postage paid at New York, NY and additional mailing offices. POSTMASTER: Send address change to The Journal of Engineering for Gas Turbines and Power, c/o The AMERICAN SOCIETY OF MECHANICAL ENGINEERS, 22 Law Drive, Box 2300, Fairfield, NJ 07007-2300.

CHANGES OF ADDRESS must be received at Society headquarters seven weeks before they are to be effective. Please send old label and new address.

PRICES: To members, $24.00, annually; to nonmembers, $100.00. Add $6.00 for postage to countries outside the United States and Canada.

INDEXED by the Engineering InJex, Inc.

Journal of Engineering for Gas Turbines and Power

Published Quarterly by The American Society of Mechanical Engineers

VOLUME 107 • NUMBER 3 • JULY 1985

TECHNICAL PAPERS

(Contents Continued on Inside Back Cover)

(Contents Continued)

K. V. Bury
Associate Professor.
Department of Mechanical Engineering,
University of British Columbia

K. J. W. Spurr
Previously Senior Engineer
and Test Director.
Development Department,
Hydroelectric Generation
Projects Division,
British Columbia Hydro
and Power Authority

J. H. Lang
Supervisor.
Turbines & Valves,
Mechanical Department,
Hydroelectric Generation
Projects Division,
British Columbia Hydro
and Power Authority

Recent Developments in the Field Testing of Large Turbines

A new test procedure is proposed for the field acceptance testing of large hydroelectric turbines. This procedure is an improvement over existing procedures in that it generates test data from which a statistical estimate of turbine efficiency as well as a confidence band on that estimate can be calculated.

1 Introduction

In recent years hydroelectric power developments have increasingly shifted toward lower-head, larger-volume Francis (and other) turbine installations. These higher specific speed machines tend to exhibit less stable performance characteristics due to higher blade loading and greater sensitivity to slight changes in the approach flow regime. This frequently results in an increased variability among measurements taken during turbine acceptance tests. With the increase in machine size and cost of energy, the treatment of test data and the associated error analysis have become a critical part of the turbine acceptance test.

The turbine evaluation procedures commonly used are based on International Test Codes [1, 2]. The state of the art, as discussed in [3, 4], shows that the evaluation procedures had been developed for installations where inherent variations in the measured variables were relatively small and where a careful, unambiguous error analysis had not been generally established. However, because of the economic consequences of errors[1] inherent in performance estimates, the need to estimate machine performance statistically has become important.

This paper proposes an alternative test and evaluation procedure which modifies the traditional approach to Field Acceptance Test (FAT) by generating a coherent data base to which statistical analysis can be applied. The resulting turbine efficiency estimate, and its confidence band, allows a more rational settlement of turbine contracts.

[1] Typical contractual penalties may exceed 4–5 percent of the original turbine price per one-tenth of one percent efficiency deviation.

Contributed by the Power Division for publication in the JOURNAL OF ENGINEERING FOR GAS TURBINES AND POWER. Manuscript received by the Power Division July 1983.

2 Traditional Efficiency Evaluation

The traditional approach to the efficiency evaluation of an installed turbine is to measure developed power at a number of measured levels of available power, to convert the resulting calculated efficiency and output values to rated head, and to fit a "smooth curve" to these test points ([1], p. 53). The single decision quantity, which is then compared with the contractual design ("guarantee") efficiency, is often a weighted average of efficiencies obtained from the smooth curve at a number of predefined power levels.

When comparing measured and guaranteed values, a common procedure is to place a measurement tolerance band around the weighted average test efficiency. This band consists of a systematic error and a random error which, in engineering practice, are usually combined in the RMS sense. The existing 1963 IEC code [1] only recommends estimated values for the systematic errors, which implies that random errors are negligible. However, with the increased accuracy of modern instruments and the added variability of lower head units, systematic and random errors tend to be of the same order of magnitude for the typical FAT of 30–40 test points, so that both error components must be considered in an error analysis.

Given an efficiency estimate and its error band, the turbine contract provides for a price adjustment in proportion to the deviation of the guarantee efficiency from the estimated tolerance band. Thus the magnitude of the error band becomes economically significant.

In determining the magnitude of the error band there are two areas of concern. One is the error due to a chosen smooth curve (see Fig. 1). This fit imposes on the test data a model for which an intrinsic justification does not appear available. The other is that the systematic and random error components be

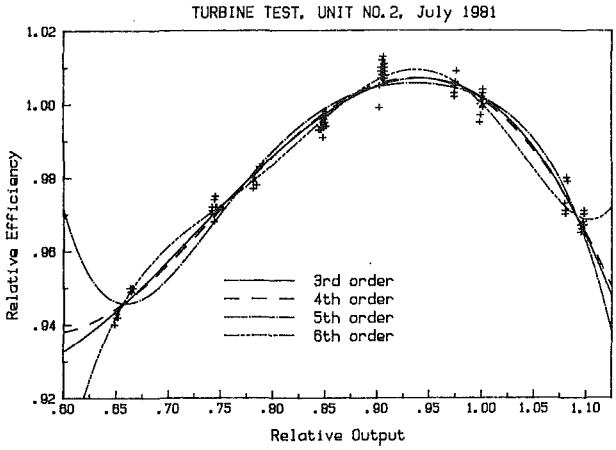

Fig. 1 Test data obtained with the proposed procedure, and superimposed least-squares polynomial curve fits; scales are relative to a chosen reference value

explicitly recognized in a rational error analysis which results in a reasonable efficiency estimate and a justifiable tolerance band.

3 Development of New Procedure

In 1981 an alternative FAT procedure was developed by the British Columbia Hydro and Power Authority in order to better evaluate turbine efficiency. This developed procedure was used as a basis to contractually evaluate four 240,000 Bhp Francis turbine units in the B.C. Hydro system. The following outlines a proposed procedure, formulated after the above field test experience.

3.1 Determination of Efficiency Values. The required overall turbine efficiency estimate E is obtained by a weighted average procedure which requires individual efficiency estimates E_j at K specified power levels P_j

$$E = \sum_{j=1}^{K} a_j \cdot E_j \tag{1}$$

where $\Sigma_{j=1}^{K}\ a_j = 1$, and the weights a_j are contractually specified. Since the estimates E_j, as well as their associated uncertainties, vary with power level in a manner for which a justifiable engineering model is not available, the values E_j and their error bands should be determined independently of each other. In this way the unknown model error, which is inherent in an assumption of a smooth curve fit to the efficiency data, is avoided. Furthermore, straightforward statistical techniques can then be used to establish a best efficiency estimate E_j at each required power level P_j with a confidence band at a given level of confidence ϕ.

In general, it is not possible to set the physical field test conditions so that a specified output power P_j is precisely achieved for a given test, since the actual characteristics of the turbine are not known at this stage. To overcome this difficulty, the turbine wicket gates may be physically blocked at two settings which closely bracket each required power level P_j from above and below. The approximate value of these settings can be estimated from the manufacturer's physical model turbine performance curves or better from a preliminary power-gate test done prior to the FAT. The objective is to choose prototype gate settings such that the corresponding output power, when converted to rated head, lies within ± 2 percent of P_j (see Appendix 1). Test data can then be linearly transformed to equivalent values corresponding to the predefined power level P_j (see Appendix 2). The resulting n_j calculated efficiency values E_{ij} now form a coherent data base for estimating the turbine efficiency E_j and its standard deviation s_j at power P_j.

3.2 Preliminary Field Test. In order to conduct the FAT at a desired level of statistical control, the variabilities of installed instruments and measured variables must be assessed. Since these variabilities are installation- and site-dependent, a preliminary test series is considered an essential prerequisite to the contractual FAT. Preliminary tests may be performed immediately prior to the FAT and require only a small but reasonable number of test points bracketing some of the power levels. The cost of such tests is not large relative to the costs of potential errors in the final efficiency evaluation in today's contracts.

From the results of preliminary tests the suitability of instrumentation may be verified, the required number of instrument readings, whose average will constitute a test point average, established, and preliminary estimates of standard deviations obtained for measured variables.

3.3 Error Analysis. The turbine efficiency is related to the measurable quantities of power P, discharge Q, and hydraulic head H by

$$\eta = C\frac{P}{H\,Q} \tag{2}$$

where C is a dimensional constant. Errors in the measurements of P, Q, H translate into an error in the derived efficiency E with two components: systematic and random.

Systematic errors comprise the residual bias errors remaining in measurement processes after the most precise calibrations possible have been carried out in order to remove any bias of known direction. Neither the magnitudes of these residual errors, nor their directions, are measurable. The (absolute) magnitudes B_P, B_Q, B_H of systematic errors may be estimated from instrument calibration statements and/or envelope values suggested by test codes. The *relative* systematic errors, $b_P = B_P/P$, $b_Q = B_Q/Q$, $b_H = B_H/H$, may be combined to estimate the relative systematic efficiency

Nomenclature

P, Q, H = power output, hydraulic discharge, hydraulic head
B_P, B_Q, B_H = absolute systematic errors of P, Q, H
b_P, b_Q, b_H = relative systematic errors of P, Q, H
η = average weighted turbine efficiency
E = estimate of η
B_E, b_E = absolute, relative systematic errors of E
P_j = contractually defined power level
K = total number of power levels P_j
η_j = turbine efficiency at P_j
n_j = number of repeated observations transferred to P_j
E_{ij} = ith test point efficiency estimate at P_j
E_j = mean efficiency estimate at P_j (estimate of η_j)
a_j = weighting factor of E_j in the calculation of E
r_{Tj} = total efficiency error at P_j
s_{Tj} = estimated standard deviation of r_{Tj}
r_j = random component of r_{Tj}
s_j = estimated standard deviation of r_j
s_{Ej} = estimated standard deviation of E_j
s_E = estimated standard deviation of E
$\pm\Delta\eta_j$ = error band on E_j at confidence level ϕ
$\pm\Delta E$ = error band on E at confidence level α
t = Student's t-variate

error b_E by means of the "root-mean-square" relation (see, for example, [5], p. 361):

$$b_E = \pm (b_P^2 + b_Q^2 + b_H^2)^{1/2} \tag{3}$$

Thus the *absolute* systematic error of the efficiency evaluation is estimated as

$$B_E = \pm E \cdot (b_P^2 + b_Q^2 + b_H^2)^{1/2} \tag{4}$$

where E is an efficiency estimate.

The systematic error contributed by the linear data transfer procedure (Appendix 2) is assumed negligible relative to B_E. Likewise, errors due to discrepancies in the repeatability of wicket gate settings are ignored, since these errors are exceedingly small when gates are set against machined blocks.

Random errors of the efficiency determination result from random variations of the measurement variables P, H, Q and their associated measuring systems. These errors may be established directly from the efficiency values E_j obtained during the FAT (see section 3.4).

At each power level P_j the random efficiency error r_j is assumed to be a normal random variable with mean zero and standard deviation which is estimated as

$$s_j = \left(\frac{1}{n_j - 1} \cdot \sum_{i=1}^{n_j} (E_{ij} - E_j)^2 \right)^{1/2} \tag{5}$$

where the mean efficiency E_j is estimated by

$$E_j = \frac{1}{n_j} \cdot \sum_{i=1}^{n_j} E_{ij} \tag{6}$$

Thus the standard deviation of the mean efficiency estimate E_j is obtained as

$$s_{Ej} = s_j / n_j^{1/2} \tag{7}$$

The *total error* r_{Tj} in E_j is made up of the constant systematic component B_E and the random variable component r_j. Although it is not statistically justifiable to combine a fixed error with the variance of a random error, the following formula is offered by the current draft revision of the IEC code [1] to estimate the "variance" of the total error r_{Tj} as

$$s_{Tj}^2 \doteq B_E^2 + s_{Ej}^2 \tag{8}$$

In order to determine the number n_j of test points at each power level P_j for the FAT, such that the (unknown) efficiency η_j is bracketed by a specified confidence band of width $\pm \Delta\eta_j$ at a chosen confidence level ϕ, it is assumed that each total error r_{Tj} is a normal random variable with mean zero and variance s_{Tj}^2. Thus the following relation is obtained using equation (8)

$$\Delta\eta_j \doteq t_{(\gamma, n_j - 1)} \cdot (B_E^2 + s_j^2 / n_j)^{1/2} \tag{9}$$

and may be used to determine n_j, where t is the (tabulated) t-variate with $(n_j - 1)$ degrees of freedom at the probability level $\gamma = 1 - (1 - \phi)/2$. In practice this may be done by substituting for s_j^2 the variance obtained during the preliminary field tests. Otherwise, one would evaluate s_j^2 for an initial number n_j of actual readings, and then increase n_j until equation (9) is satisfied. In this way the test is controlled at the level of individual power settings P_j.

Since it is assumed that the total errors r_{Tj} are normal random variables, it follows [6] that the *overall* efficiency estimate E, equation (1), is also a normal random variable with mean η (unknown) and standard deviation estimated as

$$s_E = \left(\sum_{j=1}^{K} a_j^2 \cdot s_{Tj}^2 \right)^{1/2} \tag{10}$$

3.4 Formal Acceptance Test. The power levels P_j, weights a_j, error bands $\pm \Delta\eta_j$, confidence level ϕ, and the bias values B_P, B_Q, B_H should be chosen prior to the FAT.

From the preliminary field test it is known how many readings are required from each instrument to yield an average value of acceptable accuracy for each test point.

As the turbine is moved through the sequence $j = 1, 2, \ldots, K$, test points are taken above and below each required power level P_j. Each calculated efficiency test point is first converted to rated head (see Appendix 1), and then linearly transposed to correspond to P_j (see Appendix 2). The resulting efficiency value for the ith test point at power P_j is E_{ij}.

The above test sequence is repeated in whole or in part, going up and down through the power spectrum a sufficient number of times, so that at each P_j the relation (9) is satisfied. That is, as test points accumulate, the efficiency E_j and its standard deviation s_{Ej} are estimated by relations (6) and (7) until there are n_j test points such that E_j estimates the (unknown) turbine efficiency η_j to within $\pm \Delta\eta_j$ at the statistical confidence level ϕ.

The overall efficiency estimate E is then obtained from relation (1), and its standard deviation s_E may be estimated from equation (10).

If an overall error band of width $\pm \Delta E$ has been stipulated in the turbine contract, its associated confidence level α may be estimated approximately from

$$z_{(1-(1-\alpha)/2)} \doteq \Delta E / s_E \tag{11}$$

where z is the (tabulated) standard normal variate, evaluated at the probability level $(1 - (1 - \alpha)/2)$.

If, on the other hand, the confidence level α for an error band on E has been stipulated in the contract, the value ΔE can likewise be obtained approximately from equation (11).

In either case, the position of $(E \pm \Delta E)$ relative to the guarantee efficiency E_g determines the outcome of the turbine contract.

4 Recent Field Experiences

The considerations underlying the above proposed procedure formed the basis for the recent FAT of four B.C. Hydro turbines. The following is a very brief summary of that experience which served to finalize the procedure proposed in section 3.

For the turbine units in question, a total error band $\pm \Delta\eta$ on each E_j had not been contractually defined. However, the *systematic* efficiency error was agreed on as $B_E = 0.588$ percent. On the basis of a preliminary test series and a preceding, but annulled FAT, it was agreed that the *random* efficiency error was to be held below $\Delta r = \pm 0.1$ percent at the 95 percent confidence level for a total number of test points not exceeding 100. In addition, at least eight test points were to be taken at each of the five specified power levels P_j, where each test point was to be the average of seven sets of instrument readings.

Due to the nonstationary nature of the penstock flow regime, it was found necessary to set the turbine wicket gates by mechanically blocking the servomotor operating ring against machined blocks, as well as to control the adjacent turbine units so as to produce the minimum disturbance to the flow distribution approaching the unit under test.

Because the turbine contract *specified* the random error to be below 0.1 percent, an unprecedented 92 test points were recorded during this FAT. This resulted in an estimated overall 95 percent random efficiency error of $\pm$ 0.0813 percent and a total efficiency error of $\pm$ 0.594 percent was given by expression (8). The same FAT with only 30–40 test points, however, would have resulted in a random efficiency error of roughly 1/4 of the total error.

Figure 1 presents the (nondimensionalized) results of the FAT. The plotted test points show clearly that an independent data set was available at each required power level P_j, so that the efficiencies E_j could be estimated directly and the overall

efficiency estimate E obtained rationally. Also shown in Fig. 1 are a number of least-squares polynomial curve fits which indicate the arbitrary nature of the traditional smooth curve approach. It is seen that the fit becomes unstable as the order of the polynomial increases, despite the large number of test points.

5 Conclusions

The proposed Field Acceptance Test procedure overcomes the ambiguities inherent in the present international test codes, by providing a rational method of estimating an overall turbine efficiency value together with its associated measure of uncertainty.

It is suggested that the proposed procedure falls within the intent of "method A" described in the current draft revision of IEC code [1], that it leads to a more rational evaluation of turbine contracts than traditional procedures, and that it provides a coherent data base from which more refined decision procedures may be developed.

6 Acknowledgments

Acknowledgment is due to the British Columbia Hydro and Power Authority for permission to describe this recent development work, and to Mr. N. H. Latimer and Dr. W. W. Bell for their useful discussion. The responsibility for the technical content of this paper rests solely with the authors.

7 References

1 *International Code for the Field Acceptance Tests of Hydraulic Machines*, Central Bureau of the Electrical Commission, Publication No. 41, Geneva, Switzerland, 1963.

2 *Power Test Code*, ASME, No. 18.1, 1949.

3 Johnson, G. D., et al., "Evaluation of Measurement Uncertainties in Performance Testing of Hydraulic Turbines and Pump/Turbines," ASME JOURNAL OF ENGINEERING FOR POWER, Apr. 1975, pp. 145-152.

4 Discussions of [3], pp. 153-161.

5 Herschy, R. W., *Hydrometry: Principles and Practices*, Wiley, New York, 1978.

6 Bury, K. V., *Statistical Models in Applied Science*, Wiley, New York, 1975, Chap. 2.

APPENDIX 1

Data Conversion From Test Head to Rated Head

The following is a brief summary of the accepted procedure [1]. Two cases are considered for the conversion of efficiency and power from test head to rated head. In both cases the efficiency at test head is computed from the measured power and discharge values.

(*a*) The test head lies within ±3 percent of the rated head. Then power at rated head is calculated as

$$P_R = P_T\left(\frac{H_R}{H_T}\right)^{3/2}$$

and the efficiency at rated head is taken as

$$E_R \doteq E_T$$

where the subscripts R and T refer to conditions at the rated and test heads, respectively.

(*b*) The test head lies outside ±3 percent, but inside ±10 percent, of the rated head. The power at rated head is then calculated as

$$P_R = P_T\left(\frac{H_R}{H_T}\right)^{3/2} \cdot \frac{P''}{P'}$$

and the efficiency at rated head is taken as

$$E_R \doteq E_T \cdot \frac{\eta''}{\eta'}$$

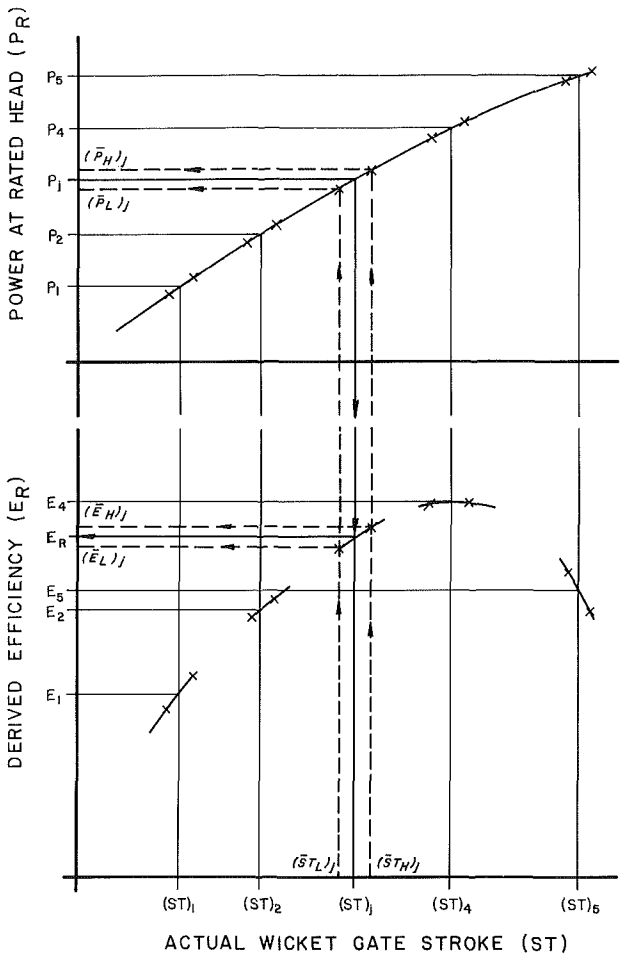

Fig. 2 Output and derived efficiency at rated head

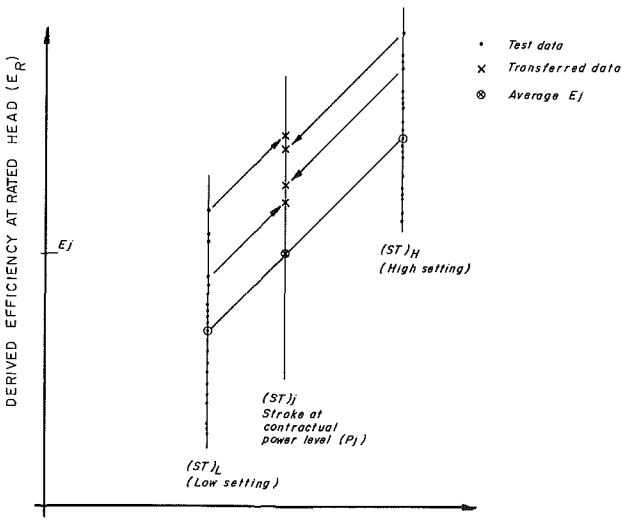

Fig. 3 Linear data transfer procedure

where P' = unit output of model turbine at the unit speed corresponding to the test head and the tested output

P'' = unit output of model turbine at the unit speed corresponding to the rated head and at a gate position corresponding to P'

η'' = efficiency of model turbine at the unit speed corresponding to the rated head and at the gate position corresponding to P'

η'' = efficiency of model turbine at the unit speed corresponding to the rated head and at the gate position corresponding to P'

APPENDIX 2

Linear Data Transfer Procedure

In the following, all quantities refer to a specific contractual power level P_j (subscript j is dropped for clarity) and are assumed to have been converted to rated head where applicable.

Each required power level P is bracketed by a low and a high wicket gate stroke setting (subscripts L and H, respectively), such that both P_L and P_H lie within ± 2 percent of P. At the stroke settings ST_L and ST_H, power is measured and efficiency is calculated (P_{Li}, P_{Hi}, E_{Li}, E_{Hi}) for n_L and n_H test points, respectively. Hence average values can be calculated as

$$\bar{P}_L = \frac{1}{n_L} \cdot \sum_{i=1}^{n_L} P_{Li};\ \bar{P}_H = \frac{1}{n_H} \cdot \sum_{i=1}^{n_H} P_{Hi}$$

and

$$\bar{E}_L = \frac{1}{n_L} \cdot \sum_{i=1}^{n_L} E_{Li};\ \bar{E}_H = \frac{1}{n_H} \cdot \sum_{i=1}^{n_H} E_{Hi}$$

The stroke setting ST to produce the required power P is calculated as (see Figs. 2, 3)

$$ST = ST_L + \frac{P - \bar{P}_L}{\bar{P}_H - \bar{P}_L} \cdot (ST_H - ST_L)$$

Given the required stroke value ST, each efficiency value derived for a test point is linearly transposed to correspond to the required power level P (see Figs. 2, 3) as follows

$$E_i = E_{Li} + \frac{ST - ST_L}{ST_H - ST_L} \cdot (\bar{E}_H - \bar{E}_L)$$

or

$$E_i = E_{Hi} - \frac{ST_H - ST}{ST_H - ST_L} (\bar{E}_H - \bar{E}_L)$$

Thus n_L derived efficiency values at the low setting ST_L and n_H such values at the high setting ST_H result in $(n_L + n_H)$ values at the contractual power level P. These $(n_L + n_H)$ values comprise the coherent data base for estimating the efficiency E and its error band at the power level P.

Justification for the local linearization in the range ± 3 percent of power P_j is found in the observed behavior of hydraulic turbines. Discharge and power are, to the first order, essentially proportional to gate opening, and the second-order effects of changing flow incidence angles can be neglected over this limited range. Experience on two tested installations has shown that the repeatability of blocked-gate tests is remarkably good.

A Universal Correlation for the Thermal Efficiency of Open Gas Turbine Cycle With Different Fuels

E. Y. W. Leung
Consultant.
Lexington, MA 02173
Mem. ASME

It is well known that, unlike the thermal efficiency of closed gas turbine cycles, the thermal efficiency of open gas turbine cycles varies with the fuel used in the combustion process. Presented in this paper is a thorough investigation of the effects of hydrocarbon fuels and alcohol fuels on the thermal efficiency of open gas turbine cycle. Among the open cycles with different fuels and otherwise identical specifications, the computed thermal efficiencies show a variation of about 2 percent between the extremes, which is appreciable. It was found that the thermal efficiency increases with a parameter of the fuel, $c_1 + c_2$*, taken from the equation of reaction,*

$$c(Fuel) + O_2 \rightarrow c_1(CO_2) + c_2(H_2O),$$

and that the thermal efficiency of open gas turbine cycles is likely to be higher if the original fuel is replaced by a fuel which has a higher fuel parameter, $c_1 + c_2$*. A universal correlation for both hydrocarbon fuels and alcohol fuels is presented in Fig. 1, plotting the thermal efficiency maximized from the pressure ratio variation, versus the parameter,* $c_1 + c_2$*. Alternatively, this correlation is also generalized by equation (2).*

Introduction

Although the thermal efficiency of closed gas turbine cycles is independent of the fuel, the thermal efficiency of open gas turbine cycles varies with the fuel used in the combustion process. In comparison with the precise concept of the thermal efficiency of closed gas turbine cycles, the thermal efficiency of open gas turbine cycles is merely an empirical term. It is understood that the present definition of thermal efficiency of open gas turbine cycles is used simply because there is no better alternative. From the practical point of view, since there is no other alternative, it becomes advantageous to understand the empirical characteristics of this thermal efficiency as much as possible.

In this paper, the investigation followed the same methods used by the serious researchers of the past. The specifications of the actual gas turbine were mostly based on an up-to-date paper on combined cycles [1]. The gas properties were taken from [2], which is well known for gas turbine cycle analysis.

The principle result of this investigation is a correlation between the variation of the thermal efficiency with both hydrocarbon fuels and alcohol fuels, and the fuel parameter, $c_1 + c_2$, taken from the equation of reaction

$$c(\text{Fuel}) + O_2 \rightarrow c_1(CO_2) + c_2(H_2O) \qquad (1)$$

This correlation is presented as either a plot, shown in Fig. 1, or the following equation,

$$\eta_{max} = [(25.47 + 29.2\tau) + (2.2 + 3.3\tau)\ln(c_1 + c_2)] \text{ percent}, \qquad (2)$$

where, if T_{max} is in degrees K, $\tau = \ln(T_{max}/1000)$, and if T_{max} is in degrees R, $\tau = \ln(T_{max}/1800)$. Of course, presented in this paper is also an explanation for the reason that the thermal efficiency should correlate with the fuel parameter $c_1 + c_2$.

Gas Turbine Cycle

Figure 2 shows the schematic diagram of a simple gas turbine assembly. A set of general specifications, or assumptions, for the actual gas turbine is summarized in Table 1. Some of these specifications were based on [1], while the others were concluded from a few recent publications.

In addition to the general specifications, or assumptions, in Table 1, the following are a few more. The compressed fuel was assumed to enter the combustor at 298.15 K, or 25°C. The net work output of the cycle was assumed to be reduced by 1 percent, allowing work for bearing friction, auxiliaries, and others in the system. The heat supplied to the cycle was assumed to be equal to the enthalpy of combustion of the fuel at 298.15 K, plus an additional 2 percent, which takes into account the effect of imperfect combustion and heat transfer loss from the combustor external surface. This low figure of 2 percent is based on an almost perfect combustion, because of the large amount of excess air present in the combustion gases. Figure 3 shows an example of the amount of theoretical air of the combustion gases with the hydrocarbon fuel, $(CH_2)_z$. The amount of excess air is always above 100 percent.

Following the common practice of gas turbine cycle analysis, the compressor pressure ratio r_p was treated as a

Contributed by the Gas Turbine Division for publication in the JOURNAL OF ENGINEERING FOR GAS TURBINES AND POWER. Manuscript received by the Gas Turbine Division December 27, 1983.

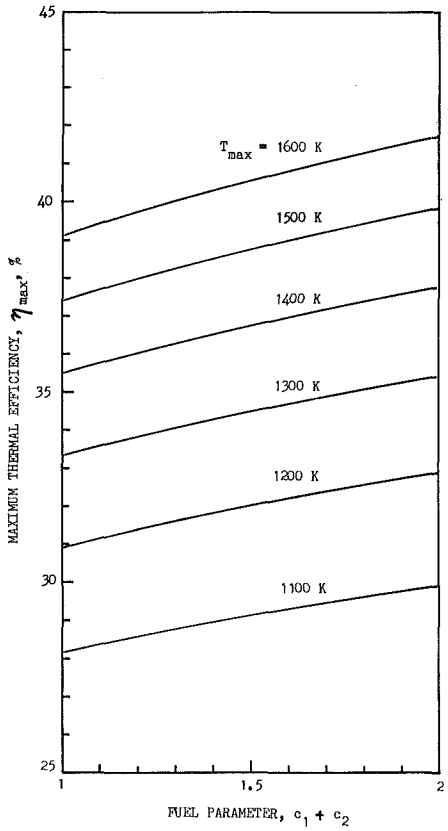

Fig. 1 Universal correlation for both hydrocarbon fuels and alcohol fuels

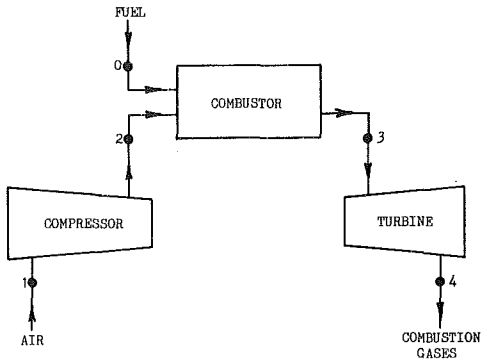

Fig. 2 Schematic diagram of a gas turbine

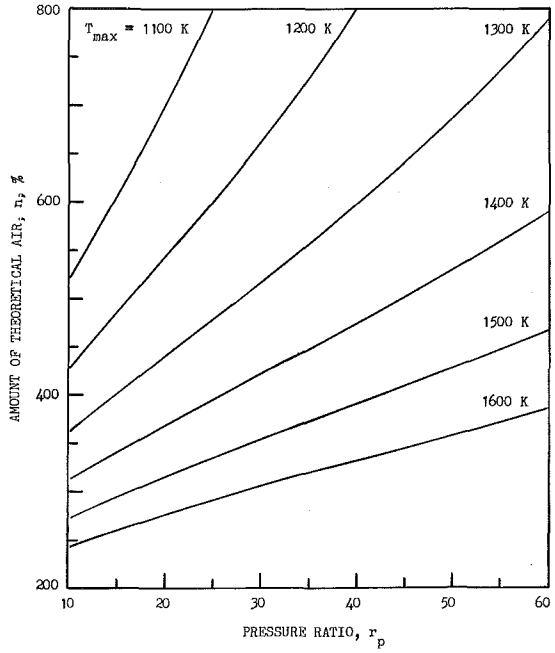

Fig. 3 Amount of theoretical air for cycles with fuels, $(CH_2)_z$

continuous variable, and the maximum temperature of the cycle T_{max} was treated as a variable, which changes with steps of 100 K, from 1100 K to 1600 K. The maximum cycle temperatures T_{max} of 1500 K and 1600 K were included in this investigation with a futuristic projection that the application of ceramic turbine and combustor parts for the gas turbine would eventually become practical.

It should be mentioned that, in order to provide a consistent analysis for this investigation, some of these specifications had to be overly generalized. For example, the combustion efficiency was assumed to be constant while it is known to be slightly dependent on the fuel. The compressor adiabatic efficiency was assumed unchanged while it tends to

Nomenclature

c, c_1, c_2 = coefficients in equation (1)
c_p = dh/dT, specific heat of air per mole of air
c_{pc} = dh_c/dT, specific heat of combustion gases per mole of combustion gases
h = enthalpy of air per mole of air
h_c = enthalpy of combustion gases per mole of combustion gases
h_{RP} = enthalpy of combustion per mole of fuel, at 298.15 K
h' = function of T, defined by equation (12)
m = number in alcohol formula, $(CH_2)_m HOH$
M = molar mass
n = amount of theoretical air
P = pressure
q_s = heat supplied per cycle per mole of air
r = number of moles of combuston gases per mole of air
r_p = compressor pressure ratio
r' = parameter of fuel, defined by equation (14)
R = universal gas constant
s = entropy of air per mole of air
s_c = entropy of combustion gases per mole of combustion gases
s_p = $\int(c_p/T)dT$, entropy of air at fixed pressure per mole of air
s_{pc} = $\int(c_{pc}/T)dT$, entropy of combustion gases at fixed pressure per mole of combustion gases
s'_p = function of T, defined by equation (13)
T = temperature in absolute scale
w_c = compressor work per mole of air
w_n = net work output per cycle per mole of air
w_t = turbine work per mole of combustion gases
x = mole fraction of oxygen in air
y, z = numbers in hydrocarbon formula, $(CH_y)_z$
η = thermal efficiency
η_c = compressor adiabatic efficiency
η_{max} = maximum thermal efficiency
η_t = turbine adiabatic efficiency
τ = function in equation (2)

Subscripts

0 = denoting properties at temperature T_0, equal to 298.15 K
CO_2 = denoting properties of CO_2
H_2O = denoting properties of H_2O
O_2 = denoting properties of O_2

be slightly lower if the pressure ratio gets too high. The effects of cooling the turbine and combustor parts on the cycle analysis were neglected because the methods of cooling lack a consistent pattern. The slight deviations of compressed gas properties from the ideal gas conditions were neglected. The fuels were assumed to be pure. The combustion gases were assumed to be the result of complete combustion, although the actual combustion is not complete, but very close to perfect.

Methods of Computation

In the compressor, air enters at state 1, and leaves at state 2, giving the following equations

$$s_{2s} = s_1, \text{ or } s_{p2s} = s_{p1} + R \ln (P_2/P_1) \tag{3}$$

$$W_c = (h_{2s} - h_1)/\eta_c \tag{4}$$

and

$$h_2 = h_1 + w_c \tag{5}$$

Air is assumed to be a mixture of dry, nonreactive ideal gases, of which the properties are given by [2]. The method of computation of these properties with the aid of a microcomputer is described in [3]. A thorough check of this new method was made by comparing the values in the air table of [2] and a similar table composed by the computer readout. A total of 2501 values for each of the properties, h and s_p, were compared, ranging from 500 R to 3000 R, at every degree R. The air table gives values of h to two decimal places, and the standard deviation of h was found to be 0.006 Btu/lb, equivalent to a temperature deviation of 0.02 R. The air table gives values of s_p to five decimal places, and the standard deviation was found to be 0.000006 Btu/lb•R, equivalent to a temperature deviation of 0.04 R. From these results, one can expect that the present investigation should be in close agreement with the investigations of previous researchers who used [2] to compute similar cycles.

In the turbine, combustion gases enter at state 3 and leave at state 4, giving the following equations,

$$s_{c4s} = s_{c3}$$

or

$$s_{pc4s} = s_{pc3} - R \ln (P_3/P_4) \tag{6}$$

$$w_t = \eta_t (h_{c3} - h_{c4s}) \tag{7}$$

and

$$h_{c4} = h_{c3} - w_t \tag{8}$$

The properties of combustion gases, h_c and s_{pc}, are given by the following equations

$$h_c = \frac{1}{r}\left(h + \frac{h'}{n}\right) \tag{9}$$

$$s_{pc} = \frac{1}{r}\left(s_p + \frac{s'_p}{n}\right) \tag{10}$$

and

$$r = 1 + \frac{r'}{n} \tag{11}$$

It should be added that n is the amount of theoretical air, of which an example is shown in Fig. 3. The functions h' and s'_p and the parameter r' are given by the following equations

$$h' = x(c_1 h_{CO_2} + c_2 h_{H_2O} - h_{O_2}) \tag{12}$$

$$s'_p = x(c_1 s_{p,CO_2} + c_2 s_{p,H_2O} - s_{p,O_2}) \tag{13}$$

and

$$r' = x(c_1 + c_2 - 1) \tag{14}$$

A detailed derivation of these equations is given by [3]. The mixture of combustion gases is, again, assumed to be a mixture of nonreactive ideal gases after the completion of the combustion process. The present method bypasses the tedious interpolations recommended in [2], but it retains the accuracy of the methods recommended by [2].

In the combustor, the combustion process is assumed to be complete. Air enters at state 2, fuel enters at T_0, and combustion gases leave at state 3, giving the following equation for adiabatic combustion,

$$r(h_{c3} - h_{c0}) - (h_2 - h_0) + \left(\frac{xc}{n}\right) h_{RP} = 0 \tag{15}$$

It should be reminded that the subscript 0 denotes properties at T_0 which is equal to 298.15 K, or 25°C. The substitution of equation (9) into the first two terms of equation (15) gives the equation

$$n = (-xch_{RP} - h'_3 + h'_0)/(h_3 - h_2) \tag{16}$$

from which the amount of theoretical air n can readily be computed. A detailed derivation of equation (16) is, again, given by [3].

According to the assumptions in the preceding section, the net work output per cycle per mole of air is

$$w_n = (rw_t - w_c)/(1.01) \tag{17}$$

and the heat supplied per cycle per mole of air is

$$q_s = (-xch_{RP}/n)/(0.98) \tag{18}$$

The thermal efficiency of the open gas turbine cycle is, as usual,

$$\eta = w_n/q_s \tag{19}$$

Table 1 Specifications of the gas turbine cycle

T_1	P_1	η_c	P_2/P_1	T_3	$(P_2 - P_3)/P_2$	η_t	$(P_4 - P_1)/P_1$
288 K	1 atm	85 %	r_p	T_{max}	4 %	88 %	1 %

Table 2 Specifications of hydrocarbon fuels, $(CH_y)_z$

y	FORMULA	PHASE	h_{RP}/M, kJ/kg	$c_1 + c_2$
0	C	SOLID	-32,750	1
1	$(CH)_z$	LIQUID	-40,000	$1\frac{1}{5}$
2	$(CH_2)_z$	LIQUID	-45,000	$1\frac{1}{3}$
3	$(CH_3)_z$	LIQUID	-47,000	$1\frac{3}{7}$
4	CH_4	LIQUID	-49,500	$1\frac{1}{2}$
∞	H_2	GAS	-120,000	2

Table 3 Maximum thermal efficiency of fuels, $(CH_2)_z$, in percent

	MAXIMUM TEMPERATURE OF CYCLE, T_{max}, K					
h_{RP}/M, kJ/kg	1100	1200	1300	1400	1500	1600
-42,750	28.80	31.64	34.14	36.36	38.33	40.09
-45,000	28.78	31.62	34.12	36.34	38.31	40.08
-47,500	28.77	31.60	34.10	36.32	38.29	40.06

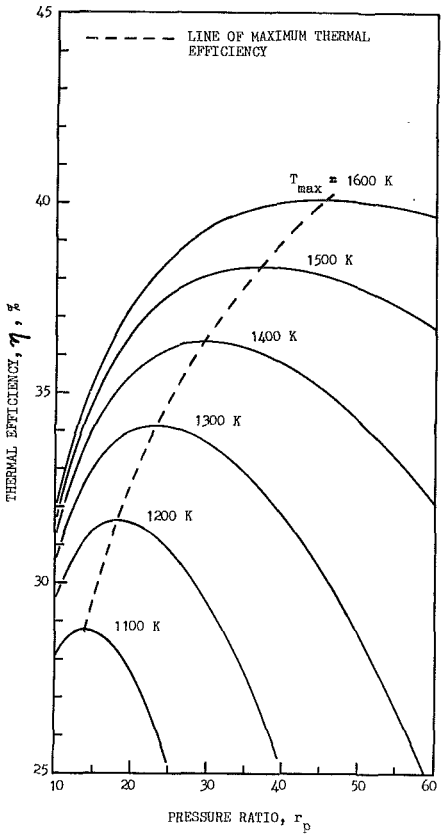

Fig. 4 Thermal efficiency of cycles with fuels, $(CH_2)_z$

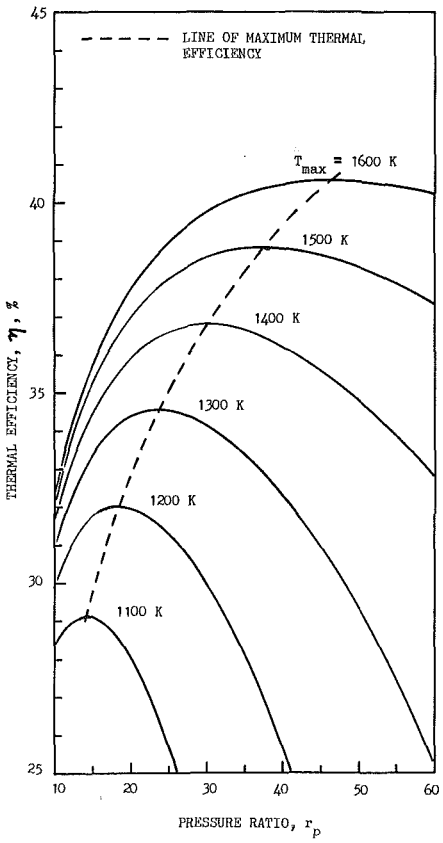

Fig. 5 Thermal efficiency of cycles with fuel, CH_4

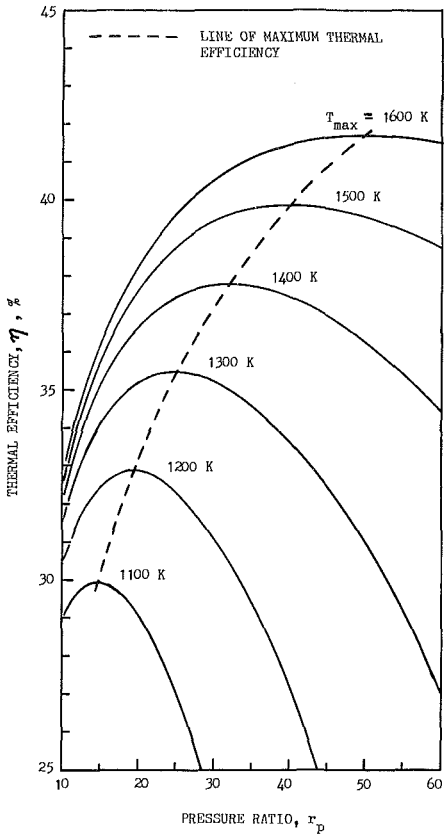

Fig. 6 Thermal efficiency of cycles with fuel, CH_3OH

Fuels

The most common type of gas turbine fuels is the group of hydrocarbon fuels $(CH_y)_z$, in which the number y plays an important role in this investigation. For example, octane, C_8H_{18}, can be rewritten as $(CH_{2.25})_8$, in which y is equal to 2.25. The values of y of most hydrocarbon fuels lie in the range between 1 and 4.

In this investigation, four basic values of y were chosen, which are 1, 2, 3, and 4. The two extremes of y, zero and infinity, were also included. With y equal to zero, the formula becomes that of carbon, C, and with y approaching infinity, the formula becomes that of hydrogen, H_2.

The average values of the enthalpy of combustion per unit mass of the hydrocarbon fuel h_{RP}/M are listed in Table 2. In this investigation, most fuels entering the combustor are compressed liquids, except carbon which is a solid and hydrogen which is a gas.

It is understood that the enthalpy of combustion per unit mass, for a series of hydrocarbon fuels with identical values of y, varies among different isomers of the same compound and, worst of all, among fuels which have different values of z. For the case of y equal to 2, the enthalpy of combustion per unit mass of ethene, C_2H_4, with z equal to 2, is about 6 percent higher than that of 1-Dedene, $C_{10}H_{20}$, with z equal to 10. This is the reason that the values of enthalpy of combustion per unit mass, in Table 2, are chosen from the average values between the extremes. It was found that the thermal efficiency of open gas turbine cycles is not sensitive to small variation of the enthalpy of combustion; the universal correlation of this investigation was made possible partially because of this characteristic. Shown in Table 3 are the variations of the maximum thermal efficiency for the series of hydrocarbon fuels $(CH_2)_z$, due to the variations of the enthalpy of combustion. It can be observed from Table 3 that the variations of maximum thermal efficiency are merely $\pm$ 0.02 percent, which result from ± 5 percent variations of the enthalpy of combustion. The ± 5 percent variations are beyond the upper and lower limits of those used in this investigation.

Table 4 Specifications of alcohol fuels, $(CH_2)_m HOH$

m	FORMULA	PHASE	h_{RP}/M, kJ/kg	$c_1 - c_2$
1	CH_3OH	LIQUID	-19,700	2
2	C_2H_5OH	LIQUID	-26,800	$1\frac{2}{3}$
3	C_3H_7OH	LIQUID	-30,600	$1\frac{5}{9}$
4	C_4H_9OH	LIQUID	-33,100	$1\frac{1}{2}$

In this investigation, the effects of the series of alcohols $(CH_2)_m HOH$ on the thermal efficiency were studied. Although this series only covers part of the alcohol family, included in this series are the most commonly used alcohol fuels, methyl alcohol, CH_3OH, and ethyl alcohol, C_2H_5OH, with m equal to 1 and 2 respectively in the formula. In order to demonstrate the universal applications of the present correlation, the list of alcohols was expanded to isopropyl alcohol, C_3H_7OH, so-called rubbing alcohol, with m equal to 3, and isobutyl alcohol, C_4H_9OH, with m equal to 4, though these alcohols are usually not used as fuels. The enthalpy of combustion per unit mass of the alcohols is listed in Table 4.

Results

Shown in Figs. 4, 5, and 6 are plots of the thermal efficiency of open gas turbine cycles η versus the compressor pressure ratio r_p for the fuels $(CH_2)_z$, CH_4, and CH_3OH. It can be observed from these plots that the complete sets of curves of thermal efficiency versus pressure ratio can be arranged in ascending order, from Fig. 2 to Fig. 4. Each of the curves in Fig. 4 is higher than each of the corresponding curves in Fig. 3, and each of the curves in Fig. 3, in turn, is higher than each of the corresponding curves in Fig. 2. Since the same pattern of ascending order is true among the maxima of these curves, these maxima, or these maximum thermal efficiencies η_{max}, which are essential in practical applications, were chosen as the principle characteristic of the curves. The maximum thermal efficiencies η_{max} for six cases of hydrocarbon fuels and four cases of alcohols, were computed and summarized in Table 5.

When the coordinates of the maximum thermal efficiency η_{max} versus the parameter $c_1 + c_2$ were plotted, it was observed that, for a fixed T_{max}, the locus of the hydrocarbon fuels and the locus of the alcohol fuels merged into one line, which became a universal correlation for both hydrocarbon fuels and alcohol fuels. Figure 1 shows a set of smooth lines for T_{max}, ranging from 1100 K to 1600 K. These lines were fitted within $\pm$ 0.05 percent of the computed points given by Table 5. Each of these lines shows that the maximum thermal efficiency increases monotonously with the fuel parameter $c_1 + c_2$. This set of lines was also fitted into equation (2), which has a standard deviation of 0.13 percent from the computed values given in Table 5.

In Table 5, there are two rows in which the parameter $c_1 + c_2$ is equal to 1.5, one row for the hydrocarbon group CH_4, and another row for the alcohol group C_4H_9OH. The discrepancies of the maximum thermal efficiency between these two fuels vary from 0.05 to 0.10 percent, which are small, although these two fuels are quite different. In Table 5, there are also two rows in which the parameter $c_1 + c_2$ is equal to 2, one row for the hydrocarbon group H_2, and another row for the alcohol group CH_3OH. The discrepancies of the maximum thermal efficiencies between these two fuels vary from 0 to 0.09 percent, which are, again, small. These small maximum thermal efficiency discrepancies, between fuels with identical fuel parameters $c_1 + c_2$, confirm the universal characteristic of the correlation proposed in this paper.

Table 5 Maximum thermal efficiency, in percent

		MAXIMUM TEMPERATURE OF CYCLE, T_{max}, K					
FORMULA	$c_1 - c_2$	1100	1200	1300	1400	1500	1600
C	1	28.14	30.90	33.33	35.48	37.38	39.09
$(CH)_z$	$1\frac{1}{5}$	28.53	31.34	33.82	36.01	37.95	39.70
$(CH_2)_z$	$1\frac{1}{3}$	28.78	31.62	34.12	36.34	38.31	40.08
$(CH_3)_z$	$1\frac{3}{7}$	28.99	31.85	34.37	36.60	38.59	40.38
CH_4	$1\frac{1}{2}$	29.14	32.02	34.55	36.80	38.80	40.60
C_4H_9OH	$1\frac{1}{2}$	29.09	31.95	34.48	36.72	38.71	40.50
C_3H_7OH	$1\frac{5}{9}$	29.19	32.06	34.60	36.84	38.84	40.64
C_2H_5OH	$1\frac{2}{3}$	29.38	32.27	34.82	37.09	39.10	40.91
CH_3OH	2	29.93	32.87	35.47	37.78	39.84	41.70
H_2	2	29.84	32.80	35.41	37.74	39.82	41.70

In addition, a plot of the maximum thermal efficiency of the hydrocarbon fuels versus the number y is shown in Fig. 7. It can be observed that the curves of maximum thermal efficiency increase with the number y. The abscissa has an unavoidable break between 4 and infinity. A plot of the maximum thermal efficiency of the alcohols versus the number m is shown in Fig. 8. It can be observed that the curves of maximum thermal efficiency decrease with the number m. A reasonable extrapolation is that, if m becomes very large, the curves of the thermal efficiency of $(CH_2)_m HOH$ should almost be identical to those of $(CH_2)_z$, shown in Fig. 4. In comparison, the plots in Figs. 7 and 8 surely lack the uniqueness of the plot in Fig. 1.

Discussion – Part 1

The correlation between the thermal efficiency and the fuel parameter $c_1 + c_2$ can best be explained from the basic equation relating these two quantities. The substitution of equations (17), (11), and (14) into equation (19) gives a detailed equation for the thermal efficiency

$$\eta = \frac{\left(\frac{w_t - w_c}{1.01}\right) \cdot \left[1 + \left(\frac{0.2099 w_t}{w_t - w_c}\right) \cdot \left(\frac{c_1 + c_2 - 1}{n}\right)\right]}{q_s} \tag{20}$$

Equation (20) shows that the thermal efficiency η depends on the terms w_c, w_t, n, q_s, and $(c_1 + c_2)$. The effects of these terms on the thermal efficiency are analyzed in the following paragraphs. The analysis is made on cycles with different fuels and otherwise identical specifications.

Equations (3) and (4) show that, if r_p and T_1 are constant, w_c remains constant. Equations (6) and (7) show that, if r_p and T_3 are constant, w_t depends only on c_{pc}, which depends on the fuel. However, the dependence of w_t on c_{pc} is a minor one because of the following reasoning. Equation (7) shows that, if the temperature change $T_3 - T_{4s}$ is assumed constant, w_t increases with c_{pc}. But a large c_{pc} in equation (6) reduces the temperature change $T_3 - T_{4s}$. Thus, c_{pc} has two effects on w_t. While one tends to increase w_t, another tends to reduce w_t. In this investigation, w_t was found to change very little because of the limited variation of c_{pc}. Therefore, for a rough

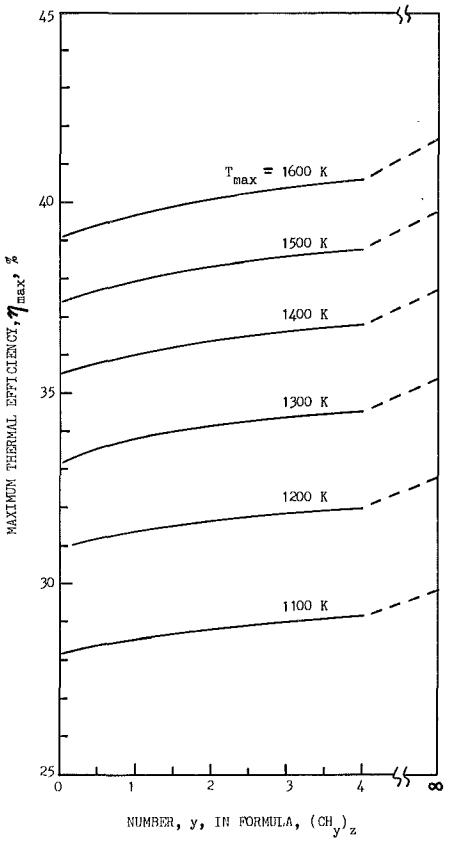

Fig. 7 Correlation for hydrocarbon fuels

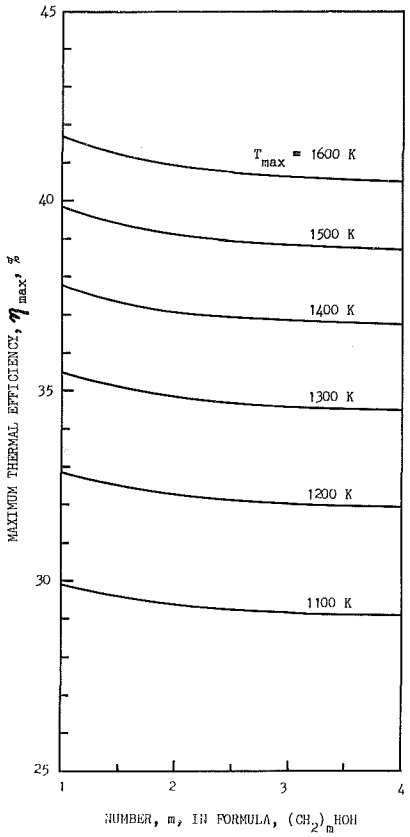

Fig. 8 Correlation for alcohol fuels

estimate of the thermal efficiency from equation (20), the terms $(w_t - w_c)/(1.01)$ and $(0.2099w_t)/(w_t - w_c)$ can be considered as constants.

Next, the combined effect of n and q_s on the thermal efficiency is analyzed. It can be observed that a large n tends to reduce the numerator in the right-hand side of equation (20), but equation (18) shows that a large n also reduces q_s, which is the denominator in the right-hand side of equation (20). In this investigation, the variation of n is, again, small, and the net effect of n and q_s on the thermal efficiency was found to be very small.

In equation (20), the only appreciable effect on the thermal efficiency is the term, $c_1 + c_2 - 1$, because while the fuel parameter $c_1 + c_2$ varies from 1 to 2, the term $c_1 + c_2 - 1$ varies from 0 to 1, or 100 percent. This is the reason for the dependence of the thermal efficiency on the fuel parameter $c_1 + c_2$ for cycles with different fuels and otherwise identical specifications.

Discussion – Part 2

It can be observed from Fig. 1 that hydrogen gas and methyl alcohol, with fuel parameter $c_1 + c_2$ equal to 2, have the highest maximum thermal efficiency among open gas turbine cycles with otherwise identical specifications. At a glance, this conclusion almost points to the replacement of hydrocarbon fuels with either hydrogen gas or methyl alcohol for gas turbines. At this point, the inadequacy of the definition of the thermal efficiency for open gas turbine cycles from the overall energy point of view becomes evident, because this definition cannot take into account events which happen outside of the gas turbine.

For the case of hydrogen, the compression of hydrogen, which is a gas, into the high-pressure combustor requires much more work than the compression of any liquid fuel to the same pressure. If this compression work were subtracted from the net work output per cycle w_n, given by equation (17), the resulted thermal efficiency for hydrogen fuel completely loses its attractiveness.

For the case of methyl alcohol, unlike hydrogen gas, it is a liquid, and does not have the requirement of excessive compression work to enter the combustor. Among the liquid fuels, methyl alcohol has the highest thermal efficiency among cycles with otherwise identical specifications. However, it is understood that the least expensive industrial method to produce methyl alcohol is to synthesize it from carbon monoxide and hydrogen at pressures above 200 atm, which are much higher than any pressure in the normal combustor of a gas turbine. Figures 4, 5, and 6 show that the thermal efficiency reaches its maximum while the combustor pressure is below 50 atm. The compression work in the synthesis of methyl alcohol simply cannot be accounted for in the definition of the thermal efficiency for open gas turbine cycles.

The arguments of the preceding paragraphs demonstrate the fact that a fuel that has a higher thermal efficiency in comparison with other fuels for cycles with otherwise identical specifications does not necessary imply that it is more suitable from the overall energy point of view. Actually, the thermal efficiency for open gas turbine cycles can only be used as an empirical standard to compare the open gas turbine cycles, and the universal correlation presented in this paper merely provides an additional guideline for the comparison.

References

1 Rice, I. G., "The Combined Reheat Gas Turbine/Steam Turbine Cycle: Part I—A Critical Analysis of the Combined Reheat Gas Turbine/Steam Turbine Cycle," ASME Journal of Engineering for Power, Vol. 102, No. 1, Jan. 1980, pp. 35-41.

2 Keenan, J. H., and Kaye, J., *Gas Tables*, Wiley, New York, 1945.

3 Leung, E. Y. W., "Algorithm for Gas Properties," *Computers in Engineering 1983 (Proceedings of the 1983 International Computers in Engineering Conference and Exhibit, ASME)*, Vol. 3, pp. 247-252.

Analysis of Single-Phase Cascade Flow in Power Plant Drain Systems

S. A. Hout[1]
Process Engineer.
Orange, CA

The performance of a typical drain system was checked through a pressure drop analysis and the determination of valve sizing coefficients. The operation checks that two-phase flow does not occur upstream of the control valve. Erosion checks are performed at any elbow installed downstream of the control valve where flashing may take place. The analysis does not cover the performance of the feedwater heater or moisture separator and reheater drain systems under transient conditions such as load rejection, i.e., turbine trip. It is believed that accurate valve sizing and appropriate drain cascade are vital to proper drainage.

Introduction

Two-phase pressure drop depends on flow regime and system geometry and is not a simple application in power plant complex drain systems. Benjamin and Miller [2] proposed an analytic approach for sizing lines carrying flashing mixtures. Isbin et al. [7] and later Fauske [5] proposed experimental data that apply to steam-water critical flow under fixed conditions.

Laio [8] considered that the drain systems calculations must be performed for all possible operating conditions to assure its adequacy; any system in a power plant must be operated with varying process conditions.

Proper design of the drain system from turbine periphery facilities requires correct line layout and control valve sizing [1]. From a purely economic viewpoint, an undersized valve cannot do the job and must be replaced; too large a control valve costs more initially and has high maintenance costs since the seating surfaces wear rapidly. Considering the operation, an oversized valve provides poor control and can cause system instability [4]. The most expensive, sensitive, and accurate controller is of little value if the control valve cannot correct the flow properly to maintain the control point.

Normally, the drain system is designed to avoid flashing upstream of the control valve. This has been accomplished by maintaining sufficient static head up to the control valve to suppress flashing [8]. This proved to be a limitation and some drain systems are designed for flashing mixtures.

Process

Power plant drain systems may generally operate under conditions of saturated or slightly subcooled liquid, which has a flashing potential. To maintain a flow in the drain system between the upstream heater and the downstream vessel, the pressure relationship should be satisfied as follows:

$$P_u + \rho H - \Delta p = P_b \tag{1}$$

(ρH may be negligible, e.g., drains to deaerator).

For single-phase liquid flow the differential pressure between pipe end critical pressure and back pressure is usually negligible [8].

The static head should be satisfied to avoid two-phase flashing flow before the control valve assuming that heat losses are negligible, then

$$H \geq \frac{1}{\rho}\left(\Delta P_u - (P_u - P_s)\right) \tag{2}$$

If the drain system is handling saturated liquid, then

$$P_u = P_s$$

and

$$H \geq \frac{\Delta P_u}{\rho} \tag{3}$$

If the liquid is subcooled, then

$$\Delta P_u > P_u - P_s \tag{4}$$

and system A is above system B (see Fig. 1), or

$$\Delta P_u < P_u - P_s \tag{5}$$

and system B is above system A.

If the heaters are at the same elevation, the drain line should still contain the control valve loop as the upstream heater is usually operated at a higher pressure.

Darcy's equation gives the friction loss

$$\Delta P_f = \frac{3.36 \times 10^{-6} \times f \times L \times W^2}{\rho d^5} \tag{6}$$

The elevation changes are given by

$$\Delta P_h = \frac{\rho H}{144} \tag{7}$$

The velocity head is accounted for with respect to the velocity at previous section

$$\Delta P_v = \frac{(V^2 - V_L^2)^{\rho}}{144 \times 64.4} \tag{8}$$

If the fluid entering the control valve is saturated liquid,

[1]Currently at Procter & Gamble, Geneva, Switzerland

Contributed by the Power Division for publication in the JOURNAL OF ENGINEERING FOR GAS TURBINES AND POWER. Manuscript received by the Power Division 1983.

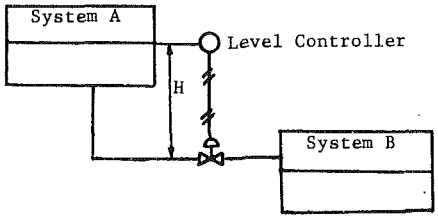

Fig. 1 Typical drain system

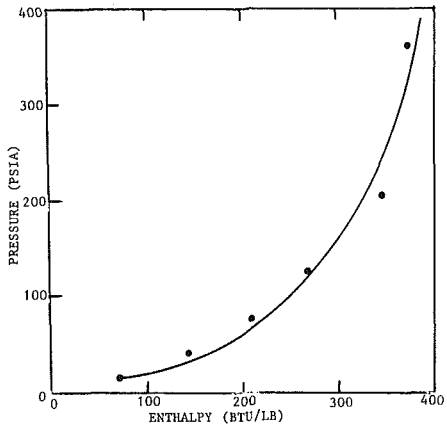

Fig. 2 Pressure-enthalpy plot of feedwater heater shell pressure and enthalpy of the feedwater heater drain

then sonic flow exists downstream of the valve orifice; the presence of the liquid phase shifts the sonic point downstream. The critical pressure ratio is defined by

$$r_c = \frac{P_c}{P_s} \tag{9}$$

The maximum allowable pressure drop that is effective in producing flow is not necessarily the maximum ΔP that may be handled by the valve. The maximum allowable differential pressure for sizing purposes is then given by [6]

$$\Delta P = K_m(P_i - r_c P_{iv}) \tag{10}$$

K_m is determined from empirical tests for liquid flow, and it is a function of the physical geometry of the valve.

After ΔP is determined, then it is used in the liquid sizing equation (6)

$$W = C_v\left(\frac{\Delta P}{G}\right)^{1/2} \tag{11}$$

to determine the flowrate W or the valve sizing coefficient C_v. Equation (11) may be used to calculate the body pressure drop at which significant cavitation can occur. It is recognized that minor cavitation may occur at a pressure drop slightly less than the one predicted by equation (11).

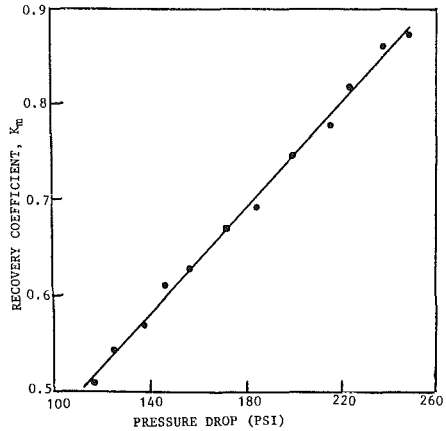

Fig. 3 A plot of the pressure drop across the valve against the recovery coefficient; single-ported, multiple-seat globe control valve

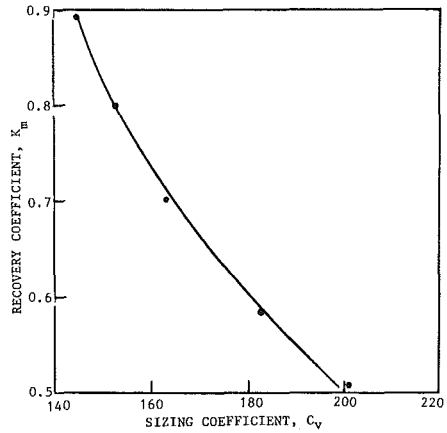

Fig. 4 The variation of the recovery coefficient with the valve sizing coefficient; single-ported multiple-seat globe control valve

Results

Forty-six drain lines were individually analyzed. Single ported with multiple seats globe control valves were used. The feedwater heaters had an integral drain cooler for the purpose of reducing the flashing potential. Figure 2 is a pressure-enthalpy plot of feedwater heater shell pressure against enthalpy of the feedwater heater drain.

The differential pressure across the valve correlated well with the valve recovery coefficient (see Fig. 3). Figure 4 is a plot of the recovery coefficient against the sizing coefficient. The flow upstream of the valves was single-phase liquid over the range of data. Some flashing occurred downstream of the valve. This was accepted and not considered crucial as flashing upstream was completely suppressed and served the purpose of design.

Nomenclature

C_v = sizing coefficient
d = inside diameter
f = friction factor
G = specific gravity
H = static head
K_m = recovery coefficient
L = length
M = Mach number $= \dfrac{V}{V_s}$
P = pressure
P_{iv} = vapor pressure of liquid at body inlet
r = pressure ratio
Re = Reynolds number $= \dfrac{\rho dV}{\mu}$
V = fluid velocity
V_s = speed of sound in the fluid
W = mass flowrate
Δ = differential
ϵ = absolute roughness
ρ = fluid density
μ = fluid viscosity

Subscripts

b = back
c = critical
f = friction
h = elevation
i = inlet
L = section
s = saturated
u = upstream
v = velocity
v = vapor

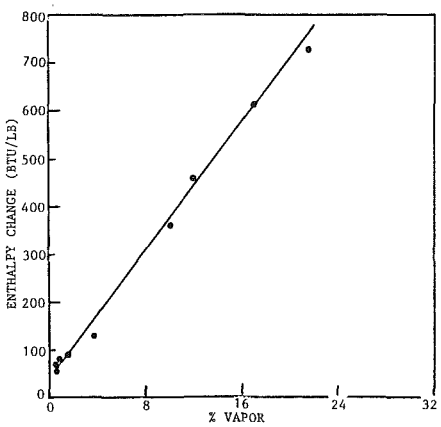

Fig. 5 A plot of the percentage of vapor downstream of the control valve against enthalpy change

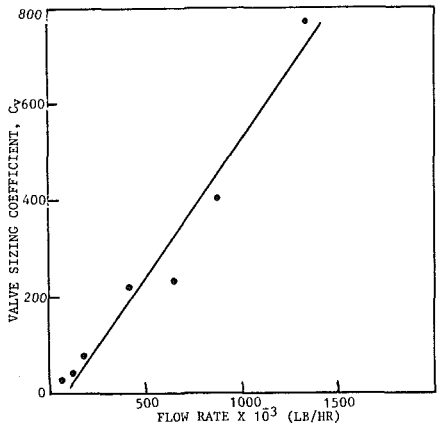

Fig. 6 Valve sizing coefficient against flow rate; single-ported, multiple-seat globe control valve

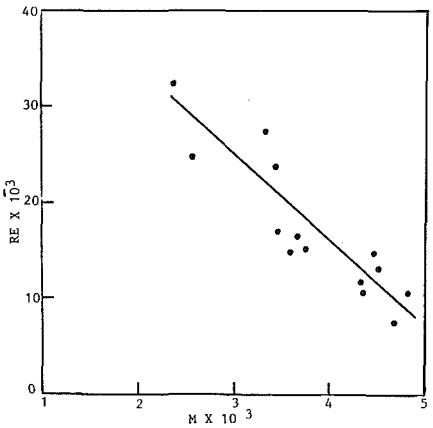

Fig. 7 A plot of Reynolds number against Mach number; single phase flow

Figure 5 is a plot of the percentage of vapor downstream of the control valve line against the existing enthalpy change of the drain system. A direct linear relationship is established over the range of data gathered.

Table 1 SI units conversion

Quantity	Multiply by	SI (metric)
Pressure, psia	703.1	kg/m^2
Enthalpy, Btu/lb	2326	J/kg
Flowrate, lb/hr	0.454	kg/hr

The valve sizing coefficients showed a direct proportionality to flowrate as predicted by equation (11) (see Fig. 6).

The Reynolds and Mach numbers were evaluated for the purpose of determining the kind of flow existing and relevent turbulence. Figure 7 shows a plot of Re against M. The data showed some scatter as the flow showed dependence on the variations in viscosity and density of the fluid. The scatter is attributed to geometry, pressure drop, and two-phase variations which affect the thermodynamic equilibrium of the system.

Discussion

The sizing criterion for a drain line carrying a flashing flow downstream of the control valve is to maintain the pressure at the control valve outlet less than the pressure at the valve orifice, in order that the mixture flow will not limit the flow through the control valve. Therefore, the control valve will have full control of the flowrate of the drain system.

The procedure used to size control valves for liquid service should consider the possibility of cavitation and flashing since they can limit the capacity and produce physical damage to the valve.

Data were obtained from the results of a computer analysis. The program used upstream heater conditions; upstream heater pressure, pressure drop to heater outlet, and temperature at heater outlet to find the saturation pressure and water data (specific gravity and viscosity). The geometric configuration of the upstream line was analyzed to account for the fittings in the pressure drop calculation. Downstream conditions and line configuration were also used.

Conclusion

Over the range of data, the design criteria for power plant drain systems have been established. Single-phase flow in the upstream cascade of the control valve in the drain line should be common practice while two-phase flashing downstream is acceptable. The sizing coefficient of the control valve and the prevention of flashing in the drain system are greatly dependent on the flowrate and cascade layout.

References

1 "Recommended Practices for the Prevention of Water Damage to Steam Turbines Used for Electric Power Generation," No. TWDP5-1, ASME Turbine Water Damage Prevention Committee, July 1972.

2 Benjamin, M. W., and Miller, J. G., *Trans. ASME*, Oct. 1942, pp. 657–669.

3 Crane Co., "Flow of Fluids," Technical Paper No. 410, 20th printing, 1981.

4 Driskell, L., "Control Valve Sizing with ISA Formulas," *Instrumentation Technology*, July 1974.

5 Fauske, H., "Critical 2-Phase, Steam-Water Flows," *Proc. Heat Transfer and Fluid Mechanics Institute*, Stanford University Press, 1961.

6 *Sizing and Selection Data*, Catalog 10, Fisher Controls, IA, 1974.

7 Isbin, H. S., et al., *J. AIChE*, Vol. 3, No. 2, Sept. 1957, pp. 361–365.

8 Liao, G. S., and Larson, J. K., ASME Winter Annual Meeting, New York, Dec. 1976.

9 Liao, G. S., ASME Winter Annual Meeting, Houston, TX, Nov. 1975.

C. M. Harman
Professor of Mechanical Engineering.
Duke University,
Durham, NC

S. Loesch
Simulation Software Engineer.
Dynalantic, Inc.,
Farmingdale, NY

Energy Storage Using Low-Pressure Feedwater

A method for increasing the peak output of steam power plants through use of a low-pressure feedwater storage system is presented. The generalized availability analysis involves only the low-pressure turbine, low-pressure feedwater heaters, and the storage system. With daily cycling and storage charging at near base load conditions, the turnaround efficiency of the energy storage system was found to approach 100 percent. Storage system turnaround efficiency is decreased when the energy is stored during plant part-load operation.

Introduction

Storage of heated feedwater to help meet peak load demands at power plants is a concept which has received considerable attention in the past few years. A comprehensive study project reviewed over 40 concepts for thermal energy storage [1]. The more promising of these concepts were examined in detail and it was concluded that none had the performance and costs to justify its adoption [2]. This conclusion was in large part due to the costs associated with storing large quantities of water at high pressure. The system considered here involves storing relatively less water at lower pressures and, therefore, at much lower cost. Storage of lower pressure and hence lower temperature feedwater does not allow as great an increase in the peak turbine output power as the high-temperature and pressure system concepts. However, only a few percent increase in the output of a large station is a significant amount of power.

The system analyzed in this study includes only the feedwater heaters on the low-pressure side of the boiler feed pump. In typical power plant practice, these heaters would be fed by extraction steam from the low-pressure turbine. The turbine, feedwater heaters, and storage unit of the system are each identified in the steam flow schematic diagram for a typical power plant shown in Fig. 1. This diagram also indicates how the system operates. When the storage system is being charged, water from the cold storage flows through the heaters into the hot storage. This flow is in addition to the system feedwater flow and causes an increase in the extraction steam flow to the heaters involved. This reduces the fraction of steam flow through the lower turbine stages and therefore reduces the output of the low-pressure turbine. During the peaking operation, the stored hot water flows to the boiler feed pump and the condensate flows into cold storage. The turbine output is increased since the extraction steam flow to the low-pressure heaters is eliminated. The system may also operate during peaking with partial flow from storage and the remainder through the heaters. This would increase power less, but would permit a longer period of operation for a given amount of stored hot water. The expected increase in the peak output of a typical power plant would be about 2.5 percent with 1/2 of the feedwater flow from hot storage.

A significant parameter for any energy storage system is the turnaround efficiency, which is defined as the ratio of the energy output from storage to the energy input to storage. Since the energy form of concern in a power plant is work, turnaround efficiency will be restricted to the ratio of loss of plant work during storage (work into storage) to increase in plant work during discharge (work out of storage). The analysis which follows provides a general method for predicting the turnaround efficiency of the low-pressure feedwater storage system. The operating variables investigated include storage charging and discharging rates, the effect of part-load plant operation during charging, and the effect of storage system operation on the low-pressure turbine leaving loss.

Analysis

Since work is the energy form of interest, this analysis makes extensive use of the steady-state thermodynamic availability property, defined as

$$a = h - T_0 s \tag{1}$$

Thermodynamic effectiveness, which is a ratio of work-related terms, is also basic to the analysis and is defined for the turbine as the ratio of output power to the net availability flowing into the turbine. For part-load operation this definition may be written:

$$\epsilon_{t,f} = P_f / A_{n,f} \tag{2}$$

The net availability flow into the turbine may be written in terms of the availability flow in the various streams. Equation (2) upon substitution and rearrangement takes the form

$$P_f = \epsilon_{t,f}\left(A_{i,f} - \sum_{k=1}^{n} A_{k,f}\right) \tag{3}$$

In this analysis the thermodynamic sink temperature is selected as equal to the temperature of the condensing steam, which is rational if only the steam cycle is considered. The result of this selection is that the availability flow from the

Contributed by the Power Division for publication in the JOURNAL OF ENGINEERING FOR GAS TURBINES AND POWER. Manuscript received by the Power Division December 1982.

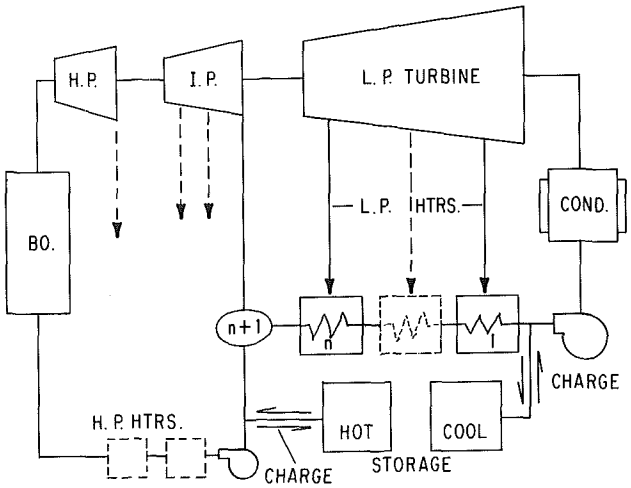

Fig. 1 Power plant schematic diagram illustrating the low-pressure feedwater storage system

turbine to the condenser is negligible. Therefore it is not accounted for in equation (3).

The increased extraction steam flow during charging of the storage system causes a decrease in the steam flow at the low-pressure turbine exhaust. This change in exhaust flow causes a change in the thermodynamic effectiveness of the low-pressure turbine. When this change is accounted for, equation (3) becomes

$$P_c = (\epsilon_{t,f} + \Delta\epsilon_{t,c})\left(A_{j,f} - \sum_{k=1}^{n} A_{k,c}\right) \tag{4}$$

The loss in output of the low-pressure turbine due to charging the storage system is obtained by subtracting the power during charging from the ordinary part-load power. Equation (4) minus equation (3) gives

$$\Delta P_c = P_f - P_c = \epsilon_{t,f}\left[(A_{j,f} - A_{j,c}) - \sum_{k=1}^{n}(A_{k,f} - A_{k,c})\right] - \Delta\epsilon_{t,c}A_{n,c} \tag{5}$$

For low-pressure feedwater storage, thermal charging does not affect steam flows from the intermediate turbine exhaust or to the boiler feed pump (for a fixed plant heat input) so

$$A_{j,f} = A_{j,c} \tag{6}$$

Combining equations (5) and (6) yields

$$\Delta P_c = \epsilon_{t,f}\sum_{k=1}^{n+1}(A_{k,c} - A_{k,f}) - \Delta\epsilon_{t,c}A_{n,c} \tag{7}$$

Applying the definition of thermodynamic effectiveness to the low-pressure heater system as part load results in

$$\epsilon_{h,f} = \frac{A_{p,f}}{\sum_{k=1}^{n+1} A_{k,f}} \tag{8}$$

Neglecting the small effect of feedwater storage on feedwater heater thermodynamic effectiveness and noting that operation of the charging system does not affect the availability flow of the feedwater into and out of the system, the low-pressure heater system thermodynamic effectiveness during charging is written as

$$\epsilon_{h,f} = \frac{A_{p,f} + m_c a_c}{\sum_{k=1}^{n+1} A_{k,c}} \tag{9}$$

An expression for the availability flow into storage obtained by subtracting equation (8) from equation (9) is

$$m_c a_c = \epsilon_{h,f}\sum_{k=1}^{n+1}(A_{k,c} - A_{k,f}) \tag{10}$$

Finally, an expression for the change in turbine output due to charging the storage system is developed by combining equations (7) and (10)

$$\frac{\Delta P_c}{m_c} = \frac{\epsilon_{t,f}}{\epsilon_{h,f}}a_c - \frac{\Delta\epsilon_{t,c}}{m_c}A_{n,c} \tag{11}$$

An expression for the change in turbine output during feedwater storage discharging may be developed in a manner similar to that just completed for charging. The result is

$$\frac{\Delta P_d}{m_d} = \frac{\epsilon_{t,0}}{\epsilon_{h,0}}a_d + \frac{\Delta\epsilon_{t,d}}{m_d}A_{n,d} \tag{12}$$

In equations (11) and (12), the first term on the right represents the change in power output due to the change in extraction steam flow to the low-pressure feedwater heater system. The second term on the right in these equations is a correction for the change in turbine effectiveness which results from the operation of the feedwater storage system.

A general expression for the turnaround efficiency of the feedwater storage system may be written

$$e = \frac{\Delta P_d t_d}{\Delta P_c t_c} \tag{13}$$

Turnaround efficiency is meaningful in performance evaluation only when a complete cycle is considered. Therefore, the total mass of water charged should equal the total mass discharged during a cycle used to evaluate turn-

Nomenclature

- a = specific thermodynamic availability
- A_i = thermodynamic availability flow into low-pressure turbine
- A_k = thermodynamic availability flow in steam to feedwater heater k of low-pressure feedwater heater systems
- A_n = net thermodynamic availability flow to low-pressure turbine
- A_p = thermodynamic availability flow from feedwater leaving the low-pressure feedwater system
- c = exhaust cross-sectional area, low-pressure turbine
- e = turnaround efficiency
- h = specific enthalpy
- m = mass flow rate
- n = number of feedwater heaters in the storage system
- P = power output, low-pressure turbine
- s = specific entropy
- t = time
- T_0 = temperature of thermodynamic sink
- V = velocity
- ϵ_h = thermodynamic effectiveness, low-pressure feedwater heaters
- ϵ_t = thermodynamic effectiveness, low-pressure turbines
- ρ = density

Subscripts

- c = charging storage system
- d = discharging storage system
- e = exit conditions from low-pressure turbines
- f = fractional or part-load operation
- 0 = design or base-load operation

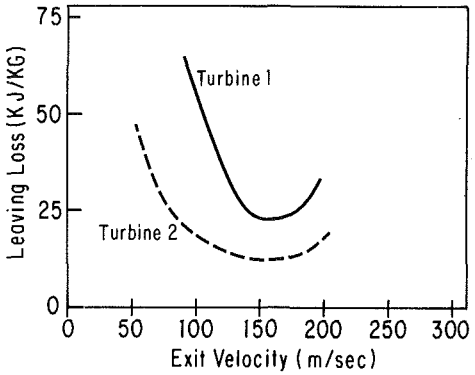

Fig. 2 Leaving loss characteristics of the example low-pressure turbines (Hausz et al. [1])

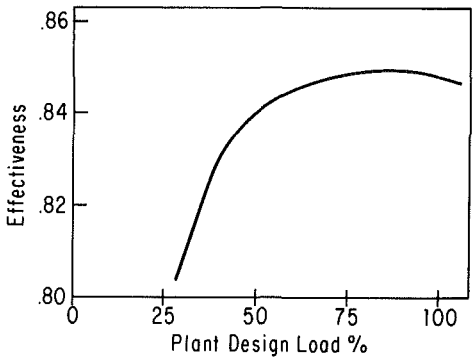

Fig. 3 Effect of part-load operation on low-pressure turbine thermodynamic effectiveness (Loesch [4])

around efficiency. This total mass is the product of the time required and the average flow rate during charging or discharging. It may be written

$$t_c m_c = t_d m_d \tag{14}$$

Substitution of equation (14) into equation (13) yields

$$e = \frac{\Delta P_d / m_d}{\Delta P_c / m_c} \tag{15}$$

which can readily be evaluated through substitution of values directly from equations (11) and (12).

Evaluation of Operational Parameters

The application of the preceding analysis requires information on the variation of performance with load for both the low-pressure turbine and the low-pressure feedwater heater system. Data of this type, taken from particular but typical equipment, will now be used to illustrate the procedure.

Information concerning the variation in the thermodynamic effectiveness of the low-pressure turbine with respect to design load may be used when it is available. Otherwise a simple approximation may be used. The variation in the thermodynamic effectiveness of the low-pressure turbine during plant operation has been found to be primarily dependent on the velocity of steam exiting the turbine according to Spencer [3]. The kinetic energy of this exhaust steam is referred to as the leaving loss. The effect of exit velocity on turbine leaving loss can be expected to vary considerably among particular installations. However, the relationship between the axial component of the exhaust velocity and leaving loss is shown in Fig. 2 for the two low-pressure turbines used as illustrative examples [2]. One of these turbines was presented as typifying nuclear power plant practice and is labeled Turbine 1; the other was presented as typifying fossil plant practice and is labeled Turbine 2 in this

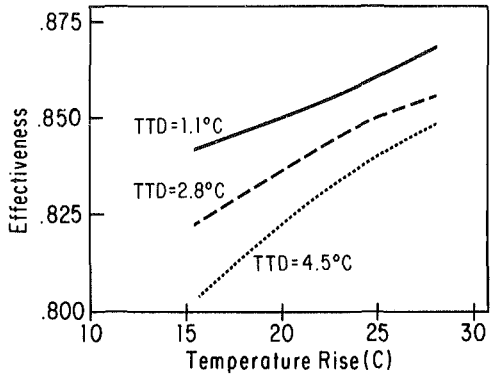

Fig. 4 Effect of the average low-pressure heater temperature rise on the thermodynamic effectiveness of the low-pressure heater system for various heater terminal temperature differences (TTD)

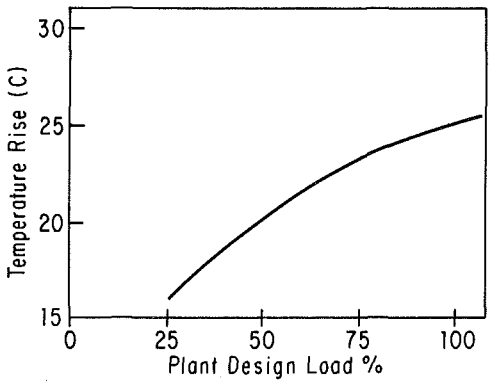

Fig. 5 Effect of storage system charging at part load on the average feedwater temperature rise in the low-pressure heaters

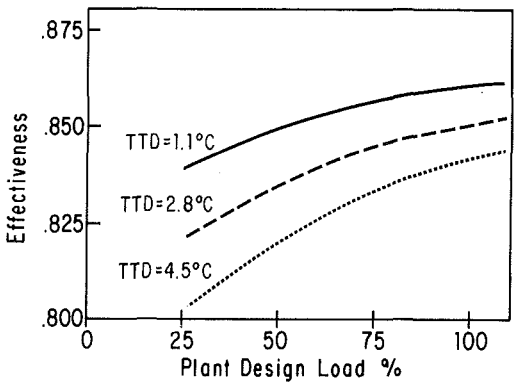

Fig. 6 Effect of storage system charging at part load on the low-pressure feedwater heat system thermodynamic effectiveness for various heater terminal temperature differences (TTD)

and subsequent figures. Since the axial velocity component of the exhaust steam is directly related to steam flow rate and plant load and since the leaving loss directly affects low-pressure turbine thermodynamic effectiveness, a relationship exists between the low-pressure turbine thermodynamic effectiveness and the plant load. An illustration of the variation of low-pressure turbine thermodynamic effectiveness with load [4] is shown in Fig. 3.

The thermodynamic effectiveness of the low-pressure feedwater heater system depends on the feedwater temperature rise and terminal temperature difference for each heater. The relationship beween heater system effectiveness and average feedwater temperature rise was calculated using mass and heat balances. The results of these calculations over the temperature range of interest are shown in Fig. 4. However, the average temperature rise in the feedwater

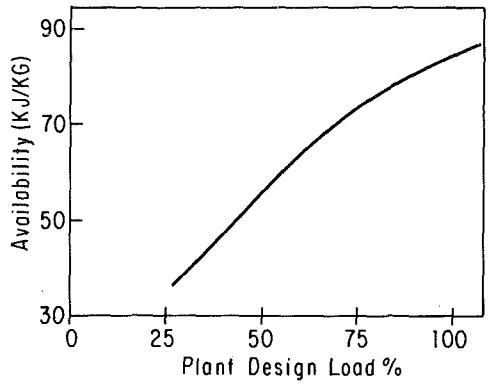

Fig. 7 Effect of storage system charging at part load on the thermodynamic availability of the stored feedwater

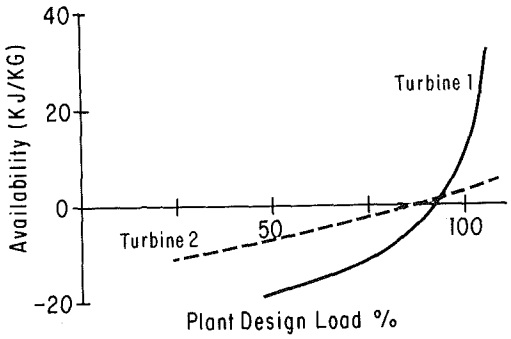

Fig. 8 Effect of storage system charging at part load on the availability of leaving losses

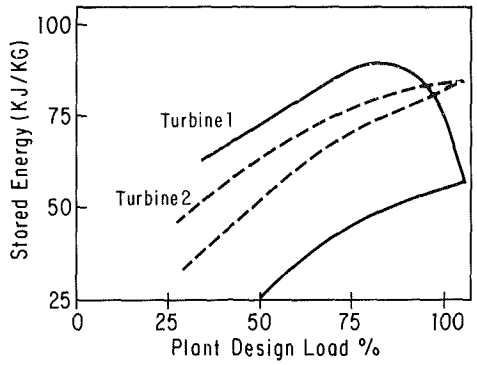

Fig. 9 Effect of storage system charging at part load on the incremental power of the low-pressure turbine

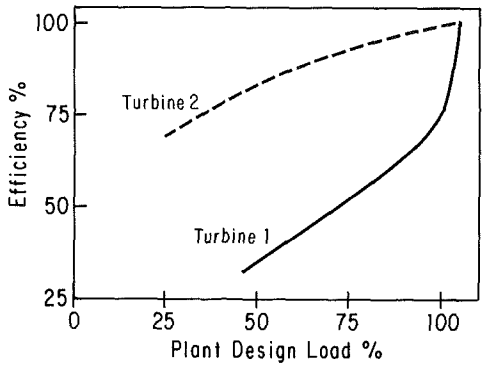

Fig. 10 Effect of storage system charging at part load on the turnaround efficiency of the low-pressure turbine

heaters decreases as the plant load decreases, due to lower extraction steam pressures. Figure 5 shows this relationship for the plant used in the example. The desired relationship between thermodynamic effectiveness of the low-pressure heater system and the plant load, as shown in Fig. 6, is obtained by combining the results of Figs. 4 and 5.

The lower extraction steam pressures associated with part-load operation imply a lower temperature for the feedwater stored at part-load conditions. The stored feedwater is at a thermodynamic state close to saturation. Since the specific availability of saturated water depends closely on temperature alone and since the temperature of the stored feedwater depends on the plant load, the availability of the water stored can be determined as a function of plant load. The availability of the feedwater at part-load conditions was calculated using equation (1) with the properties determined from part-load extraction temperature and heater performance data of the example plant used. The results are shown in Fig. 7. A heat transfer analysis shows that the water in storage loses only a negligibly small amount of availability during storage if daily cycling and moderate storage tank insulation are used [4]. The availability curve of Fig. 7 therefore indicates the feedwater availability during discharge also.

The change in the thermodynamic effectiveness of the low-pressure turbine during storage operation depends directly on the change in leaving loss and is given by

$$\Delta\epsilon_l = -\frac{m_e \Delta h_e}{A_n} \tag{16}$$

The change in the leaving loss can be expressed as the product of the change in exhaust velocity and the slope of the leaving loss curve. This is written as

$$\Delta h_e = \left(\frac{\Delta h_e}{\Delta V}\right)\Delta V \tag{17}$$

The exhaust flow is related to the exhaust velocity by

$$m_e = \rho c V \tag{18}$$

where ρ and c are constants. Also

$$\Delta m_e = -\Sigma \Delta m_k \tag{19}$$

Equations (16)–(19) are combined to yield for charging and discharging, respectively

$$\frac{A_{n,c}\Delta\epsilon_c}{m_c} = \frac{-V\left(\frac{\Delta h_e}{\Delta v}\right)\Delta m_{e,c}}{m_c} = \frac{V\left(\frac{\Delta h_e}{\Delta V}\right)\Delta m_{k,c}}{m_c} \tag{20}$$

$$\frac{A_{n,d}\Delta\epsilon_d}{m_d} = \frac{-V\left(\frac{\Delta h_e}{\Delta v}\right)\Delta m_{e,d}}{m_d} = \frac{V\left(\frac{\Delta h_e}{\Delta V}\right)\sum_{k=1}^{n}\Delta m_{k,d}}{m_d} \tag{21}$$

The expressions in equations (20) and (21) may be evaluated using low-pressure turbine data. V and $\Delta h_e/\Delta V$ can be read directly from the low-pressure turbine leaving loss curve and the ratio of the total change in extraction steam flow to the mass charging or discharging flow can be computed for a plant from simple mass and heat balances on the low-pressure heater system. Equations (20) and (21) have been evaluated using the leaving loss curves of Fig. 2 and the results are shown in Fig. 8.

Results and Summary

The values of the parameters ϵ_t, ϵ_h, a_c, and $\Delta\epsilon_{t,d}A_{n,d}/m_d$ are dependent on specific turbine and low-pressure heater characteristics. Significant differences occur in these characteristics among plants operating at the design condition and significant variation occurs for a specific plant over its

operating load range. These variations were illustrated in Figs. 3, 6, 7, and 8 by the nuclear turbine, conventional turbine, and low-pressure feedwater heater system selected. The results illustrated in these figures were used to provide the independent variables for equations (11), (12), and (15). These equations were then solved and the results summarized in Figs. 9 and 10. The analysis is general but the results are specific to the plant elements used for illustration.

When the low-pressure feedwater storage system is used to increase the maximum output of a plant, the results of this analysis show that the turnaround efficiency depends on the plant load during storage charging. Significantly, the turnaround efficiency approaches 100 percent when the storage charging is done at base load, as shown in Fig. 10. This is a considerable advantage compared with virtually any other energy storage system for power plants. The total energy stored is also greatest for a given size storage system when storage charging is done at base load. These two important factors favor charging the system when it is operating at nearly the base load or design condition.

The turnaround efficiency is reduced when storage charging is done at part load as shown in Fig. 10 and the total amount of stored energy is also decreased, as shown in Fig. 9. Charging under these conditions might be attractive, however, as an aid in reducing plant cycling and consequent problems. As an aside, charging the storage system at near base load and discharging at part load might seem to be an attractive option. The stored energy would have been produced under more efficient operating conditions than the part-load conditions prevailing at the time of discharge. However, this mode of operation increases the fluctuation in plant load, which in turn adversely affects plant reliability [5]. It also decreases the output and therefore the efficiency of the balance of the plant. This mode of operation of the storage system is felt to have little merit for these reasons.

Feedwater storage systems are less suited to plants where the turbine operates at high design exhaust velocity. These turbines are generally more sensitive to variation in exhaust flow in addition to having higher leaving losses. The increased sensitivity increases the dropoff of feedwater storage system turnaround efficiency at off-design load. Installations having turbine design exhaust velocities which approach the choked condition are essentially base-load limited. Feedwater storage systems are totally unsuited for these unusual installations.

Turnaround efficiency is virtually independent of the rate of storage charging and discharging. The storage charging rate is limited by feedwater flow rate through the heaters so at near base-load operation the feedwater storage rate would be relatively limited. Storage discharging at up to full feedwater flow would be possible and would provide the maximum peak power output from the storage system.

A case study was made of the economics of adding a low-pressure feedwater storage system at a selected nuclear power plant [6]. The maximum power increase the system could provide was calculated to be 41,600 kW or 6.9 percent of the low-pressure turbine output. Storage for 3 hr at this level was assumed. Cost estimates for shop-fabricated tanks 3 m in diameter and 30 m in length were obtained. The total cost including insulation and installation of the 57 tanks needed for the system was estimated at $3.84 million, making the capital cost about $92/kW. If the system is operated for 3 hr per day for 5 days per week and 11 months per year, a 20 percent fixed cost rate would yield a capital cost of $0.029/kWh. These cost figures are presented only to indicate a possible economic feasibility for the system. They are time and site specific and are based on extensive details and assumptions. The results, however, suggest that the system may be economically attractive in some situations.

References

1 Hausz, W., Berkowitz, B. J., and Hare, R. C., "Conceptual Design of Thermal Energy Storage Systems for Near-Term Electric Utility Application, Volume 1: Screening of Concepts," EPRI EM-1037, Apr. 1979.

2 Hall, E. W., et al., "Conceptual Design of Thermal Energy Storage Systems for Near-Term Electric Utility Applications," EPRI EM-1218, Nov. 1979.

3 Spencer, R. C., Cotton, K. C., and Cannon, C. N., "A Method for Predicting the Performance of Steam Turbine-Generators . . . 16,500 kW and Larger," ASME JOURNAL OF ENGINEERING FOR POWER, Vol. 85, No. 4, Oct. 1963, pp. 249-301.

4 Loesch, S. B., "An Availability Analysis for Predicting the Performance of Low Pressure Feedwater Storage Systems," M.S. thesis, Duke University, 1982.

5 Anson, D., "Availability of Fossil Fuel Fired Steam Power Plants," EPRI FP-422-SR, June 1977.

6 Mazzola, D. E., "Energy Storage in Low Pressure Feedwater," Duke University, unpublished work.

Steam Cycle Regeneration Influence on Combined Gas-Steam Power Plant Performance[1]

G. Cerri
Professor.
Assoc. Mem. ASME

A. Colagé
Engineer.

Dipartimento di Meccanica e Aeronautica,
Università degli Studi "La Sapienza",
Rome, Italy

The influence of steam cycle regeneration on combined plant performance has been analyzed from the thermodynamic point of view. A mathematical model has been developed and calculations have been performed according to a cycle analysis criterion. The higher the number of extractions the lower the relative efficiency gain. The influence of the intermediate feedwater temperatures is very small when these temperatures are slightly changed in relation to the equally spaced values. Results are given for a gas turbine firing temperature equal to 1000°C. They show a positive influence on combined cycle efficiency for small regeneration degrees. Gas turbine firing temperature in the range of 800-1400°C has been considered. The influence of the economizer inlet temperature lower limit is shown.

Introduction

To analyze thermodynamic regeneration of steam cycles used in combined gas steam plants a different approach is needed with respect to the traditional steam cycles. In the latter plants (owing to the boiler's air preheater) the exhaust gas stack temperature is independent of the regeneration degree.[2] Because of the relatively high temperature of the compressed air the combined gas steam cycle stack temperature depends on the status (i.e., pressure and temperature) of the feedwater at the waste heat boiler inlet.

To obtain the best compromise between combined cycle efficiency and specific work (related to the compressed air which takes part in the combustion), steam cycle parameters have to be varied with respect to nonregenerative steam cycles when thermodynamic regeneration is taken into account.

The aim of this paper is to analyze the influence of regeneration on combined cycle performance according to the previous analysis proposed in [1] where combined gas steam plants having steam cycles with one pressure level and without regeneration were dealt with. Thermodynamic analysis was carried out by means of some parameters which were recognized to be of interest in the study.

Cycle Analysis Criterion and Model Identification

The analysis is performed on combined gas steam plants shown in Fig. 1, the thermodynamic cycle of which is given in Fig. 2. Z extractions are considered in the bottomed steam cycle: The extracted steam masses condense in the respective heaters. The feedwater temperature is then increased from the condensation point up to the economizer inlet temperature: $T_{fw}(1)$. The mathematical model of the plants here considered

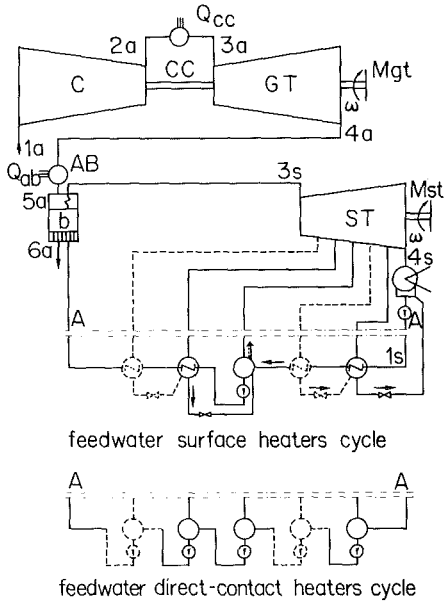

Fig. 1 Schematic flow diagram of a combined plant with regenerative feedwater cycle

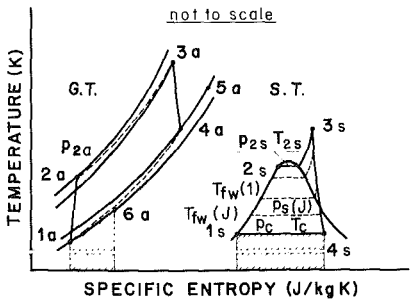

Fig. 2 Temperature entropy diagram of a combined cycle

[1]Financially supported by M.P.I. (Ministry of Education), Italy.

[2]According to [2], regeneration degree of (R) is defined as the ratio between the feedwater enthalpy rise due to regeneration and the feedwater enthaly difference between the boiler saturation and the condenser extraction pump outlet.

Contributed by the Power Division for publication in the JOURNAL OF ENGINEERING FOR GAS TURBINES AND POWER. Manuscript received by the Power Division November 1983.

was studied from a thermodynamic point of view and was given in the previous paper [1]. Variations and additions that this study deals with are:

- the waste heat boiler treatment
- the turbine expansion and regenerative heating of the feedwater

The waste boiler heat exchange, the diagram of which is given in Fig. 3, depends on the feedwater enthalpy

$$h_{fw}(1) = h_{co} + R\lambda \tag{1a}$$

or

$$h_{fw}(1) = (1-R)h_{co} + Rh_{2s} \tag{1b}$$

The energy conservation is expressed as:

$$\left(1+\frac{1}{\alpha}\right)C_{pa56}(T_{5a}-T_{6a})\eta_b = s[H_{3s}-h_{fw}(1)] \tag{2}$$

The pinch point temperature difference can be obtained by the energy balance of the economizer

$$\left(1+\frac{1}{\alpha}\right)C_{paec}(T_{aei}-T_{6a})\eta_b = s[h_{2s}-h_{fw}(1)] \tag{3}$$

and by the saturation steam temperature

$$T_{2s} = T(p_{2s}) \tag{4}$$

Finally the pinch point is

$$\Delta T_{pp} = T_{aeci} - T_{2s} \tag{5}$$

The feedwater inlet temperature in the economizer is

$$T_{fw}(1) = T\,[h_{fw}(1), p_{2s}] \tag{6}$$

and then the economizer inlet temperature difference is

$$\Delta T_{eci} = T_{6a} - T_{fw}(1) \tag{7}$$

Steam turbine expansion and thermal feedwater regeneration have been studied considering the elementary cell which describes the cycle between two successive extractions (Fig. 4). In this way the first and the last elementary cells have two fictitious heaters, both surfaces of which are equal to zero.

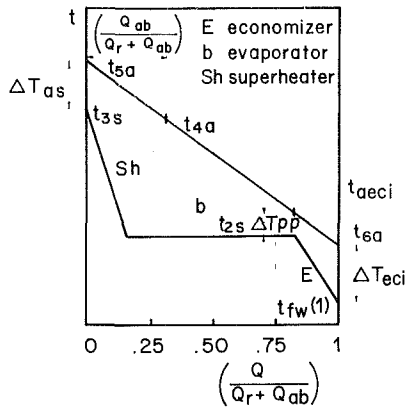

Fig. 3 Typical temperature-heat transfer diagram in the waste heat recovery boiler

Each elementary cell is known by means of an index (J) which specifies the downstream cell heat exchanger. Then $z+1$ cells have been considered.

For each elementary cell the pressure ratio is defined as

$$\beta_{st}(J) = p_s(J-1)/p_s(J) \tag{8}$$

where

$$p_s(0) = p_{3s} \tag{9}$$

and

$$p_s(z+1) = p_{co} \tag{10}$$

Polytropic efficiency can be expressed [3] as

$$\eta_{pst}(J) = \eta_{pds} = \text{const} \tag{11a}$$

in the superheated steam region and as

Nomenclature

C_p = specific heat at constant pressure, J/kg K
D = dryness steam fraction
e = excess of air in combustion
H, h = enthalpy, J/kg (steam and liquid)
J = index
m = mass, kg
p = pressure, Pa
Q = heat, J
q = ratio between the heat at the afterburner and the heat at the gas turbine combustion chamber
R = regeneration degree
S = entropy, J/kg K
s = stream air mass ratio
T, t = temperature, K, °C
W = work, J
W_0 = specific work, related to the compressed air, J/kg (air)
z = number of extractions
α = compressed air fuel ratio
α_{st} = stoichiometric air fuel ratio
β = gas turbine pressure ratio
Γ_i = net calorific power, J/kg
η_b = boiler efficiency: ratio between the heat absorbed by the water (steam) and the heat given up by the exhaust gas stream
η = efficiency
λ = enthalpy difference of the water between the boiler saturation and the condenser extraction pump outlet $\lambda = h_{2s} - h_{co}$
$\nu = R/C_p$ = ratio between the constant of the gas and the mean specific heat at constant pressure in the transformation
Δ = difference

Subscripts

a = air; exhaust gas
ad = adiabatic
b = combustion; boiler
ab = afterburning
c = compressor
co = condenser
d = drain
ds = dry steam
ec = economizer
e = extraction
es = extracted steam
ex = exhaust gas
fw = feedwater
gt = gas turbine
i = inlet
is = isentropic
m = mechanical
o = outlet
p = polytropic
pp = pinch point
s = steam
ss = saturated steam
st = steam turbine
1, 2, 3, . . . = initial and end points of thermodynamic transformations

Superscripts

h = thermodynamic limit
l = lower limit
t = technological limit
u = upper limit
$*$ = maximal

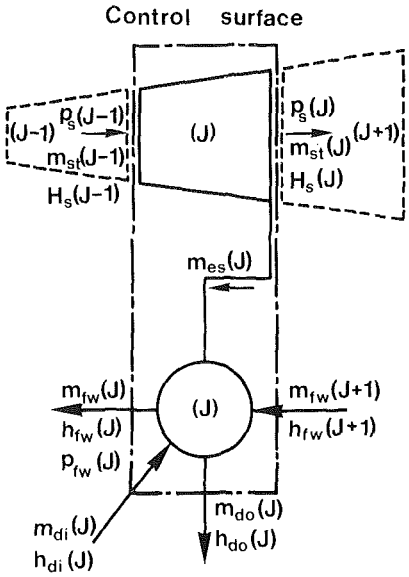

Fig. 4 Elementary steam cycle cell

$$\eta_{pst}(J) = \eta_{pds} - 1 + \frac{D(J-1) + D(J)}{2} \tag{11b}$$

in the wet steam region. When the expansion line crosses the saturation line $D(J-1)$ equals one.

Properly evaluating the isentropic expansion coefficient the cell's adiabatic efficiency is expressed as[3]

$$\eta_{adst}(J) = \eta[\beta_{st}(J), \eta_{pst}(J), p_s(J-1), T_s(J-1)] \tag{12}$$

The above relationships lead to the calculation of the steam expansion line points at the turbine extractions.[4] The work delivered by a steam turbine cell is:

$$W_s(J) = m_{st}(J-1)[H_s(J-1) - H_s(J)]\eta_m \tag{13}$$

Both surface and direct-contact regenerative heaters can be studied with two similar mathematical models (Fig. 5). The temperature differences at the inlet ($\Delta t_i(J)$) and at the outlet[5] ($\Delta t_o(J)$) are assumed to be known.

[3] The dependence of η_{adst} on $p_s(J-1)$ and $T(J-1)$ is connected with the isentropic expansion coefficient ν which depends on the status of the steam which expands in the cell.

[4] According to [1] the expansion end point enthalpy for each elementary cell can be evaluated using the isentropic end point expansion enthalpy

$$H_{sis}(J) = H[S_s(J-1), p_s(J)] \tag{14}$$

and then the actual end expansion point enthalpy is

$$H_s(J) = H_s(J-1) - [H_s(J-1) - H_{sis}(J)]\eta_{adst}(J) \tag{15}$$

Expansion line characteristic points can be then calculated once pressures $p_s(J)$ for $J = 0$ to $J = z + 1$ have been assigned; of course

$$H_s(0) = H_{3s} \tag{16}$$

[5] Surface regenerative heater condensed water leaving the exchanger is the sum of the extracted steam and water, drained from other heat exchangers, entering into it. Terminal temperature difference at the exit ($\Delta t_o(J)$), Fig. 5, may be $\neq 0$: Usually it is higher than zero; only in high-pressure regenerators it may be less than zero. Drains from other exchangers and the condensed water leave the direct-contact regenerator mixed with the feedwater. The outlet direct-contact heater temperature difference is equal to zero; the inlet temperature difference loses its meaning. Equations which express mass conservation and temperature inlet difference for surface heaters are

$$m_{fw}(J) = m_{fw}(J+1) \tag{17a}$$

$$\Sigma m_{di}(J) + m_{es}(J) = \Sigma m_{do}(J) \tag{18a}$$

$$T_{do}(J) = T_{fw}(J+1) + \Delta T_i(J) \tag{19}$$

Equations expressing the same things for direct-contact regenerators are

$$m_{fw}(J) = m_{fw}(J+1) + \Sigma m_{di}(J) + m_{es}(J) \tag{17b}$$

$$m_{do}(J) = 0 \tag{18b}$$

Since no drain leaves the heat exchanger, equation (19) loses its meaning.

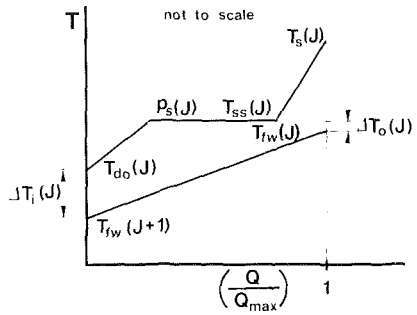

surface regenerator heat transfer diagram

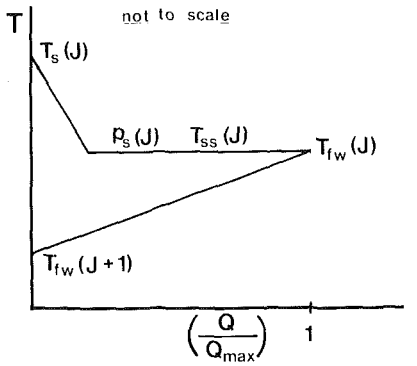

direct-contact regenerator heat transfer diagram

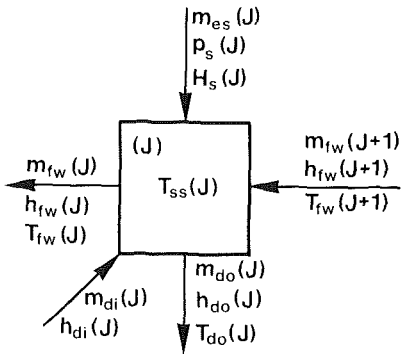

model Jth heater

Fig. 5 Typical surface and direct-contact regenerators heat transfer diagrams and model of a heater

The saturation temperature of the condensing extracted steam is

$$T_{ss}(J) = T_{fw}(J) + \Delta T_o(J) \tag{20}$$

and the extraction pressure is[6]

$$p_s(J) = p[T_{ss}(J)] \tag{21}$$

Knowing the feedwater enthalpy

$$h_{fw}(J) = h[T_{fw}(J), p_{fw}(J)] \tag{22}$$

The regenerators' energy balance is expressed by

$$m_{fw}(J)h_{fw}(J) = m_{fw}(J+1)h_{fw}(J+1) + \Sigma m_{di}(J)h_{di}(J) + m_{es}(J)H_s(J) - m_{do}(J)h_{do}(J) \tag{23}$$

Mass conservation and thermal conditions have to be considered.

[6] In the present study, pressure and heat losses have not been considered because they do not lead to any noteworthy statement.

The above equations can be written for each elementary cell.

Once the kind of regenerator (surface and direct-contact) is established in its relative position in the plant and once the terminal temperature differences are given, it is possible to calculate the thermodynamic configuration of the steam cycle, the extracted steam masses, and the work delivered by the steam as a function of

- number of extractions z
- regeneration degree R
- $z-1$ intermediate feedwater temperatures

$$\{T_{fw}(J)\}_{J=2-z}$$

The following conditions have to be satisfied

$$0 \le R \le 1 \tag{24}$$

$$T_{fw}(J+1) \le T_{fw}(J) \le T_{fw}(J-1) \text{ for } J=2-z\ (25^1)\ \ldots\ (25^{z-1})$$

$$\Delta T_{pp} \ge \Delta T_{pp}{}^{l} \tag{26}$$

$$T_{6a} \ge T_{6a}{}^{l} \tag{27}$$

$$T_{3s} \le T_{3s}{}^{u} \tag{28}$$

where $T_{3s}{}^{u}$ is the lower of $T_{3s}{}^{ul}$ (538°C) and $T_{5a} - \Delta T_{as}$.

A further condition has to be established concerning the terminal temperature difference at the inlet of the economizer

$$\Delta T_{eci} = T_{6a} - T_{fw}(1) \tag{29}$$

which has to be higher than a lower limit

$$\Delta T_{eci} \ge \Delta T_{eci}^{l} \tag{30}$$

It must be noticed that the value of ΔT_{eci}^{l} might be taken independently of the regeneration degree R (i.e., independently of $T_{fw}(1)$) but it seems to be a much too restrictive assumption. The heat exchanged by the exhaust gases should really be nearly independent, if possible, of the regeneration degree R; that means the surface of the boiler in relation to the compressed air does not depend on $T_{fw}(1)$. This is possible if ΔT_{eci}^{l} is taken as a decreasing function of R. If we define the minimal acceptable value ΔT_{eci}^{lo} for $R=0$ (this is an economical factor) the lower limit of such a terminal temperature difference can be written as

$$\Delta T_{eci}^{l} = \Delta T_{eci}^{lo} - R(\Delta T_{eci}^{lo} - \Delta T_{pp}^{l}) \tag{31}$$

In this way when R equals one, the economizer doesn't exist and ΔT_{eci}^{l} coincides with the pinch point lower limit, and when R equals zero ΔT_{eci}^{l} is equal to ΔT_{eci}^{lo}; both these values are connected with economic evaluations.

In conclusion, taking into consideration what has been written in [1] and the equations herein established, combined gas steam cycle efficiency and specific work can be calculated for each set of the following quantities

$$T_{3a},\ \beta,\ s,\ p_{2s},\ T_{3s},\ q,\ R,\ z,\ \{T_{fw}(J)\}_{J=2-z}$$

which satisfy the stated conditions.

It must be noticed that instead of the $z-1$ feedwater temperatures $\{T_{fw}(J)\}_{J=2-z}$, other quantities might be used, such as extraction steam pressures $\{p_s(J)\}_{J=2-z}$, or extracted steam masses $\{m_{es}(J)\}_{J=2-z}$, or any combination of them. Specifically $T_{fw}(1)$ or $p_s(1)$ or $m_{es}(1)$ can be used instead of R.

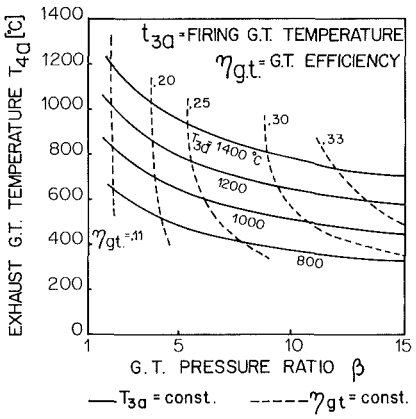

Fig. 6 Exhaust gas turbine temperature versus gas turbine pressure ratio for constant firing gas turbine temperature, and isoefficiency curves

Analysis of Results and Discussion

The thermodynamic model described in the previous section has been used to calculate combined gas steam cycle performance; a regenerative steam cycle has been considered.

Assumptions underlying the analysis are

p_{1a}	= 100. kPa	t_{1a}	= 15.°C
p_{co}	= 5. kPa	t_{co}	= 32.5°C
η_{pc}	= 0.89	η_{pgt}	= 0.87
η_{pds}	= 0.87	$\eta_{m,c,gt,st}$	= 0.98
$(p_{2a} - p_{3a})/p_{2a}$	= 0.03	ϵ_b	= 0.96
Γ_i	= 42700 kJ/kg	$p_{4a} - p_{1a}$	= 0.5 kPa
e^l	= 0.06	α_{st}	= 14.7
Δt_{as}^{l}	= 50°C	t_{3s}^{ul}	= 538°C
Δt_{pp}^{l}	= 30°C	S_{3s}^{l}	= 6.24 kJ/kg K ($D_{4s}^{l} \cong 0.70$)
Δt_{eci}^{lo}	= 50°C	t_{6a}^{l}	= 160°C

Steam turbine polytropic efficiency has been assumed to obtain a maximal adiabatic efficiency $\eta_{adst} = 0.88$.

Steam cycle pressure drops, thermal losses, and feedwater pumps have not been taken into account.

To simplify the analysis direct-contact heaters have been considered.

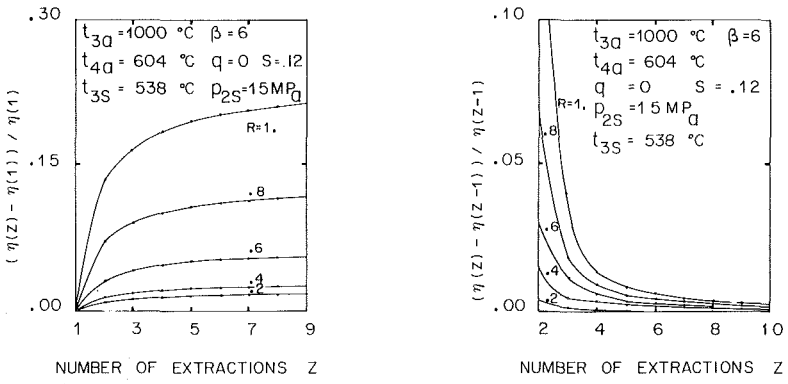

Fig. 7 Influence of number of extractions on efficiency

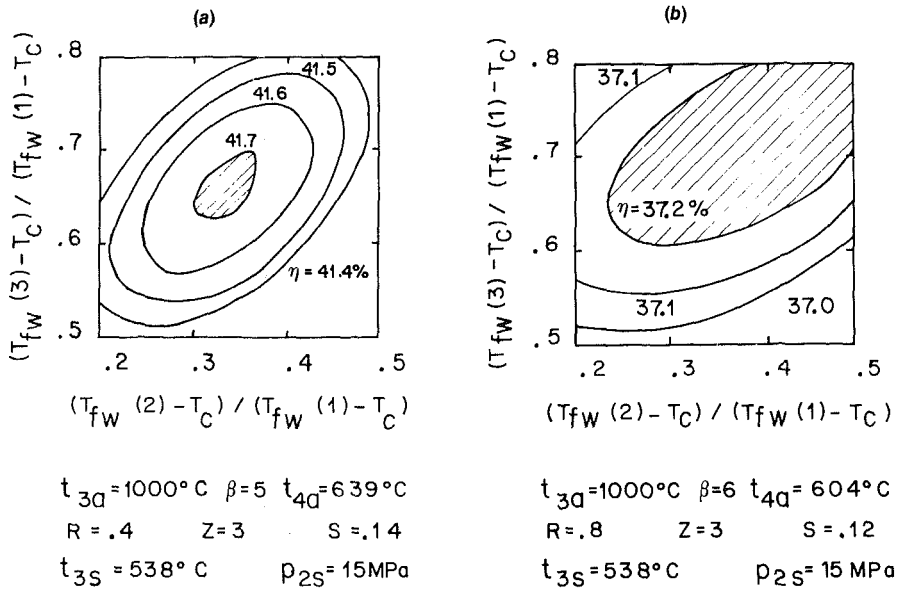

Fig. 8 Isoefficiency curves in the intermediate feedwater temperatures domain, z = 3: (a) R = 0.4; (b) R = 0.8

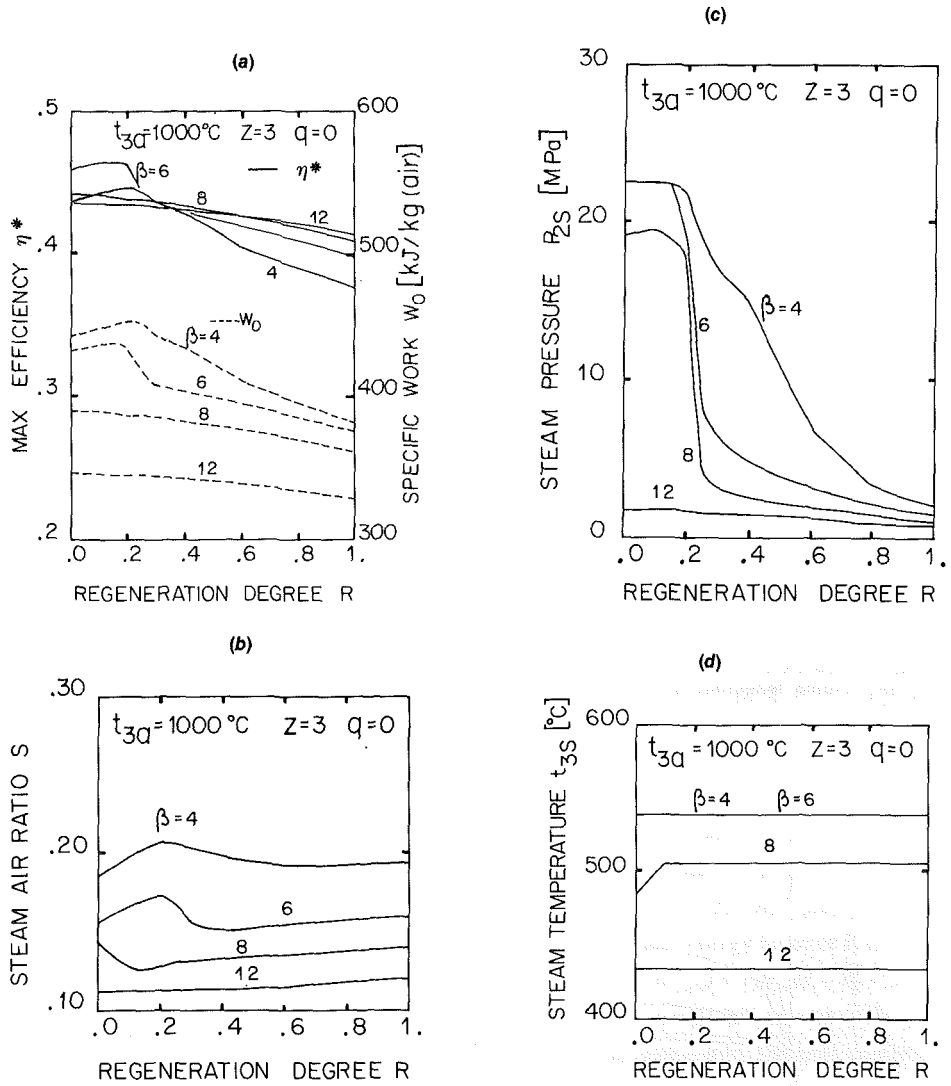

Fig. 9 Combined cycle performance versus regeneration degree: (a) maximal efficiency and specific work; (b) steam air mass ratio; (c) steam pressure; (d) steam temperature

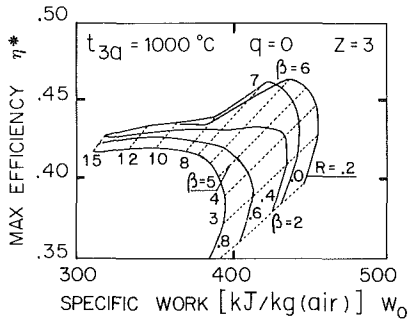

Fig. 10 Maximal efficiency versus specific work

Regeneration degree R, number of extractions z, and intermediate feedwater temperatures $T_{fw}(J)_{J=2-z}$ have been selected as independent quantities.

The relationship between the G.T. exhaust gas temperature, the G.T. firing temperature, and G.T. pressure ratio is shown in Fig. 6. In the same figure the G.T. isoefficiency curves are given too.

The relative influence of extraction number is shown in Fig. 7. Relative efficiency gain with respect to one extraction $[(\eta(z)-\eta(1))/\eta(1)]$ is given in Fig. 7(*a*) versus extraction number z. The efficiency gained by one more extraction $[(\eta(z)-\eta(z-1))/\eta(z-1)]$ versus z is shown in Fig. 7(*b*). The intermediate feedwater temperatures have been selected equally spaced between $T_{fw}(1)$ and T_{co}; therefore

$$T_{fw}(J)=T_{co}+(T_{fw}(1)-T_{co})(z-J+1)/z \text{ for } J=1-z \quad (32)$$

Curves of Fig. 7(*a*) and 7(*b*) are for constant regeneration

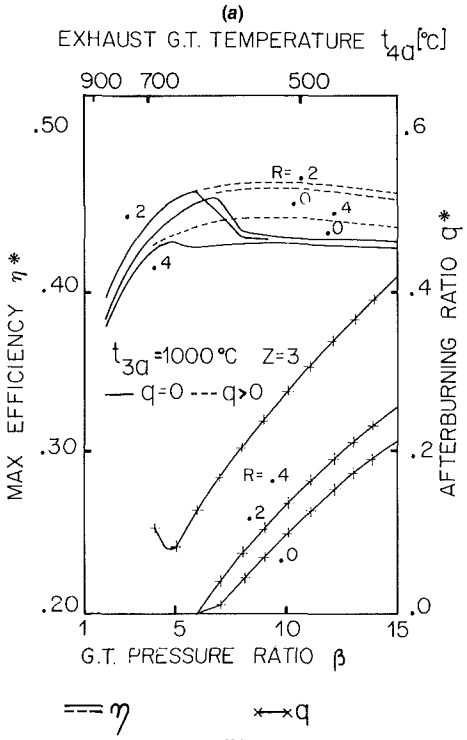

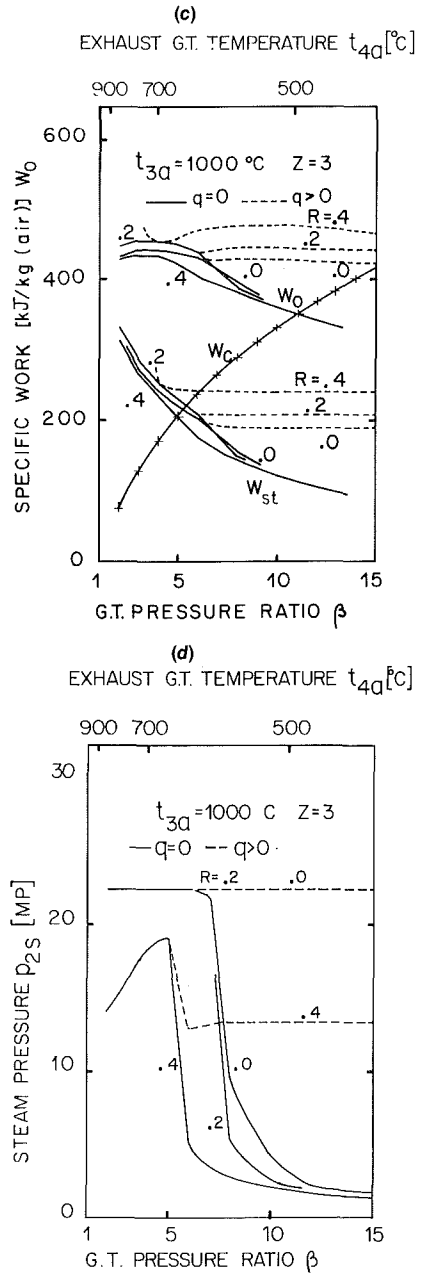

Fig. 11 Combined cycle performance versus gas turbine pressure ratio with and without fuel fired in the afterburner: (*a*) maximal efficiency and afterburning ratio; (*b*) steam air mass ratio; (*c*) overall specific work W_0, compressor work W_c, and steam work W_{st}; (*d*) steam pressure

degree R, and clearly show that by increasing the number of extractions over three the more negligible the rise in efficiency becomes chiefly for low regeneration degrees, $R<0.6$; consequently plants with three steam extractions have been presented.

Isoefficiency curves for $z=3$ are given in Fig. 8 where for abscissa and ordinate axes the difference between the second extraction and the condenser temperature as well as the difference between the third extraction and the condenser temperature are shown normalized by the feedwater regenerative total temperature increase. Curves are for $R=0.4$ and $R=0.8$; they show the maximal efficiency is reached in the region around the point (dashed region)

$$(T_{fw}(2)-T_{co})/(T_{fw}(1)-T_{co})=0.33$$
$$(T_{fw}(3)-T_{co})/(T_{fw}(1)-T_{co})=0.66$$

and the efficiency surface is quite flat.

Therefore the assumption that the intermediate feedwater temperatures are equally spaced between the condenser and the first extraction temperatures ($T_{fw}(1)$, depends on the steam pressure p_{2s} and on the regeneration degree R) is not far from the thermodynamic optimum conditions. Moreover this position is strengthened by technical reasons; turbine manufacturers can't provide extraction points at precisely the correct pressures for every steam cycle. Even if these manufacturers knew the correct extraction pressures, it would be nearly impossible to provide these exact pressures without, in many cases, compromising the design and perhaps the steam turbine efficiency.

The abovementioned assumption underlies the further analysis carried out in the present study.

The maximal efficiency η^* reached in the range of variability of the quantities s, p_{2s}, t_{3s}, versus the regeneration degree R is given in Fig. 9(a) which is for gas turbine firing temperature $T_{3a}=1000°C$, extraction number $z=3$, and without any afterburning fuel $q=0$; curves in Fig. 6 are for gas turbine pressure ratio $\beta=$ const (i.e., for constant exhaust gas turbine temperature). For the higher pressure ratios ($\beta=8$, 12) maximal efficiency η^* reaches its maximum when $R=0$. For the lower pressure ratios maximal efficiency η^* reaches its maximum when $R>0$ depending on the value of β. Specific work curves are also given in Fig. 9(a). Figures 9(b, c and d) show s, p_{2s} and T_{3s} corresponding to the curves of Fig. 9(a).

Maximal efficiency η^* rises, increasing the steam air mass ratio s (Fig. 9) when R assumes low values and the steam pressure is high

Maximal efficiency η^* versus specific work W_o is given in Fig. 10; curves are for constant regeneration degree R and for constant gas turbine exhaust temperature, which means a constant pressure ratio β. This figure clearly shows that when R is in the range 0. -0.2, efficiency can reach higher values with respect to that for $R=0$, only if gas turbine pressure ratios are in a proper range ($\beta<6.5$).

When fuel is fired in the afterburner ($q\neq 0$) thermodynamic regeneration influences combined cycle performance in a different way. Maximal efficiency η^* versus gas turbine pressure ratio is given in Fig. 11(a); curves are for constant regeneration degree ($R=$const); solid lines are for $q=0$ (without afterburning fuel), dashed lines are for $q\neq 0$. In this figure the afterburning rate (q^*) corresponding to η^* is given too. The maximal efficiency η^* is not, practically speaking, influenced by firing fuel in the afterburner when the pressure ratio assumes low values ($\beta<6$). This means high gas turbine exhaust temperatures, whatever the regeneration degree is. Maximal efficiency η^* is positively influenced by steam cycle regeneration degree, when R is in the range 0. -0.2 and for values of β higher than $6-7$ (for $T_{3a}=1000°C$). That means low exhaust gas turbine temperatures. This is due to the higher steam temperatures, steam pressures, and steam air

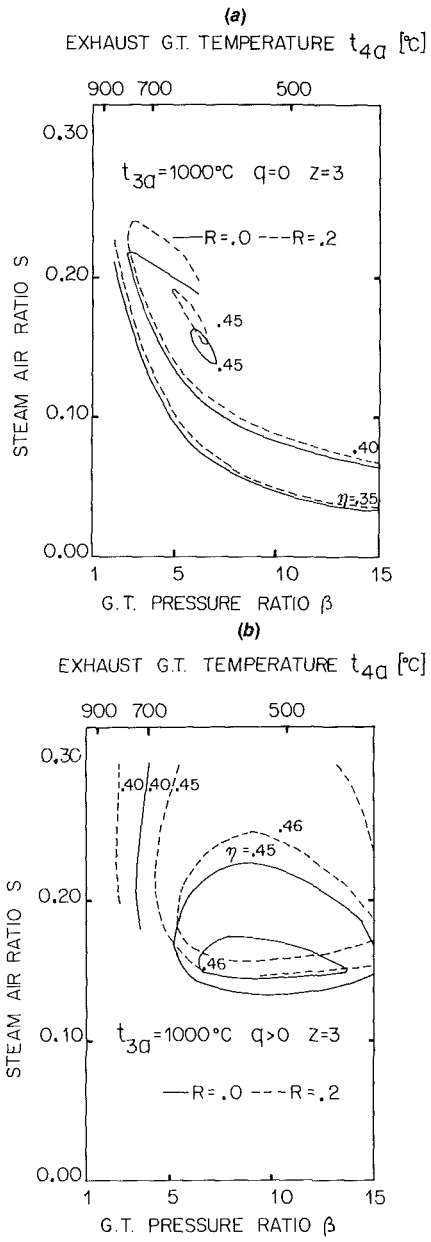

Fig. 12 Isoefficiency curves in the steam air mass ratio-gas turbine pressure ratio domain: (*a*) without extra fuel fired in the afterburner $q=0$; (*b*) with extra fuel $q\neq 0$

mass ratios which the afterburning fuel makes possible (Fig. 11). Specific work (W_o), steam turbine work (W_{st}), and compressor work (W_c) versus gas turbine pressure ratio are shown in Fig. 11(c). Values of β and R in which W_c is equal to W_{st} seem of interest for a particular arrangement of the plant.

Isoefficiency and isoregeneration-degree curves are given in Figs. 12 (a, b); on the abscissa and ordinate axes, steam air mass ratio and pressure ratio are respectively indicated. The curves in Fig. 12(a) are for $q=0$ (without afterburning rate) and those of Fig. 12(b) are for $q\neq 0$; they show the area in the curves is of a different extent whether q is equal to or different from zero.

It is worth noticing the curves for $R=0.2$ and $\eta=0.45$ and the position of the maximal values $\eta=0.46$ and $\eta=0.47$ for $q=0$ and $q\neq 0$, respectively.

Combined cycle efficiency depends on the economizer inlet temperature difference lower limit (ΔT_{ei}^{lo}); the influence of this parameter is shown in Fig. 13 where efficiency (η) versus ΔT_{ei}^{lo} is given for $T_{3a}=1000°C$; $\beta=5$; for $T_{4a}\simeq 600°C$, $q=0$ and $z=3$.

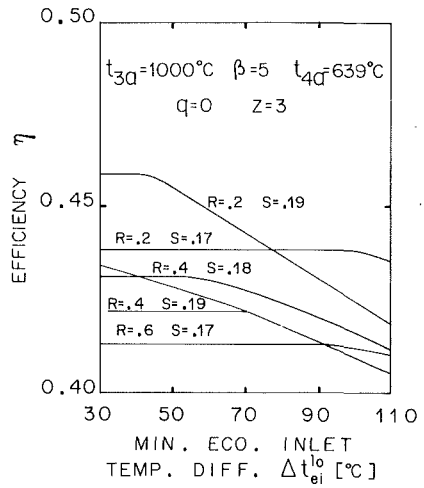

Fig. 13 Efficiency versus minimal economizer inlet temperature difference

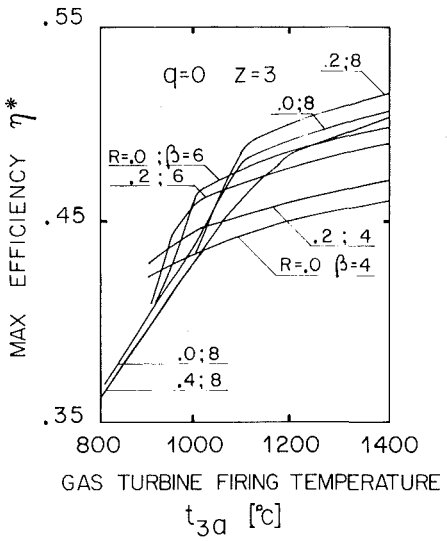

Fig. 14 Maximal combined cycle efficiency versus gas turbine firing temperature for both constant pressure ratio β and regeneration degree

Maximal efficiency η^*, for $q=0$, versus the gas turbine firing temperature (T_{3a}) is shown in Fig. 14 where curves are for $\beta=$ const and $R=$ const; the greater the gas turbine firing temperature the lower the slope of the curves.

Concluding Remarks

Steam cycle regeneration influences performance of combined plants; the analysis in the present study shows:

- The number of extractions raises the efficiency; the relative efficiency gain, making z extractions instead of $z-1$, becomes smaller and smaller by increasing z by one when z rises.
- Equally spaced feedwater temperatures represent a nearly optimal solution. The efficiency surface in the intermediate feedwater temperature domain is quite flat.
- Efficiency can rise for small β, high exhaust gas turbine temperature, and for small regeneration degree $R\simeq 0.2-0.3$ due to the possibility of reaching the maximal steam temperature and pressure and increasing steam air mass ratio. Specific work goes up too.
- Firing fuel in the afterburner makes the efficiency increase for high values of pressure ratio (i.e., low exhaust gas turbine temperatures); the regeneration degree causes an increase of efficiency only when R is small enough ($R<0.2-0.3$ for $T_{3a}=1000°C$).
- The higher the maximal gas turbine temperature is the higher the efficiency is for every value of R but the smaller the effect of its variation is. Whatever the gas turbine firing temperature T_{3a} is, efficiency rises only for low regeneration degrees $R\simeq 0.2-0.3$ depending on the exhaust gas turbine temperature, i.e., T_{3a} and β.
- The economizer inlet temperature difference influences the maximal combined cycle efficiency related to the gas turbine parameters and to the regeneration degree. For a given steam air mass ratio s, the higher the regeneration degree is the smaller is the ΔT_{ei}^{lo} range in which efficiency is practically independent.

Steam cycle thermodynamic regeneration in combined plants appears important because low regeneration degrees ($R\simeq 0.2-0.3$) make an efficiency increase possible whatever the gas turbine firing temperature is. It is interesting to note the possibility of having the steam turbine work equal to the compressor shaft work in the gas turbine pressure ratio range for which an increase of combined plant efficiency can be obtained by means of steam cycle regeneration.

References

1 Cerri, G., "Parametric Analysis of Combined Gas Steam Cycles," ASME Paper No. 82-GT-95.

2 Salysbury, J. K., "Steam Turbines and Their Cycles," Wiley, New York, 1950.

3 Kehlhofer, R., "Calcul du Comportament à Charge Partielle des Centrales Combineés à Turbines à Gaz et à Vapeur," *Revue Brown Boveri*, Vol. 10-78, pp. 672-679.

4 Priddy, A. P., and Sullivan J. J., "Engineering Considerations of Combined Cycles," *Combustion*, Mar. 1973, pp. 19-25.

5 Wunsch, A., "Centrales Combinées à Turbines à Gaz et à Vapeur. Situation Actuelle et Développements Futurs," *Rev. Brown Boveri*, Vol. 65, No. 10, Oct. 1978, pp. 646-655.

6 Pfenninger, H., "Combined Steam and Gas Turbine Power Stations," *Brown Boveri*, Paper No. CH-T 040013E.

7 Fraize, W. E., and Kinney, C., "Effects of Steam Injection on the Performance of Gas Turbine Power Cycles," ASME JOURNAL OF ENGINEERING FOR POWER, Vol. 101, Apr. 1979, pp. 217-227.

8 Tomlinson, L. O., and George, R. L., "Scelta di una Turbina a Gas e di un Ciclo a Vapore per il Massimo Rendimento di un Ciclo Combinato," Nuovo Pignone, Energia Totale dalle Turbine a Gas, Firenze, Nov. 6-7, 1981, pp. 1-9.

9 Sonneuschain, H., "A Modular Optimizing Calculation Method of Power Station Energy Balance and Plant Efficiency," ASME JOURNAL OF ENGINEERING FOR POWER, Vol. 104, Apr. 1982, pp. 255-259.

10 McClintock, R. B., and Silvestri, G. J., "Formulation and Iterative Procedures for the Calculation of Properties of Steam," ASME, 1968.

11 McClintock, R. B., and Silvestri, G. J., "Some Improved Steam Property Calculation Procedures," ASME JOURNAL OF ENGINEERING FOR POWER, Vol. 92, Apr. 1970, pp. 123-134.

S. J. Palaszewski
Bell Laboratories,
Whippany, NJ 07981
Assoc. Mem. ASME

S. Weinbaum
Professor.
Mem. ASME

L. M. Jiji
Professor.
Mem. ASME

Department of Mechanical Engineering,
The City College of the
City University of New York,
New York, NY 10031

Power Plant Spray Cooling: Design and Performance Studies

A new three-dimensional model for determining the flow and thermal characteristics of spray units is utilized in an effort to predict and improve the cooling efficiency of spray units. In a marked departure from present theories, which are based on the behavior of an average droplet in a uniform average environment, the model examines the local variation in properties of both the air and the droplets throughout the flow field encompassing the spray umbrella. Model predictions of droplet return temperature along the spray perimeter, downwind wet-bulb temperature, and downwind air-velocity were compared with field data on a commercial spray. Good agreement was observed. A parametric study was then performed to determine the optimum droplet size and discharge angle for a spray unit. It was found that substantial improvements in the cooling obtained for a given spray power input can be achieved over currently used floating spray units.

Introduction

During the past decade considerable interest has been generated in waste heat dissipation from power generation. Public pressure and concern have precipitated stringent state and federal laws regulating traditional once-through open-cycle cooling. Aside from those regulations, the difficulty of waste heat management is compounded by increasing needs for power and accelerating demands on water resources.

Recognizing these developments and trends, the power industry has intensified its activity in exploring alternate methods for waste heat dissipation. A closed-cycle approach which has received favorable attention is spray canal cooling. The spray system consists of floating modules each spraying a small percentage of the condenser discharge water into the air. Typically spray modules, each consisting of several spray units, are aligned parallel to the edge of a canal which can be up to several miles long. Spray systems are attractive from the standpoint of economy of construction and ease of maintenance.

The present work demonstrates that the theoretical model proposed herein can accurately predict the performance of a single spray unit, and can be utilized to optimize design. Since the new model identifies all parameters governing the performance of spray units, it allows one to systematically investigate new designs and carry out parametric studies for purposes of optimization.

Previous models for predicting the performance of spray units and modules [1-6] have been based on some average droplet in variously defined uniform average environments and have introduced semi-empirical interference factors to either describe the effect of the wind or the interaction between successive spray units. In marked contrast to these models, the theoretical model [7, 8] used for the present design and performance analysis examines the local variation in properties of both the air and the droplets throughout the flow field of the spray umbrella for any prescribed upwind velocity profile. Furthermore, the model does not require any empirical interference factors for the interaction of the spray with the wind or with other spray units. The only empirical factors required are the correlation equations for the local droplet heat and mass transfer coefficients and the turbulent mixing models for the air-vapor phase. An important objective of the present paper is to show how the basic mathematical model developed in [7, 8] can be utilized to perform parametric optimization studies on spray nozzle designs leading to significant improvements in spray cooling efficiency.

Model Description

The basic model described in detail in [7, 8] examines the local mass, momentum, and energy interaction between spray droplets and air-vapor elements. An air-vapor element is a finite volume of the gas phase that traverses the spray domain (Fig. 1). Separate conservation equations are written for both the individual droplets and air-vapor elements including a conservation equation for droplet number density along droplet trajectories. Air-vapor element streamlines and droplet trajectories are found by solving the differential momentum equations for each phase. These three-dimensional momentum equations consider the local buoyancy force, droplet drag, and turbulent diffusion of momentum. The magnitude of the local interaction between droplets and air-vapor elements is related to the number of droplets passing through each element as the element follows a streamline. The air-vapor conservation equations incorporate terms which arise from the presence of the droplets. These terms characterize the droplets as sources of mass, momentum, and energy to the air-vapor phase. Integrating the air-vapor equations along selected streamlines yields the

Contributed by the Power Division for publication in the JOURNAL OF ENGINEERING FOR GAS TURBINES AND POWER. Manuscript received by the Power Division December 1983.

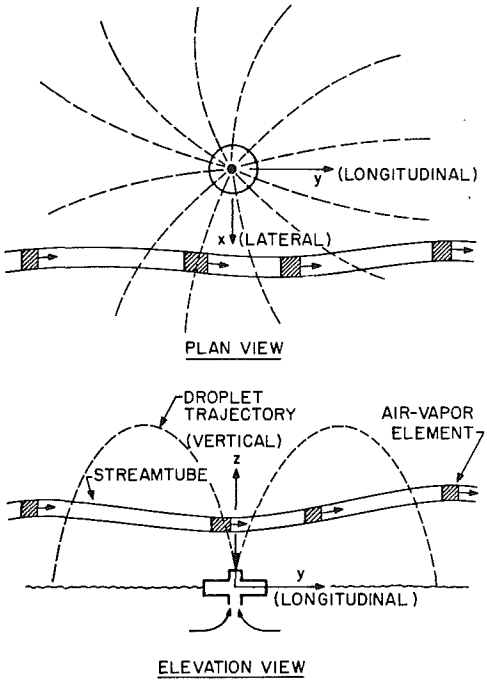

Fig. 1 Trajectory of a fluid element as it crosses the spray field

local conditions of air-vapor velocity, dry-bulb temperature, and absolute humidity. Droplet velocity, mass, and temperature along a trajectory are determined relative to the local air-vapor properties. Since the local conditions of the air-vapor continuum and of the droplets are all unknown initially, an iterative scheme is employed to obtain convergent solutions. A maximum of four iterations is required. A numerical Runge-Kutta technique is used to obtain solutions to the coupled set of two-phase conservation equations. Calculations are made for half of the symmetrical spray domain including eighteen droplet trajectories and two hundred air-vapor streamlines. Computation time per iteration is under 1 min on a high-speed computer such as the Cray-1.

The interference between successive downwind spray units [1, 3] is automatically determined by the present model from the computed exit air conditions of the single spray. The dry-bulb temperature, absolute humidity, and air velocity downwind of the first spray in a pass are the entrance conditions for the next spray, etc. The effects of interference between sprays and the modeling of an entire spray system will be the subject of a future paper.

Conservation Equations

Conservation of Mass for a Droplet. To determine the amount of evaporation that a droplet experiences during its time of flight, one relates the time rate of change of droplet mass to the evaporative flux across the concentration boundary layer of the droplet

$$dM/dt = -\rho_a h_D \pi d^2 [\omega_s(T_d) - \omega] \tag{1}$$

The mass transfer coefficient h_D is determined by an empirical correlation given by Ranz and Marshall [9]

$$h_D = (D/d)[2 + 0.6(\mathrm{Re})^{1/2}(\mathrm{Sc})^{1/3}] \tag{2}$$

Conservation of Droplet Momentum. Droplet velocities are determined by applying Newton's law for a particle. Consideration is taken of gravitational forces and the drag induced by the local vector-velocity difference between the droplet and the air-vapor continuum. The resulting equation is

$$M d\mathbf{v}/dt = M\mathbf{g} - (C_D \rho_a \pi d^2/8)|\mathbf{v} - \mathbf{u}|(\mathbf{v} - \mathbf{u}) \tag{3}$$

where [10]

$$C_D = 0.44 = \text{drag coefficient for Re} > 1000 \tag{4a}$$

$$C_D = (24/\mathrm{Re})(1 + 0.15\mathrm{Re}^{0.687}),\ \mathrm{Re} \le 1000 \tag{4b}$$

A droplet trajectory is found from

$$d\mathbf{s}_d/dt = \mathbf{v} \tag{5}$$

Conservation of Energy for a Droplet. Taking into consideration surface convection and evaporation, and neglecting temperature gradients within the droplet, the energy balance gives

Nomenclature

A = cross-sectional area of streamtube
B = Bowen ratio = ratio of convective to evaporative heat transfer = $C_{pa}(T_{d0} - T_{wb\infty})/[L_0(\omega_s(T_{d0}) - \omega_\infty)]$
C_D = drag coefficient
C_p = constant pressure specific heat
$C_p{}^*$ = specific heat ratio (air to droplet) = C_{pa}/C_{pd}
C_{psv} = specific heat ratio (air-vapor to water vapor) = C_{av}/C_{pv}
c = number characterizing the size of an air element
D = diffusion coefficient
d = droplet diameter
d_c = droplet diameter upon canal reentry
E_{ref} = reference theoretical power input to a spray unit
Fr = Froude number = $v_0^2/(gd_0)$
g = gravitational acceleration
g_c = dimensional constant = 1.0 kg-m/nt-s^2
Gr = Grashof number = ratio of buoyancy to viscous forces = $c^3\beta_T g d_0^3(T_{d0} - T_{wb\infty})/v_a^2$
H = velocity head of spray nozzle = $v_0^2/(2g)$
H_0 = surface heat flux
h = droplet heat transfer coefficient
h_D = droplet mass transfer coefficient
h_f = enthalpy of water at saturation temperature
i = enthalpy of air-vapor mixture
k = thermal conductivity
k' = von Karman's constant
K_m = turbulent viscosity of air
K_{wv} = turbulent thermal diffusivity of water vapor in air
L = latent heat of vaporization of water
L_{mo} = Monin-Obukhov length scale = $\dfrac{\rho_a C_{pa} T_{db} u_*^3}{k' g H_0}$
l = lateral dimension of streamtube
M = droplet mass
m = vertical dimension of streamtube
$\dot{m}_0$ = mass flow rate of a spray unit
$\dot{m}_e$ = evaporation rate from a spray unit
N = total number of trajectories
$\dot{n}_j$ = number of droplets ejected along a trajectory per unit time
NTU = number of transfer units
n = number of droplets in an air-vapor element
Po = Power ratio = ratio of theoretical spray power input to a reference power input = $[\dot{m}_0 v_0/(2g_c)]/E_{\mathrm{ref}}$

$$-MC_{pd}dT_d/dt = \pi d^2 h(T_d - T_{db}) + \pi d^2 \rho_a h_D[\omega_s(T_d) - \omega]L \quad (6)$$

The terms on the right-hand side of equation (6) are the energy given up by the droplet due to convection and evaporation, respectively.

The heat transfer coefficient h is obtained from an empirical correlation for a droplet given by Ranz and Marshall [9]

$$h = (k_a/d)[2 + 0.6(\mathrm{Re})^{1/2}(\mathrm{Pr})^{1/3}] \quad (7)$$

Water Vapor Continuity Equation. To determine the variation of absolute humidity along any air-vapor streamline in the spray field, species conservation along a streamline is required. Conservation of mass for the water vapor in a fluid element gives

$$\rho_a V d\omega/dt = \rho_a \pi d^2 n h_D[\omega_s(T_d) - \omega] + \rho_a V K_{wv} \partial^2 \omega/\partial z^2 \quad (8)$$

where $d\omega/dt$ is the total derivative following the fluid motion. The first term on the right-hand side of equation (8) represents the droplets as sources of water vapor to the air-vapor elements. The second term is the net efflux of water vapor across the boundaries of the element due to turbulent diffusion.

If an element is considered to have the shape of a rectangular parallelepiped, the volume of an element can be characterized by an equivalent cube, whose side dimension is some multiple of the initial mean droplet diameter

$$V = (cd_0)^3 \quad (9)$$

Equation (8) is integrated along the gas-phase streamlines to determine ω. These streamlines are obtained from the momentum equation for the air-vapor element.

Conservation of Air Momentum. The velocity of an air-vapor element is found from a Lagrangian form of the momentum equation. Forces on the element are droplet drag, buoyancy, and turbulent shear. The air momentum equation can be written as

$$\rho_a V d\mathbf{u}/dt = (n\rho_a C_D \pi d^2/8)|\mathbf{v} - \mathbf{u}|(\mathbf{v} - \mathbf{u}) - \rho_a \beta_T V \mathbf{g}(T_{db} - T_{db\infty}) + \rho_a V K_m(\partial^2 u_y/\partial z^2)\mathbf{j} \quad (10)$$

Air Continuity Equation. The continuity equation for the air-vapor phase is formulated for a rectangular streamtube. The cross-sectional area of the streamtube upwind of the spray is given by the frontal area of an air-vapor element. This area changes as the element moves through the spray domain according to

$$\rho_a u_y A = \rho_a U_\infty A_\infty \quad (11)$$

where the cross-sectional area of a streamtube is given by

$$A = lm \quad (12)$$

The lateral and vertical streamtube dimensions and velocity components are obtained by utilizing a ratio of the lateral and vertical components of the air momentum equation as detailed by Palaszewski [7]. The air-vapor streamline itself is found from

$$d\mathbf{s}_a/dt = \mathbf{u} \quad (13)$$

Air Energy Equation. Neglecting conduction in comparison with turbulent diffusion of heat, one can write for conservation of energy along an air-vapor streamline

$$\rho_a V di/dt = n\pi d^2(T_d - T_{db}) + n\pi d^2 L h_D \rho_a(\omega_s(T_d) - \omega) + \rho_a C_{pa} V K_h \partial^2 T_{db}/\partial z^2 \quad (14)$$

The terms on the right-hand side of equation (14) represent convective and evaporative heat transfer from the droplets and turbulent diffusion of heat in that order. The enthalpy i of an air-vapor mixture is given by

$$i = C_{pa}(T_{db} - T_{ra}) + \omega[h_f(T_{wb}) + L(T_{wb}) + C_{pv}(T_{db} - T_{wb})] \quad (15)$$

After substituting equation (15) into equation (14) and dropping small terms equation (14) become

$$\rho_a V C_{pav} dT_{db}/dt = \rho_a \omega V C_{pv} dT_{wb}/dt + n\pi d^2 h(T_d - T_{db}) + \rho_a C_{pa} V K_h \partial^2 T_{db}/\partial z^2 \quad (16)$$

where

Nomenclature (cont.)

Pr = Prandtl number = $\mu_a C_{pa}/k_a$
$\dot{Q}$ = rate of heat transfer from a spray unit
Re_0 = initial Reynolds number = $\rho_a v_0 d_0/\mu_a$
S = distance along a streamline or droplet trajectory
Sc_0 = initial Schmidt number = $\mu_a/(\rho_a D_0)$
Sf = Stefan number = latent to sensible heat = $L_0/[C_{pd}(T_{d0} - T_{wb\infty})]$
SER = Spray Energy Release
T = temperature
T_{d0} = spray supply temperature
$Tu_{wv\infty 2m}$ = diffusivity turbulent number = ratio of turbulent thermal diffusivity to kinematic viscosity = $K_{wv\infty 2m}/\nu_a$
$Tu_{m\infty 2m}$ = momentum turbulent number = ratio of turbulent viscosity to kinematic viscosity = $K_{m\infty 2m}/\nu_a$
U_{2ml} = air velocity at a 2 m height downwind of the spray
$\mathbf{u}$ = air velocity vector
u_* = friction velocity
V = volume of a finite air-vapor element
Ve = velocity ratio = $U_{\infty 2m}/v_0$
v_0 = initial speed of the mean size drop
$\mathbf{v}$ = drop velocity vector
z = vertical distance above canal surface
z_0 = roughness height
α_s = wind shear velocity ratio = $u_*/(k' U_{\infty 2m})$
β_T = coefficient of thermal expansion of air
ΔT_{wb2ml} = change in local wet-bulb temperature of air passing through the spray
μ = viscosity
ν = kinematic viscosity
ξ = wind angle to the canal
ρ = density
ρ^* = density ratio = ρ_a/ρ_d
ϕ = spray discharge angle
ω = absolute humidity

Superscripts

* = dimensionless variable

Subscripts

0 = initial value at nozzle discharge
$2m$ = ambient value at a 2 m height
∞ = ambient value at any height
a = air
d = droplet
db = dry bulb
j = trajectory number
s = saturated air
v = water vapor
wb = wet bulb
y = horizontal space coordinate in the wind direction

Table 1 PSM experimental conditions

Exp. No.	$L_{mo}(m)$	$T_{do}(°C)$	$T_{db\infty}(°C)$	$T_{wb\infty}(°C)$	$U_{\infty 2m}(m/s)$
2	-4.5	34.4	22.5	14.0	4.27
3a	-8.5	30.2	21.0	16.2	4.64
3b1	-4.5	31.3	22.3	15.5	2.30
3b2	-4.5	31.4	22.7	14.9	2.50
5a1	-4.5	25.7	15.5	11.9	1.28
5a2	-2.5	25.9	16.3	13.3	1.80
5b	-13.5	26.4	17.5	13.6	2.43
5bES	-4.5	26.0	17.5	13.8	2.02
5bS	-13.5	26.0	17.5	13.5	2.68

Note: $z_0 = 0.04$ m for all experiments

Data from Reference [12].

$$C_{pav} = C_{pa} + \omega C_{pv} \tag{17}$$

Meteorological Considerations

The initial upwind profiles of dry-bulb temperature and absolute humidity can be considered uniform since the variation of these quantities is small over heights typical of sprays (5 m). The wind velocity profile is given [11] as

$$U_\infty(z) = (u_*/k')\left[\ln\left(\frac{z}{z_0}+1\right)+\psi(z)\right] \tag{18}$$

$\psi(z)$ takes on different forms depending on the stability condition of the atmosphere [11]. Values of the turbulent transport properties and the turbulent length scale L_{mo} are given in [11]. While the spray heat and moisture release will affect atmospheric stability, their effect on changes in stability is assumed small compared to convection and evaporation in determining drop and air-vapor temperatures.

Comparisons With Data

The predictions of the present model for a single spray unit have been compared with data [12] for one spray of the Powered Spray Module (PSM) manufactured by the Ceramic Cooling Tower Company. A typical spray module consists of four spray units aligned parallel to the edge of a canal. The module is powered by a 56-kW pump. Each nozzle sprays approximately 9470 L of water per minute. The nozzles are located 0.92 m (3.0 ft) above the water surface, and produce a spray pattern with a maximum height of 6.1 m and a radius of 6.1 m at the water surface in the absence of wind [13].

The initial droplet velocity is 11.64 m/s and the spray discharge angle is 74 deg [13]. In the model, droplets were discharged from 36 sites around the nozzle perimeter, producing a droplet trajectory every 10 deg. Although the model can handle any number of discharge sites, the number 36 was chosen to limit computation time and conserve computer resources. A sensitivity study was not carried out since the objective was to create as fine a flow field as possible within computation budgetary constraints.

The spray was assumed to be monodisperse. The value of the initial droplet diameter (d_0 = 1.5 cm) was obtained by varying the drop diameter until the single particle momentum equation [7, 8] matched the experimentally observed trajectory [13] in the absence of wind.

The data for the PSM were obtained from field measurements at Dresden and Quad-Cities Nuclear Stations by the Illinois Institute of Technology. Measured values of ambient wet-bulb and dry-bulb temperature, wind speed, wind direction to the canal, and initial droplet temperature were used as input to the model. Predictions were compared with measurements of the droplet return (cold) temperature at four positions around the spray perimeter and of the downwind horizontal air velocity and wet-bulb temperature 2.0 m above the canal and 6.1 m from the nozzle along a line perpendicular to the canal edge. The theory was compared with data only for the operating spray units nearest the canal

Table 2 Comparison of theory and experiment for droplet cooling range of *PSM*

Experiment No.	$\xi°$		Droplet Cooling Range (°C) Catch Pan No. 1	2	3	4
2	10	experiment	1.5	1.8	2.7	2.2
□		theory	1.7	2.1	2.2	2.0
3a	19	experiment	0.9	1.2	1.5	1.2
□		theory	1.1	1.4	1.4	1.3
5bES	73	experiment	1.0	1.1	0.8	0.8
		theory	1.0	1.0	0.8	0.8
5bS	79	experiment	1.2	1.2	1.0	1.0
		theory	1.0	1.0	0.9	0.9
5b	83	experiment	1.0	0.9	0.7	1.0
		theory	1.0	1.0	0.9	0.9

Note: Data from Reference [12].

Table 3 Comparison of theory and experiment for *PSM* downwind wet-bulb temperature and air-velocity

Exp. No.	$\xi°$	$\Delta T_{wb2ml}(°C)$ exp.	theory	$U_{2ml}(m/s)$ exp.	theory
3b2	14	3.8	2.9	1.50	1.57
3b1	27	3.1	3.2	1.40	1.43
5a1	29	2.7	5.0	1.26	0.47
5a2	62	3.9	4.2	1.20	1.12
5bES	73	3.3	5.9	1.75	0.78
5bS	79	3.0	3.2	2.41	1.70
5b	83	-	-	1.74	1.36

Note: Data from Reference [12].

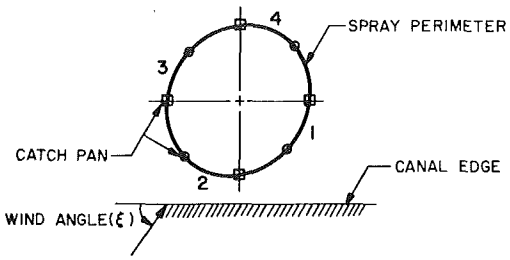

TOP VIEW

Fig. 2 Location of catch pans around spray perimeter

upwind edge, since the most upwind sprays are the only ones that see ambient air. Table 1 lists the experimental conditions. Comparisons between theoretical predictions and the data are given in Tables 2 and 3. In Table 2, the square or circle underneath each experiment number, along with the catch pan number, indicates where the droplet temperature measurement was made. Figure 2 shows the location of the catch pans and the direction of the wind, ξ. Agreement between the theoretical and measured values of the droplet cooling range is generally within the reported experimental error of 0.2°C. Droplets ejected on the upwind side of the nozzle experience a greater amount of cooling than droplets ejected downwind of the nozzle. This is due to the progressive humidification and heating of the air flowing through the spray. Upwind droplets see air close to ambient conditions, while downwind droplets see air that has undergone substantial interaction with the spray. The data and theoretical predictions in Table 2 clearly indicate this trend. For experiments 2 and 3*a*, the upwind catch pans are #2 and #3 and the downwind catch pans are #1 and #4. For both of these experiments, the sprayed water collected by pans 2 and 3 shows a greater cooling range than the water collected by pans 1 and 4. For experiments 5*b*, 5*b*ES and 5*b*S, the upwind pans (1 and 2) also collected cooler water than the downwind pans (3 and 4).

Table 3 shows comparisons between predicted and measured values of the change in wet-bulb temperature at a 2-m height (ΔT_{wb2ml}) of the air passing through the spray, and the horizontal air-velocity at a 2-m height downwind of the spray. Temperature and velocity measurements were obtained midway between the first and second sprays in a pass. A correlation between air-velocity and wet-bulb temperature may be noted in Table 3. The predicted and measured values of local air velocity show good agreement for the experiments in which the change in wet-bulb temperature is closely predicted (e.g., experiments 3*b*1, 3*b*2, and 5*a*2). The observation is consistent with expected behavior. If the predicted air velocity is lower than the data, the predicted local wet-bulb temperature is expected to be higher than the data. The smaller the local air velocity, the less ventilation the spray experiences and the greater the buildup of heat and water vapor in the spray domain. For experiments 5*a*1 and 5*b*ES, predicted air velocities substantially lower than the data result in local wet-bulb temperatures substantially higher than the data.

Although these trends exist, good agreement between data and predictions can be considered fortuitous in part since the wet-bulb temperature and wind speed data are average values over many hours. The fact that the droplet cooling range is more closely predicted is due to the relative stability of the ambient wet-bulb temperature for each experiment. Eighty percent of droplet heat transfer is due to evaporation, which depends upon the difference between the droplet temperature and the local wet-bulb temperature. Therefore, the droplet cooling is expected to be easier to predict if the thermal driving force is accurately measured.

Parametric Studies

The Governing Parameters. Formulation of the governing equations and boundary conditions for the present model in dimensionless form reveals the parameters which affect the performance of spray units. Of primary interest in sprays is their cooling effectiveness within the constraints of power requirements and mass loss due to evaporation. The dimensionless dependent variable $\dot{Q}/(\dot{m}_0 v_0^2/(2g_c))$ represents the ratio of the heat removed from the spray to the theoretical power needed to operate it. Examination of the governing equations and boundary conditions shows that for the general case of a liquid spray in atmospheric air, this ratio depends on seventeen parameters. For the special case of water sprays in atmospheric air, the Prandtl number Pr, Schmidt number Sc_0, specific heat ratio C_p^*, and density ratio ρ^* are approximately constant. In addition, the diffusivity turbulent number is equal to the momentum turbulent number times a constant [7] which depends on atmospheric stability. These considerations reduce the number of governing parameters to eleven. Thus

$$\dot{Q}^* = \frac{\dot{Q}}{\dot{m}_0 v_0^2/(2g_c)} = f(\mathrm{B,Fr,Gr},Po,\mathrm{Re}_0,\mathrm{Sf},Tu_{m\infty 2m},Ve,\alpha_s,\phi,z_0^*) \quad (19)$$

Of the eleven parameters given in equation (19), only five can be controlled by design considerations. These are: Fr, *Po*, Re_0, *Ve*, and ϕ. The power ratio *Po* is the ratio of the theoretical power input to the spray to a specified reference power input. The reference power input used here (10.7 kW) is the theoretical power required to operate a single spray of the PSM. Power ratio can be expressed as

$$Po = [\dot{m}_0 v_0^2/(2g_c)]/E_{\mathrm{ref}} \quad (20)$$

where E_{ref} = reference theoretical spray power input. For a given discharge velocity v_0, the power ratio distinguishes between sprays having different mass flow rates. The remaining six parameters in equation (19), B, Gr, Sf, $Tu_{m\infty 2m}$, α_s, and z_0^* depend on meteorological conditions and water temperature. Therefore, for optimum design we have

$$\dot{Q}^* = f(\mathrm{Fr},Po,\mathrm{Re}_0,Ve,\phi) \quad (21)$$

Parametric studies of equation (21) define the optimum spray design. Although the number of parameters is large, such a study is nevertheless feasible due to the additional considerations outlined below.

The phenomenon of liquid jet breakup into droplets has been extensively studied. Correlations have been developed for the mean droplet size resulting from the breakup of jets issued from nozzles, many of which are given by Masters [14]. Considerable work has been done in the development of empirical correlations for the mean droplet size formed by centrifugal spray nozzles [14]. It is generally known that the velocity head exerts a major influence on the size of droplets produced by spray nozzles. Masters [14] suggests correlations of the form

$$d_0 = c_1 H^{c_2} \quad (22)$$

where

c_1 and c_2 are constants and
H = velocity head of spray nozzle = $v_0^2/(2g)$

Soo [6] shows that for two "test" sprays, droplet diameter is affected by head. Little work has been done to develop correlations for the mean drop size of sprays formed by cone impact diffusers (e.g., Powered Spray Module). For the purposes of the present parametric studies, the authors developed correlations based on available information. Substituting the definition of velocity head H into equation (22) yields

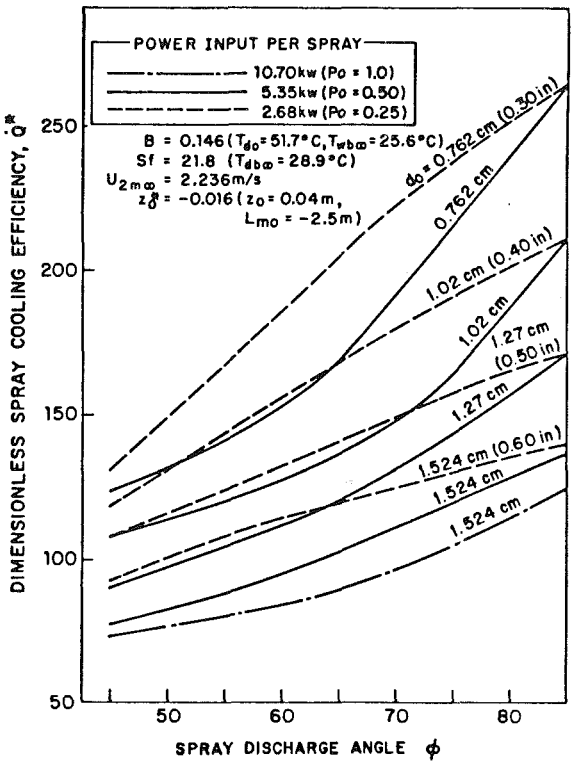

Fig. 3 Cooling efficiency for a single spray

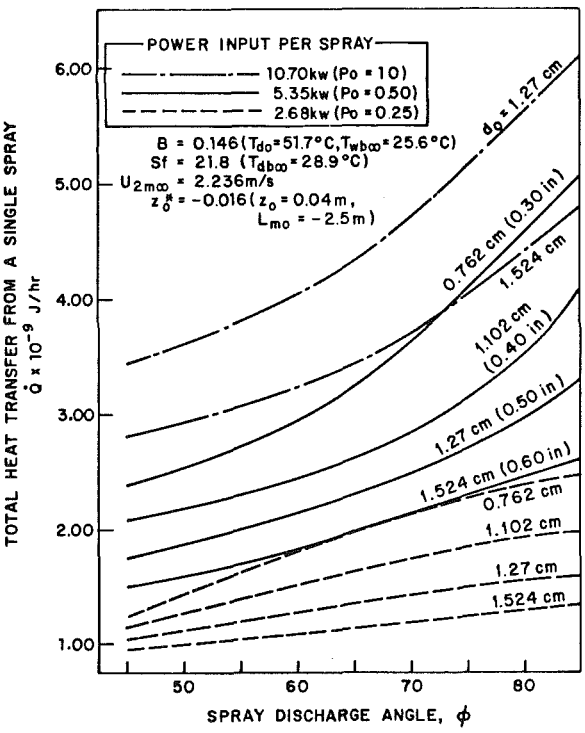

Fig. 4 Total heat transfer for a single spray

$$d_0 = c_1 v_0^{2c_2}/(2g)^{c_2} \tag{23}$$

Equation (23) reveals the interrelationship between discharge velocity and mean droplet diameter. The dependence of d_0 on v_0 further reduces the number of independent parameters governing spray cooling efficiency. In particular, the Reynolds number and Froude number cannot be varied independently of each other, reducing the number of independent dimensionless parameters to four. Equation (21) can now be written

$$\dot{Q}^* = f(Po, \mathrm{Re}_0, Ve, \phi) \tag{24}$$

Design Charts. A theoretical study of equation (24) was carried out for summer design conditions. These conditions are: $T_{d0} = 51.7°C$, $T_{db\infty} = 28.9°C$, $T_{wb\infty} = 25.6°C$, $U_{2m\infty} = 2.236$ m/s (5 mph), $z_0 = 0.04$ m (atmospheric surface layer over 30 cm weeds), $L_{mo} = -2.5$ m (strong daytime solar insolation: extremely unstable air).

Values of z_0 and L_{mo} were obtained from [15]. The velocity ratio $Ve = U_{2m\infty}/v_0$ was not held constant in this study since the nozzle discharge velocity v_0 varied with mean droplet diameter. The results, therefore, are valid only for the design wind speed. The correlation between d_0 and v_0 used in this study was found as described in [7]. The resulting correlation is

$$d_0 = 9.17 \times 10^{-4} v_0^{-6.36} m \tag{25}$$

where v_0 is in m/s.

Figure 3 shows the effect of mean droplet diameter (or Re_0), power ratio Po, and discharge angle ϕ, on spray cooling efficiency. The reference theoretical power input (10.7 kW) is of one unit of the PSM, representing a pump efficiency of 76.4 percent, where pump efficiency is the ratio of theoretical power input to the actual power input to the pump. The chart does not reveal a single set of parameters giving optimum spray cooling efficiency, $\dot{Q}^*$. Cooling efficiency rises with increasing discharge angle and decreasing droplet size. Maximum efficiency occurs at a 90 deg (vertical) discharge angle for any size droplet. A droplet discharged vertically undergoes the largest temperature change due to maximum contact time with the air. Also, there is little buildup of water vapor or heat in the spray domain at large discharge angles since there is insufficient time for humidity and heat to accumulate in the narrow spray field that is formed at large discharge angles when there is a significant crosswind.

At a given mean droplet diameter, cooling efficiency increases with decreasing power ratio. Lower power ratios result in lower spray flow rates. At a given discharge angle, the lower the flow rate, the fewer droplets there are in the spray domain and the lower the rise in local wet-bulb temperature. Lower power ratios exhibit improved efficiency due to local conditions that are closer to ambient conditions.

It is seen from Fig. 3 that the curves for a power ratio of 0.25 for a given droplet size are higher than the $Po = 0.5$ curves for the next smallest droplet size in the figure, over a certain range of ϕ. For example, the $Po = 0.25$ curve for $d_0 = 1.524$ cm is above the $Po = 0.5$ curve for $d_0 = 1.27$ cm and discharge angles of 45 to 64 deg. This indicates that even for sprays discharging large drops, there is a range of the governing parameters where such sprays are more effective dissipators of heat than sprays having smaller drops.

An important economic consideration is the cost of a spray system incorporating efficient sprays versus a second system incorporating less efficient sprays with a higher rate of heat dissipation. This aspect of the optimization problem can be analyzed with the help of Figs. 3 and 4.

Using the example cited above, a spray unit with a discharge angle of 64 deg, a droplet diameter of 1.524 cm, and a power ratio of 0.25 has the identical cooling efficiency of a unit with the same discharge angle, a drop diameter of 1.27 cm, and a power ratio of 0.5. Although having the same cooling efficiency, the second unit dissipates twice as much heat as the first unit. For any given spray system, half as many units of type 2 are necessary to dissipate a given amount of heat as of type 1, thus greatly reducing the length of the spray canal and the cost of the spray system.

The dependence of total heat transfer from a spray unit on the governing parameters can be seen in Fig. 4. For a given

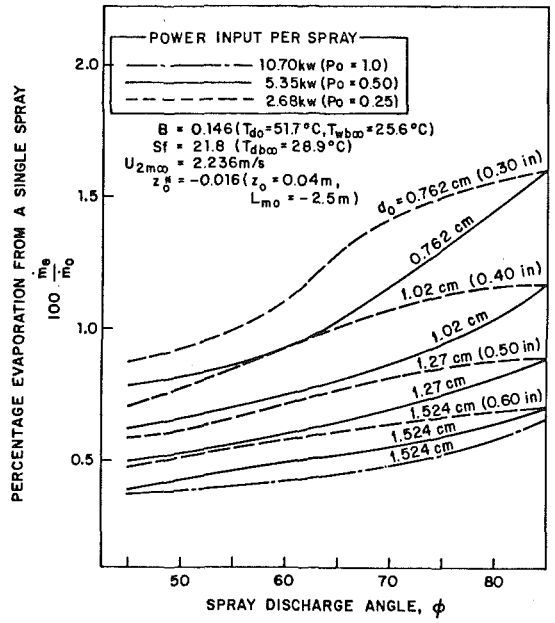

Fig. 5 Evaporation as a percentage of spray flow rate for a single spray

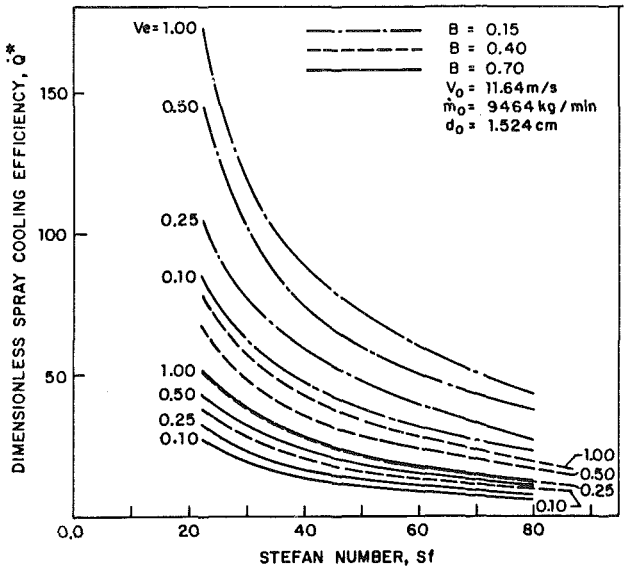

Fig. 6 Performance chart for PSM single spray in unstable air

power ratio, total heat transfer increases with decreasing droplet size. The curve for $Po = 1.0$ and $d_0 = 1.524$ cm is for the PSM. It can be seen that the performance curve for $Po = 0.50$ and $d_0 = 0.762$ cm crosses the PSM curve at $\phi = 73$ deg. Thus, the total cooling achieved by the PSM can be obtained with half the PSM's power input by a spray unit producing drops of diameter $d_0 = 0.762$ cm, which is half the droplet diameter of the PSM. This suggests that substantial savings in the power cost of operating a spray system can be realized by the use of this alternative spray unit design.

The alternative design would be unacceptable were it to produce excessive loss of water through evaporation. Figure 5 shows that at $\phi = 73$ deg, the PSM evaporation is 0.51 percent of the sprayed water whereas evaporation is 1.25 percent for the alternative design, which is well within the criteria given by Soo [6] of 2.5 percent evaporation for summer operation. The evaporative mass ratio $\dot{m}_e/\dot{m}_0$ for the spray unit is given by

$$\frac{\dot{m}_e}{\dot{m}_o} = \frac{\pi \rho_d}{6\dot{m}_0} \sum_{j=1}^{N} \dot{n}_j (d_{0j}^3 - d_{cj}^3) \tag{26}$$

where $\dot{m}_e$ is the evaporation rate from the spray unit.

An additional observation on performance can be made by considering the curve for $Po = 1.0$, $d_0 = 1.27$ cm in Fig. 4. This curve suggests that greater cooling can be achieved for the PSM for the same power input by a change in pump design. Using a pump that produces a larger head will result in smaller droplets. A nozzle discharging 1.27-cm droplets will increase the PSM efficiency at $\phi = 74$ deg by about 28 percent.

Performance Charts. For sprays of fixed design, the number of independent parameters is reduced to six: B, Sf, $Tu_{m\infty 2m}$, Ve, α_s, $z_0{}^*$. The Grashof number is not an independent parameter since it is a constant multiple of the Stefan number for a fixed design. The turbulence parameters $Tu_{m\infty 2m}$, α_s, and $z_0{}^*$ are determined by the stability of the atmosphere and the roughness of the earth's surface. Atmospheric stability depends on the amount of solar insolation and the wind speed. In the present study, the atmosphere was assumed to be unstable under strong solar insolation, and the earth's surface covered with 30-cm high weeds ($z_0 = 0.04$ m). For these conditions $T_{um\infty 2m}$, α_s, and $z_0{}^*$ are determined by wind speed and are not independent of velocity ratio Ve. Additional performance charts may be constructed for different amounts of solar insolation, different atmospheric stabilities, and surface roughnesses. With the specification of atmospheric stability and surface roughness, the performance of a fixed design depends on Bowen ratio, Stefan number, and velocity ratio.

The fixed design analyzed in this study is one unit of the Powered Spray Module. In Fig. 6 the spray cooling efficiency is plotted versus the Stefan number Sf for values of the velocity ratio Ve and the Bowen ratio B. The range of the Stefan number Sf covers the normally encountered atmospheric conditions and condenser discharge temperatures. Lower Stefan numbers reflect a greater potential for heat transfer due to a larger difference between the initial droplet temperature and the ambient wet-bulb temperature. For a given Stefan number, the Bowen ratio B indicates the influence of evaporation on performance. Figure 6 shows that at a given velocity ratio, a low Bowen ratio (high percentage of evaporative heat transfer) is associated with improved spray efficiency over a high Bowen ratio. For a given Bowen ratio, efficiency improves with velocity ratio over the entire range of Stefan number. It is interesting to note that for a Bowen ratio of 0.4 and a velocity ratio of 0.1, spray performance is better than for a Bowen ratio of 0.7 and velocity ratios of 0.10 and 0.25. This shows that, contrary to the results obtained from both the NTU and SER models, spray efficiency is not solely a function of wind speed, but depends on the difference between the total enthalpy of the air and the enthalpy of saturated air at the temperature of the droplet. This consideration helps to explain the spread in NTU values in Fig. 3 of [16] between the "best fit" curve of Porter and Chen and their summer data.

Acknowledgments

This work was supported by the National Science Foundation Grant No. ENG. 78-20709. Appreciation is extended to the City University of New York Computer Center for the use of their facilities. The above work was done in partial fulfillment of the requirements of the Ph.D degree of S. Palaszewski from The School of Engineering of the City College of the City University of New York.

References

1 Chen, K. H., and Trezek, G. J., "Spray Energy Release (SER) Approach to Analyzing Spray System Performance," *Proceedings of the American Power Conference*, Vol. 38, 1976, pp. 1435–1442.

2 Frediani, H. A., and Smith, N., "Mathematical Model for Spray Cooling Systems," ASME JOURNAL OF ENGINEERING FOR POWER, Vol. 99, No. 2, Apr. 1977, pp. 279–283.

3 Chaturvedi, S., and Porter, R. W., "Air-Vapor Dynamics in Large-Scale Atmospheric Spray Cooling Systems," *Journal of Fluids Engineering*, Vol. 100, No. 1, Mar. 1978, pp. 65–72.

4 Porter, R. W., Jain, M., and Chaturvedi, S. K., "Unit Thermal Performance of Atmospheric Spray Cooling Systems," ASME *Journal of Heat Transfer*, Vol. 102, No. 2, May 1980, pp. 210–214.

5 Berger, M. H., and Taylor, R. E., "An Atmospheric Spray Cooling Model, Environmental Effects of Atmospheric Heat/Moisture Releases," *The Second AIAA/ASME Thermophysics and Heat Transfer Conference*, Palo Alto, CA, May 1978, pp. 59–64.

6 Soo, S. L., "Power Spray Cooling—Unit and System Performance," ASME Paper No. 75-WA/Pwr-8, Nov. 1975.

7 Palazewski, S. J., "An Air-Vapor-Droplet Local Interaction Model for Spray Units," Doctoral dissertation, The City University of New York, 1980.

8 Palaszewski, S. J., Jiji, L. M., and Weinbaum, S., "An Air-Vapor-Droplet Local Interaction Model for Spray Units," ASME *Journal of Heat Transfer*, Vol. 103, No. 3, Aug. 1981, pp. 514–521.

9 Ranz, W. D., and Marshall, W. R., Jr., "Evaporation from Drops," *Chemical Engineering Progress*, Vol. 48, No. 3, Feb. 1952, pp. 141–146, 173–180.

10 Wallis, G. B., *One-Dimensional Two-Phase Flow*, McGraw-Hill, New York, 1969.

11 Panofsky, H. A., "The Atmospheric Boundary Layer Below 150 Meters," *Annual Review of Fluid Mechanics*, Vol. 6, 1972, pp. 147–177.

12 Yang, U. M., and Porter, R. W., "Thermal Performance of Spray Coolings Systems—Theoretical and Experimental Aspects," Waste Energy Management Technical Report TR-76-1, Illinois Institute of Technology, Dec. 1976.

13 Wilson, D. C., "Thermal Performance of Powered Spray Modules," Master's thesis, University of Illinois, Urbana-Champaign, 1972.

14 Masters, K., *Spray Drying*, Leonard Hill, London, 1972.

15 Hoffert, M. I., "Atmospheric Transport, Dispersion and Chemical Reactions in Air Pollution: A Review," *AIAA Journal*, Vol. 10, No. 4, Apr. 1972, pp. 377–387.

16 Ryan, P. J., and Myers, D. M., "Spray Cooling: A Review of Thermal Performance Models," *Proceedings of the American Power Conference*, Vol. 38, 1976, pp. 1473–1481.

A Mathematical Model for Ringbom Engine Operation

J. R. Senft
University of Wisconsin—River Falls,
River Falls, WI 54022

The Ringbom or hybrid Stirling engine, essentially dormant for some 70 years, is experiencing a vigorous rebirth following recent fundamental discoveries concerning its unique mode of operation. In this paper the author's earlier mathematical model of Ringbom engine operation is extended to include volume variation effects due to the displacer rod. This injects a new parameter, the rod-to-displacer area ratio, into the theory improving its fidelity and increasing its predictive power. It is rigorously shown that the main theorem characterizing overdriven mode operation, the basic regime of stable running for hybrids, remains valid in the extended model and is presented here in a new form.

Introduction

The Ringbom engine is a Stirling engine with a free displacer and a crank-coupled piston. It is also often referred to as the hybrid Stirling engine, since it conceptually lies between the full kinematic Stirling and the completely free piston engine. Chronologically however it preceded the free piston Stirling, being the 1907 invention of Ossian Ringbom. Figure 1 is a drawing of the Ringbom engine based on his 1907 patent [1]. Now, as then, the idea is appealing because it appears to offer the versatility of a shaft output engine without the complication of a mechanical drive for the displacer. However, apparently little was done with the idea until recently.

Interest in the hybrid concept was revived by the pioneering efforts of Walker in 1970 [6]. In 1980 the present author demonstrated the attainability of stable running with a small model hybrid; Fig. 2 shows a photograph of this engine and [4] presents full constructional details. At the same time a conceptual model was put forward which explained the operational characteristics observed, particularly the stable operation over a wide range of shaft speeds; the key concept introduced was *overdriven mode operation*, a mode of operation in which the displacer is in a sense forced to keep in proper phase with the piston.

Following this an elementary isothermal linear pressure model was developed to quantify these concepts in an attempt to sharpen understanding of hybrid operation and to provide rudimentary design tools; these results were published in [2]. Interest in large-scale Ringbom engine conversions at the University of Calgary blossomed again in parallel with these developments [5, 7].

Recently it was found that the mathematical model could be extended to more faithfully reflect engine pressure variation [3]. This paper presents in detail the development of an improved version of the original theory and concludes with a new statement of a necessary and sufficient condition for stable overdriven mode operation.

Contributed by the Power Division for publication in the JOURNAL OF ENGINEERING FOR GAS TURBINES AND POWER. Manuscript received by the Power Division December 1982.

The Conceptual Model

The mathematics of this paper models the concept of overdriven mode operation, which was rather thoroughly introduced and discussed in [2]. We therefore give only a brief version in this section for the sake of completeness, but adopt a slightly different view for the sake of those who have already read the earlier exposition.

The Modified Ringbom. Ringbom's patented engine used rising gas pressure acting on a rather large displacer rod to lift the displacer from the hot to the cold end as the piston approached its inner dead center, but relied on gravity to effect its return [1, 2]. This of course limits the potential speed of the engine. A spring could be fitted to augment the effect of gravity in seeking higher speeds, but an alternative is the use of gas pressure difference across the displacer rod to drive it in

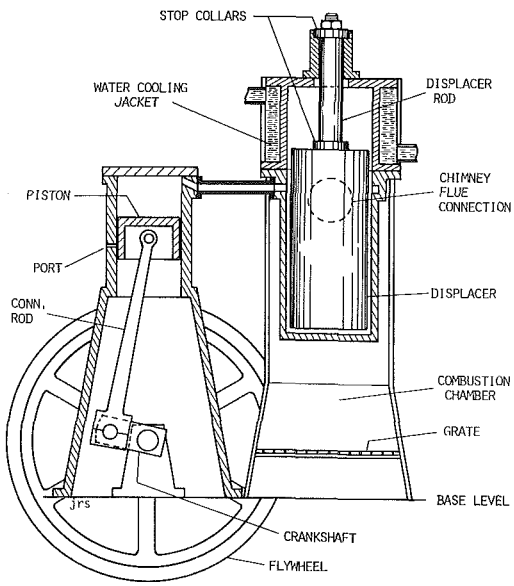

Fig. 1 The hybrid Stirling engine of Ossian Ringbom

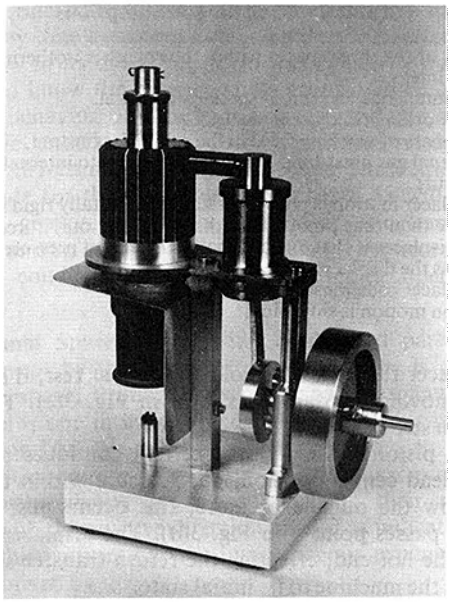

Fig. 2 The author's miniature hybrid engine

both directions. This latter approach is the fruitful one, for it not only gives the higher speeds desired, but also makes it possible for the engine to operate in the overdriven mode which is, as will be shown, stable steady operation over a wide range of speeds.

This dual direction pressure drive on the displacer is quite easy to arrange in practice. One has only to omit the small port specified by Ringbom passing through the cylinder wall and located just above the bottom dead center of the piston stroke; it is plainly visible in Fig. 1.

Omitting this port forces the mean cycle pressure to be approximately equal to the surrounding pressure because of inevitable leakage past the piston or displacer rod seals. Thus, the engine pressure will fluctuate above and below the external pressure more or less equally, producing nearly similar driving forces on the displacer rod in *each* direction. By choosing engine geometry appropriately, these driving forces can be made large enough to render the effect of gravity negligible, and accordingly its effect is usually totally disregarded in typical engine analyses.

Overdriven Mode Operation. Overdriven mode operation of the modified Ringbom is illustrated in Fig. 3. We begin in Fig. 3(*a*) with the displacer in the hot end of its cylinder and the crankshaft rotating and bringing the piston inward on the compression stroke. We assume a heavy flywheel and hence

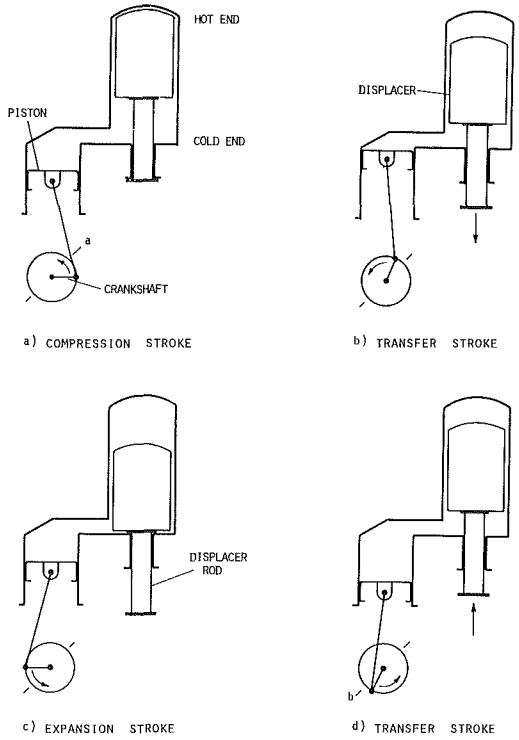

Fig. 3 Operation of the modified Ringbom engine

have very uniform (and nearly sinusoidal) piston motion. Now if the mean cycle pressure is equal to the external pressure, then with the piston at midstroke, the displacer will still be held in the hot end by pressure difference. The piston must advance beyond midstroke before this pressure difference across the displacer rod drops to zero; the point where this occurs is at *a* on the crankpin circle.

As the piston passes this point, the displacer is accelerated toward the cold end as indicated in Fig. 3(*b*). This is the first transfer stroke of the Stirling cycle in which gas is displaced from the cold to the hot end by flowing around the moving displacer. Since the piston is near top dead center, its movement is relatively small during the transfer. The pressure within the machine rises because of the increase in temperature of a large portion of the workspace gas.

For simplicity in our analysis, we assume that the displacer stops instantly at the ends of its stroke. This is a reasonable simplification since in practice the halts can be made very rapidly and with negligible rebound when appropriate dissipative cushions or dashpots are fitted. Continuing with

Nomenclature

A = cross-sectional area of displacer
A_p = cross-sectional area of piston
A_R = cross-sectional area of displacer rod
L_P = amplitude of piston motion = 1/2 piston stroke
L = maximum amplitude of displacer motion = 1/2 maximum displacer stroke
x_P = piston position at time t
x_D = displacer position at time t
V_e = instantaneous volume of expansion space
V_c = instantaneous volume of compression space
V_D = volume of dead space
T_E = temperature of working fluid in the expansion space
T_C = temperature of working fluid in compression space
T_D = temperature of working fluid in the dead space
p = instantaneous pressure of the working fluid
p_c = cycle pressure at midstroke of piston and displacer
Δp = $p - p_c$, pressure difference across displacer rod
R = gas constant of working fluid
M = mass of working fluid
M_D = mass of displacer assembly
ω = angular velocity of crankshaft
K = $[Ap_c\rho(1-\tau-\rho)]/[M_D L(1+\tau-\rho+\kappa\lambda+\sigma)]$
t_0 = $\omega^{-1}\arcsin(\beta^{-1})$
τ = T_C/T_E
τ' = T_C/T_D
λ = L_P/L
κ = A_P/A
σ = $\tau' V_D/AL$
ρ = A_R/A
γ = $\sqrt{K}/\omega$
β = $(\lambda\kappa)/(1-\tau-\rho)$
χ = $\sqrt{\beta^2-1}$

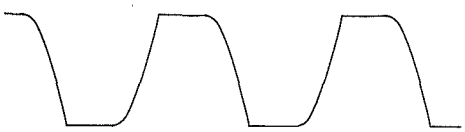

Fig. 4 Overdriven displacer motion showing dwell periods

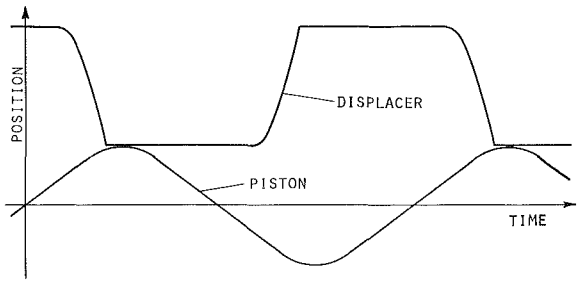

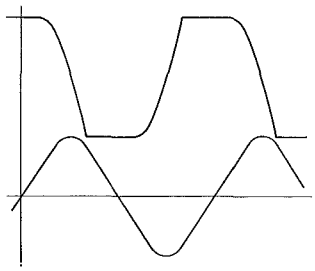

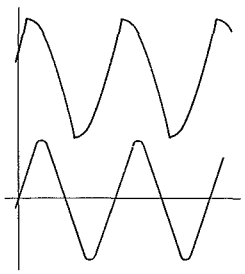

Fig. 5 Displacer phasing change with increasing engine speed

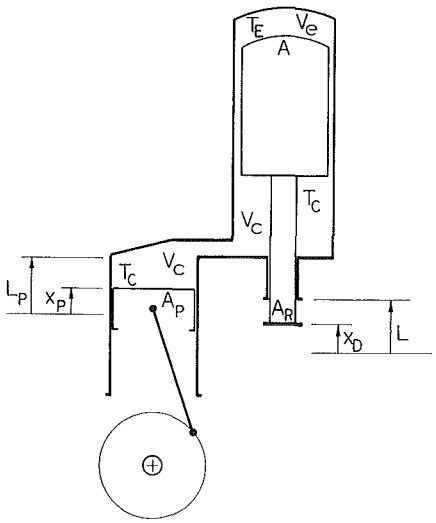

Fig. 6 Schematic representation of the Ringbom Stirling engine

Table 1 Modeling Assumptions

(*i*) Each of the three spaces within the engine is isothermal in space and time.
(*ii*) Instantaneous pressure is spatially constant.
(*iii*) The working fluid is an ideal gas.
(*iv*) The mass of working fluid in the engine is constant.
(*v*) External gas pressure is constant and equal to internal midstroke pressure.
(*vi*) Displacer motion is physically limited by totally rigid stops.
(*vii*) Other than that provided by the stops, the only force acting on the displacer is that due internal and external pressure difference across the displacer rod.
(*viii*) Displacer collisions are totally inelastic.
(*ix*) Piston motion is sinusoidal.

the displacer fully into the cold end and at rest, the piston is rapidly moving outward as shown in Fig. 3(*c*). This is the expansion stroke.

As the piston passes midstroke and continues toward its bottom dead center position, gas pressure within the engine falls below the outside pressure; this occurs just after the crankpin passes point *b* in Fig. 3(*d*). The displacer is driven back to the hot end, effecting the return transfer stroke and returning the machine to its initial state.

An important point to note in this description is that the displacer completed its *full* stroke *before* the piston had moved enough to change the gas pressure bias to drive the displacer back. This condition is the essence of the overdriven mode concept. *Overdriven mode operation is operation in which the displacer contacts its physical travel limits before the gas pressure difference across its rod changes sign to oppose the motion.*

Stable Steady-State Operation. A little thought will reveal that overdriven mode operation as defined above is in fact also steady-state operation, which is stable with respect to shaft speed. Overdriven mode operation implies the existence of dwell periods following unidirection displacer motions as illustrated in Fig. 4. These dwells are not due to mere truncation of motion; the displacer is physically stopped while under a nonnegative acceleration with respect to its direction of motion. At all speeds below the limiting one, after the displacer comes to rest, a positive time interval must pass before the gas pressure difference across the displacer rod reverses sense and the displacer begins to move the other way. This ensures that the displacer is driven exactly the same way and in the *same relation to the piston* from cycle to cycle. Thus, with a constant crankshaft speed, displacer phasing is constant; hence, the overdriven mode is *steady-state* operation.

Overdriven mode operation is also *stable* operation. The main result of the mathematical analysis below will clearly show this. For the present, however, intuition will suggest that the displacer motion will adjust to changes in crankshaft speed primarily by changing the length of its dwell periods. The sequence of graphs in Fig. 5 illustrates this as piston period decreases. In the last graph the overdriven speed limit has been reached with zero length dwell segments; just beyond this speed, engine operation becomes irregular.

The Mathematical Model

Modeling Assumptions. We shall assume the engine configuration shown in Fig. 6. The modeling assumptions we adopt are summarized in Table 1 and will be discussed as we proceed. As usual the assumptions represent a compromise between reality and mathematical tractibility. Most of the assumptions here are typically made in first order level Stirling engine analyses and appear to capture the major features of the real machine. Recent comparisons with higher-order analyses and actual engine performance indicate a surprisingly high degree of predictability for this model [5].

However, one must always keep in mind the limitations imposed by one's assumptions. The mathematical model given below in its developed form was primarily inspired by the wish to know the dimensionless groups which determine the basic behavior of Ringbom engines, and the desire for some basic understanding of the conditions under which stable overdriven mode operation occurs. These are the only claims made for the model described here. As will be seen, only two groups, γ and χ, determine Ringbom engine behavior, and an easily applied theorem giving necessary and sufficient conditions for overdriven mode operation is presented.

Isothermal Spaces. Following established parlance, the volume swept by the displacer on its hot side is called the expansion space. Primarily for mathematical manageability, our model is one in which the expansion space is isothermal (assumption (*i*)). We take all gas in this space to be at the constant temperature T_E. Piston and displacer position, x_P and x_D respectively, are measured from their midstroke position with the positive direction inward as indicated in Fig. 6. With this convention, the instantaneous expansion space volume is given by

$$V_e = A(L - x_D) \tag{1}$$

The compression space consists of the volume above and swept by the piston plus the volume swept by the cool face of the displacer. All gas in this space is assumed to be at the temperature T_c. The instantaneous compression space volume is

$$V_c = (A - A_R)(L + x_D) + A_P(L_P - x_P) \tag{2}$$

in which the volume variation due to the displacer rod has been included (cf. [2]).

Not shown in Fig. 6 is the dead space which consists of all volume within the engine not swept by the piston or the displacer. This includes for example the space around the displacer, the volume in the connecting passage between the two cylinders, etc. For simplicity we consider all dead space as one volume V_D at a constant temperature T_D. T_D can usually safely be taken as the mean of T_E and T_c.

Applying the ideal gas law to the expansion, compression, and dead spaces, we obtain the following expression for the total mass of the working gas

$$M = \frac{pV_e}{RT_E} + \frac{pV_c}{RT_C} + \frac{pV_D}{RT_D}$$

Note that the pressure p is the same in each space by assumption (*ii*) from which it follows that

$$p = MR\left(\frac{V_e}{T_E} + \frac{V_c}{T_C} + \frac{V_D}{T_D}\right)^{-1} \tag{3}$$

Substituting equations (1) and (2) into (3), and making use of our nomenclature, we get p explicitly as a function of x_D and x_P

$$p = \frac{MRT_C}{A(1-\tau-\rho)x_D - A_P x_P + AL(1+\tau-\rho+\lambda\kappa+\sigma)} = p(x_D, x_P)$$

Of course only the case where

$$1 - \tau - \rho > 0$$

is of interest to us, since other machines have rods too large relative to the temperature ratio to function as Ringbom engines.

Linear Pressure Function. The pressure difference across the displacer rod is by assumption (*v*)

$$\Delta p = p - p_C = p(x_D, x_P) - p(0,0)$$

In order to make the analysis more yielding, we shall replace the above expression for Δp by its best linear approximation at (0,0). We find

$$\left.\frac{\partial p}{\partial x_D}\right|_{(0,0)} = -C_0(1-\tau-\rho)$$

and

$$\left.\frac{\partial p}{\partial x_P}\right|_{(0,0)} = C_0\kappa$$

where

$$C_0 = \frac{MRT_C}{AL^2(1+\tau-\rho+\lambda\kappa+\sigma)^2} \tag{4}$$

Henceforth we shall regard Δp as given by its linear approximation at (0,0), that is

$$\Delta p(x_D, x_P) = -C_0(1-\tau-\rho)x_D + C_0\kappa x_P \tag{5}$$

where C_0 is the constant given by equation (4).

Displacer Motion. In keeping with the goal of a model clear enough to provide a genuine understanding of overdriven mode operation with a minimum of obscuring details, we adopt assumption (*vii*). Thus viscous forces on the displacer are ignored, and we do not take up the case where external springs or dampers are arranged to act on the displacer. The only force acting on the displacer when not held against one of its stops is

$$A_R \Delta p(x_D, x_P)$$

Accordingly, the prevailing differential equation is

$$\ddot{x}_D = -(A_R/M_D)\Delta p(x_D, x_P) \tag{6}$$

where M_D is the mass of the displacer assembly. From equation (5), (6) becomes

$$\ddot{x}_D - Kx_D = -K\frac{\kappa}{1-\tau-\rho}x_P \tag{7}$$

where K is the constant given by

$$K = \frac{A_R}{M_D}(1-\tau-\rho)C_0 \tag{8}$$

Our final assumption is sinusoidal piston motion

$$x_P = L_P \sin \omega t \tag{9}$$

This is quite close to actual practice where relatively heavy flywheels and long connecting rods are usually used. With equation (9) the differential equation (7) describing the motion of the displacer assumes a familiar form:

$$\ddot{x}_D - Kx_D = -K\frac{\kappa}{1-\tau-\rho}L_P \sin \omega t \tag{10}$$

The general solution of (10) can be written as

$$x_D = a\exp(\sqrt{K}t) + b\exp(-\sqrt{K}t) + \frac{\lambda\kappa}{1-\tau-\rho}\frac{KL}{K+\omega^2}\sin \omega t \tag{11}$$

where a and b are constants depending upon initial conditions.

Analytic Statement of Overdriven Mode Operation. Equation (6) applies only when the displacer is not being held against one of its stops, for if the displacer is being so held, then the stop is applying a balancing force which was not included. Thus solution (11) applies only to individual intervals of displacer motion; in general the constants a and b in (11) change from one interval of motion to the next.

With the displacer initially in its full inward position, i.e., $x_D = L$, and the piston at midstroke, i.e., $x_P = 0$ (or $t = 0$), the displacer is held in this position because from (5)

$$\Delta p(L, 0) = -C_0(1-\tau-\rho)L < 0$$

that is, the external pressure exceeds the internal. Equation (6)

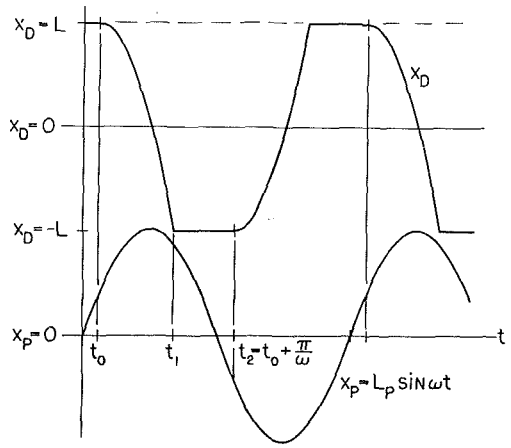

Fig. 7 Graph of piston and displacer motions in an overdriven Ringbom

will not apply until Δp diminishes to zero as the piston moves inward. We find that

$$t_0 = \frac{1}{\omega} \arcsin \frac{1-\tau-\rho}{\lambda\kappa} \tag{12}$$

is the point where $\Delta p = 0$ when $x_D = L$. One should note that the inequality

$$\frac{1-\tau-\rho}{\lambda\kappa} < 1 \tag{13}$$

must be satisfied in order to initiate displacer motion.

The point t_0 is shown in Fig. 7 where the lower curve is piston position and the upper curve displacer position as functions of time. The dashed horizontal line depicts the innermost possible position of the displacer and hence the vertical distance from the upper curve to the line is proportional to the expansion or hot space. The vertical distance between the two curves represents the compression or cold space volume.

Figure 7 depicts the displacer completing its full allowed travel, from resting position L at time t_0 to resting position $-L$ at time t_1, in an elapsed time $t_1 - t_0$, which is less than π/ω, the half-period of the piston motion. If this does in fact occur, then the return travel of the displacer will be identical because of the symmetry of the Δp function given by equation (5) (in the actual case the symmetry is close enough for the return to be practically the same). Thus steady-state overdriven motion occurs at a given shaft speed ω if the initial elapsed time is less than π/ω. We have thus arrived at the following criteria for overdriven mode operation:

Overdriven mode operation occurs at the shaft speed ω if and only if from $x_D = L$ and $\dot{x}_D = 0$ at $t = t_0$ the displacer reaches $x_D = -L$ at a time $t = t_1 \le t_0 + \pi/\omega$.

Now the initial conditions $x_D = L$ and $\dot{x}_D = 0$ when $t = t_0$ yield the following particular version of displacer motion equation (11)

$$x_D = \frac{L\omega^2}{K+\omega^2}\left(\frac{1}{2}(1-\gamma\chi)\exp(\sqrt{K}(t-t_0)) + \frac{1}{2}(1+\gamma\chi)\exp(-\sqrt{K}(t-t_0)) + \beta\gamma^2 \sin \omega t\right) \tag{14}$$

where

$$\gamma = \frac{\sqrt{K}}{\omega}, \quad \beta = \frac{\lambda\kappa}{1-\tau-\rho}, \text{ and } \chi = \sqrt{\beta^2 - 1}$$

This leads to a simpler analytic statement of the above overdriven mode condition:

Lemma 1 Overdriven mode operation occurs if and only if x_D given by equation (14) assumes the value $-L$ for a value of t in the interval $(t_0, t_0 + \pi/\omega]$.

Lemma 1 provides an analytic test for overdriven mode operation. Let $x_D = -L$ in equation (14) and solve for t, numerically of course. If the solution lies within the interval specified in Lemma 1, then the engine will run in steady overdriven mode operation. If there is no solution in the interval it will not run in the overdriven mode.

The result however does not supply a great deal of insight. Of course some insight is usually lost whenever a numerical solution of a crucial equation must be accepted. The complex form of equation (14) also precludes gaining much information directly. Nor does the result identify the independent dimensionless parameters determining overdriven mode operation; it does however narrow down the field of possibilities.

The Main Result. It is possible to show, by entirely elementary means, that the right-hand side of (14) considered as a function of t is decreasing on the interval $I = [t_0, t_0 + \pi/\omega]$ if $\gamma\chi > 1$. The demonstration is purely mathematical and completely independent of the object being modeled; we consider (14) as a mathematical function only, temporarily separated from the fact that it describes displacer position during a subinterval of I.

Therefore the statement that the equation $x_D(t) = -L$ has a solution in the interval I is equivalent to the statement that x_D has a value not more than $-L$ at the right endpoint of I, given the facts that the function x_D is continuous on the interval and has a positive value at the left end. Moreover, the inequality

$$x_D(t_0 + \pi/\omega) \le -L$$

can be reduced to a particularly simple form

$$\gamma\chi + 1 \le (\gamma\chi - 1)\exp(\pi\gamma) \tag{15}$$

This gives us the following result:

Lemma 2 If $\gamma\chi > 1$, then overdriven mode operation occurs if and only if inequality (15) holds.

Lemma 2 is very close to our main result; it only requires logical paring of the antecedent. Suppose that for a given set of parameters we find that $\gamma\chi \le 1$. Then $1 - \gamma\chi \ge 0$ of course so that by examining equation (14) we see that

$$x_D(t) > \frac{L\omega^2}{K+\omega^2}\beta\gamma^2 \sin \omega t \tag{16}$$

for all t in the interval of displacer motion. If the engine is operating in the overdriven mode, then $x_D(t_1) = -L$ for some t_1 in the interval $(t_0, t_0 + \pi/\omega]$ by lemma 1. Thus (16) would give

$$-L = x_D(t_1) > \frac{L\omega^2}{K+\omega^2}\beta\gamma^2 \sin \omega t_1 \tag{17}$$

But $0 < t_0 \le \pi/2\omega$ so that

$$\sin \omega t_1 \ge \sin \omega(t_0 + \pi/\omega) = -\sin \omega t_0 = -\frac{1}{\beta}$$

Thus (17) implies

$$-L > \frac{L\omega^2}{K+\omega^2}\beta\gamma^2\left(-\frac{1}{\beta}\right) = -L\frac{\gamma^2}{1+\gamma^2}$$

which is absurd since L is positive. This demonstrates the following:

Lemma 3 If overdriven mode operation occurs, then $\gamma\chi > 1$.

Finally, we make the purely mathematical and trivial observation that inequality (15) implies $\gamma\chi > 1$. This implication, together with lemmas 2 and 3 yield our main result that overdriven mode operation is logically equivalent to inequality (15)

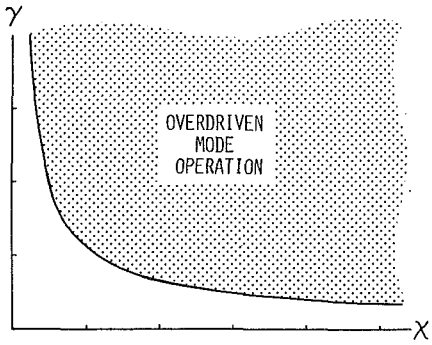

Fig. 8 The region of overdriven mode operation in the γ-χ plane

Theorem A Ringbom engine operates in the overdriven mode if and only if $\gamma\chi + 1 \leq (\gamma\chi - 1) \exp(\pi\gamma)$.

Using the definitions of the hyperbolic functions the inequality in the theorem can be rewritten in the following way

Corollary A Ringbom engine operates in the overdriven mode if and only if $\gamma\chi \sinh(\pi\gamma) - \cosh(\pi\gamma) \geq 1$.

This is the form of the main result given in [2].

Conclusion

By the theorem above, only two dimensionless products, γ and χ, determine the operating mode of the Ringbom engine. This makes the result very practical as a preliminary design tool or as a quick check of stability for new operating conditions or a hardware modification; only a simple hand-held calculator is required. Furthermore, because only two variables are involved, the condition for overdriven mode operation can be represented by a region in the γ-χ plane. This region is shown in Fig. 8. The boundary curve of course has equation

$$\chi = \frac{1}{\gamma} \frac{e^{\pi\gamma} + 1}{e^{\pi\gamma} - 1}$$

If a given engine geometry with given temperatures and shaft speed has its point (χ,γ) lying within the shaded region or on the boundary curve, then it is operating in the overdriven mode. If the point lies outside the region, then it is not running in the overdriven mode.

The most universal value of this model, however, is the insight it gives. By examining the form of χ and γ one can predict important general effects resulting from variable changes, e.g., increasing displacer rod diameter, or decreasing displacer stroke increases the overdriven speed range to a higher value. Reference [3] provides more examples of a less trivial nature. As a final example here, we point out how easily the stability of overdriven Ringboms can be deduced. From Fig. 8 it is clear that if an engine runs in the overdriven mode at some speed ω, then it will run overdriven at all lower speeds, since decreasing only ω increases γ and leaves χ unchanged and thus the new (χ,γ) point lies in the shaded region.

References

1 Ringbom, O., "Hot Air Engine," U.S. Patent 856102, June 4, 1907.
2 Senft, J. R., "The Hybrid Stirling Engine," *Proc. 16th Intersociety Energy Conversion Engineering Conference*, Paper No. 819785, ASME, Atlanta, August 1981.
3 Senft, J. R., "Parameter Effects in Hybrid Stirling Engines," *Consultant Reserch Report* prepared for University of Calgary, December 29, 1981.
4 Senft, J. R., "A Hybrid Stirling Engine," *Engineering in Miniature*, September 1982.
5 Srinivasan, V., Walker, G., Fauvel, R., and Senft, J. R., "Ringbom-Stirling Engine Simulation and Parametric Study," in preparation.
6 Walker, G., *Stirling Cycle Machines*, Clarendon Press, Oxford, 1973.
7 Walker, G., et al., "Future Coal-Burning Stirling Engines," *Proc. I. Mech. E.*, Stirling Engine Conference, University of Reading, March 1982.

On Prediction of Off-Design Multistage Turbine Pressures by Stodola's Ellipse[1]

D. H. Cooke
Stone and Webster
Engineering Corporation,
Houston, TX

The variation of extraction pressures with flow to the following stage for high backpressure, multistage turbine designs is highly nonlinear in typical cogeneration applications where the turbine nozzles are not choked. Consequently, the linear method based on Constant Flow Coefficient, which is applicable for uncontrolled expansion with high vacuum exhaust, as is common in utility power cycles, cannot be used to predict extraction pressures at off-design loads. The paper presents schematic examples and brief descriptions of cogeneration designs, with background and theoretical derivation of a more generalized "nozzle analogy" which is applicable in these cases. This method is known as the Law of the Ellipse. It was originally developed experimentally by Stodola and published in English in 1927. The paper shows that the Constant Flow Coefficient method is really a special case of the more generalized Law of the Ellipse. Graphic interpretation of the Law of the Ellipse for controlled and uncontrolled expansions, and variations for sonic choking and reduced number of stages (including single stage) are presented. The derived relations are given in computer codable form, and methods of solution integral with overall heat balance iteration schemes are suggested, with successful practical experience. The pressures predicted by the relations compare favorably with manufacturers' data on four high-backpressure, cogeneration cycle turbines and three large utility low-pressure ends.

Introduction

In power plant cycle analysis of predesigned or existing equipment systems, using high-speed digital computer heat-and-mass-balance codes, the determination of turbine extraction pressures at various off-design stage flows is extremely important. Such pressures directly affect the thermal balance around each heater, and iteratively establish the cycle flows for each final solution. It is important that the manufacturer's design pressures be matched as closely as possible, and, in flow deviations away from design or predicted loads, that a correct and consistent set of pressure-flow relations be followed.

There are many times during design of a power plant, and after commencement of commercial operation, when an owner or engineer needs to explore off-design and/or abnormal conditions between and beyond the normal data provided by the manufacturer. Heaters out of service or degraded in performance, emergency bypass of turbine generators after a load-trip, steady-state extremes for transient system analyses, economic effect of possible cycle modification alternatives, and matching of test data in plant performance diagnoses are but a few occasions where accurate exploratory heat balance analysis is necessary.

The ability to accomplish this work expeditiously has been greatly enhanced in the last few years by the availability of generalized heat-and-mass-balance codes by independent software firms, e.g., SYNTHA, PEPSE, and THERM. With these codes, using the basic "thermal-kit" data provided by the manufacturer, the owner or engineer can interpolate and/or extrapolate from the normal load points to determine with reasonable accuracy the two essential unknowns for off-design performance: (1) bowl and shell *pressures*, and (2) turbine group *efficiencies*. To accomplish this, the codes provide consistent but limited sets of rules, the most common of which is that of [1].

Another phase of power plant design where the pressure and efficiency "rules" become even more important is that of early, conceptual cycle design work before selection of a turbine manufacturer. The economic optimization of a conceptual cycle must conform to reasonable and correct design and off-design criteria, so that the desired operating range may be readily achieved by prospective turbine-generator and heat transfer equipment suppliers.

The purpose herein is to describe and derive general relations for determining bowl and shell pressures in controlled and uncontrolled turbine expansions, including individual stage choking effects. These relations are based on an extensive research of the literature. Their exposition is theoretical rather than empirical, but design and off-design data provided by turbine manufacturers is presented for practical comparison. It is hoped that this work may enhance

[1] Winner of the 1985 Prime Movers Committee Award

Contributed by the Gas Turbine Division and presented at the Joint Power Generation Conference, Toronto, Ontario, Canada, September 30–October 4, 1984. Manuscript received at ASME Headquarters June 21, 1984. Paper No. 84-JPGC-GT-14.

industry theoretical and practical understanding in these areas.

Theoretical Bases

One of the most useful of engineering parameters in turbine design work is known as the mass flow coefficient,

$$\phi = \frac{W}{\sqrt{\frac{P}{v}}}, \quad \text{or} \quad \phi_T = \frac{W\sqrt{T}}{P}. \tag{1}$$

Whereas the volume form of this parameter is generally correct for all compressible fluids, the temperature form on the right is applicable only when the perfect gas law $Pv = RT$ can be assumed to apply. Either parameter is an index of total mass flow entering the nozzle throat of an expansion, according to relations for compressible, isentropic flow in a single nozzle, from [2]:

$$\frac{\phi}{A} = \frac{1}{12}\sqrt{\frac{2Gk}{k-1}}\left(r^{\frac{2}{k}} - r^{\frac{k+1}{k}}\right)^{1/2}, \text{ or} \tag{2}$$

$$\frac{\phi_T}{A} = \sqrt{\frac{2GJc_p}{R}}\left(r^{\frac{2}{k}} - r^{\frac{k+1}{k}}\right)^{1/2}. \tag{3}$$

The mass flow coefficient ϕ should not be confused with the closely related *nozzle* flow coefficient, which accounts for the reduction in effective flow area due to nonuniform velocity profile, as with boundary layer buildup at low flow and Reynolds number.

It will be noted that as long as the effective flow area remains fixed, flow coefficient is a constant times the radical on the right, which is a function of the outlet pressure ratio r across the nozzle. The r function maximizes at a pressure ratio

$$r^* = \left(\frac{2}{k+1}\right)^{\frac{k}{k-1}}. \tag{4}$$

Thereafter, for lower outlet pressure ratios, which can be caused either by higher inlet or lower outlet pressure, the flow coefficient is truly constant, unless the effective area changes, and the nozzle is said to be "choked." Under choked conditions the acoustic velocity for the flowing fluid exists in the nozzle throat (whether or not the flow is isentropic), and decreases in outlet pressure cannot be sensed upstream. Downstream of the choked throat, expansion to lower backpressures will occur through an expansion wave in supersonic flow, which may be followed by one or more compression shocks.

The row-by-row turbine performance calculation method generally follows the theory for a *single nozzle* as in equations (1)–(4). Another method, known as the stage-group method, features the idea of the "nozzle analogy." In such an analogy, entire groups of turbine stages are treated as if they were single nozzles. This concept is the predominant subject of the remaining theoretical discussions in this paper. Prior to embarking on these discussions, however, a review of practical multistage turbine designs is in order.

Uncontrolled Versus Controlled Expansion

A schematic example of the typical utility power uncontrolled expansion to high vacuum is shown in Fig. 1. Downstream of the throttle, the entire expansion is characterized by *fixed flow areas*, inasmuch as the reheat stop valve (RSV) and intercept valve (IV) are designed to remain fully open during all normal operating modes. This is in contrast to the throttle, which is designed to modulate at all loads below absolute maximum throttle flow, in order (in U.S. systems) to maintain constant pressure at boiler outlet.

The numbered dots in Fig. 1 represent locations of bowl and shell pressures at significant points in the turbine expansion. The term "bowl" refers to the average inlet *total* pressure upstream of a nozzle or stationary blade row, usually at an extraction point. The term "shell" refers to outlet *static* pressure immediately downstream at the pitch diameter of

Nomenclature

A = nozzle effective throat area, ft^2
a = effective critical pressure ratio for group, outlet/inlet
B = backpressure (exit static pressure), psia
c_p = specific heat at constant pressure, BTU/lb-R
D = parameter grouping for acoustic formulation
G = gravitational constant, 4.1698×10^8 ft/hr^2
g = gravitational constant, 32.174 ft/s^2
J = mechanical equivalent of heat, 778.17 ft lb/BTU
K = proportionality constant for Stodola's ellipse
k = isentropic expansion exponent
n = number of pressure stages in group
P = inlet total pressure to the first stage nozzle of group, psia
R = gas constant, ft/R
r = nozzle pressure ratio, outlet/inlet
r^* = nozzle critical pressure ratio, outlet/inlet
T = absolute temperature, R
U = blade speed at pitch diameter, ft/s
V = absolute velocity, ft/s
v = specific volume, ft^3/lb
VWO = valves wide open
W = mass flow, lb/hr
w = relative velocity, ft/s
X = the ratio B/P for multistage group
Y = Stodola constant in formulation
Z = surrogate variable in acoustic derivation (for X)
η_{ST} = turbine total to static efficiency
ξ = pressure ratio factor in acoustic formulation
ρ = reaction, fraction of stage head expanded in rotor
Φ = ratio of mass flow coefficient to that at choking
ϕ = mass flow coefficient, volume form, in.-ft$^{3/2}$/hr
ϕ_T = mass flow coefficient, temperature form, in.^{2}-R$^{1/2}$/hr
Δ = stack shift, difference in relative design flow ratio between adjacent multistage groups at any given load

Conditional Subscripts and Superscripts

av = average
D = design
i = any multistage group
s = volume form (P); according to Stodola (W/A)
t = temperature form (P); true (W/A); throat choking (B)
x = extraction
1,2,3 . . = specific multistage group, or stage in group
0,1,2 = inlet, after stator, after rotor
$*$ = value at choking (throat Mach number unity)
n = nth stage, counting upstream from exit

the last stage exit from a given group. The shell pressures are usually taken as true extraction pressures, although there may be a significant radial vortex pressure differential at the exit of a given stage or group, particularly at far off-design loads, and account must be taken for pressure losses at exit from the turbine shell, if significant, and in the extraction piping.

Controlled Expansion. A simplified controlled expansion arrangement typical of a recent cogeneration application is shown in Fig. 2. The expansion is broken up into several separately controlled segments, each preceded by variable flow area control devices represented as valves A, C, and F. The backpressures at the end of each segment, at points B, D, and J, are held constant at high levels to meet the owner's process steam requirements. These backpressures must remain constant at all flows. As the process steam demand increases at point B, for example, valve C will automatically close to restore the pressure in the header. This reduces flow in the following segment. Theoretically, such increased demand at point B could proceed until the flow to the downstream segment reached zero. In practice, maximum limits are placed on process steam demand from the turbine at each controlled extraction, with emergency "letdown" as at valve K, if necessary to maintain header pressure, in order to avoid damage to downstream turbine and boiler components by reduced flow.

Controlled extractions may be integral with the turbine casing as at point B, or between turbine casings as at point D, with pressure control at E. The extraction and backpressure control devices at C, E, and F are most efficiently designed as sequential valve steam chests with variable admission control stages to reduce throttling, but various simpler and less expensive devices, equivalent to the single throttle valves shown in the figure, are also commonly used.

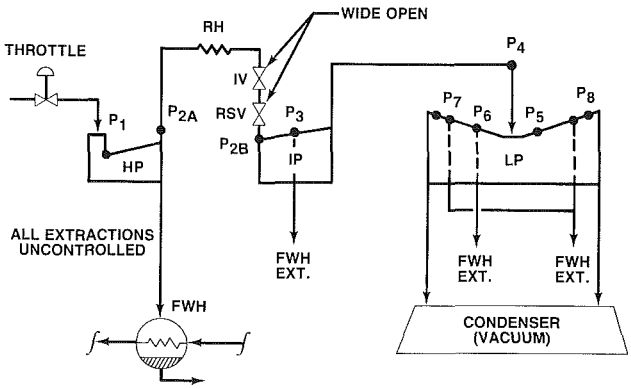

Fig. 1 Uncontrolled multistage expansion to high vacuum

Uncontrolled extractions for feedwater heating are usually included in the design as at G and H. The controlled backpressure segment between F and J is typical of pressure modeling on any uncontrolled (fixed flow area) segment in the cycle, and is therefore the example for derivations in theoretical sections to follow.

Constant Flow Coefficient for Uncontrolled Expansions. For the system shown in Fig. 1 it has long been recognized [3], [4] that at any point i in the expansion downstream of the throttle, the bowl pressures are related to the mass flow entering the immediate nozzle throat by the relation

$$\phi_i = \frac{W_i}{\sqrt{\frac{P_i}{v_i}}} = \text{constant.} \tag{5}$$

This is empirically known to be true for uncontrolled multistage expansion to high vacuum, regardless of the fact that stages upstream of the very last stage are seldom, if ever, acoustically choked, even at maximum design flow. Figure 3 is a plot of bowl pressures for four utility power turbine-generator units by major manufacturers of this equipment, showing that all bowl pressures are linear with W^2v, which is the implication of equation (5).

The term "relative design flow index" refers to the ratio of W^2v to its value at the design point, taken as the valves-wide-open (VWO), 5 percent overpressure condition. Each "position ray" has its own reference design value and the abscissa plots for a given load shift from ray to ray as shown in Fig 3. This shifting phenomenon will be termed "stack shift."

The W^2v index and its temperature form counterpart, $W\sqrt{T}/W_D\sqrt{T_D}$ have roughly the same numerical values as W/W_D at any given part load point. Pressures are almost directly linear with flow, therefore, in designs of this type, and the use of the temperature form of the equation introduces but a small error depending on the region of steam properties traversed.

The points in Fig. 3 have been scaled for display from their actual values to pressures for corresponding positions for the 607.2 MWe unit, so that it appears that each manufacturer designed the same unit. This is valid procedure only if the relations are linear. The small scatter of the points can be attributed in most cases to round-off error, or possible errors in transposing manufacturers' heat balance data.

There are two significant issues which are apparent from the linear multistage pressure relations shown in Fig 3. The first is that, regardless of pressure ratio, the flow coefficient is constant, and bowl pressures are independent of intermediate backpressures, even though the individual stages are not

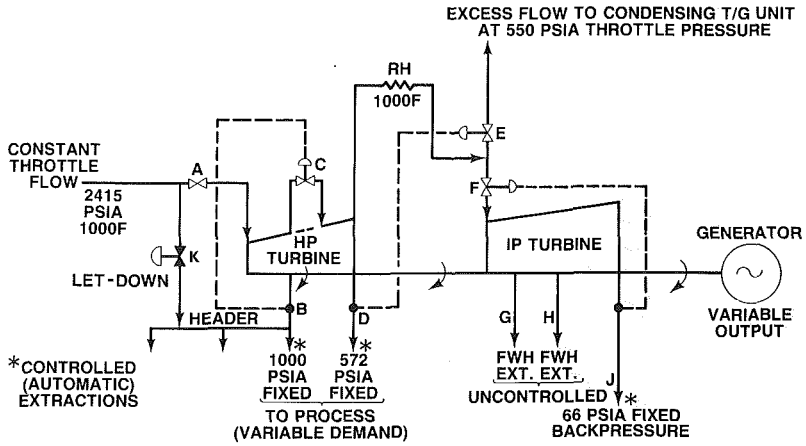

Fig. 2 Controlled expansion cogeneration schematic

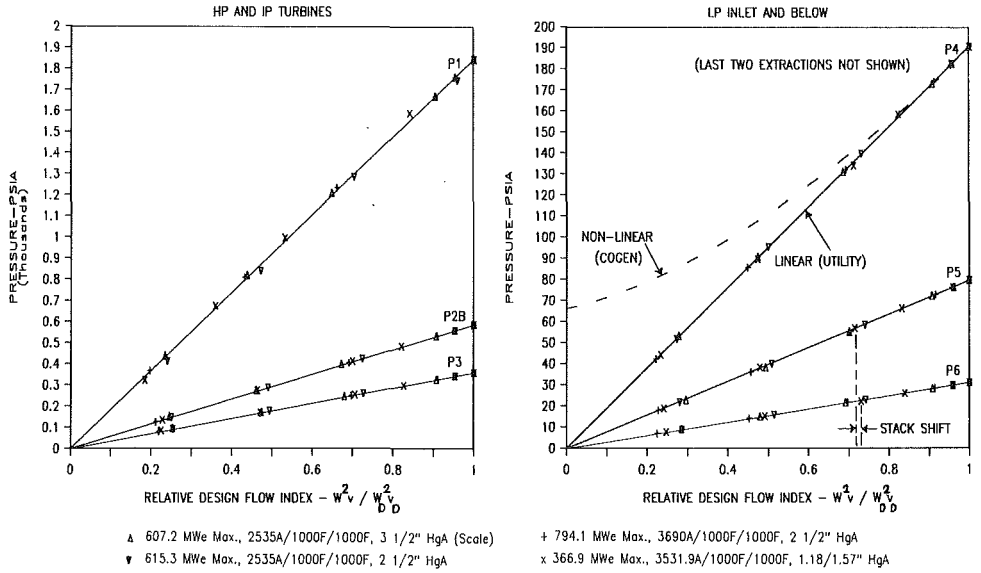

Fig. 3 Constant flow coefficient design comparison (uncontrolled extractions)

acoustically choked. The second is that such linear relations, passing through the graph origin, could not be valid for controlled expansions like Fig. 2 or, for that matter, any variable flow expansion to fixed high backpressure, as indicated schematically by the dashed "cogen" curve in Fig 3. These two issues are resolved in the paragraphs to follow.

Law of the Ellipse for Many Stages

Consider the multistage turbine expansion segment with several uncontrolled extraction groups as shown in Fig. 4, where the final backpressure is some fixed value. For any extraction group i where i is 1, 2, or 3, as in the figure, a nozzle analogy may be developed which treats each entire group expansion as if it were a single nozzle. This analogy is known as Stodola's Ellipse [5, 6], and states that

$$\phi_i \propto \sqrt{1 - \left(\frac{B_i}{P_i}\right)^2}. \tag{6}$$

This proportionality is mathematically valid only for an infinite number of pressure stages, but it is empirically valid down to as few as eight 50-percent reaction stages, as determined by Stodola using an eight-stage laboratory turbine at the Polytechnicum in Zurich early in this century. The assumption is that all nozzle flow areas remain constant. The calculation of the bowl pressure on the variable admission control stage is therefore not included, although the relations for single stage to be developed later in this paper could be used on each admission arc segment bowl, if the individual VWO design flows and bowl pressures are known.

Since the limit of the right-hand radical in relation (6) is unity as the backpressure approaches zero, the proportionality explains why the flow coefficient is constant in the multistage expansions to high vacuum previously discussed. In the multistage groups of Figs. 1 and 3, the backpressure of each succeeding group "floats" on the "stacked" downstream backpressures, culminating in vacuum, so that the radical in relation (6) approaches unity when the ratio B_i/P_i becomes very small, which is effectively the case for each cumulative stack of groups relative to the high-vacuum exhaust. The resulting constant flow coefficient condition implies that the pressure ratio for each individual stage does not change appreciably with flow for a large number of stages with low backpressure. A constant value of r is, of course, the only way flow coefficient can be constant in equations (2) and (3) other than by choking.

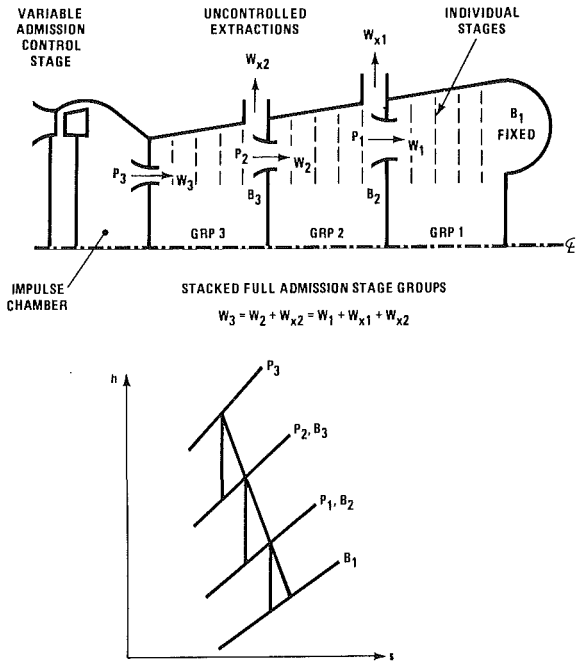

Fig. 4 Pressure-flow arrangement, multistage segment

The development of the proportionality into the familiar elliptical equation, with semimajor axis unity, is shown in Fig. 5 from [7]. Some observers have said that the elliptical relation holds down to some outlet pressure ratio B_i/P, well below the single nozzle choking value of about 0.5, below which the curve is flat. It is more precise to say the relation applies mathematically for an infinite number of stages, so that choking *never* occurs, and the ellipse holds infinitesimally close to zero B/P. The progressive reduction in overall choking pressure ratio with increasing numbers of choked, cascaded nozzles is indicated in Fig. 5, which illustrates how the "flat" disappears for a large number of stages.

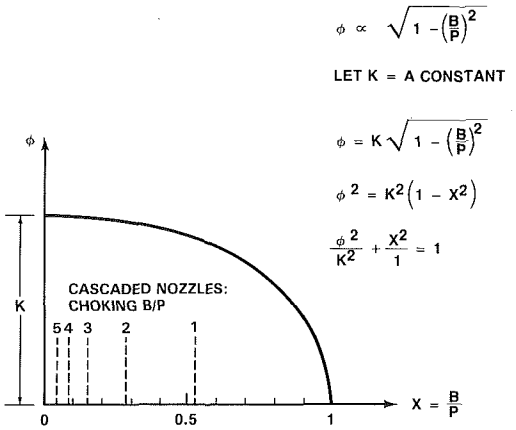

Fig. 5 Stodola's ellipse for infinite number of stages (unchoked)

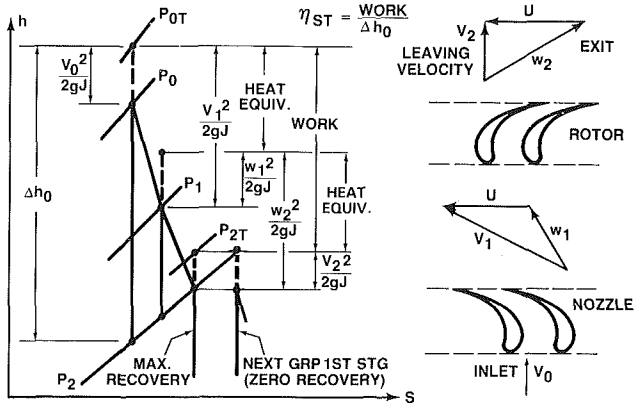

Fig. 6 Group last stage pressure-velocity relations

Derivation of Codable Equations. The proportionality in (6) can be restated as

$$\frac{\phi_i}{\phi_{iD}} = \frac{\sqrt{1-\left(\frac{B_i}{P_i}\right)^2}}{\sqrt{1-\left(\frac{B_{iD}}{P_{iD}}\right)^2}}, \tag{7}$$

where the subscript D refers to the "design set" of the four variables W, P, v, and B, for the volume form of the flow coefficient, or W, P, T, and B for the temperature form. This set is determined from any known load where all flows and pressures in each group are established in relation to each other "by design." In the initial cycle design, this is usually the most efficient operating condition where the pressures of all extractions are set to give nearly equal feedwater temperature rise. For conventional utility cycles this is usually near the maximum flow condition, but in cogeneration cycles the "design load" may be as low as 50 percent of maximum.

By algebraic rearrangement and reduction of equation (7) the following results

$$P_i = \frac{B_i}{\sqrt{1-\phi_i^2 Y_{iD}}}, \tag{8a}$$

or

$$B_i = P_i\sqrt{1-\phi_i^2 Y_{iD}}, \tag{8b}$$

where

$$Y_{iD} = \frac{P_{iD}^2 - B_{iD}^2}{P_{iD}^2 \phi_{iD}}. \tag{9}$$

The "Stodola constant," Y_{iD}, is fixed for all loads. The flow coefficient ϕ_i and ϕ_{iD} may be either of the forms in equation (1) and is the same as that used in most programs based on constant flow coefficient, which should facilitate computer application of these relations.

Equation (8*a*) permits solving for the group inlet pressures "backwards," starting with the known fixed backpressure B_1, in Fig. 4, and working upstream.

For each iteratively established set of flows W_1, W_2, and W_3 for the uncontrolled segment, a new set of pressures P_1, P_2, and P_3 can be calculated for the next iteration.

Equation (8*a*) is, of course, not explicit since ϕ_i contains P_i. Further reduction is necessary depending upon the form of flow coefficient. For the "volume" form, a quadratic equation,

$$P_i^2 - W_i^2 v_i Y_{iD} P_i - B_i^2 = 0 \tag{10}$$

results, so that

$$P_i = \frac{W_i^2 v_i Y_{iD} + \sqrt{W_i^4 v_i^2 Y_{iD}^2 + 4B_i^2}}{2}. \tag{11}$$

In using the quadratic formula to derive equation (11), the sign before the radical must be positive, because a negative sign will always give a negative pressure (squared first term under the radical).

For the "temperature" form of flow coefficient the derivation is much simpler, resulting in

$$P_i = \sqrt{W_i^2 T_i Y_{iD} + B_i^2}. \tag{12}$$

The temperature form of flow coefficient always seems to result in much simpler algebraic formulations and has been recommended by Brown Boveri Corporation and Siemens-Allis, Inc. as sufficiently accurate for superheated steam.

Solving the group inlet pressures backward as in Fig. 4 and equations (8*a*), (11), and (12), is usually necessary during some part of the cycle analysis, but is the reverse of the iterative progression in some heat balance codes. The form in equation (8*b*) allows solving "forward" for progressive backpressures, working downstream in each segment, starting with an assumed value for P_3 in Fig. 4. Simple reductions result for each form of flow coefficient. For the volume form

$$B_i = P_i\sqrt{1-\frac{W_i^2 v_i}{P_i} Y_{iD}}, \tag{13}$$

and for the temperature form,

$$B_i = \sqrt{P_i^2 - W_i^2 T_i Y_{iD}}. \tag{14}$$

Equations (11)–(14) have been successfully used by Syntha Corporation in converging on multiple controlled-segment cycles.

Total and Static Pressures. The *h–s* plot in Fig. 4 shows that these relations assume that the leaving velocity from the last stage of each group is completely dissipated (zero recovery), in order that the exit static pressure from each group is the same as the inlet total pressure to the next group as shown in Fig. 6. This will cause no error if the upstream group efficiency is properly adjusted to account for any velocity recovery (carryover). In further work using dynamic similarity relations to determine leaving energy, it is planned to refine this approach.

Graphic Visualization (Unchoked). Figure 7 shows a graphic visualization of pressure-flow variations according to the foregoing relations for three stacked multistage groups as in Fig. 4. The curves are for an imaginary design wherein the pressure is linear with flow when acoustically choked, as defined at equations (2), (3), and (4). An example of such a design would be a turbine expanding a perfect gas at constant inlet temperature over the entire load range.

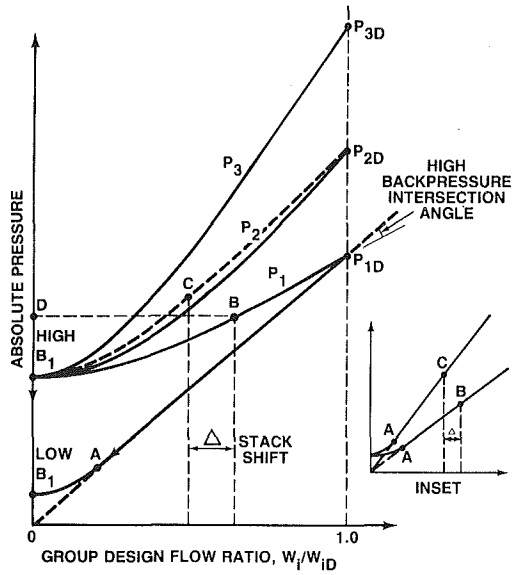

Fig. 7 Graphic visualization pressure versus flow (unchoked)

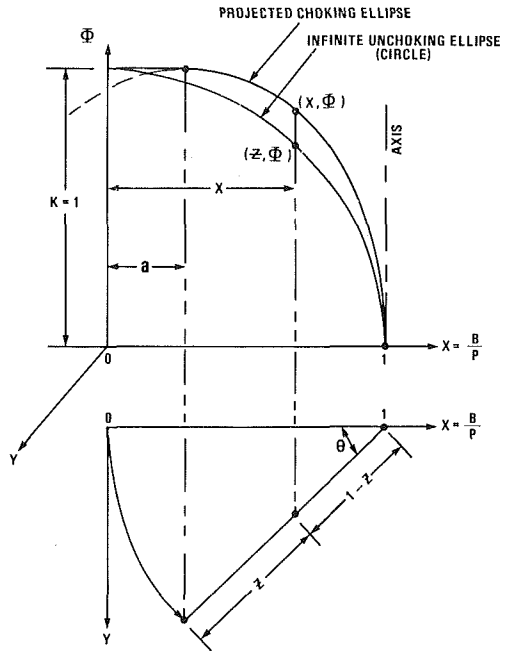

Fig. 8 Construction of finite acoustic choking form of Stodola's ellipse

For high backpressure, the pressure relations are curves intersecting rays from the origin at an angle as shown at point P_{1D}. As the backpressure is decreased, and point B_1 moves downward along the ordinate, the pressure curves stretch until curve P_1 is tangent to the ray at P_{1D}, then the curve lies along the ray as point A moves down the ray toward the origin. Point A is where the curve significantly departs from the ray. Between points A and P_{1D} the radical in equation (6) is very nearly unity, and the pressure acts as if the flow in the group were acoustically choked (flow coefficient constant). This is the condition of all groups plotted in Fig. 3.

It will be noted that the slope of all curves is zero at zero flow, as the derivative of pressure with respect to flow, at zero flow, in equations (11) and (12) would indicate.

The design flow ratio can be different for each group at any given load between zero and 1.0. The difference between W_i/W_{iD} for adjacent group pressure curves for a given load is termed stack shift. For standard utility power designs as in Fig. 3, the normal design stack shift is usually less than 6 percent, but for variable abnormal operating conditions, such as heaters out of service or high reheat attemperation spray, the stack shift can be as high as 15 or 20 percent.

For high backpressure, stack shift changes the shape of the curves. For example, say bowl pressure curve P_1 is operating at point B. Curve P_2, operating at a lower flow ratio, senses a higher backpressure than if the downstream group were at the same flow ratio. The effect is to reduce the "bow" in the curve to that at point C. (Curve P_2 instantaneously tries to head for point D on the curve as the flow is lowered, but ultimately must end up at B_1.)

The above phenomenon does not occur for adjacent groups at low backpressure for operating flows between A and P_{1D} in Fig. 7. The stack shift cannot affect the bow in the curve, because there is none (see inset). This proves that constant flow coefficient is a valid assumption for all utility power designs similar to Fig. 3 regardless of stack shift.

Sonic and Finite Stage Effects

It has been shown that if the Law of the Ellipse, as expressed in relation (6), is taken to be mathematically valid only for an infinite number of stages, the ellipse holds infinitesimally close to zero B/P, as shown in Fig. 5. In that figure, K is the limit of the value of flow coefficient as B/P approaches zero. There is no limit on flow per unit area W/A since theoretically, for any flow, however large, with a correspondingly high inlet pressure P a sufficient number of stages can be assumed so that the individual nozzles do not choke acoustically.

Suppose, as suggested by Csanady in [5], we define a relative choking flow coefficient Φ as the ratio of the actual ϕ to the value ϕ^*, where one or more of the stages in the group chokes acoustically, at a corresponding effective group outlet critical pressure ratio a. We then can establish a direct correlation between the radical in relation (6) with the r function in equations (2) and (3), in terms of a finite number of stages and an average single isentropic nozzle critical pressure ratio r^*.

Figure 8 shows the construction of relations needed to establish the above correlation. The value of K for the infinite unchoking ellipse previously defined is now unity because of the definition of Φ. The equation of the infinite ellipse in terms of a surrogate variable Z is

$$\Phi = \sqrt{1 - Z^2}, \tag{15}$$

which is, of course, a circle.

The point (x, Φ) is any point on a projected ellipse generated by swinging the infinite circle out by an angle θ and projecting it back onto the plane, so that the finite ellipse chokes at a. The remaining steps are as follows:

$$X = 1 - (1 - Z)\cos\theta \tag{16}$$

$$Z = 1 - \frac{(1 - X)}{\cos\theta} \tag{17}$$

$$\cos\theta = 1 - a \tag{18}$$

$$\Phi = \sqrt{1 - \left(\frac{X - a}{1 - a}\right)^2} \tag{19}$$

$$\Phi = \sqrt{1 - \left(\frac{B - Pa}{P - Pa}\right)^2} \tag{20}$$

Equation (20) is the basic finite acoustic choking form of Stodola's ellipse. There are now two ways the radical can effectively become unity: (1) when the ratio B/P is very low, as before, and (2) when $B - Pa$ is zero, which corresponds to acoustic choking. The product Pa is the same as the choking backpressure B_t which Csanady [5] suggests should be subtracted from B. The same quantity must also be subtracted

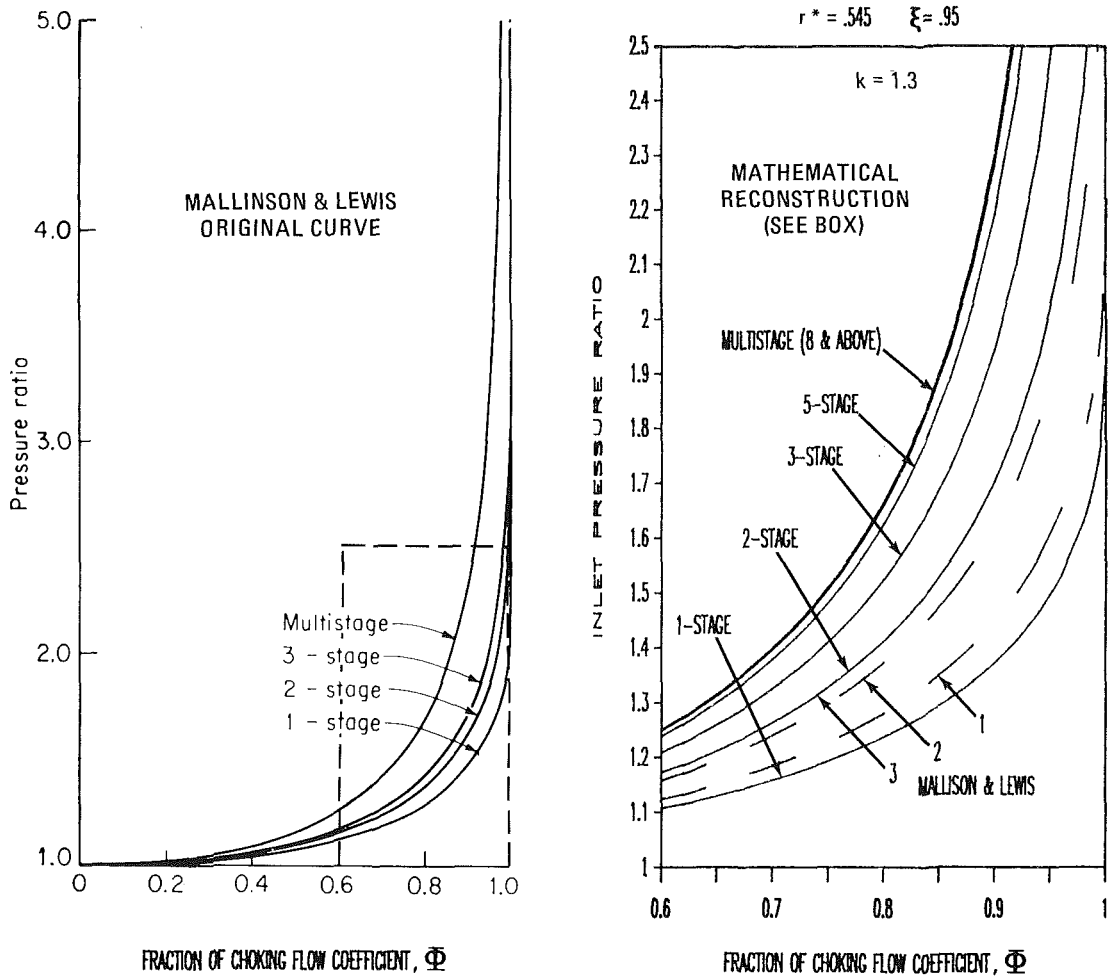

Fig. 9 Effect of number of stages

from P in the denominator, however, in order for the relation to be reasonable.

The quantity $B-Pa$ can never be allowed to become negative, in order to conform to the physical choking phenomeon (a negative value implies a negative absolute pressure, which is not a physical reality). Once the stage group becomes choked, Φ remains unity for higher values of P, and the points lie along the straight line segment to the left of the upper dot in Fig. 8. If negative $B-Pa$ were allowed, the ellipse would continue mathematically as shown by the dashed curve.

The effective choking pressure ratio a for the group can be defined as

$$a = (\xi r_n^*)^n \tag{21}$$

where n is the number of *pressure* stages in the group, and ξ is a pressure-ratio loss factor slightly less than unity. Equation (21) is based on the fact that the group outlet/inlet pressure ratio is the product

$$\frac{B_1}{P_n} = \frac{B_1}{P_1} \times \frac{P_1}{P_2} \times \frac{P_2}{P_3} \times \ldots \times \frac{P_{n-1}}{P_n} \tag{22}$$

for which the intermediate stage pressures cancel. It can be assumed that when the group chokes, one or more stages in the group will be operating at the inlet isentropic critical pressure ratio r_n^* for the first nozzle in the group, which may be determined from [8], according to the group inlet pressure and enthalpy. This is a reasonable assumption where the expansion is completely in either the superheated or wet region, because the critical pressure ratio usually does not change appreciably during an isophase expansion. Where there is a significant change, or the expansion line crosses the saturation line, an average value

$$r_{av}^* = (r_1^* r_2^* r_3^* \ldots \ldots r_n^*)^{1/n} \tag{23}$$

may be used.

The foregoing approach tacitly assumes that each *work* stage (i.e., stator-rotor combination) is designed at about the same relative choking flow coefficient Φ. It is not implied that each pressure stage in the group must choke simultaneously. The number of pressure stages for a pure impulse work stage is one. The number of pressure stages for a 50-percent reaction work stage is two. For intermediate reactions less than 50 percent, the rotor blades will not be near choking when the group chokes, but the fractional number of pressure stages included for intermediate reaction rotors affects the value of a according to equation (21).

The factor ξ accounts for the fact that the expansion is not isentropic. In order to achieve sonic conditions in the nozzle throat, a slightly larger pressure drop than that corresponding to r^* must be taken on account of the energy dissipation between inlet and throat. Based on enthalpy-drop efficiency coefficients of 0.95 for typical nozzle blades and 0.90 for rotor blades, from [9], values of *pressure ratio factor*, ξ = 0.95 for high pressure stages, and ξ = 0.97 for low pressure stages have been used in applying these relations.

Stage-Number Correlation. Figure 9 shows an original curve of small stage-number effects on Stodola's ellipse by Mallinson and Lewis [10] as discussed by Csanady [5]. The pressure ratio is the *inlet* pressure ratio (inverse B/P). Otherwise, the "multistage" curve is a plot of equation (15).

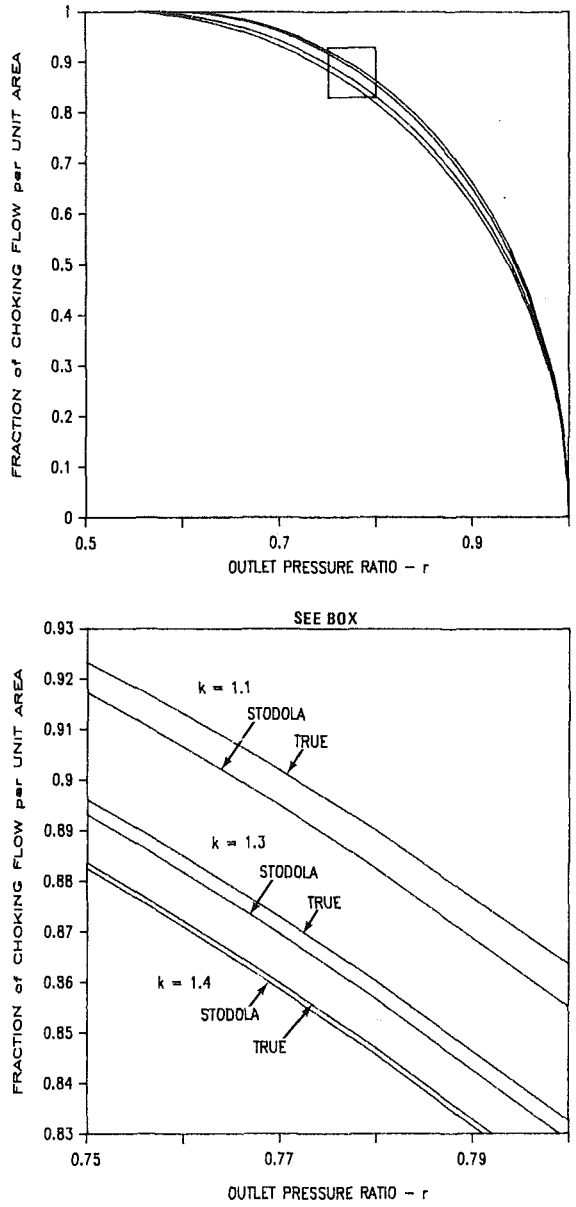

Fig. 10 Single isentropic nozzle correlation

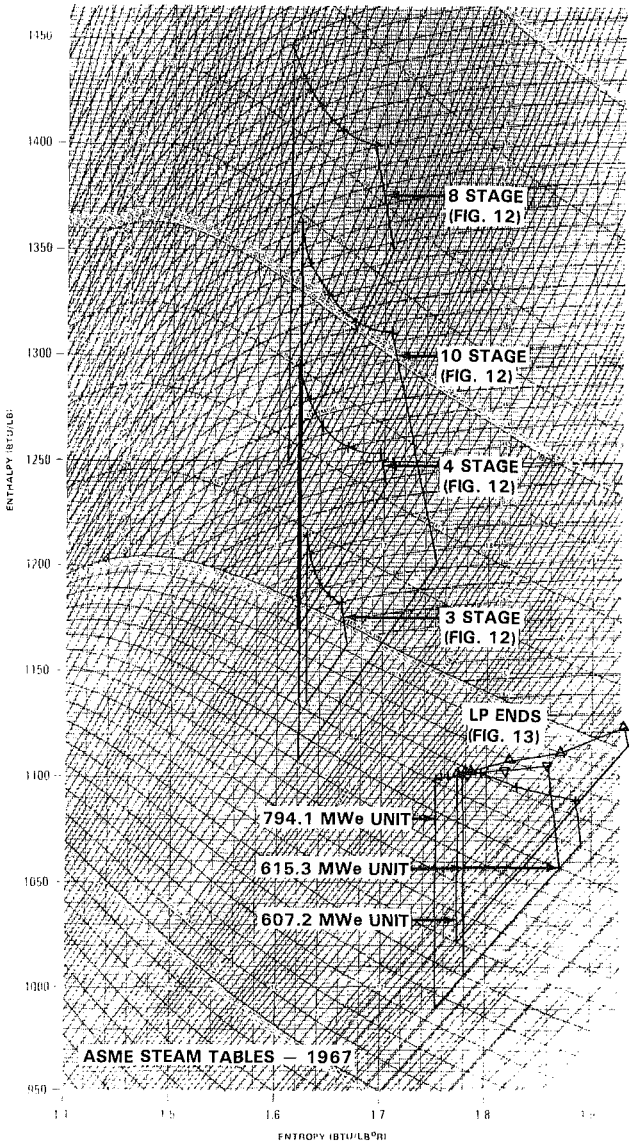

Fig. 11 Thermodynamic property regimes of designs compared

The curves have been mathematically reconstructed according to equations (20) and (21) in Fig. 9. Using the correlation thus provided with n, it can be seen that for eight pressure stages (four 50-percent reaction stages) the infinite Stodola relation coincides within a heavy line, as shown in the figure. For 16 pressure stages (corresponding to Stodola's eight-stage reaction machine) the coincidence is within a very light line.

The Mallinson and Lewis small stage-number curves were based on experimental data for 1, 2, and 3 *work* stages. Their single-stage curve chokes at a considerably higher inlet pressure ratio, indicating that the test turbine may have had considerable reaction. The two and three-stage data fall below the relations based on equations (20) and (21). If their machines were impulse turbines, they would conform to $a \propto 1/\sqrt{n}$. This function has no apparent rational basis and predicts coincidence with the infinite multistage curve at much higher n values than Stodola or the body of manufacturers' data compared in this paper. Rather than assume their test turbines had negative reaction, it is thought more likely that Mallinson and Lewis plotted the flow coefficient relative to *design* for the two and three-stage machines instead of relative to choking. The recognition of the abscissa as relative to choking was made by Csanady, but does not seem to have been recognized by Mallinson and Lewis.

Incidence and Speed Effects. Mallinson and Lewis [10] and others have stated that the Law of the Ellipse is only valid for blade flow angles near design. Using the pressure ratio factor ξ the increased incidence loss at far off-design loads can be properly accounted for so that the relations will hold at any design load. In the same vein, Csanady [5] notes that the elliptical relation would not be completely independent of rotative speed, and would not hold down to zero speed. With correction for incidence using ξ, the entire expansion can be regarded as a series of stationary nozzles with the "heat equivalent" of shaft work removed as shown in Fig. 6. Rotative speed should, therefore, have no effect.

Single Nozzle Correlation. If the foregoing relationships are valid, it should be possible to represent a single isentropic nozzle using (at fixed inlet thermodynamic conditions) equations (19) and (21), wherein $\xi = 1.0$ and $n = 1$. Figure 10 is a comparative plot of the "true" relation according to equations (2), (3), and (4)

$$\frac{(W/A)_T}{(W/A)_T^*} = \sqrt{\frac{r^{\frac{2}{k}} - r^{\frac{k+1}{k}}}{r^{*\frac{2}{k}} - r^{*\frac{k+1}{k}}}} \tag{24}$$

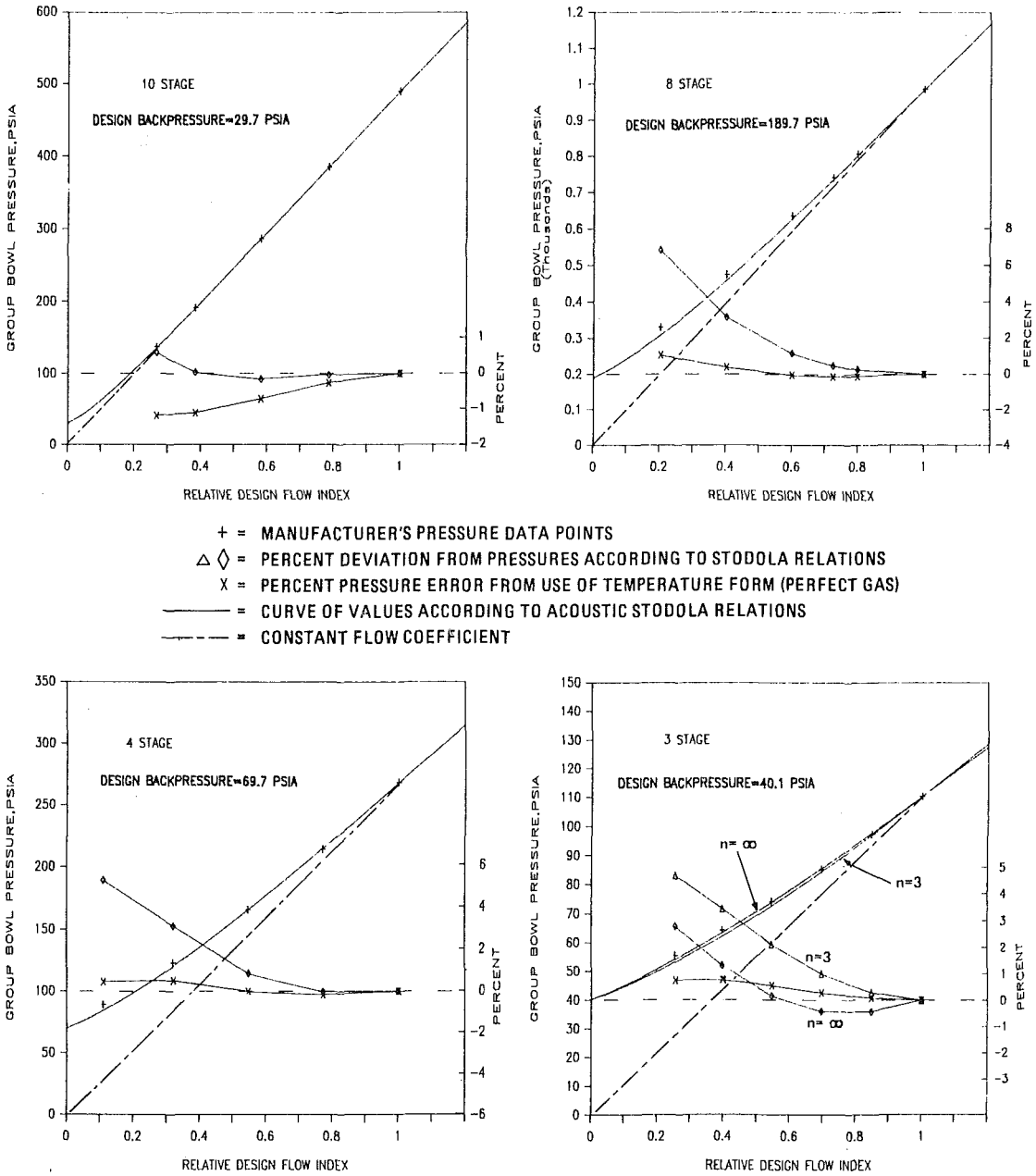

Fig. 12 Comparison of controlled expansion designs

against that predicted by the simpler acoustic form of Stodola's equation

$$\frac{(W/A)_s}{(W/A)_s^*} = \sqrt{1-\left(\frac{r-r^*}{1-r^*}\right)^2}. \tag{25}$$

The close correlation of the two distinct functions can be seen in the blow-up of the small box in Fig. 10. Even for $k = 1.1$ (wet steam), the agreement is within 1/2 percent. If these functions were expanded in series it is conjectured that the significant terms may be identical. This close correlation is believed to be the main reason the Law of the Ellipse works so well.

Modification of Codable Equations. The basic proportionality from which all of the infinite form equations were derived was stated in relation (7). This proportionality can be restated in the finite acoustic form as

$$\frac{\phi_i}{\phi_{iD}} = \frac{\sqrt{1-\left[\dfrac{B_i - P_i a}{P_i(1-a)}\right]^2}}{\sqrt{1-\left[\dfrac{B_{iD} - P_{iD} a}{P_{iD}(1-a)}\right]^2}}. \tag{26}$$

The Stodola constant (9), which is fixed for all loads, takes the form:

$$Y_{iD} = \frac{(P_{id} - P_{iD}a)^2 - (B_{iD} - P_{iD}a)^2}{P_{iD}^2 \phi_{iD}^2}. \tag{27}$$

In coding equation (27), the first of two choking tests to prevent negative values of $B - Pa$ should be made. If $B_{iD} - P_{iD}a$ is negative, the *design* is choked and Y_{iD} takes the form

$$Y_{iD} = \frac{(1-a)^2}{\phi_{iD}^2}. \tag{28}$$

For the volume form of flow coefficient the bowl pressure of each group may be determined from

$$D_i = W_i^2 v_i Y_{iD} - 2a B_i \tag{29}$$

and

$$P_i = \frac{D_i + \sqrt{D_i^2 + 4(1-2a)B_i^2}}{2(1-2a)} . \tag{30}$$

Here the second of the two choking tests should be made. Having calculated P_i from (31), if $B_i - P_i a$ is negative, the group is operating choked and equation (30) should not be used.

$$P_i = P_{iD}\left(\frac{W_i^2 v_i}{W_{iD}^2 v_{iD}}\right) \tag{31}$$

Equation (31) will be recognized as the constant flow coefficient relation.

The choked forms in the above relations are simply the forms taken when $B_{iD} - P_{iD}a$ or $B_i - P_i a$ are set to zero.

Current Design Comparisons

The foregoing relations have been applied in comparing with manufacturers' data for a number of currently operating turbine designs. Figure 11 shows the steam property regimes traversed by each design over the load range. Bowl pressure, enthalpy, and flow at five or six operating load points from approximately 25-percent to 100-percent design flow were provided on four controlled-extraction, cogeneration designs by General Electric Company [11].

Data were also compared on three low-pressure ends from three of the large utility units of several major manufacturers plotted in Fig. 3. The three LP ends chosen were all nearly at the same backpressure.

In all of the comparison plots in the next figures, the curves and manufacturers' data are plotted against volume form relative design flow index, $W^2 v / W_D^2 v_D$. This allows plotting of the Stodola relation curves without thermodynamic property values, since the properties for the compared designs were known only at the discrete data points. The relative $W^2 v$ plots also show clearly the departure of the high backpressure curves from linearity, or the linearity of the choked or low backpressure groups, which is a definite advantage to the use of this parameter. One salient feature to be noted, however, is that the slope of the curves at zero flow is no longer zero as it would be for direct flow plotting or for the temperature form $W\sqrt{T}/W_D\sqrt{T_D}$. Again, the correctness of this is evident from the derivative of the equations relative to $W^2 v$.

Controlled Expansion Designs. All four of the designs shown in Fig. 12 are designed and operating acoustically unchoked. The finite acoustic form of the Stodola relations is used for all four curves as shown by the solid lines. There is, of course, no significant difference between the finite and infinite curves for the eight and ten-stage designs as would be expected from the coincidence of the finite and infinite curves in Fig. 9. For the four-stage design, the shown deviation of the GE data from the curves is about 1 percent greater than the infinite form would have shown, at flow index values less than 0.8. In the three-stage plot both the infinite and finite deviation curves are shown, and a pressure deviation increase of about 2 percent due to low number of stages is indicated. In all four cases it was assumed that the turbine designs were impulse, so that the number of pressure stages was set equal to the number of work stages.

In all except the ten-stage design there is a pronounced increase in deviation, with the manufacturers' pressures higher than the curve prediction, at low flows. This is probably due to the manufacturer's lower *nozzle* flow coefficients from boundary layer buildup at low Reynolds number, hence reduced effective flow areas.

The error from use of the temperature (perfect gas) form of

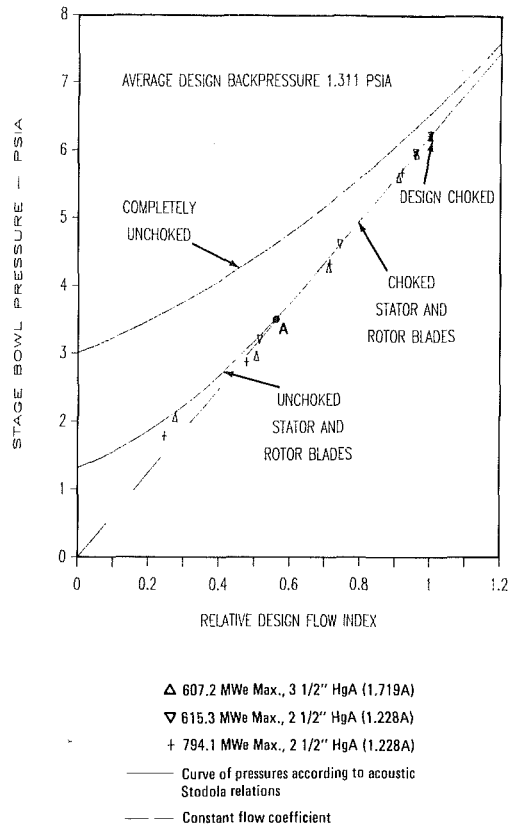

Fig. 13 Low-pressure end design comparison operating acoustically choked and unchoked at mean diameter

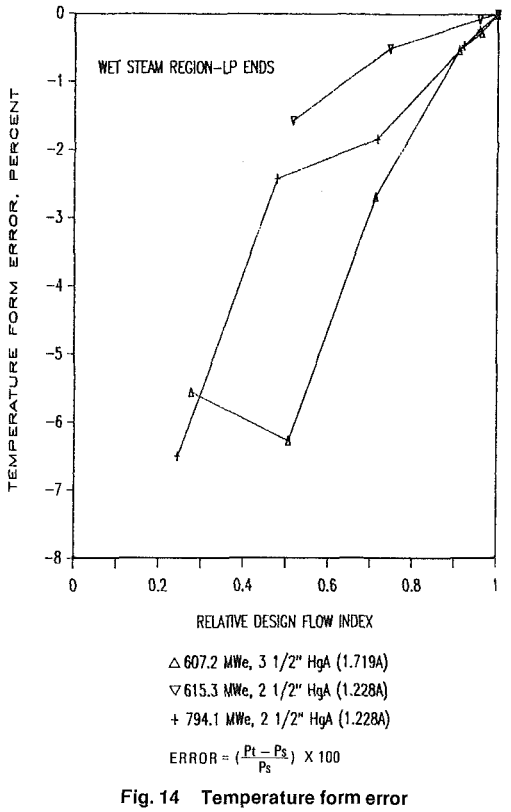

Fig. 14 Temperature form error

the equation is shown in all four plots to be on the order of 1 percent or lower. This shows the suitability of the temperature form relations for superheated steam, as recommended by Brown-Boveri Corporation and Siemens-Allis, Inc. The

acoustic forms of the temperature relations are similar to equations (29), (30), and (31), and may be easily derived from equations (26), (27), and (28).

Low-Pressure Ends. The three low-pressure end designs compared in Fig. 13 show quite reasonable agreement of the manufacturers' data with the finite acoustic form of the Stodola relations. The low-pressure ends in all three cases are single 50-percent reaction stages at the mean diameter. A value of $n = 2$ has been assumed.

The LP end is usually the only stage in a large utility machine which is designed to operate acoustically choked. Because of the choked condition, constant flow coefficient does apply for most of the design operating range. It will be noted that all designs remain choked almost down to the nominal 50-percent load point, even though the condenser pressure is assumed to remain fixed at the 100 percent value. In actuality, the condenser pressure is lower at reduced loads so that the choked condition will persist at even lower loads.

At high backpressure, such as would occur under abnornal conditions (possibly with alarm or trip), it will be noted that the operation can be completely unchoked, and, at 100-percent flow, the bowl pressure is higher than that at design, affecting the upstream stage. The use of constant flow coefficient in such cases will predict bowl pressures lower than exhaust pressure.

The temperature form error for the wet steam region is shown to be quite significant in Fig. 14.

Summary and Closure

The Law of the Ellipse, as formulated herein, has been shown to provide a rational and universally applicable mathematical method of predicting off-design multistage turbine pressures, in reasonable agreement with both theory and practice. The same formulation covers the complete range of turbine stage group pressure ratio and number of stages, whether acoustically choked or not. The ten-stage comparison in Fig. 14, for example, is a case where the backpressure is low relative to the stage group bowl pressure. The linear Stodola prediction correctly coincides with constant flow coefficient and data for that case, while still conforming with allowance for low-flow area restriction to the manufacturer's data for the unchoked, nonlinear, three-stage case at a much higher relative backpressure. The formulation further conforms to data for the acoustically choked low-pressure ends in Fig. 13.

The deviation of the Stodola curves from the data points shown in Figs. 12 and 13 does not in any way imply that the empirically substantiated manufacturers' data are not correct. It is acknowledged that the theory presented herein is not entirely complete, but the formulations provide an explainable, rational means of matching, and then extrapolating, manufacturers' or test pressure data to off-design operating modes. The formulations are therefore suitable for use in generalized heat-and-mass-balance codes which do not now provide such a universally applicable, correct, pressure modeling technique.

Acknowledgments

The assistance and support of John Bayers, Tom Valentino, and George Rohde of the Bechtel Houston Mechanical Engineering Staff is gratefully acknowledged. Thanks is also due to Bill Printup of General Electric Co. and Ewald Kohl of Siemens-Allis, Inc. for help and information provided.

References

1 Spencer, Cotton, and Cannon, *A Method of Predicting the Performance of Steam Turbine Generators 16,500 kW and Larger*, General Electric Co., Publication GER-2007C, July 1974.

2 Salisbury, J. K., *Steam Turbines and Their Cycles*, Krieger, Huntington, N. Y., 1950, pp. 105, 106.

3 Spencer, Cotton, and Cannon, op. cit., p. 6, para. III, 1.

4 Energy Incorporated, *PEPSE Manual*, Vol. 1, User Input Description, Rev. 9, p. 91-B, Equation 5.5-1.

5 Csanady, G. T., *Theory of Turbomachines*, McGraw-Hill, New York, 1964, p. 67 ff.

6 Stodola, A., and Lowenstein, L. C. (tr.), *Steam and Gas Turbines*, McGraw-Hill, New York, 1927, Vol. 1, p. 316 ff.

7 Hsuan, Yeh, Graduate Course Notes: *Turbomachinery*, University of Pennsylvania, ME610, 1958 (unpublished).

8 Steltz, W. G., "The Critical and Two-Phase Flow of Steam," ASME JOURNAL OF ENGINEERING FOR POWER, Apr. 1961, p. 148.

9 Balje, O. E., *Turbomachines: A Guide to Design, Selection and Theory*, Wiley, New York, 1981.

10 Mallinson, D. H., and Lewis, W. G. E., "The Part-Load Performance of Various Gas-Turbine Engine Schemes," *Proc. Inst. Mech. Engrs. (London)*, 159 (W. E. P. No. 41), 1948, pp. 200–201.

11 Printup, W. O., Manager—Thermodynamic Engineering, General Electric Company, Lynn, Mass., private communication, Mar. 20, 1984.

APPENDIX

SI Unit Conversion Table

Quantity	SI units	Conversion factor
Absolute temperature	K	R/1.8
Pressure	kPa	6.8948 × (psia)
Length	m	0.3048 × (ft)
	mm	25.4 × (in.)
Enthalpy	kJ/kg	2.3260 × (BTU/lbm)

G. Theoclitus
Chief Staff Engineer.
Engineering Technologies Department,
C-E Air Preheater Company,
Wellsville, NY 14895

Heat Exchanger Fires and the Ignition of Solid Metals

Solid metals can ignite and burn from the heat released through the oxidation reaction and related to the rate in which heat is dispersed. The fires can be promoted by the preignition of combustible accumulations at temperatures normally considered as relatively safe oxidation conditions. Experimental studies for fire and theoretical ignition temperatures are described in the paper.

Introduction

This paper is prepared as an introduction to heat exchanger fires, to serve as a guide to maintenance engineers, and as a reference to heat exchanger designers and suppliers.

Fires in heat exchangers are not common occurrences. Cook [1] explains that heat exchanger fires are caused by the preignition of combustible deposits that accumulated on the heat transfer surface. In particular, he referred to Ljungstrom® air preheaters which recover heat from the exhaust gas of an oil or coal fired boiler and use the heat to preheat the incoming combustion air. The majority of these fires were found to have occurred during poor firing conditions brought on by transient periods such as light-off and cold startup. At such times, a fuel-rich condition may exist within the combustion boiler and raw fuel can be carried to the preheater by the flue gas.

Eventually such deposits will build up to the level where they will ignite spontaneously leading to a metal fire, with temperatures reaching 3000°F (1649°C) and damage to the heat transfer surface and the heat exchanger structure will usually occur.

Most heat exchanger fires can be prevented. Cook emphasized the need to prevent combustible deposit accumulation on the heat transfer surface by frequent cleaning of the surface, and through proper control over combustion conditions. During steady-state firing, periodic soot blowing must be established and unerringly maintained.

When a heat exchanger fire occurs, it is usually valid to conclude that it is the result of an accidental or careless incident.

An innocent deviation from the cleaning or firing procedure may appear of minor concern not worth reporting, but it may significantly contribute to the combustible deposit accumulation which ultimately could be the genesis of a fire.

It is hoped that the work in this paper will strengthen the fire prevention recommendations stated here and by [1].

Experimental Program

An experimental program was initiated to investigate the mechanism of heat exchanger fires, particularly the process which leads to the ignition of steel metal. Typical combustible deposit accumulations were simulated on the heat transfer surface and ignited by exposure to an environment of hot air. In order to understand the effect of the combustible deposits, a series of tests was first designed to determine the ignition temperature of the steel surface in the absence of combustible deposits on the surface.

The heat transfer surface that was tested was the mild steel crimped plate (matrix) type which is usually installed in the Ljungstrom air preheater. A photograph of this surface is shown in Fig. 1.

The thickness of the crimped sheets shown in Fig. 1 was 0.026 in. (0.66 mm) and the minimum plate spacing was 0.099 in. (2.5 mm). The properties of the heat transfer matrix obtained by stacking the plates were: the ratio of free flow to frontal area or surface porosity 0.871; surface area density 124 ft^2/ft^3 (406.8 m^2/m^3); and hydraulic diameter 0.0281 ft (0.00856 m).

The oxides on the metal sheets were examined by the metallurgical laboratory and the oxide thickness was reported to be on the average 0.00004 in. (0.001 mm). Each separate test was begun with new sheets as delivered from the crimping production process with the sheets having the appearance shown on Fig. 1.

The test setup for the metal ignition tests is shown schematically in Fig. 2 which shows the type of equipment used for the test program.

Air was supplied with a Roots Conoville Blower and was heated with a direct fired natural gas combustor. All the air ducts were stainless steel 3 in. (76.2 mm) i.d. The hot air from

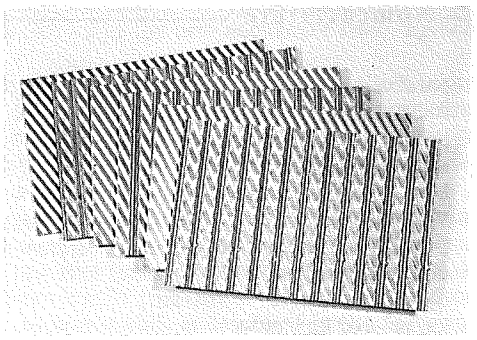

Fig. 1 Heat transfer surface used in ignition experiments

Contributed by the Power Division and presented at the ASME Winter Annual Meeting, Washington, D.C., November 15-20, 1981. Manuscript received by the Power Division March 1983.

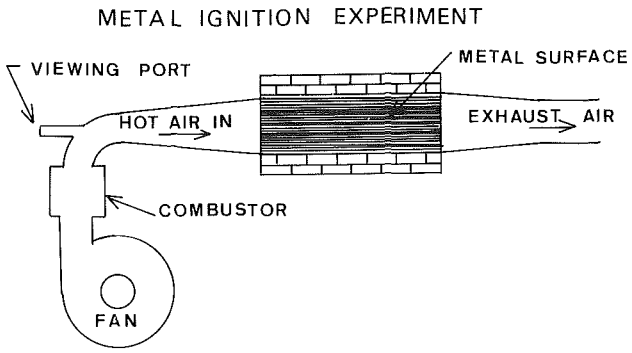

Fig. 2 Schematic of test setup for metal ignition experiment

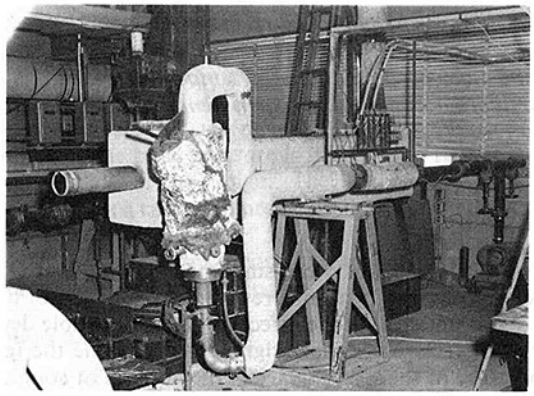

Fig. 3 Photograph of metal ignition test setup

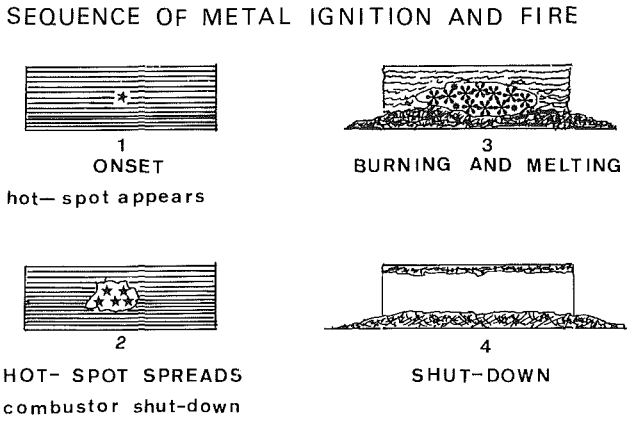

Fig. 4 Sequence of metal ignition and fire

the combustor at the temperatures described in the tests as inlet air was delivered to a fire-brick lined furnace box which contained the steel heat exchanger surface to be tested.

A right angle turn was included in the hot air duct as it entered the furnace box. This right angle was included to permit the installation of a viewing glass which could be air cooled and would avoid direct impingement by the heated air.

The furnace box provided the space for installation of the heat exchanger surface. The test core dimensions were 1 ft × 1 ft (0.305 m × 0.305 m) as the flow frontal area and the surface length was 3 ft (0.913 m) in the flow direction.

A grid of thermocouples was installed within the furnace box to monitor the air temperatures entering and leaving the heat exchanger surface. The thermocouples and the viewing glass were replaced at the beginning of each new test.

A photograph of the experimental test setup is shown in Fig. 3; the viewing port and combustor are in the foreground. Space limitations and safety precautions required a compact arrangement, reflecting some departures from the high standards established for obtaining uniform velocity distribution, accurate orifice flow measurements, and accurate fluid temperatures. Although some accuracy was sacrificed, it was felt that the results presented a new understanding of the conditions which lead to heat exchanger fires and should be useful for fire prevention.

The test setup was calibrated *in situ* with pitot tube traverses and the nonuniformity of flow was found to be the overriding source of error in determining the reliability of the results.

Air flow ± 8 percent,
Air temperatures ± 25°F (± 14°C),
Heat transfer coefficient (± 10 percent)

The metal oxide thickness was estimated to have an uncertainty of ± 15 percent.

In the first few tests, thermocouples were installed within the heat exchanger surface. This was soon discontinued because they were slow in sensing a fire unless they were fortuitously located in the area of the fire onset; then they became the first casuality. Continuous observation of the heat exchanger surface through the viewing port proved to be the best way to identify a fire at the earliest time.

Many of the ignition experiments will be presented. Figure 4 described schematically the observed sequence of metal ignition and fire.

The first indication of a fire is the appearance of a dull red spot deep within the heat exchanger surface. The hot spot soon grows and enlarges. Eventually the hot spot is sufficiently established that it no longer needs the support of heated air and the combustor can be shut down. If the hot spot is indeed well established, the ambient air causes the hot spot to continue to grow and spread; its color progresses to cherry red and white hot, and subsequently melting is observed. Eventually, total destruction of the surface occurs. If the hot spot is not well established, the ambient air cools the metal and no fire develops.

Nomenclature

A_p = parabolic oxidizing constant for metal, kg^2 O_2/m^4-s
E_p = parabolic oxidizing activation energy, J/mol
h = heat transfer coefficient, W/m^2 °C
h_p = parabolic heat transfer, defined by equation (7)
k = oxidation rate constant, kg/m^2-s or kg^2/m^4-s
Q = heat of oxidation reaction per unit weight of oxygen, J/kg O_2
R = universal gas constant = 8.3141 J/kg-mol-K
T = absolute temperature, K
T_{ig} = ignition temperature, K
T_p = parabolic ignition temperature, defined by equation (5)
w = weight of oxygen reacted with metal per unit area, kg O_2/m^2
γ = ratio of mass of oxide to mass of oxygen forming it, kg oxide/kg O_2
δ = thickness of oxide film, m
ϵ = emissivity
θ = time, s
ρ_{oxide} = density of oxide, kg oxide/m^3
σ = Stefan-Boltzmann constant = 5.6697 × 10^{-8} W/m^2 K^4
η_p = parabolic pyrophoricity, defined by equation (6)

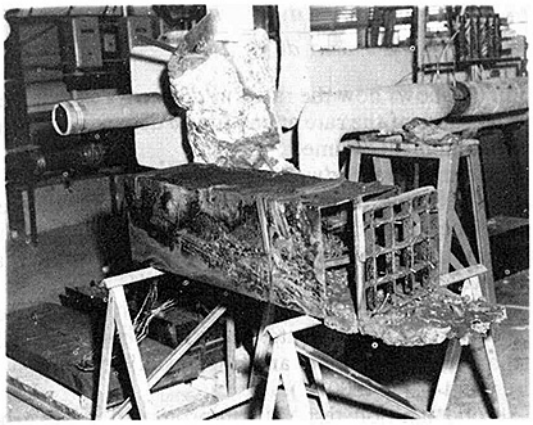

Fig. 5 First test sample after burning

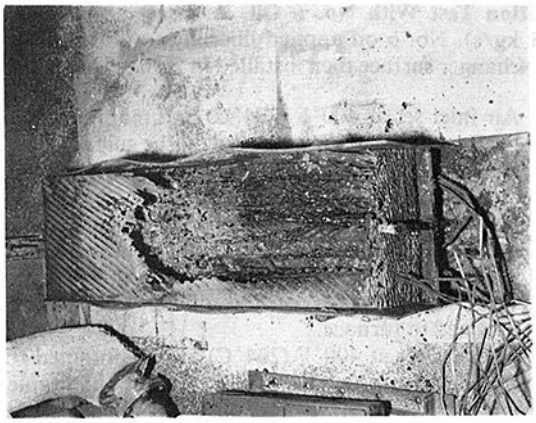

Fig. 6 Second burning test terminated early

Ignition Tests With Unpromoted Metal Surfaces. The first ignition test was exploratory where unpromoted heat exchanger surface was exposed to an air flow of 640 lb/hr (0.081 kg/s) which was increasing in temperature. After a period of 9 hr, the inlet air to the core reached 1300°F (700°C) and the outlet air temperature registered a temperature increase. This was the first indication of heat being generated within the surface. The inlet air temperature was immediately stabilized while the air temperature rise through the surface was observed. In a period of 15 min, the air outlet reached a maximum value of 1350°F (730°C) then began to decrease and within an hour had dropped to the inlet temperature of 1300°F (700°C). The inlet air was again increased resuming the prior heating procedure.

After a period of 90 min the inlet air temperature reached 1470°F (800°C) and a temperature rise through the surface was again observed. The inlet air temperature was stabilized at 1470°F (800°C). Visual inspection of the surface noted a dull red spot (hot spot) within the surface. The hot spot grew rapidly and in 10 min a very violent burning fire was in effect. By visual observation, the heat exchanger surface was collapsing and melting. Eventually the test surface was reduced to a large opening with melted steel at the bottom. The air flow was shut down and after an overnight period, the test surface was removed and inspected. Figure 5 is a photograph of this burned surface. The outlet end is in the foreground; note the melted and solidified steel and the outlet thermocouples.

A post-mortem analysis of the first test resulted in a decision to further investigate the temperature of 1300°F (700°C) where a temperature rise within the surface was first detected. Also, it was hypothesized that the heating period was too slow because the internal heat generated was decaying at a faster rate. In other words, the heating rate of the air could not keep pace with the decrease in oxidation rate. This is discussed in more detail under the theoretical analysis section.

The second test was carried out with unpromoted surface: an air flow of 640 lb/hr (0.081 kg/s) with an instant and sustained air temperature of 1300°F (700°C). The behavior of the heat exchanger surface at this temperature and flow was surprising. In less than 3 min a hot spot appeared which grew rapidly and by 3 min the entire heat exchanger surface was in a fully established fire. The experiment was terminated early before full destruction of the surface occurred. After an overnight cooling period, the tested surface was removed from the furnace and inspected. Figure 6 is a photograph of the second test and illustrates some of the early stages of the ignition and burning sequence. In the foreground is the outlet end of the test surface. The origin of the fire and hot spot is in the center which shows the hottest and melted regions. Initially the fire rapidly spreads downstream while spreading more slowly upstream. In the foreground, note the internal thermocouples, all of which have failed.

The third ignition test was with unpromoted surface, an air flow of 640 lb/hr (0.081 kg/s), and with an initial and sustained temperature of 1250°F (675°C). The purpose of this test was to find if a temperature less than 1300°F (700°C) could ignite the metal. The heat exchanger surface reacted to this temperature by generating some internal heat and the outlet air temperature reached 1275°F (675°C) within 10 min; but in the next 10 min the heat generation began to decrease and there was no sign of fire.

After a period of 30 min the inlet air was increased to 1300°F (700°C) which resulted in some internal heat generation with the outlet air reaching 1325°F (730°C) and 5 min later a hot spot appeared. The hot spot refused to grow and enlarge but remained visible for an hour. After this hour, the air flow was decreased to half of its value, but the air temperature was unchanged. The hot spot immediately began to grow and spread, finally leading to a full metal fire.

Ignition Tests With Promoted Metal Surfaces. The initial ignition tests with unpromoted metal surface demonstrated that mild steel heat exchanger surfaces can ignite and burn at temperatures as low as 1300°F (700°C). These temperatures are surprisingly low particularly considering that the only source for internal heat generation is the oxidation of the steel (rusting). This fire threat should be of sufficient dissuasion to avoid the use of mild steel heat exchanger surfaces when such temperatures are expected.

Air preheating applications seldom encounter temperatures as high as 1300°F (700°C) but an additional source of heat could have a cumulative effect and, together with the steel oxidation, result in a still lower ignition temperature. An additional source of heat has been claimed to be the combustible deposits accumulated on the heat exchanger surface. The cumulative effect of these deposits has been asserted and experimental verification seemed an appropriate supplement to the ignition tests on the unpromoted surface.

The plan for the promoted surface ignition tests called for limiting the air inlet temperature to a maximum of 800°F (427°C), and simulating the type of combustible material that could be carried to the heat exchanger from the combustion process.

The maximum temperature of 800°F (427°C) was selected because historical data had been obtained from our records reporting that most heat exchanger fires had occurred at or below this temperature. Also this is the approximate range in which most air preheaters operate.

The type of combustible material that could originate from a combustion process was defined as raw fuel from a cold startup, raw fuel from loss of combustion control, soot, and carbon from loss of combustion control. The method used to simulate such materials is described in the following section on ignition tests with No. 6 oil.

Ignition Test With No. 6 Oil. Air flow set at 640 lb/hr (0.081 kg/s). No. 6 oil applied liberally to both sides of the heat exchanger surface then installed in furnace box.

1 Air inlet set at 400°F (204°C) and maintained for 7.5 hr. Result: no action observed on the surface.
2 Air inlet set at 500°F (260°C) and maintained for 7.5 hr. Result: no action observed on the surface.
3 Surface cooled, removed from furnace and inspected. Result: a thin layer of hard, black, tarry deposit observed on the surface.
4 Second application of the oil to the surface and returned to furnace.
5 Air inlet set at 400°F (204°C) and maintained for 7.5 hr. Air inlet set at 500°F (260°C), and maintained for 7.5 hr. Result: no action observed on the surface at either temperature.
6 Surface cooled, removed from furnace and inspected. Result: a heavier layer of hard, black, tarry deposit observed on the surface.
7 Surface returned to the furnace without adding more oil.
8 Air inlet set at 700°F (371°C) for 20 min. Result: sparks observed in outlet air stream but ceased after twenty minutes.
9 Surface cooled, removed from furnace and inspected. Result: The hard, black, tarry deposit was brittle and loosely adhering to the surface.
10 Surface returned to the furnace without adding more oil.
11 Air inlet set at 715°F (379°C). Result: immediate ignition of the deposits with flames observed. Metal eventually ignited and heat exchanger surface destroyed.

Other examples of combustible deposits were prepared and tested in the same manner as the No. 6 oil. The various materials and the results of the tests follow:

1 Light rust preventive oil. Results: Repeated applications with the exposures to the heated air failed to develop a deposit accumulation and the tests were discontinued.
2 Light rust preventive oil (same as above) mixed with lampblack forming a thick paste. Results: After the third application of the mixture with each application exposed to the heated air, the third application ignited at 530°F (277°C) and metal ignition followed.
3 No. 6 oil mixed with lampblack. Results: After the fourth application of the mixture with each application exposed to the heated air, the fourth application ignited at 690°F (366°C) and metal ignition followed.

Theoretical Analysis

An excellent theoretical analysis of solid metal ignition temperature has been carried out by Reynolds [2]. Some portions of this analysis will be discussed here which will help to explain some of the experimental results.

The oxidation of metals follows two different modes of oxidation:

$$\text{Linear rate} \quad w = k\theta \tag{1}$$

$$\text{Parabolic rate} \quad w^2 = k\theta \tag{2}$$

where w is the weight gain of the oxidized metal, which represents the oxygen that has combined with the metal, kg/m^2. The time in seconds is represented by θ, and k is the oxidation rate constant. Low carbon steel follows the parabolic rate above 1000°F (538°C). The oxidation rate can be obtained by differentiating equation (2):

$$\frac{dw}{d\theta} = \frac{k}{2w} \tag{3}$$

Equation (3) shows how the rate $dw/d\theta$ decays as w increases. The actual value of the rate at any time θ depends on the value of w at that moment in time.

The oxidation rate $dw/d\theta$ represents the internal heat generation resulting from the oxidation of steel (exothermic reaction). The behavior of the heat exchanger surface during the unpromoted ignition tests can be explained somewhat by the heat rate equation (3).

The first ignition test with unpromoted surface was carried out at a very slow heating rate. Sufficient time was available for the oxide to build up and the resulting ignition temperature was 1470°F (800°C).

The second ignition test with unpromoted surface began with an instant exposure to to 1300°F (700°C) air temperature with the original low oxide thickness existing. Metal ignition (at 1300°F) immediately followed.

The third test with unpromoted surface included a time delay period at a temperature of 1250°F (657°C) which provided the time for the oxide to grow. Metal ignition occurred at 1300°F (700°C) but only after the air flow was decreased to 50 percent. The reduction of air flow decreased the convective heat losses.

The factors which influence the ignition temperature of solid metals are numerous and varied. The resulting equations for ignition temperature are complex. The known oxidation rates data for the metal were extrapolated to temperatures near ignition and then the ignition temperature could be expressed mathematically. Reynolds developed a simplified expression for the ignition temperature by defining certain dimensionless groupings

$$e^{-(1/T_p)} = (1/\eta_p)\,(T_p)^5 + (h_p)\,(T_p)^2 \tag{4}$$

The dimensionless groups are:

(*a*) Parabolic ignition temperature

$$(T_p) = T_{ig}[R/E_p] \tag{5}$$

(*b*) Parabolic pyrophoricity

$$(\eta_p) = \left[\frac{Q\gamma A_p}{8\sigma\epsilon\,\rho_{\text{oxide}}\delta}\right]\left[\frac{R}{E_p}\right]^4 \tag{6}$$

(*c*) Parabolic heat transfer

$$(h_p) = \frac{2\,\rho_{\text{oxide}}\delta h}{Q\gamma A_p}\left[\frac{E_p}{R}\right] \tag{7}$$

The dimensional quantities are defined in the nomenclature. Their values for mild steel are provided in the appendix. Reference [2] was the source for these values.

The solution of equation (4) for the case of mild steel is graphically shown in Fig. 7. The influence of the factors which affect the ignition temperature can be observed in this figure.

The initial thickness of the oxide layer (δ) relates to the oxide presently existing on the metal, which has been explained in this section.

The emissivity of the oxide layer (ϵ) and the convective heat transfer coefficient (h) both influence the ignition temperature because they represent modes in which heat is carried away from the oxidation area.

The points shown on Fig. 7 are those that were experimentally found during the ignition tests on the unpromoted surface.

The thickness of the oxide layer (δ) was determined in the metallurgical laboratory by microscopic examination, and found to be on the average 0.00004 in. (0.001 mm).

The emissivity of the oxide layer (ϵ) for the steel surface was obtained from McAdams [3], listed as follows:

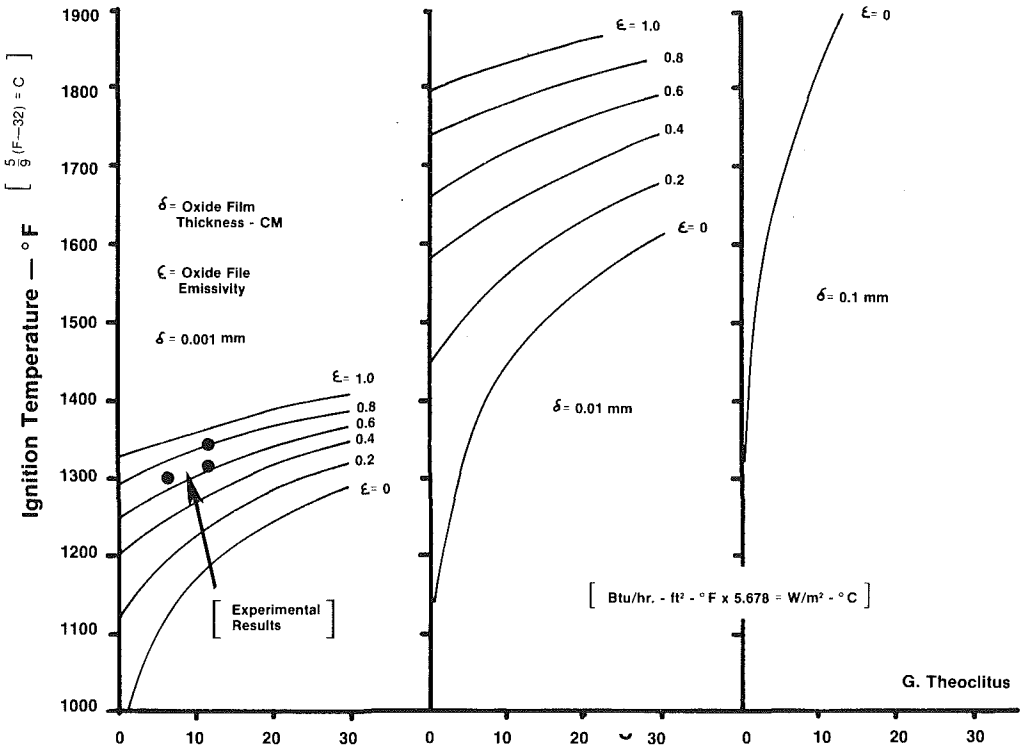

Fig. 7 Theoretical ignition temperature of mild steel

(*a*) Rolled sheet surface with an oxidized layer

$$\epsilon = 0.52 - 0.66$$

(*b*) Oxidized sheet steel $\epsilon = 0.80$

(*c*) Iron oxide $\epsilon = 0.85 - 0.89$

Using the above values for δ and ϵ, the experimental results fall virtually on the theory.

Discussion

Metal Ignition. The ignition and burning of solid metals is a hazard which can exist for all types of heat exchangers including compact heat exchangers. Metal ignition experiments were reported by McDonald [4] on plate-fin type heat transfer surfaces. McDonald also found that temperatures of 1300°F to 1350°F (704°C to 732°C) appeared to be the point where ignition of mild steel would occur.

Heat exchanger designers normally consider temperatures when selecting materials of construction from the viewpoint of structural strength. Metal ignition temperatures should be an additional consideration during the design and the material selection period.

The materials selected must safely withstand the expected operating temperature environment. Precedence must also be given to any conceivable high temperature excursions. Such excursions may be adequate to ignite solid metals. In anticipation of such possible excursions, the heat exchanger designer should upgrade the metal specification or call for protection against the expected types of high temperature excursions.

For a regenerative type heat exchanger, a high temperature excursion can occur by the ignition of combustible deposits which have accumulated on the heat exchanger surface. Adequate means must be provided to prevent the accumulation of these combustible deposits. Soot blowers have proven to be effective as cleaning devices. Cleaning schedules must be established according to the firing conditions and the procedures that have been defined by Cook. The heat transfer surface must not contain any "blind" zones which cannot be reached by the soot blowers. Zones that cannot be cleaned will permit combustible deposit to accumulate and auto-ignition of the deposits will eventually occur.

Fire Detection. Considerable thought has been given to the best method for fire detection.

From the experience gained in the metal ignition experiments, the earliest time to detect an incipient metal fire is when the hot spot first appears. Although the hot spot is visible,[1] there is no other indication that the onset of a metal fire has been reached. Thermocouples in the fluid stream will probably not sense any increase in fluid temperature. Progress of the fire is very rapid from this point and costly damage will occur unless the fire is immediately detected.

Since the hot spot is the first visual indication of an incipient fire, an infrared radiation detection device was chosen as a means to sense a red glowing hot spot. Such a device, developed by C-E Air Preheater [5], could detect a cigarette glow 30 to 40 feet away.

Concluding Remarks

The ignition and burning of mild steel heat exchanger surface has been demonstrated in experiments in which the steel ignited in an air environment of 1300°F (700°C). At this temperature the heat generated by metal oxidation exceeds the heat losses and auto-ignition takes place. Analytical means have been presented which can be utilized by heat exchanger engineers to evaluate the potential threat of solid metal ignition.

The presence of any other sources of heat can stimulate the metal ignition at lower temperatures. This also has been experimentally demonstrated.

[1] If a provision is made to visualize the heat exchanger surface

Acknowledgments

The author gratefully acknowledges the contributions from W. E. Hammond who initiated the experimental investigation.

References

1 Cook, W. C., "Air Preheater Fires," presented at American Public Power Association, Engineering and Operations Workshop, Atlanta, Georgia, March 14-17, 1977, Paper No. 158, C-E Air Preheater, Wellsville, NY.

2 Reynolds, W. C., "Investigation of Ignition Temperatures of Solid Metals," National Aeronautics and Space Administration, Technical Note D-182, Oct. 1959.

3 McAdams, W. H., *Heat Transmission*, 3rd ed., McGraw-Hill, New York, 1954.

4 McDonald, C. F., "The Potential Danger of Fire in Gas Turbine Heat Exchangers," ASME Paper No. 69-GT-38.

5 Wixson, D. F., "C-E Air Preheater Infrared Detection System," Paper No. 154, C-E Air Preheater, Wellsville, NY, 1980.

APPENDIX

Values and properties for mild steel and ferrous oxide (FeO)

$A_p = 37\ \text{kg}^2\ \text{O}_2/\text{m}^4\text{-s}$

$E_p = 1.3816 \times 10^8\ \text{J/mol}$

$\rho_{\text{oxide}} = 5.7 \times 10^3\ \text{kg oxide/M}^3$

$\gamma = 4.49\ \text{kg oxide/kg O}_2$

$Q = 1.674 \times 10^7\ \text{J/kg O}_2$

$$\frac{E_p}{R} = \left[\frac{1.3816 \times 10^8\ \text{J/mol}}{8315.1\ \text{J/mol-K}} \right] = 16{,}617.6\ \text{K}$$

C. R. Tong[2]
M. J. Tan[3]
S. G. Bankoff[4]
Chemical Engineering Department,
Northwestern University,
Evanston, IL 60201

A Model for Convective Boiling in a Narrow Eccentric Annular Gap[1]

A steady-state model is developed for convective boiling and dryout in an eccentric annulus with line contact between the heated inner wall and the adiabatic outer wall. The geometry and heat transfer conditions resemble those in a PWR steam generator, except for the lower pressure. Good agreement is shown with experimental data reported elsewhere.

I. Introduction

One of the major problems in steam generator operation is the corrosion-erosion of the primary tubes which may be made of Inconel-600, leading to denting of tubes in the tube support plate (TSP) and thinning and cracking of these tubes. Rupture of the primary tube implies that radioactive water from the primary loop will leak into the secondary system, and then possibly through the purge system into the environment. Tests using a single Inconel-600 tube with a carbon-steel TSP indicated that dryout or very poor heat transfer occurred at or near the metal-to-metal contact region between the primary tube and the TSP [1]. It has also been shown that denting increases with elevated temperature and chloride concentration [2]. Using radioactive salt deposition, it has been shown that crevices due to TSP contact in steam generators caused local dryout, which leads to salt deposition and corrosion damage of the tube [3, 4]. Thus, the majority of tube rupture incidents occur at the crevice region.

Research into methods of preventing, or at least delaying, such incidents can be divided into thermal-hydraulic, corrosion, and ameliorative design and operation studies. The present work falls into the first category. The experimental portion, involving heat transfer measurements in a single-tube geometry under simulated Westinghouse PWR conditions, has been reported elsewhere [3, 4]. This paper deals with the construction of a steady-state computer model to predict mean axial velocities, qualities, and wall temperatures as a function of position in a short eccentric annulus. Some comparisons with experimental results are shown which give reasonably good agreement with the predicted temperature profiles.

II. Literature Review

Katto et al. performed experiments on boiling in a space bounded by two horizontal coaxial disks in a pool of saturated liquid at atmospheric pressure. It was found [5, 6] that the CHF was reduced when the supply of liquid to the heating surface was restricted. They concluded that the dominant heat transfer mechanism is thin-film evaporation, and thus suggested that at the critical heat flux the average life of liquid films on the heated surface is equal to the average detachment period of the vapor masses. A general correlation was derived, based on their CHF data, which took into account inertial, buoyancy, capillary, and geometric effects [7].

Jensen, Cooper, and Bergles [8] performed experiments on natural-convection pool boiling of saturated water at atmospheric pressure in horizontal annular geometries with an electrically heated inner tube. It was found that the dryout heat flux was proportional to the radial clearance. The mechanism for dryout was again identified as thin-film evaporation. A dimensionless correlation was developed in terms of the vapor Reynolds number in the confined space.

Ishiibashi and Nishikawa [9] examined pool boiling of saturated liquid in a vertical annular gap for pressures up to 1.1 MPa. They classified saturated boiling in a narrow space into two regimes: an isolated bubble regime and a coalesced bubble regime, depending upon the gap dimension and the pressure. Based upon the observation that the occurrence of dryout is preceded by the generation of coalesced bubbles at a low frequency, the heat transfer data for the coalesced bubble regime were correlated by a Nusselt number and a modified Reynolds number in which the effects of gap width and pressure were accounted for. The bubble emission frequency data were also correlated in terms of a Fourier number and the Nusselt number.

Markatos, Sala, and Spalding [10] considered a different, but related, problem, consisting of the adiabatic steady flow of a single-phase fluid in a narrow skewed annulus. The flow was treated as two-dimensional, with the velocity and pressure variations in the radial direction assumed negligibly small. Numerical solutions for the static pressure and velocity fields were obtained.

To summarize, the earlier studies of concentric-gap boiling revealed the existence of a transition region which may exhibit periodic dryout and rewetting, accompanied by bubble emission from the periphery of the confined space. More recently, Baum and Curlee [21] have experimentally and analytically examined dryout and chemical concentration in confined geometries typical of PWR steam generators. An analytical model was developed for predicting the shape of the liquid-vapor dryout region, assuming that saturated liquid

[1]Work supported by a contract with the Electric Power Research Institute, Palo Alto, CA.
[2]Now with Universal Oil Products, Des Plaines, IL.
[3]Now with Texaco USA, Bellaire, TX.
[4]To whom communications regarding this paper should be addressed.
Contributed by the Power Division for publication in the JOURNAL OF ENGINEERING FOR GAS TURBINES AND POWER. Manuscript received by the Power Division October 1983.

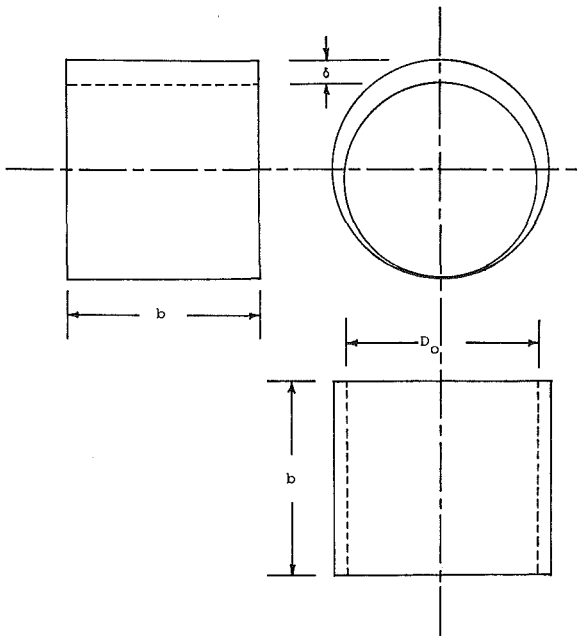

Fig. 1 An eccentric annulus with line contact

flows into the crevice, but saturated vapor properties alone can be used to describe the one-dimensional flow in the crevice, both before and after the dryout point. The present work employs a more detailed model, in which these assumptions are relaxed.

III. Model Assumptions and Conservation Equations

A locally-homogeneous-equilibrium two-phase model is presented here for flow inside an eccentric annular gap with the inside tube heated. Figure 1 is a sketch of the configuration. The crevice geometry under consideration is a gap region formed between the primary tube and the tube hole of the TSP in which the tube maintains a line contact with the plate metal. The circumferential coordinate θ is defined with respect to the origin at the contact line at the entrance to the gap. Assumptions used in developing the model include:

1 Non-oscillatory steady flow conditions.

2 Flow volume in the crevice can be divided into two regions: two-phase and dryout (vapor only) regions. The dryout region is symmetric about the contact line, with increasing width in the axial flow direction.

3 The two-phase region contains a homogeneous equilibrium mixture while the dryout region contains superheated vapor.

4 The outer wall of the gap is adiabatic.

5 Negligible tangential flows, implying that circumferential pressure gradients in the annulus region are everywhere small.

Assumptions 1 and 2 are in accord with macroscopic visual observations [4]. Assumption 3 is based on measurements of very small superheats required to initiate and maintain boiling in this geometry. Assumption 4 was a reasonable first estimate, and was later modified to take into account heat losses in the contact region, as detailed below. An analytical study of heat conduction losses in the contact region is given elsewhere [3, 4, 22]. Assumption 5 is not in accord with visual observations of strong tangential flows at the boundary of the dryout region. However, since excellent heat transfer, and hence very low wall superheats, are obtained in this region, this assumption results in negligible error, and allows a considerable simplification of the numerical calculations. A theoretical analysis of these tangential flows is given elsewhere [22].

With these assumptions it is straightforward to show [11] that the conservation equations for any particular circumferential position can be written as follows:

I. *Subcooled liquid*

$$\left[\left(\frac{\partial v}{\partial i}\right)_P \left(\frac{\partial i}{\partial P}\right)_x + \frac{1}{G^2}\right]\frac{dP}{dz} + \left(\frac{\partial v}{\partial i}\right)_P i_{lv}\frac{dx}{dz} = -\frac{2fv}{D_{hy}} \tag{1}$$

$$\left(\frac{\partial i}{\partial P}\right)_x \frac{dP}{dz} + i_{lv}\frac{dx}{dz} = \frac{4q}{GD_{th}} \tag{2}$$

II. *Liquid-vapor two-phase mixture*

$$\left[\left(\frac{\partial v}{\partial P}\right)_x + \frac{1}{G^2}\right]\frac{dP}{dz} + v_{lv}\frac{dx}{dz} = -\frac{2fv}{D_{hy}} \tag{3}$$

$$\left(\frac{\partial i}{\partial P}\right)_x \frac{dP}{dz} + i_{lv}\frac{dx}{dz} = \frac{4q}{GD_{th}} \tag{4}$$

III. *Superheated vapor*

$$\left[\left(\frac{\partial v}{\partial P}\right)_T + \frac{1}{G^2}\right]\frac{dP}{dz} + \left(\frac{\partial v}{\partial T}\right)_P \frac{dT}{dz} = -\frac{2fv}{D_{hy}} \tag{5}$$

$$\left(\frac{\partial i}{\partial P}\right)_T \frac{dP}{dz} + \left(\frac{\partial i}{\partial T}\right)_P \frac{dT}{dz} = \frac{4q}{GD_{th}} \tag{6}$$

where P, T, v, and i are pressure, temperature, specific volume, and specific enthalpy, respectively; D_{hy} and D_{th} are the hydraulic and thermal equivalent diameters of each longitudinal element; G is the mass velocity; f is wall friction factor; q is heat flux; and x is the thermodynamic mass quality defined by

$$x(z) = \frac{i(z) - i_{ls}}{i_{vs} - i_{ls}} \tag{7}$$

Nomenclature

C_p = specific heat
D = diameter
F = Reynolds number factor in Chen correlation
f = wall friction factor
G = mass velocity
h = heat transfer coefficient
i = enthalpy
k = thermal conductivity
p = pressure
q = heat flux
r = radius
S = suppression factor in Chen correlation
T = temperature
U = overall heat transfer coefficient
u = velocity
v = specific volume
x = mass quality
z = axial position
Pr = Prandtl number
Re = Reynolds number
δ = maximum gap size
δ_w = thickness of tube wall
ρ = density
θ = circumferential position
μ = viscosity
τ = wall shear stress
χ_{tt} = Lockhart-Martinelli parameter

Subscripts

c = critical
hy = hydraulic
i = inside primary tube
in = inlet to test section
l = liquid phase
m = meniscus
o = outside primary tube
s = saturated
th = thermal
v = vapor phase
w = primary tube wall

The thermodynamic mass quality is used to determine whether the flow is single-phase subcooled or saturated, two-phase, or single-phase superheated.

I. *Subcooled or saturated:* $x \le 0$

II. *Two-phase:* $0 < x < x_c$

III. Superheated vapor: $x_c \le x \le 1$

A fourth-order Runge–Kutta method is used to solve for P, u, T, and x as functions of z and θ. The algorithm is:

1 Set inlet flow conditions and outlet pressure.
2 Fix $\Delta\theta = \pi/N$.
3 Guess u_{in}.
4 Evaluate x to determine in which region the flow belongs and integrate the appropriate balance equations.
5 Calculate the pressure drop and evaluate u; iterate until convergence is achieved ($u \rightarrow u_{in}$).
6 Increment in z and repeat steps 2 to 5 until the complete axial profile is calculated.
7 Increment in θ and repeat steps 2 to 6 until the complete θ direction profile is obtained.

The first version of a code [11] for dryout of an eccentric annular gap (DEAG-1) is described below, since it was used to obtain stability and natural frequency estimates, to be described elsewhere [13]. Some changes in the constitutive equations in recognition of the narrow-gap annular geometry, which improved the agreement between predicted and experimental temperature distributions, will be described in Section IV.

The constitutive equations used in DEAG-1 are summarized as follows [11]

(A) *Equivalent diameters*

$$D_{hy} = \delta\left[1 - \left(2 + \frac{\delta}{D_o}\right)^{-1} \frac{\sin\theta_j - \sin\theta_{j-1}}{\theta_j - \theta_{j-1}}\right] \tag{8}$$

$$D_{th} = \delta\left[\left(2 + \frac{\delta}{D_o}\right) - \frac{\sin\theta_j - \sin\theta_{j-1}}{\theta_j - \theta_{j-1}}\right] \tag{9}$$

(B) *Friction factor*

$$f = \begin{cases} 16\,\mathrm{Re}^{-1} & \text{for } \mathrm{Re} < 2000 \quad (10a) \\ 0.079\,\mathrm{Re}^{-0.25} & \text{for } \mathrm{Re} > 2000 \quad (10b) \end{cases}$$

where

$$\mathrm{Re} = \frac{GD_{hy}}{\mu} \tag{11}$$

with

$$\mu = \begin{cases} \mu_l & \text{for subcooled liquid} \quad (11a) \\ \left(\frac{x}{\mu_v} + \frac{1-x}{\mu_l}\right)^{-1} & \text{for liquid-vapor mixture} \quad (11b) \\ \mu_v & \text{for superheated vapor} \quad (11c) \end{cases}$$

(C) *Heat Flux*

$$q = U(T_i - T) \tag{12}$$

$$U = \left(\frac{1}{h_i} + \frac{D_i \ln(D_o/D_i)}{2k_w} + \frac{D_i/D_o}{h_o}\right)^{-1} \tag{13}$$

(C.1) *Primary heat transfer coefficient*

$$h_i = 0.023\,\mathrm{Re}_{li}^{0.8}\,\mathrm{Pr}_{li}^{0.33} k_{li}/D_i \tag{14}$$

where

$$\mathrm{Re}_{li} = \frac{G_i D_i}{\mu_{li}} \tag{15a}$$

$$\mathrm{Pr}_{li} = \frac{C_{pli}\mu_{li}}{k_{li}} \tag{15b}$$

(C.2) *Secondary heat transfer coefficient*

I. Single-phase subcooled region:

$$h_o = 0.023\left(\frac{k_l^{0.6} G^{0.8} C_{pl}^{0.4}}{\mu_l^{0.4} D_{th}^{0.2}}\right) + \frac{(0.00122)S}{T_w - T}\left(\frac{k_{ls}^{0.79} C_{pls}^{0.45} v_{vs}^{0.24}}{\sigma^{0.5}\mu_{ls}^{0.29} i_{lv}^{0.24} v_l^{0.49}}\right) \times (T_w - T_s)^{1.24}(P_w - P)^{0.75} \tag{16}$$

II. Two-phase region:

$$h_o = F(0.023)\frac{k_{ls}^{0.6} G^{0.8}(1-x)^{0.8} C_{pls}^{0.4}}{\mu_{ls}^{0.4} D_{th}^{0.2}} + S(0.00122)\left(\frac{k_{ls}^{0.79} C_{pls}^{0.45} v_{vs}^{0.24}}{\sigma^{0.5}\mu_{ls}^{0.29} i_{lv}^{0.24} v_l^{0.49}}\right) \times (T_w - T_s)^{0.24}(P_w - P)^{0.75} \tag{17}$$

III. Single-phase superheated region:

$$h_o = \begin{cases} \frac{3.66 k_v}{D_{th}} & \text{for } \mathrm{Re}_v < 2000 \quad (18a) \\ 0.023\,\mathrm{Re}_v^{0.8}\mathrm{Pr}_v^{0.33} k_v/D_{th} & \text{for } \mathrm{Re}_v > 2000 \quad (18b) \end{cases}$$

$$\mathrm{Re}_v = \frac{GD_{th}}{\mu_v} \tag{19a}$$

$$\mathrm{Pr}_v = \frac{C_{pv}\mu_v}{k_v} \tag{19b}$$

(d) *Dryout criterion*

$$x_c = 0.99 = \text{const} \tag{20}$$

Equations (14) and (18*b*) represent the well-known Dittus–Boelter correlation for single-phase heat transfer (14) and equations (16), (17) the Chen correlations for subcooled and saturated convective nucleate boiling [15]. The Reynolds number factor F and the suppression factor S are given in [15].

The pressure gradient across the TSP is estimated using the Chisholm correlation [16]:

$$\frac{dP}{dz} = \frac{v_l}{2C_D^2} G(1-x)^2(1 + C\chi_{tt}^{-1} + \chi_{tt}^{-2}), \tag{21}$$

where C_D and C are constants. χ_{tt} is the Lockhart-Martinelli parameter:

$$\chi_{tt} = (v_l/v_v)^{0.5}(1/x - 1) \tag{22}$$

IV. Improved Model (DEAG-3)

Comparisons with data [12] revealed that DEAG-1 was unable to predict dryout in cases where it was observed experimentally [4]. Further, although the model was able to predict the general shape of the tube wall temperature profile, the estimated peak wall temperature was consistently higher than the data value.

The constitutive equations for flow and heat transfer used in the model are in the form of empirical corrrelations. Since these correlations were developed for relatively unrestricted flow geometries, they are at best rough approximations when applied to boiling in a narrow eccentric gap. For an improved model, the following changes were introduced:

(A) Friction Factor Correlations. The eccentricity of the inner tube introduces circumferential variations of the local

Table 1 Summary of operating conditions for selected runs [4]

Fig. No.	2	3	4	5	6	7
Quality, x	0.006	0.133	0.0	0.0	0.0	0.029
Primary flowrate, kg/s	0.500	0.496	0.505	0.498	0.498	0.500
Secondary flowrate, kg/s (10^{-2})	3.46	1.98	3.43	8.58	17.06	9.07
Primary temperature °C	197.6	201.5	185.9	196.2	203.5	191.7
Secondary inlet temperature, °C	165.8	165.1	164.9	163.9	162.8	165.3

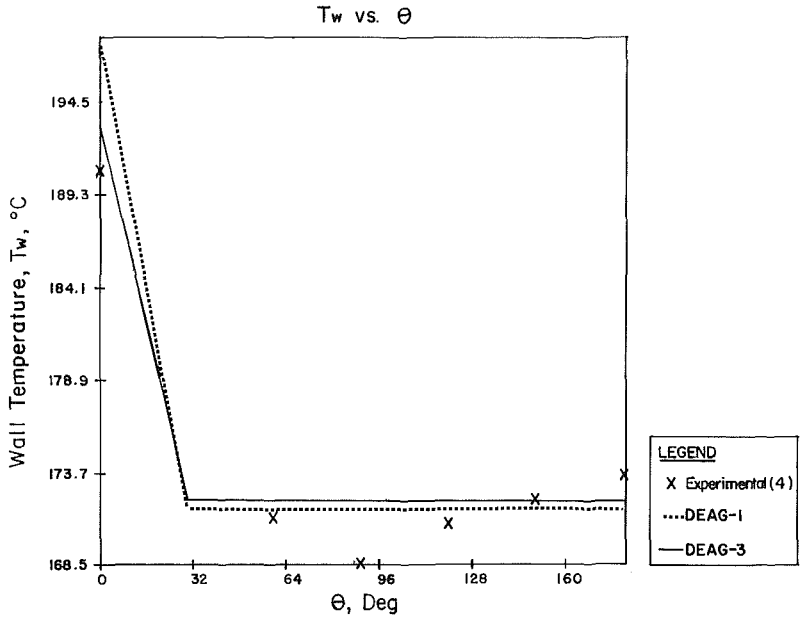

Fig. 2 Wall temperature as function of angle from contact line (see Table 1)

shear stress and hence the friction factor. Snyder and Goldstein [17] proposed that for fully developed laminar flow in completely eccentric annuli

$$f = \frac{r_i f_i + r_o f_o}{r_o + r_i} \tag{23}$$

For the present geometry

$$f = 22.2/\mathrm{Re} \tag{24}$$

Equation (24) was used for Re <2000 in place of equation (10*a*). For flow in the turbulent region, a modified Blasius equation [18] was used

$$f = 0.085\ \mathrm{Re}^{-0.25};\ \mathrm{Re} > 2200 \tag{25}$$

According to Knudsen and Katz [19], for transition flow in smooth cylinders

$$f^{-0.5} = 26.28 - 4\log(4.67 \times 10^6\ \mathrm{Re}^{-1} f^{-0.5}) \tag{26}$$

Solving for f at Re $=2000$ and Re $=2200$, and approximating the relationship with a linear function, one obtains:

$$f = 0.0164 - (2 \times 10^{-6})\mathrm{Re} \tag{27}$$

Equation (27) was employed for the region $2000 \leq \mathrm{Re} \leq 2200$.

(B) Heat Transfer Correlations. For Re < 2000 equation (18*a*) was replaced by the Rohsenow–Choi equation [20]

$$h_v = 4k_v/D_{th} \tag{28}$$

The Dittus–Boelter equation for heat transfer in the superheated turbulent flow region, equation (18*b*), was replaced by the Colburn equation [20]

$$h_i = 0.023\ \mathrm{Re}_{li}^{0.8}\ \mathrm{Pr}_{li}^{0.4} k_{li}/D_i \tag{29}$$

A large number of correlations have been developed for forced-convection nucleate boiling. These correlations can be divided into two main groups: low-quality (subcooled boiling) and high-quality (saturated boiling) flows. These include the Thom correlation for the former and the Dengler–Addoms, Wright, and Schrock–Grossman equations for the latter [20]. Although these are of simple form and are easier to use than the Chen correlation, their domain of applicability is highly restricted. Tests with different correlations suggested that the Chen correlation was adequate to correlate data for both low and high-quality boiling in the narrow gap.

(c) Dryout Criterion. In DEAG-1 dryout is said to have occurred when a predefined critical quality x_c is reached or exceeded. However, dryout was observed close to the line of contact in all experimental runs, although the dry patch width was dependent on the operating conditions. According to Jensen et al. [8], the longer residence time of the vapor in the restricted area allows thin-film evaporation to occur at lower critical heat flux levels, and hence incipient dryout occurs at lower qualities than in the unrestricted area. The influence of gap size on x_c can be expressed with a θ-dependent relationship which meets these criteria:

1 x_c is a minimum at $\theta = 0$ deg.
2 x_c is a maximum at $\theta = 180$ deg.
3 $0 < x_c < 1$.
4 x_c is a symmetrical function about the diameter that passes through the line of contact.
5 x_c is sensitive to inlet flow quality.

A function that meets these criteria is

$$x_c(\theta) = x_{in} + \sin(\theta/2) \tag{30}$$

An arbitrary upper boundary for this function has been set; for $x_c(\theta) > 0.9999$

$$x_c(\theta) = 0.9999 = \mathrm{const} \tag{31}$$

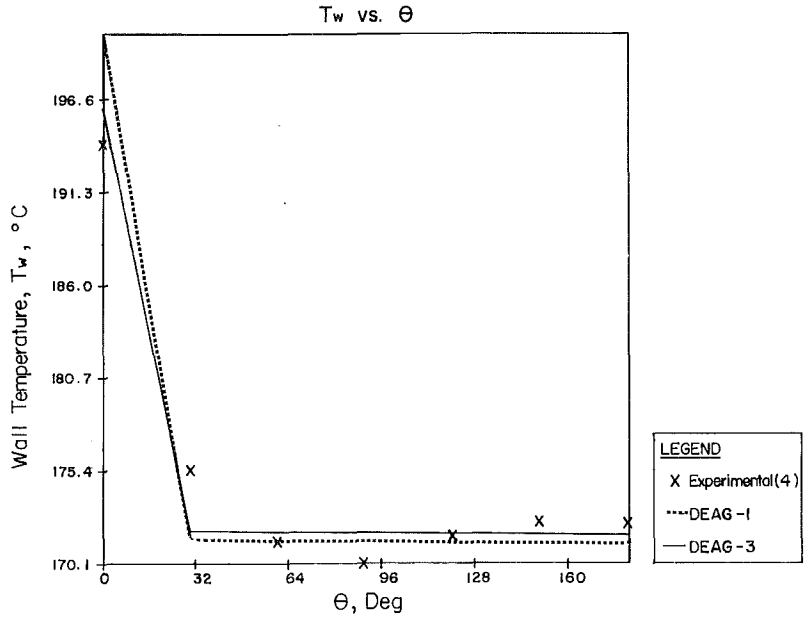

Fig. 3 Wall temperature as function of angle from contact line

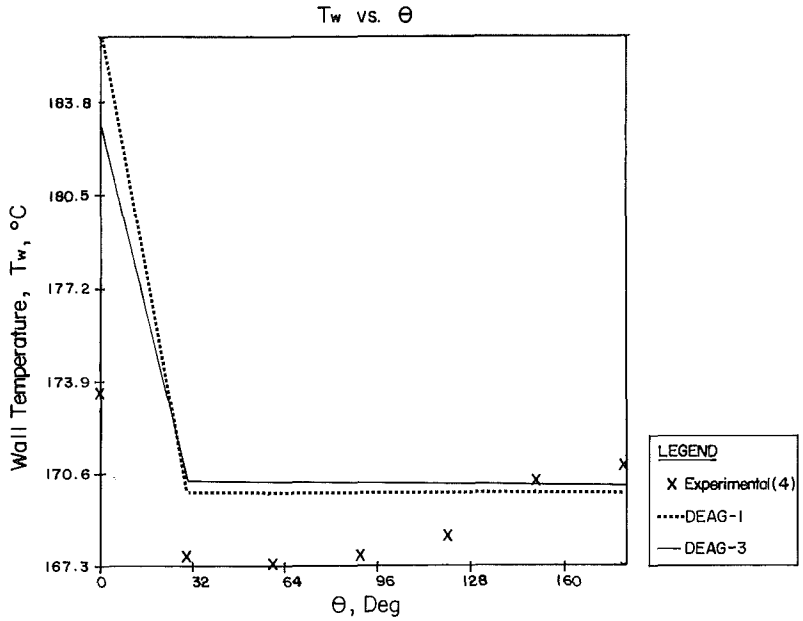

Fig. 4 Wall temperature as function of angle from contact line

Equations (30) and (31) were substituted for equation (20) in the improved model.

(D) Radial Heat Loss. Since the TSP was not insulated in the experiments for visualization purposes, assumption 4 is suspected to be a cause for overpredicting the maximum wall temperatures in DEAG-1. In the improved model, a term to account for radial heat loss through the TSP in the dryout region along the line of contact was included

$$U' = (1/h_v + \delta_w/k_w - \delta_{rp}/k_{rp} + 1/h_i)^{-1} \quad (32)$$

The presence of entrained water droplets in the dryout region considerably increased the heat transfer from the wall. To account for this effect, the coefficient in equation (28) for the laminar-gap vapor-side heat transfer was sharply increased in the model

$$h_v = 20\, k_v/D_{th} \quad (23)$$

V. Results

(A) Influence of Gap Size. DEAG-1 was first used to study the effects of gap size variations on the thermal-hydraulic behavior of boiling in a narrow eccentric gap, using parameters from experimental runs [3]

tube hole diameter	21.1 mm
tube wall thickness	1.14 mm
flow-hole [4] diameter	6.35 mm
inlet quality	0.52
primary flowrate	0.492 kg/s
secondary flowrate	0.523 kg/s
secondary pressure	0.687 MPa
primary temperature	198.7°C
secondary temperature	164.5°C

With this set of operating parameters, the following maximum gap sizes were used for three independent simulations: 0.53, 0.885, and 2.80 mm.

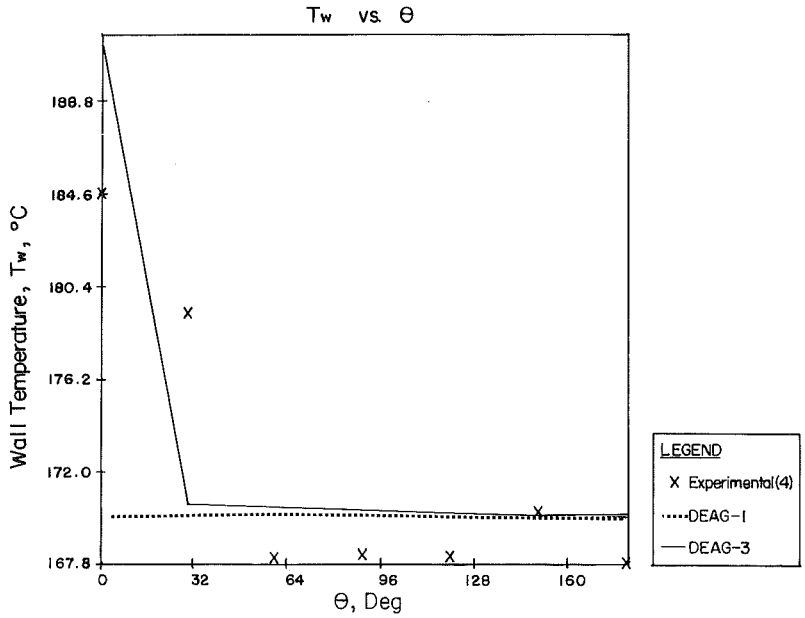

Fig. 5 Wall temperature as function of angle from contact line

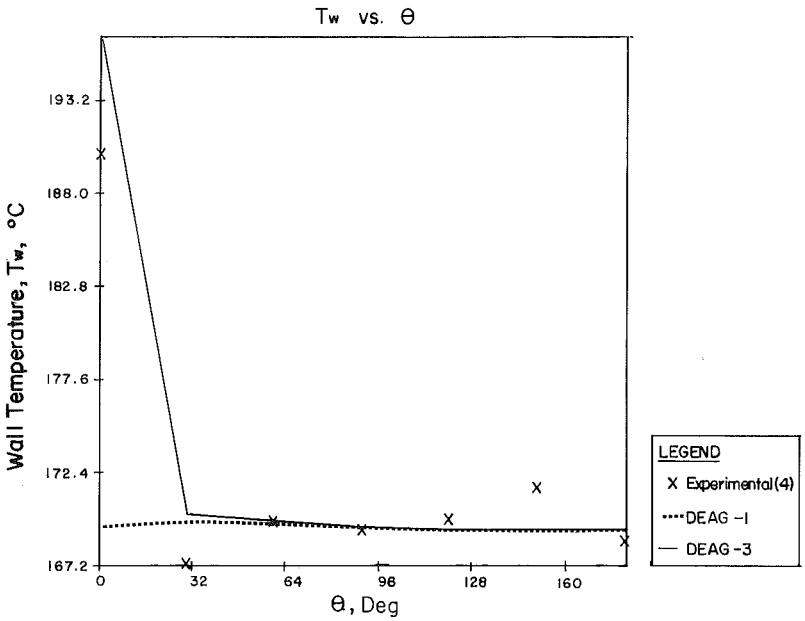

Fig. 6 Wall temperature as function of angle from contact line

Some selected results are shown here. Additional results and a program listing are given for DEAG-1 and DEAG-3 elsewhere [12]. Local wall temperatures are shown in Figs. 2 and 3 as a function of the circumferential position for diametral gap widths of 0.53 and 2.80 mm, respectively. Dryout is predicted for the smaller gap, and the maximum wall superheat of 34°C is in close agreement with the experimental result. For the 2.80 mm gap, the characteristic W-shaped temperature profile of the data is observed, owing to the behavior of the Chen correlation [12]. However, no dryout is predicted, contrary to observation, and hence this correct shape is due to cancellation of opposing errors.

The final model, DEAG-3, gave more realistic predictions of dryout and of maximum wall temperatures. This was shown by a comparison of predicted and observed temperatures for twelve experimental runs [4], all with a gap size of 0.885 mm. Some of these comparisons are shown in Figs. 2–7; the experimental conditions for these runs are given in Table 1. It should be noted that axial temperature variations on both the primary and secondary sides in this short annular geometry were found to be negligible [4].

One sees that the predicted width of the dryout region, the peak wall temperature, and the mean temperature in the two-phase boiling region far from the contact line all agree reasonably well with the data trends. The peak temperature is usually still overpredicted, but this is not as important as the correct estimation of the dryout gap width. Similarly, the nucleate-boiling region wall temperature for the contact line is sometimes slightly underpredicted, but this may be due to the use of the Chen convective nucleate-boiling correlation, which is based largely on round-tube data, in this narrow-gap configuration.

VI. Summary

A steady-state model for dryout and wall temperatures in a

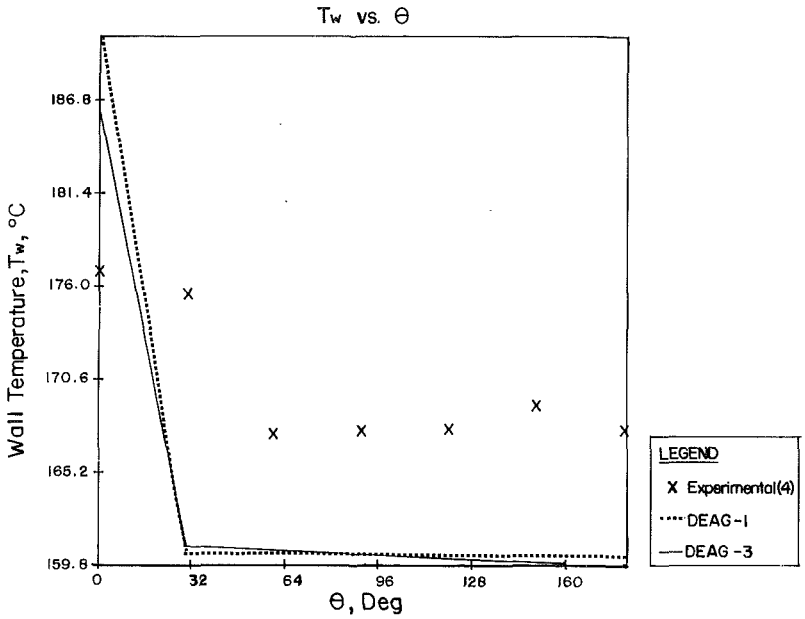

Fig. 7 Wall temperature as function of angle from contact line

narrow eccentric annulus with line contact has been developed which is generally in good agreement with experimental data at 0.1–0.69 MPa. However, the model remains to be verified for the higher pressures typical of steam generators. Dryout always occurs with line contact, so that the possibility of thermal stress and corrosion is always present. However, true line contact may be rare in actual practice, and experiments [4] have shown that misalignment as small as 0.002 in. will generally prevent dryout.

References

1 Green, S. J., and Steininger, D. A., "Pressurized Water Steam Generators—Problems of PWR Steam Generators," ASME Paper No. 80-C2/NE-8, Nucl. Engg. Conf., San Francisco, CA, 1980.

2 Shah, M. M., "A General Correlation for Critical Heat Flux in Annuli," *Int. J. Heat Mass Transfer*, Vol. 23, 1980, pp. 225–234.

3 Bankoff, S. G., et al., "Boiling Heat Transfer in a Narrow Eccentric Annulus," EPRI NP-2610, Sept. 1982.

4 Johnston, B. S., Ph.D. thesis, Chemical Engineering Department, Northwestern University, Evanston, IL, 1981.

5 Katto, Y., and Yokoya, S., "Experimental Study of Nucleate Pool Boiling in Case of Making Interface-Plate Approach to the Heating Surface," *Proceedings of the Third International Heat Transfer Conference*, Vol. 3, 1966, pp. 219–227.

6 Katto, Y., and Yokoya, S., "Principal Mechanism of Boiling Crisis in Pool Boiling," *Int. J. Heat Mass Transfer*, Vol. 11, 1968, pp. 993–1002.

7 Katto, Y., and Kosho, Y., "Critical Heat Flux of Saturated Natural Convection Boiling in a Space Bounded by Two Horizontal Co-axial Disks and Heated From Below," *Int. J. Multiphase Flow*, Vol. 5, 1979, pp. 219–224.

8 Jensen, M. K., Cooper, P. E., and Bergles, A. E., "Boiling Heat Transfer and Dryout in Restricted Annular Geometries," *AIChE Symp.*, Vol. 73, No. 164, 1976, pp. 205–214.

9 Ishiibashi, E., and Nishikawa, K., "Saturated Boiling Heat Transfer in Narrow Spaces," *Int. J. Heat Mass Transfer*, Vol. 12, 1969, pp. 863–894.

10 Markatos, N. C. G., Sala, R., and Spalding, D. B., "Flow in an Annulus of Non-Uniform Gap," *Trans. Ind. Chem. Engg.*, Vol. 56, 1978, pp. 28–35.

11 Tan, M. J., M.S. thesis, Chemical Engineering Department, Northwestern University, Evanston, IL, 1980.

12 Tong, C. R., M.S. thesis, Chemical Engineering Department, Northwestern University, Evanston, IL, 1981.

13 Tan, M. J., and Bankoff, S. G., "Stability and Natural Frequency of a Dry Patch in Narrow-Gap Eccentric Annulus Convective Boiling," to be submitted for publication.

14 Dittus, F. W., and Boelter, L. M. K., "Heat Transfer in Automobile Radiators of the Tubular Type," University of California Engineering Pubs., Vol. 2, 1930, p. 443.

15 Chen, J. C.,. "Correlation for Boiling Heat Transfer to Saturated Fluids in Convective Flow," *Ind. Engg. Chem. Process Design and Develop.*, Vol. 5, No. 3, 1966, pp. 322–329.

16 Chisholm, D., and Leisham, J. M., "The Metering of Wet Steam," *Chem. and Process Engg.*, Vol. 50, No. 7, 1969, pp. 103–106.

17 Snyder, W. T., and Goldstein, G. A., "An Analysis of Fully Developed Laminar Flow in an Eccentric Annulus," *AIChE J.*, Vol. 11, No. 3, 1965, pp. 462–467.

18 Brighton, J. A., and Jones, J. B., "Fully Developed Turbulent Flow in Annuli," ASME *J. Basic Engg.*, Vol. 86, 1964, pp. 835–844.

19 Knudsen, J. C., and Katz, D. L., *Fluid Dynamics and Heat Transfer*, McGraw-Hill, New York, 1958, p. 176.

20 Rohsenow, W. M., and Harnett, J. P., *Handbook of Heat Transfer*, McGraw-Hill, New York, 1973, pp. 7-32, 13-34.

21 Baum, A. J., and Curlee, N. J., Jr., "An Experimental and Analytical Investigation of Dryout and Chemical Concentration in Confined Geometries," ASME Paper No. 80-C2/NE-6, Nucl. Engg. Conf., San Francisco, CA, 1980.

22 Johnston, B. S., and Bankoff, S. G., "Boiling Heat Transfer in a Narrow Eccentric Annulus, Part III: A Model of Dry Patch Extent and Temperature Distribution," ASME/JSME Joint Thermal Engineering Conference, Honolulu, HI, 1983.

Calculation of Heat Transfer to Convection-Cooled Gas Turbine Blades

W. Rodi
Universität Karlsruhe,
Karlsruhe, Federal Republic of Germany

G. Scheuerer
Universität Erlangen-Nürnberg,
Erlangen, Federal Republic of Germany

A mathematical model is presented for calculating the external heat transfer coefficients around gas turbine blades. The model is based on a finite-difference procedure for solving the boundary-layer equations which describe the flow and temperature field around the blades. The effects of turbulence are simulated by a low-Reynolds number version of the k–ϵ *turbulence model. This allows calculation of laminar and transitional zones and also the onset of transition. Applications of the calculation method are presented to turbine-blade situations which have recently been investigated experimentally. Predicted and measured heat transfer coefficients are compared and good agreement with the data is observed. This is true especially for the pressure-surface boundary layer which is of a rather complex nature because it remains in a transitional state over the full blade length. The influence of various flow phenomena like laminar-turbulent transition and of the boundary conditions (pressure gradient, free-stream turbulence) on the predicted heat transfer rates is discussed.*

1 Introduction

The thermal efficiency and specific thrust of gas turbines can only be improved significantly by increasing the turbine-inlet temperature. This approach is limited, however, by the availability of appropriate materials that withstand the high temperatures. For instance, present-day blade materials cannot be exposed to temperatures above 1250 K without dramatic losses in their lifetime. In order to make possible turbine-inlet temperatures of more than 1600 K, which are common practice in modern military jet engines, the turbine blades must be cooled. In presently operating engines, convective cooling and film cooling (or a combination of both) are used exclusively. In both techniques, the cooling air is diverted from the mainstream at the exit of the compressor, and the mass flux through the combustion chamber and the turbine is thereby reduced. This and associated losses, which are discussed by Cohen et al. [1] decrease the thermal efficiency of the system. Poor design may lead to a situation where the efficiency gained by higher turbine-inlet temperatures is completely offset by the additional cooling losses.

An important task in the design of modern gas turbines is therefore to minimize the cooling air stream and with it the cooling losses. To this end, the blade surface is allowed to reach locally the critical temperature dictated by the lifetime requirements. An important prerequisite for the design of such highly optimized cooling arrangements is the actual knowledge of the temperature distribution over the blade surface which, for a certain arrangement, is determined by the heat transfer from the hot gas to the blade. The prediction of this heat transfer and its variation around the turbine blade is therefore of great practical importance. As prototype experiments are usually extremely expensive (Daniels [2] quotes a number of 1 million pound sterling per rig test of the Rolls-Royce RB-211 engine) and often not of high accuracy, there is a great need for theoretical prediction methods. Such methods are particularly suitable for parameter studies and, due to the recent development of fast digital computers and efficient numerical solution procedures, fairly powerful techniques are available now.

The present paper describes a differential (or field) method for calculating the external heat transfer rates to convection-cooled gas turbine blades. The method, which is restricted to two-dimensional situations without flow separation, is based on the numerical boundary-layer procedure of Patankar and Spalding [3]. A refined turbulence model has been incorporated into this procedure which is an extended version of the widely used k–ϵ model. The extensions concern the simulation of viscous and near-wall effects and of the laminar-turbulent transition and its dependence on the free-stream turbulence. The calculation method is applied to various turbine blade situations for which Daniels and Browne [4] have recently carried out measurements. Predicted and measured heat transfer rates are compared, and the paper discusses the influence of phenomena like laminar-turbulent transition, relaminarization, free-stream turbulence, curvature, etc. on the variation of the heat transfer coefficient along the suction and pressure surfaces of turbine blades.

2 Mean Flow Equations

Under two-dimensional stationary conditions, the velocity and temperature field in boundary layers along blade surfaces is governed by the following equations [5]

Contributed by the Gas Turbine Division for publication in the JOURNAL OF ENGINEERING FOR GAS TURBINES AND POWER. Manuscript received by the Gas Turbine Division August 1984.

continuity equation:

$$\frac{\partial(\rho U)}{\partial x}+\frac{\partial(\rho \tilde{V})}{\partial y}=0 \tag{1}$$

x-momentum equation:

$$\rho U\frac{\partial U}{\partial x}+\rho \tilde{V}\frac{\partial U}{\partial y}=-\frac{dP}{dx}+\frac{\partial}{\partial y}\left(\mu\frac{\partial U}{\partial y}-\rho\overline{u'v'}\right) \tag{2}$$

total-enthalpy equation:

$$\rho U\frac{\partial H}{\partial x}+\rho \tilde{V}\frac{\partial H}{\partial y}=\frac{\partial}{\partial y}\left\{\frac{\mu}{\mathrm{Pr}}\frac{\partial H}{\partial y}-\rho\overline{h'v'}+U\left[\left(1-\frac{1}{\mathrm{Pr}}\right)\mu\frac{\partial U}{\partial y}-\rho\overline{u'v'}\right]\right\} \tag{3}$$

In these equations, the x coordinate follows the blade surface and y is normal to x. As the ratio of boundary layer thickness to the radius of curvature of the blade surface is usually fairly small, the extra terms arising from the curvature in such a coordinate system have been neglected. This is justified by Bradshaw's [6] dimensional arguments and the discussion in section 6. U, V, u', v' are the mean and fluctuating velocities in the x and y direction, respectively; P represents the static pressure which is approximately constant across the boundary layer. The total enthalpy

$$H=h+U^2/2+k \tag{4}$$

is the sum of the static enthalpy h and the kinetic energy of the mean and fluctuating motion. The fluid properties are characterized by the density ρ, the viscosity μ, and the Prandtl number Pr. An overbar indicates conventional time averaging of fluctuating quantities while the tilde over V indicates mass averaging so that

$$\rho \tilde{V}=\rho V+\overline{\rho' v'} \tag{5}$$

The first term represents the product of the conventionally averaged quantities ρ and V and the second that of their fluctuations. Both are of the same order of magnitude in compressible boundary layers, whereas ρU is much larger than $\overline{\rho' u'}$ which is therefore neglected. The ideal gas law

$$\rho=\frac{P}{RT} \tag{6}$$

is used to link the density to the static temperature T and hence to the static enthalpy $h=c_pT$.

The above system of equations was solved with the following boundary and initial conditions. At the wall, the velocity components U and V were set to zero (no-slip condition), while the solution of the enthalpy equation (3) requires the specification of either the heat flux or the temperature at the wall. The heat flux depends on the internal cooling processes and could only be determined by solving simultaneously the internal heat transfer problem. Hence, only the external heat transfer is considered and here the wall temperature T_w is prescribed from measurements so that the boundary condition for H at the wall is

$$H=c_pT_w \tag{7}$$

In the free stream, the conditions

$$U=U_e(x),\quad H=H_e=\text{const} \tag{8}$$

are prescribed, where the free-stream velocity U_e is determined from static pressure measurements via the Bernoulli equation. The total enthalpy in the free stream assumes a constant value.

The calculations were started near the stagnation point with a laminar boundary layer, as explained in greater detail in section 6. At the initial station, the U-velocity profile was prescribed with the well-known Pohlhausen formula (see White [7])

$$\frac{U}{U_e}=2\frac{y}{\delta}-2\left(\frac{y}{\delta}\right)^3+\left(\frac{y}{\delta}\right)^4+\frac{\Lambda}{6}\frac{y}{\delta}\left(1-\frac{y}{\delta}\right)^3 \tag{9}$$

where δ is the boundary layer thickness and

$$\Lambda=\frac{\delta^2\rho_e}{\mu_e}\frac{dU_e}{dx} \tag{10}$$

is the Pohlhausen parameter. The temperature and hence the enthalpy distribution at the initial station is related linearly to the velocity profile

Nomenclature

a_1 = empirical parameter
c = chord length of blade
c_p = specific heat
$c_\mu, c_{\epsilon 1}, c_{\epsilon 2}$ = empirical constants in turbulence model
f_μ, f_1, f_2 = empirical functions in turbulence model
H = total enthalpy $= h+U^2/2+k$
h = mean static enthalpy
h' = fluctuating static enthalpy
K = acceleration parameter $= (\mu_e/\rho_e U_e^2)dU_e/dx$
k = turbulent kinetic energy
L = turbulent length scale
P = mean static pressure
P_k = production of k
Pr = molecular Prandtl number
Pr_t = turbulent Prandtl number
R = radius of curvature of surface, gas constant
q_w = heat flux at the surface
Re_c = chord Reynolds number $= U_1 c\rho_1/\mu_1$
Re_{2k} = momentum thickness Reynolds number $= U_e\delta_{2k}\rho_e/\mu_e$
Re_y, Re_T = turbulence Reynolds numbers defined in equation (15)
T = mean static temperature
T_0 = total temperature in free stream
Tu = turbulence level $= (\overline{u_e'^2})^{1/2}/U_e$
U = mean streamwise velocity
U_τ = friction velocity $= \sqrt{\tau_w/\rho_w}$
u' = fluctuating streamwise velocity
V = mean lateral velocity
v' = fluctuating lateral velocity
x = streamwise coordinate
y = cross-stream coordinate
y^+ = dimensionless wall distance $= yU_\tau\rho_w/\mu_w$
δ = boundary layer thickness
δ_{2k} = momentum thickness
δ_v = thickness of viscous sublayer
ϵ = dissipation rate
Λ = Pohlhausen parameter
μ = molecular viscosity
μ_t = turbulent (eddy) viscosity
α = heat transfer coefficient $= q_w/(T_w-T_0)$
ρ = mean density
ρ' = fluctuating density
$\sigma_k, \sigma_\epsilon$ = empirical constants in turbulence model
τ_w = wall shear stress

Subscripts

e = external (free stream)
w = wall
1 = inlet station

$$\frac{T}{T_w} = 1 + \left(\frac{T_e}{T_w} - 1\right)\frac{U}{U_e} \tag{11}$$

Further details on the starting procedure are discussed in section 6.

3 Turbulence Model

The turbulent stress $-\rho\overline{u'v'}$ and the turbulent heat flux $-\rho\overline{v'h'}$ appearing in equations (2) and (3) have to be determined with the aid of a turbulence model. In the present work, Lam and Bremhorst's [8] low-Reynolds number version of the well-tested k–ϵ model has been adopted. This model as well as extensions necessary for the simulation of the laminar-turbulent transition as well as for calculating the turbulent heat flux are presented below.

3.1 The k–ϵ Model. The k–ϵ model uses the eddy viscosity concept relating the turbulent stress to the mean rate of strain

$$-\rho\overline{u'v'} = \mu_t \frac{\partial U}{\partial y} \tag{12}$$

In this and the following turbulence-model equations curvature terms arising from the use of a curvilinear coordinate system have again been neglected. This will be justified in section 6. The eddy viscosity μ_t is related to the turbulent kinetic energy k and the rate of its dissipation ϵ by

$$\mu_t = c_\mu f_\mu \rho \frac{k^2}{\epsilon} \tag{13}$$

where c_μ is an empirical constant and f_μ a function which expresses viscous and near-wall effects on the stress $-\rho\overline{u'v'}$. The function f_μ given by Lam and Bremhorst [8] reads

$$f_\mu = \left[1 - \exp(-0.0160\mathrm{Re}_y)\right]^2 \left(1 + \frac{19.5}{\mathrm{Re}_T}\right) \tag{14}$$

where the turbulence Reynolds numbers Re_y and Re_T are defined as

$$\mathrm{Re}_y = \frac{\sqrt{k}y\rho}{\mu};\quad \mathrm{Re}_T = \frac{k^2\rho}{\epsilon\mu} \tag{15}$$

The distributions of k and ϵ are determined from the following model transport equations for these quantities

$$\rho U\frac{\partial k}{\partial x} + \rho\tilde{V}\frac{\partial k}{\partial y} = \frac{\partial}{\partial y}\left[\left(\mu + \frac{\mu_t}{\sigma_k}\right)\frac{\partial k}{\partial y}\right] + P_k - \rho\epsilon \tag{16}$$

$$\rho U\frac{\partial \epsilon}{\partial x} + \rho\tilde{V}\frac{\partial \epsilon}{\partial y} = \frac{\partial}{\partial y}\left[\left(\mu + \frac{\mu_t}{\sigma_\epsilon}\right)\frac{\partial \epsilon}{\partial y}\right] + \frac{\epsilon}{k}\left[c_{\epsilon 1}f_1 P_k - c_{\epsilon 2}f_2\rho\epsilon\right] \tag{17}$$

where the production P_k of k is:

$$P_k = \mu_t\left(\frac{\partial U}{\partial y}\right)^2 \tag{18}$$

The empirical low-Reynolds number functions f_1 and f_2 appearing in the ϵ-equation (17) read:

$$f_1 = 1 + \left(\frac{0.06}{f_\mu}\right)^3,\quad f_2 = 1 - \exp(-\mathrm{Re}_T^2) \tag{19}$$

For the remaining empirical constants, the "standard" values cited by Rodi [9] have been adopted: $c_\mu = 0.09$, $c_{\epsilon 1} = 1.44$, $c_{\epsilon 2} = 1.92$, $\sigma_k = 1.0$, $\sigma_\epsilon = 1.3$. A detailed discussion of the low-Reynolds number k–ϵ model is provided in Patel et al. [10]. It should be noted that the constants in the functions f_μ, f_1, and f_2 are slightly different from Lam and Bremhorst's [8] original proposal. They have been adjusted to give better results for a variety of boundary layers (see Rodi et al. [11]).

Boundary and initial conditions need to be specified also for the turbulence quantities k and ϵ. At the wall, the following conditions are used

$$k = \frac{\partial \epsilon}{\partial y} = 0 \tag{20}$$

which follows from the no-slip condition and the continuity equation at the wall. The free-stream values of k and ϵ are determined from the solution of the simplified k and ϵ equations prevailing in the free stream

$$\rho_e U_e \frac{dk_e}{dx} = -\rho_e \epsilon_e \tag{21}$$

$$\rho_e U_e \frac{d\epsilon_e}{dx} = -\rho_e c_{\epsilon 2}\frac{{\epsilon_e}^2}{k_e} \tag{22}$$

The streamwise variation of k_e and ϵ_e is obtained by integrating these ordinary differential equations, starting from prescribed values at the initial station. The prescription of initial values is discussed in section 6.

3.2 Calculation of the Laminar-Turbulent Transition. For relatively large free-stream turbulence levels (say above 1 percent) the model is capable of simulating, at least qualitatively, the physical transition mechanism which is governed by the diffusion of turbulent kinetic energy k from the free stream into the laminar boundary layer. The calculations start with a laminar boundary layer; some distribution of k and ϵ between the wall and the free-stream values k_e and ϵ_e given from the experiments has to be prescribed at the starting station (the starting profiles for mean velocity and total enthalpy have already been given in section 2). The following empirical profiles are used for k and ϵ

$$k = k_e(U/U_e)^2 \tag{23}$$

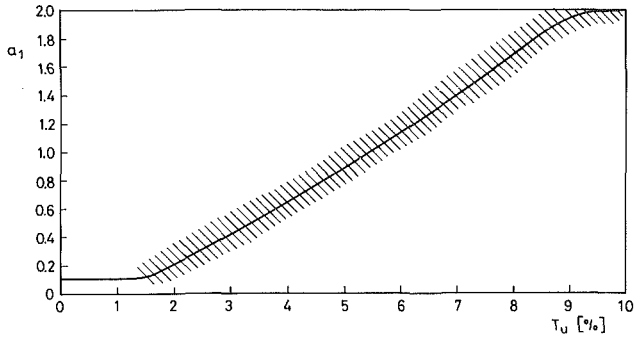

Fig. 1 Variation of coefficient a_1 with turbulence level

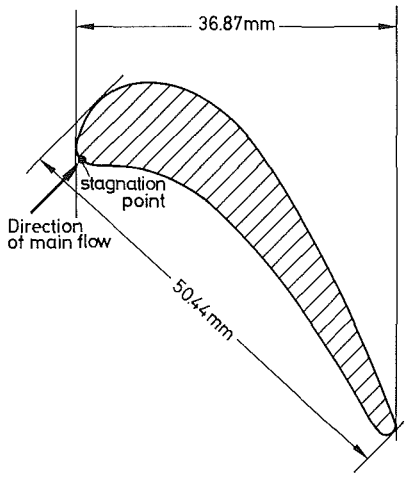

Fig. 2 Blade profile in Daniels and Browne's [4] experiments

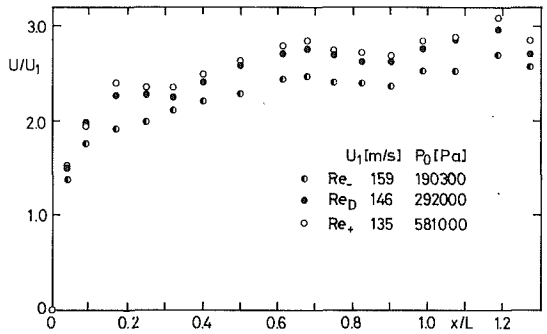

Fig. 3 Measured distribution of free-stream velocity along suction surface

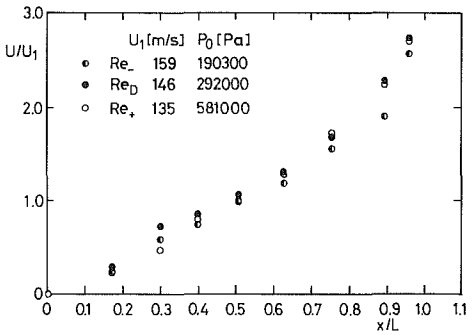

Fig. 4 Measured distribution of free-stream velocity along pressure surface

$$\epsilon = a_1 k \partial U/\partial y; \quad \epsilon \geq \frac{k_e^{3/2}}{L_e} \tag{24}$$

Equation (23) forces k to vanish at the wall and increases k quadratically with distance from the surface until it takes its prescribed free-stream value at the edge of the boundary layer. The initial profile for ϵ is based on the assumption that the rate of dissipation is proportional to the rate of production of k and that the proportionality coefficient a_1 depends on the turbulence level Tu. The variation of a_1 with Tu used in the model is shown in Fig. 1; it has been determined by simulating various boundary-layer experiments involving laminar-turbulent transition. A detailed discussion on these is provided by Scheuerer [12]. Equation (24) also imposes a limit on ϵ which prevents the turbulence length scale $L = k^{3/2}/\epsilon$ inside the boundary layer from exceeding its free-stream value L_e.

As the calculation proceeds from the initial station, turbulent kinetic energy diffuses from the free stream into the boundary layer. When, after a certain distance, the higher k values of the free stream reach the near-wall zone of the boundary layer, they cause increased turbulence production by interaction with the larger velocity gradients so that the magnitude of k is augmented and gradually renders the boundary layer turbulent.

3.4 Modeling of the Turbulent Heat Flux $-\rho\overline{v'h'}$. The turbulent heat flux $-\rho\overline{v'h'}$ appearing in the total enthalpy equation (3) is modeled with the aid of the eddy diffusivity concept and the additional assumption that the eddy diffusivity is equal to the eddy viscosity divided by the turbulent Prandtl number Pr_t

$$-\rho\overline{v'h'} = \frac{\mu_t}{\mathrm{Pr}_t}\frac{\partial h}{\partial y} \tag{25}$$

The eddy viscosity μ_t is provided from the k-ϵ model described above. For the turbulent Prandtl number, a constant value of $\mathrm{Pr}_t = 0.86$ is used in agreement with a large number of experimental data collected by Kays and Moffat [13].

4 Solution Procedure and Computational Details

The mean-flow and turbulence-model equations presented in the previous sections were solved with an adapted version of the GENMIX computer code described by Spalding [14] which originates from the earlier Patankar-Spalding [3] procedure. The method is implicit and forward marching in space so that only one-dimensional storage of the variables is required. A dimensionless stream function is used as normal coordinate which causes the numerical grid to expand automatically as the boundary layer grows so that a constant number of grid nodes is distributed across the boundary layer at each station, resulting in a fairly economical solution procedure.

In order to obtain grid-independent solutions, a nonequidistant grid was used with 100 nodes in the cross-stream direction, and with considerably finer mesh sizes near the wall than near the edge of the boundary layer. At the starting location, the first grid node away from the wall was typically at the dimensionless wall distance $y^+ = 0.2$, where y^+ is defined in the Nomenclature. The streamwise step size was specified as one quarter of the momentum thickness δ_{2k}, defined as

$$\delta_{2k} = \int_0^\infty \frac{U}{U_e}\left(1 - \frac{U}{U_e}\right)dy \tag{26}$$

In order that fast changes in the viscous sublayer can be followed, the step size was further limited to five sublayer thicknesses, corresponding to $\Delta x \leq 25\mu_w/(\rho_w U_\tau)$.

The calculation time per forward step was 0.125 s on a CDC CYBER 173 computer. The total computing times were of the order of 20 min for the suction surfaces and 10 min for the pressure surfaces.

5 Description of the Test Cases

The computer program was applied to various blade situations for which Daniels and Browne [4] have recently conducted heat transfer measurements. The blade profile is shown in Fig. 2 and is typical of high-pressure turbines in modern high-bypass-ratio fan jets. Three test cases were selected for simulation and these are characterized by chord Reynolds numbers Re_c of 4.8×10^5, 6.7×10^5, and 1.3×10^6 where

$$\mathrm{Re}_c = \frac{U_1 c \rho_1}{\mu_1} \tag{27}$$

The index "1" in equation (27) relates to values at the inlet, and c is the axial chord of the blade. The three different test cases will subsequently be referred to as Re_-, Re_D, and Re_+. The variation in Reynolds number was achieved by altering the stagnation pressure P_0.

The outlet Mach number of the cascade flow was equal to 0.94 for all cases. Figures 3 and 4 show respectively the distributions of the measured free-stream velocities along the suction and pressure surfaces. The coordinate system originates at the stagnation point. The total temperature T_0 in the free stream was 432 K and the blade surface temperature T_w was constant at 288 K for all test runs. Although these temperatures are not representative for real turbines, their ratio $T_w/T_o \approx 0.7$ is quite characteristic of modern jet engines. The heat transfer rates were determined in the experiments from the temporal variation of the blade surface temperature by means of a transient technique. Daniels and Browne [4] give an uncertainty of ± 10 percent for their measurements of the wall heat flux.

In order to simulate operational conditions in a real cascade, Daniels and Browne [4] placed a turbulence-

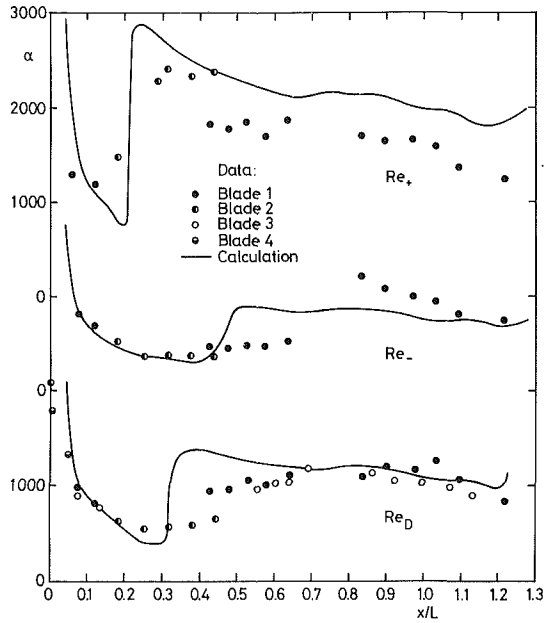

Fig. 5 Distribution of heat transfer coefficient along suction surface

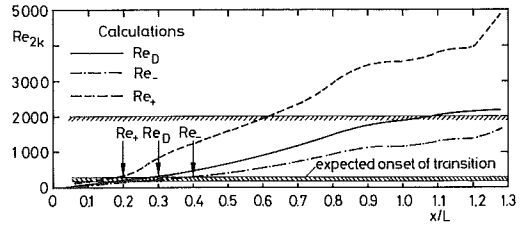

Fig. 6 Calculated variation of momentum-thickness Reynolds number along suction surface

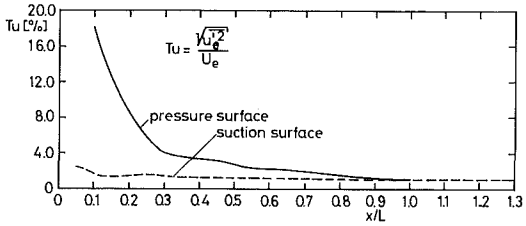

Fig. 7 Calculated variation of free-stream turbulence intensity along suction and pressure surfaces for case Re_D

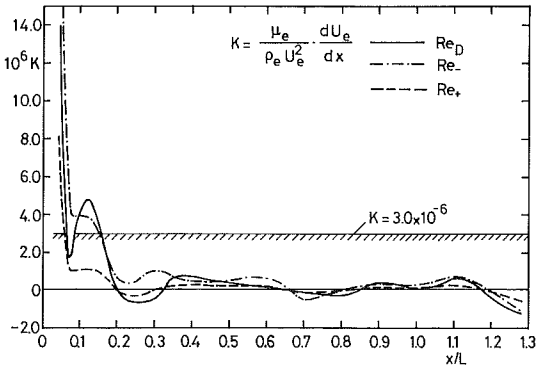

Fig. 8 Variation of acceleration parameter K along suction surface

generating grid in the inlet channel. At 12.7 cm upstream of the blade profile, they measured a turbulence level of $Tu=4.2$ percent with a hot wire. For the calculations reported here, the turbulence level at the entrance of the cascade was obtained with the aid of an empirical formula for the decay of grid turbulence due to Townsend [15]. This yielded the value of 3 percent used in the computations. The turbulence length scale in the free stream was set equal to the diameter of the rods of the turbulence-generating grid ($L_e=1.8$ cm); this choice is supported by an analysis of the predominant frequency of the free-stream turbulence field conducted by Daniels [1]. The initial value for the dissipation rate ϵ was calculated from $\epsilon_e=k_e^{3/2}/L_e$.

Daniels and Browne [4] examined the two-dimensionality of the blade boundary layers by visualizing the surface streak lines. With the exception of small areas at hub and tip of the blades, the surface flow was observed to be parallel to the x direction. The aspect ratio (pitch to blade height) of the cascade was 2.2.

6 Results and Discussion

In this section, the calculated results are compared with the experimental data. The suction and pressure surface flows are discussed separately in subsections 6.1 and 6.2. After comparing the heat transfer coefficients for each surface, the influence of laminar-turbulent transition, pressure gradient, free-stream turbulence level, surface curvature, compressibility, and surface roughness on the heat flux distributions is assessed.

6.1 Suction Surface. The calculations for the suction surfaces were initialized at $x/L=0.04$. The momentum-thickness Reynolds numbers, $Re_{2k}=\delta_{2k}U_e\rho_e/\mu_e$ at this position were calculated with a theory of Thwaites [16] which is based on a linear increase of the free-stream velocity in the vicinity of the stagnation point. Re_{2k} emerged as 42.5, 53, and 80 for the Re_-, Re_D, and Re_+ cases respectively. Even the largest Reynolds number is well within the laminar regime so that the chosen initial profiles described in section 2 represent adequately the physical situation. In order to determine the local turbulence level at the starting location, the absolute value of $\overline{u_e'^2}$ was assumed to remain constant over the small distance from the inlet reference station "1" to the initial station of the calculation. Due to the change in free-stream velocity U_e there results

$$Tu=Tu_1(U_1/U_e) \tag{28}$$

The free-stream turbulence was assumed to be isotropic so that the turbulent kinetic energy k_e is related to Tu by

$$\frac{k_e}{U_e^2}=1.5\ Tu^2 \tag{29}$$

Figure 5 compares the distribution of the calculated and measured heat transfer coefficient α (for definition see Nomenclature) for the three test cases. The individual symbols characterize blades that were instrumented differently. The largest number of data has been taken for the design condition Re_D, and this will be discussed first. The flow is initially laminar; in this region the predicted results are in very good agreement with the measurements. In the model simulation, the laminar-turbulent transition occurs somewhat earlier than in the experiments and also proceeds faster, which leads to certain differences with the data in this region. In the fully turbulent region beyond $x/L>0.5$, the experimental heat transfer coefficients are again reproduced very well by the model. A similar picture emerges for the Re_- case, where good agreement results in the laminar and turbulent regions, but discrepancies arise in the transitional regime. In that case, however, the transition data appear somewhat suspect because in another set of measurements without a turbulence-generating grid [4], where the turbulence level was only 0.4 percent, the laminar-turbulent transition occurred much

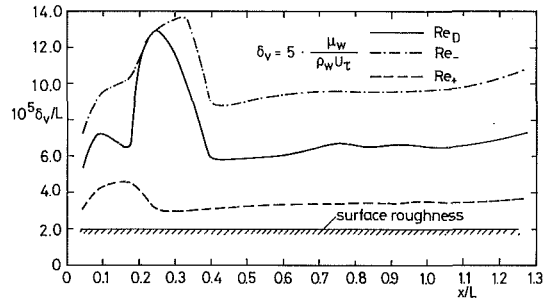

Fig. 9 Calculated variation of viscous sublayer thickness along suction surface

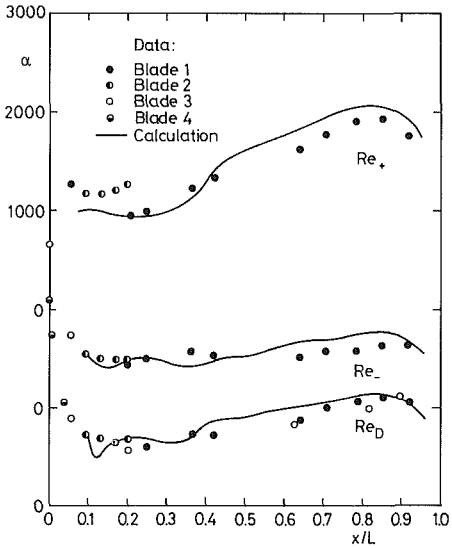

Fig. 10 Distribution of heat transfer coefficient along pressure surface

earlier. Hence, it is not clear whether the measured transition process for the lowest Reynolds-number case is representative of a two-dimensional boundary-layer flow. The α distribution for the higher Reynolds-number flow is shown at the top of Fig. 5. It displays a strong variation of the heat transfer coefficient as the flow undergoes transition, which is simulated well by the model. In the turbulent region, the heat transfer coefficient is somewhat overpredicted. It should be noted, however, that the experimental values show a discontinuity at $x/L = 0.42$, which is roughly of the same magnitude as the difference between calculations and measurements. In the following, the various flow phenomena governing the distribution of the heat transfer coefficient are discussed in greater detail.

Laminar-Turbulent Transition. From empirical correlations collected by Abu Ghannam [17], laminar-turbulent transition for the flow considered is expected in the Reynolds number range $200 \leq Re_{2k} \leq 300$. Figure 6 compares the calculated momentum thickness Reynolds number with this criterion, and it can be seen that the predicted onset of transition (indicated by arrows) agrees with the expected values. It is interesting to note that, for the Re_D case, the Reynolds number exceeds only slightly a value of 2000 usually considered as the lower limit for fully turbulent boundary layers. This means that strong viscous effects are present over most of the suction surface. These are increased further by reducing the Reynolds number, i.e., for the Re_- case. It is obvious therefore that only a turbulence model can be used that takes proper account of the viscous effects, as does the one employed in the present work.

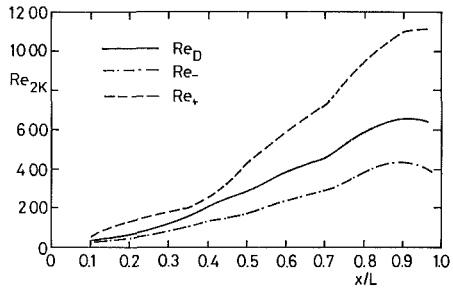

Fig. 11 Calculated variation of momentum-thickness Reynolds number along pressure surface

Free-Stream Turbulence. The main effect of free-stream turbulence on the boundary layer development is to promote laminar-turbulent transition which, in turn, leads to increased heat transfer coefficients. In addition, the heat transfer in the fully turbulent boundary layer is enhanced, although only by a small amount (approximately 4 percent per 1 percent *Tu*, see Bradshaw [18]). The variation of *Tu* with surface length, as calculated from equations (21) and (22), is shown in Fig. 7 for the Re_D case. Although the magnitude of the turbulence intensity in the simulated experiments is less than in real engines, its variation along the blade surface is comparable. As a consequence of the rapid acceleration near the stagnation point (see Fig. 3), *Tu* is decreased to about 50 percent of its inlet value and displays only a mild decay thereafter. This distribution is quite typical for suction surfaces and points to the importance of using local values of *Tu*, especially for transition calculations, rather than a characteristic reference value as was done in older methods.

Pressure Gradient. Apart from the free-stream turbulence, the longitudinal pressure gradient exerts the largest effect on transition and hence on the distribution of the heat transfer coefficient. The pressure gradient is often characterized by the dimensionless parameter K, defined as

$$K = \frac{\mu_e}{\rho_e U_e^2} \frac{dU_e}{dx} \tag{30}$$

For values of K larger than 3.0×10^{-6}, transition is suppressed for small *Tu*, and turbulent boundary layers start to relaminarize. Figure 8 shows that high accelerations occur only for $x/L < 0.2$, while the effect of the pressure gradient is negligible for the rest of the suction surface. This behavior is quite representative of general suction-surface situations, as the initial increase of the free-stream velocity usually takes place over small distances and, thereafter, yields low values of K and consequently a small effect on the momentum and enthalpy equations. It should be stressed that adequately small forward steps are required in the numerical solution procedure in order to resolve the steep variations in the pressure gradient and the associated thin boundary layer in the leading-edge zone.

Surface Curvature. The effects of surface curvature on the boundary-layer behavior increase with the ratio of local boundary-layer thickness δ to radius of curvature R (where R is positive for convex and negative for concave surfaces). Skin friction and heat transfer rates are reduced for convex curvature, i.e., on the suction surfaces, and augmented on the concave pressure surfaces. Bradshaw [6] states that the change of these rates due to curvature is of the order of δ/R for laminar flow and almost one order of magnitude higher for turbulent flow. The calculations have shown that δ/R values of 0.02 are not exceeded in the laminar regime and that δ/R is around 0.005 in the turbulent region. Hence the neglect of the curvature terms in the mean-flow equations and also in the turbulence model appears justified.

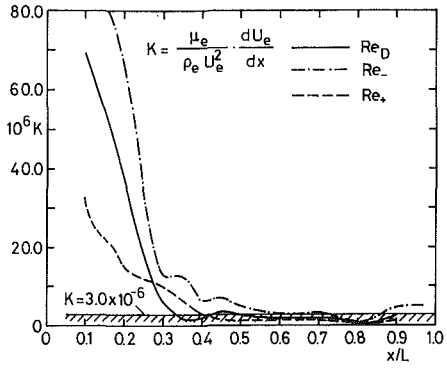

Fig. 12 Variation of acceleration parameter K along pressure surface

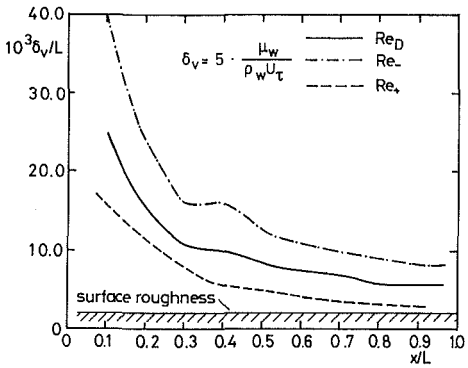

Fig. 13 Calculated variation of viscous sublayer thickness along pressure surface

Variation of Fluid Properties. In the present test cases, the local Mach numbers exceeded unity only slightly along the suction surfaces. Hopkins and Inouye's [19] correlation of experimental data suggests that, for these values, the density variations due to compressibility cause only small reductions (of the order of 10 percent) in the skin friction and heat transfer coefficients. In many cases, the influence of Mach number is counterbalanced by the effects of the variation in fluid properties caused by the surface cooling, which leads to higher heat transfer and skin friction values. Here, for a temperature ratio of $T_w/T_0 \approx 0.5$, increases of 20 percent in the heat transfer rates have been observed in comparison with isothermal flow (see Sill [20]). Further, for Mach numbers around unity, Schlichting [21] reports only a small compressibility effect on the laminar-turbulent transition. Altogether, the variation of fluid properties has no significant influence on the boundary-layer development along turbulent blades.

Surface Roughness. Roughness effects become noticeable whenever the height of the roughness elements exceeds the viscous sublayer thickness δ_v, which may be estimated as

$$\delta_v = 5 \frac{\mu_w}{\rho_w u_\tau} \tag{31}$$

For the blades under investigation, the surface roughness height k_s was approximately 1 micron, resulting in $k_s/L \approx 2\times10^{-5}$. This value is compared with the computed sublayer thicknesses δ_v in Fig. 9. As can be seen, the roughness elements are well within the viscous sublayer so that their effect is negligible and the assumption of a smooth surface justified. This situation is representative of present-day turbine blades; it should be stressed, however, that the smoothness requirements for blade surfaces increase with the Reynolds number because of the decreasing thickness of the viscous sublayer.

6.2 Pressure Surface. The calculated heat transfer coefficients along the pressure surface are compared with the experimental data in Fig. 10. The computations were started at $x/L = 0.1$ for the Re_- and Re_D cases and at $x/L = 0.075$ for the Re_+ case. The corresponding momentum thickness Reynolds numbers were 30 and 33, respectively. The results for the design condition Re_D are displayed at the bottom of Fig. 10. Due to the relatively high free-stream turbulence, the laminar-turbulent transition occurs shortly after the initial station as will be discussed further below. The continuous acceleration prevents the heat transfer coefficient from increasing rapidly so that it grows only slightly from the point of transition to the trailing edge. The numerical model reflects this behavior very well and shows good agreement with the data. For the Re_- condition, the heat transfer coefficient is nearly constant along the blade surface because the acceleration parameter K increases with decreasing Reynolds number so that stronger relaminarization effects are present. This behavior is also reproduced well by the computations. In the case of the highest Reynolds number, Re_+, the free-stream turbulence effect dominates over the acceleration effect and leads to markedly higher heat transfer rates toward the trailing edge, which are reproduced within the experimental uncertainties. In the following, the influence of various parameters on the heat transfer behavior is again discussed.

Laminar-Turbulent Transition. The high free-stream turbulence levels in the leading-edge region of pressure surfaces lead to a very early transition. However, the boundary layers do not attain a fully turbulent state because of the relaminarizing effect of the pressure gradient. The flow remains transitional over the entire blade surface, especially so for the lower chord Reynolds numbers. This conclusion is supported by Fig. 11 which shows the calculated momentum thickness Reynolds number along the pressure surface. For the Re_D and Re_- case, maximum values of 650 and 450 result, respectively, which indicate clearly that the boundary layers are not fully turbulent.

Free-Stream Turbulence. Figure 7 includes also the calculated variation of Tu along the pressure surface. The low free-stream velocities in the leading-edge region yield, according to equation (28), turbulence intensities of 19 percent which are an order of magnitude larger than those on the suction surface. As was mentioned already, these high values cause a rapid onset of transition.

Pressure Gradient. Figure 12 shows the acceleration parameter K for the pressure surface. A comparison with Fig. 8 indicates that this parameter is much higher on the pressure surface than on the suction surface. For the Re_D and Re_- conditions, the criterion for relaminarization, $K = 3.0 \times 10^{-6}$, is exceeded over most of the surface length. From the last two figures it is therefore obvious that the flow on the pressure surface is controlled almost entirely by free-stream turbulence and pressure-gradient effects.

Surface Curvature. On the pressure surface, the absolute value of δ/R is somewhat larger than on the suction surface in the initial region, but it does not exceed 0.03; beyond $x/L = 0.4$ it is constant at about 0.002. Hence, on the pressure surface, the neglect of curvature effects in the theoretical model is again justified.

Surface Roughness. The calculated thicknesses of the viscous sublayer on the pressure surface are compared in Fig. 13 with the value of the surface roughness height. As in the case of the suction surface, the roughness elements are embedded in the viscous sublayer and hence do not exert any effect on the skin friction or heat transfer rates. In fact, the

problem of surface roughness is less critical on the pressure than on the suction side of turbine blades.

7 Conclusions

The following conclusions can be drawn from the study presented in this paper:

- The distribution of the heat transfer coefficient on the suction sides of turbine blades is governed mainly by the onset of the laminar-turbulent transition. This process in turn is controlled by the local values of the free-stream turbulence intensities and the pressure gradient. Surface curvature, variable fluid properties, and surface roughness (if the blades are well finished) exert only a negligible influence on the external heat transfer. The calculation method used in the present study predicts the heat transfer coefficients with good accuracy; discrepancies with the measurements occur only in the transitional region, where the method yields a somewhat faster transition than was observed in the experiments.
- On the pressure surface, transition usually starts very near the leading edge because of the high relative turbulence intensity on this side of the blade. After this onset, there is a delicate balance between free-stream turbulence and pressure-gradient effects, the former tending to promote and the latter to retard the transition to fully turbulent flow. Due to the relaminarizing effect of the pressure gradient, the boundary layer does not become fully turbulent on the pressure surface. Again curvature, variable properties, and roughness effects are negligible. As the free-stream turbulence level and the pressure gradients are both about one order of magnitude larger than on the suction side, the boundary layer is very sensitive to these parameters and a refined turbulence model is required that can handle the interaction of free-stream turbulence and pressure-gradient effects in such complex boundary layers. The excellent results obtained for the heat transfer coefficients on the pressure surface with the present model show that this model is indeed capable of simulating adequately these effects.

8 Acknowledgments

Financial support of the Forschungsvereinigung Verbrennungskraftmaschinen is gratefully acknowledged. The calculations were carried out on the CDC computer of the Regionales Rechenzentrum Erlangen. The authors would like to thank Mrs. R. Zschernitz for the efficient typing of the manuscript.

9 References

1 Cohen, H., Rogers, G. F. C., and Saravanamutto, H. I. H., *Gas Turbine Theory*, Longman, London, 1973.

2 Daniels, L. C., "Film Cooling of Gas Turbine Blades," Univ. of Oxford, Dept. Eng. Sc., OUEL-Rept. No. 1302/79, 1979.

3 Patankar, S. V., and Spalding, D. B., *Heat and Mass Transfer in Boundary Layers*, 2nd ed., Intertext, London, 1970.

4 Daniels, L. C., and Browne, W. B., "Short Duration Measurements of Heat Transfer Rate to a Gas Turbine Rotor Blade," *Int. J. Heat Mass Transfer*, Vol. 24, 1981, pp. 871-879.

5 Cebeci, T., and Smith, A. M. O., *Analysis of Turbulent Boundary Layers*, Academic Press, New York, 1974.

6 Bradshaw, P., "Effects of Streamline Curvature on Turbulent Flow," AGARDograph No. 169, 1973.

7 White, F. M., *Viscous Fluid Flow*, McGraw-Hill, New York, 1974.

8 Lam, C. K. G., and Bremhorst, K. A., "Modified Form of the k-ϵ Model for Predicting Wall Turbulence," *J. Fluids Eng.*, Vol. 103, 1981, pp. 456-460.

9 Rodi, W., *Turbulence Models and Their Application in Hydraulics*, International Association for Hydraulic Research, Delft, The Netherlands, 1980.

10 Patel, V. C., Rodi, W., and Scheuerer, G., "Evaluation of Turbulence Models for Near-Wall and Low-Reynolds Number Flow," *Proceedings 3rd Turbulent Shear Flow Symposium*, Davis, CA, Sept. 1981.

11 Rodi, W., Celik, I., Demuren, A. O., Scheuerer, G., Shirani, E., Leschziner, M. A., and Rastogi, A. K., "Calculations for the 1980-81 AFOSR-HTTM Stanford Conference on Complex Turbulent Flows," *Proceedings* of this conference, Vol. III, ed. S. J. Kline, B. J. Cantwell, and G. M. Lilley, 1982.

12 Scheuerer, G., "Entwicklung eines Verfahrens zur Berechnung zweidimensionaler Grenzschichten an Gasturbinenschaufeln," Ph.D. thesis, Universität Karlsruhe, 1983.

13 Kays, W. M., and Moffat, R. J., "The Behaviour of Transpired Turbulent Boundary Layers," in: *Studies in Convection*, ed. B. E. Launder, Vol. 1, Academic Press, London, 1975, pp. 223-319.

14 Spalding, D. B., "GENMIX—A General Computer Program for Two-Dimensional Parabolic Phenomena," Pergamon Press, Oxford, 1977.

15 Townsend, A. A., "The Structure of Turbulent Shear Flow," 2nd ed., Cambridge Univ. Press, Cambridge, 1976.

16 Thwaites, B., "Approximate Calculation of the Laminar Boundary Layer," *Aero Quarterly*, Vol. 7, 1949, p. 245.

17 Abu-Ghannam, B. J., "Boundary Layer Transition in Relation to Turbomachinery Blades," Ph.D. thesis, Univ. of Liverpool, 1979.

18 Bradshaw, P., "Effect of Free-Stream Turbulence on Turbulent Shear Layers," ARC-Paper 35648, 1974.

19 Hopkins, E. J., and Inouyé, M., "An Evaluation of Theories for Predicting Turbulent Skin Friction and Heat Transfer on Flat Plates at Supersonic and Hypersonic Mach Numbers," *AIAA Journal*, Vol. 9, 1971, pp. 993-1003.

20 Sill, H., "Wärme- und Stoffübertragung in turbulenten Strömungsgrenzschichten längs verdunstender welliger Wasserfilme," Ph.D. thesis, Universität Karlsruhe, 1982.

21 Schlichting, H., "Boundary Layer Theory," Verlag G. Braun, Karlsruhe, 1968.

Heat Transfer Enhancement in Channels With Turbulence Promoters

J. C. Han
Associate Professor.

J. S. Park
Research Assistant.

C. K. Lei
Research Assistant.

Turbomachinery Laboratories,
Mechanical Engineering Department,
Texas A&M University,
College Station, TX 77843

Repeated rib roughness elements have been used in advanced turbine cooling designs to enhance the internal heat transfer. Often the ribs are perpendicular to the main flow direction so that they have an angle of attack of 90 deg. The objective of this investigation was to determine the effect of rib angle of attack on the pressure drop and the average heat transfer coefficients in the fully developed turbulent air flow in a square duct with two opposite rib-roughened walls for Reynolds number varied from 7000 to 90,000. The rib height-to-equivalent diameter ratio (e/D) *was kept at a constant value of 0.063, the rib pitch-to-height ratio* (P/e) *was varied from 10 to 20, and the rib angle of attack* (α) *was varied from 90 to 60 to 45 to 30 deg, respectively. The thermal performance comparison indicated that the increased heat conductance for the rib with an oblique angle to the flow* ($\alpha = 45$-30 *deg*) *was about 10–20 percent higher than the rib with a 90 deg angle to the flow, and the pumping power requirement for the angled rib was about 20-50 percent lower than the transverse rib. Semi-empirical correlations for friction factor and heat transfer coefficients were developed to account for rib spacing and rib angle. The correlations can be used in the design of turbine blade cooling passages.*

Introduction

Fully developed turbulent heat transfer and friction in tubes or between parallel plates with repeated-rib rougheners have been studied extensively [1–7]. Considerable data also exist for repeated-rib-roughness in an annular flow geometry in which the inner annular surface is rough and the outer surface is smooth in order to simulate the geometry of fuel bundles in an advanced gas-cooled nuclear reactor [8–10]. Based on those previous studies, the effects of rib height-to-equivalent diameter ratio e/D, rib pitch-to-height ratio P/e, and rib angle of attack α on the heat transfer coefficients and friction factor over a wide range of Reynolds numbers are well established. Semi-empirical correlations have been developed for the heat transfer designer. It should be noted that the increase in heat transfer is accompanied by an increase in the pressure drop of the fluid flow. Many investigations have been directed toward establishing a geometry which gives the best heat transfer performance for a given pumping power. In annular flow, White and Wilkie [9] found that the greatest heat transfer rate per unit pumping power was obtained with $P/e = 8$ at 33 deg helix angle. In parallel-plate flow, Han et al. [5] concluded that the rib with a 45 deg angle of attack at $P/e = 10$ provided superior performance per unit friction expenditure. In circular tube flow, Gee and Webb [6] and Sethumadhavan and Raja Rao [7] reported that the best performance was identified with $P/e = 10 \sim 15$ at the rib angle of attack about $50 \sim 60$ deg.

In some applications, such as gas turbine airfoil cooling design, the heat transfer enhancement is required on two opposite walls of the cooling passages in order to remove more heat transferred from airfoil external surfaces which are directly exposed to the hot gases flow. The current advanced gas turbine blade cooling system, as sketched in Fig. 1, the turbulence promoters (i.e., repeated ribs) with a 90 deg angle to the flow have been cast onto the two opposite walls of the shaped internal passages [11–12]. The internal passages can be approximately modeled as that in the flow in rectangular channels with two opposite rib-roughened walls. The heat transfer and friction characteristics in channels of this kind may be different from those of circular tubes, parallel plates, or annuli. The earliest experimental data were reported by Burggraf [13], who studied the turbulent air flow in a square duct with two opposite ribbed walls with $\alpha = 90$ deg, $P/e = 10$, and $e/D = 0.055$. The results indicated that the augmentation of the Nusselt number on the ribbed side wall and on the smooth side wall was 138 and 19 percent, respectively, higher than the four-sided smooth duct flow values; whereas the friction factor was about 8.6 times higher. In this study the emphasis was placed on the effect of entrance conditions, such as long duct entrance, short duct entrance, and 180 deg bend entrance, on the heat transfer coefficients. Only one particular rib geometry ($\alpha = 90$ deg, $P/e = 10$, $e/D = 0.055$) was tested. Recently, Han and Lei [14] systematically investigated the effects of rib pitch-to-height and rib height-to-equivalent diameter ratios on the friction factor and heat transfer coefficients for fully developed turbulent air flow in a square duct with two opposite rib-roughened walls. The P/e ratio was varied from 10 to 40, the e/D ratio was varied from

Contributed by the Heat Transfer Division and presented at the ASME Winter Annual Meeting, New Orleans, Louisiana, December 9-14, 1984. Manuscript received by the Heat Transfer Division July 1984. Paper No. 84-WA/HT-72.

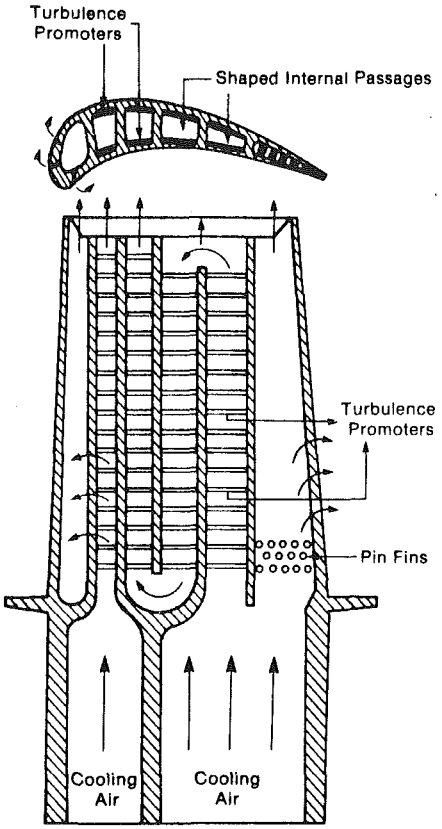

Fig. 1 Cooling concept of a modern multipass turbine blade

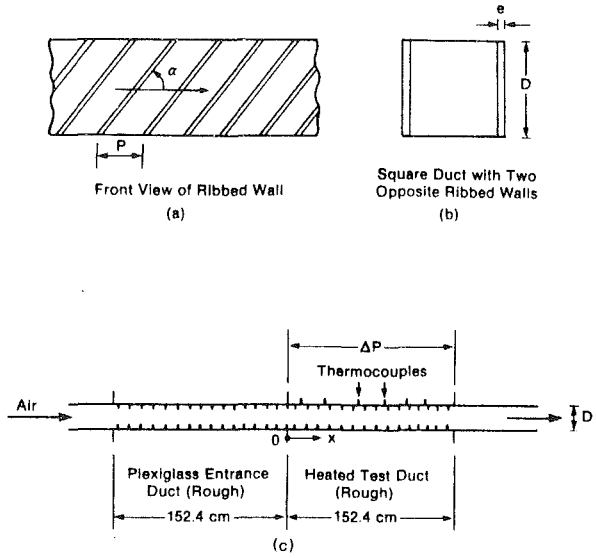

Fig. 2 (a) Rib geometry; (b) cross section of test duct; (c) sketch of test section

0.021 to 0.063, but the α was kept at a constant value of 90 deg. Based on the four-sided smooth duct correlation and the four-sided ribbed duct similarity law, a general prediction method for average friction factor and average Stanton number in rectangular channels with two opposite ribbed walls with $\alpha = 90$ deg was developed [15].

In general, the turbine airfoil cooling designer would like to optimize the rib geometry in order to obtain the best heat transfer coefficients for either a given coolant flowrate or a given available pressure drop across the cooling passages. The previous studies suggested that the rib with an oblique angle to the flow provided a better performance when compared to the rib with a 90 deg angle to the flow. However, those results were primarily obtained for flow in annuli, between parallel plates, or in circular tubes with a rib-roughened wall. The technical literature provides no information on the optimum rib angle for flow in turbine airfoil cooling passages. This paper examined the effect of rib angle of attack on the pressure drop and heat transfer coefficients in the fully developed turbulent flow in a square duct with two opposite rib-roughened walls as shown in Fig. 2. The rib height-to-equivalent diameter ratio was kept at a constant value of 0.063, the rib pitch-to-height ratio was varied from 10 to 20, and the rib angle of attack was varied from 90 to 60 to 45 to 30

Nomenclature

D = side-to-side dimension of the square duct
e = rib height
e^+ = roughness Reynolds number $= (e/D)\mathrm{Re}(f/2)^{1/2}$
$\bar{e}^+$ = average roughness Reynolds number $= (e/D)\mathrm{Re}(\bar{f}/2)^{1/2}$
f = friction factor in a four-sided smooth duct
$\bar{f}$ = average friction factor in a two-sided ribbed duct
g_c = conversion factor
G = mass flux $= \rho \bar{V}$
h = heat transfer coefficients
H = heat transfer roughness function
$\bar{H}$ = average heat transfer roughness function
k = thermal conductivity of fluid
$\bar{K}/K$ = increased heat conductance $= (\overline{\mathrm{St}}/\mathrm{St})/(\bar{f}/f)^{1/3}$
L = test section length for friction pressure drop
Nu = Nusselt number $= hD/k$
$\overline{\mathrm{Nu}}$ = average Nusselt number in a two-sided ribbed duct
Δp = pressure drop across the test section
P = rib pitch
$\bar{P}/P$ = reduced pumping power $= (\bar{f}/f)/(\overline{\mathrm{St}}/\mathrm{St})^3$
Pr = Prandtl number of fluid
q'' = heat transfer rate per unit area
R = momentum transfer roughness function
$\bar{R}$ = average momentum transfer roughness function
Re = Reynolds number $= GD/\mu$
R_{av} = average ray length of the duct
St = Stanton number $= \mathrm{Nu}/(\mathrm{Re}\,\mathrm{Pr})$
$\overline{\mathrm{St}}$ = average Stanton number in a two-sided ribbed duct
T^+ = dimensionless temperature
$\bar{T}^+$ = dimensionless average temperature
T_b = bulk mean temperature of fluid
$\bar{T}_w$ = average lateral wall temperature
u^+ = dimensionless velocity
$\bar{u}^+$ = dimensionless average velocity
V = average velocity of fluid
X = the axial distance from the heated test duct
Y = distance from the wall
α = flow attack angle
ρ = average density of fluid
μ = average viscosity of fluid
η = efficiency index $= (\overline{\mathrm{St}}/\mathrm{St})/(\bar{f}/f)$

Subscripts

s = smooth side walls in a two-sided ribbed duct
R = ribbed side walls in a two-sided ribbed duct
r = four-sided ribbed duct

deg, respectively. The Reynolds number range of this investigation extended from 7000 to 90,000. Air was the working fluid; constant wall heat flux was the boundary condition. This paper will first describe the experimental results. The thermal performance comparison will then be discussed and the semi-empirical correlations for friction factor and heat transfer coefficients will be presented.

Experimental Results

The Experimental Apparatus. An experimental facility was constructed to test the enhancement technique and to provide the smooth duct reference data. A schematic of the test rig is shown in Fig. 2. A detailed description of the test section is referred to [14–15]. Only a brief discussion will be addressed here. Air was forced through a 10.16 cm (4 in.) diameter tube equipped with a 5.08 cm (2 in.) diameter calibrated orifice plate to measure flow rate. An unheated entrance duct (152.4 cm, or 60 in.) was used between the tube and the heated test duct (152.4 cm). This plexiglass entrance duct served to establish hydrodynamically fully developed flow at the entrance to the heated test section. At the end of the test duct, the air was exhausted into the atmosphere.

The test duct, which consisted of four heated parallel aluminum plates, 0.635 cm (0.25 in.) thick, had 7.6 cm by 7.6 cm (3 in. by 3 in.) cross-sectional dimensions and a heated length of 20 duct diameters. The brass rib had a square cross section (0.476 cm by 0.476 cm, or 0.1875 in. by 0.1875 in.) and was glued onto the two opposite walls of the square duct (both entrance and test duct) in a required distribution (P/e) and angle of attack (α). The glue thickness of this investigation was estimated to be less than 0.0127 mm (0.005 in.). Woven heaters embedded in silicone rubber were adhered uniformly between the aluminum plate and a wood panel to insure good contact. Each aluminum plate had one woven heater; each heater could be independently controlled by a variac transformer and provided a controllable constant heat flux for the test plate. The entire test section was well insulated by fiberglass material. The test section was instrumented with 36 thermocouples distributed along the length and across the span of the aluminum plates. Thermocouples were also used to measure the bulk mean air temperature entering and leaving the test section. Five pressure taps along the test duct (three on the smooth side and two on the ribbed side) were used to measure the static pressure drop across the test section.

Analysis of Data. In the hydrodynamically fully developed duct flow, the friction factor can be calculated from

$$\bar{f} = \Delta p/[4(L/D)(G^2/2\rho g_c)] \tag{1}$$

During the runs, it was observed that the magnitude of the pressure drop over the test duct was about the same when measured from the pressure taps, either on the smooth side wall or on the ribbed side wall. The friction factor calculated from equation (1) was an average value between the smooth side wall and the ribbed side wall over the test duct. The average friction factor of the present investigation was based on the adiabatic conditions (tests without heating). The maximum uncertainty in the average friction factor was estimated to be less than 6.6 percent for Reynolds number greater than 10,000 by using the uncertainty estimation method in [16].

During the rib-roughened duct test, it was found that the wall temperature paralleled the bulk mean air temperature at downstream distances ranging from 3 to 5 duct diameters from the start of heating. This implied that the flow was in the thermally fully developed region after $X/D \geq 5$. In fully developed region, the Nusselt numbers can be calculated from

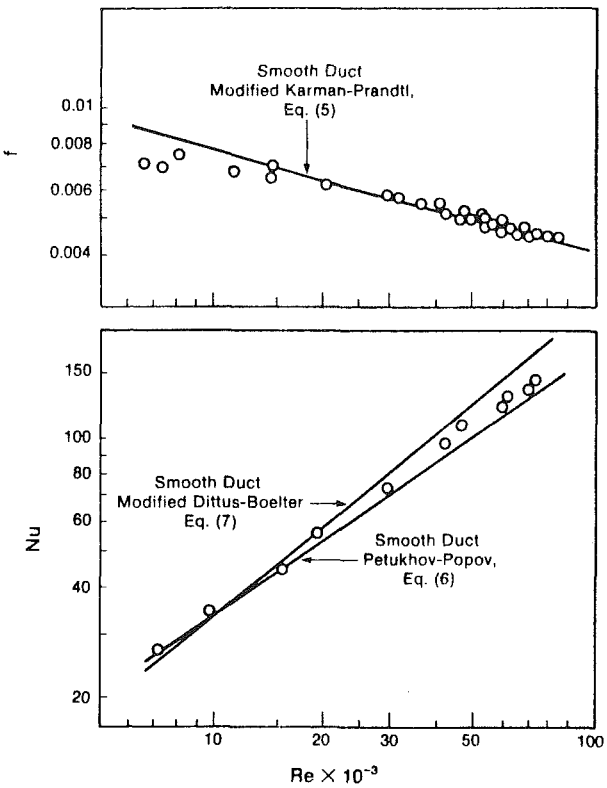

Fig. 3 Friction and heat transfer results for smooth duct

$$\mathrm{Nu}_s = [q_s''/(\bar{T}_w - T_b)_s](D/k) \tag{2}$$

$$\mathrm{Nu}_R = [q_R''/(\bar{T}_w - T_b)_R](D/k) \tag{3}$$

$$\overline{\mathrm{Nu}} = \tfrac{1}{2}(\mathrm{Nu}_s + \mathrm{Nu}_R) \tag{4}$$

The q_s'' and q_R'' represent the net heat flux from the smooth side wall and the ribbed side wall to the fluid, respectively, whereas $(\bar{T}_w - T_b)_s$ and $(\bar{T}_w - T_b)_R$ are the thermal driving forces averaged over the span of the smooth wall and the ribbed wall in the fully developed region, respectively. The net heat flux is the heat flux generated from the heater, subtracting from heat loss to the environment through the insulation material, i.e., q'' (net) $= q''$ (heater) $- q''$ (loss). The maximum heat loss from the smooth side wall and the ribbed side wall was estimated to be less than 5 and 3 percent, respectively, for Reynolds numbers greater than 10,000. Equation (2) was used for the smooth side wall Nusselt number calculation and equation (3) was for the ribbed side wall while equation (4) was for the average Nusselt number in a duct with two opposite ribbed walls. Notice that the ribbed side heat flux q_R'' was based on the projected heat transfer area (not including the increased rib surface area). The maximum uncertainty in the Nusselt number was estimated to be less than 6.8 percent for Reynolds number greater than 10,000.

Experimental Results for Smooth Duct. Before initiating experiments with rib-roughened walls, the friction factor and heat-transfer coefficients were measured for a fully developed four-sided smooth duct and compared with the results given in the literature, as shown in Fig. 3. As seen by the figure there is good agreement between existing correlations and the experimental results for the present smooth duct with 7.6 cm by 7.6 cm cross section. The friction factor differs by up to 9.0 percent from the modified Karman–Prandtl equation [17], and the Nusselt number differs by up to 9.5 percent from either the Petukhov–Popov equation [18] or the modified Dittus–Boelter equation. The modified Karman–Prandtl equation for the four-sided smooth duct friction factor by Brundrett [17] is

Table 1 Rib geometry tested for $e/D = 0.063$

	$P/e = 10$		$P/e = 20$	
	Friction	Heat transfer	Friction	Heat transfer
$\alpha = 90$ deg	X	X	X	X
$\alpha = 75$ deg	X	X	X	X
$\alpha = 60$ deg	X	X		
$\alpha = 45$ deg	X	X	X	X
$\alpha = 30$ deg	X	X	X	X
$\alpha = 15$ deg	X		X	

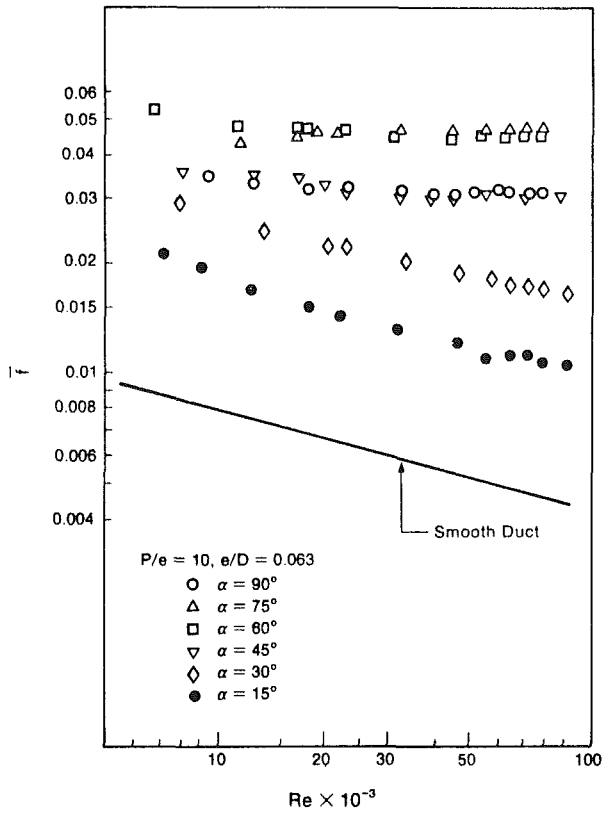

Fig. 4 Average friction factor with varied α for $P/e = 10$

$$1/(f)^{1/2} = 4.0 \log_{10}[\mathrm{Re}(f)^{1/2}] - 0.4 + 4.0 \log_{10}(2R_{av}/D) \quad (5)$$

where $2R_{av}/D = 1.156$ for a square duct. The Petukhov–Popov equation for the four-sided smooth duct heat transfer [18] is

$$\mathrm{Nu} = (f/2)\mathrm{Re}\ \mathrm{Pr}/[1.07 + 12.7(f/2)^{1/2}(\mathrm{Pr}^{2/3} - 1)] \quad (6)$$

The modified Dittus-Boelter equation for the four-sided smooth duct heat transfer is

$$\mathrm{Nu} = 0.023\ \mathrm{Re}^{0.8}\ \mathrm{Pr}^{0.4}(2R_{av}/D)^{-0.2} \quad (7)$$

Experimental Results for Rib-Roughened Duct. The ribs had a square cross section and were glued in-line onto the surfaces in patterns to achieve the desired spacing and angle of attack. A total of 11 rib geometries was tested for the square duct with two opposite ribbed walls, as shown in Table 1.

The average friction factor versus Reynolds number for the different rib angle is shown in Figs. 4 and 5. For the $\alpha = 90$, 75, 60, and 45 deg, the friction factor approaches an approximately constant value as the Reynolds number increases while the friction factor decreases with Reynolds number when $\alpha = 30$ and 15 deg. For the case of $P/e = 10$ as seen from Fig. 4, the friction factor with $\alpha = 90$ deg is about three to ten times higher than the four-sided smooth duct over the range

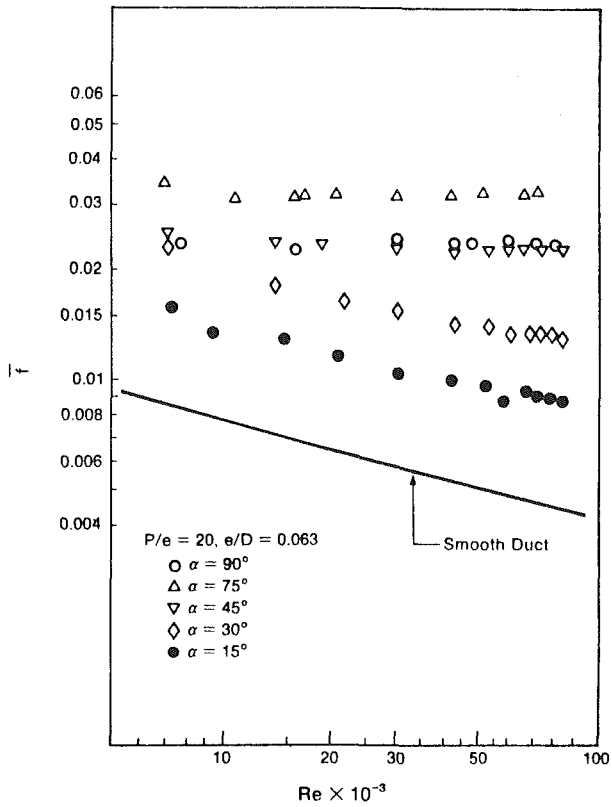

Fig. 5 Average friction factor varied with α for $P/e = 20$

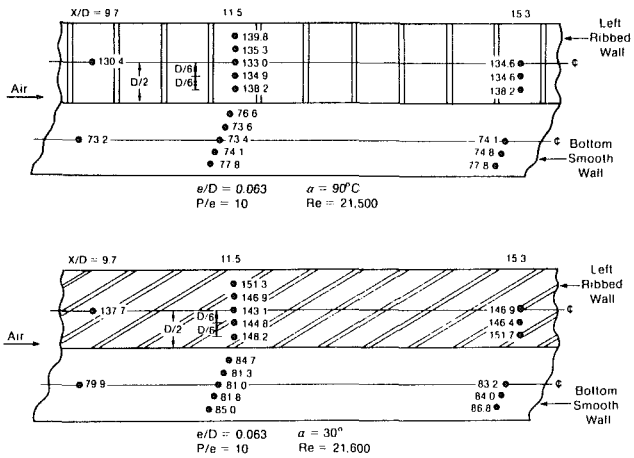

Fig. 6 Local Nusselt number for $\alpha = 90$ and 30 deg

of Reynolds numbers. The friction factor with $\alpha = 45$ deg is about the same as $\alpha = 90$ deg; however, it decreases by 20–40 percent when the α changes from 90 to 30 deg. It is noted that the friction factor with $\alpha = 60$ deg (or 75 deg) is about 50 percent higher than $\alpha = 90$ deg. The results with $P/e = 20$ have similar trends to $P/e = 10$; however, the friction factor is relatively reduced, as shown in Fig. 5.

The orientation of the ribs with respect to the thermocouples in the fully developed region ($X/D = 9.7 \sim 15.3$) is shown in Fig. 6. It is seen that the local Nusselt number variation in both streamwise and spanwise directions is less than 6 percent for $\alpha = 90$ and 30 deg. The Nusselt numbers shown in Figs. 7–8 were based on the average value in the fully developed region results ($X/D = 9.7 \sim 15.3$). The data show that the Nusselt number (therefore the heat transfer coefficients) increases with increasing Reynolds number as the

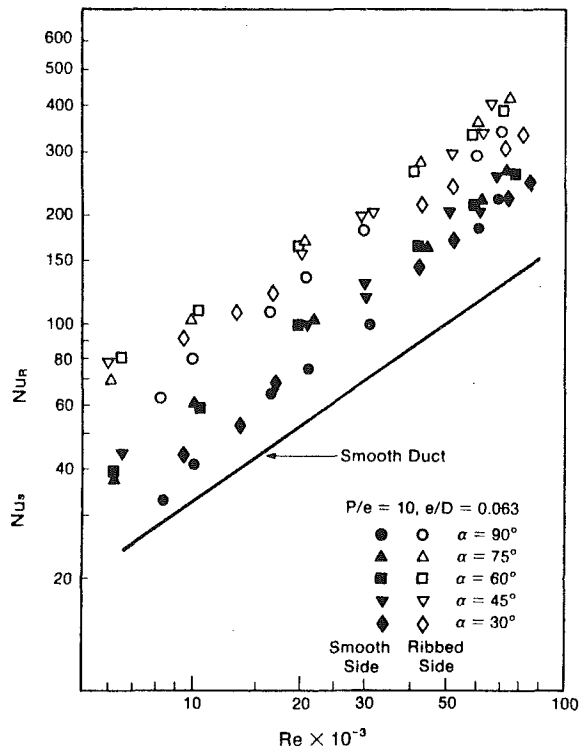

Fig. 7 Nusselt number varied with α for $P/e = 10$

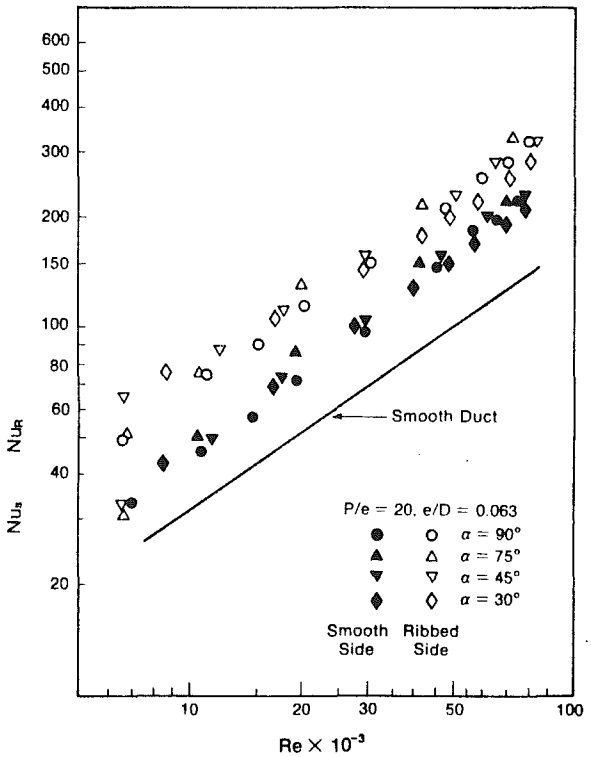

Fig. 8 Nusselt number varied with α for $P/e = 20$

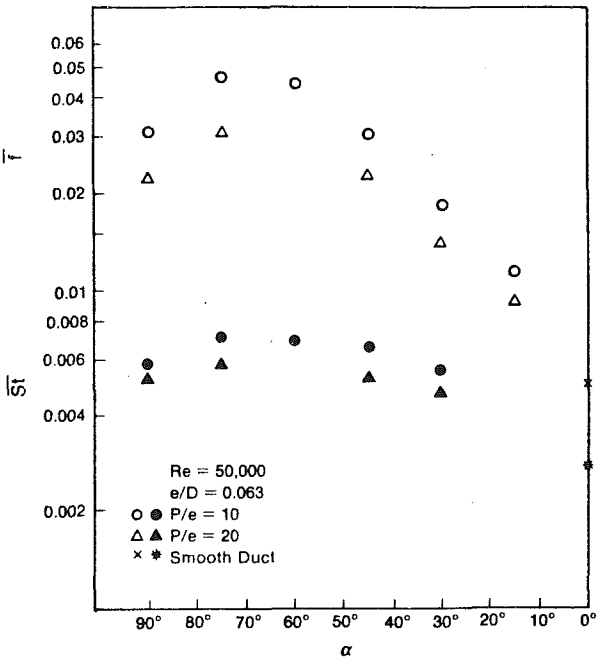

Fig. 9 Average friction and Stanton number varied with α

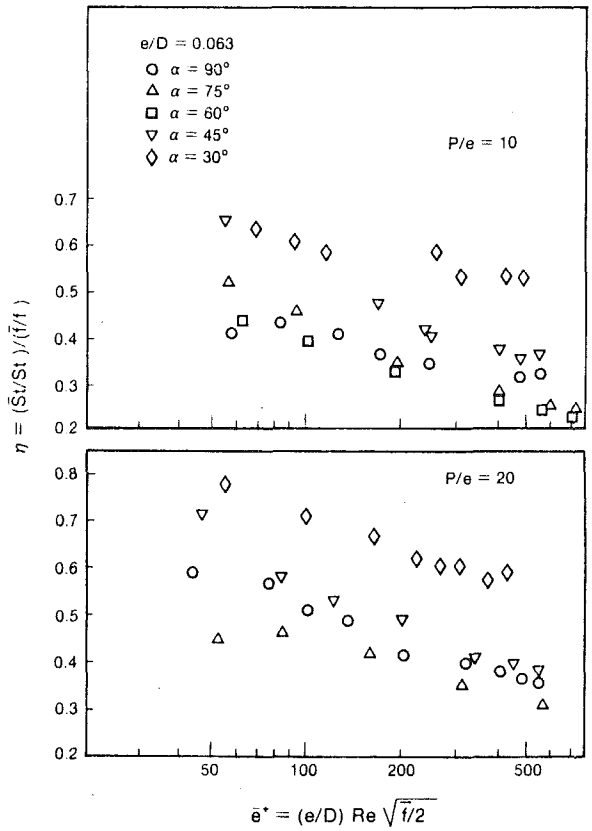

Fig. 10 Efficiency index varied with α for different P/e

conventional turbulent pipe flow. As indicated in Fig. 7, the Nusselt number of the ribbed side wall with $\alpha = 90$ deg is about 2.5 times higher than that of the four-sided smooth duct. The Nusselt number with $\alpha = 30$ deg is about 5–10 percent higher than $\alpha = 90$ deg, whereas the Nusselt number with $\alpha = 45$ deg (60, and 75 deg) is about 25 percent higher than $\alpha = 90$ deg. The Nusselt number of the smooth side wall is also higher than that of the four-sided smooth duct by 30–80 percent due to the presence of the ribs on the adjacent walls. It is observed that the ribs with an oblique angle to the flow have more influence on the smooth side walls. Therefore, the average Nusselt number (average of the ribbed side and the smooth side walls) for the ribs with an oblique angle to the flow is higher than that of the rib with a 90 deg angle to the flow. The results for $P/e = 20$ have the similar trends to $P/e = 10$. However, the heat transfer is relatively reduced as shown in Fig. 8.

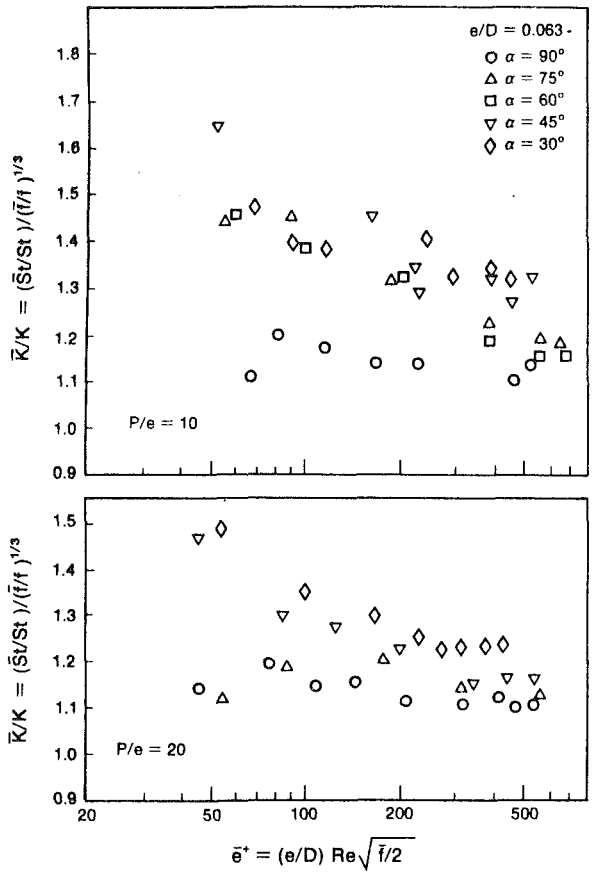

Fig. 11 Increased heat conductance varied with α for different P/e

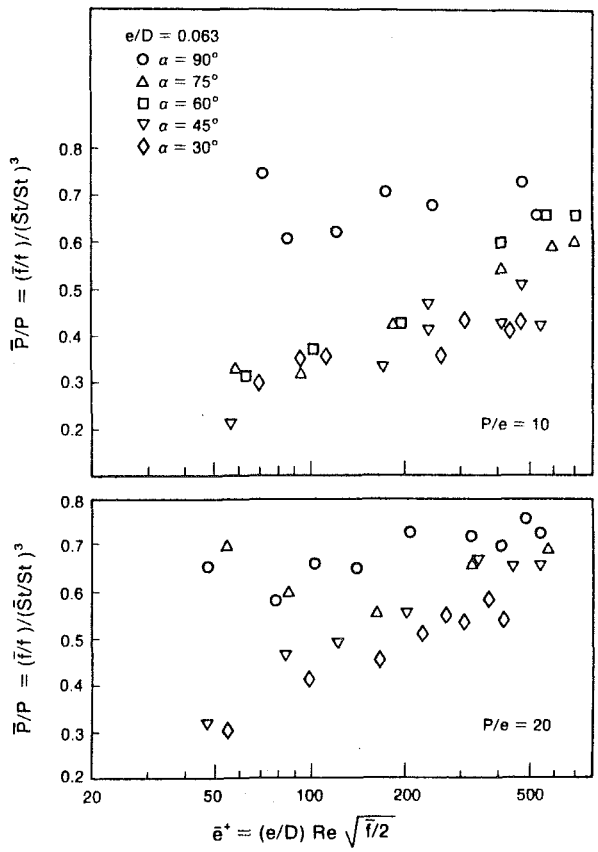

Fig. 12 Reduced pumping power varied with α for different P/e

Thermal Performance Comparison

The average friction factor and the average Stanton number versus the rib angle of attack for Re = 50,000 and $P/e = 10$ and 20 are shown in Fig. 9. The data of the 0 deg angle of attack were obtained from the present smooth duct results. Both the friction and heat transfer increase with decreasing α, and reach a maximum value at α approximately 60–70 deg, then decrease with further decreasing α. It is noted that the amount of the friction factor decrease is relatively larger than of the Stanton number when the rib angle of attack changes from 60 to 30 deg. This suggests that the best thermal performance may be obtained at the rib flow attack angle around 45–30 deg.

The efficiency index η versus the average roughness Reynolds number $\bar{e}^+$ is presented in Fig. 10. It is clearly seen that the best η is obtained with the 30 deg flow attack angle. These comparisons also suggest that the preferred operating condition is for smaller $\bar{e}^+$ (i.e., either smaller e/D or Re) for a given rib spacing and rib angle of attack.

Three design objectives for internally rib-roughened surfaces when compared to the smooth surface as discussed in [6] are

1 reduced heat transfer surface area for equal pumping power and heat duty
2 increased heat conductance for equal pumping power and heat transfer surface area; a higher heat conductance may be used to obtain increased heat duty
3 reduced pumping power for equal heat duty and heat transfer surface area

According to the analysis shown in [6], the performance equation of the present study can be expressed as

$$\frac{\bar{K}/K}{(\bar{P}/P)^{1/3}(\bar{A}/A)^{2/3}} = \frac{\bar{\mathrm{St}}/\mathrm{St}}{(\bar{f}/f)^{1/3}} \tag{8}$$

Equation (8) provides an expression containing the parameters $\bar{K}/K$, $\bar{P}/P$, and $\bar{A}/A$ defined in terms of $\bar{f}/f$ and $\bar{\mathrm{St}}/\mathrm{St}$.

The turbine airfoil cooling designer would like to have either increased heat conductance ($\bar{K}/K$) for equal pumping power ($\bar{P}/P = 1$) and heat transfer surface area ($\bar{A}/A = 1$), or reduced pumping power ($\bar{P}/P$) for equal heat conductance ($\bar{K}/K = 1$) and heat transfer surface area ($\bar{A}/A = 1$). Increased heat conductance versus $\bar{e}^+$ is shown in Fig. 11. Reduced pumping power for the data of this study is depicted in Fig. 12. The increased heat conductance increases with decreasing α and reaches a maximum value at α approximately 45–30 deg, while the pumping power requirement (reduced pumping power) decreases with decreasing α and reaches a minimum value at α approximately 45–30 deg. It is seen that the increased heat conductance with $\alpha = 45$–30 deg is about 10–20 percent higher than at $\alpha = 90$ deg, whereas the pumping power requirement with $\alpha = 45$–30 deg is about 20–50 percent lower than $\alpha = 90$ deg over the range of $\bar{e}^+$. It is noted that the $\bar{K}/K$ should be greater than 1.0 and $\bar{P}/P$ should be smaller than 1.0, respectively, in order to have advantages in using the turbulence promoters. The pumping power requirement for the $P/e = 10$ is about 20 percent lower than the $P/e = 20$ at the same rib oblique angle. Again the preferred operating condition is for smaller $\bar{e}^+$.

In general, the performance is greatly improved when α varies from 90 to 60 deg, and gradually reaches a maximum value at α about 45–30 deg, then returns to the smooth duct result when α further varies from 30 to 0 deg. It is noted that the best performance angle was reported about 45–50 deg for flow between parallel plates and in tubes by the previous investigations [5–6]. Based on these observations, it may be concluded that the best rib angle is shifted from a 45–50 deg for flow between parallel plates to a smaller angle of 45–30 deg for flow in a square duct with two opposite ribbed walls.

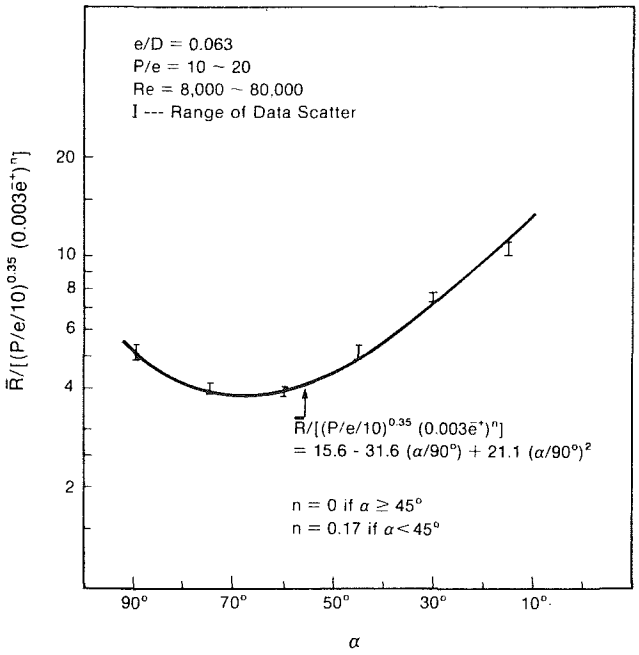

Fig. 13 Friction factor correlation

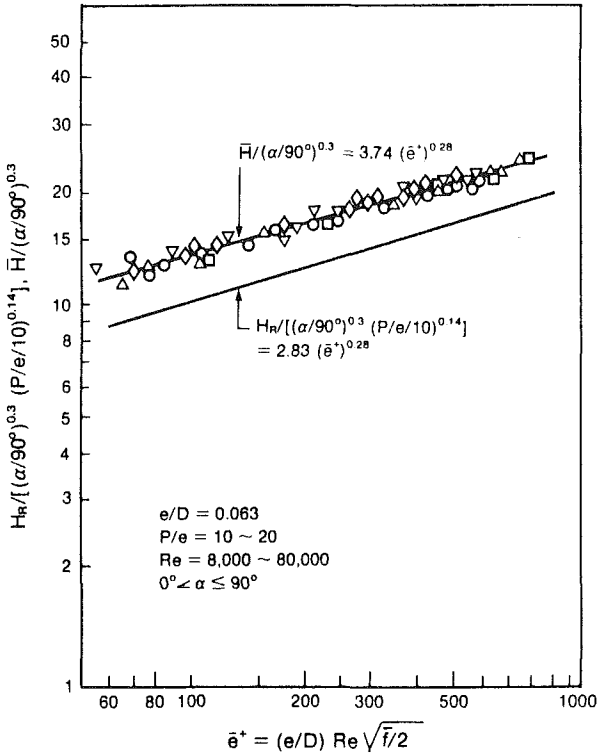

Fig. 14 Heat transfer correlation

Friction and Heat Transfer Correlations

For the results of rib-roughened surfaces to be most useful, general correlations are required for both the friction factor and the heat transfer coefficients which cover a wide range of parameters (e/D, Re, P/e, α).

Since Nikuradse [19] found the law of the wall and developed the so-called friction similarity law to correlate the friction data for fully developed turbulent flow in tubes with sand roughness, the method has been successfully extended to correlate the friction data for turbulent flow in tubes with repeated-rib roughness [2]. Assuming that the same method can be applied to flow in a four-sided ribbed duct, the law of the wall can be expressed by the dimensionless velocity profile normal to the wall

$$u^+ = 2.5\ ln(y/e) + R(e^+) \tag{9}$$

Integration of equation (9) across the cross-sectional area of a flow channel gives

$$\bar{u}^+ = -2.5 + 2.5\ ln(l/e) + R(e^+) \tag{10}$$

where l is the distance between the ribbed wall and the position of zero shear stress (i.e., $l = 1/2\ D$). The dimensionless average velocity across the channel in a four-sided ribbed duct can be written in terms of the friction factor f_r as: $\bar{u}^+ = (2/f_r)^{1/2}$. Inserting $\bar{u}^+$ into equation (10), the friction similarity law for flow in a four-sided ribbed square duct yields

$$R(e^+) = (2/f_r)^{1/2} + 2.5\ ln(2e/D) + 2.5 \tag{11}$$

Assuming that equation (11) can be applied for flow in a square duct with two opposite ribbed walls, by replacing $\bar{R}$ and $\bar{f}$ for R and f_r, the friction similarity law of the present study becomes

$$\bar{R}(\bar{e}^+) = (2/\bar{f})^{1/2} + 2.5\ ln(2e/D) + 2.5 \tag{12}$$

It should be noted that $R(e^+)$ and f_r is for flow in a four-sided ribbed duct, whereas $\bar{R}(\bar{e}^+)$ and $\bar{f}$ is for flow in a two-opposite-ribbed duct. It is expected that $\bar{R}$ is larger than R for a given e/D ratio because $\bar{f}$ is smaller than f_r. It was found that all the data of the different e/D ratios ($e/D = 0.021$–0.063) were approximately correlated into a constant value of $\bar{R}$ in fully rough regime for a given rib angle of attack ($\alpha = 90$ deg), and rib pitch-to-height ratio ($P/e = 10$ or 20) [14]. Once $\bar{R}$ is experimentally determined, the friction factor can be predicted from equation (12) for a given e/D ratio.

Correlation of the present friction data is shown in Fig. 13. The $\bar{R}$ is independent of $\bar{e}^+$ for $\alpha = 90$ to 45 deg while the $\bar{R}$ increase with increasing $\bar{e}^+$ (because $\bar{f}$ decreases with increasing Reynolds number) for $\alpha < 45$ deg. The dependence of $\bar{R}$ on P/e and α shown in Fig. 13 is:

$$\bar{R}/[(P/e/10)^{0.35}(0.003\bar{e}^+)^n] = 15.6 - 31.6(\alpha/90\text{ deg}) + 21.1(\alpha/90\text{ deg})^2 \tag{13}$$

where

$$n = 0 \quad \text{if } \alpha \geq 45 \text{ deg}$$
$$n = 0.17 \quad \text{if } \alpha < 45 \text{ deg}$$

Equation (13) is the average friction factor correlation of the present data with a confidence level of ±5 percent. For the given e/D, P/e, α, and Re, the average friction factor can be found by combining equations (12) and (13).

Dipprey and Sabersky [20] developed the so-called heat transfer similarity law to correlate heat transfer data for fully developed turbulent flow in tubes with sand roughness. This similarity method has been extended to correlated heat transfer data for turbulent flow in rib-roughened tubes [2]. It is assumed that the same method can be applied for flow in a four-sided ribbed duct using the heat and momentum transfer analogy, giving a dimensionless temperature profile normal to the ribbed wall as:

$$T^+ = 2.5\ ln(y/e) + H(e^+, \text{Pr}) \tag{14}$$

Integrating equation (14) over the flow channel cross section and combining with equations (10) produces

$$\bar{T}^+ = (2f_r)^{1/2} - R(e^+) + H(e^+, \text{Pr}) \tag{15}$$

where the dimensionless average temperature profile can be expressed by: $\bar{T}^+ = (f_r/2)^{1/2}/\text{St}_r$. Substituting $\bar{T}^+$ into

equation (15), the heat transfer similarity law for flow in a four-sided ribbed duct yields

$$H(e^+, \mathrm{Pr}) = R(e^+) + [f_r/(2\mathrm{St}_r) - 1]/(f_r/2)^{1/2} \quad (16)$$

Assuming that equation (16) can be applied for flow in a square duct with two opposite ribbed walls by replacing $\bar{H}$, $\bar{R}$, $\bar{f}$, $\overline{\mathrm{St}}$ for H, R, f_r, and St_r, respectively, the heat transfer similarity law of the present study becomes:

$$\bar{H}(\bar{e}^+, \mathrm{Pr}) = \bar{R}(\bar{e}^+) + [\bar{f}/(2\overline{\mathrm{St}}) - 1]/(\bar{f}/2)^{1/2} \quad (17)$$

Correlation of the present heat transfer data is shown in Fig. 14. No significant dependence of $\bar{H}$ on P/e is observed. For a Prandtl number of 0.7 of the present study, the dependence of $\bar{H}$ on α and $\bar{e}^+$ shown in Fig. 14 can be represented by

$$\bar{H}(\bar{e}^+) = 3.74(\alpha/90 \text{ deg})^{0.3}(\bar{e}^+)^{0.28} \quad (18)$$

The deviation of equation (18) is about ±10 percent. If $\bar{H}$, $\bar{R}$, and $\bar{f}$ are known, the average Stanton number ($\overline{\mathrm{St}}$) can be found by combining equations (17) and (18).

In design consideration, correlations for the ribbed side wall Stanton number (St_R) and the smooth side wall Stanton number (St_s) may be useful. Assuming that equation (17) can be used to correlate the ribbed side wall heat transfer data by replacing H_R and St_R for $\bar{H}$ and $\overline{\mathrm{St}}$, one obtains

$$H_R(\bar{e}^+, \mathrm{Pr}) = \bar{R}(\bar{e}^+) + [\bar{f}/(2\mathrm{St}_R) - 1]/(\bar{f}/2)^{1/2} \quad (19)$$

Heat transfer correlation of the ribbed side wall shown in Fig. 14 is

$$H_R/(P/e/10)^{0.14} = 2.83(\alpha/90 \text{ deg})^{0.3}(\bar{e}^+)^{0.28} \quad (20)$$

The deviation of equation (20) is about ±10 percent for $P/e = 10$, and ±13 percent for $P/e = 20$. If H_R, $\bar{R}$, and $\bar{f}$ are known, the ribbed side wall Stanton number (St_R) can be determined by combining equations (19) and (20). After obtaining $\overline{\mathrm{St}}$ and St_R, the smooth side wall Stanton number can be found by $\mathrm{St}_s = 2\overline{\mathrm{St}} - \mathrm{St}_R$.

Conclusions

An experimental study of fully developed turbulent air flow in a square duct with two opposite rib-roughened walls has been performed. The effects of rib angle of attack and rib spacing on the heat transfer coefficients and friction factor have been investigated. The following conclusions can be drawn:

1 For $P/e = 10$, the average Nusselt number of $\alpha = 90$ deg is about two times higher than the four-sided smooth duct value, whereas the average friction factor is about four-six times higher. Best thermal performance is achieved at angles of attack of 30 and 45 deg for both P/e ratios. The average Nusselt number of $\alpha = 30$ deg is about 5 percent higher than $\alpha = 90$ deg while the average friction factor is about 20–45 percent lower. At $\alpha = 45$ deg the average heat transfer is 25 percent greater than at $\alpha = 90$ deg, and the average friction factor remains the same. The results for $P/e = 20$ show trends similar to those of $P/e = 10$; however, the friction and heat transfer enhancement are relatively reduced.

2 The efficiency index for $\alpha = 30$ deg is about 30–50 percent higher than that for $\alpha = 90$ deg. The increased heat conductance with $\alpha = 45$–30 deg is about 10–20 percent higher than that with $\alpha = 90$ deg; the pumping power requirement for the $\alpha = 45$–30 deg is about 20–50 percent lower than for $\alpha = 90$ deg. The pumping power requirement for $P/e = 10$ is about 20 percent lower than $P/e = 20$ at the same rib angle. It is concluded that the ribs with an oblique angle (30–45 deg) to the flow provide a better performance than the ribs with a 90 deg angle to the flow which is currently being used in the modern gas turbine internal cooling passages.

3 Correlations for the average friction factor, the average heat transfer, and the ribbed side wall heat transfer have been obtained to account for e/D, P/e, α, and Re for flow in a square duct with two opposite ribbed walls. The correlations can be used for turbine blade internal cooling design.

Acknowledgments

This work was funded by Mr. Curtis Walker at the U.S. Army Research and Technology Laboratories (AVRADCOM) and was monitored by Mr. Robert Boyle at the NASA-Lewis Research Center under NASA Grant No. NAG 3-311. Their support is gratefully acknowledged.

References

1 Nunner, W., "Heat Transfer and Pressure Drop in Rough Tubes," AERE lib/Trans. 786, 1958.

2 Webb, R. L., Eckert, E. R. G., and Goldstein, R. J., "Heat Transfer and Friction in Tubes With Repeated-Rib Roughness," *Int. J. Heat Mass Transfer*, Vol. 14, 1971, pp. 601–617.

3 Lewis, M. J., "An Elementary Analysis for Predicting the Momentum and Heat Transfer Characteristics of a Hydraulically Rough Surface," ASME *Journal of Heat Transfer*, Vol. 97, 1975, pp. 249–254.

4 Kader, B. A., and Yaglom, A. M., "Turbulent Heat and Mass Transfer From a Wall With Parallel Roughness Ridges," *Int. J. Heat Mass Transfer*, Vol. 20, 1977, pp. 354–357.

5 Han, J. C., Glicksman, L. R., and Rohsenow, W. M., "An Investigation of Heat Transfer and Friction for Rib-Roughened Surfaces," *Int. J. Heat Mass Transfer*, Vol. 21, 1978, pp. 1143–1156.

6 Gee, D. L., and Webb, R. L., "Forced Convection Heat Transfer in Helically Rib-Roughened Tubes," *Int. J. Heat Mass Transfer*, Vol. 23, 1980, pp. 1127–1136.

7 Sethumadhavan, R., and Raja Rao, M., "Turbulent Flow Heat Transfer and Fluid Friction in Helical-Wire-Coil-Inserted Tubes," *Int. J. Heat Mass Transfer*, Vol. 26, 1983, pp. 1833–1844.

8 Hall, W. B., "Heat Transfer in Channels Having Rough and Smooth Surfaces," *J. Mech. Eng. Sci.*, Vol. 4, 1962, pp. 287–291.

9 White, L., and Wilkie, D., "The Heat Transfer and Pressure Loss Characteristics of Some Multi-start Ribbed Surfaces," in: *Augmentation of Convective Heat and Mass Transfer*, ed. A. E. Bergles and R. L. Webb, ASME, New York, 1970.

10 Donne, D., and Meyer, L., "Turbulent Convective Heat Transfer From Rough Surfaces With Two-Dimensional Rectangular Ribs," *Int. J. Heat Mass Transfer*, Vol. 20, 1977, pp. 582–620.

11 Suo, M., "Turbine Cooling," in: *The Aerothermodynamics of Aircraft Gas Turbine Engines*, ed. G. Oates, Air Force Aero Propulsion Lab., AFAPL TR 78-52, 1978.

12 Taylor, J. R., "Heat Transfer Phenomena in Gas Turbine," ASME Paper No. 80-GT-172.

13 Burggraf, F., "Experimental Heat Transfer and Pressure Drop With Two-Dimensional Turbulence Promoter Applied to Two Opposite Walls of a Square Tube," in: *Augmentation of Convective Heat and Mass Transfer*, ed. E. E. Bergles and R. L. Webb, ASME, New York, 1970, pp. 70–79.

14 Han, J. C., and Lei, C. K., "Heat Transfer and Friction in Square Ducts With Two Opposite Rib-Roughened Walls," ASME Paper No. 83-HT-26.

15 Han, J. C., "Heat Transfer and Friction in Channels With Two Opposite Rib-Roughened Walls," ASME *Journal of Heat Transfer*, Vol. 106, No. 4, Nov. 1984, pp. 774–781.

16 Kline, S. J., and McClintock, F. A., "Describing Uncertainties in Single-Sample Experiments," *Mechanical Engineering*, Vol. 75, Jan. 1953, pp. 3–8.

17 Kakac, S., and Spalding, D. B., "Turbulent Forced Convection in Channels and Bundles," Vol. 1, Hemisphere, New York, 1979, pp. 361–367.

18 Karlekar, B. V., and Desmond, R. M., *Heat Transfer*, 2nd ed., West Publishing Company, New York, 1982, pp. 496–498.

19 Nikuradse, J., "Laws for Flow in Rough Pipes," NACA TM 1292, 1950.

20 Dipprey, D. F., and Sabersky, R. H., "Heat and Momentum Transfer in Smooth and Rough Tubes at Varied Prandtl Number," *Int. J. Heat Mass Transfer*, Vol. 6, 1963, pp. 329–353.

The Transpired Turbulent Boundary Layer in Various Pressure Gradients and the Blow-Off Condition

D. P. Georgiou

J. F. Louis

Department of Aeronautics and Astronautics, Massachusetts Institute of Technology, Cambridge, MA 02139

An experimental study of the reduction in heat transfer to a transpiration-cooled flat surface subjected to pressure gradients (zero, negative, and positive) is presented for flow conditions similar to those encountered in gas turbines. The investigation is carried out for high injection rates and determines the blow-off conditions under which the boundary layer is lifted away from the wall by the transpired coolant. The study was conducted in a hot blow-down wind tunnel facility. The transient nature of the facility ensures that the wall remains isothermal. The Reynolds number, the ratio of the gas to wall temperatures, and the pressure gradient parameters K *are chosen to be representative of the conditions found in advanced gas turbines. The effect of the pressure gradient was found to be small. However, a local strong acceleration can reduce the cooling effectiveness. The heat transfer rates or Stanton numbers on a solid surface downstream of a transpiration cooled wall are found to be sensitive to the upstream injection ratio (b) and to the pressure gradient parameter. The data indicate that the ratio of Stanton numbers with and without cooling is nonzero for values of the injection parameters larger than values obtained theoretically by Kutateladze. The predicted value of the critical injection ratio (b_{cr}) determined from this study agrees well with the experimental data of Liepmann and Laufer for a free mixing layer, which is similar to a transpired boundary layer near blow-off as pointed out by Coles.*

Introduction

Cooling by mass transfer is a most effective means to reduce high heat fluxes. It can be accomplished by several different methods: film, transpiration, and ablation. The first two methods are the only feasible means in devices and machines with long life expectancy.

In transpiration cooling, the coolant is introduced through a porous wall. In this process, the wall is convectively cooled and the external heat transfer coefficient is decreased. Thus, transpiration cooling is considered to be the most effective scheme for air cooling. However, the use of a porous wall creates structural problems and more importantly a risk of fast oxidation associated with clogging.

The effective utilization of transpiration cooling requires a good understanding of its performance under conditions representative of operating gas turbines, particularly when large coolant flows are used to reduce the risk of oxidation. Therefore, the objectives of this study are:

1 To investigate the relationship between coolant flow rates and cooling effectiveness in a turbulent boundary layer, under conditions similar to those found in modern gas turbine engines. The emphasis is on conditions with high coolant flow rates. Configurations with uniform and uneven injections are also studied.

2 To determine the conditions for which blow-off occurs. The purpose of this study is to determine the validity of one of two criteria: The first is based on the conventional modeling of a turbulent wall boundary layer and the second is based on the ability of the layer to entrain the transpired flow rate.

Contributed by the Heat Transfer Division and presented at the ASME Winter Annual Meeting, New Orleans, Louisiana, December 9–14, 1984. Manuscript received by the Heat Transfer Division July 1984. Paper No. 84-WA/HT-71.

The Transpired Laminar Boundary Layer

The laminar case is well understood and solutions exist for different configurations such as the flat plate, the cylinder, the cone, and aerofoils. These solutions relate the ratios of skin frictions (C_f/C_{f0}) and heat fluxes ($\mathrm{St}/\mathrm{St}_0$) with and without transpiration to the product $F\cdot\mathrm{Re}^{0.5}$ where F is the coolant-to-mainstream mass flux ratio and Re is the Reynolds number. The limit of effective coolant injection is reached at the blow-off point when the skin friction and/or the heat flux vanish. Emmons and Leigh [1] studied the case of blow-off for a transpired laminar boundary layer in a constant velocity main flow and uniform injection. Their study indicates that blow-off will occur when the product of $F\cdot\mathrm{Re}^{0.5}$ is equal to 0.619. This corresponds to a value of the injection parameter: $b=(F/\mathrm{St}_0)=(2F/C_{f0})=1.5$ for a Prandtl number $\mathrm{Pr}=0.7$.

The Transpired Turbulent Boundary Layer

The transpired turbulent layer has been much studied although much effort has been spent for low injection rates and uniform near isothermal conditions. Extensive reviews are given by Jeromin [2], Hartnett and Sastri [3], Kays [4], Kays and Moffat [5], and by Coles [6]. For values of the injection parameter $b<4$, measurements of heat transfer and velocity [7] profiles agree well with the results of analyses based on a model of the turbulent boundary layer following the "law of the wall." The blow-off condition has been studied for turbulent boundary layers, by Hacker [8], Kutateladze and Leont'ev [9], Mironov [10], Bayley and Turner [11], and Coles [6]. Based on the data of Mickley and Davis [12], the analysis of Hacker estimated that at blow-off $F \cdot \mathrm{Re}^{-0.2} = 0.09$ which corresponds to $b = 2.4$. Kutateladze and Leont'ev predicted $b = 4.0$ at blow-off in their analysis valid for constant velocity, for uniform injection under isothermal conditions, and Reynolds numbers close to infinity. Their analysis uses a conventional "law of the wall" representation of the turbulent boundary layer at conditions near the blow-off. Later they provided corrections for a wider range of conditions while Bayley and Turner developed a correction for streamwise acceleration. A general form of the prediction is $b = 4.0\,(1 + 0.83/\mathrm{Re}_m^{0.14})$. Coles pointed out that the transpired boundary layer at the blow-off point should be equivalent to a free mixing layer. Since the integral momentum equation becomes $d\theta/dx = F$ at the blow-off point for a transpired boundary layer over a flat plate and since the experimental data of Liepmann and Laufer [13] for the free mixing layer yield: $d\theta/dx = 0.035$, Coles proposed that $F = 0.035$ at the blow-off point. This criterion means that blow-off will occur when the injection rate is larger than the entrainment rate of the turbulent layer. Both the work of Bayley and Turner in a turbine cascase and of Morris et al. [14] have found that the analysis of Kutateladze and Leont'ev did not accurately predict the measured heat transfer and the flow conditions near blow-off. Kutateladze and Mironov [15] reviewed experimental studies of the turbulent boundary layer with strong injection.

The Experiment, Its Design and Operation

(a) The Experiment. The basic flow configuration involved a smooth flat wall, low Mach number with temperature and pressure ratios similar to those of advanced gas turbines. The Reynolds number was about 10^6 and tests were performed for four values of the pressure gradient parameter $K = 0.0$, $-0.30 \cdot 10^{-6}$, $0.65 \cdot 10^{-6}$, and $1.2 \cdot 10^{-6}$. The porous section of the flat wall was made of a sintered bronze plate. The tests were performed in a hot blow-down wind tunnel facility using transient measuring instruments and data acquisition system. The details on the experimental facility are given in [16].

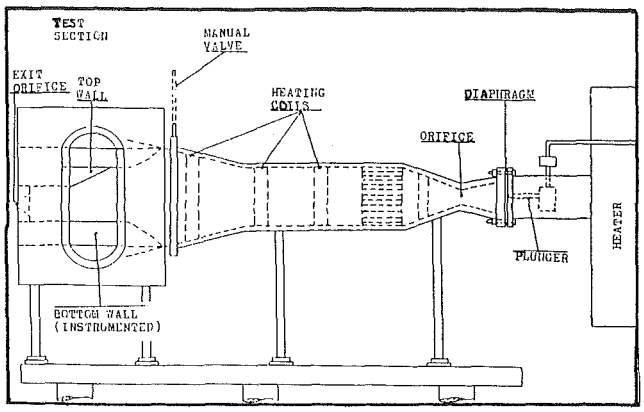

Fig. 1 The hot blow-down facility

(b) The Blow-Down Facility. Figure 1 shows a high-temperature blow-down wind tunnel. Air is heated in an electric heat exchanger and expands through the facility after rupture of a diaphragm which is initiated by the motion of an electrically controlled plunger. The mass flow of air is controlled and measured by a calibrated orifice. After the orifice, the hot air expands through a supersonic nozzle which ends in a matrix of small tubes acting as a supersonic flow diffuser and flow straightener. The cross section of the flow area is then changed from circular to rectangular. This is followed by a constant width subsonic diffuser. A manually operated valve is located between the heated diffuser and the room temperature test section. The valve is opened just before the test.

(c) The Test Section. The test section is made of three parts: a nozzle, a test channel, and an outlet section with an exit orifice designed to maintain a Mach number of 0.155 at the inlet of the test channel. The test channel was designed to minimize any three-dimensional flow. The dimensions of the channel are width of 50.8 mm, an inlet height of 104.8 mm, and a channel length of 228.6 mm. The flow conditions were determined using the similarity rules given in Louis [17]. The turbine conditions to be simulated are flow temperature and pressure of 1700 K and 12 bar respectively for a metal temperature of 1100 K.

Similarity considerations lead to the selection of the following conditions: inlet Mach number of 0.157, flow temperature of 490 K, pressure of 2.7 bar, density of 1.92 kg/m^3, and a wall temperature of 300 K. The transient nature of the facility ensures that the wall remains isothermal. The test channel is made of two close tolerance Plexiglas walls, one flat instrumented with its porous section and one a top wall with a contour that generated a streamwise pressure gradient.

Nomenclature

b = injection parameter = (F/St_0) or $(2F/C_{f0})$
c = specific heat
C_f = skin friction coefficient
F = blowing parameter = $(\rho v)_w/(\rho u)_\infty$
H = shape factor = δ^*/θ
k = conductivity
K = pressure gradient parameter = $(\nu/u_\infty^2)\,(du_\infty/dx)$
l_B = thickness of the porous calorimeter
q_w = wall heat flux
q_c = conduction losses
q_r = radiation losses
Re = Reynolds number
St = Stanton number
T = temperature
u = velocity (streamwise)
v = velocity (transverse)
δ = boundary layer thickness
δ^* = boundary layer displacement thickness
θ = boundary layer momentum thickness
δ_E = boundary layer enthalpy thickness
μ = dynamic viscosity
ν = kinematic viscosity
ρ = density
τ_w = skin friction
τ_D = diffusion time

Subscripts

0 = solid wall
∞ = free stream
w = wall
B = calorimeter
c = coolant

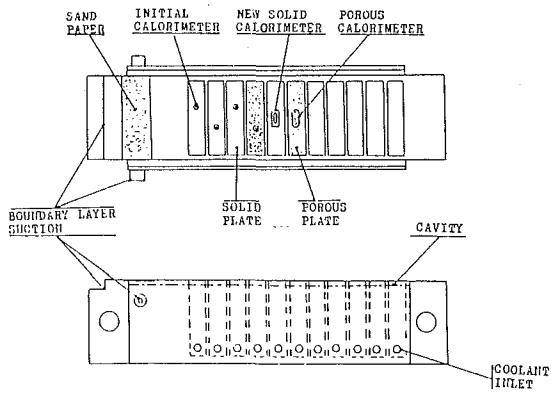

Fig. 2 The instrumented wall

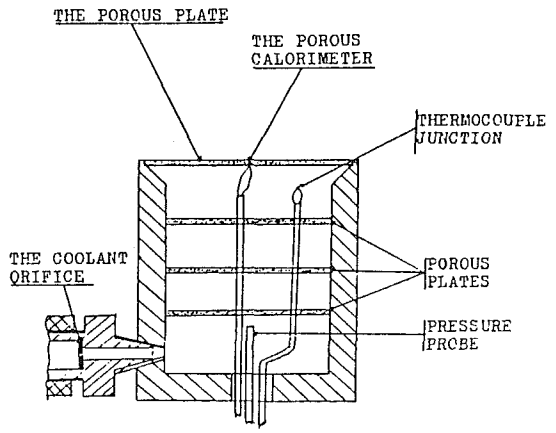

Fig. 3 Details of the cavity design

(*d*) **The Instrumented Wall (Fig. 2).** A boundary layer suction slot is located at the entrance of the channel. A sandpaper strip is positioned upstream of the porous wall to provide a turbulent trip of the boundary layer. The location of the strip is such that it initiates a uniform two-dimensional boundary layer with a maximum thickness equal to 10 percent of the channel width. The injection of the transpired air can be introduced through 11 cavities. The top of each cavity can be covered by either a solid or porous plate.

A calorimeter is installed in each solid wall at midwidth. The porous plates were cut from a sheet of sintered bronze with an average roughness of about 160 microinches.

(*e*) **The Coolant Injection System.** The system was designed to provide a uniform pressure and flow distribution at the injection plate and, to assure a short fill-up time (150 ms) of the cavities. The coolant injection system consists of a main reservoir, air valves, secondary reservoirs, calibrated choked orifices, and the injection cavities. In order to achieve uniformity of the transpired flow, the coolant air is first brought along the bottom wall of each cavity and three additional porous plates are inserted inside each cavity (Fig. 3).

(*f*) **Instrumentation and Data Acquisition.** Pursuant to the objectives of the experiment, the following parameters were measured:

1 mainstream total pressure and temperature
2 static pressure along the solid walls
3 coolant pressure and temperature in the reservoirs and the cavities
4 heat flux in the solid and porous walls

The pressure measurements were made using Setra 204E and 202E transducers. The temperature measurements used

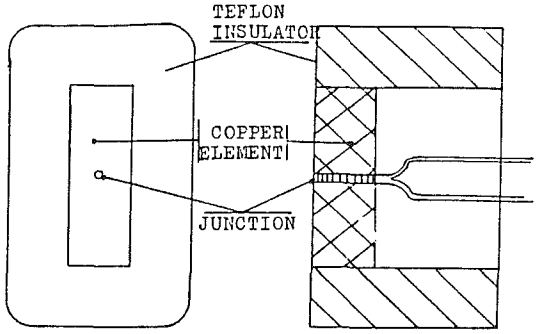

Fig. 4(*a*) The new solid calorimeter

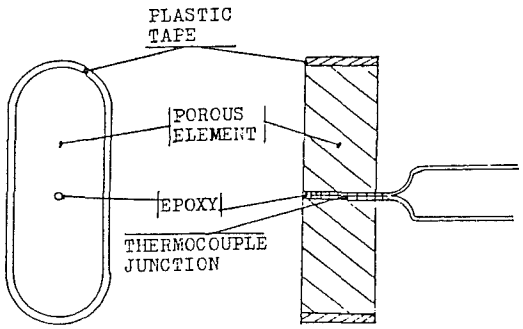

Fig. 4(*b*) The porous calorimeter

copper-constant on thermocouples. The outputs of these gages were amplified, digitized, stored in memory, and later sent to a minicomputer for analysis. Although initial experiments used solid calorimeters in the porous wall, most of the data were taken with porous calorimeters located in the porous wall and with solid calorimeters for measurements made in the solid wall. The porous calorimeter was designed to provide better accuracy near blow-off conditions.

(*g*) **The Calorimeters.** These were used to measure the heat flux in a transient experiment lasting 1.3 s; steady flow conditions were reached after 0.35 s. Diagrams of the two types of calorimeters are given in Fig. 4. The solid calorimeter was made of a small rectangular block of copper. The side exposed to the heat flux was 1.58 mm and 3.17 mm in the directions respectively parallel and transverse to the flow. The thickness of the copper was 0.92 mm. The back side of the copper element was exposed to the air sealed in the cavity of the Teflon holder. The thermocouple wires (0.075 mm in diameter) were attached to the copper element by inserting them through a small hole in the center of the element and soldering them to the copper. The wires were separated as they emerged from the copper. An analysis [16] indicated a diffusion time of 7.3 ms, a conduction heat loss of 2.4 percent at 0.4 s in the test, and a characteristic rate of temperature rise of 15.9 K/s. The comparison of measured heat flux data for the solid wall with existing correlations showed very good agreement, indicative of a well-behaved turbulent boundary layer.

The porous calorimeter was made of the same material as the transpired plate. Since the plate and the calorimeter have the same temperature rise, the conduction losses are insignificant for equal injection rates. The gage has a streamwise length of 4.76 mm and a maximum length of 7.94 mm, and the diffusion time is calculated to be 150 ms. The average temperature of the gage was measured by putting the thermocouple junction in intimate contact over the depth of a hole in the center of the element with silver epoxy. The perimeter of the gage was taped. The gage was inserted into the slot cut in the porous plate.

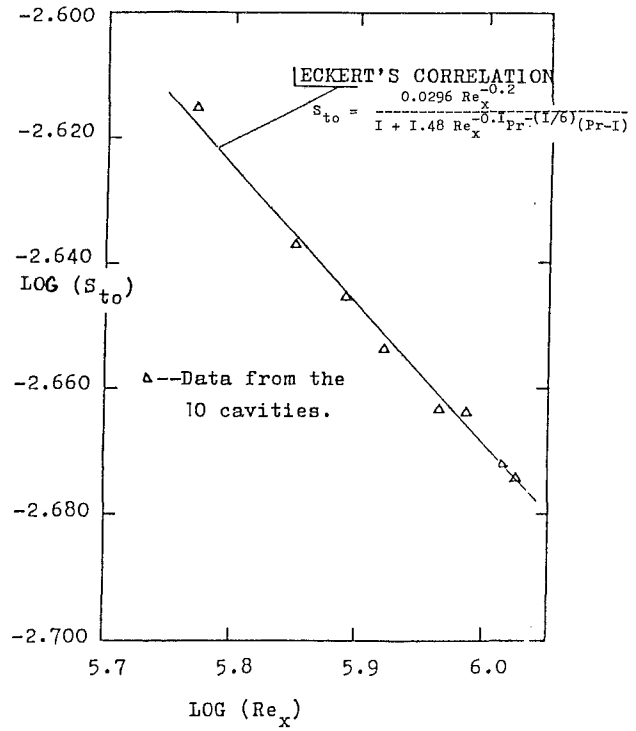

Fig. 5 The variation of the Stanton number with Reynolds number for the solid wall case; the Reynolds number was calculated by applying the standard correlation on the ninth cavity, and then using the known distances among the calorimeters

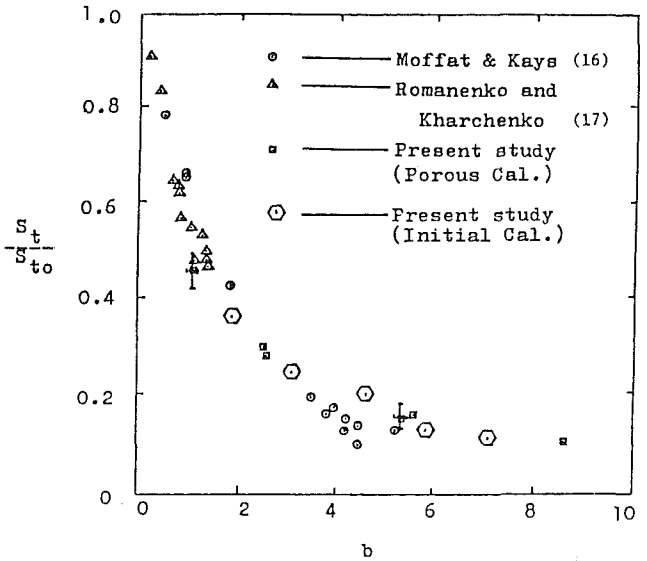

Fig. 6 Comparison of the measured cooling effectiveness with those of others; constant free-stream velocity

The heat flux can be calculated from the gage thermocouple as follows:

1 The energy balance of the porous gage can be written as

$$q_w = \rho_B c_B 1_B \frac{d\bar{T}_B}{dt} + (\rho v)_c c_c (T_w - T_c) + q_c + q_r$$

2 Since the conduction and radiation losses are negligible and since the mainstream conditions are constant, the small rise in wall temperature can be equated with the rise in gage temperature and the energy balance can be written as

$$q_w = \rho_B c_B 1_B \frac{d\bar{T}_B}{dt} + \left(1.0 + \frac{(\rho v)_c c_c}{(\rho_B c_B 1_B)} t\right)$$

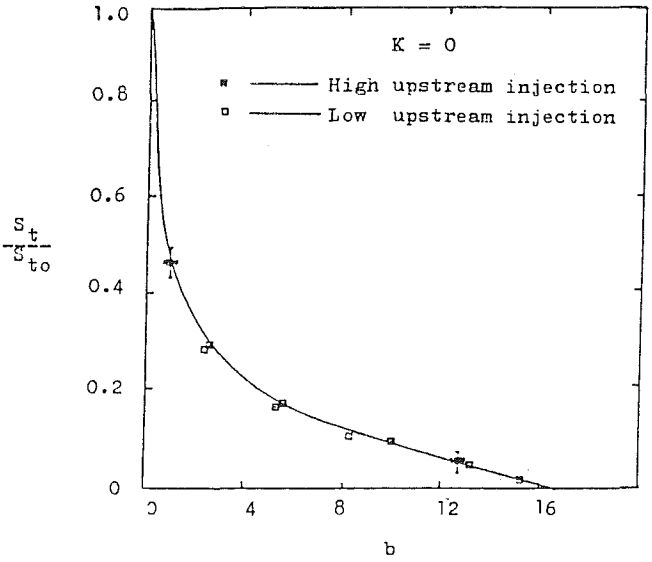

Fig. 7 The effect of upstream injection; constant free-stream velocity

The value of the derivative ($d\bar{T}B/dt$) was determined using a third-order polynomial approximation in a least-square method when the heat flux is calculated.

Experimental Results and Their Analysis

(*A*) Solid Wall Heat Fluxes. The fluxes were measured for reference and calibration. The results for the case of zero pressure gradient are shown in Fig. 5 and compared with existing correlations given in Eckert and Drake [18]. The agreement is indicative of a well-behaved two-dimensional turbulent boundary layer.

(*B*) Transpired Wall Heat Fluxes in Zero Pressure Gradient. Figure 6 shows a comparison of the transpired wall heat fluxes with the other results; the studies of Moffat and Kays [19] used a small temperature difference of 15 K between wall and main flow and a velocity of 15 m/s while Romanenko and Karchenko [20] used 100 K and 50 m/s.

The results of the three studies are in good agreement for moderate values of b. Measurements with the initial solid and porous gages are in reasonable agreement. A difference arises for values of $b>4$ while the difference is of the same order as the absolute uncertainty of the results [19]. The local variation of the Stanton number ratio as a function of b is given in Fig. 7 for two levels of injection upstream of the cavity on which the measurement is taken. It can be seen that the boundary layer adjusts itself quickly to the local injection level.

For $b>6$, the variation of the Stanton number ratio is nearly linear (Fig. 7). A linear extrapolation of the data for large injection rates yields a value of $b=16.5$ at the blow-off point. This value agrees with the criterion of Coles that the boundary layer at blow-off should be equivalent to a free mixing layer and consequently that $F=0.035$ or $b=F/\mathrm{St}_0=0.035/0.00218=16.1$, indicating the blow-off occurs when the injection rate equals or surpasses the entrainment rate of the layer. These results suggest that for $b>4$, the transpired turbulent boundary layer cannot be accurately described by a layer following the "law of the wall." But more likely, it could be described by an "outer boundary layer" entraining the injected flow which at blow-off acquires the characteristics of a free mixing layer.

A review article by Kutateladze and Mironov recently known to the authors, provides data which correlate the above analysis. First, the data also indicate that the injection becomes dominant in the inner layer at value of $b>6.0$. Data also indicate that the intermittency decreases toward the wall

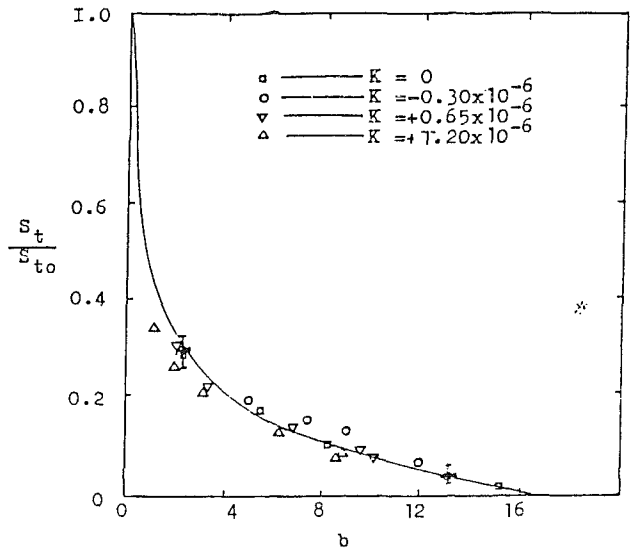

Fig. 8 The pressure gradient effect; low upstream injection rate; the data refer to cavity number 7; the upstream coolant flux was uniform; the value of b in cavity number 3 was about 1.7

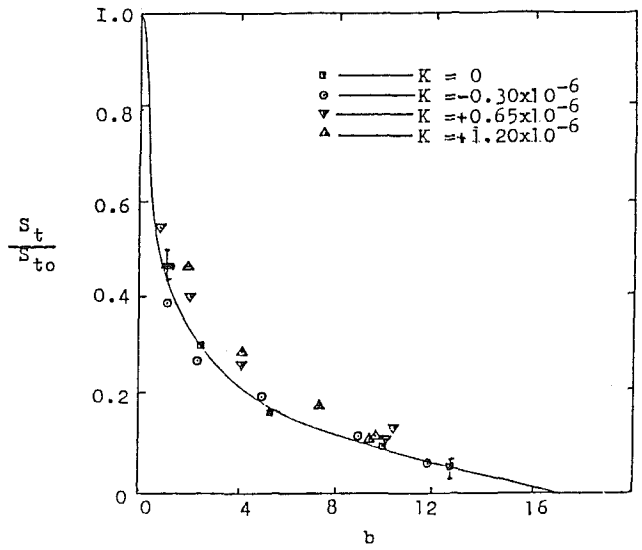

Fig. 9 The pressure gradient effect; high upstream injection rate; the data refer to cavity number 7; the upstream coolant flux was uniform; the value of b in cavity number 3 was about 2.5

as would be expected when the inner layer takes after a free mixing layer. Temperature profiles in the vicinity of the wall corroborate our data indicating that blow-off conditions occur at values of $b > 16.5$.

(C) The Effect of Pressure Gradients. In the range tested the pressure gradients are found to have relatively little influence on the ratio of Stanton numbers as can be seen in Figs. 8 and 9. The turbulent boundary layer integral equations

$$\frac{d(\mathrm{Re}_D)}{d\mathrm{Re}_x} = F_{\infty 0}\left(\frac{F_\infty}{F_{\infty 0}} - \frac{F}{F_{\infty 0}}\right) - K \cdot \frac{1}{\rho_\infty}\mathrm{Re}_D$$

$$\frac{d(\mathrm{Re}_m)}{d\mathrm{Re}_x} = \frac{C_{f0}}{2}\left(\frac{C_f}{C_{f0}} + b_u\right) - K(1+H)\mathrm{Re}_m$$

$$\frac{d(\mathrm{Re}_H)}{d\mathrm{Re}_x} = \mathrm{St}_0\left(\frac{\mathrm{St}}{\mathrm{St}_0} + b_H\right)$$

where

$$\mathrm{Re}_D = \frac{\rho_\infty u_\infty \delta^*}{\mu_\infty}$$

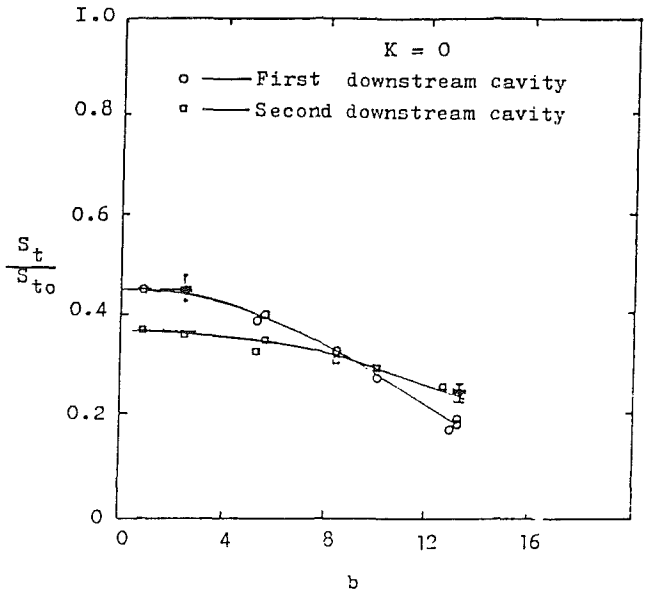

Fig. 10 Local variation of the Stanton number ratio as a function of upstream injection rate; constant free-stream velocity

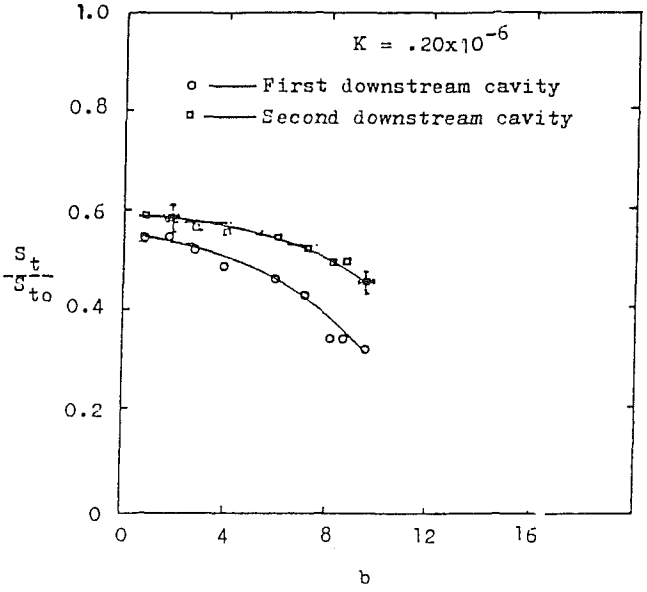

Fig. 11 Local variation of the Stanton number ratio as a function of upstream injection rate; strong acceleration

$$\mathrm{Re}_m = \frac{\rho_\infty u_\infty \theta}{\mu_\infty}$$

$$\mathrm{Re}_H = \frac{\rho_\infty u_\infty \delta_E}{\mu_\infty}$$

$$d\mathrm{Re}_x = \frac{\rho_\infty u_\infty}{\mu_\infty} dx$$

indicate that the pressure gradient parameter influences the displacement and momentum thicknesses directly while the energy thickness does not show any direct effect. Although the value of the St_0 is influenced by the pressure gradient parameter K, the ratio of Stanton numbers shows little influence of the pressure gradient parameter (Figs. 8 and 9) but a slight influence of the upstream injection is found which is characterized by a small reduction of the ratio of Stanton numbers with increasing upstream injection level.

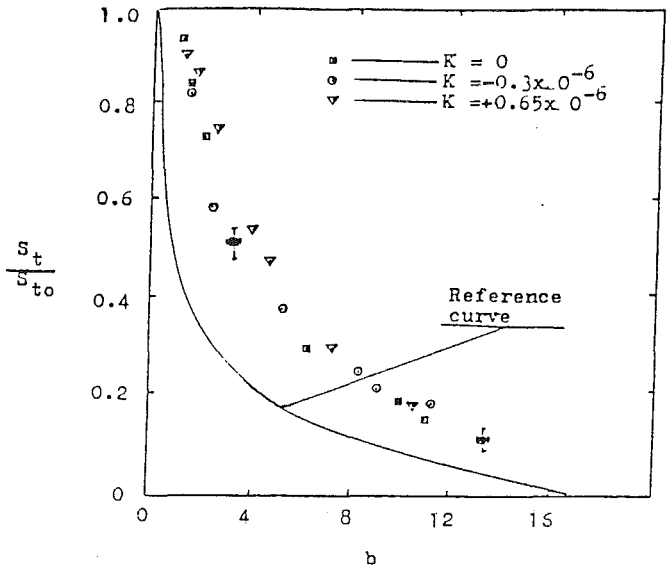

Fig. 12 The cooling effectiveness in a sudden step in the injection; data taken in cavity number 7; cavities numbers 1 to 6 had a solid plate on top

(*D*) Effect of Nonuniform Injection. As shown above, changes in upstream injection have been found to have a negligible influence on the downstream heat fluxes on smooth porous surface. The following experiments study two cases of practical importance. The first is representative of the cooling in the region close to the trailing edge of a turbine blade where the coolant feed rate is small, and it is important to determine the reduction in heat flux achievable with increasing upstream injection rates. The only previous study of this case was made by Whitten et al. [21] who observed that the boundary layer quickly relaxes to the "uniform injection" state downstream of a change in level of injection. They reported a relaxation length of about four boundary layer thicknesses for values of $b<4$. Figs. 10 and 11 show the measurements obtained at two adjacent cavities operating with a low injection rate. The measurements were made for increasing upstream injection rates for three different values of pressure gradient parameter. It can be seen that for $b<4$, there is no significant change in heat fluxes. However, the heat flux decreases slowly with increasing injection rates for $b>4$. Flow acceleration tends to enhance this effect. The second case (Fig. 12) considers the heat flux on a smooth process cavity located downstream of a solid wall. The comparison of the data with the reference uniform injection indicates an appreciable boundary layer relaxation effect.

Conclusions

The following conclusions can be drawn from the results of the present study:

1 The results obtained for low values of the injection parameter agree well with other available data.

2 The results indicate a linear drop of the ratio of the heat flux with increasing injection rate for the values of the injection parameter larger than the predicted value $b\simeq 4$ for blow-off conditions by the theory of Kutateladze and Leont'ev who assumed that the turbulent layer follows a "law of the wall."

3 The results yield a value of the injection parameter $b=16.5$ at blow-off conditions which compares well with $b=16.1$ predicted using the criterion proposed by Coles who suggested that the turbulent boundary layer behaves as a free mixing layer near the blow-off conditions.

4 The two above conclusions suggest that for $b>4.0$, the transpired boundary layer cannot be modeled by a layer following the "law of the wall," because the region close to the wall becomes dominated by the transpired layer which is entrained by the "outer layer."

5 The pressure gradients investigated are found, as expected, to have small effect on the ratio of Stanton number for a given injection rate.

6 The local heat flux is negligibly influenced measured at constant injection rate by increasing upstream injection rates up to a value of the injection parameter near 4; beyond that value a small reduction of heat flux is observed for increasing injection rates.

Acknowledgments

The authors wish to express their gratitude to Professor M.A. El-Masri, and Messrs. G. Power, J. Watts, D. Jenkins, R. Andrew, and H. Kozlu who have helped make this work possible. This work was supported by the Department of Energy under Contract Number E(49-18)-2295.

References

1 Emmons, H., and Leigh, D., "Tabulation of the Blasius Function With Injection and Suction," ARC CP 157, 1955.

2 Jeromin, L., "The Status in Research in Turbulent Boundary Layer With Injection," *Progress in Aeronautical Sciences*, Vol. 10, 1970.

3 Hartnett, J., and Sastri, V., "Heat Transfer in Transpired Turbulent Boundary Layer," in: *Heat and Mass Transfer in TBL*, ed. Spalding, Hemisphere, 1968.

4 Kays, W. M., "Heat Transfer to the Transpired Turbulent Boundary Layer," *Int. J. of Heat and Mass Transfer*, Vol. 15, 1972, p. 1023.

5 Kays, W. M., and Moffat, R. J., "The Behavior of Transpired Turbulent Boundary Layer," in: *Studies in Convection*, VI, ed. B. Launder, Academic Press, 1976.

6 Coles, D., "A Survey of Data for the Turbulent Boundary Layer With Mass Transfer," AGARD CP-93, 1971.

7 Cebeci, T., and Smith, A. M. O., "Analysis of Turbulent Boundary Layers," Academic Press, 1974.

8 Hacker, D., "Empirical Prediction of Turbulent Boundary Layer Instability Along a Flat Plate With Constant Mass Addition at the Wall," *Jet Propulsion*, Sept. 1956.

9 Kutateladze, S., and Leont'ev, A. I., *Turbulent Boundary Layer in Compressible Gases*, Academic Press, 1964.

10 Mironov, B., and Yarygina, N. I., "Heat Transfer and Friction in a Boundary Layer on a Porous Surface," *Inzh. Fiz. Zh.*, Vol. 23, No. 5, 1972.

11 Bayley, F., and Turner, A., "The Heat Transfer Performance of Porous Gas Turbine Blades," *Aero J. of the R.Ae. Soc.*, Dec. 1968.

12 Mickley, H., and Davis, R. S., "Momentum Transfer for Flow Over a Flat Plate With Blowing," NACA TN 4017, 1957.

13 Liepmann, H., and Laufer, J., "Investigations of Free Turbulent Mixing," NACA TN 1257, 1947.

14 Morris, et al., "Experimental Evaluation of a Transpiration Cooled Nozzle Guide Vane," AGARD CP-229, 1977.

15 Eckert, R. G., edited by J. P. Hartnell, "Studies in Heat Transfer: A Festschrift for E.R.G. Eckert," Hemisphere, 1980.

16 Georgiou, D. P., "The Transpired Turbulent Boundary Layer in Various Pressure Gradients and the Blow-Off Condition," Sc.D. thesis, Department of Aeronautics and Astronautics, Massachusetts Institute of Technology, Feb. 1983.

17 Louis, J. F., "Systematic Studies of Heat Transfer and Film Cooling Effectiveness," *Proceedings of the Symposium on High Temperature Problems in Gas Turbine Engines*, AGARD, Middle East Technical University, Faculty of Engineering, Conference Hall, Ankara, Turkey, Nov. 19-23, 1977.

18 Eckert, E., and Drake, R., *Analysis of Heat and Mass Transfer*, McGraw-Hill, 1972.

19 Moffat, R. J., and Kays, W. M., "The Turbulent Boundary Layer on a Porous Plate: Experimental Heat Transfer With Uniform Blowing and Suction," *Int. J. of Heat and Mass Transfer*, Vol. 11, 1968, p. 1547.

20 Romanenko, P. N., and Karchenko, V. N., "The Effects of Transverse Mass Flow on Heat Transfer and Friction Drag in a Turbulent Flow of a Compressible Gas Along an Arbitrary Shaped Surface," *Int. J. of Heat and Mass Transfer*, Vol. 6, 1963, p. 727.

21 Whitten, D., Moffat, R. J., and Kays, W. M., "Heat Transfer to a Turbulent Boundary Layer With Non-Uniform Blowing and Surface Temperature," *Proc. 4th Int. H. Trans. Conf.*, Versailles, Paper No. FC8.8, 1970.

Metallurgical Factors Affecting the Reliability of Fossil Steam Turbine Rotors

R. Viswanathan

R. I. Jaffee

Electric Power Research Institute
Palo Alto, CA 94303

The reliability of steam turbine rotors is of concern both from the point of view of avoiding premature failures prior to the end of the design life and from the point of view of extending the plant life beyond the end of the design life. With respect to rotors that are already in service, improved methods for assessing the remaining life of the rotors are needed. Although some progress has been made toward repairing of damaged rotors, many utilities still consider it risky and would rather replace these rotors than repair them. With respect to new rotors, methods for improving their reliability under cyclic operational conditions and other higher temperature conditions may be needed. All these concerns can be addressed adequately only with improvements in our understanding of the metallurgical behavior of the rotors. This paper is intended to review the various metallurgical factors that affect the reliability of rotors.

1.0 Introduction

Steam turbine rotors are among the most critical and highly stressed components of steam power plants. Failures of rotors have resulted in a wide spectrum of eventualities ranging from catastrophic burst to lengthy forced outages imposing severe economic penalties on the affected utilities. There have been only a few instances of catastrophic bursts of rotors. There is, however, great concern about the potential for such bursts because of the consequences of such incidents. The rotors made prior to 1950 and during the 1950s are of major concern because of their poorer quality compared to current rotors. There has also been an increasing awareness of the inadequacy of the original design database and of unanticipated in-service degradation of the rotor materials. Deviations in operational practice such as unforeseen or intentional cycling have also contributed to this concern. To forestall the possibility of a catastropic burst, several rotors are retired annually, based essentially on the recommendations of the turbine manufacturers. The criteria and the decision methodology for retirement are proprietary and vary from manufacturer to manufacturer. In addition to avoiding premature failures prior to the end of design life, many utilities would like to extend the life of the rotors beyond their design life, for economic reasons. Knowledge of the metallurgical factors affecting the remaining useful life of the rotor is of paramount importance.

While it is true that significant improvements in the casting and fabrication technology of rotors over the last 20 years have resulted in reduced risk against bursts from bore cracks where center quality and fracture toughness are limiting, surface cracking by high cycle fatigue, and corrosion fatigue have occurred in rotors made in later years. There is evidence to indicate that crack growth by these mechanisms is relatively unaffected by cleanliness of the rotor. For instance, the effect of steel cleanliness on the rate of fatigue crack growth is illustrated in Fig. 1 [1]. The data show that the crack growth

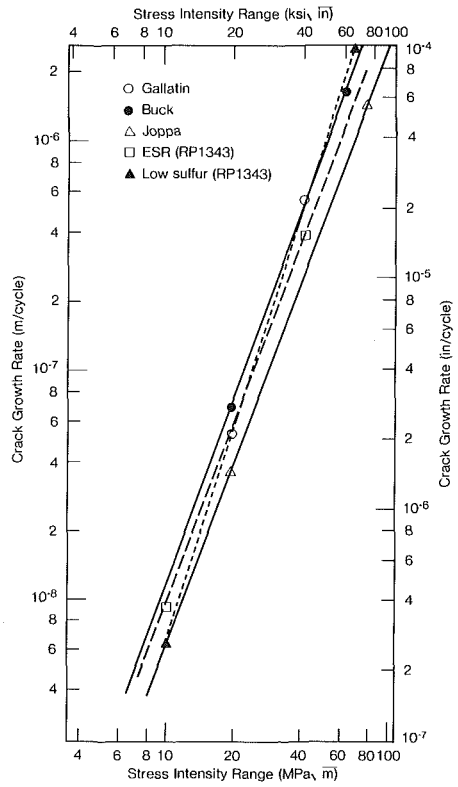

Fig. 1 Fatigue crack growth data for Cr-Mo-V steel: tests conducted in air at 25°C at 1 Hz at an *R* ratio of 0.1 [1]

Contributed by the Power Division for publication in the JOURNAL OF ENGINEERING FOR GAS TURBINES AND POWER. Manuscript received by the Power Division April 1983.

Table 1 Steam turbine rotor failures

Rotor component	Unit name	Year	Failure description
LP Shaft	Ridgeland #4	1954	burst while in service [1]
	ENESCA (Spain)	1950	burst while in test pit [1]
	Nijmijen (Netherlands)	1950	fracture, in service
	Not available	1951	burst while in test pit
	Connor Creek #16	1977	with 5 × 16-in. crack [3]
	Didcot (England)	1972	water induction
	Unnamed (England)	1972	water induction
	Aberthaw (England)	1973	water induction
	Wurgassen (W. Germany)	1974	2 shafts transverse cracking [2]
	Ferrybridge C (England)	1977	3 shafts transverse cracking [2]
	R. S. Wallace	1974	transverse cracking [3]
	Fort Martin #1	1976	2 shafts transverse cracking [2]
	Ravenswood #3	1978	transverse cracking [2]
	Astoria #5	1978	transverse cracking [2]
	Oak Creek #7	1980	transverse cracking [2]
	Waukegan #8	1981	transverse cracking [2]
	St. Clair #6	1981	transverse cracking [3]
	Pennelec	1981	transverse cracking
	State #4	1983	transverse cracking [4]
	Campbell	1984	transverse cracking
IP Shaft	Shawnee #1	1954	steeple fracture [2]
	Weadock #1	1955	steeple fracture [2]
	Tanners Creek #1	1953	wheel fracture
	Gallatin #2	1974	burst in service [1]
	Muskingum River #2	1968	transverse cracking [2]
	Cumberland #2	1976	coupling cracking [2]
	Mitchell #2	1980	coupling cracking [2]
	St. Claire #3	1983	
HP Shaft	Philo #5	1962	shaft transverse fracture [1]
	El Segundo #3 and 4	1978	shaft wheel fracture [1]
	Alamitos #3 and 4	1978	shaft transverse cracking [1]

Notes:
[1]Crack plane in axial-radial direction.
[2]Rotor was shut down due to high vibration prior to complete fracture.
[3]Cracking discovered by nondestructive testing.
[4]Cracking found after charge out.

rates are unaffected by the degree of cleanliness and are comparable for the 1950 vintage rotors (Gallatin, Joppa, and Buck Stations) and for high purity steel rotors made in the 1980s using advanced techniques.

There are many instances of LP rotor forgings made in the late 1960s to much cleaner specifications than the 1950 vintage forgings, in which circumferential cracks initiating at the shaft surface by corrosion fatigue propagated almost to the bore. The cracks were generally detected by abnormal vibration and the rotors had to be replaced or repaired at considerable expense. In such cases, methods of repairing and salvaging the rotor need to be investigated. In the rotors to be used in future machines, there is a need to further improve their quality, material properties, and design to increase economy operation (e.g., by eliminating prewarming requirements) and cycling capability.

The purpose of this document is to review the materials related issues affecting the reliability of fossil power plant rotors, so that the direction for future R&D can be delineated.

2.0 Failure of Rotors in Service

The failure of a rotor can be defined as its inability to perform the intended function so that it has to be replaced prior to end of the design life. On the basis of this definition, it is impossible to gather information regarding all the rotor failures. Table 1 is a list of rotor failures known to have occurred, based partly on the information published by Bush [2] and partly on unpublished information. The principal modes of cracking encountered in the LP and HP/IP Rotors and current remedies are summarized in Table 2.

2.1 LP Shafts/Rotors

2.1.1. Bore Cracks. The bore of a rotor is a highly stressed region of the rotor. The peak stresses at the bore are tangential and are conducive to formation of radial axial cracks. Several shafts and rotors are replaced every year due to bore indications and cracks. The principal metallurgical cause of these cracks is the poor quality of the near bore material in rotors made in early 1950s. During this period, ingots for rotor forging were air melted in open hearth furnaces. These forgings were characterized by severe segregation bands of sulfide and other inclusions, tramp elements and alloying elements and overall high concentration

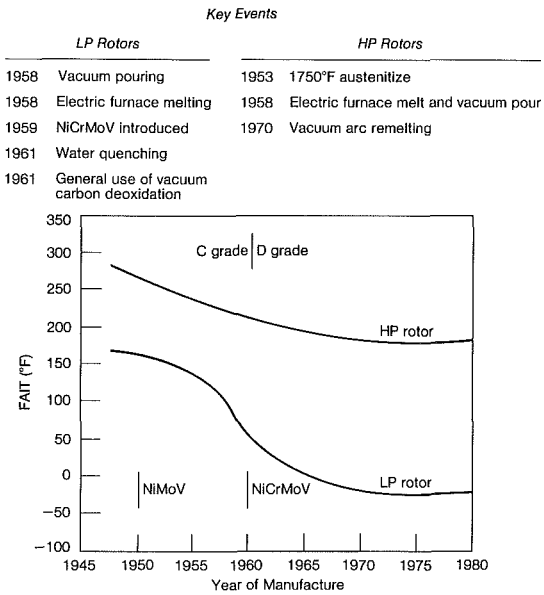

Fig. 2 Trends in impact toughness of steam turbine rotors (based on ref. 3.4)

Table 2 Types of cracking found in rotors

Component	Type of cracking	Cause of cracking	Remedial actions: Current rotors	Remedial actions: New rotors
LP Rotor/shaft	Radial axial bore cracks	Poor toughness and transient thermal stresses	Retire; grind, overbore or bottle-bore cracked areas	Improved toughness by control of cleanliness, H_2, and temper embrittlement
	Transverse cracks	High cycle fatigue with or without corrosion assistance	Retire; weld repair	Need to develop materials with improved pitting resistance; improved design to minimize stress concentration; reduce da/dn; coatings
HP/IP Rotors	Radial axial bore cracks	Creep with or without low cycle fatigue; poor creep ductility due to faulty heat treatment (class c) coupled with poor center quality facilitating initiation poor toughness	Retire; grind, overbore or bottle-bore derate machine steam-cool control start-stops	Improve center quality; heat treatment has been modified
	Blade grove wall cracking	Poor creep ductility	Retire; machine off cracks and use lighter blades; steam cool	Heat treatment has been modified
	Rotor surface cracking	Thermal fatigue	Machine off cracks; enlarge radius	Improved materials with resistance to thermal fatigue

of hydrogen, phosphorus, antimony, tin, arsenic, and sulfur. The presence of large amounts of inclusions can promote initiation and propagation of low-cycle fatigue cracks [3] during start-stop cycles. This, coupled with the fact that the material has very low inherent toughness, results in a high risk of rotor failure. Numerous improvements have been made since the latter part of the 1950s in steel making and rotor fabrication technology and the quality of forgings near the center has improved steadily over the years with a concomitant improvement in the toughness of rotor, as may be seen from Fig. 2 [3, 4]. The significant events contributing to the toughness improvements depicted in Fig. 2 are electric furnace melting and vacuum pouring of rotor ingots introduced in 1958, changeover from NiMoV to NiCrMoV steels for LP rotors in 1959, introduction of water quenching heat treatment practice in 1961, and use of vacuum carbon deoxidation (VCD) practice starting about 1961.

With respect to the older vintage rotors currently in service, removal of damaged bore material is sometimes performed by grinding, overboring, or bottle boring. The effectiveness of this practice has not been completely validated. In one case, a 10 cm × 40 cm radial axial bore crack was detected in a LP rotor by the Detroit Edison Co. [5]. The crack was machined out and the rotor was returned to service for 14 months, when it was re-examined. Further crack extension was revealed and the rotor was then retired. It has also been suggested that the machining processes can leave irregularities in the bore surface which makes subsequent ultrasonic inspection unreliable [6].

2.1.2. Transverse Cracks. This mode of cracking has been observed in the shafts of shrunk on disk-shaft construction. The cracks are often located near regions of high stress concentration on the surface. They generally (not always) initiate at corrosion pits and subsequently propagate by rotational bending fatigue. The cracks sometimes penetrate almost to the bore without burst of the rotor because of the higher toughness and lower stresses associated with the cracking. The toughness is not the limiting factor in such cases, and final failure can occur by ductile overload. Ultimate failure, however, is never reached since rotor instability results well ahead of that time, allowing the operator enough time to shut down the machine.

Metallurgical failure analyses have been carried out in detail in three recent instances of transverse cracking of shafts by investigators from the Battelle Columbus Laboratories [7–9]. In the first two instances [7] corrosion pits approximately 0.025 cm deep were found to have resulted in the initiation of cracks which subsequently propagated by fatigue. The average crack growth rates determined from the fractographic features were alarmingly high (40 cm/hr). The Battelle investigation suggested that failure of the two shafts was governed principally by the pit initiation event. Once pits of about 0.01-in. depths developed, failure followed in a matter of hours. In the case of the third failure, no evidence of cracking initiation from corrosion pits could be found [8, 9]. Crack propagation was once again found to have resulted from rotational bending fatigue, although the estimated rates of crack growth were much lower (2.5×10^{-4} cm/hr) compared to the other two shaft failures.

Since transverse cracking initiates at the shaft surface and propagates by high-cycle fatigue, improving the cleanliness, particularly the center quality of the rotor forgings, has not significantly affected the incidence of failure. This type of cracking therefore continues to be a problem even in rotors made in the 1960s and 1970s. Typical solutions to the problem have consisted of design changes to eliminate stress concentrations and control of steam chemistry to prevent pitting. The cracked shafts are mostly replaced by redesigned shafts,

Table 3 Highlights of utility survey relating to creep problems in HP/IP rotors

o Utilities with creep problems in the last 5 years	42 percent [1]
o Utilities to whom manufacturers have expressed concern	49 percent
o HP/IP rotors retired due to creep or end-of-design life	0.75 percent [2]
o HP/IP rotors reaching end-of-design life in next	
5 years	3.6 percent
10 years	5.3 percent
o Turbines derated or on accelerated inspection schedule due to suspected creep damage	1.2 percent

[1] Based on survey of 70 utilities
[2] Based on a total of about 3600 rotors

although in some instances weld repair has been accomplished successfully [10, 11].

2.2 HP-IP Rotors. A recent questionnaire survey of 70 utilities by EPRI indicates creep of rotors to be a major industry concern [12]. Highlights from the survey are shown in Table 3. The anticipated cost of purchase of replacement rotors alone will be in excess of $300 million in the next ten years. Additional costs will also be incurred due to installation costs, outage costs, and other related costs. Improved methods for assessing and extending the life of these rotors can result in significant savings for the utility industry. The different types of cracks generally encountered in these rotors are reviewed below.

2.2.1. Bore Cracking. As discussed earlier, rotors of the 1950 vintage have poor quality of the near bore material and are characterized by clusters of inclusions, segregation streaks, and locally high concentrations of embrittling impurities. The inclusions serve as favorable sites for crack initiation. Crack propagation by low-cycle fatigue, creep, or a combination of both is also facilitated by inclusion clusters and severe temper embrittlement of the grain boundaries. Another cause of cracking in some of these rotors is claimed to be their poor creep rupture ductility (and notch sensitivity) resulting from the use of a 1010°C austenitizing heat treatment. Most CrMoV rotors made after the mid-1950s were austenitized at 954°C since the reduced austenitizing treatment was found to reduce the rupture strength and improve the rupture ductility. With respect to the older rotors however, the utilities continue to face the dilemma of whether to run or to retire the rotors. Utilities have retired numerous rotors of the old class C type due to their poor rupture ductility characteristics. Other options that have been exercised include derating of the machine, removal of the damage by grinding, overboring, or bottle-boring [12].

2.2.2. Rim Cracking. This form of cracking was first identified in the LP rotors at Shawnee (TVA) and at Weadock (Consumers Power Co.) [2]. The cracks were in the outer corner of the T grooves for the blades and usually started at the blade entrance slots. The cracking in the Shawnee rotor was identified to be due to the poor long term creep rupture strength of the NiCrMoV steel used. In the case of the Weadock rotor cracking was attributed to the low creep ductility and hence notch weakening of the CrMoV steel (class C austenitized at 1010°C). The remedial actions consisted of use of CrMoV steel austenitized at 954°C for all future rotors; design modifications were also implemented to lower the stresses. Numerous rotors of this vintage have had to be replaced. Creep cracking at the blade attachment areas continues to be a problem for many utilities. It has sometimes been possible to extend rotor life by grinding or machining off the cracks and simultaneously reducing the stresses by use of lighter weight blades. Steam cooling has also been employed at times, to lower the temperature at the critical regions.

2.2.3. Rotor Surface Cracking. This is a problem generally experienced in HP rotors and is attributed to thermal fatigue resulting from cycling. The cracks usually occur in heat grooves and other relatively small radii at labyrinth seal areas along the rotor. These cracks are generally shallow and in most instances can be removed by machining a few thousandths of an inch (known as skin peeling). To prevent reoccurrence the radii are enlarged to lower the local stress concentration [13]. The skin peeling process can be continued repeatedly until it is no longer practical.

3.0 Life Assessment of In-Service Rotors

The useful life of rotors in service may well exceed or fall considerably short of the design life. The reasons for this wide spectrum of behavior are related to design, operational, and metallurgical factors. Among the factors that tend to shorten the life are unforeseen residual stresses and stress concentrations, operating under conditions not originally envisioned in the design (e.g., cycling, excessive temperature, corrosive environments) degradation of the material in service due to temper embrittlement, creep embrittlement, and other time-dependent phenomena which had not been sufficiently characterized and anticipated 20-30 years ago; the main reason why rotors can have life remaining even after the end-of-design life, in spite of the above vagaries in design, operational, and material parameters is the factor of safety, and conservatism built into the original design. The balance between these various factors as they affect rotor life is specific to each rotor; hence the need for the systematic methodology to assess the life of in-service rotors.

3.1 Fracture Mechanics. As the starting point in the analysis it is assumed that a small crack of size a_0 pre-exists or has formed during service of the rotor. The crack grows as a function of further service time (da/dt) or as a function of cyclic operation (da/dn) depending upon whether crack growth occurs under static loads (e.g., creep, stress corrosion) or under cyclic loads (e.g., fatigue, corrosion fatigue). The crack eventually reaches a critical size a_c at which time catastrophic burst of the rotor occurs.

The critical crack size a_c is given by the approximate formula [14,15]

$$a_c = \frac{Q}{1.21\pi}\left(\frac{K_{IC}}{\sigma}\right)^2 \tag{1}$$

where

a_c is the critical crack half-length
Q is a flaw shape parameter
σ is the tangential stress at the location of interest
K_{IC} is the material fracture toughness at the flaw location under the temperature and stress conditions of interest

K_{IC} is a material property and can be determined by testing the material at the relevant temperature. Since the stress can be estimated, the critical crack size a_c can be calculated. Various formulae exist for expressing crack growth rates. For instance, fatigue crack growth in rotor steels can be expressed by the relation

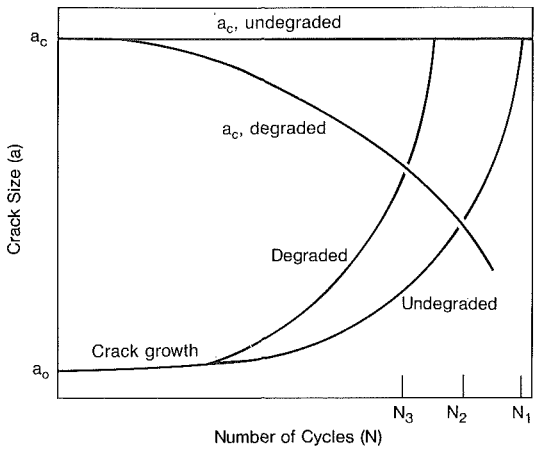

Due to in-service degradation of material, the rate of crack growth as well as the critical crack size may be affected adversely, leading to premature failure at N_3 cycles rather than the anticipated life of N_1 cycles.

Fig. 3 Illustration of remaining life concept

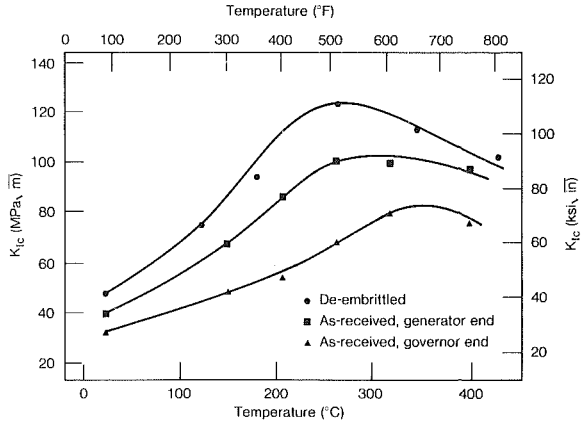

Fig. 4 Degradation of fracture toughness due to temper embrittlement in-service; Cr-Mo-V rotor retired after 17 years of service at Buck #6 of Duke Power Company [1]

$$da/dN = C_0 \Delta K^m \quad (2)$$

where a is the crack length, N is the number of cycles, ΔK is the stress intensity range, C_0 and m are material constants.

Knowing the initial crack size a_0 in the rotor (from nondestructive evaluation), the crack growth rates da/dn or da/dt, and the critical crack size a_c (from the standard material property data), the remaining life of the rotor is estimated.

One major source of uncertainty in assessing the remaining life of the rotor using the above approach is the lack of material property data for the rotor in the service degraded condition. Prolonged service exposure often causes degradation of the fracture toughness (K_{IC}), creep strength, yield strength, and other properties as described in the later sections of this paper. Consequently, the properties of the rotor in its service exposed condition must be determined by testing or estimated based on a knowledge of the original material properties and the operational history of the rotor.

Figure 3 illustrates the problem schematically. In the absence of any in-service degradation of the toughness of the material, the a_c will remain unaffected and will have a constant value. The crack growth will occur from the initial size a_0 until the crack size reaches a_c at point N_1, at which time unstable fracture will occur. In actual practice, the toughness of the rotor is known to degrade due to temper embrittlement and other microstructural changes so that a_c is reduced and failure will occur at $N_2 \leq N_1$. In addition, service degradation of the material may also affect the rate of fatigue crack growth da/dN itself so that failure may now occur at N_3, instead of N_1 or N_2. Designs based on original undegraded properties would predict failure at N_1 cycles whereas premature failure may occur due to the unanticipated in-service degradation of the steel at N_3 cycles.

3.2. Current Methodologies and Improvements Needed. The methods and criteria by which turbine manufacturers make run/retire decisions for rotors are often proprietary. The general principles involved are however known. The key element of the procedure are NDE evaluation, stress analysis, and material property data. The NDE evaluation gives an indication of the size and distribution of flaws present. For an assumed duty cycle of the turbine, the distribution of stresses as a function of location, time, and temperature can be calculated. The worst combination of stress and material properties (K_{IC}) is expected to occur in the near bore region during transient conditions. The critical flaw size for this set of circumstances is then estimated. Based on current flaw size indications, available fatigue crack growth rate data, and the estimated critical flaw size in the material, the remaining life of the rotor is estimated for various operating conditions. The results may be further modified using an "experience factor." In this type of analysis it is conservatively assumed that all indications are cracks located in the worst orientation (radial-axial). The tolerable flaw sizes are expected to be conservative since in converting the service modified fracture appearance transition temperature (FATT) values to K_{IC} type values, the lower end of the scatterband is used. Since fatigue crack growth rate data for steels exhibit wide scatter, the highest rates are assumed. The present methods for estimating remaining life thus involve the most conservative assumptions relating to the NDE data, operating conditions, and the material property data.

One example of a life prediction system that has been widely publicized is the STRAP Program, based on finite element thermoelastic stress analysis and fracture mechanics, and details of field NDE inspection results as input to the calculations [6, 16]. The automated Steam Turbine Rotor Analysis Program (STRAP) has been developed by EPRI to facilitate the prediction of rotor lifetime given the duty cycle of the turbine and the results of ultrasonic examination from the rotor bore. STRAP consists in part of a preprocessor code that generates the boundary conditions and finite element mesh for transient and steady-state temperature and stress analysis employing the ANSYS general-purpose structural analysis code. A postprocessor contains fracture toughness, stress-rupture, yield strength, and fatigue crack growth rate data for air-melted 1 CrMoV forgings, on the basis of which the local stress and temperature values are screened to determine the critical crack size, the initial crack size that could grow to critical size within a specified number of hours or cycles, and the minimum area fraction of defects that could link up to result in a significant crack. A boresonic data reduction code allows rapid sorting of indicated flaw sizes and locations to determine the regions of greatest defect density.

While the EPRI effort represents a major step in life prediction analysis, the failure modes analyzed are limited to fatigue growth of crack from flaws near the bore. Other mechanisms such as stress corrosion, thermal fatigue, high cycle bending, or torsional fatigue are not addressed. Several gaps remain in the materials, NDE, and stress analysis areas which need to be filled, before the methodology can be more widely applied. While the fracture mechanics routine represents the state of the art, the data base does not take into account subcritical crack growth by creep fatigue. The interaction between creep and low-cycle fatigue which can be an important crack growth mechanism for bore cracks has not been addressed, simply for lack of data. Linkup between

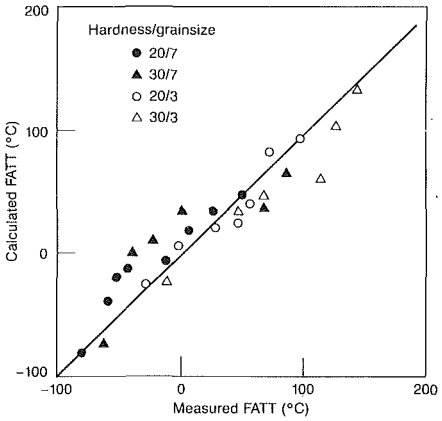

Fig. 5 Correlation between calculated and measured values of FATT for Ni-Cr-Mo-V steels [17]

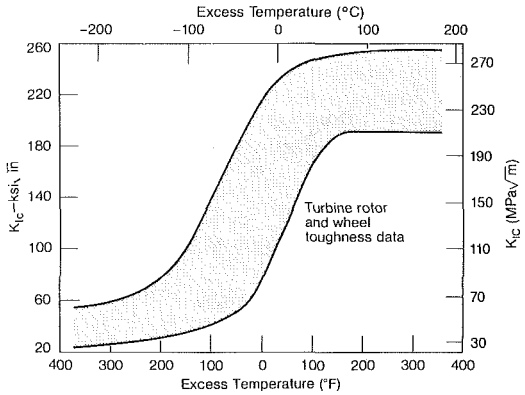

Fig. 6 Correlation of the K_{IC} of rotor and disk steels with the excess temperature; excess temperature is defined as the temperature of interest minus the FATT at that temperature [3]

clustered defects that is caused by crack growth across the ligaments has not been taken into consideration. The change in material toughness in service due to temper embrittlement is not included in the analysis.

The ultrasonic test (UT) and interpretation methods also need further improvements. The UT is not capable of distinguishing between different types of flaws such as porosity, inclusions, and cracks and they are all lumped together for the fracture mechanics analysis. Regions of high density indications are simply assumed to be cracks, whether in fact they are so or not. There is considerable uncertainty in evaluating the data on a volumetric basis and assumptions have to be made regarding the connectivity of individual flaws. Assumptions made regarding subsurface flaws may also need to be further verified. The UT examination is also incapable of detecting microscopic damage, such as grain boundary cavitation due to creep, and grain boundary segregation of impurity elements; these damage mechanisms may reflect severe deterioration of the material with impending cracking, but can go undetected by the current NDE procedures. Finally, the current version of the code incorporates only a deterministic approach to failure prediction so that the prediction is a lower bound, conservative value. Incorporation of a probabilistic approach into the code can result in more realistic predictions of life time, corresponding to different risk levels.

In conclusion, current methods for life prediction can provide a foundation for further R&D work in the area of remaining life prediction of rotors. Additional work is needed in extending the methodology to cover additional failure modes and metallurgical factors which are important but have not been addressed in the past. In the materials area, the most important issues that need further study are toughness degradation by temper embrittlement (LP and HP), crack initiation and growth under creep, low-cycle fatigue and creep-fatigue conditions (for IP-HP only). In the case of LP rotors, creep is not a consideration and crack initiation and growth under low cycle fatigue would seem to be the most important issues.

3.2.1 In-Service Degradation of Toughness. Toughness degradation due to temper embrittlement can affect the remaining life of both CrMoV and NiCrNoV rotors. The CrMoV rotors operate over the entire range of temperature (316–538°C) that is critical for temper embrittlement. At the same time, they are inherently less susceptible to temper embrittlement due to the absence of nickel. In extreme cases where the impurity levels are very high (e.g., Buck rotor HP-IP), significant embrittlement of CrMoV steel has been observed and the fracture toughness is appreciably lowered [1] (see Fig. 4). The NiCrMoV steels generally operate below about 370°C. Since this is in the bottom range of the critical range for temper embrittlement (343–538°C), one would expect that degradation by embrittlement may not be appreciable. While this is generally true, significant in-service degradation of some rotor materials is known to occur at very long times ($\geq$ 15 years) even at temperatures as low as 343°C. In view of the wide variability of the chemical compositions of rotors, there is a definite need to characterize each rotor individually with respect to in-service degradation. It is often impossible to remove samples from a rotor in order to evaluate its toughness by conducting destructive tests. EPRI research in the last few years under Research Project 559 has focused on nondestructive methods, whereby the toughness of a rotor could be estimated by examining very small samples. One approach has consisted of developing embrittlement equations correlating FATT with microstructural observations using small auger samples. Since the FATT is related primarily to the concentration of impurities at grain boundaries, hardness, and grain size, it can be estimated readily using small samples. Figure 5 shows the correlation between predicted and actual measured values of FATT for NiCrMoV rotors generated under the RP559 project [17]. The correlation is good. Further work is needed to validate this diagnostic technique with respect to field rotors. If an FATT can be estimated reliably, it can be converted to K_{IC} values needed for life assessment using empirical relationships of the type shown in Fig. 6. Other methods for estimating K_{IC} of rotors from miniature specimens should also be investigated. It has also been the practice of some turbine manufacturers to age core samples of all rotors utilized by their company, in the laboratory to monitor the degradation of toughness under operating conditions. This information is however unavailable to the public at this time.

3.2.2 Creep and Stress Rupture. In the case of HP-IP rotors operating in the creep regime, the relaxed long term bore stresses and wheel radial stresses are assessed against the creep rupture data for the steel. The design stresses are generally based on the 10^5 hr smooth bar creep rupture stress divided by some appropriate safety factor. Since it is impossible to obtain 10^5 hr creep rupture data on every rotor material, the general practice is to evaluate the short-time rupture strength of the material at temperatures well above the service temperature, then use the Larson-Miller type time-temperature parameter to extrapolate the data. There are three main problems associated with this approach. The creep rupture properties of rotor steels vary widely even with minor differences in composition and heat treatment, resulting in a broad scatterband of data. Turbine manufacturers have traditionally used the lower bound of the scatterband for design, thus building in an unknown degree of

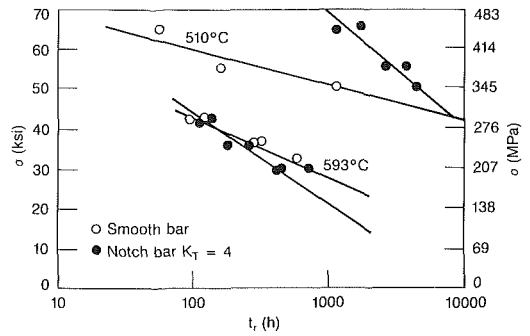

Fig. 7 Variation of time of rupture (t_r) with applied stress (σ) for smooth and notched specimens of Cr-Mo-V steel tested at 510 and 593°C [18]

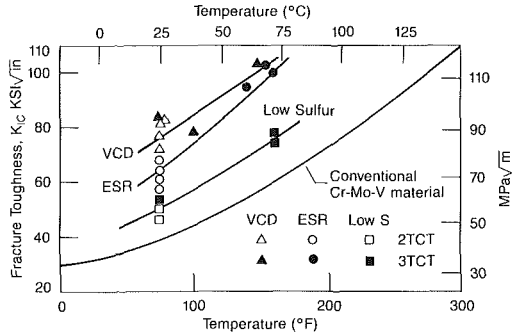

Fig. 8 Variation of K_{IC} with temperature for three Cr-Mo-V rotor forgings manufactured to high cleanliness standards using advanced steel making technology [20, 21]

conservatism. Secondly, the standard scatterband of data is based on rupture tests of conventional creep specimens tested in air. Since the tests are conducted in air at elevated temperatures, oxidation effects would exert an adverse influence on the rupture behavior. In actual rotors, however, the effect of such oxidation with respect to the large section size may be minimal. Use of laboratory data to predict the rupture behavior of large rotors may thus contribute additionally to the conservatism in the original design. Thirdly, long-term microstructural changes and degradation phenomena lend considerable uncertainty to the validity of any of the available time-temperature extrapolation procedures to predict long-term behavior.

Approaches that use stress rupture criteria alone for design ignore the importance of rupture ductility. Unfortunately, improving the strength of materials often results in a corresponding lowering of ductility. Reduced ductilities imply an inability to accommodate strains by creep deformation rather than by cracking. Consequently, in presence of notches and other stress concentrations, the creep rupture strength drops drastically compared to that under smooth bar conditions as may be seen from Fig. 7 [18]. This allegedly is the reason for cracking in numerous class C rotors heat treated at 1010°C. These problems brought into focus the importance of ductility and creep rupture behavior in presence of stress concentrations. Many manufacturers employ testing of notch bars in creep in order to detect tendencies for notch sensitivity. Unfortunately, notch sensitive steels also happen to be stronger in short duration tests and the manifestation of the notch sensitive behavior does not occur except in long duration tests. It is difficult to predict the onset of notch sensitive (low ductility) behavior based on accelerated tests. Again, notch sensitivity is not an inherent material property, but depends on the test temperature, stress state, and stress. Since this type of behavior implies that the onset of creep cracking is strain limited, the ability to model creep strain accumulation in terms of time, temperature, stress, and stress state is essential in predicting the remaining life. The creep strain in turn must be relatable to damage and eventual crack nucleation under the multiaxial stress conditions. The principal form of damage in "notch sensitive" situations is nucleation of cavities and wedge cracks at grain boundaries. Once the cavities and cracks form, linkup between them to form large cracks can occur rapidly, because the ductility is low. Since the incipient cavitation and microcracking cannot be detected by current inspection techniques, this type of failure is insidious and can occur without much forewarning.

There is a major need for understanding the initiation and growth of creep cavities as a function of creep strain, temperature, stress and stress state. Armed with this knowledge, examination of small metallographic samples removed from the critical locations of a rotor can provide a rapid, inexpensive, and nondestructive method to estimate remaining life. Periodic assessment of the remaining life will also be possible with such a technique. There will be no limitation in terms of the number of locations or type of locations that can be examined.

The cavitation type of damage is generally associated with low ductility, notch sensitive material and conditions. In these cases, in the absence of other pre-existing flaws, the critical failure event is crack nucleation by creep, since, once the cracks are nucleated, rapid linkup and eventual failure are envisioned. Most rotors made after the mid-1950s, however, are relatively creep ductile under operating conditions. In these cases, creep cracks, once initiated, grow slowly with time until eventual linkup and failure occurs. In such cases, failure is limited by creep crack growth rate and not by crack (cavity) nucleation. A knowledge of creep crack growth rate is, however, essential in all cases for prediction of remaining life since pre-existing defects may obviate initiation consideration. The limited published information, relating to creep crack growth in CrMoV rotor steels, has been reviewed by Curzon and Wells [19].

3.2.3. Low-Cycle Fatigue. Cyclic thermal stressing under start-stop cycles can lead to initiation and propagation of cracks by low-cycle fatigue. The stress distribution in the rotor during various cold starts, warm starts, and under steady-state conditions can be computed with existing techniques. The peak stresses are generally found to occur tangentially in the bore at a temperature well below the steady-state operating temperature. Repeated cold starts can result in low-cycle fatigue in the stress range where the minimum stress might be zero and the maximum stress is the peak transient stress. Superimposed on this fatigue damage is the creep damage occurring at the operating temperature both due to repeated relaxation of the stresses from the peak value to the steady-state value and due to long time creep under the steady-state relaxed stress. The interaction of the fatigue and creep damage can lead to significant deterioration of the expected life. This issue is now of particular concern since many older fossil units (rotors made from dirty steel) which were not designed to operate cyclically are now being used in a cyclic mode. The utilities have made this change for economic reasons fully knowing that there is a penalty associated with it in terms of reduced life. What needs to be done is to quantify this penalty so that guidelines can be provided both in terms of operating procedures and in terms of remaining life estimation. The methodology for dealing with the low-cycle fatigue problem per se exists, but the methodology for dealing with the combined effects of fatigue and creep does not exist. Many approaches have been proposed to estimate cumulative damage under creep-fatigue conditions, but none have been verified adequately with extensive long-term test results.

4.0 Repair and Refurbishment

In view of the very high cost associated with replacing

rotors, procedures for extending life by rotor repair and refurbishment have aroused considerable interest among utilities.

In the case of high-temperature rotors, the practice of refurbishing the bore by grinding, overboring, or bottle-boring is used by some utilities. The potential life extension through removal of the bore material is based on two premises. Firstly, it is believed that since the bore is the highest stressed region and the stresses diminish rapidly away from the bore, all forms of high-temperature damage are confined to the near bore region. Secondly, it is believed that even substantial increases in the bore diameter will not result in increased stresses. Both of these premises, put forward by the manufacturers, have to be independently verified by experiments. There is also the possibility that in those rotors where the poor center quality extends well beyond the bore, removal of bore material may expose new and potentially more dangerous sites for crack initiation. Further work should be undertaken to validate the efficacy of bore repair techniques.

In the case of circumferential cracks in LP shafts, weld repair has gained increasing attention recently. The know-how for performing this repair seems to be confined to a few organizations. For instance, the Brown Boveri Corp. views the weld repair as feasible and viable, in view of their experience with welded disk construction. Recently Westinghouse Electric Corporation has also successfully weld repaired a cracked LP shaft. To date, three U.S. utilities have applied weld repair to salvage LP shafts containing circumferential cracks. Several utilities are believed to be seriously evaluating the potential of this method. Besides concerns about unknown long-term performance of the welded rotors, rotor bowing, distortion, and material properties of the heat-affected zone are among some of the immediate concerns [10].

In the case of cracks in blade attachment areas, a common practice has been to grind or machine off the cracks, at the same time lowering the stresses by using lighter blades. In the case of rotor surface cracking, the cracks have been generally found to be confined to a few mils from the surface and removal of this skin layer has been shown to be adequate to restore the material [13].

5.0 Improvements Needed for Future Rotors

As discussed earlier, further improvements in reliability, efficiency, and economy of operation (cycling capability) can result by improving the toughness, creep strength, and low-cycle fatigue strength of CrMoV rotors and by improving the low-cycle fatigue strength, toughness, and resistance to corrosion fatigue of the NiCrMoV rotors. The materials technology needed for achieving some of these improvements is discussed in this section.

5.1. Improved Toughness of HP-IP Rotors. The toughness of the CrMoV steels in current use, notwithstanding the improved cleanliness achieved over the last two decades, is still poor. The fracture appearance transition temperature (FATT) is well above room temperature, so that during each cold start, the rotors have to be prewarmed to a temperature above the FATT over a period of several hours prior to imposition of full load.

The controlled startup and shutdown requirements lead to increased capital costs and operational costs for the plant and decreased flexibility and total power generation. These considerations have become especially important in the context of the increased cyclic duty requirements imposed on the older fossil units resulting from the use of nuclear units for base-load operation. Design of new units in large sizes (1000 MW) with cycling capability is also incumbent upon the availability of rotors with improved toughness since the number of fatigue cycles the rotor can withstand prior to reaching the critical of crack size increases with toughness. Fracture toughness considerations relating to the HP and IP rotors thus have a major influence on the reliability, efficiency, and the overall plant economy. There are currently two methods to achieve improved fracture toughness in HP-IP rotors as follows:

1 Improved cleanliness
2 Modification of alloy content and heat treatment

5.1.1. Improved Cleanliness. Improved cleanliness of HP-IP rotor steels is being studied under several projects funded by EPRI [20]. Three processes for casting the CrMoV rotor steel ingots have been evaluated: electroslag remelting (ESR), silicon deoxidized low sulfur (Low S), and vacuum carbon deoxidized low sulfur (VCD). Production forgings from the ingots have been made, to be installed in utility turbines. Large test ends and bore bars have been evaluated. In all cases, the sulfur content is kept at or below 0.002 percent S, with low residual contents of P, Sn, As, and Sb. Other alloy contents are nominal except for the VCD forging, where silicon is low. The low sulfur content has resulted in a major improvement in the fracture toughness of CrMoV, as shown in Fig. 8. At room temperature, the fracture toughness of CrMoV has doubled for the VCD forging and has increased 60 percent and 25 percent, respectively, for the ESR and low S forgings. The ductile-to-brittle fracture transition temperatures (FATT) for the three forgings were 60°C, 73°C, and 95°C for VCD, ESR, and Low S, respectively. If the FATT were at room temperature or below, the HP-IP rotor would not require prewarming before cold starting, a significant operational advantage. Significantly, the high-temperature strength was not affected by the improved low-temperature properties, and actually improved slightly.

In a related effort, the effect of reducing Si and Mn is also being investigated [21]. Generally, manganese is added to steel in amounts of 20 times the sulfur content. At 0.001–0.002 percent sulfur level, only 0.02–0.04 percent manganese is needed, about 1/10 of the nominal manganese content. This area of steel metallurgy is relatively unexplored. Some data from the University of Leeds suggest that the low Mn–Low S steels will be extremely tough. Work done by the University of Pennsylvania has shown that low Mn–Low S steels are not only tough but resist the grain boundary segregation and embrittlement caused by the residual P, Sn, As, and Sb when the steel is heated in the temper embrittlement range of 343–538°C. The CrMoV alloy is being modified to compensate for the loss of hardenability accompanying the absence of manganese by increased nominal alloy content of Ni, Cr, and Mo (0.9Ni, 1.5Cr, 1.4Ni versus 0.35Ni, 1.1Cr, 1.2Mo). The philosophy being used is to stay as close to the normal alloy specifications as possible, because commercialization of a clean steel within existing specifications will be easier than for a completely new steel.

5.1.2. Modification of Alloy Content and Heat Treatment to Improve Toughness. In the past, one of the constraints to the development of CrMoV steels with improved toughness has been the inability to make significant changes in the alloy content and heat treatment procedures, for fear of adversely affecting the creep strength of the alloy. It has been found that as the rupture strength increases, the FATT is also found to increase. The best creep rupture properties of CrMoV steels are achieved with a microstructure consisting of upper bainite. Unfortunately, the upper bainitic structure also leads to inferior toughness; in order to achieve good toughness, lower bainitic and martensitic structures are preferred, but they result in poor creep properties. In the manufacture of turbine shafts it has therefore to be considered whether creep strength at high temperatures or

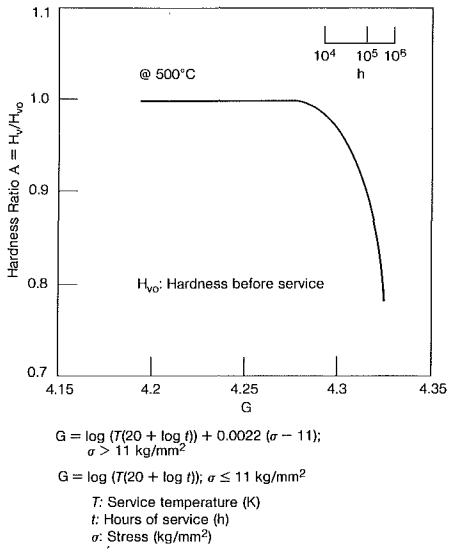

Fig. 9 Softening of Cr-Mo-V rotor steel with duration of service exposure [13]

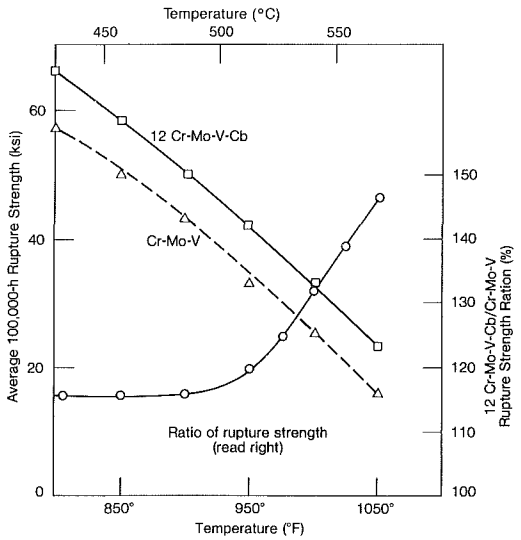

Fig. 10 Comparison of the mean predicted rupture strengths of 12Cr-Mo-V-Cb and Cr-Mo-V rotors [3]

toughness at low temperatures is to be preferred. Each manufacturer makes this tradeoff in different ways based on his design. For instance, the European practice of oil quenching CrMoV rotors has resulted in slightly improved toughness but at the sacrifice of some creep strength. The U.S. manufacturers, on the other hand, preferred to air cool CrMoV rotors, thus opting in favor of creep strength.

Recent analysis of Finkler and Potthast has shown that in a 120-cm-dia CrMoV rotor, the beneficial effect of quenching on the toughness is confined only to the surface region and that improvements near the bore are only marginal [22]. They have advocated that heat treatment modifications may have to be coupled with alloy modifications to improve hardenability, before significant improvements in toughness can be realized. In line with this reasoning they have developed an alloy with a preliminary designation ATRIX 382S, containing higher levels of Ni and Cr and a slightly lower level of carbon compared to ASTM 470 class 8 grade CrMoV steel. An experimental ingot of the new alloy weighing about 150 kg has been made, forged, and heat treated similar to the core of a 120-cm-dia shaft. Depending on the preliminary heat treatment and the final heat treatment the FATT values were found to range from $-10°C$ to $+55°C$. The tensile and creep properties were comparable to the conventional grade. Based on these encouraging preliminary results, Finkler and Potthast believe that the new steel can be expected to give a ferrite-free bainitic structure at the core of oil quenched forgings of up to 150 cm diameter with a tensile strength of 800 MPa and an FATT of room temperature.

An alternate approach to circumventing the creep strength–toughness tradeoff that has to be made in HP rotors has been to produce an integral HP-LP rotor with an axial gradient in properties [23]. The impact toughness gradually increases, while the creep strength gradually decreases from the HP to the LP side of the rotor, in a manner compatible with the service requirement. This approach requires modification of the alloy as well as the heat treatment procedure. Modification of the conventional 1 percent CrMoV steel was conducted to enhance hardenability and make grain size refinement easier. It was found that increasing the nickel content up to 1 percent gives sufficient hardenability to ensure good toughness at the center of the forging, without any sacrifice of the creep rupture strength. The addition of about 0.03 percent niobium gives rise to easier grain size control, coupled with additional creep rupture strengthening. The silicon content was reduced to compensate for the increased nickel content and to avoid temper embrittlement. A prototype rotor made from the modified composition was given a differential heat treatment such that the HP side was austenized at 980°C and water spray cooled prior to tempering while the LP side was austenized at 945°C and fan cooled.

The FATT values at both the HP and LP ends are well below the ASTM specifications for this class of steel. In addition, the creep rupture strength of the HP side of the rotor was also found to be equivalent and in some cases even better than that of conventional CrMoV steels.

5.2. Improved High-Temperature Strength. The temperature limit of the 1 CrMoV steel for HP-LP rotors is about 538°C. Some softening will occur after a 1 CrMoV rotor is in service at 538°C for 100,000 hr (Fig. 9) [13, 24]. At higher temperatures, up to 566°C, the 12 CrMoVCb rotor steel is used. The 100,000 rupture strength of this steel is 133 percent higher than that of 1 CrMoV at 538°C and 148 percent higher at 566°C (Fig. 10) [4]. At service temperatures of 593°C, it is generally conceded that the 12 CrMoVCb is marginal, and steam cooling must be used to keep the rotor within its strength capabilities. At still higher temperatures, austenitic steels such as A316, Discaloy, or A286 will have to be used. The main problem with austenitic steel forgings is the manufacturing capability to produce austenitic forgings large enough to satisfy the design size requirements with satisfactory mechanical properties. Alloy segregation that occurs during solidification of large austenitic steel ingots severely limits forgeability. However, reasonable success has been achieved with special practices such as electroslag remelting (ESR).

5.3. Low-Cycle Fatigue. In order to obtain higher reliability for cyclic duty turbine, once again, higher center quality of forgings must be assured so that the risk or crack initiation and propagation by low-cycle fatigue can be ensured. Research efforts described in Section 5.1 are major steps in the right direction. In addition, further optimizations of microstructure may result in additional improvements in LCF resistance. Current CrMoV rotors are heat treated to produce an upper bainitic microstructure which has excellent creep resistance but very poor ductility and toughness. It has been suggested by many turbine manufacturers that the microstructure that gives the best creep properties may not necessarily be desirable from an LCF point of view. For cycling service, the rotors may have to be optimized with

respect to LCF rather than creep. Further studies are needed to evaluate the effect of microstructure on creep and LCF behavior of CrMoV steels so that the best tradeoff can be made for cyclic duty.

5.4. LP Rotors. The most important issues with respect to LP rotors are toughness, LCF resistance, and corrosion fatigue. In the area of toughness, the technology for producing rotors with excellent toughness already exists. The high center qualities achievable and the high ductilities have also resulted in the desired low-cycle fatigue properties. Methods for further improving the LCF resistance for cycling rotors is not clear. Avoidance of circumferential corrosion fatigue needs to be addressed. The effects of corrosives and stress concentration factors on the initiation of pitting may be a fruitful area of research. Methods of reducing the susceptibility to pitting, such as surface modifications, coatings, and steam purity control will also have to be addressed.

References

1 Viswanathan, R., and Jaffee, R. I., "Toughness of CrMoV Steels for Steam Turbine Rotors," ASME *Journal of Engineering Materials and Technology*, Vol. 105, Oct. 1983, p. 286.

2 Bush, S. H., "Failures in Large Steam Turbine Rotors," in: *Rotor Forgings for Turbines and Generators*, ed. R. I. Jaffee, EPRI Report WS 79-235, 1979, p. 1.1.

3 Timo, D. P., Curran, R. M., and Plazek, R. J., "The Development and Evaluation of Improved Rotor Forgings for Modern Large Steam Turbines," Ibid., p. 3-115.

4 Curran, R. M., Newhouse, D. L., and Newman, J. C., "The Development of Improved Rotor Forgings for Modern Large Steam Turbines," ASME Paper No. 82-JPGC-Pwr-25, Joint Power Generation Conference, Denver, 1982.

5 Takhar, J. S., et al., "Run/Retire Decision on a 25 Year Old LP Turbine Rotor," American Power Conference, Apr. 1979.

6 Ammirato, F. V., and Gelhaus, F., "Electric Power Research Institute Developments in Turbine Rotor Inspection and Evaluation," Joint Power Generator Conference, ASME, Toronto, Oct. 1984.

7 Leis, B. N., et al., "Fatigue and Fracture Analysis of Two Turbine Shafts," ASME Paper No. 81-PVP-27, Joint Conference of the Pressure Vessels and Piping Materials Nuclear Engineering and Solar Divisions of the ASME, 1981.

8 Buchait, R. D., Viswanathan, R., and Jackson, C. M., "Fatigue Cracking of Steam Turbine Shafts," in: *FATIGUE 84*, Birmingham, UK, Sept. 1984.

9 Bucheit, R. D., and Jackson, C. M., "Metallurgical Investigation of a Cracked Low Pressure Steam Turbine Shaft From an Electric Utility," EPRI Report CS2984, RP700-4, Mar. 1984.

10 Gaitonde, R., Commonwealth Edison Co., Maywood, Illinois, G0153, personal communication, Sept. 1983.

11 Saha, S. K., General Public Utilities, Reading, PA 19603, personal communication, June 1983.

12 Richman, R. H., et al., "Creep and Creep Fatigue Damage in Steam Turbine Rotors and Casings," Results of a utility survey conducted in 1982 for EPRI, to be published.

13 Hirota, Y., et al., "Changes of Material Properties and Life Management of Steam Turbine Components Under Long Term Service," *Mitsubishi Heavy Industries Technical Review*, Vol. 19, No. 3, 1982.

14 Tiffany, C. F., and Masters, J. J., "Applied Fracture Mechanics," ASTM STP 381, 1964, p. 249.

15 Greenberg, H. D., Wessel, E. T., Clark, W. G., Jr., and Doyle, W. H., "Critical Flaw Sizes for Brittle Fracture of Large Turbine Generator Rotor Forgings," International Forge Masters Conference, Terni, Italy, 1970.

16 Cook, T. S., Pennick, H. G., and Wells, C. H., "Life Time Prediction Analysis System in Steam Turbine Rotor Reliability," EPRI Report NP923, Nov. 1978.

17 McMahon, C. J., et al., "Temper Embrittlement of CrMoV and NiCrMoV Rotor Steels," EPRI Final Report No. RP559, 1983.

18 Viswanathan, R., and Beck, C. G., "Effect of Aluminum on the Stress Rupture Properties of CrMoV Steels," *Met. Trans. A*, Vol. 6A, Nov. 1975, p. 1997.

19 Curzon, A. M., and Wells, G. H., "Developing of a Crack Growth Algorithm for Time-Dependent Analysis of Steam Turbine Rotors."

20 Steiner, J. E., Swaminathan, V. P., and Jaffee, R. I., "Evaluation of Advanced Melting Technology for Large High Temperature Steam Turbine Rotor Forgings," *Proc. of the Forge Masters Conference*, Dusseldorf, 1980.

21 Jaffee, R. I., Unpublished work, EPRI, Palo Alto, 1982.

22 Finkler, H., and Potthast, E., "Heat Treatment of 1% Cr-Mo-V Steel With Special Regard to the Effects of Quenching Rates on the Properties," in: *Rotor Forgings for Turbines and Generators*, ed. R. I. Jaffee, EPRI Report W.S. 79-235, 1979.

23 Sawada, S., Ohnishi, T., and Kawaguchi, S., "Development of an Integral HILP Combination Rotor Forging," Ibid.

24 Werner, F. E., Eichelberger, T. W., and Hahn, E. K., "The Effect of Austenitizing, Tempering and Microstructure on the Properties of a Cr-Mo-V Steel," *Trans. ASME*, Vol. 52, 1960, p. 376.

Performance and Flowrate Control of the Kinetic Extruder Coal Powder Pump

J. W. Meyer

J. H. Bonin

Applied Mechanics Laboratory,
Lockheed Palo Alto
Research Laboratory,
Palo Atlo, CA 94304

The kinetic extruder is a novel centrifugal machine for feeding powdered material, in particular coal, against gas back pressure. The nonmechanical method of flow-rate control in the machine is described. Performance data obtained in tests of the kinetic extruder are presented and compared with theoretical predictions. It is found that a one-dimensional model of the material flow through the device gives accurate predictions of most aspects of the machine's performance. However, some details of the limiting behavior evidently require a more refined analysis.

1 Introduction

Over the past several years a novel centrifugal pump-type machine has been developed for pumping dry powdered materials. This U.S. Department of Energy (DOE) sponsored development was aimed toward improving means for introducing pulverized coal into the high-pressure gas environments characteristic of coal gasification reactors. The machine, termed a kinetic extruder, behaves functionally as a compressor or pump since coal powder is drawn from an atmospheric hopper, fed through the pump rotor, and delivered at a high gaseous pressure existing inside the rotor housing. However, in terms of its basic physics the kinetic extruder is not a true pump in that it does not of itself generate any pressure, it merely injects the powder into the pressurized environment. Development and testing of early models of the unit have been documented in a number of previous papers and reports [1-6]. The purpose of the present paper is to report on the performance of the latest version of the kinetic extruder, Model #6. This machine was equipped with an interesting system for throttling the rate of coal flow through the rotor. It performed well, and considerably more test data and running hours were obtained with this latest model, than with all previous models combined. This paper describes the basic operation and performance characteristics of the machine. Various test data obtained are compared with theoretical predictions made based on the current view of the physics of the material flow through the device.

The classical, and heretofore only commercially available, hardware for injecting coal into high pressure is a batch "lockhopper" system. This typically consists of an atmospheric supply hopper, a pressure cycling lockhopper, and a pressurized receiver hopper, the three vessels being stacked vertically and equipped with large connecting valves. The middle lockhopper is cyclically filled with coal, pressurized, emptied into the receiver hopper, and then depressurized. Lockhopper systems have been criticized on the grounds of large size as well as low efficiency and reliability. Alternate devices under development in recent years, mostly under DOE sponsorship, include the kinetic extruder and various types of volumetric pocket [7] or piston feeders [8, 9]. A comparison of the relative merits of these approaches would be of interest but is beyond the scope of this paper on the kinetic extruder. A general overview of different coal feed system types has been given by Gall [10].

A cross-section assembly drawing of the Model #6 kinetic extruder is given in Fig. 1. As shown, the device has as its main elements a rotor, a stationary feed pipe through which coal is fed to the eye of the rotor, and a loose fitting pressure housing enclosing the rotor. In operation, coal is continuously drawn into the rotor from a fluidized atmospheric hopper. The pressure in the rotor eye is kept slightly subatmospheric by venting it through a second passage in the feed pipe to a vacuum dust collector. As the pulverized coal enters the rotor, centrifugal forces cause it to flow into radial channels, termed sprues, and to form moderately compacted, moving, porous plugs of material in each of the sprues. These continuously renewing coal plugs form the pressure seal. The term sprue is here restricted to only the pressure sealing portion of the flow channel.

The rate of coal flow through the sprues is stabilized and controlled by structures, termed control nozzles, at the outboard end of each radial sprue. The control nozzle orifice forms the choke point in the material flow. Flow-rate throttlability is achieved by varying the gas pressure differential across the control nozzle orifice. This in turn is accomplished by introducing an independent gas flow into the inboard end of the nozzle structure. The control gas flow is brought into the rotor via a set of shaft seals and thence goes through a system of passages which connect to each nozzle. A conventional controller and control valve throttles the gas supply flow, thereby controlling the nozzle pressure differential. This method of varying the coal flow is covered in detail in Section 3.

The coal is discharged from the rotor into the pressurized

Contributed by the Power Division for publication in the JOURNAL OF ENGINEERING FOR GAS TURBINES AND POWER. Manuscript received by the Power Division April 1984.

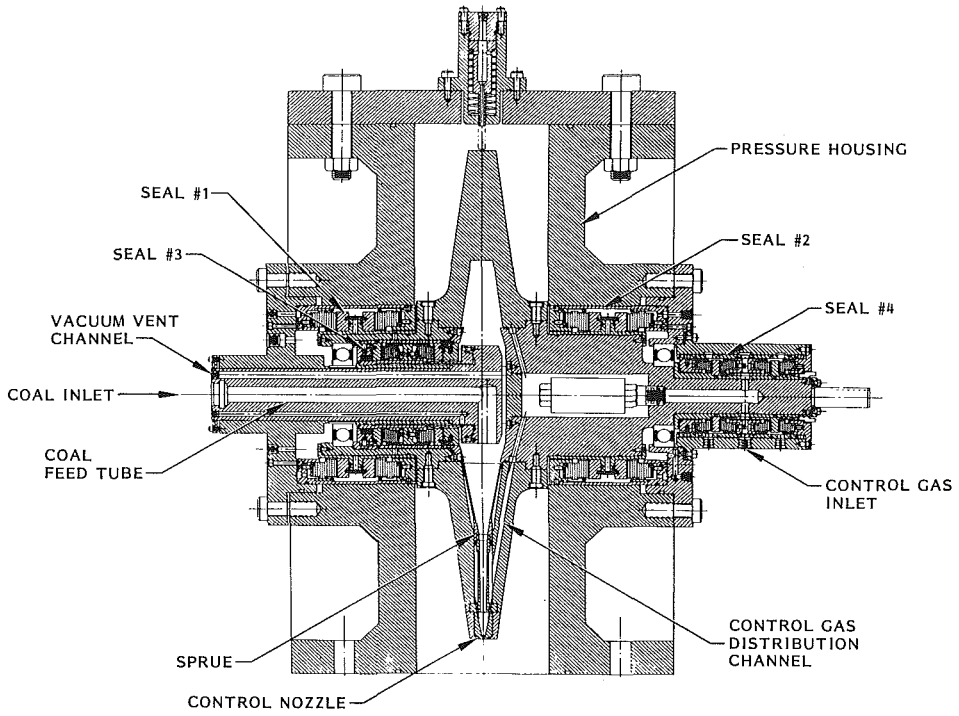

Fig. 1 Model #6 kinetic extruder pulverized coal pumping machine

housing in the form of rapidly dispersing particle jets. The jet penetration into the high-pressure gas slipstream at the rotor rim is very limited, and the coal velocity is almost instantly equilibrated with a strong gas vortex which is set up inside the housing. The dispersed particles tend to concentrate near the periphery of the housing due to the cyclone action of the vortex. The particle phase in suspension inside most of the casing remains extremely dilute. Sampling near the perimeter of the rotor has indicated coal densities of less than 3 kg/m^3. From the casing, a number of schemes are available for transferring the coal pneumatically to a gasification reactor or a pressurized surge hopper. In the present tests, the coal was discharged through a large port directly into a pressurized receiver, which was attached immediately below the kinetic extruder housing.

The main objective of the program of testing with the Model #6 machine was demonstration of durability. Toward this end, the machine was run for a total of 265 hr pumping coal. Due to test loop limitations, primarily those of a limited gas supply, the test time was noncontinuous and for the most part at a relatively low pressure (6 bar). However, intermittently the kinetic extruder was run throughout its range of operation to verify performance and to determine if any operational changes occurred during the test program. The data obtained during these more limited tests are analyzed in the present paper. Wear rate data and other aspects of the durability testing are covered in [11]. Generally, the range of operation of the machine was up to 28.6 bar (400 psig) and a flow-rate range of 0.6 to 2.0 tons/hr (metric).

2 Sprue Material Flow

The flow of material through the kinetic extruder sprues is a

Nomenclature

a = sprue cross-sectional area, m^2
A = constant in equation (10), kg/s
B = constant in equation (10), bar^{-1}
d = particle diameter, m
D = channel diameter, m
g = gravitational acceleration, m/s^2
j = constant in equation (6)
J,J' = rate parameters in gravity flow equations
k = coal bed permeability, cm^2
L = sprue length, m
$\dot{m}_c$ = coal flow rate, kg/s
N = number of channels in rotor
P = gas pressure, bar
ΔP_N = nozzle pressure differential, bar
ΔP_c = control gas pressure differential at injection point, bar
Q_s = gas flow rate through sprue, g/s
Q_v = vacuum system gas flow rate, g/s
Q_b = seal #3 purge flow rate, g/s
Q_3 = seal #3 leakage flow rate, g/s
Q_c = flow of transport gas entering rotor, g/s
Q_g = control gas flow rate, g/s
Q_n = permeation flow through nozzle coal, g/s
r = radial distance from axis of rotor, m
u = coal velocity through sprue, m/s
v = gas superficial velocity through sprue, m/s
ϵ = coal bed porosity or void fraction
ρ = gas density, kg/m^3
ρ_c = coal bed density, kg/m^3
ρ_c^o = reference coal bed density (800 kg/m^3)
σ = sprue coal bed radial compression stress
τ = sprue coal bed wall shear stress
μ = gas viscosity
ω = rotor speed, s^{-1}

Subscripts

o = nozzle orifice
1 = sprue inlet
2 = sprue outlet
N = nozzle inlet or sprue outlet
H = rotor housing

Superscript

o = standard state conditions

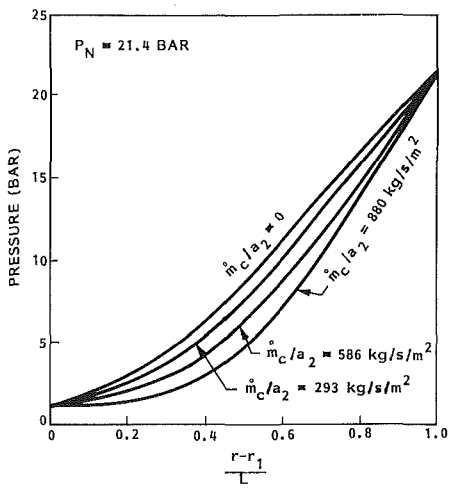

Fig. 2 Calculated gas pressure distributions within coal plug porosity as a function of coal mass flux; sprue outlet pressure 21.4 bar

low-velocity (order of 1 m/s) packed bed type of flow. Basic aspects of the mechanics of the sprue flow have been discussed by Meyer [2] and will only be briefly reviewed here. Under the condition that the radial velocity is low, so that radial and coriolis acceleration terms are negligible, the basic force balance equation for a disk element of material across the sprue cross section may be written as follows:

$$\rho_c r\omega^2 - \frac{dP}{dr} = \frac{d\sigma}{dr} + \frac{4\tau}{D} \tag{1}$$

where P is the gas pore pressure within the material plug interstices, D is the channel diameter, σ is the solid normal stress in the radial direction averaged across the cross section, and τ is the frictional wall shear stress on the material.

In [2] it is argued that at least in the narrow and relatively straight sections of the kinetic extruder sprues, the normal stress term σ, and consequently its derivative, remains small relative to the other terms in equation 1. This is due to the well-known Jannsen asymptotic limit to normal stresses in granular material columns. This lack of buildup of really high values of solid compaction stresses is significant to the operation of the machine since it results in the material bed properties (e.g., bulk density, porosity, and permeability) remaining relatively constant throughout the sprue.

In predicting performance of the kinetic extruder a simple view is taken in that the right-hand side of equation (1), containing the solid stress terms, is left undetermined. It is assumed that if the left-hand side remains positive, so that the material remains stressed to some degree, the sprue flow will be stable. It may be noted that since the solid compaction stresses are subject to the Jannsen limit and do not build up to high values, it might be expected that conditions where the pore pressure term exceeded the centrifugal force term locally, over just a short length of sprue, would cause bed expansion and abrupt loss of sealing integrity of the material plug. As discussed in Section 8, the actual limiting behavior observed is somewhat different.

Since the details of the solid stress state are left unaddressed, the only significant computational problem is the determination of the gas pressure gradient distribution in the sprue. The gas flow solution has also been covered in [2] and will only be summarized here, and typical calculation results given. The basic equations solved are those representing porous media permeation flow of a compressible gas through the moving plug of sprue material. Specifically, the governing equations are the Darcy permeation equation

$$v - \epsilon u = \frac{k}{\mu}\frac{dP}{dr} \tag{2}$$

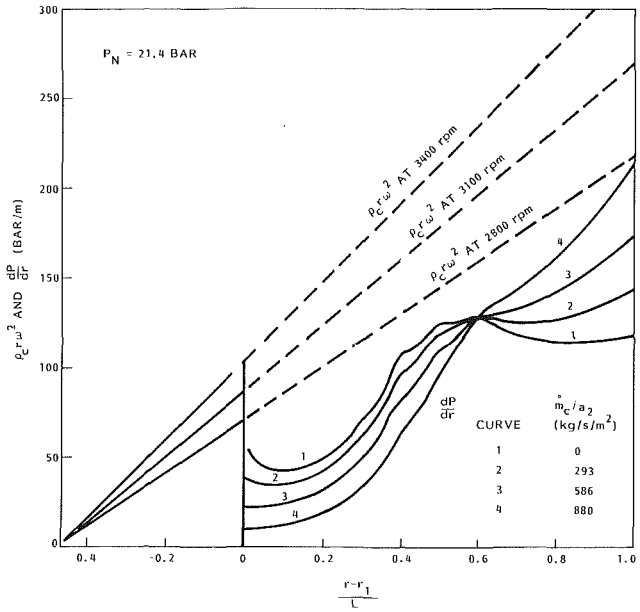

Fig. 3 Gas pressure gradient distributions (solid lines) as function of coal mass flux compared with centrifugal force distributions

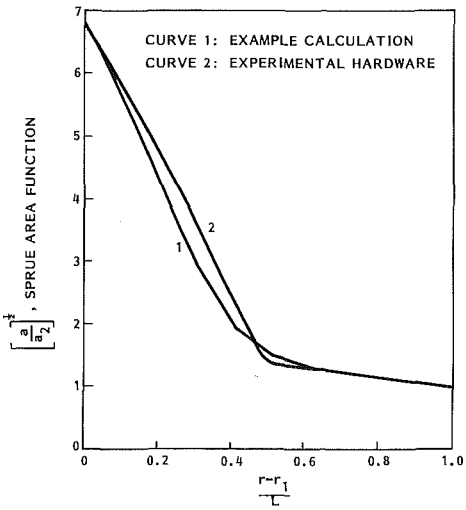

Fig. 4 Sprue cross-sectional area ratio as a function of position

the gas and coal continuity equations,

$$\rho v a = Q_s = \text{const} \tag{3}$$

$$\rho_c u a = \dot{m}_c = \text{const} \tag{4}$$

and a gas equation of state (isothermal)

$$\frac{P}{\rho} = \text{const} \tag{5}$$

with the pressure boundary conditions of $P = P$(eye) at the sprue inlet and $P = P$ (nozzle) at the sprue outlet.

The major approximations made in formulating and solving these equations are those of one dimensionality, that is uniform velocity of both solid and gas phases across the sprue cross section, and use of uniform bed properties (ρ_c, ϵ, and k). The validity of these assumptions must be tested by comparing theoretical predictions with the performance of the kinetic extruder. Details of the numerical method of solution of the equation system are given in [2].

Generally, the theoretical predictions show that the gas pressure and pressure gradient distributions in a given sprue depend mainly on the variables of P(outlet), coal velocity or mass flux, and the bed property of permeability. Figures 2 and 3 show pressure and pressure gradient distributions for a

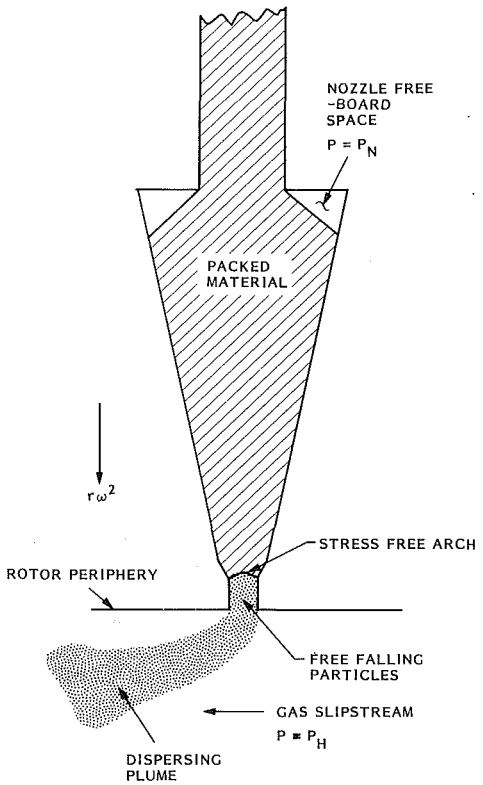

Fig. 5 Control nozzle structure and solid flow pattern

sprue shape and operating conditions similar to those used in tests of kinetic extruder #6. The precise area profile used in the calculations is given as curve #1 in Fig. 4 and the sprue length was 0.22 m. As shown in Figs. 2 and 3, the pressure and pressure gradient distributions vary with coal mass flux through the sprue (outlet mass flux is the distinguishing parameter between the plotted curves). Figure 3 also includes the centrifugal force term $\rho_c r\omega^2$ for three differing rotor speeds as a comparison. As shown, the centrifugal force term exceeds the pressure gradient term at all conditions of speed and flow rate considered in this example.

The rate of gas flow through the sprue is also computed in the theoretical calculation. Representative results are given in [2], and also in Section 6 of this paper, where theory and experimental measurements are compared. Calculations generally show that the gas flow through the sprue may be in either direction depending on operating conditions in relation to bed permeability. If the pressure difference across the sprue is low, or the rate of coal flow is high, then the gas flow direction is radially outward; some gas originally in the coal interstices at the sprue inlet is then carried through with the coal into the higher pressure region. If the pressure is high and/or the coal velocity low, then gas leaks upstream faster than the coal moves and a net flow of gas into the eye region takes place. At one particular condition the gas flow in the sprue is exactly zero. The gas originally in the coal is then, in effect, precisely displaced by gas permeating upstream from the high-pressure end of the sprue.

3 Control Nozzle Material Flow

The control nozzle is an approximately conical structure which is placed at the distal end of each sprue. Its function is both to provide distal support to, and thereby stabilize, the moving plug of material in the sprue channel, and also to constitute the coal flow-rate controlling element in the machine as a whole. Figure 5 illustrates the flow pattern and functioning of the control nozzle element. This shows a to-scale sketch of the control nozzle profile and sprue outlet geometry used in the present machine. The moving packed material within the sprue and nozzle is denoted by the shaded area. The control nozzle outlet at the rotor periphery is the narrowest point in the flow channel and acts as the choke point for the material flow. The gas pressure P_N in the freeboard space above the nozzle solids is connected to the "control gas supply" via rotor passages (not shown), and is controllable to a set differential relative to the gas pressure downstream of the nozzle P_H, which is the rotor housing pressure. This gas pressure differential $P_N - P_H$, in combination with the centrifugal force, serves to control the rate of coal flow through the nozzle orifice.

The rate of coal flow through the nozzle can be represented by expressions which are similar to those representing gravity flow of particulate materials through bin and hopper apertures. In contrast to the behavior of liquids, the mass rate of particulate flow through orifices is independent of head (at least for heads greater than a few orifice diameters). Experimentally and by dimensional analysis it can be shown that the rate of gravity flow through circular orifices is given by [12, 13]

$$\dot{m}_c = J\frac{\pi}{4}\rho_c(D_o - jd)^{5/2}g^{1/2} \tag{6}$$

where $\dot{m}_c$ is the mass flow rate, J is a fixed parameter depending on the geometry and, perhaps, the material friction or wall roughness, ρ_c is the bulk density, g is the gravitational acceleration, D_0 is the orifice diameter, d is the particle diameter, and j is an empirical constant of order one.

Accurate theoretical prediction of the critical parameter J has so far eluded investigators. The rate of flow is mainly determined by phenomena in the immediate vicinity of a stress-free arch which is said to form immediately over the orifice (see Fig. 5). The arch represents a boundary between a stressed, packed flow mode and particle free fall. A number of theories have been advanced to analyze this flow and quantitatively predict J, but all seem to be lacking in one regard or another [12]. However, this is of little practical concern here since J can be treated as an empirical constant, which can be rather easily determined by experiment in a given case.

Extension of the above equation to account for both the higher than earth surface g forces, and the gas pressure forces due to the nozzle pressure differential, is quite simple. It may be assumed that the gas pressure gradient per unit mass in the vicinity of the stress-free arch acts essentially as an effective addition to the g force. The equation that describes the control nozzle flow rate of coal may then be conveniently written as follow

$$\dot{m}_c = NJ'\frac{\rho_c}{\rho_c^o}(D_o - jd)^{5/2}\left[\frac{r\omega^2}{g} - \frac{1}{\rho_c g}\left(\frac{dP}{dr}\right)_o\right]^{1/2} \tag{7}$$

where N is the number of channels in the rotor, $r\omega^2$ is the centrifugal force, $(dP/dr)_o$ is the gas pore pressure gradient in the solids immediately above the nozzle outlet, and $J' = J(\pi/4)\rho_c^o g^{1/2}$.

The magnitude of the outlet pressure gradient may be calculated in a straightforward manner using the same computer code as is applied to the sprue flow. Such calculations would not be expected to yield very quantitatively accurate predictions of $(dP/dr)_o$ because the basic model assumptions of one dimensionality and uniform properties are weak in the vicinity of the nozzle orifice. However, calculations do give two key results which are of some importance. First, they show that the nozzle pressure gradient is highly peaked at the outlet end, with most of the total pressure drop taking place within just a few orifice diameters from the orifice. This means that large outlet pressure gradients, and hence large changes in coal flow rate, can be obtained with relatively small total nozzle pressure differentials. Second, the computations also show that under a wide range of con-

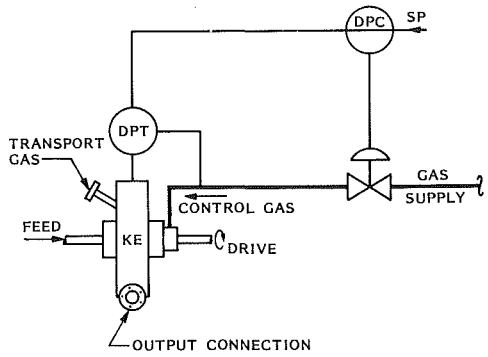

Fig. 6 Control gas pressure control schematic

ditions, the calculated outlet pressure gradient goes very nearly linearly with the pressure difference, $\Delta P_N = P_N - P_H$, imposed on the nozzle.

Making this linear approximation, which serves to define the pressure gradient constant B

$$-\frac{1}{\rho_c g}\left(\frac{dP}{dr}\right)_o = B\Delta P_N$$

and with

$$A = NJ'(D_o - jd)^{5/2} = \text{another constant}$$

for a particular set of nozzle hardware and feed material, the flow rate equation representing the kinetic extruder may be written as

$$\dot{m}_c = A\frac{\rho_c}{\rho_c^o}\left(\frac{r\omega^2}{g} + B\Delta P_N\right)^{1/2} \tag{8}$$

The constant B is then viewed as an empirical constant which is to be determined in calibration tests of the kinetic extruder. The other constant A is also empirical but, as discussed below, it can be determined by independent means.

One additional complication is the fact that the true nozzle pressure differential ΔP_N exceeds that at the point of injection of the control gas into the machine ΔP_c, due to a centrifugal head imposed by the column of control gas within the passages in the rotor. This augmentation of the control pressure is easily calculated as follows

$$\Delta P_N = \Delta P_c + \rho^o \frac{P_N}{P^o}\frac{r^2\omega^2}{2} \tag{9}$$

The magnitude of the centrifugal increment in ΔP_N can be up to several bar, depending on rotor speed and housing pressure. The final form of the flow-rate control equation for the kinetic extruder is thus given by

$$\dot{m}_c = A\frac{\rho_c}{\rho_c^o}\left[\frac{r\omega^2}{g} + B\left\{\Delta P_c + \rho^o\frac{(P_H + \Delta P_c)}{2P^o}r^2\omega^2\right\}\right]^{1/2} \tag{10}$$

This equation can be used to map out the flow-rate performance curves of the kinetic extruder as a function of speed, control pressure ΔP_c, and housing pressure P_H.

The parameter A can be determined independently by the simple expedient of bench calibration of the nozzles using a free flowing sand. All 12 nozzles were tested in this fashion by timing their passage of 100 g of -50 mesh $\times$ $+100$ mesh, 1300 kg/m^3, bulk density calibration sand. This test has been found to give very reproducible results and was used to check for nozzle wear at the end of the test program. The 12 nozzles' average flow rate was 0.393 g/s in the bench sand calibration. The maximum excursion from the average value for an individual nozzle was 9 percent. Repetitions of the calibration tests after 220 hr of coal flow test time duplicated the original calibrations to ± 2 percent for individual nozzles, and to the third significant figure for the average of the 12 nozzles. Based on these bench tests, the equation (10) constant $A = 0.00290$ kg/s. Applying this value to the kinetic extruder flow assumes the value of the jd term is similar for both the test sand and the coal feedstock.

In the test equipment, a conventional process controller system was used to control the differential pressure of the control gas stream at its injection point at the shaft of the machine. A system of this type is shown schematically in Fig. 6. The main control elements were a Foxboro Model 11DM differential pressure transmitter, a Foxboro Model 43AB controller, a throttling valve, and a remote loading and display station. The ΔP_c range that could be set was -2.75 bar to $+2.75$ bar ($\pm$ 40 psid). The ΔP_c control setpoint was manually input, as such, and was not tied to any additional mass flow control elements.

4 Experimental Hardware and Instrumentation

A description of the kinetic extruder Model 6 is covered in detail in [11], which contains a full set of engineering drawings of the machine. Only a few relevant attributes of the machine will be touched on here. The rotor was 0.71 m in diameter and contained 12 sprues and control nozzles. The sprues were approximately 5 $\times$ 5 cm in square cross section at their inlets and tapered to an 8.2 mm circular diameter at their outlets. The sprues had a length of 0.22 m and an area profile according to curve 2 in Fig. 4. The inlets were positioned at 0.10 m from the rotational axis where their square shapes nestled together, minimizing locations where stagnant zones of coal could accumulate. The control nozzles were 36 mm long, terminating in a 2.2-mm orifice. The rotor could be driven at speeds up to 3600 rpm by a diesel engine prime mover with a hydraulic pump/motor power transmission unit. Speeds were manually adjusted from the control room by means of a remote actuator on the hydraulic motor displacement control. Speeds could easily be stabilized within a few rpm during test runs.

Critical components of the kinetic extruder were the four rotating seals denoted by numbers 1–4. Seals #1 and #2 were the main shaft seals, seal #3 sealed between the rotor and the stationary feed pipe which delivered coal into the rotor eye, and seal #4 was a pair of seals which allowed injection of the control gas into the shaft. All of the seals were Crane Type 28 nitrogen-buffered double seals. These seals are similar in appearance to conventional face type double seals, except that high-pressure gas rather than seal oil is used as the pressurizing buffer fluid supplied between each set of seals. In the present case, nitrogen buffer gas at a pressure of 33.8 bar (475 psig) was fed to all the seals from a regulated supply. The flow of seal gas varied slightly with speed and temperature but normally was approximately 4 g/s (7 scfm) for all four seals in aggregate. This represents the leakage through a total of ten rotating seal faces. The split in the leakage flow between that into the process and that outboard would be roughly even. The sealing faces float slightly out of contact so that frictional torque is negligible.

The test loop and instrumentation is also well documented in [11]. Only those instruments directly used in obtaining the present experimental data will be listed here. The test loop may be briefly described as consisting of two 50-cu-ft hoppers, one serving as an atmospheric, gas-fluidized, feed hopper, and the other being the pressurized receiver. The pressurizing gas, as well as all other test loop gas flows, was nitrogen. Coal was delivered to the suction side of the kinetic extruder via a 3/4-in. pipe from the feed hopper. The kinetic extruder housing was mounted directly above the receiving hopper and discharged the coal fed through the rotor directly into the receiver. While the receiver and kinetic extruder housing were pressurized, coal could be recycled back from the receiver to the feed hopper through a 3/4-in. transfer pipe. During tests, the kinetic extruder was run continuously, transferring coal from the feed hopper into the pressurized receiver hopper. Periodically, as the receiver became full, the recycle pipe valve was opened and the coal allowed to flow

back to the feed hopper. The feed hopper was mounted on three BLH Model U3L1 load cells with Weston digital displays. Load cell readings were summed to determine hopper weight and the coal flow rate was established from weight versus time plots. The test coal was nominally 45 percent passing 200 mesh grind of a Utah Bituminous coal. It was scalped with an 18 mesh screen on loading it into the test loop to remove any oversize material which could clog the control nozzle orifices. Shaft torque and speed were monitored with a Lebow Model 1605 torque meter with a speed pickup, and Datronic Model 3240 and 3278 signal conditioner-indicators. Receiver hopper pressure was controlled by a Fisher Model 4150 controller and instrumented with redundant 600 psig Marsh 1 percent gages. Control nozzle pressure differential was measured by a Foxboro Model E11DM transmitter and also by a redundant Dwyer gage. Rotor eye pressure was monitored by a Foxboro Model E11AH transmitter and also by two compound gages. A Cox Model GL8-4 turbine meter, which was specially calibrated for 500 psig nitrogen, was used for the control gas flow-rate measurement. Seal buffer gas flows were measured with 3 Brooks Model 3602 high-pressure purge meters. The seal #3 eye side purge flow was periodically verified by diverting the flow through a Dwyer Model RMB-56 rotameter at atmospheric pressure. Gas/coal temperature in the receiver was monitored with a Fluke 2170A digital thermometer. The rotor eye vent system flow was measured by a 5/8-in. metering orifice in a vertically downward section of the 1-in. Sch 40 suction pipe. The orifice pressure instrument was Dwyer Capsuhelic differential gage.

Special instrumentation was a device termed the sprue flow detector. This was a PCB Model 121A02 piezoelectric pressure transducer which was in a fixed mounting inside the kinetic extruder housing, close to the nozzle outlets in the periphery of the rotor. The coal jets issuing from each nozzle struck the detector in sequence, producing a signal which was monitored on an oscilloscope that was phase referenced to the rotor shaft speed. A normal display was a 12-pulse wave train on the scope, each pulse corresponding to the flow from a particular control nozzle. The transducer head was protected from erosion by a cap and wear rod of hard material.

Estimated accuracy of the experimental data is as follows: coal flow rate ±5 percent, housing pressure ±2 percent, control gas pressure ±0.1 bar, control gas flow rate ±10 percent, rotor speed ±1 percent.

5 Sprue Gas Flow Data

Under many, though not all, operating conditions of the kinetic extruder at elevated pressures, the gas flow direction inside the sprue is radially inward, with a measurable amount of net leakage of control nozzle gas through the plug of coal in the sprue into the eye of the rotor. In the present tests of the machine, the sprue gas flow was determined by means of a gas material balance on the eye region of the rotor. Comparison of this leakage flow rate with theoretical predictions provides the only really direct evidence that the material flow in the sprue is in accordance with the present view of it.

Experimentally, the sprue gas flow was determined from the following material balance

$$-Q_s = Q_v - Q_b - Q_3 - Q_c \tag{11}$$

where

- Q_s = gas flow rate in sprue (positive outward)
- Q_v = measured gas flow rate in vacuum system suction pipe; this was the primary experimental measurement
- Q_b = a seal area purge flow which entered the rotor eye
- Q_3 = seal #3 leakage flow
- Q_c = gas entering eye with the coal feed

Table 1 Sprue gas flow data

Run ID	$\dot{m}_c$ (kg/s)	P_N (bar)	$-Q_s$ (g/s)	k(sample) (10^{-9} cm^2)
462	0.33	23.2	1.7	3.4
462	0.41	23.4	1.2	3.4
462	0.39	7.9	-0.5	3.4
483	0.54	17.0	-0.2	4.0
483	0.19	13.1	0.8	4.0
483	0.19	13.1	0.5	4.0
483	0.57	22.8	0.3	4.0
483	0.22	22.1	1.8	4.0
483	0.32	23.0	2.2	4.0
490	0.40	7.6	-0.2	4.0
490	0.37	26.6	1.4	4.0
490	0.32	29.7	1.8	4.0
490	0.32	29.7	3.3	4.0
491	0.28	29.3	3.4	3.5
491	0.40	30.8	2.3	3.5
495	0.23	15.2	0.5	3.9
496	0.35	16.5	-0.1	2.9
496	0.28	15.8	-0.3	2.9
500	0.40	27.2	0.9	2.7
500	0.50	27.7	0.3	2.7
501	0.32	26.8	1.2	2.9
505	0.34	26.6	1.3	2.6
505	0.39	25.8	1.0	2.6

The Q_v measurement was difficult to obtain reliably because a minor amount of extremely fine coal dust was contained in the suction gas flow, and this dust plugged the metering orifice taps in a short time, if they were left connected. This problem was countered by leaving the taps disconnected from the pressure instrument, allowing an inward air bleed, and only connecting them briefly when an actual reading was taken. This reduced the amount of data that could be gathered conveniently, but gave confidence in what was obtained.

The seal purge Q_b was a relatively large term in the material balance. However, it could be accurately measured and was a constant quantity controlled by a needle valve in choked flow. A rate of purge flow of $Q_b = 3.4$ g/s was used throughout the experimental program. The remaining terms, Q_3 and Q_c, could not be measured directly but fortunately are small. The seal #3 leakage flow into the eye is estimated at $Q_3 = 0.34$ g/s based on 20 percent of the total measured flow into seals #1 and #3. This combined flow was all that was available because the buffer gas supplies for these two seals are internally common in the machine. The 20 percent figure represents a reasonable estimate based on the number (4) and sizes of the seal faces leaking. Finally, for the purposes of data reduction the Q_c term was estimated as 0.13 percent of coal flow, which makes it typically only slightly greater than Q_3. This quantity was arrived at from a coal density of 500 kg/m^3 in the feed pipe flow into the rotor eye. This is a fluid bed regime density representative of the coal in the fluidized feed hopper. In view of the several uncertainties, the probable accuracy of the reduced Q_s data is estimated to be no better than plus or minus 0.5 g/s.

Theoretical model predictions of the sprue gas flow Q_s show a first-order dependence on sprue outlet pressure, coal flow rate, and the permeability of the compacted coal plug within the sprue. The permeability of the feedstock was monitored by periodic sampling from the test loop and subjecting the sample to a standardized test. This test method is covered in more detail in [1, 2], but briefly it involves compacting a test tube sample of coal at a standard 1000g in a laboratory centrifuge, and then measuring the permeability of the compacted plug directly by a gas flow test. The same test yields a value for compacted bulk density. The compaction stress on the coal in the lab test is believed to be reasonably similar in magnitude to that on the coal plug in the kinetic extruder sprues.

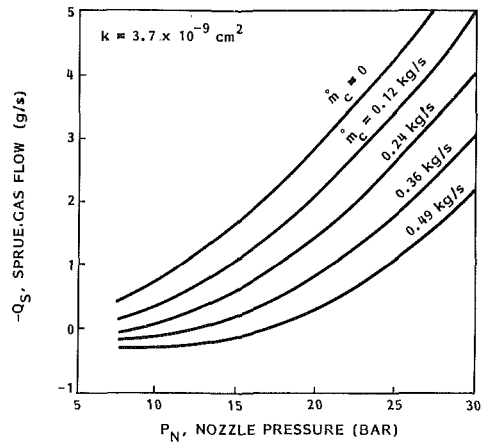

Fig. 7 Sprue gas flow as a function of nozzle pressure and coal flow rate; theoretical predictions for $k = 3.7 \times 10^{-9}$ cm^2

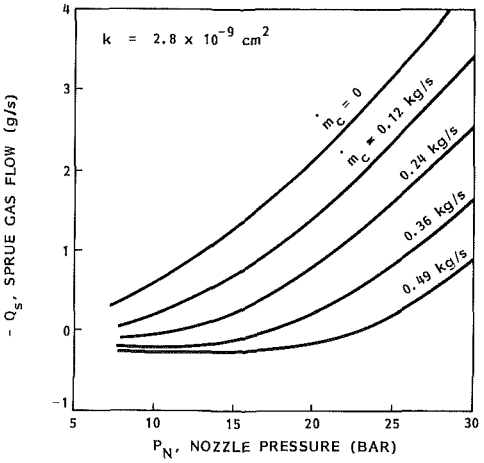

Fig. 8 Sprue gas flow as a function of nozzle pressure and coal flow rate; theoretical predictions for $k = 2.8 \times 10^{-9}$ cm^2

In the present test program, the coal inventory in the test loop was recycled through the kinetic extruder an average of approximately 30 times before removal and replacement with fresh material. This resulted in some gradual changes in material properties due to attrition and drying. Typically the fresh coal had a lab test permeability of approximately 7×10^{-9} cm^2 and this value decayed asymptotically to about 2.5×10^{-9} cm^2 with repeated passes around the test loop. Generally, the initial decay rate was fairly rapid, and the bulk of the performance data was taken when the test loop coal inventory was 4×10^{-9} cm^2, or lower, in permeability. Sample bulk density test results were always in the 775-825 kg/m^3 range. The coal true material density, and a porosity value of 37 percent at 800 kg/m^3 bulk density, were determined by an alcohol displacement technique. Test loop samples were taken frequently enough so that the coal properties during a particular performance test run are known with reasonable confidence.

As stated, theory indicates that sprue gas flow is a function of three key variables: nozzle pressure, coal flow rate, and permeability. The experimental sprue gas flow data are listed in Table 1. This shows Q_s, as calculated from equation (11), together with the corresponding values of pressure, coal flow rate, and the permeability determined from test samples. Theoretical predictions may be presented in the form of multiple sets of predicted Q_s versus P_N curves, with coal flow rate as a parameter, each full set of curves representing a single value of permeability. One set of theoretical Q_s curves, for a permeability value of $k = 3.7 \times 10^{-9}$ cm^2, is given in Fig. 7. A second set, for the lower value of $k = 2.8 \times 10^{-9}$ cm^2, is shown in Fig. 8. A void fraction of 37 percent and a bulk density of 800 kg/m^3 was taken for all the theoretical calculations.

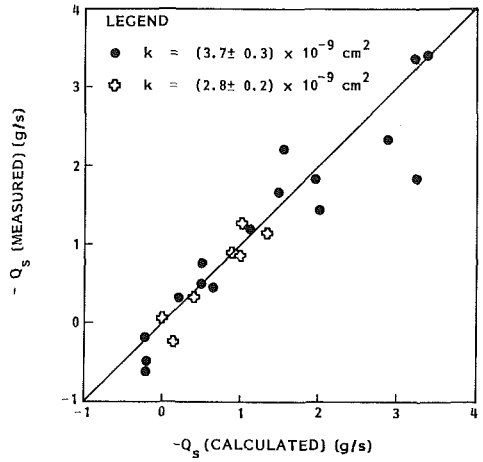

Fig. 9 Comparison of theoretical and experimental sprue gas flow data

Comparison of the Table 1 data with theoretical predictions, as determined from Figs. 7 and 8, shows agreement within the estimated probable error of the data. No systematic deviations can be identified. Figure 9 illustrates the comparison by plotting the measured data as a function of calculated values. As shown, most of the data fall quite close to the 45-deg line in the graph. It may be concluded from this favorable comparison that (1) the bench permeability tests yield values of k and bulk density that are representative of the state of the coal in the kinetic extruder sprues, and (2) the basic assumptions of the theory (i.e., one dimensionality and uniform properties) are reasonably accurate in their application to the permeation flow of gas through the moving coal plug.

6 Coal Flow Rate Performance Data

Experimental kinetic extruder coal flow-rate data are presented as a function of control gas differential pressure setting in Fig. 10. The three groups of data correspond to three combinations of housing pressure and rotor speed: 7.9 bar, 2700 rpm; 14.8 bar, 2850 rpm; and 24.5 bar, 3600 rpm, respectively. The range of experimental flowrates shown represents the minimum and maximum rates that could be stably achieved with the control pressure range available. The lower limit is characterized by the condition that the actual nozzle pressure differential ΔP_N becomes negative. Attempts to operate with $\Delta P_N < 0$ yielded unreliable behavior characterized by frequent interruptions in the flow from individual nozzles. The upper limit corresponds either to the maximum ΔP_c setting of the controls, or to a suction side limit caused by excessive pressure drop in the feed pipe.

The three curves also plotted in Fig. 10 are predicted performance curves for the above pressure-speed combinations, as calculated from equation (10). Values of the equation (10) A and B parameters that were used are $A = 0.00290$ kg/s, and $B = 7200$ bar^{-1}. This value of A is that obtained from the bench experiments with sand. The B value was determined by adjusting for a best fit to the Fig. 10 data. As shown, with this value of B, the agreement between the prediction from equation (10) and the data are quite good at all three combinations of speed and housing pressure.

7 Control Gas Flow Rate Data

The rate of flow of control gas was monitored and these

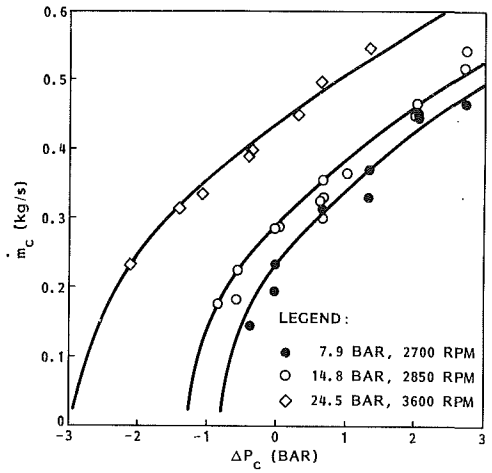

Fig. 10 Kinetic extruder coal flow rate as a function of control gas pressure differential; comparison of experimental data with predictions of equation 10

data may also be compared with predictions. The control gas flow requirement is mainly that needed to pressurize the interstitial porosity of the feed material up to the control nozzle pressure. As such, the volume rate of gas flow per unit coal flow through the nozzle should be a fixed quantity equal to ϵ_o/ρ_{co}, where ϵ_o and ρ_{co} are the void fraction and coal bulk density at the control nozzle outlet position. This picture must be slightly modified since some control gas may escape upstream through the sprue plug and also some may permeate through the nozzle coal. The nozzle gas material balance may be written as:

$$\frac{Q_g}{\rho_N \dot{m}_c} = \frac{\epsilon_o}{\rho_{co}} - \frac{Q_s}{\rho_N \dot{m}_c} + \frac{Q_N}{\rho_N \dot{m}_c} \tag{12}$$

If Q_s and Q_N are small, then the volume gas flow per unit coal flow would be constant, independent of operating pressure (neglecting minor temperature variations). Based on the observed range of Q_s data (see Table 1), the maximum Q_s contribution would have an effect of about 25 percent in the above equation. There is no information on the magnitude of Q_N.

Figure 11 shows the control gas flow data, in actual cubic meters at nozzle pressure per kg of coal feed, as a function of nozzle pressure. The data are divided into high (solid points) and low (open points) nozzle pressure differential groupings. These would also approximately correspond to higher and lower rates of coal throughput. As shown, the relative constancy of the control gas flow in these terms hold fairly well. Some scatter occurs, a portion of which can be attributed to differing amounts of gas leakage upstream through the sprues. The scatter band is perhaps a little wider than would be expected based on the sprue gas flow data. The lower rate at the lowest pressures is due to the lack of any sprue leakage, and also the fact that the shaft seal #4 leaks some seal gas into the control gas stream. This seal leakage is a fixed mass flow which becomes significant in terms of volume flow at low pressure. If it is assumed that the lower limit of the data scatter band, about 7.5×10^{-4} m^3/kg, represents the actual interstitial volumetric flow, this would correspond to a void fraction of 49 percent and a coal bulk density of 650 kg/m^3 at the nozzle outlet. This seems a reasonable value, considering the relatively high velocity and rate of area change in this location, in comparison to the sprue.

8 Limiting Behavior

Under conditions where the rotor speed is insufficient for the gas pressure against which the kinetic extruder is pumping, operation becomes unstable. If the speed is so low that

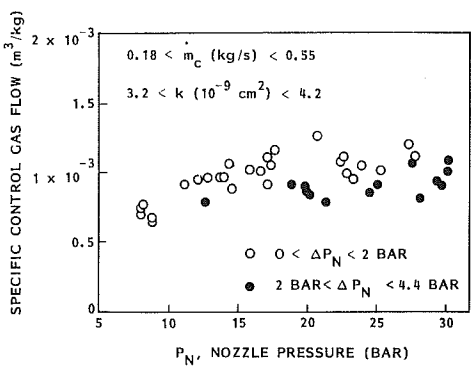

Fig. 11 Control gas volumetric flow data (actual m^3 per kg of coal) as a function of control nozzle pressure

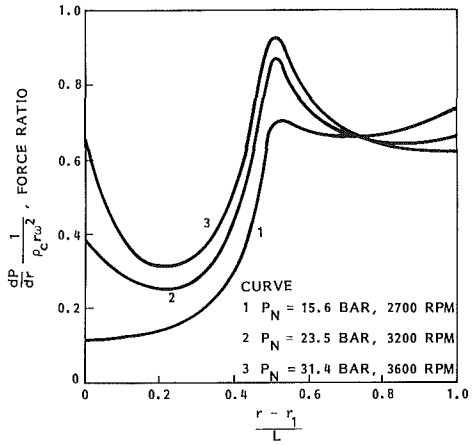

Fig. 12 Predicted ratio of sprue pressure gradient to centrifugal force at marginal speed conditions; coal flow rate 0.365 kg/s

the integrated pressure gradient exceeds the integrated effect of the centrifugal force, the plug of coal in the sprue is forced back toward the eye of the rotor, loses its sealing integrity, and a blowback of gas into the rotor eye would then occur. In practice, however, it is found such events do not take place because before such a low speed is reached, another type of flow instability takes place which is considerably less dramatic. The manifestation of this instability, which is here termed a nozzle flow upset, has been investigated by experimenting with the machine under marginal speed conditions.

Experimentally, such an upset is marked by a cessation of flow from one nozzle orifice, as indicated by the sprue flow detector signal, coupled with a drop in control nozzle pressure differential and a large increase in control gas flow as the ΔP_c controller attempts to compensate. No changes in rotor eye pressure are observed, indicating that the sealing properties of the plug of coal in the nonflowing sprue are maintained. The only conclusion that can be drawn is that the coal is somehow forming a stable arch near the end of the sprue, which stops the flow, allowing the control nozzle to drain free of coal. Control gas may then flow freely out the now empty nozzle, immediately leading to a loss of pressure differential in all the nozzles (which have a common supply) and the large increase in gas flow. Once such a condition occurs, the flow in the offending sprue will only restart if the housing pressure is reduced substantially, typically by at least 50 percent.

Based on a number of experiments, what may be termed marginal operating speeds were identified for three housing pressure levels. These marginal speeds are defined as those for which a nozzle flow upset typically occurred within the time period available for one test run at pressure, generally 10-20 min. The marginal speeds as a function of housing pressure level are given in Table 2.

Table 2 Marginal operating speeds

Housing pressure (bar)	Housing pressure (psig)	Avg. nozzle pressure (bar)	Experimental marginal speed (rpm)
14.8	200	15.6	2700
21.7	300	23.5	3200
28.6	400	31.4	3600

The nozzle flow upsets were, of course, a statistical event and critical speeds could not be established with great precision. However, it is felt that the Table 2 data give a consistant indication of the boundary between stable and unstable operation as observed in the tests, within an estimated accuracy of 100 rpm.

Predictions of the pressure gradient and centrifugal force distributions in the sprue coal plug for the above three marginal operating conditions have been made using the theoretical model. The most usual coal properties were assumed for the calculations ($k = 3.7 \times 10^{-9}$ cm^2, $\epsilon = 37$ percent, and $\rho_c = 800$ kg/m^3). Results of the theoretical computations are summarized in Fig. 12. This shows the predicted ratio of pressure gradient to centrifugal force plotted as a function of radial position along the sprue, for the three cases. A value of one or greater over a significant length of sprue would indicate definite instability. All three curves are for a flow rate which was midrange to the experimental conditions, $\dot{m}_c = 0.365$ kg/s.

As shown in Fig. 12, the predicted excess of centrifugal force over the pressure gradient is fairly consistent under the three marginal conditions. In the outboard half of the sprue, where most of the pressure drop takes place, the force ratios average about 0.7. This value can evidently be taken as defining the boundary of unstable operation for this sprue shape. It also may be noted that the first half of the sprue is rather lightly loaded. An improved sprue shape, which would give a better match between the pressure gradient and centrifugal force over the whole sprue, could improve overall performance.

To conclude, the precise mechanism by which a stable sprue outlet arch forms at marginal operating conditions, leading to the nozzle flow upset, is not known. It does not appear to be explainable in light of the simple, uniform properties analysis of the sprue flow. It is the authors' view that the cause is most likely a small random slug of coal with significantly differing properties, i.e., lower permeability, that forms the bridge. Analysis of this situation will have to wait for a more elaborate theory which takes into account the solid stress state and its coupling to the bed properties governing gas permeation flow. On the other hand, as a general predictor of minimum operating speeds the simple theory still appears quite useful, if tempered with prudent margins of safety.

9 Conclusions

It may be concluded from the present work that the kinetic extruder's status of development is now relatively mature in terms of the basic engineering understanding of the material flow behavior in the device. The theoretical calculations of the sprue gas flow are in good agreement with test data in terms of prediction of rates of leakage flow, and are in fair agreement in terms of predicting speed versus pressure limits of operation. A semi-empirical equation for the rate of flow through the kinetic extruder is very successful in predicting characteristic operating curves over the machine's range of performance. Average bed properties at the state of compaction within the sprue passages appear to be adequately determined by bench testing of material samples. However, the constant bed properties flow theory falls short of predicting the precise mode of limiting behavior in the sprue.

Acknowledgments

This research was supported by the U.S. Department of Energy under Contract No. DE-AC21-82MC19299. The technical project monitor was Mr. Dave Dubis. The authors also wish to acknowledge Mr. Joseph Sedy of John Crane-Houdaille, Inc., for his contribution to the kinetic extruder development.

10 References

1 "Coal Feeder Development Program," *DOE Report No. FE-1792-61*, Phase III Report, Lockheed, Sunnyvale, Sept. 1979.

2 Meyer, J. W., "A Channel Flow Analysis for Porous Beds Moving Under High G-Forces," *AICHE Journal*, Vol. 26, No. 3, May 1980, pp. 363-371.

3 Bonin, J. H., Daniel, A. D., and Meyer, J. W., "Instrumentation and Controls for the Kinetic Extruder—A Novel Pulverized Solids Feeder," *Instrumentation in the Mining and Metallurgy Industries*, Vol. 9, Instrument Society of America, 1982, pp. 159-178.

4 "Development of a Pilot-Scale Kinetic Extruder Feeder System and Test Program," *DOE Report No. DE8200954*, Phase I Report, Lockheed, Sunnyvale, Mar. 1982.

5 Meyer, J. W., Daniel, A. D., and Bonin, J. H., "Means and Apparatus for Throttling a Dry Pulverized Solid Material Pump," *U.S. Patent No. 4,362,441*, Dec. 7, 1982.

6 Meyer, J. W., Daniel, A. D., and Bonin, J. H., "The Kinetic Extruder, A Dry Pulverized Solid Material Pump," *U.S. Patent No. 4,376,608*, Mar. 15, 1983.

7 Flemming, J. R., et al., "Final Report: Development and Testing of a Linear Pocket Feeder for High Pressure Coal Feeding," Foster Miller Associates, Waltham, MA, prepared for U.S. Dept. of Energy, Mar. 1982.

8 "Final Report Phase II: Verification Tests, Conspray Dynamic Sleeve Piston Coal Feeder," Conspray Systems, Santa Ana, CA, *DOE Report No. DOE/MC/14603-1562*, Jan. 1984.

9 Mistry, D. K., "Quarterly Report, Coal Feeder Development," *DOE Report No. FE-14600-19*, Ingersoll-Rand Research, Princeton, N.J., Apr. 1982.

10 Gall, R. L., and Johnson, E. K., "An Overview of Coal-Feed Systems," *Chem Eng. Progress*, May 1983, pp. 31-36.

11 "Development of a Pilot-Scale Kinetic Extruder Feeder System and Test Program, Phase II—Verification Testing," *DOE Report No. FE-19299-14*, Lockheed, Sunnyvale, Jan. 1984.

12 Savage, S. B., and Sayed, M., "Gravity Flow of Cohesionless Granular Materials in Wedge-Shaped Hoopers," *Mechanics Applied to the Transport of Bulk Materials*, AMD, Vol. 31, ASME, 1979, pp. 1-24.

13 Zenz, F. A., and Othmar, D. F., *Fluidization and Fluid Particle Systems*, Reinhold, 1960, pp. 136-174.

Effect of Surface Configuration During Solid Particle Impingement Erosion[1]

P. V. Rao[2]

D. H. Buckley

NASA Lewis Research Center,
Cleveland, OH 44135

A study of the progression of erosion and its detrimental effects due to solid particle impingement requires a detailed understanding of the erosion process and morphology of real surfaces of ductile metals. A series of experiments was conducted to investigate the erosion characteristics of aluminum alloy surfaces during spherical glass bead and angular crushed glass particle impingement. The effects of particle shape on cylindrical surfaces and surfaces with pre-existing holes and slits were determined. An attempt was made to understand the relationship between erosion rate and pit morphology. Based on the experimental observations, an empirical relationship between erosion rate and volume loss is presented. This technique provides an improved prediction method for a wide spectrum of ductile materials.

Introduction

The detrimental effects of erosion during solid particle impingement have been encountered in several components varying from pneumatic transport to space programs. These include erosion of coal gasification machinery due to ash particles, abrasion erosion of pipelines and valves during pneumatic and slurry transport, loss of efficiency, performance loss of aircraft turbomachinery due to sand ingestion and erosion, and erosion and abrasion damage of rocket nozzles due to condensed metallic oxide particles.

There have been several parametric studies to investigate the effect of particle velocity, angle of impact, particle size and shape (angularity), particle charge, properties of materials and abrasives, etc. on erosive wear (e.g., [1, 2]). A majority of the laboratory scale equipment, such as sand blast apparatus, wear chambers, wear pumps and nozzles, tunnels, jet and rotating arm devices, have been used to examine flat specimens for such studies (e.g., [3, 4]). The information available on ductile material erosion thus far has not resulted in a universal erosion model using properties and parameters of both erodent and eroding materials.

The surfaces in real erosion situations are continuous combinations of convex and concave curvatures. The erosion prone joints, corners, and attachment of components in machinery and other devices impart severe life limitations due to the progression of erosion. Some investigators have therefore studied the erosion phenomenon for a specific requirement using particular configurations (e.g., [5, 6, 7]). Some researchers have studied cylinders of different materials both along and perpendicular to the axis. For example, Neilson and Gilchrist [5] tested hard steel, mild steel, brass, and aluminum cylinders using 500-μm iron grit and brass using 250-μm grit. Tilly [8] tested aluminum cylinders with 60- to 125-μm quartz grit. Also tested were tubes of aluminum oxide using aluminum oxide grit [5] and tubes of aluminum using 270-μm steel shot [9]. Barklow et al. [10] have studied both experimentally and theoretically the erosion-corrosion process of cylinders with aluminum oxide grit. In all these studies the erodent particles have impinged the surface perpendicular to the axis of the cylinder. Carter et al. [11], however, impinged copper and stainless steel cylinders along their axes using 0.1-mm sand grit.

The objective of this paper is to present (1) the erosion of circular cylinders which represent features of bluff leading edges as in gas turbine blades, and (2) the erosion and morphological characteristics of circular cylindrical holes and conical holes as well as slits which represent ordered asperities, joints, corners, cooling holes on turbine blades, and attachments on erosion prone surfaces.

Background

Several theoretical attempts on the impact of particles on cylindrical surfaces and their trajectories have been made. Thus, different size particle impact trajectories around the circular cylinders [10], particle impact on a circular cylinder cascade [12] and its boundary layer effects [13], particle trajectories in the wake of a cylinder [14] (using the flow field generated by the discrete vortex method), and the particle rebound phenomenon around a cylinder [15] have been reported.

Other important analytical studies reported have been (1) solution of fluid-particle systems from the leading edge of a flat plate resulting in a new shear law and a new heat transfer coefficient appropriate to the gas-particle boundary layer even at high temperatures for constant size particles [16], (2)

[1]Modified version of the feature article presented at the ASME Cavitation and Multiphase Flow Forum, Houston, June 21-23, 1983

[2]Cleveland State University—NASA Resident Research Associate

Contributed by the Power Division for publication in the JOURNAL OF ENGINEERING FOR GAS TURBINES AND POWER. Manuscript received by the Power Division October 26, 1983.

inertial impaction efficiency calculations and experimental verification pertaining to single elements such as cylinders, spheres, plates, airfoils, rectangular traps, ribbons and ellipsoids of revolution [17], and particle trajectory calculations of spherical particles in a uniform two-dimensional fluid flow about a circular cylinder and lifting aerofoil section [18]. Well-documented reviews of the state-of-the-art of the flow of solid-fluid particle studies pertaining to aircraft structures and turbomachinery are also available (e.g., [19, 20]).

In sand blast tests the particles nearing the flat or cylindrical surface target depart or deviate from the fluid streamline trajectory resulting in different particle velocity and impact angle at the point of impact compared to the initial free stream conditions. Small particles most closely follow the flow to the streamlines, but in some instances miss the "target surface" altogether [8, 21]. It was observed in [10] that the particles of more than 11-μm size may not be influenced by the flow field and the presence of targets. Tilly [8] has defined the number of particles that strike the target relative to the total initial number of particles in the free stream as the strike efficiency. Barklow et al. [10] and Dring [12] defined this parameter as impact number density. Golovin and Putnam [17] defined the efficiency of impaction as the ratio of the number of particles flowing through the minimum cross section to the number of particles flowing through the target projected area. Tilly [8] calculated the strike efficiency for various sizes of particles as a function of velocity on cylindrical surfaces and as a function of the angle of approach for flat surfaces in uniform flows. The detailed information pertaining to the change of the angle of impact during the particle impingement is available in [12]. Golovin and Putnam [17] presented inertial impaction efficiency as a function of inertial impaction parameter for rectangular half-body, ribbon normal to flow, sphere, recessed trap, cylinder, ellipsoid of revolution, and airfoils.

The aerodynamic effects involved during normal incidence in a uniform flow have been discussed by Laitone [22, 23] and Murthy and Crowe [24]. A universal understanding of the erosion processes on real surfaces which affect friction, drag, and performance characteristics has not been fully attained.

Apparatus and Experimental Procedure

Specimens. Specimens of the aluminum alloy 6061-T6511 were used in this investigation. The aluminum cylinders of 12.7- as well as 25.4-mm diameter and 37.5 mm long were used. Both circular cylindrical holes and geometrically similar conical holes were drilled on the 6 by 25 by 37.5-mm aluminum alloy specimens. The nominal composition and mechanical properties of the aluminum alloy were available in [25]. Before erosion exposure, all specimens were polished with 600-grit emery paper, then with 3-μm diamond paste, cleaned to a clean surface and then rinsed with distilled water, and air dried.

Apparatus and Procedure. A sand-blasting facility was used to continuously impact test specimens at normal incidence. Commercial grade No. 9 (20-μm diameter) spherical micro-glass beads and commercial grade No. 10 (30 μm) angular crushed glass were used. The particle size distribution of glass beads has been presented [26]. The SEM micrographic details of the sizes and shapes of both forms of glass are available in the literature [27, 28]. In the sand-blasting facility the distance between the specimen and the nozzle (1.18 mm diameter) was 13 mm. Argon was used as the driving gas at gage pressures of 0.27 and 0.82 MPa. The average centerline particle velocities and erodent flow rates are presented in Table 1. The velocities are obtained by using a double disk arrangement similar to one discussed earlier [29]. Measurements were not made of the velocity distribution from the center to the outer radius of the jet. The jet divergence was about ± 2 deg relative to the center line. The nozzle is replaced frequently during the experiments to limit the effect of nozzle wear on jet divergence, particle velocity, erodent flow rate, etc. The nonsymmetric erosion pit is an indirect indication of the nozzle wear in this type of study.

Table 1 Particle velocity and flow rate of glass beads and crushed glass particles

Parameter	Parameter corresponding to erodent particles flowing at gas pressure			
	Glass beads		Crushed glass	
	0.27 MPa	0.82 MPa	0.27 MPa	0.82 MPa
Particle velocity, m/sec	72	130	48	87
Particle flow rate, g/sec	0.98	0.48	0.34	0.22

Volume loss was calculated from weight lost. The sensitivity of the balance used was ± 0.1 mg. Surface profiles of the eroded surfaces were recorded with a profilometer. The depths of the shallow pits were measured from surface traces and checked with a depth gage. The sensitivity of the gage is ± 2.5 μm (0.0001 in.). The eroded surfaces were observed with an SEM.

Experimental Results and Discussion

Erosion of Circular Cylinders

Erosion Characteristics. Figure 1 presents cumulative erosion data for 25.4- and 12.7-mm-dia aluminum alloy circular cylinders as a function of the abrasive charge of the spherical glass beads and angular crushed glass. The driving gas pressure was 0.82 MPa and particle velocities are 130 and 87 m/s for glass beads and crushed glass particles respectively. Results obtained on flat surfaces and micrographs taken earlier [27, 30] were included for comparison. Figure 1 shows that the erosion of cylinders exposed perpendicular to their axis is less than the erosion of flat surfaces. This is true for both forms of glass despite the fact that the average erosion rate varies by one order of magnitude between glass bead and crushed glass impingement. This is also in agreement with earlier investigations [8, 15] which attributed

Nomenclature

A, A' = coefficients
a = constant (intercept)
b = base diameter of cylindrical hole
C = coefficient (equations (6) and (7))
c = coefficient (Figs. 10 and 14)
D = diameter of circular cylindrical hole
d = depth of pre-existing hole
d_j = diameter of the nozzle
m = exponent
n = exponent
R = radius of curvature of the cylindrical surface
t = exposure time
V = cumulative volume loss
w = abrasive charge
ϵ_c = strike efficiency of a cylindrical surface
ϵ_f = strike efficiency of a flat surface

Subscripts

max = maximum

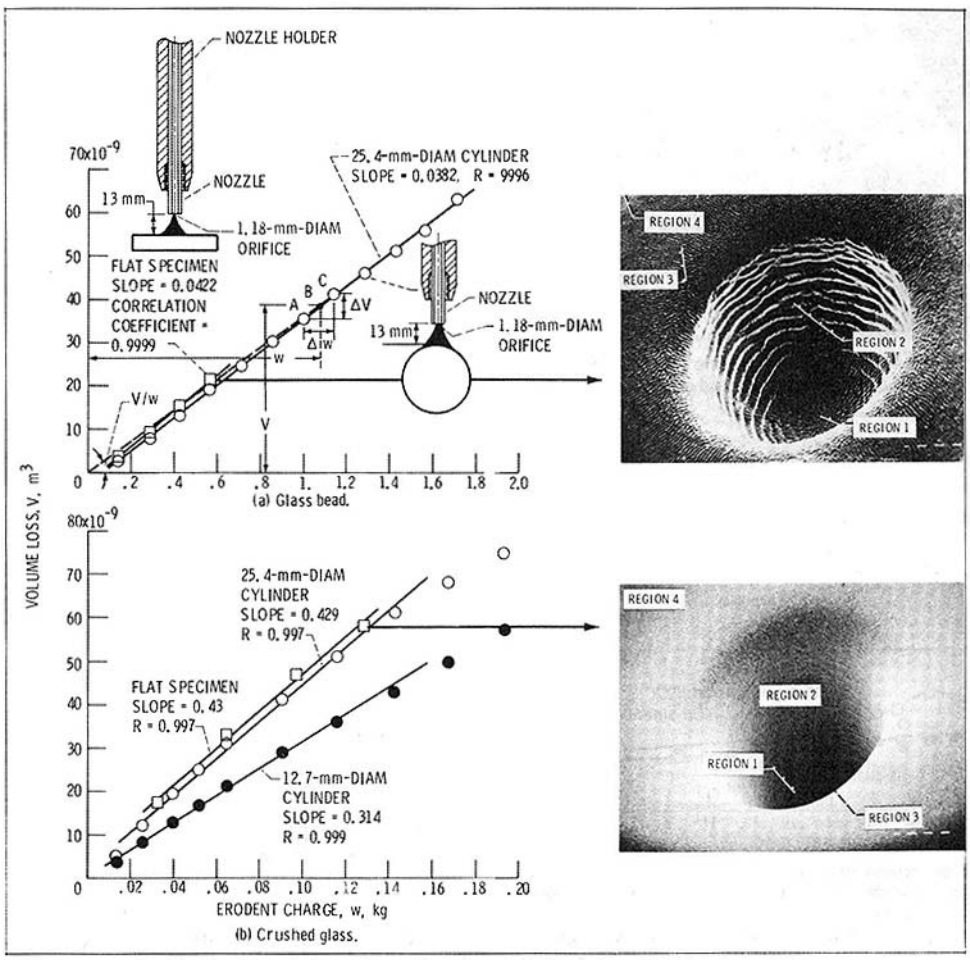

Fig. 1 Cumulative volume loss as a function of erodent impingement on circular cylinders and flat surface at normal incidence; driving gas pressure, 0.82 MPa (gage); instantaneous erosion rate at *B* equals slope of local tangent at $B = \Delta V/\Delta w$; cumulative average erosion rate at *B* equals slope of line joining origin and point $B = V/w$; experimental data variation is from 1.0 to ±7.76 percent at various exposure times, the maximum being at the inception stages of erosion

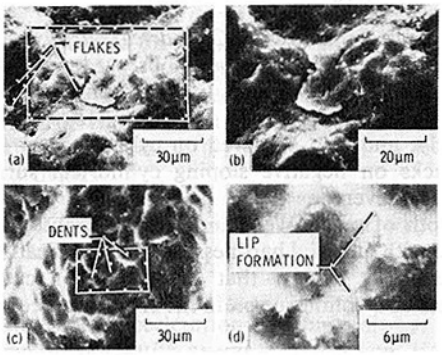

Fig. 2 SEM micrographs of eroded aluminum alloy surfaces exposed to glass bead impingement depicting flakes and dents: (*a*) dislodging flakes; (*b*) detailed view of flake in (*a*); (*c*) individual flakes and dents; (*d*) detailed individual dents in (*c*)

this effect to the reduction of strike efficiency in a uniform flow of erodent particles.

As the diameter of the cylinder decreased, the cumulative erosion also decreased (see Fig. 1). Most impinging jets induce damage by direct impact and radial outflow of the particles. On slightly convex surfaces, such as cylinders, the radial outflow component of erosion is believed to be reduced. Also, the particles deviated at a stagnation point, as discussed by earlier investigators [8, 21, 22], and may possibly miss the surface altogether. Hence, on cylinders, the angle of impingement changes from normal (90 deg) to glancing (0 deg), or to complete missing. This probably causes the reduction in erosion as theoretically predicted in [8, 10, 12, 23, 24] using particle trajectories. It is also to be remembered that a circular cylinder is a complicated form from a (two-phase) fluid flow point of view. Although other researchers [5, 8] have studied the erosion characteristics of circular cylinders, the effect of time and jet have not been reported.

Strike Efficiency. The reduction of erosion and strike efficiency of particles from a jet impinging a cylindrical surface may be attributed to the change of angle of incidence when compared with flat surfaces (see schematic in Fig. 1). The ratios of strike efficiency on a flat surface to that on a cylindrical surface for uniform flows of 20- and 30-μm size particles, without considering shape of the particles, were calculated to be 1.103 and 1.05, respectively [8]. The flat surface to cylindrical surface erosion rate ratios from steady-state regions for jet flow glass beads (20 μm) and crushed glass (30 μm) were 1.105 and 1.002 (Fig. 1). This agreement with glass beads shows that surface configuration seems to be of considerable influence during the deformation wear process. During the glass bead impingement, material appears to have been removed in the form of flakes as shown in Fig. 2. Individual dents are also seen clearly in Figs. 2(*c*) and (*d*).

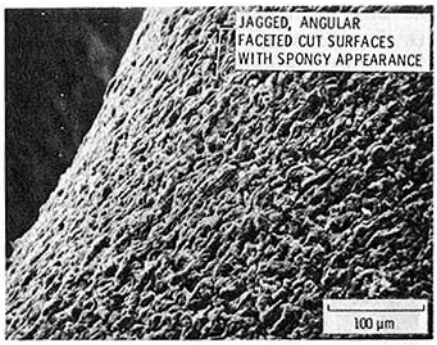

Fig. 3 SEM micrograph of eroded aluminum alloy surface exposed to crushed glass impingement depicting jagged and cut surfaces

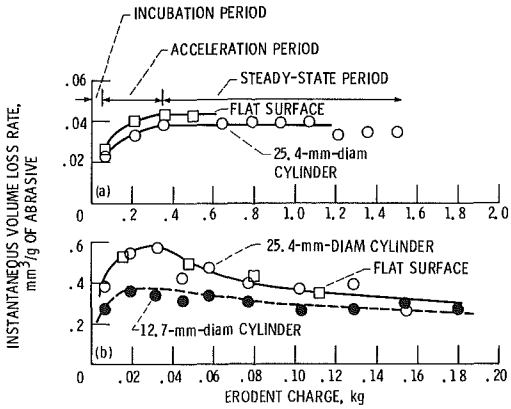

Fig. 4 Instantaneous volume loss rate as a function of erodent impingement on circular cylinders and flat surfaces at normal incidence; driving gas pressure, 0.82 MPa: (*a*) glass bead impingement exhibiting incubation, acceleration, and steady-state periods; (*b*) crushed glass impingement exhibiting incubation, acceleration, peak erosion rate, and deceleration periods

These flakes are believed to be formed by cyclic stress, deformation, extrusion and final fatigue failure, which is generally referred to as deformation wear. The disagreement for crushed glass particles is due to (1) the applicability of spherical particle theory to angular particles, and (2) the cutting wear phenomenon with angular particles. During cutting wear [30], all surfaces of the test specimens exhibit jagged, angular, cut faceted patterns as shown in Fig. 3. In this case, the surface appears to be cut by impact and subsequent outflow.

From the foregoing it may be stated that as the radius of curvature of cylindrical surface $R \rightarrow \infty$, the ratio of the strike efficiency of a cylinder to the strike efficiency of a flat surface $\epsilon_c/\epsilon_f \rightarrow 1$. On the other hand, as $R \rightarrow 0$, $\epsilon_c/\epsilon_f \rightarrow \infty$. In other words, $\epsilon_c/\epsilon_f \rightarrow 1$ as $R >> d_j$ (diameter of the nozzle) and $\epsilon_c/\epsilon_f \rightarrow \infty$ as $R << d_j$ without considering the shape of the particles.

Erosion Rate Versus Time Curves. Figure 4 presents volume loss rate versus abrasive charge curves. With glass bead impingement, curves exhibited incubation, acceleration, and steady-state periods for the cylindrical surfaces (Fig. 4*a*). With angular crushed glass, on the other hand, they exhibited incubation, acceleration, peak erosion rate, and deceleration periods on the same surfaces.

The surface configuration and shape as well as size of particles do not seem to influence the individual shape of the erosion rate versus abrasive charge curve. Curves similar to those in Fig. 4(*a*) are common type and have been discussed by several investigators (e.g., [3, 8, 11]). The shape of the curve in Fig. 4(*b*) is a less frequent type and has only been reported by the present investigators [31].

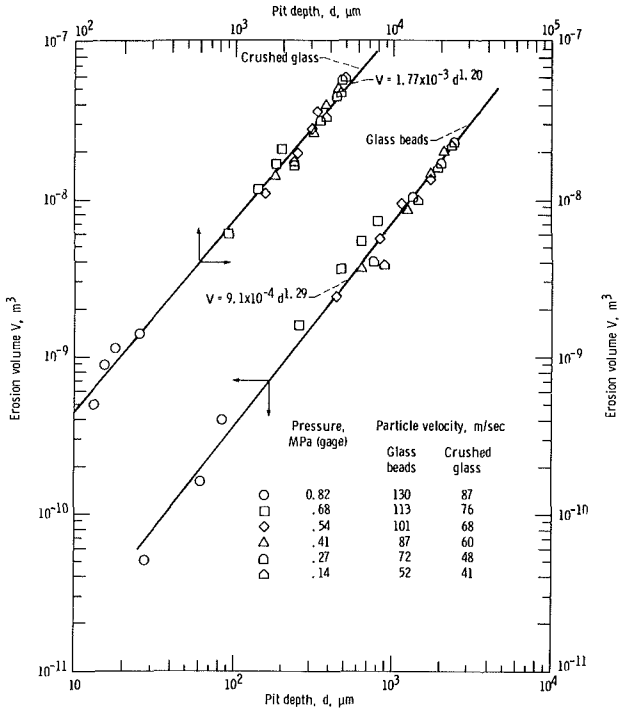

Fig. 5 Erosion volume as a function of pit depth [31]

Long-Term Exposure. In energy conversion systems erosion prone components are exposed to long-term (around 20,000 hr) erosive environments. Figure 4 shows that the erosion rate does not change for spherical erodent particles and continuously decreases for angular erodent particles. Figure 4(*b*) may be more realistic as most of the particles encountered in real situations are angular. Also, for components where erosion is prevalent, this may give the design engineers an estimate not only of how to predict erosion but also to use highly resistant material to reduce breakdown or component change time. It is evident with angular particles that for long exposures the pit becomes sufficiently deep to affect the erosion rate.

Morphological Features on Cylindrical Surfaces. Five and four different regions have been observed on flat surfaces during spherical glass bead[3] (micrograph in Fig. 1*a*) and crushed glass[4] (micrograph in Fig. 1*b*) impingement, respectively, and also observed on cylindrical surfaces. The radial tracks on negative sloping cylindrical surfaces are, however, less severe.

The depth of cut in wear and erosion processes has been correlated with material hardness for characterization of wear resistance. It is known that the depth of cut in wear phenomena and volume of pit in the erosion process represent

[3] Flat specimens exposed to glass bead impingement, at an advanced stage, exhibit five regions (micrograph in Fig. 1*a*): Region 1 consists mainly of radial deformation tracks, emanating from the center of the impact. The depth and width of the tracks increase with radial distance from the center of the pit. Region 2 consists of both radial tracks and concentric rings. For convenience, these have been called "radial-concentric" rings. It was believed to be the first observation of such patterns. Region 3 is a steep-slope region composed mainly of radial tracks. Region 4 is rougher, with irregular concentric, ripple and crest patterns. Region 5 is a transition from the undamaged zone to the incipient erosion zone.

[4] Flat surfaces exposed to crushed glass particle impingement, at an advanced stage, exhibit four regions (micrograph in Fig. 1*b*): region 1, pit bottom with no clear pattern; region 2, concentric ripple patterns on the sides of the pit; region 3, a rough undulating region with a changing slope from almost vertical to horizontal; and region 4, the transition from incipient erosion zone to the undamaged area of the specimen.

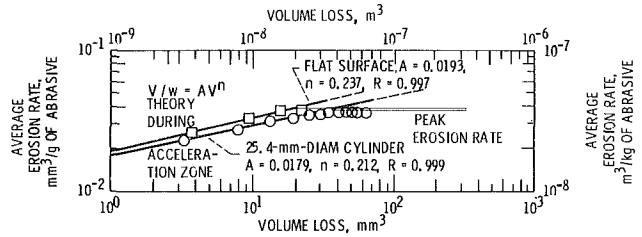

Fig. 6 Cumulative average erosion rate versus volume loss curves of aluminum alloy cylinder and flat surface during glass bead impingement; driving-gas pressure, 0.82 MPa; particle velocity, 130 m/s

material loss by wear and erosion phenomena respectively. Figure 5 is a typical plot of erosion volume as a function of the depth of the pit [31]. This is presented to investigate whether or not the depth of the pit represents the total volume loss after several millions of both forms of glass particle impact. Figure 5 shows that this type of correlation is possible for different velocities and the exponents appear to be almost equal irrespective of the shape of the erodent particle. Pit depth apparently appears to correlate well with erosion volume for both forms of glass particle impact compared to pit width, pit width/depth ratio and approximate pit volume [31]. Hence, it is also possible to compare the pit depths corresponding to steady-state period or peak erosion rate of different metals with metal properties for the characterization of erosion resistance.

Characteristic of Erosion Rate Versus Cumulative Erosion Curve. Figure 6 presents typical log-log plots of cumulative average erosion rate versus erosion of an aluminum alloy cylinder and an aluminum alloy flat impacted with glass beads. The acceleration stage of erosion may be represented by a relation of the form (with respect to abrasive charge or exposure time)

$$V/t = A' V^n \tag{1}$$

or

$$V/w = A V^n \tag{2}$$

or

$$V = [A w^{1/(1-n)}] \tag{3}$$

as $w = f(t)$, where V is the cumulative volume loss (in mm^3), t is the exposure time (in min) corresponding to V, w is the abrasive charge (in g) corresponding to V, A' and A are coefficients, and n is an exponent. The coefficients, exponents (slopes), and correlation coefficients are marked in Fig. 6. Differentiation of equation (3) with respect to w and simplification provides

$$dV/dw = A V^n/(1-n) = V/[(1-n)w] \tag{4}$$

$$dV/dt = V/[(1-n)t] \tag{5}$$

Equation (5) indicates that instantaneous erosion rate, dV/dw or dV/dt, during the acceleration stage may always appear to be a function of cumulative average erosion rate, V/w or V/t. The ratio of these two rates is therefore constant (equation (5)). Substitution of equation (3) into equation (4) results in

$$dV/dw = C w^m \tag{6}$$

where

$$C = \frac{A^{1/(1-n)}}{(1-n)} \tag{7}$$

$$m = n/(1-n) \tag{8}$$

The advantage of this relation is that values of $(dV/dt)_{max}$ and time or abrasive dosage corresponding to this peak may be calculated with just a few experimental points and with a knowledge of A, n, and V/t. The experimental points of this

LEGEND	VELOCITY, m/s	ERODENT	SIZE, μm	ANGLE, deg	EQUATION	CORRELATION COEFT.	COEFT. A	EXPONENT B	REF.
■	100	SiO_2	400	-	$W/w = AW^n$	0.996	1.8×10^{-1}	0.75	[32]
□	150					.998	2.4×10^{-1}	.72	
●	200					.997	4.5×10^{-1}	.63	
○	250					.994	6.0×10^{-1}	.56	
◇	104	SiC	60-125	90	$W/w = AW^n$	.996	7.0×10^{-3}	.26	[8]
◆				40	"	-	3.4×10^{-3}	.26	
○	10	WC-6% Co SPHERES	1580	90	$W/i = AW^n$	.999	2.0×10^{-5}	.85	[33]
●	14.5					.999	2.7×10^{-5}	.88	
						.999	1.7×10^{-4}	.76	
▷	33					.999	7.8×10^{-4}	.74	
▶	54								
▷	72					.997	1.3×10^{-3}	.59	
◣	87					.998	2.2×10^{-3}	.60	
△	101					.999	6.0×10^{-3}	.55	
▲	117					.998	6.9×10^{-3}	.61	
◇	126					.999	9.1×10^{-3}	.55	
◆	151					.999	1.1×10^{-2}	.64	
◇	64	GLASS BEADS	495-600	90	$W/w = AW^n$	.999	1.5×10^{-3}	.74	[34]
▼	100	SiC	400	-	$W/w = AW^n$	-	2.5×10^{-1}	.84	[32]
▽	150					-	9.6×10^{-1}	.96	
▲	200					-	1.05	.61	
△	250					.999	1.4	.48	
□	129	Al_2O_3	210	4	$W/w = AW^n$				[5]
□				18					
●				25					
●				40					
□				70					
□				90					

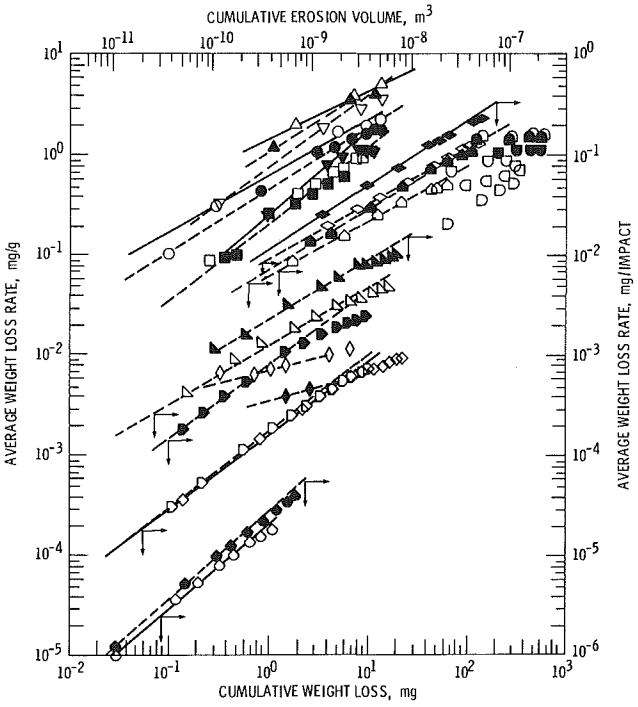

Fig. 7 Average weight loss rate as a function of cumulative erosion for aluminum and aluminum alloys

relation deviate exactly at $(V/t)_{max}$. The value of time corresponding to this peak may therefore be calculated.

To explore the validity of the proposed power law relation and to confirm the results of the authors' findings, the extensive aluminum and aluminum alloy erosion data reported by other investigators [5, 8, 32-34] are analyzed using equation (2) and presented in Fig. 7. The slight differences of equations, the values of the coefficients, exponents, and correlation coefficients are presented in the legend of Fig. 7. Hence, it appears possible to predict average erosion rate with fewer points during the acceleration period. The characteristics of this relationship require further investigation to

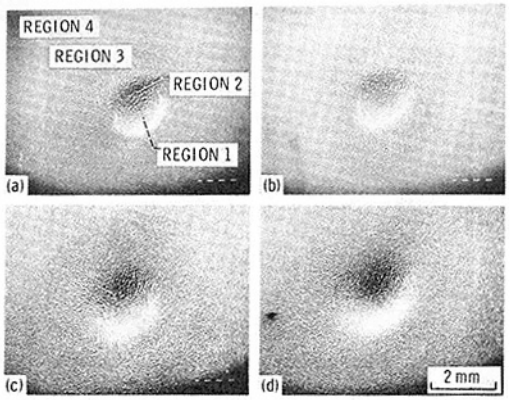

Fig. 8 Typical SEM micrographs of eroded aluminum alloy surfaces with conical hole (b = 0.76 mm and d = 0.38 mm) exposed to glass bead impingement; driving-gas pressure, 0.27 MPa; particle velocity, 72 m/s; (*a*) 15 s; (*b*) 30 s; (*c*) 120 s; (*d*) 180 s

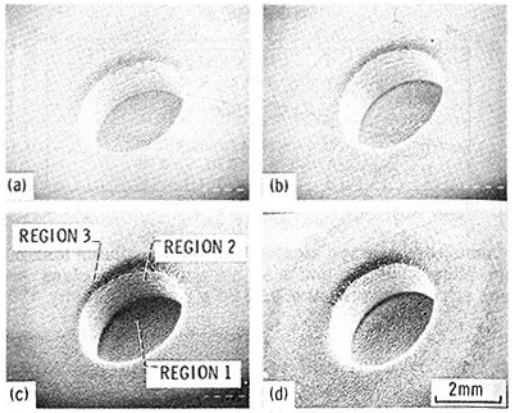

Fig. 10 Typical SEM micrographs of eroded aluminum alloy surfaces with circular cylindrical hole (D = 3.18 mm and d = 1.35 mm) exposed to glass bead impingement; driving-gas pressure, 0.27 MPa; particle velocity, 72 m/s; (*a*) 15 s; (*b*) 30 s; (*c*) 60 s; (*d*) 120 s

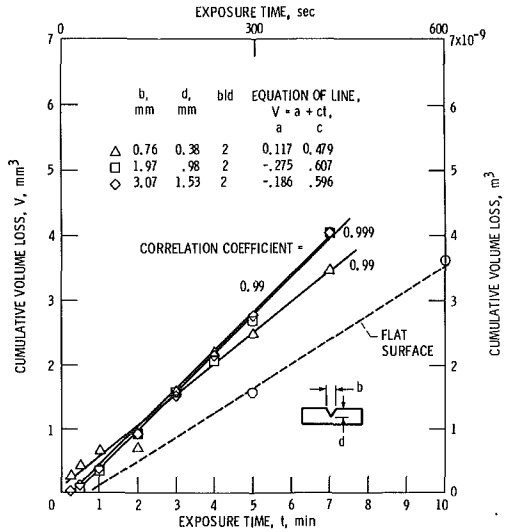

Fig. 9 Erosion of aluminum alloy surfaces with pre-existing conical holes as a function of time; driving-gas pressure, 0.27 MPa; particle velocity, 72 m/s; experimental data variation is from 0 to ±6.6 percent at various exposure times, the maximum being at the inception stages of erosion

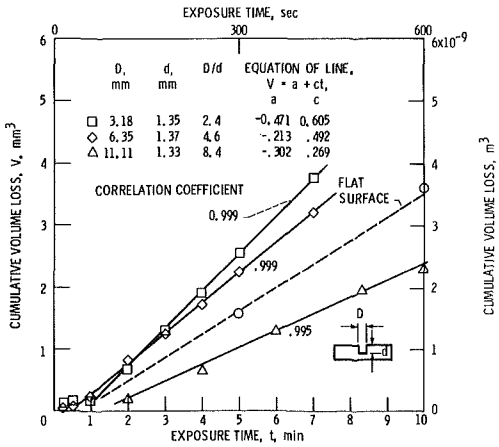

Fig. 11 Erosion of aluminum alloy surfaces with pre-existing circular cylindrical holes as a function of time; driving-gas pressure, 0.27 MPa; particle velocity, 72 m/s; experimental data variation is from 0.5 to ±5.9 percent at various exposure times, the maximum being at the inception stages of erosion

assess its advantages compared to conventional curve fit approaches.

Erosion of Pre-existing Holes and Slits

Morphological Features of Holes. Figure 8 presents a typical series of SEM micrographs of aluminum alloy specimens with pre-existent conical holes as a function of exposure to glass bead impingement time. The driving gas pressure of 0.27 MPa (average particle velocity is 72 m/s) is considered to systematically reveal morphological features. The holes examined are geometrically similar with a constant aspect ratio (base diameter b to depth d) of 2 (b/d_j = 0.6, 1.7, and 2.6, respectively, where d_j is the diameter of the nozzle). The existence of five regions as discussed by the authors [27] with respect to flat surfaces is also seen in the present study.

The main features observed with conical holes are that radial tracks form almost immediately and concentric ripples (in region 4) are very faint. The inception of radial-concentric rings is observed with b = 1.97 mm and b = 3.07 mm holes. From the photographs it appears that damage on small pits is more than on deep pits. However, this seems to be true only during the initial phases of erosion; Fig. 9 presents cumulative erosion versus time curves.

Figure 10 presents a typical series of SEM micrographs of aluminum alloy specimens with circular cylindrical holes of diameter D = 3.18 mm and depth d = 1.35 mm as a function of exposure to glass bead impingement time. The average particle velocity is 72 m/s. (The driving gas pressure is 0.27 MPa.) For small holes, radial tracks are observed around the top of the hole (Fig. 10). Radial, concentric rings always appear to develop on the side of the hole, and the central portion of hole contains only irregular patterns. For larger diameter holes, the radial tracks form at the bottom of the pit. Irregular circumferential ripple patterns are also seen at the pit bottom for wide pits. The radial tracks and radial, concentric rings appear to form earlier at 3.18 and 6.35-mm diameters than on a flat surface. Hence, more erosion is expected on these surfaces.

Figure 11 presents erosion versus time curves for circular cylindrical holes of constant depth d (1.35 mm) and diameters D of 3.18, 6.35, and 11.12 mm (D/d_j = 2.7, 5.4, and 9.4, respectively). It is evident that erosion is large on the two small diameters.

It is possible to suspect that the variations of erosion volumes in Figs. 9 and 11 may be due to workhardening during the process of the hole drilling. However, detailed studies did not show evidence to this effect. Hence, it may be stated that the volume losses obtained on individual surfaces represent the true erosion characteristics due mainly to flow differences induced by the presence of holes and their sizes.

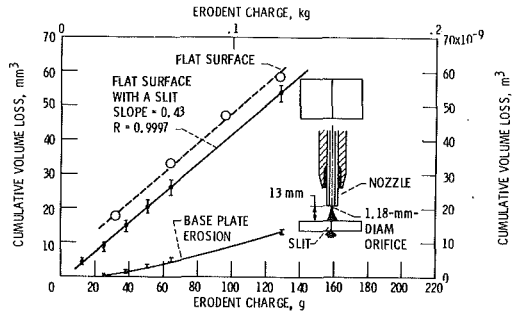

Fig. 12 Cumulative volume loss of aluminum alloy as a function of crushed glass impingement on a slit at normal incidence; driving-gas pressure, 0.82 MPa; particle velocity, 87 m/s

Erosion Characteristics. It is evident from Figs. 9 and 11 that the erosion of aluminum alloy surfaces with holes – conical and circular cylindrical – appears to be always more than the erosion on the flat surface except when the hole is very wide. However, there seems to be a different trend for these two forms of holes. The steady-state erosion rate increases with increases in the size of the conical holes (keeping the same aspect ratio b/d) (Fig. 9) and with decreases in the diameter of cylindrical holes (keeping approximately constant depth) (Fig. 11). The radial outflow pattern, particle rebound mechanism, and the strike efficiency (along with particle trajectory) seem to be the main reasons for the differences in erosion resistance. It appears that the theory proposed for rectangular traps using uniform flow theory is not applicable here.

Erosion at Holes, Edges, and Narrow Slits. The erosion rate at holes and edges of the test specimens was considerably higher than that for a flat surface in the present study (Figs. 9 and 11). Figure 12 presents a typical plot of erosion at a narrow slit (0.1 mm) with respect to exposure time of crushed glass particle impingement. This figure indicates that cumulative volume loss at a narrow slit is less than that on flat surfaces, although erosion progressed fast through the slit. This result, which is in conflict with that from shallow holes, is due mainly to the observed erosion below the slit on the neighboring component. The erosion on the base plate is also presented in Fig. 12. The total erosion on the top and base plates is equal to the erosion on a flat specimen without a slit. Slits reduce erosion but could extend and transfer the process to the adjoining or underlying components and base materials. Hence, caution should be exercised in designing this type of slits to alleviate erosion.

Figure 12 shows that slopes of the curves for both flat surfaces, with and without slits, are the same. It is generally observed that with slits the depth of the pit increases faster than the width of the pit. Hence, one may assume that most impinging particles do not flow out from the pit surface, but escape through the slit to adjoining components, possibly causing erosion inside.

Conclusions

The main observations of these studies are as follows:

1 Circular cylindrical surfaces experienced less erosion than flat surfaces with both glass bead and crushed glass impingement particles. The uniform-flow strike efficiency proposed also agrees with glass bead jets, providing almost the same ratio of erosion rate between flat and cylindrical surfaces.

2 Curves of erosion rate versus time or glass bead dosage for circular cylindrical surfaces exhibited incubation, acceleration, and steady-state periods. With crushed glass impingement, they exhibited incubation, acceleration, peak erosion, and deceleration periods.

3 A (power law) relation was observed between cumulative erosion rate and volume loss during the acceleration stage of erosion. This is believed to be advantageous for characterizing erosion using fewer experimental points.

4 Most of the pre-existing holes – circular cylindrical and conical – exhibited more erosion than flat surfaces.

5 The morphological features on an aluminum alloy surface with holes were similar to the ones on flat surfaces. The radial tracks were, however, observed on conical surfaces immediately after exposure to glass bead impingement.

6 The erosion at a narrow slit was less than that on a flat surface. A slit generally extends the erosion to the adjoining and underlying components and base materials.

References

1 "Erosion Control in Energy Systems," NMAB-334, National Materials Advisory Board, Washington, D.C., 1977.

2 Adler, W. F., "Assessment of the State of Knowledge Pertaining to Solid Particle Erosion," ETI CR 79-680, Effects Technology, Inc., Santa Barbara, CA, June 1979.

3 Finnie, I., Wolak, J., and Kabil, Y., "Erosion of Metals by Solid Particles," *Journal of Materials*, Vol. 2, No. 3, Sept. 1967, pp. 682-700.

4 Soderberg, S., et al., "Erosion Classification of Materials Using a Centrifugal Erosion Tester," *Tribology International*, Vol. 14, No. 6, Dec. 1981, pp. 333-343.

5 Neilson, J. H., and Gilchrist, A., "An Experimental Investigation Into Aspects of Erosion in Rocket Motor Tail Nozzles," *Wear*, Vol. 11, 1968, pp. 123-143.

6 Grant, G., and Tabakoff, W., "Erosion Prediction in Turbomachinery Resulting From Environmental Solid Particles," *Journal of Aircraft*, Vol. 12, No. 5, May 1975, pp. 471-478.

7 Tabakoff, W., and Hamed, A., "Three Dimensional Particles Trajectories in Turbomachinery," *Conference on Gas-Borne Particles*, The Institution of Mechanical Engineers, Oxford, June 30-July 2, 1981, Paper No. C63/81.

8 Tilly, G. P., "Erosion Caused by Airborne Particles," *Wear*, Vol. 14, 1969, pp. 63-79.

9 Maji, J., and Sheldon, G. L., "Mechanisms of Erosion of a Ductile Material by Solid Particles," *Erosion: Prevention and Useful Applications*, edited by W. F. Adler, ASTM STP 664, American Society for Testing and Materials, Philadelphia, 1979, pp. 136-147.

10 Barkalow, R. H., Goebel, J. A., and Pettit, F. S., "Erosion-Corrosion of Coatings and Super Alloys in High-Velocity Hot Gases," *Erosion: Prevention and Useful Applications*, edited by W. F. Adler, ASTM STP 664, American Society for Testing and Materials, Philadelphia, 1979, pp. 163-192.

11 Carter, G., Nobes, M. J., and Arshak, K. I., "The Mechanism of Ripple Generation on Sandblasted Ductile Solids," *Wear*, Vol. 65, No. 2, Dec. 15, 1980, pp. 151-174.

12 Dring, R. P., "Particle Impact on a Cascade of Circular Cylinders," Report No. UTRC77-30, United Technologies Research Center, East Hartford, CT, March 17, 1977.

13 Dring, R. P., "Particle Impact on a Cascade of Circular Cylinders (Boundary Layer Effects)," Report No. UTRC77-69, United Technologies Research Center, East Hartford, CT, June 22, 1977.

14 Laitone, J. A., "A Numerical Solution for Gas-Particle Flow at High Reynolds Numbers," ASME *Journal of Applied Mechanics*, Vol. 48, Sept. 1981, pp. 465-471.

15 Laitone, J. A., "Characterization of Particle Rebound Phenomena in the Erosion of Turbomachinery," *Journal of Aircraft*, Vol. 20, March 1983, pp. 275-281.

16 Marble, F. E., "Dynamics of a Gas Containing Small Solid Particles," *Combustion and Propulsion, 5th AGARD Colloquium*, Braunschweig, edited by R. P. Hagerty et al., Pergamon Press, New York, 1963, pp. 175-215.

17 Golovin, M. N., and Putnam, A. A., "Inertial Impaction of Single Elements," *Industrial and Engineering Chemistry Fundamentals*, Vol. 1, No. 4, Nov. 1962, pp. 264-273.

18 Morsi, S. A., and Alexander, A. J., "An Investigation of Particle Trajectories in Two-Phase Flow Systems," *J. Fluid Mechanics*, Vol. 55, part 2, Sept. 26, 1972, pp. 193-208.

19 Rudinger, G., *Flow of Solid Particles in Gases*, AGARD-AG-222, 1976.

20 Tabakoff, W., "Performance Deterioration on Turbomachinery With Presence of Solid Particles," *Particulate Laden Flows in Turbomachinery*, edited by W. Tabakoff, ASME, New York, 1982, pp. 3-22.

21 Tilly, G. P., "Erosion Caused by Impact of Solid Particles," *Wear*, edited by D. Scott, Treatise on Materials Science and Technology, Vol. 13, Academic Press, New York, 1979, pp. 287-319.

22 Laitone, J. A., "Aerodynamic Effects in the Erosion Process," *Wear*, Vol. 56, No. 1, Sept. 1979, pp. 239-246.

23 Laitone, J. A., "Erosion Prediction Near a Stagnation Point Resulting

From Aerodynamically Entrained Solid Particles," *Journal of Aircraft*, Vol. 16, No. 12, Dec. 1979, pp. 809–814.

24 Murthy, J., and Crowe, C. T., "Aerodynamic Effects on the Erosion of Finite Size Targets," *Particulate Laden Flows in Turbomachinery*, edited by W. Tabakoff, ASME, New York, 1982, pp. 43–48.

25 Rao, P. V., Young, S. G., and Buckley, D. H., "A Study of the Nature of Solid Particle Impact and Shape on the Erosion Morphology of Ductile Metals," NASA TM-82933, July 1982.

26 Rao, P. V., Young, S. G., and Buckley, D. H., "Solid Spherical Glass Particle Impingement Studies of Plastic Materials," NASA TP-2161, 1983.

27 Rao, P. V., Young, S. G., and Buckley, D. H., "Morphology of Ductile Metals Eroded by a Jet of Spherical Particles Impinging at Normal Incidence," *Wear*, Vol. 85, No. 2, March 1, 1983, pp. 223–237.

28 Salik, J., and Buckley, D. H., "Effect of Erodent Particle Shape and Various Heat Treatments on Erosion Resistance of Plain Carbon Steel," NASA TP-1755, Jan. 1981.

29 Ruff, A. W., and Ives, L. K., "Measurement of Solid Particle Velocity in Erosive Wear," *Wear*, Vol. 35, 1975, pp. 195–199.

30 Rao, P. V., Young, S. G., and Buckley, D. H., "Morphology of an Aluminum Alloy Eroded by a Jet of Angular Particles Impinging at Normal Incidence," NASA TP-2139, May 1983.

31 Rao, P. V., and Buckley, D. H., "Time Dependence of Solid-Particle Impingement Erosion of an Aluminum Alloy," NASA TP-2169, Aug. 1983.

32 Kayser, W., "Erosion by Solid Bodies," *Proceedings of the 2nd Meersburg Conf. on Rain Erosion and Allied Phenomena*, Vol. 2, edited by A. A. Fyall and R. B. King, Royal Aircraft Establishment, Farnborough, England, 1967, pp. 427–447.

33 Rickerby, D. G., and Macmillan, N. H., "The Erosion of Aluminum by Solid Particle Impingement at Normal Incidence," *Wear*, Vol. 60, No. 2, May 1980, pp. 369–382.

34 Hutchings, I. M., "A Model for the Erosion of Metals by Spherical Particles at Normal Incidence," *Wear*, Vol. 70, No. 3, Aug. 15, 1981, pp. 269–281.

Characterization of Solid Particle Erosion Resistance of Ductile Metals Based on Their Properties[1]

P. V. Rao[2]

D. H. Buckley

NASA Lewis Research Center,
Cleveland, OH 44135

This paper presents experimental results pertaining to spherical glass bead and angular crushed glass particle impingement. A concept of energy absorption to explain the failure of material is proposed and is correlated with the erosion characteristics of several pure metals. Analyses of extensive erosion data indicate that the properties—surface energy, specific melting energy, strain energy, melting point, bulk modulus, hardness, atomic volume—and the product of the parameters—linear coefficient of thermal expansion × bulk modulus × temperature rise required for melting, and ultimate resilience × hardness—exhibit the best correlations. The properties of surface energy and atomic volume are suggested for the first time for correlation purposes and are found to correlate well with erosion rates at different angles of impingement. It further appears that both energy and thermal properties contribute to the total erosion.

Introduction

The energy crisis has forced many power plants to use high-sulfur coals and oils. The major byproducts of combustion combined with atmospheric moisture lead to H_2SO_4 attack on mechanical and turbomachinery components. For example, in coal conversion, the combustion and gasification lead to severe corrosion and erosion problems in piping, valves, pumps, compressors, turbines, cyclone separators, etc. The power plants are expected to operate for over 20,000 hr without a major shutdown. One must, therefore, first recognize the seriousness of erosion/corrosion attack, and second, take steps early in the design phase to minimize these effects. The high number of erosion-related failures has, however, established erosion as a serious design consideration. The problems of component erosion due to particulate laden gases will continue to increase as system temperature and process speeds in various systems are increased. While coal gasification is one area where erosion is a critical problem, there are other areas such as injection of debris into aircraft engines and particle impact on space vehicles which are also of major concern. A better understanding of basic processes and mechanisms involved in erosion is therefore of utmost importance.

Many attempts have been made to correlate the erosion rate of various ductile materials with their physical, mechanical, and other properties. However, no universal correlation using a single property or a combination of properties has been established. Table 1 presents the correlation attempts and suggestions made by different investigators [1-20] using a variety of properties. The particle geometry, sizes, and shapes, the angle of impingement, and the velocity of impact are also recorded in the table.

Thus far, the following properties have been examined by various investigators: hardness [1, 3, 5, 8, 13, 14], surface layer hardness [16], dynamic hardness [20], elastic modulus [2, 8, 13], ductility [5, 8, 14, 16, 20], localized ductility [19], melting temperature [6], tensile strength [8, 14], yield stress [8 and 14], impact strength [14], fracture toughness [14], linear coefficient of expansion [14], product of hardness × elongation [1], "thermal pressure" [7], product of density × specific heat × melting temperature differential [9], (mean molecular weight/density)$^{1/3}$ × 1/(thermal conductivity × melting temperature × enthalpy of melting) [10], metal-metal bonding energy [11], ultimate resilience[3] [12], specific melting energy [15], cohesive energy [17], and mechanical energy density[4] [18]. Pure physical properties of metals such as density [4] and specific gravity [8] have also been tried with nominal success. A majority of these investigators used erosion data reported either by Finnie et al. [3] or Tadolder [21] or both.

From a physical understanding it is logical that the energy absorbed by the material until it yields or fails in a tension test is a simple property that is expected to roughly represent erosion resistance of ductile materials [22]. Although this type of correlation has recently been attempted [18] for pure metals using the data in reference [3], the correlations do not appear to be better than earlier attempts [7, 8, 10, 12, 14, 16,

[1] Modified version of a paper presented at the ASME Energy Sources Technology Conference on Liquid-Solid Flows and Erosion Wear in Industrial Equipment, New Orleans, Louisiana, February 12-16, 1984.

[2] Cleveland State University—NASA Resident Research Associate.

Contributed by the Power Division for publication in the JOURNAL OF ENGINEERING FOR GAS TURBINES AND POWER. Manuscript received by the Power Division November 1983.

[3] Ultimate resilience = (tensile strength)^2/[2 × elastic modulus].

[4] This is also called strain energy or toughness and may be defined as work done to cause failure/unit volume and can be calculated from the area of the curve of an engineering stress-strain curve.

Table 1 Material property correlations with solid particle impingement erosion

Investigator	Erosion parameter	Correlated or suggested properties of materials	Angle of impingement, deg	Particle velocity, m/s	Impinging particles (size, μm)
Wood and Espenschade [1][a]	Erosion rate	Hardness (Knoop) Hardness × elongation	90	[b]225	Silica flour (74)
Brauer and Kriegel [2]	Erosion	Elastic modulus	20, 30, 45, 50 60, 75, 90	20, 70	----------
Finnie, et al. [3]	Volume removed	Hardness (VHN)	20	76, 137	SiC (250)
Kayser [4]	Resistance to erosion	Density (metals, alloys, and plastics)	----------	143	Quartz sand (400)
Tilly [5][c]	Erosion	Hardness (VHN), ductility at fracture	90	104	Quartz (60-125)
Smeltzer, et al. [6][d]	Volume removed	Melting temperature	20	137	SiC (250)
Ascarelli [7][d]	Volume eroded	Thermal pressure (product of linear thermal expansion, temperature rise required for melting, and bulk modulus of metal)	20	137	SiC (250)
Tuitt [8][e]	Volume loss	Hardness, tensile strength, ductility, proof stress, specific gravity, elastic modulus	30, 90	305	Quartz sand (40)
Hutchings [9][d,f]	Volume loss rate	Density × specific heat × temperature rise required for melting	20 45	137 82	SiC (250) Quartz
Jennings et al. [10][g]	Volume loss	(Mean molecular weight/density)$^{1/3}$ (Thermal conductivity × melting temperature × enthalpy of melting)	20, 30, 45 90	91-253	Glass beads (200) SiC (220)
Vijh [11][d,f]	Wear resistance	Metal-metal (interatomic) bond energy	20 45	137 82	SiC (250) Quartz
Eyre [12]	Erosion	Ultimate resilience (tensile strength)^2/(2 × elastic modulus)	----------	------	----------
Sheldon [13][d,h]	Erosion wear	Hardness (VHN), elastic modulus	20	76	SiC (250)
Jones and Lewis [14][e]	Erosion wear rate	Impact strength, ultimate tensile strength, fracture toughness, elongation, hardness, coefficient of themal expansion	90	------	Quartz SiC Iron powder
Malkin [15][d,f]	Specific erosion energy[i]	Specific melting energy (melting energy per unit volume of target)	20 45	76, 137 82	SiC (250) Quartz
Soderberg, et al. [16]	Cutting erosion resistance	Surface layer hardness	15, 30, 45, 60, 75, 90	20, 66, 100	Olivine sand (350-490)
	Deformation erosion resistance	Ductility	15, 30, 45, 60, 75, 90	20, 66, 100	Olivine sand (350-490)
Buckley [17][d]	Weight loss rate	Cohesive engery	20	137	SiC (250)
Rickerby [18][d]	Volume erosion	Mechanical energy density (strain engergy)	20	76, 137	SiC (250)
Levy [19]	Erosion resistance	Localized ductility	15, 30, 90	30, 61	SiC (240)
Hutchings [20]	Erosion resistance	Dynamic hardness and ductility	90	30-75	Glass beads (212-250 and 495-600) Steel shot (600-700)

[a]Several steels were correlated.
[b]Airstream velocity (particle velocity is much smaller than this value).
[c]Several alloys were correlated.
[d]Finnie, et al [3] data have been adopted.
[e]Erosion resistance of several alloys and coatings were correlated.
[f]Tadolder [21] data have been adopted.
[g]Seven alloys were correlated.
[h]Apart from pure metals, Cu-Ni alloys were also correlated.
[i]Kinetic energy per unit volume of target material (using an analogy with grinding).

17, 19] using the same experimental data. Hence, an analysis of the energy absorption characteristics as well as thermal energy parameters due to the impinging particles and the experimental verification to assess the merit of the material properties in predicting erosion are necessary.

The mechanism of material removal during particle impingement has been attributed to extrusion, ductile fracture, melting, low-cycle fatigue, delamination, localized adiabatic shear, adhesive material transfer, and so forth [22]. Most of these postulations have resulted from wear debris and metallographic observations of the platelet or flake-type and other shapes of particles. As shown in Fig. 1 these phenomena have been named as deformation and cutting wear (with spherical and angular particle impact), respectively. The wear debris generation processes have been clearly illustrated in other papers as well [22-26].

More recently it has been made clear that two or three mechanisms can fully explain the erosion process with different shapes and sizes of particles [23, 24]. Also, Brown and Edington [27] observed that material was lost via three dif-

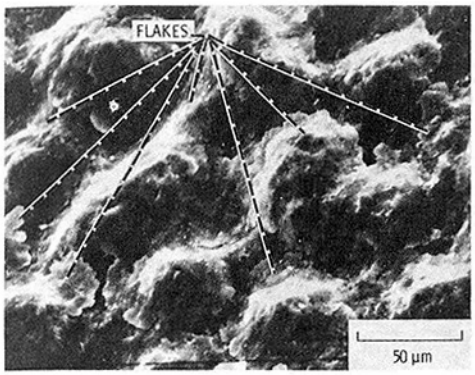

Fig. 1(*a*) Flakelike wear debris due to glass bead impingement (deformation wear)

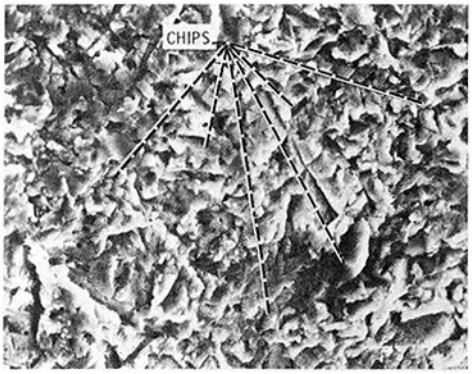

Fig. 1(*b*) Jagged, angular craters and cut surfaces with chips due to angular particle impingement (cutting wear)

Fig. 1 Wear debris during spherical and angular particle impingement erosion

ferent processes, namely, melting, dusting, and sheet formation. The micrographic observations in the literature [23, 25, 27] and those of the present authors [22, 24, 26] support the suggestion that the erosion process does not result from a single mechanism (e.g., Fig. 1).

This paper assesses the erosion characteristics and damage processes of pure metals to identify those properties best used for erosion prediction.

Background of Modeling Efforts

There have been several models proposed by different investigators for single and multiple spherical or angular particle impingement erosion. Excellent overviews of the subject have been presented by Ruff and Wiederhorn [28], Adler [29], Tilly [30], and Schmitt [31]. However, for completeness and to inform the readers, the models developed by various researchers are briefly highlighted. Finnie [32] in 1958 presented the dynamic equations governing the motion of the angular particle after it strikes the surface considering the flow stress of material (using the concept of a rigid cutting tool removing a chip of material). This model has been modified as discussed in [29, 33]. Bitter [34], categorizing deformation and cutting phenomena, developed an analytical equation based on an energy balance consideration of (1) recoverable elastic and elastic-plastic deformation energy and (2) nonrecoverable plastic deformation energy. Wood and Hafer [35] and Neilson and Gilchrist [36] have simplified the equations proposed by Bitter [34] to incorporate (1) the threshold normal velocity component and (2) the critical impingement angle of particles. The amounts of kinetic energy which have to be absorbed to remove a unit mass of material by cutting and deformation wear mechanisms have been discussed [36]. Sheldon and Kanhere [37] have provided an equation based on an energy balance between the kinetic energy of a sphere impacting normal to the surface of the target and the work done in creating the final crater dimensions in accordance with Meyer's hardness relation.

Mamoun [38] formulated a model to analytically predict material removal during spherical particle impingement using the Hertzian theory of contact and semi-empirical relationships pertaining to the fatigue life as a function of strain amplitude. He categorized the material response into six cases to consider his prediction efforts for both ductile and brittle materials. Head and co-workers [10, 39] proposed a model considering the energy transfer from (1) the impinging particles, and (2) the nature of the response of the target and the nature of the erosive media. Despite the fact that this model was develped for natural soils, it had a remarkable ability to predict particulate erosion because a parameter called modulus of toughness (similar to strain energy) was incorporated in the model. Tabakoff and his associates [40, 41] have considered both particle trajectories and erosion in turbomachinery—gas turbine and compressor—components to model solid particle erosion using the statistical nature of the impact and the rebound characteristics. The initial model was fitted with small and large impingement angle dominant mechanisms. Further development and advances of their different models have recently been discussed by Tabakoff [41].

Hutchings et al. [42] have contributed not only to an understanding of the individual mechanisms, namely, plowing, cutting I, and cutting II, but also to formulating a model based on the concept of a rigid sphere impacting normally on a rigid plastic plane. Later, Hutchings [20, 43] presented a fatigue-type model using the concept of critical fracture strain to remove an elemental volume of the target material. This model produced useful results using the dynamic hardness and the ductility of the metal.

A "localization" model has recently been proposed by Sundararajan and Shewmon [44] using the critical plastic strain criteria defined as the strain which the deformation in the target localizes, resulting in lip formation. The investigators contend that this model is superior to fatigue-type and other models proposed thus far because their model is able to demonstrate and explain the excellent correlation between the erosion rate and the thermal pressure.

Although several other investigators made modeling efforts, it would be too time consuming to discuss all of these models in this paper.

Materials, Experimental Apparatus, and Procudure

Materials. Specimens of copper, cobalt, nickel, indium, lead, magnesium, and aluminum alloy were used in this investigation. The specimens were 6 mm thick, 25 mm wide, and 37.5 mm long. Before exposure to erosion, all specimens were polished with 600-grit emery paper, then with 3-μm diamond paste, polished on a clean surface to remove any diamond paste left, and finally cleaned with distilled water and air dried.

Apparatus and Procedure. A sandblasting facility was used to impact test specimens continuously at normal incidence. Commercial grade No. 9 spherical glass beads of 20 μm average diameter and commercial grade No. 10 crushed glass of 30 μm average size were used. The particle size distribution and SEM micrographic details of the glass beads have been presented by Rao et al. [22, 24, 26]. In the sandblasting facility the distance between the specimen and nozzle (1.18 mm diameter) was 13 mm. Argon was used as the driving gas. The average jet velocity of the particles with both crushed glass and glass beads was 87 m/s. The velocities were measured by a double disk apparatus. The jet divergence was about ± 2 deg relative to the centerline and the glass bead and crushed glass flows were 0.89 and 0.22 g/s, respectively.

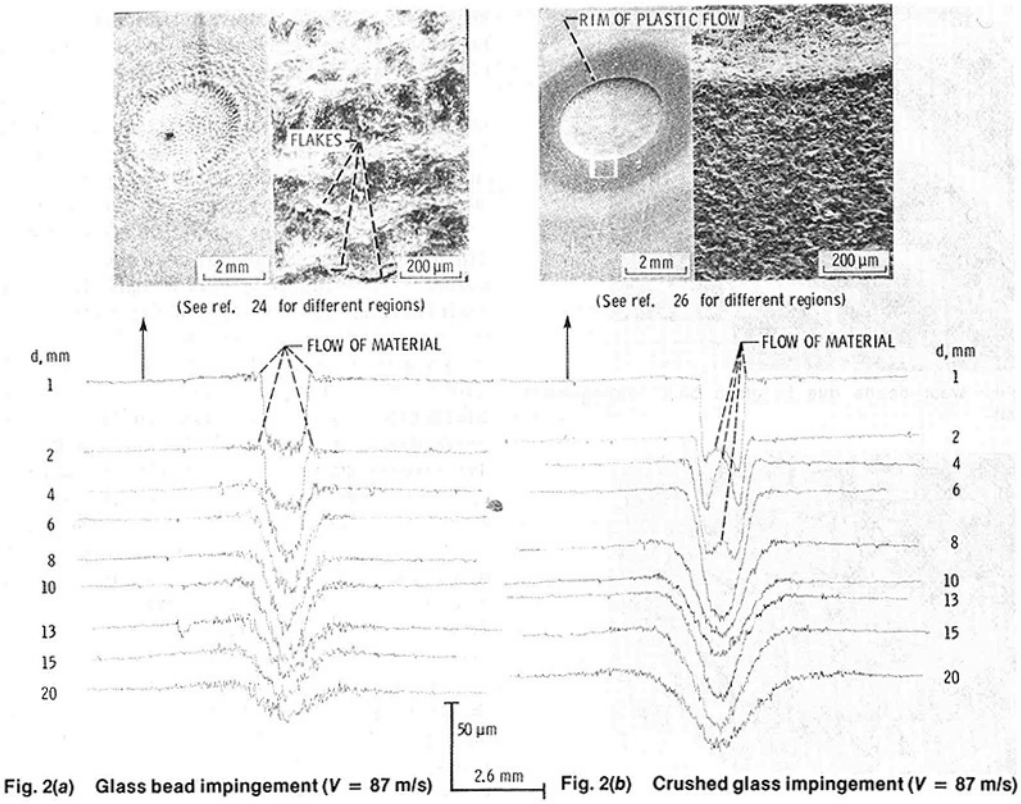

Fig. 2(a) Glass bead impingement (V = 87 m/s) Fig. 2(b) Crushed glass impingement (V = 87 m/s)

Fig. 2 Surface traces during incubation period as a function of the distance of the nozzle above the specimen surface

Profiles of the eroded surfaces were recorded with a profilometer and depths were measured with a depth gage. The eroded surfaces were observed with a scanning electron microscope (SEM) and chemical analyses were obtained by means of energy dispersive x-ray spectroscopy (EDS).

Experimental Observations

Damage and Material Debris During Incubation Period. Figure 2 presents typical profilometer traces recorded on the pure copper specimen surface after spherical glass bead and angular crushed glass impact as a function of distance d between the nozzle and the specimen. The profiles were recorded during incubation periods (2 s for crushed glass and 15 s for glass beads) for an average particle jet velocity of 87 m/s. The SEM micrographs (on top) show macroscopic (plastic) deformation and flow of the metal surface during impingement *but not strain hardening*. Figures 3(*a*) and (*b*) show individual craters on aluminum alloy surfaces during very early stages of glass bead impact. There is sufficient evidence of repeated overlapping impacts, plastic deformation and rim formation, and final "fatigue-type" failure, resulting in flake or platelet type debris (Fig. 1*a*) or extrusion type mechanism (Fig. 3*b*). The former mechanism is a manifestation of deformation wear. This is opposed to jagged, angular craters and cut surfaces with chips formed during cutting wear (Figs. 1*b* and 2*b*, SEM micrograph on the top).

Strain hardening and straining beyond elastic range of the surface layers also appear to play important roles (at advanced stages of erosion only) photographically shown in Figs. 3(*c*) and (*d*). The observations of Figs. 2 and 3 support the concept that high repetitive particle impact forces lead to plastic deformation, fracture, and final fatigue-type failure. When erodent particles strike a surface under sufficiently high contact stress (or force) they "plow" or "cut" the surface depending on the shape of the particles. The plastic deformation of top layers may, in a few cases, result in the strain softening as well.

The surface traces in Fig. 2 indicate a small material loss due to pit formation although the weight loss[5] measurements of the specimens have not shown any loss or gain of material. This contradicting result may be attributed to two factors: (1) the embedment of particles and particle dust (forming a composite layer of erodent and metal) may be more than anticipated in earlier tests [22, 24, 26] and (2) the strainhardening (Fig. 3*c*) of the surfaces of materials as discussed in [44, 45] may be extremely high so that the top thin metal layers may be of a higher density.[6]

The Concept of Energy Absorption and Material Erosion. The concepts of thermal pressure [7], specific heat × density × temperature difference between the temperature of the metal and its melting point [9], ultimate resilience [12], specific melting energy (thermal energy density) [15], mechanical energy density[7] [18], and localization model [44] using critical plastic strain have contributed to an understanding of the erosion process and characterization of erosion resistance. However, the impinging spherical and angular particles as shown in Figs. 1 and 3 and as

[5] Volume loss values were obtained by weighing specimens before and after their exposure to the erodents and dividing by density. The sensitivity of the balance was ±0.01 mg. Calculations using profile configurations in Fig. 2 indicate that volume losses vary from 0.025 to 0.085 mm^3 for glass bead impingement and from 0.027 to 0.38 mm^3 for crushed glass impingement.

[6] This momentarily increased top layer density may lead to increased weight loss in certain situations and may explain the increase in material loss during the acceleration period of erosion. Alternatively, it is also possible to believe that the material lost from the holes (seen in Fig. 2 profiles) may be compensated with the weight of the glass adhering/embedding in the surface over the entire area of impact.

[7] This is also called the strain energy per unit volume of a material in a tensile test and approximately represents the area under the curve of an engineering stress–strain curve.

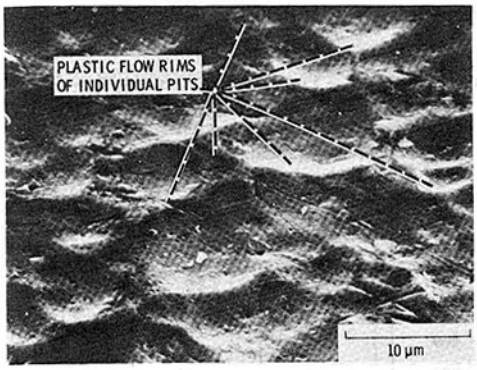

Fig. 3(*a*) Individual impacts with lips of plastically displaced metal and distorted as well as deformed surface layers on aluminum alloy surface

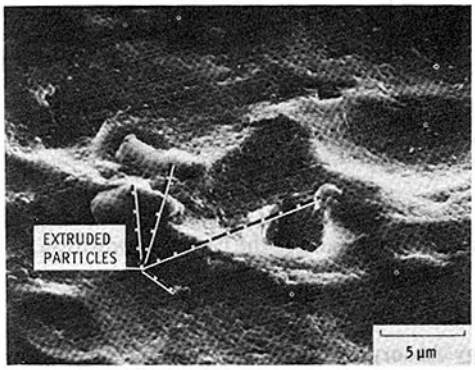

Fig. 3(*b*) Extrusion of particles on aluminum alloy surface; average particle velocity, 100 m/s; exposure time, 2.5; glass bead flow, 0.75 g/s

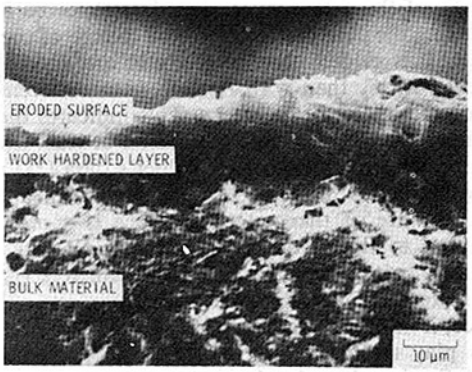

Fig. 3(c) Work-hardened layer at bottom of crater formed by erosion of annealed 6061 aluminum alloy; etched with a 5Δ HF (48Δ), 10Δ H_2SO_4

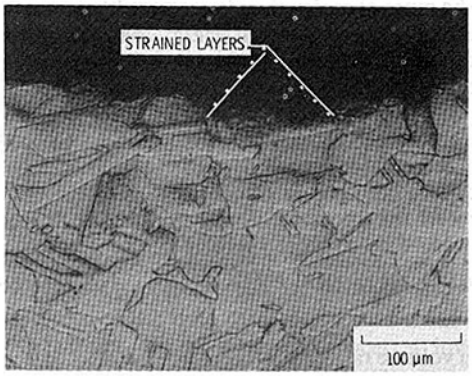

Fig. 3(*d*) Strained layers on pure OFHC copper surface during glass bead impingement

Fig. 3 SEM micrographs and optical photograph during the initial and advanced stages of damage and erosion

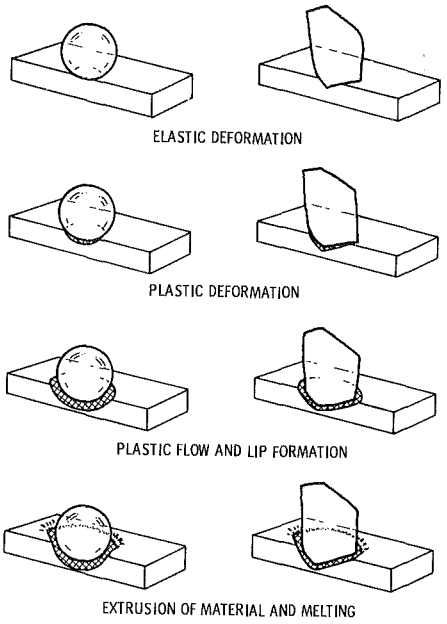

Fig. 4(*a*) Spherical particle impingement

Fig. 4(*b*) Angular particle impingement

Fig. 4 Different forms of failure modes during solid particle impingement

schematically shown in Fig. 4 are assumed to induce different deformation modes, namely, (1) elastic deformation, (2) plastic deformation, (3) plastic flow and lip formation, and (4) extrusion of material and possible melting (failure and splashing), resulting in material loss. Most of the time, the volume of the crater induced by an impact is not equal to the volume loss. This is due mainly to the fact that material deforms plastically and flows as a lip (Figs. 1*a*, 3*a*, and 3*b*).

The failure modes in Fig. 4 and the micrographs in Figs. 2 and 3 demonstrate that a single mechanism cannot completely account for the cumulative damage and final material removal. Typically elastic penetration occurs for spherical particles whereas with angular particles plastic penetration occurs possibly resulting in residual stresses. Hence, the volume loss measurement is an index of material erosion damage and it represents a part of total energy absorption efficiency of a material (to a first order approximation) during solid particle impingement. Thus, the erosion rate and material property (at a constant velocity, particle size shape and concentration and angle of impingement) is represented as

$$(\text{erosion volume rate})(\text{material property})^n \propto \text{constant} \quad (1)$$

This constant takes care of the velocity relationship,[8] the size, shape, and concentration of particles, and the angle of impact.

It is believed that only a part of the kinetic energy[9] from the impinging particles is absorbed by the surface of the material to cause damage and material removal. It was mentioned by Hutchings [20] that the energy balance during the particle impingement is as follows: 1–10 percent of the kinetic energy may rebound, 1–5 percent may be dissipated as elastic wave energy, and 90 percent may be dissipated in plastic work (>80

[8] Parametric studies from the literature have indicated that erosion rate varies as (velocity)^{2p} where p is the factor accounting for the deviations of experimental velocity exponent. An excellent explanation as to why $p > 1$ was provided by Finnie et al. [23]. The theory, however, indicated a value of $p = 1$.

[9] Erosive damage is sometimes a cumulative effect of series of impacts that do not individually produce any deformation visible under an optical microscope, but such impacts produce small increments of nucleation and expansion of dislocations in the crystalline structure surrounding the area of impact. These latter events interact to form cracks and eventually result in a low-cycle fatigue-type failure.

Table 2 Correlations of energy properties with erosion*

[(Erosion rate)(P_R or U or Se)^n = A.
P_R = proof resilience = $Y^2/2E$; U – ultimate resilience = $T^2/2E$; Se = strain energy = $(T+Y)\epsilon\ell/2$; Y = yield stress; T = tensile strength; E = elastic modulus; $\epsilon\ell$ = elongation; V = particle velocity; θ = angle of impingement.]

Energy property	Correlation parameter	Tadolder [21] data; quartz sand; V = 82 m/s; θ = 45	Finnie, et al. [3] data; SiC (250 μm size)				
			V = 136 m/s; θ = 20	V = 76 m/s; θ = 20	V = 76 m/s; θ = 30	V = 76 m/s; θ = 50	V = 76 m/s; θ = 90
Proof resilience, P_R	Corr. coef. R	0.977	0.734	0.702	0.647	0.548	0.431
	Exponent n	0.62	0.38	0.349	0.37	0.25	0.17
	Constant A	401	1943	469	546	208	89
Ultimate resilience, U	Corr. coef. R	0.995	0.76	0.733	0.571	0.444	0.341
	Exponent n	0.59	0.41	0.38	0.357	0.22	0.15
	Constant A	904	3713	862	785	239	96
Strain energy, Se	Corr. coef. R	0.996	0.971	0.955	0.94	0.874	0.837
	Exponent n	0.816	0.737	0.695	0.65	0.49	0.41
	Constant A	1568	8945	2037	1748	540	231

*All correlations were carried out using the units of erosion rate as mm^3/kg.

All values of Se are calculated using the relationship $S_e = (T+Y)\epsilon\ell/2$ for the condition described in Table 3. It is always necessary to calculate the nearest material properties to match the available extensive erosion data. It is further possible that by changing the processing history (e.g., strainhardening versus annealing) or alloy content (e.g., different steels with various heat treatments) of material, the values of P_R, U and Se change, but not the erosion behavior. The SEM micrographs in Fig. 3 clearly show all different modes such as plastic deformation, flow, strainhardening, extrusion, etc., of the erosion processes taking place during particle impingement. Hence, all three parameters P_R, U and Se are considered in order to understand their relative contribution.

percent heat and < 10 percent stored energy). It is the last part of the energy responsible for material removal.

SEM micrographs in Figs. 2 and 3 further demonstrate that different energy absorption characteristics[10] contribute to the cumulative damage to final material removal as schematically represented in Fig. 4, i.e., by (1) elastic deformation (and wave dissipation), (2) plastic deformation, and (3) fracture. In order to investigate the energy absorption characteristics and their contribution as well as relation to erosion, a simple relation of the following type is used (keeping size, shape and concentration of particles and velocity of impact constant)

$$(\text{Erosion rate})(P_R \text{ or } U \text{ or } S_e)^n = A \qquad (2)$$

where A is a constant for a given set of experimental conditions. When a particle impinges on a surface, depending on the energy absorption of the material and considering characteristics of the energy absorption in Fig. 4, the following conditions exist resulting in different deformations: *condition* (*a*) $0 \le E_p \le P_R$ (only elastic deformation); *condition* (*b*) $P_R \le E_p \le U$ (only plastic deformation); *condition* (*c*) $U \le E_p \le S_e$ (failure only by fracture); *condition* (*d*) $0 \le E_p \le U$ (elastic and plastic deformations); *condition* (*e*) $0 \le E_p \le S_e$ (elastic and plastic deformations and fracture); *condition* (*f*) $E_p \ge S_e$ (complete ductile fracture). Here E_p is the energy stored (including heat generation),[11] P_R the proof resilience ($= Y^2/2E$), U the ultimate resilience ($= T^2/2E$), S_e the strain energy to failure ([$(T + Y)\epsilon 1/2$]), Y the yield strength, T the tensile strength, E the elastic modulus, and $\epsilon 1$ the percent elongation.

Correlations

Energy Absorption Properties. In this section correlations were carried out using material (strain) energy properties P_R, U, and S_e and the relationship in equation (2). Table 2 presents the statistical parameters obtained using the least-squares fit of the extensive erosion data reported earlier [3, 21] including the data pertaining to the change of the angle of incidence. It is evident that correlations are good and more consistent with S_e than with P_R and U at different particle velocities and angles of incidence. This indicates that (1) the energy input per unit volume of erosion at least exceeds P_R and U in a majority of cases (Tadolder's data [21] indicated best correlations wth all the three parameters), and (2) the complete failure of the material surface is a *major* factor contributing to the material loss. Hence, S_e provides best correlations as it is the largest of the parameters P_R, U, and S_e. Ultimate resilience U is good for certain sets only (Table 2). Hence, it intuitively indicates that elastic and plastic strain energies play relatively *less* significant roles as elastic and plastic deflections in a simple tension test may be a negligible portion of the total failure energy (see footnote of Table 2). These correlations also suggest that the erosion process appears to be more complex than it was considered earlier.

Attempts to correlate strain energy with erosion rate have been moderately successful [18, 35]. Ultimate resilience was suggested by Eyre [12] for solid particle impingement erosion (Table 1). The concepts of strain energy and ultimate resilience were, however, originally proposed by Thiruvengadam [46] and Hobbs [47], respectively, for cavitation and liquid impingement erosion.

In view of the abovementioned limitations, it may be advisable to consider a relation similar to

$$(\text{Erosion volume rate})[A_1 P_R^{n1}] + A_2 U^{n2} + A_3 S_e{}^{n3}] = \text{constant} \qquad (3)$$

or

$$(\text{Erosion volume rate})[P_R^{n1} + U^{n2} + S_e{}^{n3}] = A \qquad (4)$$

in order to further understand the individual contributions of elastic, plastic and failure strain energies involved in the cumulative erosion process at different velocities of impact, angle of impingement, and sizes and shapes of particles.

[10] Under three modes the energy absorption expressions can be calculated in a simple tensile test using proof resilience P_R [(yield stress)^2/(2 × elastic modulus)], ultimate resilience U [(tensile strength)^2/(2 × elastic modulus)], and strain energy S_e (work done to cause failure = area under the stress–strain curve). The relative contributions of these parameters in determining damage depend upon the impact velocity, particle size, concentration, and shape, angle of impingement, and material properties (such as yield stress, ductility, tensile strength, and elastic modulus). The erosion process depends upon the strain rate, contact time and area, local melting, deformation depth and area. The resulting erosion is thus a cumulative effect of all these factors.

[11] The energy absorption efficiency may be calculated in one of the following two ways: (1) by obtaining absorbed efficiency in the form of material damage on different materials (during incubation period), calculating the total plastic work (heat and stored energy), and parametrically changing the variables, namely, the impact velocity, the size, shape of particles, and angle of impact; (2) by calculating the ratio of energy required for the erosion volume on the material surface to the total energy imparted to the surface. The latter method appears to be approximate as the energy caused for material removal is much more than the energy required for plastic work. A novel dislocation etching technique may be worthwhile to pursue.

Table 3 Correlations of material properties with solid particle erosion*

[(Erosion rate)(material property)^n = A.
V = particle velocity; θ = angle of impingement; α = coefficient of expansion; K = bulk modulus; $\Delta T = T_m - T_{atm}$; T_m = melting point; T_{atm} = temperature of specimen; C_p = specific heat at constant pressure; ρ = density.]

Property	*Parameter*	Tadolder [21] data; quartz sand; V = 82 m/s; $\theta = 45°$	Finnie, et al. [3] data; SiC (250 μm size)				
			V = 136 m/s; $\theta = 20°$	V = 76 m/s; $\theta = 20°$	V = 76 m/s; $\theta = 30°$	V = 76 m/s; $\theta = 50°$	V = 76 m/s; $\theta = 90°$
Surface energy	Constant A	141	988	256	230	126	73
	Exponent n	1.77	1.50	1.42	1.26	1.00	0.92
	Corr. coef. R	0.965	0.965	0.957	0.981	0.946	0.934
Hardness	Constant A	1284	9920	2405	2.03×10^3	1332	766
	Exponent n	0.76	0.74	0.71	0.71	0.60	0.54
	Corr. coef. R	0.985	0.910	0.844	0.844	0.697	0.552
Melting point	Constant A	1.87×10^5	1.68×10^6	3.96×10^5	7.04×10^5	2.09×10^5	9.91×10^4
	Exponent n	1.17	1.16	1.14	1.20	1.07	1.01
	Corr. coef. R	0.956	0.933	0.923	0.905	0.789	0.659
Elastic modulus	Constant A	1.29×10^4	9.74×10^4	2.20×10^4	1.82×10^4	5.93×10^3	2.74×10^3
	Exponent n	1.14	1.09	1.06	1.01	0.83	0.73
	Corr. coef. R	0.898	0.885	0.871	0.824	0.666	0.519
Bulk modulus	Constant A	7.42×10^4	3.33×10^5	8.03×10^4	7.38×10^4	2.67×10^4	1.37×10^4
	Exponent n	1.51	1.35	1.34	1.32	1.17	1.09
	Corr. coef. R	0.942	0.937	0.936	0.905	0.782	0.647
Coefficient of thermal expansion	Constant A	2.88×10^8	3.18×10^8	6.41×10^7	1.34×10^8	2.50×10^6	9.45×10^4
	Exponent n	−1.38	−1.18	−1.15	−1.19	−0.87	−0.61
	Corr. coef. R	−0.831	−0.652	−0.641	−0.652	−0.464	−0.288
Cohesive energy	Constant A	1.43×10^5	3.26×10^6	7.28×10^5	5.62×10^5	1.02×10^5	3.05×10^4
	Exponent n	1.33	1.45	1.44	1.39	1.15	0.99
	Corr. coef. R	0.746	0.765	0.766	0.768	0.636	0.477
Atomic volume	Constant A	2.04×10^6	7.42×10^7	1.41×10^7	5.21×10^8	1.75×10^8	1.75×10^8
	Exponent n	−2.28	−2.57	−2.52	−3.37	−3.20	−3.35
	Corr. coef. R	−0.754	−0.873	−0.863	−0.861	−0.798	−0.744
Metal-metal bond energy	Constant A	3.58×10^6	7.57×10^4	1.74×10^4	2.21×10^4	4.60×10^3	1.14×10^3
	Exponent n	1.50	1.11	1.10	1.11	0.82	0.57
	Corr. coef. R	0.822	0.640	0.638	0.653	0.473	0.291
Specific melting energy	Constant A	233	2077	535	*363	178	101
	Exponent n	+0.94	0.94	0.91	0.71	0.55	0.51
	Corr. coef. R	0.973	0.950	0.933	0.947	0.896	0.883
$C_p \rho \Delta T$	Constant A	4.46×10^{10}	1.26×10^{10}	3.58×10^9	2.04×10^{10}	1.12×10^9	1.08×10^8
	Exponent n	0.863	0.71	0.71	0.779	0.67	0.59
	Corr. coef. R	0.897	0.819	0.828	0.827	0.696	0.539
$\alpha K \Delta T$ (Coefficient of thermal expansion × bulk modulus × temperature differential)	Constant A	87.18	7.4×10^2	1.98×10^2	1.99×10^2	1.42×10^2	1.05×10^2
	Exponent n	1.04	0.93	0.92	0.98	0.93	0.94
	Corr. coef. R	0.971	0.991	0.989	0.978	0.906	0.808
Ultimate resilience × hardness	Constant A	1.06×10^3	5.9×10^3	1.33×10^3	9.68×10^2	2.90×10^2	1.22×10^2
	Exponent n	0.336	0.303	0.284	0.257	0.176	0.139
	Corr. coef. R	0.999	0.990	0.982	0.950	0.894	0.829
(Debye temperature)^2 × atomic weight	Constant A	1.27×10^{11}	9.52×10^{11}	1.74×10^{11}	2.12×10^{11}	5.65×10^9	4.54×10^8
	Exponent n	1.35	1.34	1.31	1.32	1.11	0.97
	Corr. coef. R	0.827	0.852	0.842	0.841	0.692	0.536

*All correlations were carried out using the units of erosion rate as mm^3/kg.

The heat treatment conditions have been explained in detail in Refs. 3 and 21. For Finnie et al. [3] data, the condition of the metal surface (heat treatment or as received condition) is identical at both velocities (136 and 76 m/s at $\theta = 20°$) and various angle of impingement ($\theta = 20°$, 30°, 50°, and 90°) conditions. Thus, Al was annealed at 700 °F for 60 min; Ag annealed at 900 °F for 60 min; Bi annealed at 450 °F for 60 min; Cd as received; Cu annealed at 1050 °F for 60 min; Fe as received (annealed); Pb (unknown); Mg annealed at 700 °F for 60 min; Mo as received (annealed); Ni as received; Sn annealed at 212 °F for 60 min; Ta as received (annealed); and W as received (annealed) [3].

Other Material Property Correlations. The main purpose of the correlations is to characterize the erosion resistance of various metals with some known energy and strength properties. Most of the time, it is necessary for the material property to exhibit all the complex processes involved in deformation or cutting erosion, yet be simple and straightforward in order to be used by design engineers. Since there is no universally accepted property to estimate erosion precisely, attempts are made in this section to explore the best material properties for correlations.

Table 3 presents statistical parameters obtained for the correlations of the extensive erosion data [3, 21] with various properties. (Heat treatment conditions are mentioned as a footnote in Table 3.) The properties considered are surface energy S, yield stress Y, tensile strength T, density ρ, hardness H, melting point T_m, elastic modulus E, bulk modulus K, coefficient of expansion α, cohesive energy Ce, atomic volume A_v, metal-metal bond energy $b(M\text{-}M)$, specific melting energy S_{me}, $C_p \rho \Delta T$, $\alpha K \Delta T$, UH, and (Debye temperature)^2 × atomic weight, $[\theta_0^s]^2 A_n$. The majority of

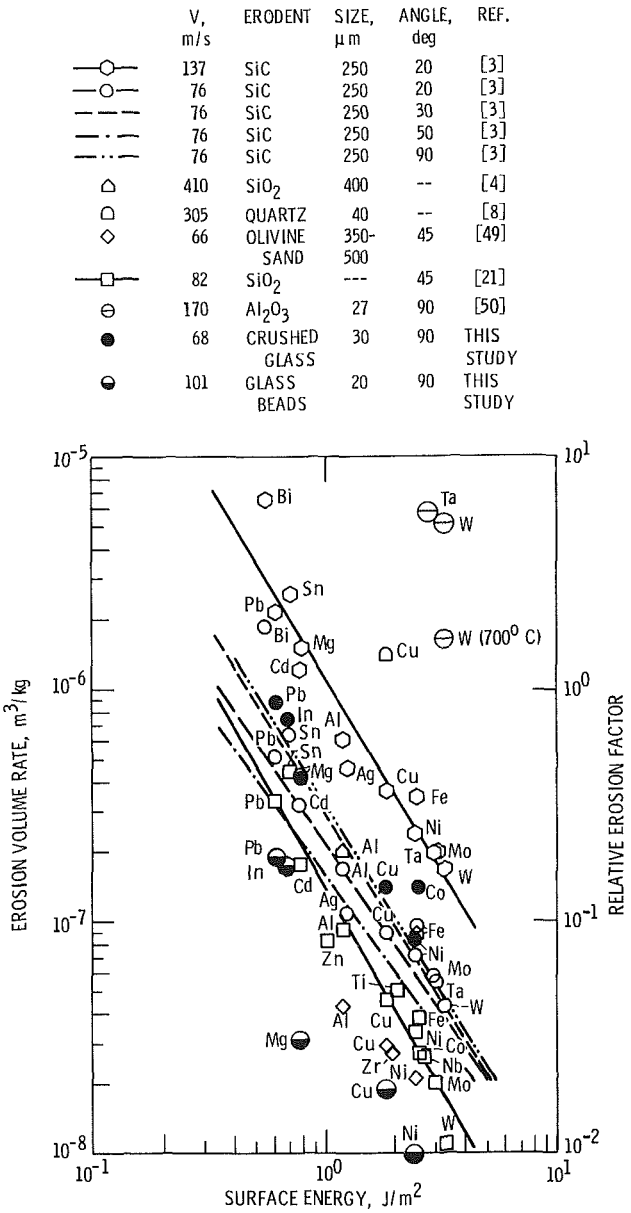

Fig. 5 Erosion rates of different metals as a function of surface energy

properties[12] were obtained from [3, 21, 48]. Data pertaining to different angles of impingement are also presented in this table.

With single properties, S, S_{me}, T_m, K, Se, H, and A_v are good for correlating erosion rates of metals (Tables 2 and 3). Most properties become less significant in representing erosion as the angle of impingement reaches 90 deg. However, S, S_{me}, A_v, and S_e seem to better represent the data even at this impingement condition than other properties.

The melting point [6] and specific melting energy [15] have been successfully correlated with erosion as explained in the introduction (Table 1). The effect of material properties on cutting erosion has been explained very clearly by Finnie et al. [23]. For certain groups of metals it is observed in the literature that $Y \propto H$ and $T \propto H$. While some sets of erosion data exhibited good correlations with H (Table 3), it is rather

[12] The properties of metals obtained depend on (1) the purity of the metal, (2) the surface treatment used, (3) the type of device employed, and (4) the method adopted for evaluation. Hence, it is necessary to assess metal properties more precisely.

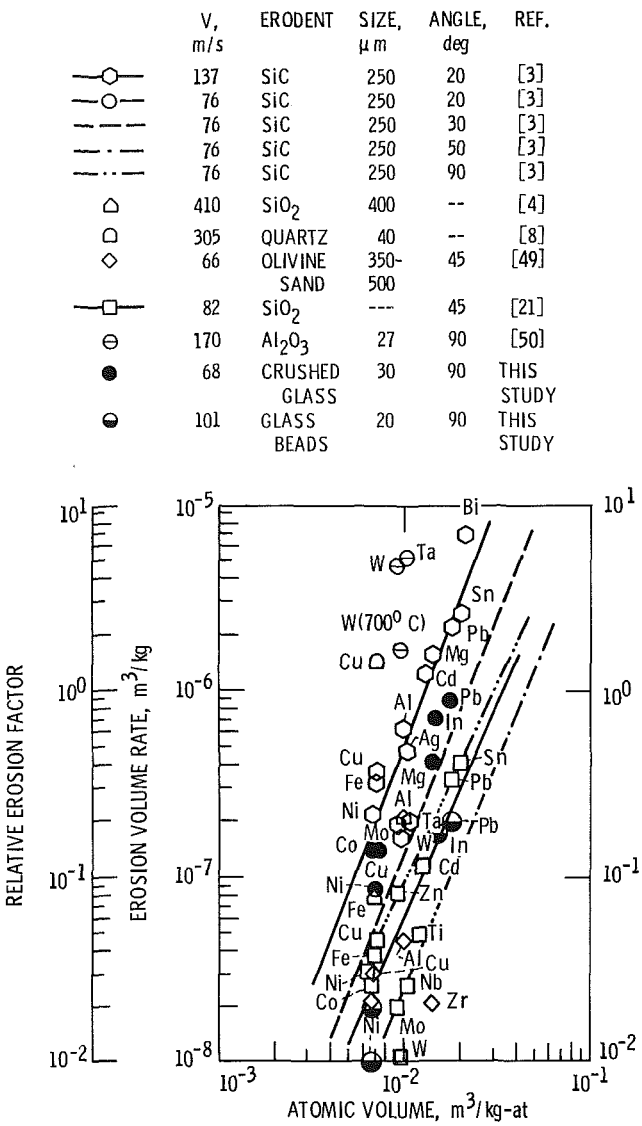

Fig. 6 Erosion rates of different metals as a function of atomic volume

surprising that P_R $(=Y^2/2E)$ and U $(=T^2/2E)$ are not *completely* successful at all impingement angles.

Multiple (products of) properties, thermal pressure $(\alpha K \Delta T)$, UH, $[\theta_0^s]^2 A_n$, and $C_p \rho \Delta T$ are listed in decreasing order of merit. There is good correlation with thermal pressure compared to other properties even at normal incidence.

Ranking of Metals and Correlation Trends. Figures 5 and 6 present data typical of the erosion rate of several metals as a function of S and A_v which were proposed by the present investigators. These figures show the permissible data scatter and the good correlation characteristics. The least-square lines of the curve fit for 30, 50, and 90 deg angle impingement were the only ones plotted omitting the data points. The data obtained by the present authors[13] and others [4, 8, 49, 50] are also presented. The good correlation with T_m, S_{me}, and S_e (Tables 2 and 3) support the *possible* melting and flow of the material surface.

Figure 7 presents a plot of erosion rate as a function of thermal pressure. It is to be remembered that thermal pressure contains both K and T_m (which are good correlating single

[13] Correlations were not obtained as only six metals were examined. The data points, however, indicate agreement with the general trend.

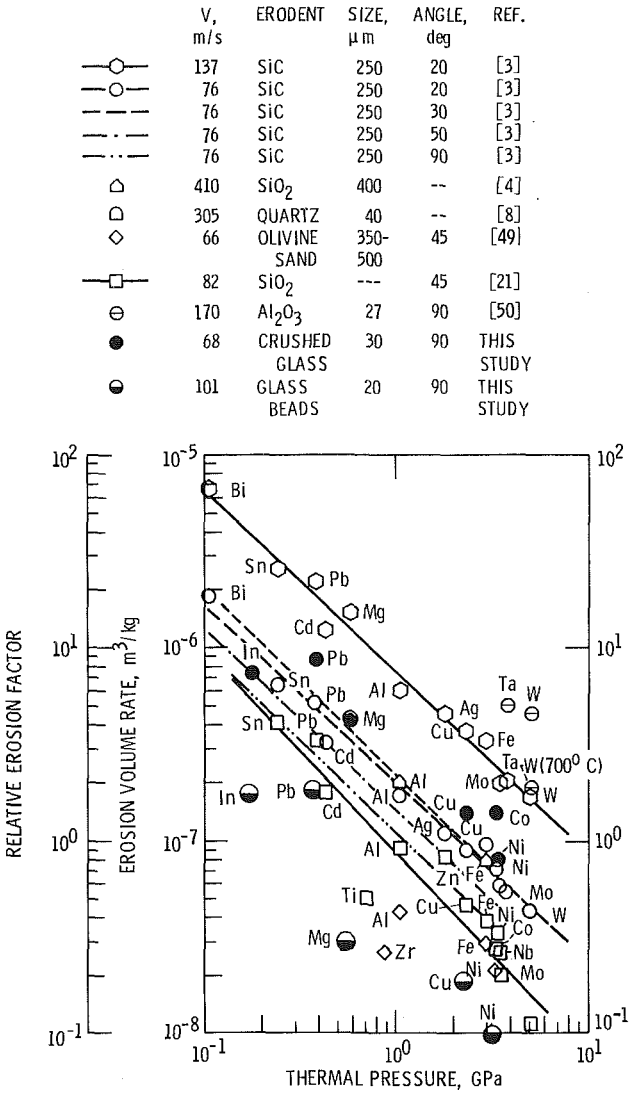

Fig. 7 Erosion rates of different metals as a function of thermal pressure

properties to represent erosion). *UH* is not much superior to *U* and *H* considered individually.

From the good correlation of properties of materials, the following inferences can be made: (1) The erosion process is either strain energy and/or thermal energy related resulting in ductile tearing or a local melting process; (2) the energy absorption capability of the material surface is always related to the erosion damage process but does not fully represent the erosion behavior; and (3) correlations are equally good for the cutting and deformation wear processes. At this juncture it is logical to assume that both fracture and thermal energy properties are interrelated during the complex erosion process.

The good correlation of erosion rate with A_v indicates that the damage process is submicroscopic in nature. Further, it is necessary to attempt to correlate other properties such as stacking fault energy and surface energy which have been successfully correlated with some forms of erosion and wear.

Erosion Resistance. It is generally observed that the erosion rates of different metals from Bi to W vary by two orders of magnitude. Despite this fact S, A_v, and S_{me}, which vary only by one order of magnitude, are better correlating properties than Ce, $b(M\text{-}M)$, ρ, α, and $C_p\rho\Delta T$.

Discrepancies in Earlier Correlations. The main reasons for the disagreement of property correlations proposed by earlier investigators [1–18] are the following: (1) Most of the earlier investigators used erosion data at 20 deg incidence [3] (a detailed statistical analysis as presented (in Tables 2 and 3) here clearly shows the importance of various properties as the angle of impingement changes); (2) data for pure metals and alloys were not separated; (3) material properties except hardness were not obtained at the time of testing; (4) the majority of correlation studies were done with angular particles (in which cutting wear predominates) except by Jennings et al. [10], Hutchings [20], and the present investigators; (5) some metals, for example, Bi and W, exhibited brittle-type metal failure similar to glass [3] instead of ductile type failure; (6) the entire spectrum of materials was not considered; and (7) the groupings of metals tested and correlated by various investigators were different.

Exponents and Coefficients. To estimate the magnitude of untested metals using equation (2), both A and n are necessary. It is evident from Tables 2 and 3 that the exponent n in most cases decreases as the angle of impingement θ increases. In the relationshp

$$n = b(\sin\theta_M/\sin\theta)^q \tag{5}$$

the exponent q values for the best properties are as follows: S, 2.3; H, 3.3; T_m, 5.1; K, 4.6; S_{me}, 1.8; Se, 1.2; and $\alpha K\Delta T$, 1.2. θ_m is the angle of impingement corresponding to maximum erosion condition. The n values obtained are fairly constant and match well with the two sets of data used [3, 21] and our own data points (Figs. 5–7).

The values of constants A also decrease as the value of θ increases from peak erosion condition (15 to 30 deg) to normal incidence (90 deg) except for A_v and $[\theta_0^s]^2 A_w$. Studies indicate that the A values appear to vary with θ and V as $[\sin\theta_m/\sin\theta]^m V^{2p}$ (p varied from 1 to 7/4 for best properties). The exponent values of m for the best properties are as follows: S, 0.78; H, 0.71; A_v, 0.52; K, 0.53; T_m, 0.45; S_{me}, 0.63; Se, 0.55; and $\alpha K\Delta T$, 1.43. Hence the final equation may take the form

$$(\text{erosion rate})(\text{material property})^n \alpha\ V^{2P}(\sin\theta_M/\sin\theta)^m \tag{6}$$

Conclusions

1 Energy absorption characteristics do not fully represent the erosion behavior of a metal.

2 Analyses of extensive data indicate that surface energy, strain energy, atomic volume, melting point, bulk modulus, specific melting energy, and hardness exhibit good correlation with erosion. However, only surface energy, specific melting energy, atomic volume, and strain energy provide good correlations at different angles of impact. Of the product parameter groups, thermal pressure (coefficient of thermal expansion × bulk modulus × melting point differential) is found to be the best parameter for correlation with erosion rate followed by ultimate resilience × hardness, and (Debye temperature)^2 × atomic weight.

3 The exponents n and coefficients A in most cases decreased as the angle of impingement θ increases. The n values generally appear to vary as $(\sin\theta_M/\sin\theta)^q$ and the A values as $V^{2p}(\sin\theta_M/\sin\theta)_m$. In this study, $5/4 \le q \le 5$, $1 \le p \le 7/4$, and $1/2 \le m \le 1.4$ depending on the property.

References

1 Wood, C. D., and Espenschade, P. W., "Mechanism of Dust Erosion," *SAE Transactions*, Vol. 73, 1965, pp. 515–523.

2 Brauer, H., and Kriegel, E., "Verschleiss von Rohrkrummern beim pneumatischen und hydraulischen Feststofftransport (Erosion of Pipe Bends in

Pneumatic and Hydraulic Solid Transport)," *Chemie. Ingenieur Tech.*, Vol. 37, 1965, pp. 265–276.

3 Finnie, I., Wolak, J., and Kabil, Y., "Erosion of Metals by Solid Particles," *Journal of Materials*, Vol. 2, No. 3, Sept. 1967, pp. 682–700.

4 Kayser, W., "Erosion by Solid Bodies," *Proceedings of 2nd Meersburg Conference on Rain Erosion and Allied Phenomena*, ed. A. A. Fyall and R. B. King, Royal Aircraft Establishment, Farnborough, England, 1967, pp. 427–447.

5 Tilly, G. P., "Erosion Caused byAirborne Particles," *Wear*, Vol. 14, July 1969, pp. 63–79.

6 Smeltzer, C. E., Gulden, M. E., and Compton, W. A., "Mechanisms of Metal Removal by Impacting Dust Particles," *Journal of Basic Engineering*, Vol. 92, No. 3, Sept. 1970, pp. 639–654.

7 Ascarelli, P., "Relation Between the Erosion by Solid Particles and the Physical Properties of Metals," AMMRC-TR-71-47, Army Materials and Mechanics Research Center, Watertown, MA, Nov. 1971, (AD-738162).

8 Tuitt, D. A., "Erosion Tests of Metallic Coatings," *Proceedings of the 4th International Conference on Rain Erosion*, ed. A. A. Fyall and R. B. King, Royal Aircraft Establishment, Farnborough, England, 1974, pp. 677–699.

9 Hutchings, I. M., "Prediction of the Resistance of Metals to Erosion by Solid Particles," *Wear*, Vol. 35, 1975, pp. 371–374.

10 Jennings, W. H., Head, W. J., and Mannings, C. R., "A Mechanistics Model for the Prediction of Ductile Erosion," *Wear*, Vol. 40, No. 1, Oct. 1976, pp. 93–112.

11 Vijh, A. K., "Resistance of Metals to Erosion by Solid Particles in Relation to the Solid State Cohesion of Metals," *Wear*, Vol. 39, No. 1, Aug. 1976, pp. 173–175.

12 Eyre, T. S., "Wear Characteristics of Metals," *Tribology International*, Vol. 9, No. 5, Oct. 1976, pp 203–212.

13 Sheldon, G. L., "Effects of Surface Hardness and Other Material Properties on Erosive Wear of Metals by Solid Particles," *Journal of Engineering Materials and Technology*, Vol. 99, No. 2, Apr. 1977, pp. 133–137.

14 Jones, M. H., and Lewis, R., "Solid Particle Erosion of a Selection of Alloy Steels," *Proceedings of 5th International Conference on Erosion by Solid and Liquid Impact*, Cambridge University, Cambridge, England, 1979, Paper No. 52.

15 Malkin, S., "Correlation Between Solid Particle Erosion of Metals and Their Melting Energies," *Wear*, Vol. 68, No. 3, May 1981, pp. 391–396.

16 Söderberg, S., Hogmark, S., and Swahan, H., "Mechanisms of Material Removal During Erosion of a Stainless Steel," *ASLE Transactions*, Vol. 26, No. 2, Apr. 1983, pp. 161–172.

17 Buckley, D. H., "Importance and Definition of Materials in Tribology," International Tribology Conference, NASA Lewis Research Center, Apr. 18–21, 1983.

18 Rickerby, D. G., "Correlation of Erosion with Mechanical Properties in Metals," *Wear*, Vol. 84, No. 3, Feb. 1983, pp. 393–395.

19 Levy, A. V., "The Role of Plasticity in Erosion," *Proceedings of 5th International Conference on Erosion by Solid and Liquid Impact*, Cambridge University, Cambridge, England, 1979, Paper No. 39.

20 Hutchings, I. M., "A Model for the Erosion of Metals by Spherical Particles at Normal Incidence," *Wear*, Vol. 70, No. 3, Aug. 1981, pp. 269–281.

21 Tadolder, Y. A., "Influence of Abrasive Grain Geometry on the Solid Particle Erosion of Metals," *Tr. Tallin Politekh Inst.*, Series A., Vol. 237, 1966, pp. 15–22.

22 Rao, P. V., Young, S. G., and Buckley, D. H., "A Study of the Nature of Solid Particle Impact and Shape on the Erosion Morphology of Ductile Metals," NASA TM-82933, July 1982; *J. Microscopy*, Vol. 135, part 1, July 1984, pp. 49–59.

23 Finnie, I., Levy, A., and McFadden, D. H., "Fundamental Mechanisms of the Erosive Wear of Ductile Metals by Solid Particles," *Erosion: Prevention and Useful Applications*, ed. W. F. Adler, ASTM STP 664, American Society for Testing and Materials, Philadelphia, PA, 1979, pp. 36–58.

24 Rao, P. V., Young, S. G., and Buckley, D. H., "Morphology of Ductile Metals Eroded by a Jet of Spherical Particles Impinging at Normal Incidence," *Wear*, Vol. 85, No. 1, Mar. 1983, pp. 223–227.

25 Ruff, A. W., "Debris Analysis of Erosive and Abrasive Wear," *Fundamentals of Tribology*, ed. N. P. Suh and N. Saka, MIT Press, Cambridge, MA, 1980, pp. 877–885.

26 Rao, P. V., Young, S. G., and Buckley, D. H., "Morphology of an Aluminum Alloy Eroded by a Jet of Angular Particles Impinging at Normal Incidence," NASA TP 2139, May 1983.

27 Brown, R., and Edington, J. W., "Mechanisms of Material Loss During the Threshold Period of Erosion by Solid Particles," *Wear*, Vol. 77, No. 3, Apr. 1982, pp. 347–353.

28 Ruff, A. W., and Wiederhorn, S. M., "Erosion by Solid Particle Impact," *Treatise on Materials Science and Technology*, Vol. 16, Materials Erosion, ed. C. M. Preece, Academic Press, New York, 1979, pp. 69–126.

29 Adler, W. F., "Assessment of the State of Knowledge Pertaining to Solid Particle Erosion," ETI CR 79-680, Effects Technology, Inc., Santa Barbara, CA, June 1979 (AD-A073034.)

30 Tilly, G. P., "Erosion by Impact of Solid Particles," *Treatise on Materials Science and Technology*, Vol. 13, ed. D. Scott, Academic Press, New York, pp. 287–319.

31 Schmitt, G. J., Jr., "Liquid and Solid Particle Impact Erosion," *Wear Control Handbook*, ed. M. B. Peterson and W. O. Winer, ASME, New York, 1980, pp. 231–282.

32 Finnie, I., "The Mechanism of Erosion of Ductile Metals," *Proceedings 3rd National Congress on Applied Mechanics*, ASME, New York, 1958, pp. 527–532; see also "Erosion of Surfaces by Solid Paticles," *Wear*, Vol. 3, 1960, pp. 87–103.

33 Finnie, I., Levy, A., and McFadden, D. H., "Fundamental Mechanisms of the Erosive Wear of Ductile Metals by Solid Particles," *Erosion: Prevention and Useful Applications*, ASTM STP 664, ed. W. F. Adler, American Society for Testing and Materials, Philadelphia, 1979, pp. 36–58.

34 Bitter, J. G. A., "A Study of Erosion Phenomena, Parts I and II," *Wear*, Vol. 6, 1963, pp. 5–21, 169–190.

35 Wood, C. D., and Hafer, C. A., "Dust Research Studies," AR-572, Southwest Research Institute, San Antonio, TX, Feb. 1966.

36 Neilson, J. H., and Gilchrist, A., "Erosion by a Stream of Solid Particles," *Wear*, Vol. 11, 1969, p. 111–122.

37 Sheldon, G. L., and Kanhere, A., "An Investigation of Impingement Erosion Using Single Particles," *Wear*, Vol. 21, 1972, pp. 195–209.

38 Mamoun, M., "Analytical Models for the Erosive Corrosive Wear Process," Rept. ANL-75-XX-2, 1975, Appendix I, Argonne National Laboratory, IL, 1975.

39 Head, W. J., and Harr, M. E., "The Development of a Model to Predict the Erosion of Materials by Natural Contaminants," *Wear*, Vol. 15, 1970, pp. 1–46; Head, W. J., Lineback, L. D., and Manning, C. R., "Modification and Extension of a Model for Predicting the Erosion of Ductile Materials," *Wear*, Vol. 23, 1973, pp. 291–298.

40 Grant, G., and Tabakoff, W., "Erosion Prediction in Turbomachinery Resulting From Environmental Solid Particles," *Journal of Aircraft*, Vol. 12, No. 5, May 1975, pp. 471–478; Kotwal, R., and Tabakoff, W., "A New Approach for Erosion Prediction Due to Fly Ash," ASME JOURNAL OF ENGINEERING FOR POWER, Vol. 103, No. 2, Apr. 1981, p. 265–270.

41 Tabakoff, W., "Performance Deterioration on Turbomachinery With Presence of Solid Particles," *Particulate Laden Flows in Turbomachinery*, ed. W. Tabakoff, C. T. Crowe, and D. B. Cale, ASME, New York, 1982, pp. 3–22.

42 Hutchings, I. M., Winter, R. E., and Field, J. E., "Solid Particle Erosion of Metals: The Removal of Surface Material by Spherical Projectiles," *Proceedings, Royal Society, London*, Series A, Vol. 348, No. 1654, Mar. 9, 1976, pp. 379–392; Hutchings, I. M., "Mechanisms of the Erosion of Metals by Solid Particles," *Erosion: Prevention and Useful Applications*, ASTM STP 664, ed. W. F. Adler, American Society for Testing and Materials, Philadelphia, 1979, pp. 59–76.

43 Hutchings, I. M., "Some Comments on the Theoretical Treatment of Erosive Particle Impacts," *Proceedings of 5th International Conference on Erosion by Solid and Liquid Impact*, Cambridge University, Cambridge, England, 1979, Paper No. 36.

44 Sundararajan, G., and Shewmon, P. G., "A New Model for the Erosion of Metals at Normal Incidence," *Wear*, Vol. 84, No. 2, Jan. 1983, pp. 237–258.

45 Cousens, A. K., and Hutchings, I. M., "A Critical Study of the Erosion of an Aluminum Alloy by Solid Spherical Particles at Normal Impingement," *Wear of Materials*, ed. K. C. Ludema, ASME, New York, 1983, pp. 382–389.

46 Thiruvengadam, A., "A Unified Theory of Cavitation Damage," *Journal of Basic Engineering*, Vol. 85, No. 3, Sept. 1963, pp. 365–376.

47 Hobbs, J. M., "Experience With a 20-kc Cavitation Erosion Test," *Erosion by Cavitation or Impingement*, ASTM STP 408, American Society for Testing and Materials, Philadelphia, 1967, pp. 157–185.

48 Gschneider, K. A., Jr., "Physical Properties and Interrelationships of Metallic and Semimetallic Elements," *Solid State Physics, Advances in Research and Applications*, ed. F. Seitz and D. Turnbull, Academic Press, New York, Vol. 16, 1964, pp. 276–426.

49 Hansen, J. S., "Relative Erosion Resistance of Several Materials," *Erosion: Prevention and Useful Applications*, ed. A. F. Adler, ASTM STP 664, American Society for Testing and Materials, Philadelphia, 1979, p. 148–162.

50 Söderberg, S., Hogmark, S., Engman, U., and Swahan, H., "Erosion Classification of Materials Using a Centrifugal Erosion Tester," *Tribology International*, Vol. 14, No. 6, Dec. 1981, pp. 333–343.

A. A. Vetter
Senior Partner.

R. S. Vetter
Junior Partner.

Humbug Mountain Research Laboratories,
Duarte, CA 91010

Balancing Pulverized Coal Flows in Parallel Piping

The distributions of the two-phase (pulverized coal in air) fuel inputs through the 24 parallel coal transport pipes of a coal-fired power plant are determined with a computer code. The orificing which would provide balanced fuel inputs through these coal transport pipes under nominal load conditions is also calculated with the code. Over the entire range of loading, the orificing determined with the code provides much smaller fuel imbalances than the imbalances which result with the previously installed orificings.

Introduction

There are a number of operational problems of coal-fired boilers which are suspected to be caused by nonuniform combustion in the furnace. One source of nonuniform combustion is uneven distribution of fuel inputs to the furnace. Combustion will then occur over a range of stoichiometric ratios and over a range of temperatures. Since the generation of nitrogen oxides is dependent upon the stoichiometry and temperature of combustion, control of nitrogen oxide generation is dependent upon control of the distribution of fuel inputs to the furnace. Uneven distribution of fuel inputs may also cause some regions of the furnace to have lower burnout of carbon from the coal, as could be indicated by a high carbon content in some of the slag.

The volume of primary air to fluidize pulverized coal is usually chosen to prevent fallout in the coal transport piping. Thus, the primary air flowrate is determined by the pipe with the lowest flow velocity. When the distributions of fuel and primary air are unbalanced, the volume of air flowing in the pipe with the highest flow velocity can be significantly higher than for the pipe with the lowest flow velocity. This situation can lead to flame instability with the flame lifting off or pulsating. Conversely, increased stability can allow a greater range for automatic generator control. Higher than necessary coal pipe flow velocities will cause more pipe erosion and short pipe lifetime.

One method to balance the flow through parallel coal transport piping is to insert segmental orifice plates in each pipeline to equalize the flow resistance for each pipe. Another method for balancing the two-phase flows is to vary the diameter of the piping to equalize flow resistances. Reorificing is usually the least expensive solution for retrofitting when an imbalance occurs.

In some cases, the orifice restrictions have been chosen to obtain balanced flow under clean-air (single phase) conditions. When pulverized coal is added to the air to form a two-phase mixture, the physical characteristics of the flow change, causing, among other effects, an increase in the pressure drop. If the piping configuration is such that the pipes have different lengths, bends, elevations, and orifices, the distribution of flow through multiple, parallel piping will no longer be balanced when particles are added to the flow [1].

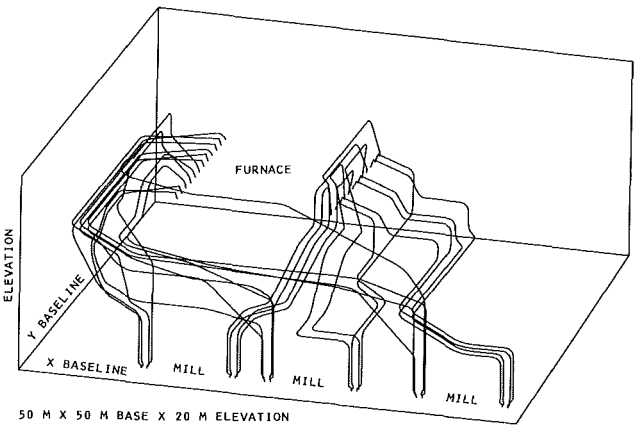

Fig. 1 A trimetric view of the coal transport piping of the Coronado Generating Station Unit I

An engineering technique has been developed to calculate the distribution of two-phase pulverized coal flows through multiple, parallel piping. This technique has been utilized to determine the orificing required to obtain balanced two-phase flow under loaded boiler conditions. The technique involves simulation of the pneumatic conveyance of pulverized coal through the piping with fluidizing air. The two-phase flow models in the simulation use current engineering art tempered with basic physical interpretations of the effects of particles in and on the flows. This technique, which has been incorporated into computer code CTS4, has been applied to the coal piping of the Salt River Project's Coronado Generating Station (CGS). The CGS is located in St. Johns, Arizona and has two units, each with a generating capacity of 400 MW.

Input Values and Cases

The flow under consideration is the fully dispersed regime

Contributed by the Power Division for publication in the JOURNAL OF ENGINEERING FOR GAS TURBINES AND POWER. Manuscript received by the Power Division July 1983.

of two-phase flow which is characteristic of the steady, loaded conditions of power plant coal transport piping. The flow regime of interest has high Reynolds number, low Mach number, near atmospheric pressures, slightly higher than ambient temperatures, no significant chemical reactions, very fine particles compared to the pipe diameter, and particle loading such that the pressure drop due to the coal being transported is comparable to the pressure drop due to the flow of air alone.

Each generating unit of the CGS has 24 coal transport pipes originating from three ball mills and terminating at the furnace. The primary air system supplies warm air for fluidization. The output of pulverized coal and air from each mill is fed to two classifiers, one at each end of each mill. At the exit of each classifier, the flow is divided into four coal pipes which convey the coal–air suspension to the furnace. A three-dimensional view of the coal transport piping of the CGS from classifier exits to the furnace is presented in Fig. 1. Just upstream of the furnace, each pipe has a downturning bend and a segmental orifice plate located immediately after the bend. The normal configuration for the segmental orifice plate has the solid, blocking segment to the outside of the bend and the open area to the inside of the bend. With this orientation, gravitational forces prevent coal "hideout" during shutdowns. The coal piping from the classifiers to the orifice plates is composed of mild steel pipe with an inside diameter of 0.533 m. Downstream of the orifice plate there is transition piping which guides the suspension into the furnace and mates the circular pipe to two rectangular ports. All of the coal pipes enter the furnace at the same elevation, twelve pipes on one side and twelve pipes located directly across on the other side. At the burners, the fluidized coal is surrounded by streams of secondary air, which supply the majority of the air for combustion.

The coal whose properties were used in the simulations is a highly volatile, high-moisture-content, high-ash-content coal which is classified as subbituminous A. The total "as-received" coal flowrate used for the simulations of a CGS unit under nominal conditions is 47.6 kg/s (377,600 lb/hr). The total as-received coal flowrates for a CGS unit under maximum and minimum loading of the mills are 60.5 and 18.9 kg/s (480,000 and 150,000 lb/hr).

The ambient conditions of temperature, pressure, and relative humidity used for these simulations are 288.7 K (60°F), 82.4 kPa (24.4 in. of mercury), and 25 percent, respectively. The classifier exit conditions for the nominal load conditions are 335.9 K (145°F), +2.0 kPa (gauge) (+8 in. of water), and 20.3 m/s (4000 ft/min) for the temperature, average static pressure, and average gas velocity in the pipes. The value of 20.3 m/s (4000 ft/min) is the design point for the coal transport piping at CGS. The moisture content of the as-received coal is 13.3 percent. All of this moisture is assumed to be removed from the coal before the pulverized coal enters the coal transport piping.

The nominal values of the coal specific gravity, coefficient of restitution, Rosin–Rammler distribution size parameter, and the Rosin–Rammler distribution exponent are 1.5, 0.45, 0.036 mm (0.0014 in.), and 0.79, respectively. The nominal value of the coal transport piping equivalent sand roughness height is 0.0038 mm (0.00015 in.).

Nine computer simulations of the CGS which were run for the three load conditions (maximum, nominal, and minimum) are listed in Table 1. The prefix numbers in the case identifier assigned in Table 1 represent the orificing source, and the suffix letter represents the load condition. Letters A, B, and C are chosen to represent the minimum, nominal, and maximum load conditions, respectively. The simulations indicated with the prefix number 1 had orificing which was determined with CTS4 to provide balanced two-phase fuel flows under the nominal load conditions. The CTS4 orificing is presently installed on both units of the CGS. The simulations indicated with the prefix numbers 3 and 2 had the originally installed and revised orificings, respectively. Both of the previously installed orificings had been chosen by the boiler manufacturer to provide balanced flow under cold, clean-air conditions.

Description of Calculational Procedure

The computer code CTS4 simulates the two-phase pneumatic conveyance of pulverized coal through multiple, parallel piping by utilizing the current engineering art tempered with basic physical interpretations of the effects of particles in and on the flows [1]. CTS4 contains a steady, one-dimensional, two-component model for the gas dynamics.

To calculate the distribution of fuel inputs through coal transport piping for a given orificing, each of the mills is considered separately. The nominal load conditions, on a per mill basis, are applied sequentially to each mill and the fuel distribution through the coal pipes from each mill is determined. The results from these calculations are combined to determine the statistical features. The distribution of fuel inputs could be determined with each mill at a different load. For the simulations presented here, all three mills were at equal load conditions.

To calculate the orifice sizing required to provide balanced fuel inputs at a given load condition, each of the pipes is assumed to have the same flows of coal and fluidizing air. For these cases, CTS4 calculates the orifice sizing required for each pipe of each mill to provide the same classifier exit through orifice pressure drop.

To calculate the pressure drop resulting from the flow of two-phase mixture of coal in air in the piping, the factors considered as contributing to pressure loss are described by the following characteristics. The flow is assumed to be steady, one-dimensional, and composed of two components, a solid phase composed of coal particles and a gas phase composed of water vapor and air. The moisture which is removed from the as-received coal in the crusher-dryers and the mills is added to the primary air as water vapor. The pressure drop of the two-phase suspension is taken as the sum of the pressure drops due to the two separate components. The pressure drop due to the air is unaffected, except for changes in the humidity and changes in the average velocity due to a change in void fraction, by the presence of coal particles. The pressure drop due to the coal component is taken to be a summation of terms which arise due to the steady motion of the particles, the acceleration of the particles, and gravitational forces for inclined pipes.

The pressure drop due to flow of the air component is taken to be represented by the Colebrook and White friction factor for high Reynolds number flow [2]. The pressure loss due to bends for the air component is represented in terms of loss of velocity head and is taken to be a function of the angle of the bend and experimentally derived factors [3, 4].

The pressure drop for fully developed, steady, horizontal flow of the coal component is represented by a friction factor which is a function of the pipe Reynolds number, Froude number, ratio of mass flowrates of coal to air, ratio of specific gravities of coal to air, coefficient of restitution of the coal with the pipe, and ratio of particle size to pipe diameter [5]. The size distribution of coal particles is represented by a Rosin–Rammler two parameter fit [6]. For inclined pipe, the effect of gravitational forces on the flow parameters is taken into account in the friction factor calculation [5], and an additional term for the static head is included. The functional dependencies of the coal component factors were obtained from detailed analyses of experimental data [5].

The additional pressure loss due to bends for the coal component is taken to be due to the loss of momentum of the particles. The maximum pressure loss is the loss of particle

Table 1 Summary of CTS4 simulations

Case number	Orificing source	Coal flow, kg/s (klb/hr)	Coefficient of variation, percent	Maximum difference percent	Maximum difference kg/s (lb/hr)
1A	CTS4	18.9 (150)	1.8	5.5	0.043 (340)
1B	CTS4	47.6 (378)	0.01†	0.03†	0.0006† (5)
1C	CTS4	60.5 (480)	0.8	2.4	0.060 (480)
2A	revised	18.9 (150)	4.0	17.6	0.139 (1100)
2B	revised	47.6 (378)	5.9	24.0	0.476 (3780)
2C	revised	60.5 (480)	6.8	26.9	0.678 (5380)
3A	original	18.9 (150)	2.8	13.6	0.107 (850)
3B	original	47.6 (378)	4.4	18.5	0.367 (2910)
3C	original	60.5 (480)	5.2	21.6	0.545 (4320)

†Nonzero due to round-off of orifice heights

Table 2 Summary of results of sensitivity analysis for variables

Variable	Nominal value	Units	Variation value	Maximum difference, percent
Ambient temperature	288.7 (60)	K (°F)	299.8 (80)	0.05
			277.6 (40)	0.04
Ambient pressure	82.4 (24.4)	kPa (in Hg)	84.1 (24.9)	0.19
			80.7 (23.9)	0.20
Ambient relative humidity	25	percent	50	0.05
Fraction of moisture removed from coal	1.00	–	0.90	0.10
Classifier exit temperature	335.9 (145)	K (°F)	337.6 (148)	0.08
			334.3 (142)	0.07
Classifier exit pressure	+2.0 (+8)	kPa (in H_2O)	+2.5 (+10)	0.07
			+1.5 (+6)	0.09
Classifier exit gas velocity	20.3 (4000)	m/s (ft/min)	23.9 (4700)	3.72
			18.8 (3700)	2.62

momentum if each particle underwent an inelastic collision with the wall so that it lost none of its momentum in the direction of the exit flow axis of the bend and all of its momentum in the direction perpendicular to the exit flow axis of the bend. To reaccelerate the particles after the bend, pressure energy is converted to kinetic energy resulting in a pressure loss above the fully developed pressure loss. This acceleration pressure drop is distributed along the length of pipe, up to a length equal to the acceleration length, according to an experimentally measured distribution function [5]. For pipe sections which are shorter than the acceleration length, the velocity defect from the fully accelerated value affects the adjacent downstream section.

The acceleration pressure drop is taken to be a function of the mass flowrate of the coal, diameter of the pipe, air velocity, pipe Reynolds number, Froude number, ratio of specific gravities of coal to air, ratio of particle size to pipe diameter, particle size distribution, inclination of the pipe, and the fully developed velocity of the coal component [5]. The fully developed velocity of the coal component is dependent upon the inclination of the pipe, air velocity, and the terminal velocity of the particles. The terminal velocity of the particles is taken to be a function of the specific gravity of

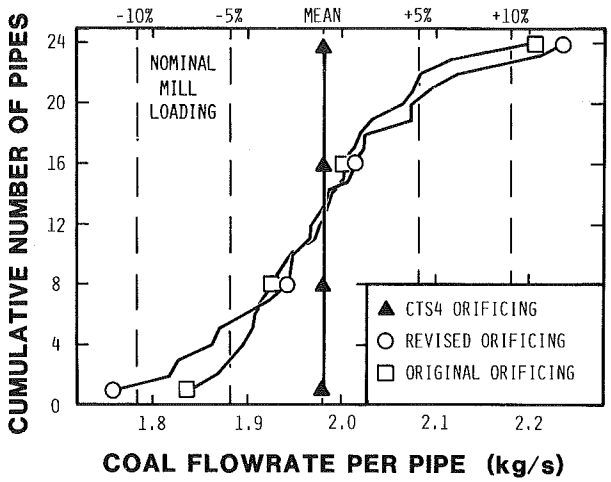

Fig. 2 Distributions of fuel flow in the coal transport pipes as a function of coal mass flowrate per pipe for the nominal load conditions

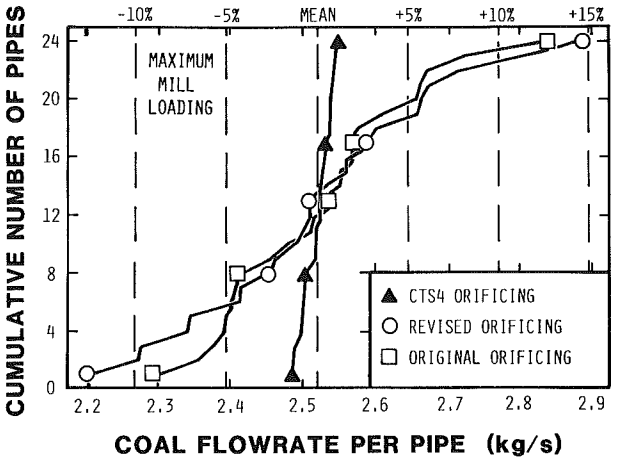

Fig. 3 Distributions of fuel flow in the coal transport pipes as a function of coal mass flowrate per pipe for the maximum mill loading

the coal, air density, shape and size factors for the particles, and the viscosity of the air. The functional dependencies of these factors were obtained from analyses of experimental data [5].

The acceleration length is taken to be a function of the coal mass flowrate, air and coal specific gravities, particle size distribution, and inclination of the pipe, with functional dependencies which were determined from analyses of experimental data [5].

The transport properties were determined from fits to experimental values. The water vapor pressure calculations were accomplished with a standard fit [7]. The viscosity of the gas was calculated by assuming an ideal mixture of air and water vapor with a power law temperature dependence for both components [8]. The absolute viscosity of the mixture was calculated assuming an equilibrium mixture and Roscoe's equation [9]. The kinematic viscosity was calculated from the absolute viscosity by assuming the equilibrium model [10]. The specific heats are obtained with an ideal mixture by volume from data for the specific heats of dry air [11] and water vapor [7]. The speed of sound of the gas phase is calculated by the perfect gas relation. The mixture sound speed was calculated assuming an equilibrium mixture [10].

The pressure drop due to the segmental orifices is calculated according to standard head meter formulas for compressible flow [12] with best-estimate discharge coefficients for the recovered pressure [13, 14, 15]. The effect of coal particles on the orifice pressure loss is assumed to be due only to the increase in velocity due to change in the void fraction [16, 17]

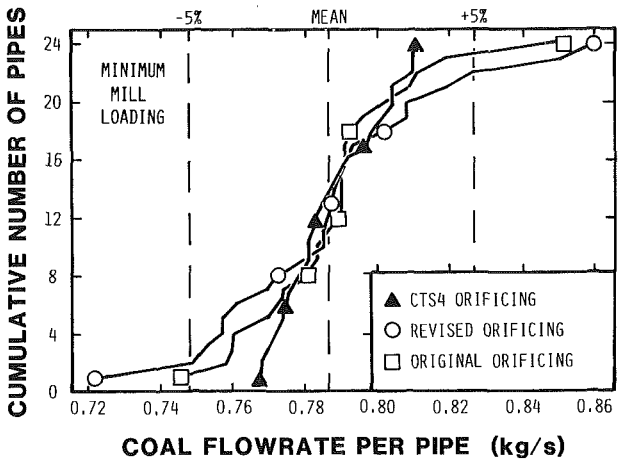

Fig. 4 Distributions of fuel flow in the coal transport pipes as a function of coal mass flowrate per pipe for the minimum mill loading

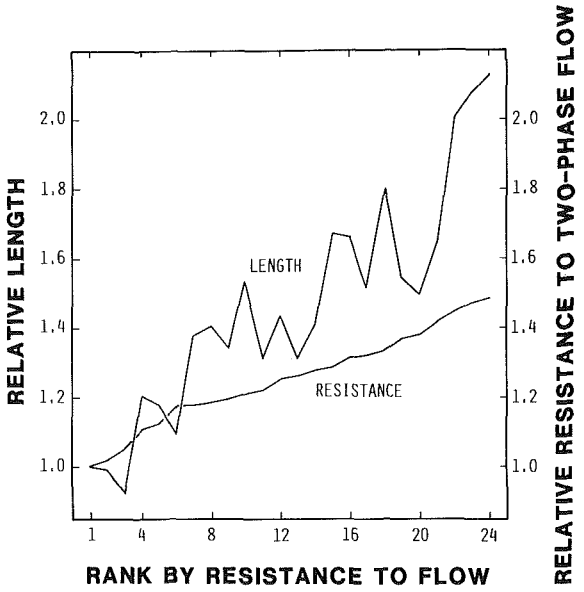

Fig. 5 Relative length and relative resistance to flow for all 24 coal transport pipes of CGS Unit I as a function of rank by resistance to flow

and the momentum loss of the particles hitting the orifice plate.

For fixed orifices, the pressure drop in each of the pipes is calculated as a function of the air and coal flowrates, then flowrates for each pipe are determined by the constraints that the sum of the mass flowrates in the two pipes is given and the pressure drops for all pipes must be equal. To balance the flows for fixed conditions by reorificing, the standard orifice is inserted in the pipe which has the highest resistance to the two-phase flow and the other orifice plate heights are determined such that equal flowrates and equal pressure drops are obtained for all pipes.

Results of the Simulations

The results of the computer simulations are summarized in Table 1. The coefficient of variation is the standard deviation of the distribution of fuel inputs, for all of the coal pipes, divided by the mean value per pipe. The mean value of the flowrate per pipe is the total flowrate for the entire unit divided by the total number of pipes from all mills. The maximum differences between the pipe with the largest fuel flowrate and the pipe with the smallest flowrate are given in Table 1 for each case. The maximum difference is given in coal flowrate and also in this coal flowrate difference divided by the mean value per pipe.

Table 3 Summary of results of sensitivity analysis for input parameters

Parameter	Nominal value	Units	Variation value	Maximum difference, percent
Coal specific gravity	1.5	–	1.65	0.04
Coefficient of restitution	0.45	–	0.35	0.21
Rosin–Rammler size	0.036 (0.00143)	mm (in.)	0.029 (0.00114)	0.06
Rosin–Rammler exponent	0.79	–	1.0	0.05
Pipe roughness	0.0038 (0.00015)	mm (in.)	0.0076 (0.00030)	0.19

Table 4 Pressure drop breakdown for a typical coal pipe

Component	Pressure drop Pa (in H_2O)	percent of total
Gas friction	232 (0.93)	16.9
Gas bends	483 (1.94)	35.2
Coal friction	335 (1.35)	24.4
Coal acceleration	98 (0.39)	7.1
Static head	144 (0.58)	10.5
Orifice	82 (0.33)	5.9

The cumulative distribution function of fuel flow in the coal transport piping as a function of as-received coal flowrate per pipe calculated for Cases 1B, 2B, and 3B, for the nominal load conditions, but with different orificings, are shown in Fig. 2. The cumulative number of pipes whose flowrate is less than or equal to a given flowrate is plotted as a function of coal flowrate in Fig. 2. Also indicated on Fig. 2 are the mean value and ±5 percent and ±10 percent values of coal flowrate. With the original and revised orificings, the imbalances in fuel inputs are within ±12 percent, and more than half of the pipes have imbalances which are within ±5 percent. The curve for Case 1B on Fig. 2 illustrates that the CTS4 orificing provides balanced flows at the nominal conditions.

The cumulative distribution function of fuel flow in the coal piping as a function of coal flowrate calculated for Cases 1C, 2C, and 3C, at the maximum load conditions, is displayed in Fig. 3. With the previously installed orificings, all of the pipes are within ±15 percent of the mean flow, and with the CTS4 orificing, all of the pipes have fuel flows which are within ±1.5 percent of the mean flow.

The cumulative distribution function of fuel flow in the coal transport piping as a function of coal flowrate calculated for Cases 1A, 2A, and 3A, at the minimum load conditions, is given in Fig. 4. With the previously installed orificings, all of the pipes have fuel flows which are within ±10 percent of the mean flow, and, with the CTS4 orificing, all of the pipes have fuel flows which are within ±3 percent of the mean flowrate.

Sensitivity analyses were performed on all of the eight input variables, with each variable changed independently. The starting conditions for these computer simulations were the balanced condition of Case 1B. The starting condition had a residual imbalance of 0.03 percent due to round-off of the values for the orifice heights. The variations and results of the sensitivity analyses for the input variables are summarized in Table 2. The only input variable which exhibits a large imbalance in this sensitivity analysis is the average transport pipe gas velocity at the classifier exit. This input variable also has the largest range of variation values.

Sensitivity analyses were performed on five of the input

parameters. The starting conditions for these computer simulations were the same as for the sensitivity analyses for the input variables. The variations and results of the sensitivity analyses for the input parameters are summarized in Table 3. The maximum imbalance increases only slightly above the starting value of 0.03 percent for the variations in coal specific gravity, Rosin–Rammler distribution size parameter, and Rosin–Rammler distribution exponent. The maximum imbalance for the variation in the value of the coefficient of restitution is greater, but is not large. The value for the maximum imbalance for the variation in coal transport piping equivalent sand roughness height as indicated in Table 3 would place it in a category similar to that of the coefficient of restitution. Since the value of the equivalent sand roughness height changes with usage of the pipe, a survey of this factor was performed. The maximum imbalance calculated for the variation of roughness height to a value of 0.042 mm (0.0017 in.), equal to that for new commercial steel pipe, is 1.3 percent. The maximum imbalance for the variation in the other direction to hydraulically smooth pipe (roughness height equal to zero) is 0.3 percent. The polishing action of the pulverized coal on the inside of the piping causes a decrease in the roughness height as a function of use [18].

Discussion of Results

All of the simulations with the previously installed orificings indicate a maximum imbalance of 14 to 27 percent for the entire range of load conditions. As the loading increases, the imbalances with the original and revised orificings increase. This behavior is expected since the orificing was chosen, in part, to achieve near balance under clean-air conditions.

Simulations with the CTS4 orificing indicate much smaller imbalances. The maximum imbalances with the CTS4 orificing for the maximum and minimum load conditions are 2.4 and 5.5 percent, respectively. The optimum balanced condition occurs at the nominal load condition with this orificing. Since the coal mass flowrate is 3.2 times greater with the maximum load than for the minimum load, the absolute value of the fuel imbalance is actually larger, as seen from Table 1, at the maximum load condition. While these imbalances are significant, they are much smaller than the corresponding imbalances calculated for the two previously installed orificings.

While some of the input variables and parameters are important to the determination of the pressure drop and imbalances, the range of probable variation from the nominal input conditions is sufficiently small that the variation is not too important to the balance of the two-phase flows. An example of this is the classifier exit temperature, which is controlled to a tight tolerance. Some of the input parameters are not under the control of the plant operator. As the input values are varied, each pipe is affected nearly equally, so that the balance of fuel inputs is nearly maintained. The two most important factors in the determination of the imbalance are the two factors which have the greatest range of variation, the as-received coal flowrate and the average transport pipe gas velocity at the classifier exit.

As is seen by the view of the coal transport piping presented in Fig. 1, each of the 24 pipes have different lengths, bends, and elevations. Thus, the resistance to the two-phase flow can be expected to vary considerably from pipe to pipe. Using the balanced condition of Case 1B, the resistances of the pipes to two-phase flow were calculated. The effects of the orifices and the static head loss were subtracted from the total resistance to obtain the resistance due to the flow. The results of these calculations are displayed in Fig. 5 as resistance to flow relative to the least resistive coal transport pipe. The pipe with the least resistance is ranked as No. 1, and the pipe with the largest resistance is ranked as No. 24. Also in Fig. 5 are the centerline pipe lengths divided by the centerline pipe length of the pipe with the least resistance. The flow resistance has a correlation coefficient of 0.92 with the length, but the length is not the only important factor. The bends and the reacceleration after the bends are also important factors in the determination of the flow resistance and, consequently, the distribution of flow in the parallel piping.

The pressure drop breakdown for a typical pipe from Case 1B is listed in Table 4. The components as listed are additive, but not independent. The gas friction component represents the pressure drop which might occur if the total length of the piping were straight and horizontal and the coal particles did not affect the flow velocity and profiles. The gas bends component represents the summation of the effects of the piping bends on the gas phase of the two-component suspension. The coal friction component represents the pressure drop due to the coal particles on the walls of the straight section of the pipe and the additive internal friction between the phases in the body of the flow. The coal acceleration component represents the pressure drops caused by reacceleration of the coal particles after a bend. The static head component represents the pressure required to suspend the column of coal along the nonhorizontal sections of pipe. The orifice component is the steady-state nonrecoverable pressure drop due to the gas and solid phases. The pressure drop due to the gas component is roughly 60 percent of the total pressure drop, while the coal particles are responsible for most of the remainder.

Summary and Conclusions

The distributions of two-phase fuel inputs through the 24 parallel coal transport pipes of the Coronado Generating Station have been balanced under loaded conditions by calculation of orifice sizing with computer code CTS4. The orificing determined in this manner has been shown to be influenced only slightly by variations of the values of most of the input variables and input parameters. The small sensitivity to these changes is due to each pipe being affected nearly equally, so the distribution of fuel inputs in the coal transport piping remains nearly balanced. The two most important input variables in the determination of the distribution of fuel inputs through the 24 parallel pipes are the average transport pipe gas velocity at the classifier exit, i.e., primary air flowrate, and the as-received coal flowrate.

The imbalance in the distribution of fuel inputs with the two previously installed orificings ranges from 13.6 to 26.9 percent for the range from minimum to maximum load. When the orificing calculated for the nominal loaded conditions by computer code CTS4 is applied to this range of loading, the fuel imbalances decrease by a factor of 3 to 10.

Not long ago a large variation of fuel flows was acceptable. Perhaps it is time to apply state-of-the-art techniques to achieve improved balance of two-phase fuel inputs to pulverized coal-fired boilers. The technique which is embodied in computer program CTS4 can be used for both retrofit of existing plants and design of piping for new plants. In both of these applications, balance can be achieved by sizing the transport pipes instead of introducing orifices into the flow.

Acknowledgments

The authors wish to thank Mr. W. D. Gauntlett, Mr. W. Greenwood, and Mr. R. M. Campbell of the Salt River Project for assistance in obtaining the data on the operating conditions and physical configuration of the CGS.

References

1 Vetter, A. A., "Theoretical Evaluation of the Differences Between Single and Two-Phase Flow as Applied to Coal Transport Piping," Humbug Mountain Research Laboratories Report HMRL-R-31:1, Sept. 21, 1981.

2 Schlichting, H., *Boundary Layer Theory*, 4th ed., McGraw-Hill, New York, 1960.

3 *Steam/Its Generation and Use*, 39th ed., Babcock and Wilcox, 1978.

4 Benedict, R. P., *Fundamentals of Pipe Flow*, Wiley, New York, 1980.

5 Rose, H. E., and Duckworth, R. A., "Transport of Solid Particles in Liquids and Gases," *The Engineer (London)*, Vol. 227, 1969, pp. 392–396, 430–433, 478–483.

6 Shotts, R. Q., "Screening," *Coal Preparation*, 3rd ed., Chap. 8, American Institute of Mining, Metallurgical, and Petroleum Engineers, 1968.

7 Meyer, C. A., et al., *1967 ASME Steam Tables*, 2nd ed., ASME, New York, 1967.

8 Kennard, E. H., *Kinetic Theory of Gases*, McGraw-Hill, New York, 1938.

9 Wallis, G. B., *One-Dimensional Two-Phase Flow*, McGraw-Hill, New York, 1969.

10 Marble, F. E., "Dynamics of Dusty Gases," *Annual Review of Fluid Mechanics*, Vol. 2, 1970, pp. 397–446.

11 Gray, D. E., ed., *American Institute of Physics Handbook*, 3rd ed., McGraw-Hill, New York, 1972.

12 Holman, J. P., *Experimental Methods for Engineers*, McGraw-Hill, New York, 1966.

13 Bean, H. S., *Fluid Meters; Their Theory and Application*, 6th ed., ASME, New York, 1971.

14 Stearns, R. F., et al., *Flow Measurements With Orifice Meters*, Van Nostrand, New York, 1951.

15 Judd, H., "Experiments on Water Flow Through Pipe Orifices," *Trans. ASME*, Vol. 38, 1916, pp. 331–366.

16 Carlson, H. M., Frazier, P. M., and Engdahl, R. B., "Meter for Flowing Mixtures of Air and Pulverized Coal," *Trans. ASME*, Vol. 70, 1948, pp. 65–79.

17 Lee, J., and Crowe, C. T., "Scaling Laws for Metering the Flow of Gas-Particle Suspensions Through Venturis," *Proc. ASME Symposium on Polyphase Flow and Transport Technology*, 1980.

18 Patterson, R. C., "Pulverized-Coal Transport Through Pipes," ASME JOURNAL OF ENGINEERING FOR POWER, Vol. 81, 1959, pp. 43–54.

N. Sitthiphong

D. Bushnell

Department of Mechanical Engineering,
Oregon State University,
Corvallis, OR 97331

Lateral Mixing of Solids in a Partially Defluidized Bed With Immersed Heat Exchange Tubes

Introduction

To turn down a fluidized bed combustor, a section of the fluidized bed needs to be defluidized by cutting off the air supply and the flow of coal to that region. With the air and coal supplies cut off, the temperature of the slumped section will decrease since the combustion stops in that part of the bed. To bring the bed up to full capacity, the air supply is returned to that stagnant part of the bed. When the refluidization of the slumped portion begins, solids in the slumped section will diffuse to the adjacent active section causing the rapid mixing of the solids in the fluidized section. If the mixing of solids is too rapid, the temperature of the fluidized section will drop below the operating temperature, and sulfur will no longer be effectively removed from the combustion gases. Thus, it should be useful to determine the rate of mixing of bed material between the slumped section with the active section after refluidization.

This paper reports on the experimental results of the lateral mixing of solids and compares them with some results from other investigators.

Apparatus and Procedures

Due to the difficulty in making measurements and observations in the high-temperature fluidized bed combustor, a dynamically similar cold phase fluidized bed was used to model the high-temperature case.

The experiment was conducted in a 0.30-m-wide by 2.40-m-long fluidized bed. A tube bundle comprising six staggered rows of horizontal tubes with 0.0125 m o.d. and 0.041 m equilateral triangular pitch was placed in the bed with the lowest row of the tubes 0.127 m above the distributor plate. The bed particles were zirconia oxide with $\bar{d}_p = 305$ μm and density 5900 kg/m^3. The static bed height was approximately at the top tube level (0.30 m). Defluidizing of a portion of the bed was achieved by using an air inlet plenum which was divided into two separate wind boxes with individual butterfly valves to control the amount of air entering the two compartments of the bed. A schematic of the apparatus is shown in Fig. 1.

The technique of using inductance probes to monitor the concentration of ferrite tracer particles which was developed and used successfully by Fitzgerald [1] was used in this study. Six inductance probes were used to measure the concentration of ferrite particles as they spread throughout the bed after the refluidization.

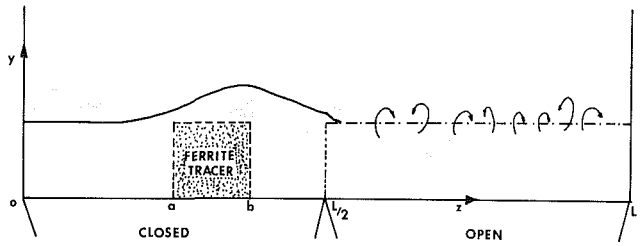

Fig. 1 Schematic representation of the test apparatus including coordinates and the location of the ferrite tracer initially introduced to the slumped bed

With half of the bed defluidized, a sufficient amount of the ferrite tracer (one percent of the total bed material by weight) with $\bar{d}_p = 1000$ μm was introduced to the slumped section of the bed. After the slumped bed was refluidized, the ferrite tracer would then spread throughout the entire fluidized bed. The output signals from the inductance probes which were found to be linear with respect to the ferrite concentration [2] were sampled once every 50 ms and then digitized. Data were also collected on six channels before introducing the ferrite tracers to the bed in order to determine accurately the background or zero level for each of the inductors. After half of the bed was refluidized, data were collected on all six probes for 300 s.

After a refluidization was made and data collected, the ferrite tracer was separated from the bed media before another set of experiments was performed. The velocity used to refluidize the slumped part of the bed was varied from 0.60 m/s to 0.90 m/s.

Experimental Results

The concentration of ferrite particles from the experiments was plotted for each of the six data channels as a function of time. Samples of the plots of concentration versus time are shown in Fig. 2. From the plot for each run, three plots on the left-hand side represent the concentration from each inductor coil in the slumped side where the locations of coils in the bed (z) are 0.1143, 0.5461, and 0.9780 m. The other three plots on the right-hand side represent the concentration from each coil in the active side where the locations of coils in the bed (z) are 1.4097, 1.8415, and 2.2733 m. The concentration scale on the plot is measured in volts. One volt is equal to 0.427 kilograms of ferrite in each cubic meter. It is important to remember

Contributed by the Power Divison for publication in the JOURNAL OF ENGINEERING FOR GAS TURBINES AND POWER. Manuscript received by the Power Division July 1983.

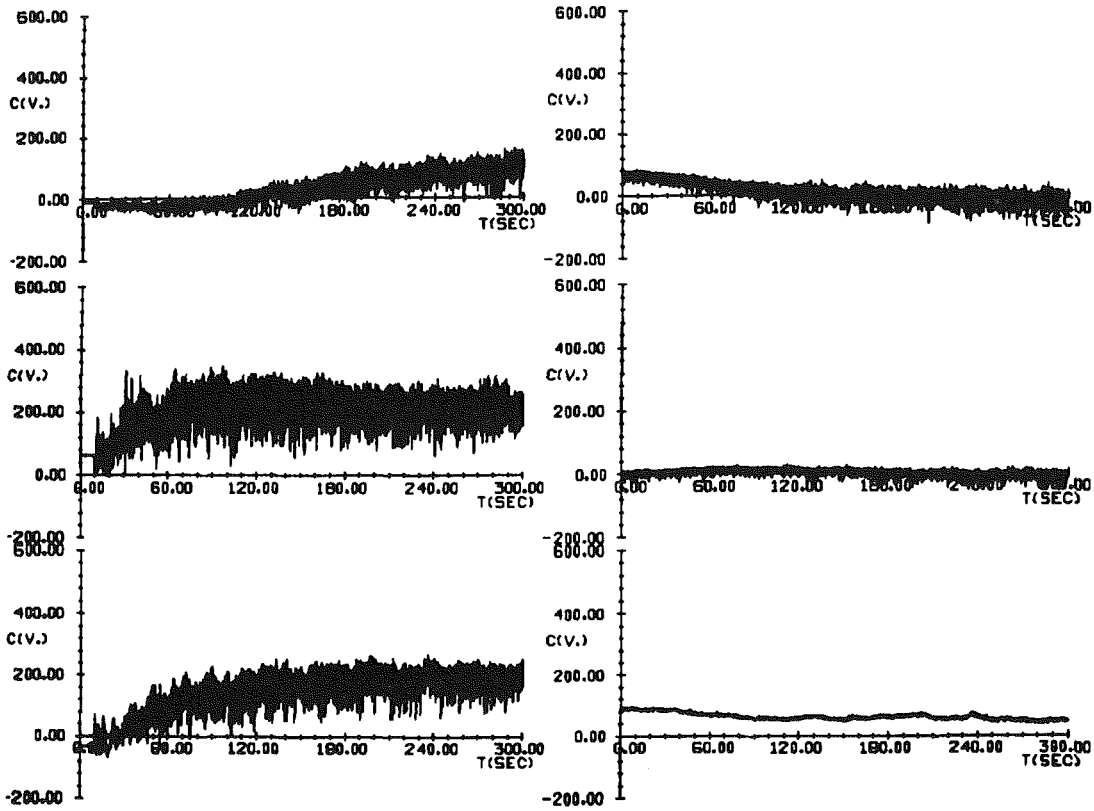

Fig. 2 Sample data of the ferrite concentration readings of all six probes

that one percent of ferrite by weight in a vicinity of a probe is approximately 32.036 kg/m^3.

The collected data as shown in Fig. 2 had to be smoothed to attenuate the effect of bubbles passing the probes. When a bubble comes close to a probe, the ferrite tracer will be separated from the probe, causing a decrease in the apparent concentration of ferrite. When the bubble moves away from that probe, the ferrite particles come back within the vicinity of the inductance probe and the concentration reading goes up again.

A computer program was developed that eliminated the effects of zero drift and the effects of bubbles passing the probes. Figure 3 shows the corrected data. A final smoothing of the raw data was also performed.

The resulting mean concentration versus time plots from all six channels were then used to obtain the ferrite concentration profile which is the distribution of the ferrite tracer as a function of the location in the bed. The concentration profile will change as time increases. The series of times from the start (t = 0) to the end (t = 290) was chosen so that the concentration profile would change dramatically and successively. A modified Fibonacci sequence of time (t = 10, 20, 30, 50, 80, 130, . . .), where each number is the sum of the previous two, was used. This series was chosen because it represented natural decaying functions or exponential functions in a characteristic manner and the changes in ferrite concentration in this study were expected to be rapid in the first 60 s, then slower as time progressed. The set of concentration profiles at different times (t = 10, 20, 30, 50, 80, 130, 210, and 290 s) from one run is shown in Fig. 4.

Since the concentration profile of the ferrite tracer in the bed at a series of times is known, a model that describes the spreading rate of the ferrite tracer or the rate that ferrite tracer disperses in a fluidized bed can be developed.

Nomenclature

A = cross-sectional area of the bed, m^2
c = concentration of ferrite tracer, kg/m^3
c_i = initial concentration of ferrite tracer = 2 c, kg/m^3
c^* = concentration of ferrite tracer at steady-state condition = 32.0, kg/m^3
d_B = bubble diameter, m
d_p = surface mean particle size, μm
D_z = lateral dispersion coefficient of solids, m^2/s
L = length of fluidized bed
M = relative amount of solids transfer
m^* = total amount of tracers from the slumped section that diffused to the active bed after the refluidization at the steady-state conditions, kg
m^* = total amount of tracers from the slumped section that diffused to the active bed after the refluidization at the steady-state conditions, kg
t = time after refluidization, s
U_{mf} = superficial velocity at the minimum fluidizing condition, m/s
$U(z), U\left(z-\frac{L}{2}\right)$ = unit step function
z = horizontal distance from the left end of the bed, m
δ = fraction of the bed consisting of bubbles
ϵ_{mf} = void fraction in the bed at the minimum fluidizing velocity

Table 1 Comparison of D_z from various investigators

Superficial velocity (m/s)	D_z (m^2/s) Equation (5)	Equation (6)	This experiment
0.60	0.038	0.0010	0.0007
0.76	0.053	0.0017	0.0012
0.90	0.063	0.0023	0.0020

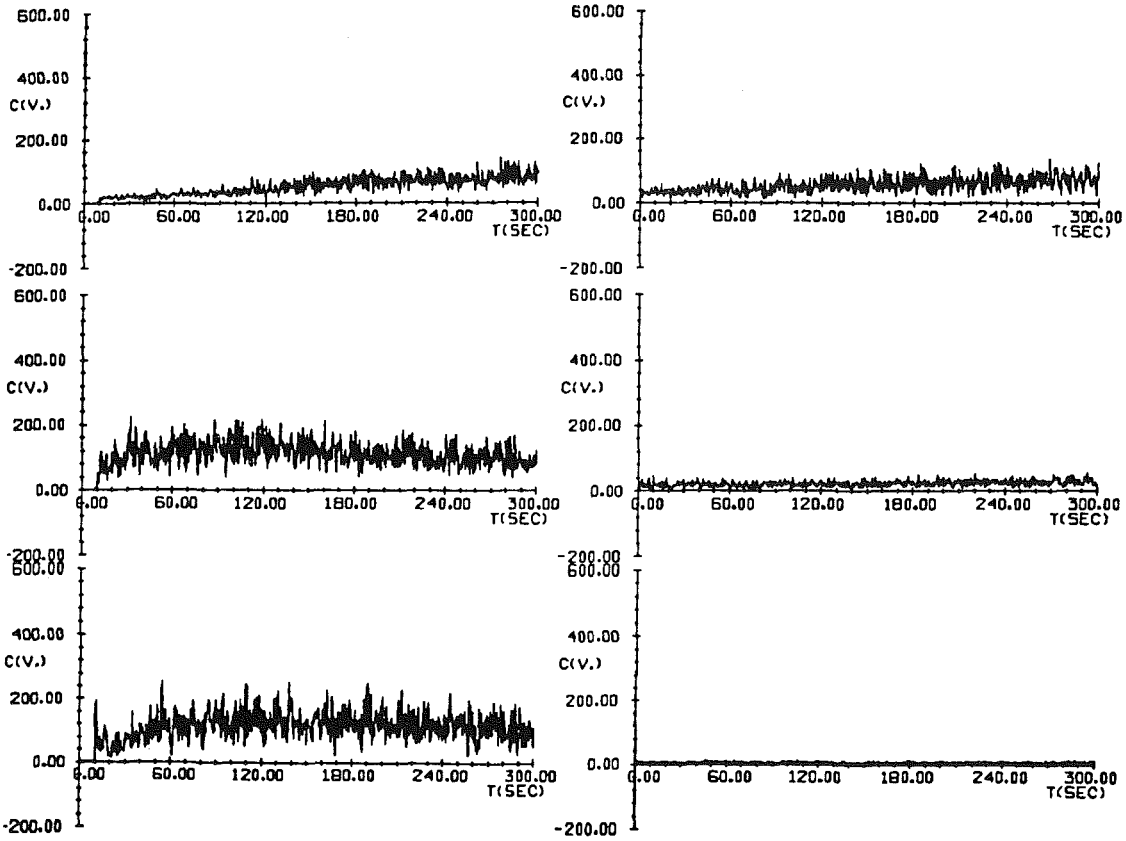

Fig. 3 Raw data corrected for bubble passing effects and for zero drift effects

Discussion

When the composition of a mixture varies from one point to another, each component has a tendency to flow in the direction that will reduce the local differences in concentration [3]. In this experiment, the concentration of ferrite particles in the bed was found to vary with location in the bed and time. The concentration of ferrite tracer in the bed satisfied the unsteady state diffusion equation.

$$\frac{\partial c}{\partial t} = D_w \frac{\partial^2 c}{\partial w^2} + D_y \frac{\partial^2 c}{\partial y^2} + D_z \frac{\partial^2 c}{\partial z^2} \tag{1}$$

However, since the width (w) of the bed is small, the concentration gradient in the w direction can be lumped. Thus

$$\frac{\partial c}{\partial t} = D_y \frac{\partial^2 c}{\partial y^2} + D_z \frac{\partial^2 c}{\partial z^2} \tag{2}$$

Furthermore, as bubbles rise in a fluidized bed, solids are drawn into the bubble wake and completely mixed in the wake. Particle circulation within the wake causes lateral displacement of the solids shed through the bed and at the surface. A consideration of these mechanisms indicates that vertical mixing should be more rapid than lateral mixing [4]. Thus, the concentration gradient in the vertical direction (y) can be neglected in comparison with the lateral concentration gradient

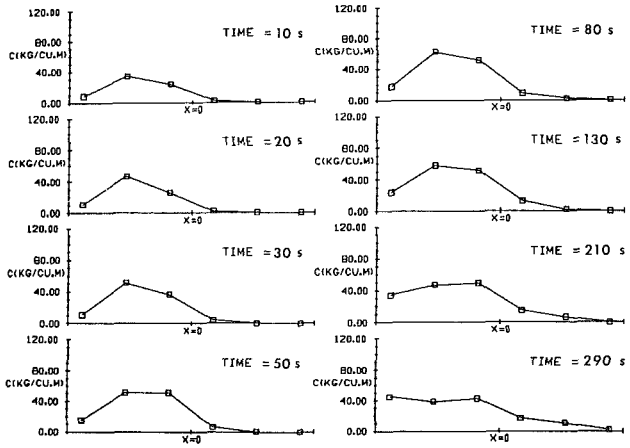

Fig. 4 Example of concentration profiles of ferrite tracer from a typical experiment

$$\frac{\partial c}{\partial t} = D_z \frac{\partial^2 c}{\partial z^2} \tag{3}$$

Equation (3) can be solved if two appropriate boundary conditions and one initial condition are known. In this experiment, the following conditions were used:

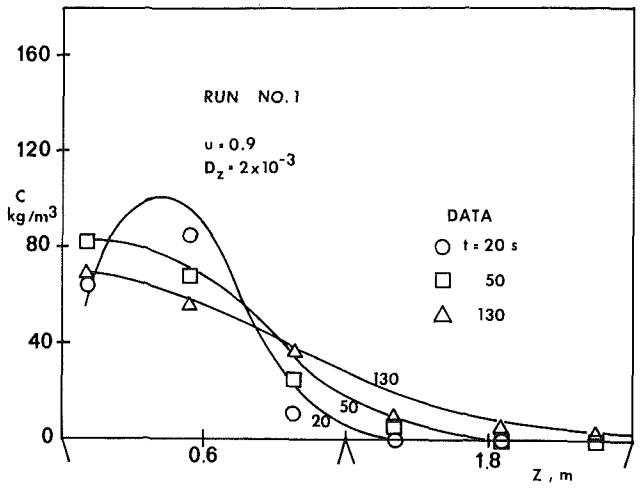

Fig. 5 Concentration profiles from run number 1 by using equation (4) with $D_z = 0.002\ m^2/s$

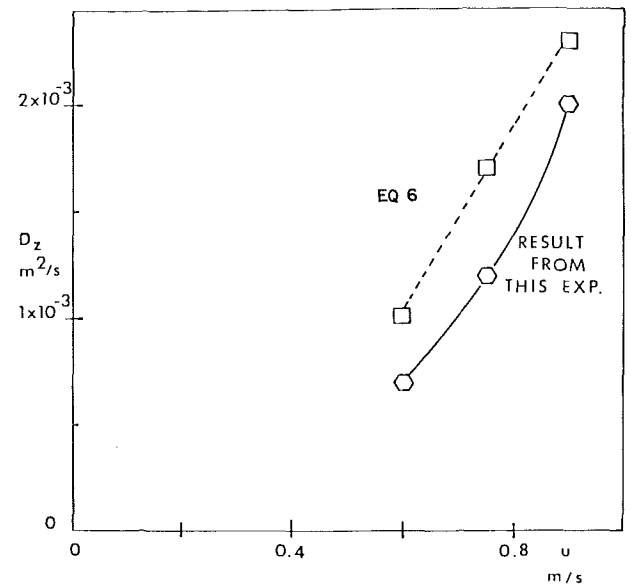

Fig. 6 Plot of dispersion coefficient of solids as a function of superficial velocity

Boundary condition $\frac{\partial c}{\partial z} = 0$ at $z = 0$ and $z = L$

Initial condition $c = c_i\left[U(z) - U\left(z - \frac{L}{2}\right)\right]$ at $t = 0$

where

$$c_i = 2c^*$$

The solution of equation (1) can be expressed as

$$c(z,t) = c^* + \frac{2c_i}{L} \sum_{n=1}^{\infty} \frac{1}{\lambda_n} \sin \frac{n\pi}{2} \exp(-D_z \lambda_n^2 t) \cos \lambda_n z \tag{4}$$

where

$$\lambda_n = \frac{n\pi}{L}$$

In equation (4), the lateral dispersion coefficient of solids (D_z) is the only unknown quantity which can be solved since $c(z, t)$ is obtained from the experimental data and the other quantities, i.e., c^*, c_i, L, t, and z are known. Newton's Root Finding method was used to determine D_z in equation (4). It

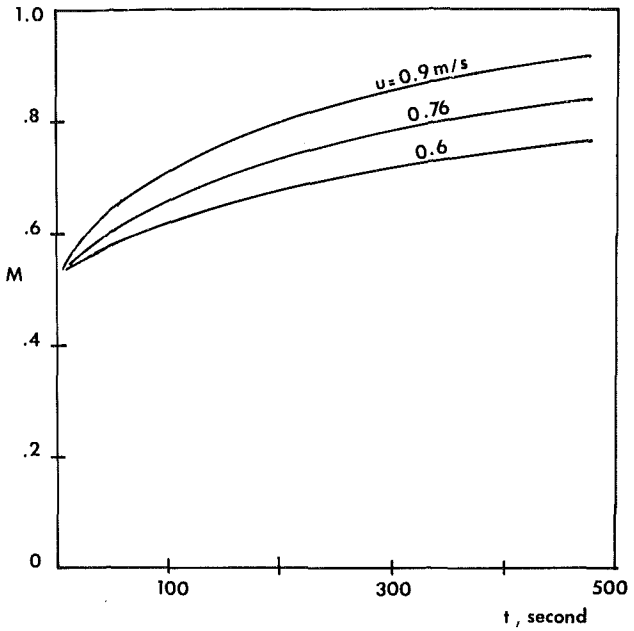

Fig. 7 The relative amount of solids transfer (M) as a function of time after refluidization

was found that D_z was mainly a function of the superficial velocity and values of D_z at various superficial velocity are shown in Table 1.

After the values of D_z were obtained, the theoretical concentration profiles were plotted by using equation (4) and compared with the experimental concentration profiles. A sample plot is shown in Fig. 5.

Mori and Nakamura [5] presented a report about solids mixing in a fluidized bed. The authors also developed a correlation from the experimental data for D_z which was expressed as

$$D_z = 2.7\ d_B^{2.0} \tag{5}$$

Kunii and Levenspiel [6] considered that the major mechanism of lateral mixing was the circulation of particles within the bubble's wake. The authors also proposed a correlation of D_z by using Einstein's random walk equation as

$$D_z = \frac{3}{16}\left(\frac{\delta}{1-\delta}\right)\frac{u\ d_B}{\epsilon_{mf}} \tag{6}$$

In equations (5) and (6) d_B can be estimated using correlations proposed by several investigators, e.g., [7, 8]. The fraction of the bed occupied by bubbles (δ) was found to vary from 0.125 at $u = 0.60$ m/s to 0.20 at $u = 0.90$ m/s. The voidage of the bed at the minimum fluidizing velocity (ϵ_{mf}) was assumed to be 0.5. The predicted values of D_z from equations (5) and (6) were calculated and are also shown in Table 1. Comparison of D_z obtained from this experiment and that from equation (6) is shown in Fig. 6 which indicates good agreement between these two numbers.

To determine the total amount of tracers from the slumped section that diffused across the interface front to the fluidized section after the refluidization at any time t, equation (4) with a known value of D_z was used

$$m_t = A\int_{\frac{L}{2}}^{L} c(z,t)\,dz$$

$$= A\left[c^*\frac{L}{2} - \frac{c_i}{L}\sum_{n=1}^{\infty}\frac{1}{\lambda_n 2}[1-(-1)^n]\exp(-D_z\lambda_n^2 t)\right] \tag{7}$$

If m^* is the total amount of tracer from the original

slumped section that diffuses to the fluidized section after refluidization at the steady-state condition, then

$$m^* = Ac^* \frac{L}{2} \tag{8}$$

Finally, the relative amount of solids transfer (M) which is defined as the ratio of m_t and m^* can be obtained and is expressed as

$$M = \frac{m_t}{m^*} = 1 - \frac{4}{L^2} \sum_{n=1}^{\infty} \frac{[1-(-1)^n]}{\lambda_n^2} \exp(-D_z \lambda_n^2 t) \tag{9}$$

The plots of M at various timed and superficial velocities are shown in Fig. 7. It was indicated that the mixing of solids from both sections would be reduced if the slumped section was refluidized with a lower velocity.

Conclusions

1 It was observed that the mechanism of solid mixing, or the dispersion of the solids from the refluidized section to the active section, can be represented by the diffusion model.

2 It was found that the dispersion coefficient of solids increased significantly with the superficial gas velocity.

3 The resulting values of M indicate that the total amount of material diffused from the slumped side to the fluidized section after refluidization increases with the refluidizing velocity.

Acknowledgments

The authors express their gratitude to Babcock and Wilcox Company for their financial support.

References

1 Fitzgerald, T. J., Catapovic, N. H., and Jovanovic, G. N., "Solid Tracer Studies in a Tube-Filled Fluidized Bed," *Proceedings of the Fifth Int. Conf. on Fluidized Bed Combustion*, Vol. 3, 1977, p. 135.

2 Deaton, W. W., "Solid Movements in a Tube-Filled Fluidized Bed," Master's thesis, Oregon State University, Corvallis, OR, 1980.

3 Skelland, A. H. P., *Diffusional Mass Transfer*, Wiley, New York, 1974.

4 Highly, J., and Merrick, D., "The Effect of the Spacing Between Solids Feed Points on the Performance of a Large Fluidized Bed Reaction," *AIChE Symp. Ser.*, Vol. 67, No. 116, 1971, p. 219.

5 Mori, Y., and Nakamura, K., "Solid Mixing in a Fluidized Bed," *Kagaku Kogaku*, Vol. 4, No. 1, 1966, p. 154.

6 Kunii, D., and Levenspiel, O., "Lateral Dispersion of Solid in Fluidized Beds," *J. of Chem. of Japan*, Vol. 2, No. 2, 1969, p. 122.

7 Mori, S., and Wen, C. Y., "Estimation of Bubble Diameter in Gaseous Fluidized Bed," *AIChE J.*, Vol. 21, No. 1, 1975, p. 109.

8 Darton, R. C., LauNauze, R. D., Davidson, J. F., and Harrison, D., "Bubble Growth Due to Coalescence in Fluidized Bed," *Trans. Inst. Chem. Eng.*, Vol. 55, No. 4, 1977, p. 274.

A Comparison of Simple Models of Turbulent Droplet Diffusion Suitable for Use in Computations of Spray Flames

P. Ward

N. Collings

N. Hay

Department of Mechanical Engineering,
University of Nottingham,
Nottingham, NG7 2RD, U.K.

An exact analysis of the diffusion of droplets in turbulent flow, taking account of the random nature of the flow and the range of length and time scales, is very involved and the equations derived are not necessarily solvable. For this reason spray models have usually not included liquid turbulent diffusion effects. Simpler models of turbulent diffusion of droplets are compared in this paper and equations suitable for insertion into existing spray models that require little extra computational effort are derived.

Introduction

An exact analysis of the diffusion of droplets in turbulent flow, taking account of the random nature of the flow and the range of length and time scales, is very involved, and the equations derived are not necessarily solvable. A description of some of these advanced treatments is given by Soo [1]. For this reason models of spray flames have usually not included liquid diffusion effects. The objective of this paper is to compare the four simpler models that have been proposed and to derive equations for each, suitable for insertion into existing spray models, and which will require little extra computational effort. Two of the models will be shown to give the same general trend as the experimental data, and the derived equations for these models will be validated by comparison with the experimental results of Snyder [2].

In spray flames the liquid phase can be represented as a continuum as described for example by Jones [3], or as a set of discrete droplets as described for example by El Banhawy [4]. The rate of diffusion of the liquid will need to be represented in a different manner in the two alternative liquid phase formulations.

In the continuum formulation the many individual droplets are averaged to define a local liquid mass fraction. A conservation equation for mass fraction of liquid can then be derived which is of the same form as the conservation equations for the gas phase. Turbulent diffusion of the droplets can be included by a diffusivity e_T where

$$J = -e_T \frac{\partial \varphi}{\partial x} \tag{1}$$

A turbulent Schmidt number can then be formed as

$$\mathrm{Sc}_T = \mu_T / e_T \tag{2}$$

A molecular diffusivity and corresponding Schmidt number could also be defined. However, for liquid droplets in air, where the density ratio is of order 1000, molecular diffusion effects will be negligible. The inclusion of turbulent diffusion will add extra terms in the equations, but will not increase the number of equations to be solved, and so the additional computing time required will be small.

In the discrete formulation representative droplets are obtained by statistically sampling the ranges of position, size, and velocity at injection. These droplets are tracked through the flow field by solving the droplet equation of motion. If turbulent diffusion is neglected, the trajectory of a droplet of given initial conditions is fully determined. However, if turbulent diffusion is included, the random nature of the flow means that the trajectory of a droplet of given initial conditions is not fully determined. In this case the number of representative droplets required will increase because a droplet of given initial conditions will need to be sampled several times. Diffusion of droplets can be simulated by a turbulent position increment to the mean trajectory, calculated by finding the response of a droplet to fluctuating gas velocity acting perpendicular to the trajectory. The turbulent increment is added perpendicularly to the trajectory, randomly in a positive or negative sense. This type of diffusion model will predict an approximately Gaussian spray distribution, centered about the trajectory due to the mean gas velocity. Inclusion of turbulent diffusion in discrete models will be simple, but will increase the solution time because the number of representative droplets required will be larger. Also convergence may be slowed down since a droplet's trajectory will change slightly from one iteration to the next, because of the random nature of the model.

Timescales

Turbulent diffusion can be characterized by the ratio of the

Contributed by the Power Division and presented at the ASME Winter Annual Meeting, Phoenix, Arizona, November 14–18, 1982. Manuscript received by the Power Division December 1982. Paper No. 82-WA/HT-2.

droplet response time to the turbulent timescale of the gas τ/T. Turbulent diffusion is assumed to occur when

$$\tau/T<1 \tag{3}$$

The equation of motion of a droplet is

$$\frac{d\,U_D}{dt}=\frac{1}{\tau}\,(U-U_D) \tag{4}$$

where

$$\tau=\frac{4}{3}\,\frac{D^2\rho_D}{C_D\mathrm{Re}\,\mu} \tag{5}$$

Diffusion is only significant for droplets where $\mathrm{Re} < 10^3$, and then

$$C_D\approx\frac{24}{\mathrm{Re}}\,(1+0.15\,\mathrm{Re}^{0.687}) \tag{6}$$

is valid. Thus τ can be determined. Regarding T, it is shown by Hinze [5] that the large energy-containing eddies are most likely to cause turbulent diffusion and for these eddies, when the relative velocity between the droplets and the surrounding fluid is small,

$$T=l/U' \tag{7}$$

When there is significant relative velocity between the droplet and the surrounding fluid, e.g. near an injector, the droplet will pass through an eddy in less than the turbulent timescale of the eddy. Following Gosman [6], to allow for this the turbulent timescale for the gas will be taken as

$$T=\text{minimum}\,(l/U', l/|\bar{U}_D-\bar{U}|) \tag{8}$$

The length scale of the turbulent eddy l can be found from the formula of Hinze [7]

$$l=(\mu_T/\rho)^{3/4}/\epsilon^{1/4} \tag{9}$$

μ_T can be found from the K–ϵ model [8]

$$\mu_T=C_\mu\rho\,K^2/\epsilon \tag{10}$$

For simplicity it is assumed that the fluctuating velocity is the same in all directions, hence

$$U'=(2K/3)^{1/2} \tag{11}$$

Thus from a knowledge of the droplet size and density and characteristics of the flow, the ratio of droplet response time to turbulent timescale τ/T can be calculated.

Alternative Models

A survey has been made of the simpler models of turbulent diffusion of droplets. These models can be divided into four basic approaches. They are briefly summarized here so that they may be compared.

Model 1. This model is based on the equation of motion of a droplet, equation (4), and gives an estimate of diffusion suitable for use in a continuum spray model. It is described by Longwell [9] and has been used in the computations of Katsuki [10].

If it is assumed that the mean velocity of the droplet is determined by the mean velocity of the gas, and the fluctuating velocity of the droplet is determined by the fluctuating velocity of the gas, equation (4) can be split into two parts

$$\frac{d\,\bar{U}_D}{dt}=\frac{1}{\tau}\,(\bar{U}-\bar{U}_D) \tag{12}$$

$$\frac{d\,U_d'}{dt}=\frac{1}{\tau}\,(U'-U_D') \tag{13}$$

Assuming that the gas has a sinusoidal fluctuating velocity given by

$$U'=U_0\,\sin\,\omega t \tag{14}$$

and

$$\mathrm{Sc}_T=\frac{\mu_T}{e_T}=\frac{l}{l_D}\left[\frac{K}{K_D}\right]^{1/2} \tag{15}$$

it is shown by Longwell [9] that equation (13) can be solved to give an estimate of the droplet turbulent Schmidt number

$$\mathrm{Sc}_T=1+\omega^2\tau^2 \tag{16}$$

If T is the time for an element of fluid to travel across the eddy

$$T=\pi/\omega$$

$$\mathrm{Sc}_T=1+(\pi\tau/T)^2 \tag{17}$$

It must be noted that if, as is sometimes the case, fluctuating components of velocity are of the same order or greater than the mean flow velocity, the above analysis may be seriously in error.

Model 2. This model, like model 1, is based on the droplet equation of motion, equation (13), but in this case the equation is solved to obtain an estimate of droplet diffusion suitable for a discrete spray model, i.e., turbulent deflections to be added to the mean path are calculated. Diffusion estimates of this type have been employed in the computations described in [6] and [11–13].

If it is assumed that U' is constant over time T and the droplet starts with no fluctuating velocity, equation (13) can be solved to find the distance traveled by a droplet in time T, due to the velocity fluctuation

$$\Delta x=U'T(1+\tau/T(\exp(-T/\tau)-1)) \tag{18}$$

This crude analysis gives an order of magnitude estimate of Δx, for $\tau < T$. Thus a power series expansion of (18) is not appropriate.

Model 3. This model, described by Liu [14] and Gudmundsson [15] and used in the computations of Abbas [16], gives a continuum estimate of droplet diffusion. It is based on a calculation of the difference in penetration of particles and turbulent eddies from the turbulent core into the boundary layer in pipe flow. The result obtained is

$$\mathrm{Sc}_T=(1+\tau/T)^{-1} \tag{19}$$

Nomenclature

C_D = drag coefficient
C_μ = constant in K–ϵ model
D = droplet diameter, m
e = diffusivity, kg m^{-1} s^{-1}
J = flux, kg m^{-2} s^{-1}
K = kinetic energy of turbulence, m^2 s^{-2}
l = length scale of turbulence, m
Re = Reynolds number
Sc = Schmidt number
t = time, s
T = turbulent timescale, s
U = velocity, ms^{-1}
x = distance, m
Δx = deflection in trajectory of droplet due to turbulence, m
σ = standard deviation
ϵ = eddy dissipation, m^2 s^{-3}
φ = mass fraction of liquid
μ = viscosity, kg m^{-1} s^{-1}
ρ = density, kg m^{-3}
τ = droplet time constant, s

Subscripts

D = droplet; all properties refer to gas phase unless subscripted by D
DIFF = diffusion
G = gaseous species
P = at the point P
T = turbulent

Superscripts

$'$ = fluctuating
$\bar{}$ = mean

The analysis is only valid for boundary layer flows and is inapplicable to more general flows.

Model 4. This model, described by Abramovich [17], also gives a continuum estimate of droplet diffusion. By making the assumption that a droplet of any size will acquire the fluctuating velocity of the gas in the duration of the turbulent timescale T it is possible to show that diffusion can be calculated by

$$\mathrm{Sc}_T = \mathrm{Sc}_{TG}\,\frac{2-\varphi}{1-\varphi} \tag{20}$$

where φ is the mass fraction of liquid. This result, unlike those obtained from models 1, 2, and 3, is independent of the timescale ratio. This is a consequence of the previously mentioned assumption.

A Method of Comparing the Models

Four models have been described above; models 1, 3, and 4 were of the continuum type and model 2 was of the discrete type. A simple formula will now be derived to convert continuum models to discrete models and vice versa. All four models can then be expressed in the same form and will be capable of comparison with the same experimental data. The model giving the best agreement with experimental results can then be used in both continuum and discrete spray models.

It is shown by Jurewicz [18] that the velocity with which droplets diffuse through the gas is given by

$$U_{\mathrm{DIFF}} = -\,\frac{e_T}{\rho\varphi}\,\frac{\partial\varphi}{\partial x} \tag{21}$$

Consider a small volume of gas containing some droplets, and no droplets in the immediate surroundings. Let the average mass fraction in the volume be φ. If the liquid diffuses distance Δx in time T

$$U_{\mathrm{DIFF}} = \Delta x/T$$
$$\partial\varphi/\partial x = (0-\varphi)/\Delta x$$

Substituting these approximations in equation (21) and rearranging

$$e_T = \rho\Delta x^2/T \tag{22}$$

A more sophisticated analysis on this point has been followed by Hotchkiss and Hirt [19] who suggest

$$\Delta x = \sqrt{4e_T T/\rho}\;erf^{-1}(y) \tag{23}$$

where y is randomly distributed $0 < y < 1$. However, this form only differs by a factor order unity from equation (22) on average and requires a very significant increase in computing time. Nevertheless better experimental data might justify the introduction of a correction factor in equation (22).

In time the particles will be distributed, rather than concentrated at one point. It can be shown that if a particle moves a distance Δx, randomly in a positive or negative sense, then after n moves, where n is large, the probability density function for the position of the particle is Gaussian, with a standard deviation given by

$$\sigma = \Delta x\, n^{1/2} \tag{24}$$

Equations (2) and (22) enable formulae for models which predict turbulent displacement Δx to be manipulated to calculate diffusivity e_T, and vice versa. Because of the level of approximation involved in the analysis above, it is appropriate to introduce a multiplying constant Sc_{TG} into the model equations, such that $\mathrm{Sc}_T \to \mathrm{Sc}_{TG}$ as $\tau \to 0$, i.e., as the droplets become gaslike.

Thus the model equations, all expressed in continuum form, become

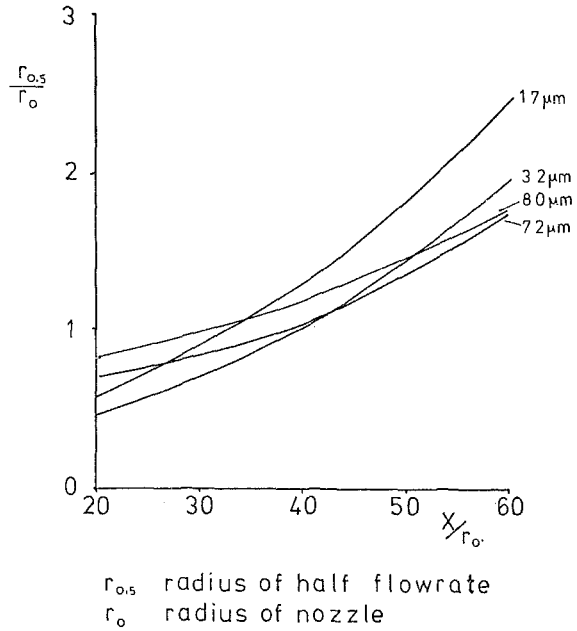

Fig. 1 Rates of dispersion of different sized particles in a gas jet; replotted from Laats and Frishman [24]

$$\text{Model 1}\quad \mathrm{Sc}_T = \mathrm{Sc}_{TG}\left(1+\left(\frac{\pi\tau}{T}\right)^2\right) \tag{25}$$

$$\text{Model 2}\quad \mathrm{Sc}_T = \mathrm{Sc}_{TG}\,\frac{l}{U'T}\left(1+\frac{\tau}{T}\left(\exp\left(\frac{-T}{\tau}\right)-1\right)\right)^{-2} \tag{26}$$

$$\text{Model 3}\quad \mathrm{Sc}_T = \mathrm{Sc}_{TG}\left(1+\frac{\tau}{T}\right)^{-1} \tag{27}$$

$$\text{Model 4}\quad \mathrm{Sc}_T = \mathrm{Sc}_{TG}\left(\frac{2-\varphi}{1-\varphi}\right) \tag{28}$$

From these results, using equations (2) and (22), the corresponding discrete equations become

$$\text{Model 1}\quad \Delta x = \sqrt{\frac{\mu_T T}{\rho\mathrm{Sc}_{TG}}}\left\{1+\left(\frac{\pi\tau}{T}\right)^2\right\}^{-1/2} \tag{29}$$

$$\text{Model 2}\quad \Delta x = \sqrt{\frac{\mu_T T^2 U'}{l\,\rho\,\mathrm{Sc}_{TG}}}\left\{1+\frac{\tau}{T}\left(\exp\left(\frac{-T}{\tau}\right)-1\right)\right\} \tag{30}$$

$$\text{Model 3}\quad \Delta x = \sqrt{\frac{\mu_T T}{\rho\,\mathrm{Sc}_{TG}}}\left(1+\frac{\tau}{T}\right)^{1/2} \tag{31}$$

$$\text{Model 4}\quad \Delta x = \sqrt{\frac{\mu_T T}{\rho\,\mathrm{Sc}_{TG}}}\left(\frac{2-\varphi}{1-\varphi}\right)^{-1/2} \tag{32}$$

Thus we have all four models expressed in equivalent forms suitable for either the continuum or the discrete formulation of spray flame models.

Choice of Model

Examination of the models, summarized in equations (25–28), shows that they give contrasting results. Models 1 and 2 predict that Sc_T will increase with τ/T, i.e., small droplets will diffuse faster than large droplets under similar conditions. This is physically plausible because of the higher inertia of the larger droplets. Model 3 predicts the opposite trend to 1 and 2, i.e., Sc_T decreases with τ/T. However, since for very large droplets there will be no diffusion, Sc_T must eventually increase with τ/T for very large τ/T. Model 4

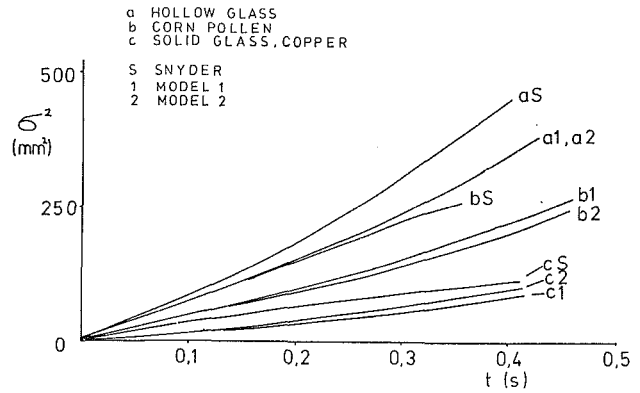

Fig. 2 A comparison of the experimental data of Snyder and Lumley [2] with models 1 and 2

predicts that Sc_T is independent of τ/T. To decide which models show the correct trend, experimental evidence must be examined.

Experiments with multiphase jets, reported in [20, 21, and 22], show that Sc_T decreases with τ/T, in agreement with model 3. The gas velocity profile assumed by Lilly [22] has been criticized by Mills [23], but this seems unlikely to fully account for the unusual trend in the results. Hinze [5] has attributed the increase in diffusivity for large droplets to overshoot effects in the nonhomogeneous flow field of the turbulent jets.

Laats [24] carried out an experiment on a multiphase jet, the results of which (expressed as radius of half-flow rate against axial distance) are shown in Fig. 1. Near the nozzle small-diameter powder is dispersed less rapidly than large-diameter powder, but far from the nozzle this trend is reversed. These results may explain the conclusion of [20–22] that Sc_T decreases with τ/T. Laats attributes the initial higher rate of diffusion of the larger particles near the nozzle to the Magnus force which acts on the larger particles when they are induced to rotate in the high-shear region near the nozzle.

Smoot and co-workers reported a series of experiments to measure the properties of two-phase jets, for use in the design of pulverized coal reactors. In early experiments [25] it was found that Sc_T decreased with $\tau/\Delta T$, but this was attributed to effects from the design of the inlet. When greater attention was paid to inlet design [26–27] Sc_T was found to increase with τ/T. Thus the apparent decrease of Sc_T with τ/T is attributed to extraneous effects.

From the experiments of Laats and Smoot it is concluded that turbulent jets are unsatisfactory flows in which to measure the turbulent diffusivity of droplets. An experiment has been performed by Snyder [2] in which particle dispersion is measured in a uniform air flow through a duct. This flow avoids the problems associated with a turbulent jet. The results show a clear trend for Sc_T to increase with τ/T, in agreement with models 1 and 2. Thus models 1 and 2 which show trends that are compatible with physical expectations are the ones to be used, in preference to models 3 and 4.

Validation of the Models

Models 1 and 2 will now be quantitatively compared with the data of Snyder [2]. Gosman [6] has already used these data to test a model similar to model 2 and has obtained good agreements for the heavier particles, but less good agreement for the lighter particles.

It has been shown above that if the turbulent timescale T is constant

$$\sigma = \Delta x\, n^{1/2} \tag{24}$$

The time after n intervals of duration T is given by

$$t = n\,T$$

$$\sigma^2 = \Delta x^2 t/T \tag{33}$$

(Note that the assumption of constant time steps taken here is merely in order to enable comparisons to be made. In actual computation, no such assumption is necessary.)

Using equations (29) and (30)

$$\text{Model 1} \quad \sigma^2 = \frac{\mu_T t}{\rho\, Sc_{TG}} \left(1 + \left(\frac{\pi\tau}{T}\right)^2\right)^{-1} \tag{34}$$

$$\text{Model 2} \quad \sigma^2 = \frac{\mu_T T\, t\, U'}{l\rho\, Sc_{TG}} \left(1 + \frac{\tau}{T}\left(\exp\left(\frac{-T}{\tau}\right) - 1\right)\right)^2 \tag{35}$$

In deriving numerical values for comparison, a value of 0.7 is used for Sc_{TG} following [8] and μ_T/ρ, T, and τ are calculated from the data of Snyder.

Figure 2 shows a comparison of equations (34) and (35) with the experimental results. The derivation of equations (34) and (35) is only approximate because the initial assumption that timescale T is constant is not true. However, Fig. 2 does give an indication of whether models 1 and 2 predict results of the correct order of magnitude.

Very close agreement is shown between models 1 and 2, which is encouraging, since they are based on fundamentally different approximations to the complex problem of turbulent diffusion. Both models underpredict the rate of diffusion for all sizes of particle by a factor of around 0.75. In view of the very approximate analysis involved this result seems quite reasonable. As noted earlier, a correction factor on e_T may be introduced in equation (22) to improve agreement. It is interesting to note that a factor of 2 produces an increase in predicted diffusion of $\sqrt{2}$ giving virtually exact agreement. However, this step does not appear to be fully justified in the absence of further experimental data.

Conclusion

The rate of diffusion of liquid drops in a turbulent flow is characterized by the timescale ratio τ/T. Experimental studies of diffusion show conflicting trends, but the most reliable results are those of Snyder [2], which show that Sc_T increases with τ/T, i.e. small droplets will diffuse faster than large ones under identical conditions. Of the models which have been proposed there are two models which predict the correct trend, though both tend to underestimate the rate of diffusion by about the same amount. Using either of these models it is possible to include droplet turbulent diffusion effects in both continuum and discrete spray prediction programs to give a reasonable degree of accuracy at little extra computational cost.

Acknowledgments

Our thanks go to the Science and Engineering Research Council for the award of a grant to one of the authors, P. Ward.

References

1 Soo, S. L., "Fluid Dynamics of Multiphase Systems," Blaisdell, 1967.

2 Snyder, W. H., and Lumley, J. L., "Some Measurements of Particle Velocity Autocorrelation Functions in a Turbulent Flow," *J. Fluid Mech.*, Vol. 48, 1971, pp. 41–71.

3 Jones, W. P., and Priddin, C. H., "Predictions of the Flow Field and Local Gas Composition in Gas Turbine Combustors," *Seventeenth Symposium (International) on Combustion*, The Combustion Institute, 1979, pp. 399–409.

4 El Banhawy, Y., and Whitelaw, J. H., "Calculation of the Flow Properties of a Confined Kerosene Spray Flame," *AIAA J.*, Vol. 18, 1980, pp. 1503–1510.

5 Hinze, J. O., "Turbulent Fluid and Particle Interaction," *Prog. in Heat and Mass Trans.*, Vol. 6, 1972, pp. 433–452.

6 Gosman, A. D., and Ioannides, E., "Aspects of Computer Simulation of Liquid Fuelled Combustors," paper presented at AIAA 19th Aerospace Sciences Meeting, St. Louis, MO, 1981.

7 Hinze, J. O., "Turbulence," 2nd edn., McGraw-Hill, New York, 1975.

8 Launder, B. E., and Spalding, D. B., "Mathematical Models of Turbulence," Academic Press, New York, 1972.

9 Longwell, J. P., and Weiss, M. A., "Mixing and Distribution of Liquids in High-Velocity Air Streams," *Industrial and Engineering Chemistry*, Vol. 45, 1953, pp. 667-677.

10 Katsuki, M., Mizutani, Y., and Ohta, M., "Theoretical Approach to Spray Combustion in Gas Turbine Combustor," Tech. Rpt. No. 1482, Osaka University, 1978.

11 Crowe, C. T., and Pratt, D. T., "Finite-Difference Methods for Calculation of Heterogeneous Combustion," paper presented at Spring Meeting of Central States Section, Combustion Institute, 1978.

12 Lockwood, F. C., Salooja, A. P., and Syed, S. A., "A Prediction Method for Coal Fired Furnaces," *Combustion and Flame*, Vol. 38, 1980, pp. 1-15.

13 O'Rourke, P. J., and Bracco, F. V., "Modelling of Drop Interactions in Thick Sprays and a Comparison With Experiments," Inst. of Mechanical Engineers Paper No. C404/80.

14 Liu, B. Y. H., and Ilori, T. A., "Aerosol Deposition in Turbulent Pipe Flow," *Envi. Sci. and Tech.*, Vol. 8, 1974, pp. 351-356.

15 Gudmundsson, J. S., and Bott, T. R., "Particle Diffusivity in Turbulent Pipe Flow," *J. Aerosol Sci.*, Vol. 8, 1977, pp. 317-319.

16 Abbas, A. S., Koussa, S. S., and Lockwood, F. C., "The Prediction of the Particle Laden Gas Flows," *Eighteenth Symposium (International) on Combustion*, The Combustion Institute, 1981, pp. 1427-1438.

17 Abramovich, G. N., and Girshovich, T. A., "Diffusion of Heavy Particles in Turbulent Gas Streams," *Soviet Physics Doklady*, Vol. 18, 1974, pp. 587-589.

18 Jurewicz, J. T., and Stock, D. E., "A Numerical Model for Turbulent Diffusion in Gas Particle Flows," ASME Paper No. 76-WA/FE-33.

19 Hotchkiss, R. S., and Hirt, C. W., "Particulate Transport in Highly Distorted Three-Dimensional Flow Fields," *Proc. Summer Simulation Conference*, SHARE, San Diego, CA, June 1972.

20 Singamsetti, S. R., "Diffusion of Sediment in a Submerged Jet," *Proc. Am. Soc. Civ. Eng.*, Vol. 92, HY 2, 1966, pp. 153-168.

21 Goldschmidt, V. W., Householder, M. K., Ahmadi, G., and Chuang, S. C., "Turbulent Diffusion of Small Particles Suspended in Turbulent Jets," *Progress in Heat and Mass Trans.*, Vol. 6, 1972, pp. 487-508.

22 Lilly, G. P., "Effect of Particle Size on Particle Eddy Diffusivity," *Industrial and Engineering Chemistry Fundamentals*, Vol. 12, 1973, pp. 268-275.

23 Mills, A. F., and Lau, H. K., "Particle Transport Across a Plane Turbulent Jet," *Industrial and Engineering Chemistry Fundamentals*, Vol. 14, 1975, pp. 134-136.

24 Laats, M. K., and Frishman, F. A., "Scattering of an Inert Admixture of Different Grain Size in a Two-Phase Axisymmetric Jet," *Heat Transfer Soviet Research*, Vol. 2, 1970, pp. 7-12.

25 Hedman, P. O., and Smoot, L. D., "Particle-Gas Dispersion Effects in Confined Coaxial Jets," *AIChE J.*, Vol. 21, 1975, pp. 372-379.

26 Memmot, V. J., and Smoot, L. D., "Cold Flow Mixing Rate Data for Pulverised Coal Reactors," *AIChE J.*, Vol. 24, 1978, pp. 466-473.

27 Tice, C. L., and Smoot, L. D., "Cold Flow Mixing Rates With Recirculation for Pulverised Coal Reactors," *AIChE J.*, Vol. 24, 1978, pp. 1029-1035.

Combustion Efficiency of a Premixed Continuous Flow Combustor

M. S. Anand
Graduate Research Assistant.

F. C. Gouldin
Professor.

Sibley School of Mechanical and Aerospace Engineering, Cornell University, Ithaca, NY 14853

Experimental data in the form of radial profiles of mean temperature, gas composition and velocity at the combustor exit and combustion efficiency are reported and discussed for a swirling flow, continuous combustor. The combustor is composed of two confined, concentric independently swirling jets: an outer, annular air jet and a central premixed fuel-air jet, the fuel being propane or methane. Combustion is stabilized by a swirl-generated central recirculation zone. The primary objective of this research is to determine the effect of fuel substitution and of changes in outer flow swirl conditions on combustor performance. Results are very similar for both methane and propane. Changes in outer flow swirl cause significant changes in exit profiles, but, surprisingly, combustion efficiency is relatively unchanged. A combustion mechanism is proposed which qualitatively explains the results and identifies important flow characteristics and physical processes determining combustion efficiency. It is hypothesized that combustion occurs in a thin sheet, similar in structure to a premixed turbulent flame, anchored on the combustor centerline just upstream of the recirculation zone and swept downstream with the flow. Combustion efficiency depends on the extent of the radial propagation, across mean flow streamtubes, of this reaction sheet. It is concluded that, in general, this propagation and hence efficiency are extremely sensitive to flow conditions.

Introduction

Swirling flows have been of interest for many years because of their potential for stabilization of high-intensity combustion processes [1]. The attractive features of swirling flows, namely better flame stability due to the formation of one or more recirculating flow zones, reduced combustion length, and increased mixing through turbulence generation, have been demonstrated in numerous experimental studies involving both diffusion and premixed flame combustors (e.g., [2, 3, 4, 5, 6]).

Recirculation in swirling flows is known to depend in part on the swirl number S, the ratio of the axial flux of angular momentum to the axial flux of linear momentum, and the Reynolds number of the flow [1, 7]. Above a critical swirl number the phenomenon of vortex breakdown [8, 9] occurs, characterized by the formation of a free stagnation point on the vortex axis, followed by reverse flow in a region of limited axial extent. Among the various forms of vortex breakdown possible [8, 10] most notable in the present context is the axisymmetric or bubble which is typically used to stabilize combustion. Unfortunately, the simultaneous presence of swirl, mean flow shear, turbulence, and heat release makes the reacting vortex flow a very complex object of study and, as a consequence, these flows are not well understood. The present work is part of a continuing program to study and characterize swirling reacting flows.

Efficiency and Pollutant Emissions. One of the present applications of the swirl combustor is in gas turbine engines. With the growth in applications for and the widespread use of gas turbines, the problem of pollutant emissions from gas turbine exhausts and the need to limit such emissions have grown. The three major pollutants from gas turbine combustors are carbon monoxide (CO), unburned hydrocarbons (UHC), and oxides of nitrogen (NO_x) which comprise nitric oxide (NO) and nitrogen dioxide (NO_2). Soot and sulfur oxides are normally not of concern in a combustor operating on lean premixed hydrocarbon–air mixtures (i.e., low-sulfur-content fuels). An understanding of the chemical mechanisms for formation of air pollutant species is required in order to interpret experimental results from laboratory combustors and to develop models to describe such combustors.

Unburned hydrocarbons are a direct indication of inefficient combustion. In addition, they are intimately connected with oxides of nitrogen in the formation of photochemical smog in the atmosphere [11, 12]. Premixed, prevaporized combustion at near-stoichiometric conditions is likely to minimize or effectively eliminate UHC emissions. Carbon monoxide in the gas turbine exhaust, in addition to being toxic, is also an indication of inefficient combustion. It is well accepted that the oxidation of CO to CO_2 in combustion systems follows the reaction [13]

Contributed by the Power Division for publication in the JOURNAL OF ENGINEERING FOR GAS TURBINES AND POWER. Manuscript received by the Power Division July 1983.

$$CO + OH = CO_2 + H \quad (1)$$

which proceeds rapidly at high temperatures but slowly at low temperatures due to reduced levels of OH. At slightly lean conditions the CO concentrations are kept to a minimum (equilibrium level) in the primary zone of the combustor where high temperatures are reached and combustion is complete. At stoichiometric conditions higher CO levels can result due to dissociation of CO_2 at high temperatures. CO increases relative to stoichiometric levels both in rich mixtures due to lack of oxygen and in very lean mixtures due to a slowing of reaction (1) (thermal quenching) at low temperatures, thus following a trend similar to that of UHC. However, since CO oxidation is slower than hydrocarbon oxidation, CO is more prone to thermal quenching and persists unreacted for many (5-6) milliseconds in fuel lean ($\phi = 0.8$) flames [14]. Thus high CO emissions from fuel lean mixtures are an indication of quenching in the secondary zone of the combustor.

Oxides of nitrogen are highly toxic. In addition, they play important roles in smog formation and depletion of ozone in the stratosphere [15]. The relative amounts of NO and NO_2 present in jet engine exhausts influence the rate of reactions in the stratosphere [12], and in recent studies the two species are reported separately. In combustion systems, NO is a prerequisite for NO_2 formation. It is generally accepted that NO formation in fuel-lean mixtures follows the Zel'dovich mechanism (thermal NO) in the absence of fuel-bound nitrogen [16]. Formation of NO is associated with high temperatures. Under lean conditions in a combustor NO increases with increase in equivalence ratio due to the accompanying increase in temperature, following a trend opposite to that of CO and UHC. But even at high temperatures NO formation is fairly slow and occurs on a time scale of several milliseconds. This understanding suggests two strategies for NO control: The first is to lower the peak temperatures in the combustor by lean, premixed operation (prevaporization of fuel may be necessary) and by exhaust gas recirculation, and the second is to reduce the residence time in the primary zone by rapid addition of secondary air through turbulent mixing. The formation of NO_2 is less well understood than the formation of NO, though several explanations have been tendered. A mechanism which is capable of explaining the high NO_2/NO_x fractions observed in many studies invokes the reaction [11]

$$NO + HO_2 = NO_2 + OH \quad (2)$$

Excess HO_2 resulting from hydrocarbon oxidation appears, through reaction (2), to be the cause of the high NO_2/NO_x fractions which are observed. Further support for this mechanism comes from the study by Chen et al. [16] who showed that when a partially reacted sample containing unburned fuel is quenched (either by mixing with cool air or in a sampling probe), large concentrations of HO_2 are produced during the accompanying low-temperature hydrocarbon oxidation. Reaction (2) is therefore favored in quenching zones, and the high NO_2/NO_x fractions can be attributed to quenching zones in the combustor.

The preceding discussion leads one to the conclusion that since conditions minimizing NO_x formation tend to maximize CO and UHC emissions or, in other words, tend to reduce combustion efficiency, and vice versa, a tradeoff is inevitable. Only advanced and radically new combustor designs involving concepts such as lean, prevaporized, premixed combustion, variable geometry, and swirl-augmented combustion can possibly meet the proposed aircraft emission standards without undue sacrifice in combustion efficiency [17].

Present Study. The combustor under investigation (Fig. 1), a confined concentric jet configuration, operates on premixed propane or methane and air with reaction stabilized by a swirl-generated recirculation zone. The inner flow is premixed fuel and air, while the outer flow is air only. Both flows may be swirled either in the same (coswirl) or opposite (counterswirl) directions. Lean operation adversely affects combustion efficiency. Adjustment of the recirculation zone and the conditions in its neighborhood by varying swirl and interjet slip velocities in a configuration such as this one seems to be a viable method for offsetting the detrimental effects of lean operation. The successful demonstration of this concept involves varied, elaborate and time-consuming experiments. Data over a range of operating conditions are needed in order to identify and understand the important fluid mechanical and combustion processes operative in the different zones of the combustor which determine overall combustor performance, namely the combustion efficiency and pollutant emissions. With this understanding, suitable models for the combustor operation can be developed to relate, over the operating range, performance to inlet conditions. In the course of the experiments it is important to develop and verify new and existing experimental techniques used in the collection of data.

In the study reported here, exhaust gas temperature, velocity, and composition measurements at various radial locations at the combustor exit were made and combustion efficiencies were calculated for propane fuel in the combustor under various outer swirl conditions. These data were compared with previous studies with methane firing [18, 19]. To keep data analysis times short, a novel gas chromatographic scheme was developed and employed for composition measurements. A pressure probe was used for velocity measurements, and it was found that *in situ* probe calibration is required to account for turbulence effects. Certain runs conducted for propane firing were repeated for methane firing in order to determine directly the effect of fuel substitution on the quantities measured. By comparison of data for propane with those for methane it is possible to ascertain whether the combustor operation is sensitive to the fuel used and whether data obtained for methane fuel can be used to characterize combustor operation with practical fuels of which propane is more representative.

A mechanism for combustion is proposed which explains qualitatively the changes in efficiency and pollutant emissions observed with changing swirl in the present and previous [19] studies. Important physical processes determining combustion efficiency are identified.

Experimental

The combustor is composed of two co-axial swirling jets (Fig. 1). Ambient air supplied to the combustor by a single blower is divided into two streams to form the inner and outer jet flows for the combustor. The inner jet, 5.1 cm in diameter, is premixed fuel and air, and the outer jet, 10.2 cm in diameter, is secondary air. Variable swirl in the inner flow is obtained by injecting air both tangentially and axially into a mixing section approximately five combustor diameters upstream of the combustor inlet. Swirl in the outer jet is regulated by variable angle vanes with both co- and counterswirl conditions possible. The combustor test section is 58.3 cm long, 10.2 cm in i.d., and is made of quartz tubing. The inner diameter of the test section is the combustor diameter (D_0). The exhaust gases exit through a 10.2-cm-i.d. stainless steel tube section and out through a chimney.

The fuel, commercial grade propane or methane, is injected radially from the inner jet centerline $5D_0$ upstream of the combustor inlet through eight sonic orifices symmetrically positioned around the circumference of a 0.95-cm-o.d. stainless steel tube lying on the centerline of the flow passage. A long reach spark plug is temporarily inserted into the combustor test section close to the centerline at the test section

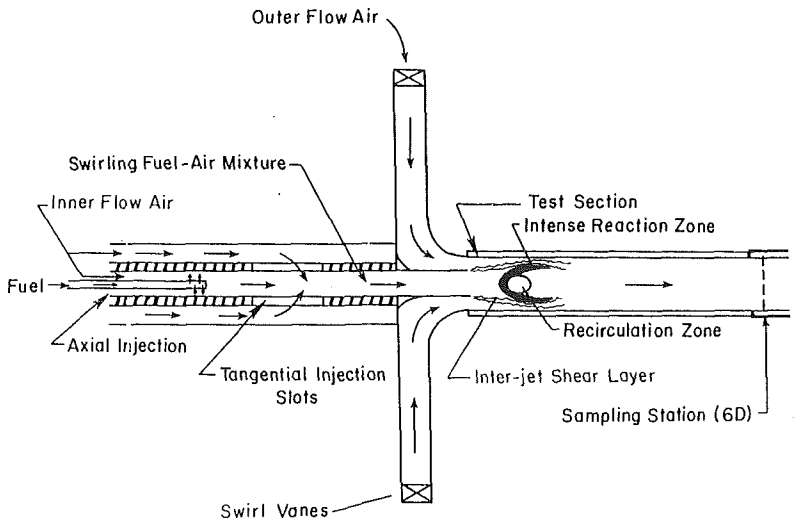

Fig. 1 Schematic diagram of the swirl combustor

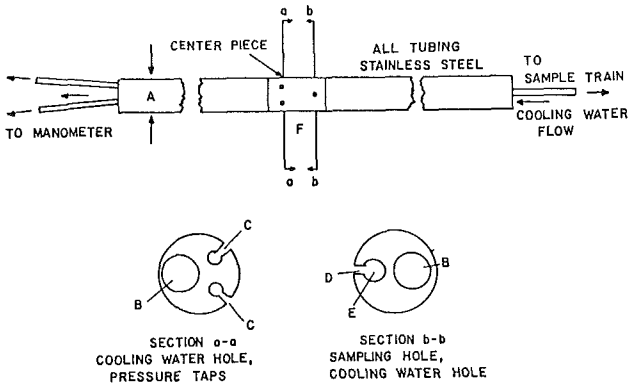

Fig. 2 Cylindrical probe for sampling and velocity measurements; dimensions: A = 7.9 mm o.d., B = 2.5 mm dia., C = 0.9 mm dia., D = 1.6 mm dia., E = 1.8 mm dia., F = 7.9 mm

inlet for the purpose of ignition. The combustor is operated at atmospheric pressure without preheat.

Test Conditions. The nondimensional swirl number for the inner or outer jet is given by

$$S = \int_{r_i}^{r_o} uvr^2 dr / r_o \int_{r_i}^{r_o} u^2 r dr \tag{3}$$

where r_i and r_o are the inner and outer radii of the jet under consideration, and u and v are the time-mean axial and tangential velocities respectively. The swirl number is positive as defined. A negative sign is used for the outer-flow swirl number under counterswirl conditions. The principal operating variables of the combustor are the inner and outer swirl numbers (S_i and S_o), the inner and outer jet flow rates, and the fuel flow rate (Q_f). The axial velocity ratio (U_i/U_o) is the ratio of the volumetric mean axial velocity of the inner jet to that of the outer jet.

Composition, velocity and temperature measurements are made at various radial locations at the exit plane ($6D_0$ downstream of the combustor inlet) for varying outer swirl, with the inner flow swirl, inner flow equivalence ratio (ϕ_i), and total volume flow rate more or less constant for all the runs. The test conditions, including the corresponding angle settings of the outer swirl vanes, are listed in Table 1. (0 deg vane angle setting corresponds to nonswirling outerflow. U_{oa} and ϕ_{oa} are the overall volumetric mean axial velocity and equivalence ratio respectively, under nonreacting conditions.)

Sampling Probe. A water-cooled cylindrical probe spanning the diameter of the combustor (Fig. 2) was used to withdraw samples and make velocity measurements. A sampling hole, two pressure taps (located 59 deg on either side of the sampling hole), and a cooling water hole are drilled into a solid cylindrical brass center piece. The sample line of the probe is connected to the sample train which draws samples for analyses. The pressure lines are connected to either end of a micromanometer enabling pressure measurements for velocity determination as well as for alignment of the probe to the flow direction. The probe can be rotated about its axis, and when the mean pressures at the two taps are equal, the bisector of the angle between the pressure taps is aligned with the mean flow direction at the radial location of the taps. Radial traverses were made by sliding the probe across the exhaust tube diameter.

The sample line from the probe is divided into two branches in the sample train, the chemiluminescent NO_x analyzer line and the syringe sampling line. All portions of the sample train except for the syringe sampling portion were heated to prevent water condensation. After water removal in the syringe sampling line by condensation in ice baths, samples were drawn into 5-ml gas-tight syringes and stored for gas chromatographic analysis.

Analysis by Gas Chromatography. The objective of the analysis was to obtain the relative amounts, on a dry basis, of oxygen, nitrogen, carbon monoxide, carbon dioxide, unburned propane, and of other possible lower hydrocarbons such as ethane, ethylene, and methane quickly and preferably with a simple scheme involving a single injection of sample.

Unfortunately, there is no single column material which allows complete separation of all the aforementioned gases (including oxygen and nitrogen) in the sample without requiring a long time for analysis (50 min or more). In addition, a few column materials irreversibly adsorb some of the component gases. For example, molecular sieve, which is the most efficient column to obtain the oxygen/nitrogen split, irreversibly adsorbs carbon dioxide. Porous polymers and silica gel which allow separation of carbon dioxide are incapable of separating oxygen, nitrogen and carbon monoxide from each other at room temperature or above. Other columns like the Alltech Associates' molecular sieve-poropak concentric (CTR) column and Supelco's carbosieve S column take nearly 80 and 50 min respectively per sample to give the required separation of all the component gases, even with temperature programming. It is crucial to keep the analysis time short since, otherwise, the total time required to complete the analyses of all the samples collected from various

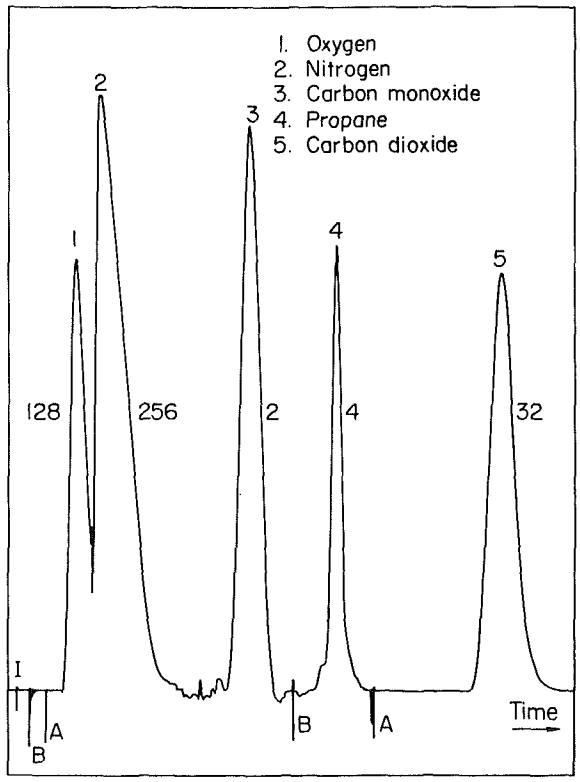

Fig. 3 Sample chromatogram: The numbers on the sides of the peaks indicate detector attenuation; the sample injection point (I) and points of valve switching to positions A and B are indicated; the time axis is compressed between peaks

radial locations in a single combustor run would be 8 to 9 hr by which time substantial leakage of ambient air into the syringes would have contaminated the stored samples.

To overcome all these difficulties, a scheme using two columns in series with a four-port switching valve was used. After a careful study of the properties of various columns, it was found that columns of poropak Q and carbosieve S would be most suitable for the purpose. The four-port valve switches between two flow arrangements, A and B. In position A the two columns are in series and the eluates from the poropak Q go through the carbosieve S column. In position B the carbosieve S column is bypassed and the eluates from poropak go directly to the detector. The gas chromatograph conditions are as follows: Column 1: Poropak Q, 1/8 in. × 6 ft, SS; Column 2: Carbosieve S, 1/8 in. × 8 ft, 100/120 mesh, SS; oven temperature: 50°C for 4 min and programmed at 25°C/min to 175°C; carrier gas: helium, 47 ml/min; detector: thermal conductivity, 270°C, 160 MA, 0.5 MV range; sample size: 0.5 ml.

Figure 3 shows a sample chromatogram obtained under the above conditions for a sample withdrawn from the combustor. The sample is injected with the four-port valve in position A. A composite peak of air, carbon monoxide, methane (if present), and carbon dioxide elutes within 0.8 min from the poropak and passes into the carbosieve column. The valve is switched to position B at the end of 2 min. Ethylene and ethane, which elute in that order at 2.5 min from poropak, pass directly to the detector. (Ethylene and ethane were not present in the sample and hence are not seen in Fig. 3.)

The valve is switched back to position A immediately after the elution of ethane (i.e., after approximately 3 min). Oxygen elutes from the carbosieve column at about 3.5 min (the exact time depends on how long the valve is kept in position B), followed by nitrogen and carbon monoxide. The valve is again switched at the end of 6 min to position B. Propane eluting from the poropak passes directly to the detector and can be detected at about 6.8 min. The valve is then switched back to position A. Methane elutes from the carbosieve at 9.5 min followed by carbon dioxide at 11.2 min. The column oven temperature is then reset to the initial temperature, 50°C. In this way the entire sample analysis including propane, ethane, and ethylene can be done within 12 min. In addition, the columns are ready for the next sample as soon as they cool to the initial temperature. The total cycle time is approximately 15 min.

Based on noise levels and the detector response to the species of interest we estimate the minimum detectable amounts to be 40 ppm for CO_2 and approximately 70 ppm for the other species. Errors in measured concentrations, as a result of inaccuracies in calibration gas samples and in reading peak areas (Fig. 3) were estimated, for typical species concentrations in the combustor, to be less than ±3 percent for all the species. These estimates do not include possible error due to air leakage into the syringes.

NO, NO_x Measurements. NO and total NO_x measurements were made using the well-established chemiluminescence method in conjunction with a NO_2 to NO converter [20]. The chemiluminescent analyzer was constructed at Cornell University [21, 22]. All lines in the chemiluminescent analyzer system and the sample transfer lines are maintained at 323 K by electrically heating with nichrome wires to prevent removal of NO_2 by water condensation. To obtain reliable and accurate NO_x measurements, preconditioning of the converter is essential [23]. Hence the converter was conditioned at 1023 K with air flow for at least one hour prior to every test run and operated at 1023 K. In addition, the entire system including the converter was purged with air between every data point thereby ensuring the oxidation of the metal surface of the converter. The difference between the NO_x and NO readings from the analyzer gives the NO_2 in the sample.

Velocity Measurements. The pressure taps in the cylindrical probe (Fig. 2) are used to find the mean flow direction θ with respect to a horizontal reference (see earlier section on sampling probe). When the pressures in the two taps are balanced the pressure (P_{59}) in either of the taps is measured. Subsequently one of the pressure taps is aligned with the flow direction to measure the total pressure (P_T). The difference ($P_T - P_{59}$) can be related to the dynamic pressure ($P_T - P_S$), where P_S is the static pressure, through calibration. The calibration was done in an unconfined, nonswirling, low turbulent intensity (laminar) jet. The mean total velocity at the measurement location can be calculated from the dynamic pressure obtained from the laminar calibration and is denoted by V_l.

Velocity measurements in turbulent swirling flows using a transverse cylindrical probe are affected by stream turbulence and swirl in the following manner. Turbulence in the flow accelerates the transition of the boundary layer on the surface of the probe from laminar to turbulent and moves the separation point further downstream on the probe surface [24] thereby altering the pressure distribution on the surface of the probe. Therefore the calibration of the probe done in a laminar flow may not be valid in a turbulent flow.

Bilger [25] has pointed out the possibility of secondary flow along the probe toward the vortex core due to the positive radial component of the mean pressure gradient present in swirling flows. The effect of the secondary flow is such that the velocity measured by the probe actually corresponds, in the undisturbed flow, to a radial location displaced approximately 0.09 of the probe diameter from the measurement point to a larger radius [26]. Since the diameter of the probe used in this study is small compared to the diameter of the combustor, swirl in the flow is not likely to cause significant displacements of this type.

Since the turbulent intensities in the combustor are high, about 10 percent of the mean flow velocity [27], the validity of the laminar calibration of the probe for use in the combustor was checked. A laser doppler velocimeter (LDV) described by Depsky [28] was used to measure velocities in the combustor (without the probe in place) and these data were compared with velocities measured by the probe. It was found that the velocities measured by LDV were about 20 percent lower than those obtained with the laminar calibration of the probe. Hence the velocity V_l has to be multiplied by a correction factor f_c in order to obtain the correct velocity V. It was found that f_c is a decreasing, nearly linear, weak function of V_l alone and is in the range of 0.88 to 0.73 for all operating conditions in this study including nonreacting (cold) and reacting (hot) flow conditions. Since the f_c values were not found to depend on the swirl condition or the presence of temperature gradients in the flow, it can be concluded that the presence of swirl and density gradients did not affect the measurement of velocity using the cylindrical probe. The factor f_c accounts for the effect of turbulence and also corrects for any probe blockage effects since LDV measurements were made without the probe in place and then compared with the probe measurements to obtain f_c. LDV measurements confirmed that the probe accurately measured the mean flow direction angle to within half a degree.

The corrected mean total velocity (V), and the axial (u) and tangential (v) components of the mean velocity are calculated from

$$V = V_l f_c, \quad u = V\cos\theta \text{ and } v = V\sin\Theta \tag{4}$$

Temperature Measurements. An uncoated fine wire Pt/Pt-10%Rh thermocouple probe was used to measure temperatures. The thermocouple junction was butt-welded using 0.127-mm-dia wires and supported with a 6.4-mm-o.d. ceramic tube. Mean values were obtained by passing the thermocouple output through an analog averaging circuit. Corrections for conduction and radiation losses were not made. In test cases, it was found that the efficiencies calculated from the temperature data increased by 2 percent or less when corrected temperatures were used.

Data Analysis. Average values of temperature and mole fraction were obtained on a mass flux weighted basis defined by

$$\bar{X} = \int_0^{R_0} \rho u X 2\pi r dr \Big/ \int_0^{R_0} \rho u 2\pi r dr \tag{5}$$

where R_0 ($=D_0/2$) is the radius of the combustor and ρ is the local density. It is important that the averaging should be done on a mass flux weighted basis since it is the only truly representative average in a flow with significant velocity, density and concentration gradients. The integrals in equation (6) were evaluated numerically using experimental data. An error analysis showed that the accuracy of the integration procedure was better than ± 0.5 percent for the profiles used in the calculations.

Combustion efficiencies were calculated by two methods. In the first method a chemical efficiency is obtained

$$\eta_c = 1 - \frac{\bar{X}_f + \bar{X}_{CO}(q_{CO}/q_f)}{[F]} \tag{6}$$

where $\bar{X}_f$ and $\bar{X}_{CO}$ are the weighted average mole fractions of fuel and CO in the exhaust; $[F]$ is the average mole fraction of fuel entering the combustor; q_{CO} is the heat release per mole of CO going to CO_2 at the inlet temperature T_{in}, and q_f is the lower heating value per mole of the fuel at T_{in}.

In the second method, a thermal efficiency η_T was calculated.

$$\eta_T = \frac{\text{(measured increase in sensible enthalpy flux in the working fluid)}}{\text{(lower heating value of the fuel)}\dot{m}_f} \tag{7}$$

$$= \dot{H}_e/\dot{m}_f q_f',$$

where

$$\dot{H}_e = \int_0^{R_0} \rho u \left(\sum_i Y_i h_i\right) 2\pi r dr \tag{8}$$

and

$$h_i \int_{t_{in}}^{T} c_{pi} dT$$

h_i is the increase in sensible enthalpy per unit mass of the species i in going from temperature T_{in} to the temperature T, and q_f' is the low heating value per unit mass of the fuel. The kinetic energy terms $u^2/2$ are small compared to the species enthalpy changes h_i and therefore are neglected. The values of specific heats c_{pi} as functions of temperature were obtained from sixth-order polynomials fitted by Prothero [29].

Results and Discussion

Visual Features. The forward portion of the flame has a capsule-shell like appearance (see the intense reaction zone depicted in Fig. 1). This shell, which is anchored on the combustor centerline upstream of the recirculation zone, surrounds the recirculation zone as determined by measurement [27, 30]. Depending on flow conditions the after portion of the luminous flame appears as a long cylinder or as a short bubble. For coswirl, the visible flame was very long, extending even past the sampling station and appearing as a long, cylindrical, luminous core in the test section. In addition, for these cases, the flames were smooth and appeared to be less turbulent than in the counterswirl cases, which were characterized by greater noise and appeared more turbulent. With counterswirl, the flame surface was not smooth but broken and showed rapid fluctuations in position indicating higher levels of turbulence. The flames for the counterswirl cases were larger in diameter, shorter in length than for coswirl and appeard as luminous bubbles. Visual features were the same for propane and methane firing under the same flow conditions.

Temperature, Velocity, and Composition Profiles. Temperature, velocity, and composition profiles for selected test conditions are presented in Figs. 4–10. Axisymmetry of conditions at the combustor exit has been well established [22, 31] and, therefore, profiles are presented for only half the diameter of the combustor. The composition profiles in the figures are presented on a dry basis.

The following terminology will be used in the discussion. "Quenching" refers to the reduction in reaction rates due to cooling (thermal quenching) as well as to the freezing or stopping of reactions by the decay and removal of active free radicals. Quenching occurs due to the "dilution" with cold outer air of zones where reactions are occurring. "Primary zone" refers specifically to the region close to the combustor inlet (up to about 1.5 D_0 axial distance from the combustor inlet) where most of the combustion is taking place. The region downstream of the primary zone will be referred to as the "secondary zone." The oxidations of CO to CO_2 and of NO to NO_2, which take several milliseconds and are slower by orders of magnitude compared to the fuel breakup reactions, are significant in the secondary zone.

Profiles of temperature and velocity are almost identical for the corresponding propane and methane cases (Figs. 4 and 5).

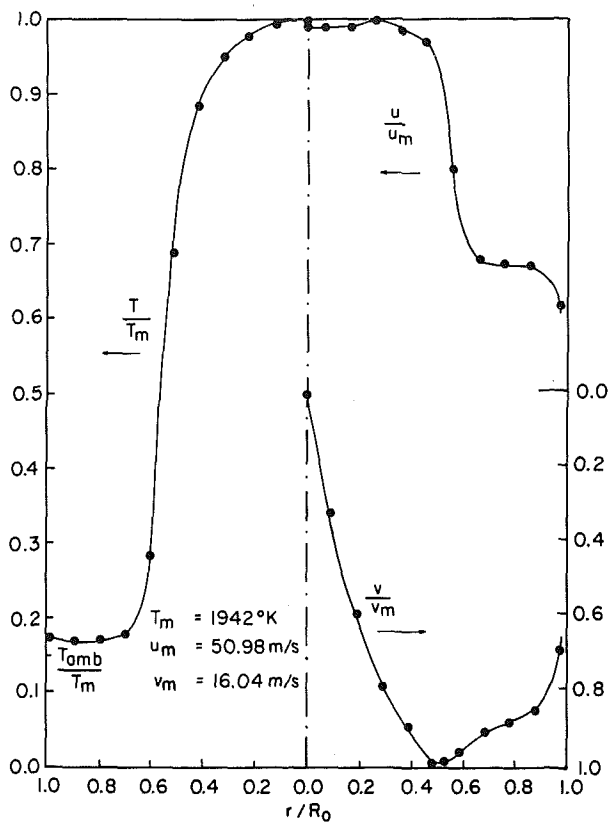

Fig. 4 Mean temperature and velocity profiles for the 55 deg coswirl, propane case

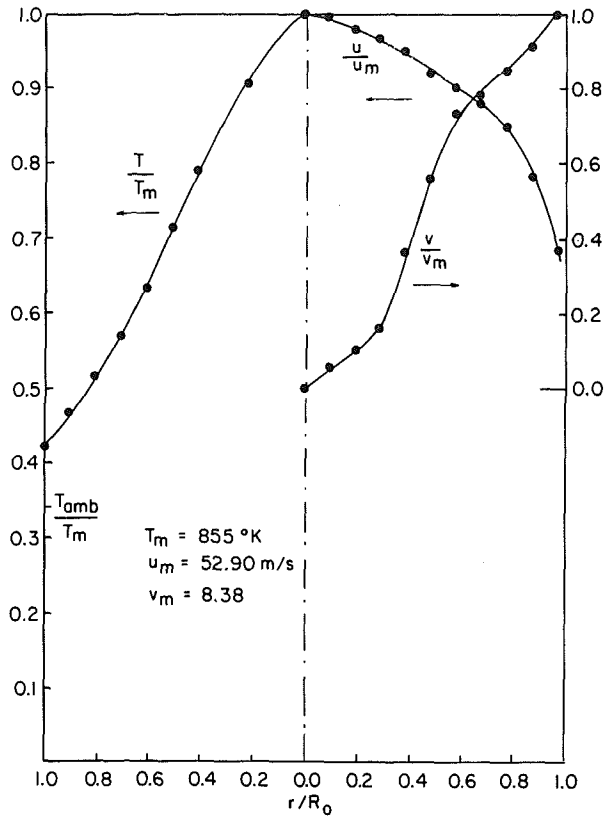

Fig. 6 Mean temperature and velocity profiles for the 30 deg counterswirl, propane case

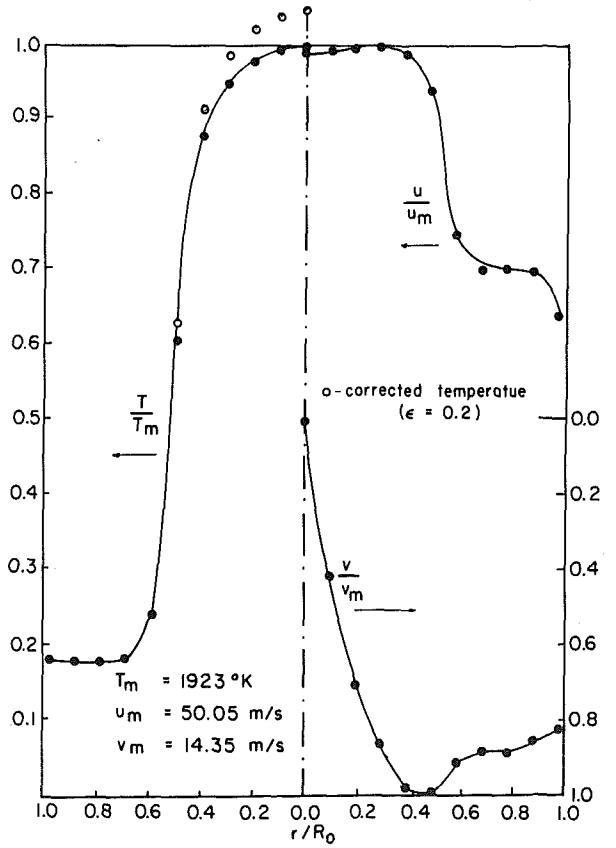

Fig. 5 Mean temperature and velocity profiles for the 55 deg coswirl, methane case; temperature values after radiation correction are also shown

Composition profiles are also qualitatively similar for the corresponding propane and methane cases. A comparison of Figs. 4 and 6 shows that the coswirl cases have very steep temperature and velocity gradients near $r/R_0 = 0.5$ (Fig. 4) compared to the counterswirl cases where the radial variations of temperature and velocity are more gradual (Fig. 6). The coswirl profiles indicate a hot, high velocity flow confined to the center of the combustor bearing out the visual observation of a long cylindrical core of hot gases. The steep radial gradients of temperature and axial velocity in the coswirl cases indicate that turbulent mixing across the combustor is poor relative to the counterswirl cases, since turbulent mixing is expected to smooth out such steep gradients.

Figures 7 and 8 show radial variations of species concentrations as well as the local equivalence ratio ϕ, calculated from the ratio of the total carbon atoms to the total oxygen atoms in the product species. At the inlet, $\phi = 0.8$ in the inner jet and $\phi = 0$ in the outer jet. Therefore, the profile of ϕ at the exit gives an indication of the extent of mixing between the inner and outer jets with the region of rapid variation of ϕ denoting the mixing layer between the two streams. The values of the overall equivalence ratio ϕ_{oa} are also shown in Figs. 7 and 8. Turbulent mixing is poor in the coswirl cases (Fig. 7) with ϕ values close to 0.8 near the centerline. The mixing layer denoted by arrows in Fig. 7 is correspondingly narrow. The ϕ profiles for the counterswirl cases are much flatter, and the ϕ values are close to ϕ_{oa} across the entire radius of the combustor. Hence the mixing layers are quite broad extending from the centerline almost to the wall of the combustor in the counterswirl cases. The composition profiles also show steep gradients in the mixing layer for the coswirl cases compared to gradual variations in the counterswirl cases.

In all the cases unburned fuel and oxygen concentrations are low on the centerline due to combustion. Correspondingly large concentrations of combustion products, namely CO and CO_2, are found in the central core. The concentrations of CO and CO_2 fall steeply while the concentrations of fuel and

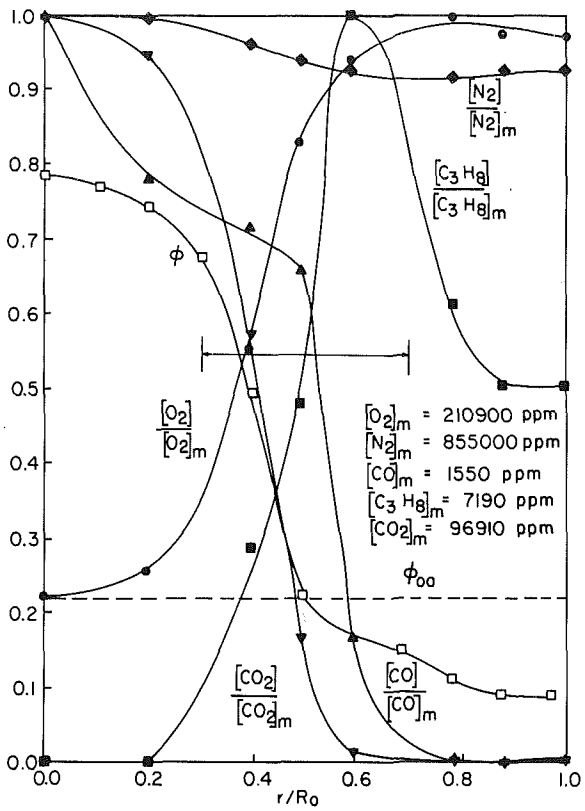

Fig. 7 Mean composition and equivalence ratio profiles for the 55 deg coswirl, propane case

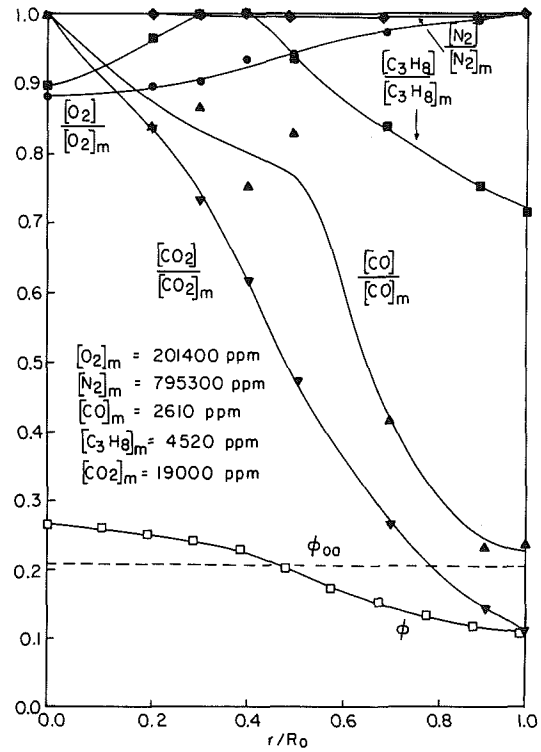

Fig. 8 Mean composition and equivalence ratio profiles for the 30 deg counterswirl, propane case

oxygen increase across the mixing layer indicating that the fuel trapped in the mixing layer is not burned. Fuel concentrations fall at the edge of the mixing layer as the wall is approached since the outer flow is only air. CO concentrations decrease less rapidly than CO_2 concentrations do in the mixing layer, with a local maximum or point of inflection in the CO profile occurring near $r/R_0 = 0.5$, apparently due to quenching of the CO oxidation reactions in the mixing layer.

Table 1 Test conditions

Outer Swirl Vane Angle Setting	S_o	U_i [m/s]	U_i/U_o	U_{oa} [m/s]	ϕ_i	ϕ_{oa}
PROPANE:						
55°Co-	+0.56	30.0	1.32	24.3	0181	0.214
30°Co-	+0.20	30.3	1.25	25.6	0.80	0.210
30°Ct-	-0.20	30.1	1.26	25.3	0.80	0.210
55°Ct-	-0.56	30.2	1.37	23.9	0.80	0.224
METHANE:						
55°Co-	+0.56	31.5	1.33	25.4	0.81	0.218
30°Ct-	-0.20	31.6	1.28	26.2	0.80	0.213

$S_i = 0.495$ $Q_f = 3.4$ SCFM (Propane)
$= 8.5$ SCFM (Methane).

Table 2 Comparison of fractions of $\overline{[CO]}/\overline{[CO_2]}$ and $\overline{[NO_2]}/\overline{[NO_x]}$ in the exhaust

	$\overline{[CO]}/\overline{[CO_2]}$	$\overline{[NO_2]}/\overline{[NO_x]}$	$\overline{[NO_x]}$ (ppm)
PROPANE:			
55° co-swirl	0.03	0.38	5.86
30° co-swirl	0.05	0.61	4.33
30° ct-swirl	0.20	0.81	3.29
55° ct-swirl	0.22	0.78	3.24
METHANE:			
55° co-swirl	0.02	-[a]	-
30° ct-swirl	0.14	-	-

[a]Oxides of nitrogen were not measured for methane firing.

Profiles of oxides of nitrogen are presented in Figs. 9 and 10. The NO_x values follow the temperature values closely with maximum local values of NO_x occurring in the coswirl cases for which the highest temperatures are observed. The importance of quenching in the NO to NO_2 conversion (discussed in the introduction) is clearly demonstrated by the profiles in Figs. 9 and 10. In the coswirl cases NO_x is predominantly NO in the central core when quenching is minimal and temperatures are high, whereas NO_2 predominates in the mixing layer due to the quenching of the hydrocarbon oxidation reactions which produces excessive amounts of HO_2. NO_x in the counterswirl cases is almost entirely NO_2 over the full radius due to the increased mixing and quenching in the secondary zone in the counterswirl cases.

Allen [32] has pointed out the possibility of NO_2 formation in the sampling probe when sampling from combustion zones, due to quenching in the cool probe. In our study, sampling was done at the exit, far away from the combustion zone, where the temperatures are low, especially for counterswirl cases. Moreover, we did not measure a high percentage of NO_2 in coswirl cases though the core temperatures were high and the flames extended past the sampling station, conditions under which probe-formed NO_2 can be expected. Hence the NO_2 measured in our study is real and not formed in the probe.

Table 2 shows that $\overline{[CO]}/\overline{[CO_2]}$ and $\overline{[NO_2]}/\overline{[NO_x]}$ fractions (the overbars indicate mass flux weighted averages) are higher in counterswirl cases compared to coswirl due to increased quenching of hydrocarbon and CO oxidation reactions in the secondary zone as a result of greater mixing in the counterswirl cases. Overall, the $\overline{[NO_x]}$ levels are low as expected for lean premixed combustion with the coswirl cases showing slightly higher values due to higher core temperatures.

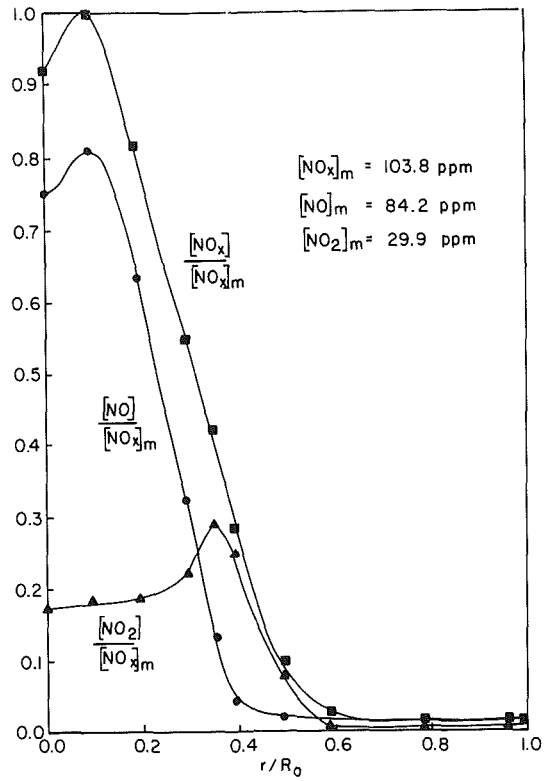

Fig. 9 Mean mole fraction profiles of oxides of nitrogen for the 55 deg coswirl, propane case

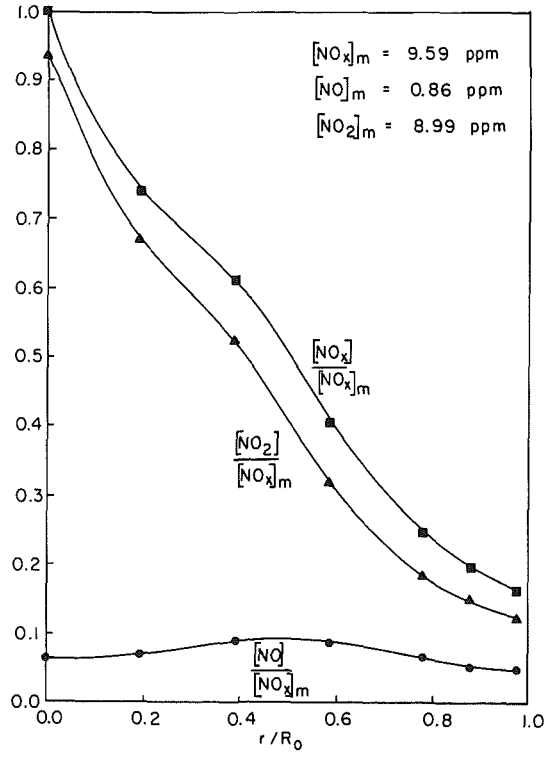

Fig. 10 Mean mole fraction profiles of oxides of nitrogen for the 30 deg counterswirl, propane case

The increased turbulent mixing in going from co- to counterswirl may be accounted for by two mechanisms: First, the tangential slip velocities across the interjet shear layer are increased in going from co- to counterswirl increasing turbulence generation and second, swirl in the presence of large positive radial density gradients suppresses turbulence production which in turn dampens the turbulent exchange of

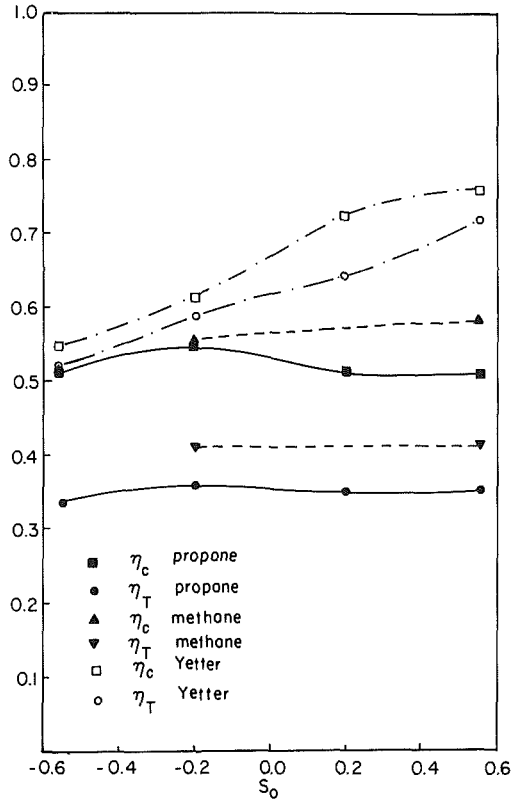

Fig. 11 Chemical and thermal efficiencies for the different outer-swirl conditions under propane and methane firing in the present study compared with those in Yetter's [19] study

mass and momentum between the two jets. Thus reduced interjet shear and high overall swirl levels significantly reduce turbulent mixing for coswirl relative to counterswirl.

Additional temperature, velocity, and composition data for this combustor have been obtained (see Table 1) which give further support to the observations made in this section. They are presented and discussed by Anand [31] but are not reported here in the interest of brevity.

Efficiencies. Combustion efficiencies are quite low (Fig. 11) since a substantial amount of fuel is trapped in the mixing layer and remains unburned due to dilution and the resultant quenching of reactions in this layer. A significant observation is that, in spite of obvious differences in temperature, velocity and composition profiles and mixing trends between the different co- and counterswirl cases, the measured efficiencies are nearly the same for all cases. Efficiencies for methane firing also are close to the efficiencies for propane firing and do not change with outer swirl. This trend of nearly constant efficiency with outer swirl is in contradiction to the observations of Yetter [19] for methane firing who observed an increase of efficiency in going from counter- to coswirl (see Fig. 11) in the same combustor under very similar operating conditions. The value of inner swirl number in the study by Yetter [19] ($S_i = 0.523$) is only slightly different from $S_i = 0.495$, the value in the present study, with the outer flow swirl vane settings being identical in the two studies. However, even a small change in S_i appears to affect the combustor operation substantially. A mechanism for the combustor operation is proposed in the following section to explain this sensitivity.

It is apparent from Fig. 11 that the calculated thermal efficiencies are much lower than the chemical efficiencies for each case. The thermal efficiencies are obtained from sensible enthalpy flux estimates based on the exhaust data and it has been shown [31] that estimated heat loss from the uninsulated

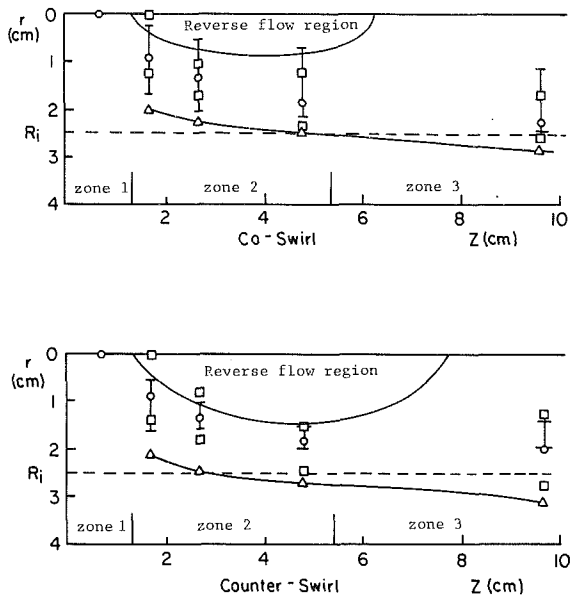

Fig. 12 Reverse flow regions, mean CH radiant emissions maxima (○) and peak axial velocity (Δ) regions near the inlet for the high co- and counterswirl cases; regions of half maxima CH emissions (□) and of large radial gradients of mean axial velocity (I) are also indicated

quartz test section of the combustor can account for the observed differences in the two efficiencies.

Combustion Mechanism. The following mechanism for combustor operation which builds on earlier work [30] is proposed in order to explain our efficiency measurements as well as those of Yetter [19]. It is hypothesized that the major combustion reactions occur in a turbulent reaction sheet, on the order of a centimeter thick and similar in structure to the reaction zone of a premixed turbulent flame. This reaction zone is anchored on the combustor centerline upstream of the recirculation zone. Chemiluminescent emission measurements of CH [30] and velocity measurements [27] for conditions very similar to those of the present study have established the shape and location of the reaction zone relative to the recirculation zone. In Fig. 12, the locations of the reverse flow zone and the reaction zone are presented for methane firing with co- and counterswirl. Circles indicate local maxima in mean CH emissions, while the squares indicate points of half maxima emissions. The curves near the centerline give the boundaries of the reverse flow (negative mean axial velocity) region.

Combustion efficiency depends upon the ability of the reaction zone (referred to as "flame" in the following discussion) to propagate outward, crossing streamtubes while being convected downstream. The factors affecting this ability are (1) inlet turbulence levels, (2) local mean velocities, (3) turbulence generation in the region through which the reaction zone passes, and (4) the local equivalence ratio in these regions. For the purpose of this discussion three zones are identified (Fig. 12) in the combustor. Different combinations of these factors influence flame propagation in each of the three zones.

Upstream of the recirculation zone, in zone 1, inlet turbulence and the mean flow pattern are the important factors. Turbulence levels significantly affect flame propagation, and in this region of flame stabilization higher inlet turbulence levels will give higher flame propagation rates. The work of Moreau and Borghi [33] shows that the influence of inlet turbulence on flame propagation can be quite dramatic. Flame propagation across streamtubes in this zone depends also on local turbulence generation which in turn is influenced by mean flow patterns which depend on the location and size of the recirculation zone. We note that if the local mean velocities are high compared to the flame speed the reaction zone will be nearly parallel to stream surfaces.

In zone 2, which is the region adjacent to the recirculation zone, turbulence generation and dissipation by mean flow shear and other mechanisms such as dilatation and pressure-velocity-density interactions alter local turbulence levels significantly from inlet levels and local flame propagation rates will depend heavily on the turbulence generated by these processes. As in zone 1, the mean velocity field also affects flame propagation. The triangles in Fig. 12 indicate points of local maxima in mean axial velocity in the combustor and the vertical lines delineate regions of large radial gradients of mean axial velocity. This shear layer is caused by the acceleration of the flow around the recirculation zone and by combustion induced flow acceleration [27]. It is evident from Fig. 12 that for both co- and counterswirl, the reaction zone is limited in its radial propagation in zone 2 to this shear layer and does not reach the interjet mixing layer. The contribution of zone 2 to efficiency is determined by the progress of the flame in crossing streamtubes in this shear layer. Higher mean velocities in the region of shear flow around the recirculation zone cause the flame to lie more parallel to streamtubes, while increased turbulence in this region due to mean flow shear and other turbulence generating mechanisms will increase flame speeds and in turn the angle of the flame with respect to the streamtubes. The latter effect should increase efficiency while the former reduces it. The mean axial flow patterns around the recirculation zone in zone 2 for co- and counterswirl cases are similar [27]. However, the local turbulence levels in this region are higher for counterswirl than for coswirl since suppression of shear generated turbulence due to interactions between density fluctuations and swirl is lower because the tangential velocities in this region are lower for counterswirl. Hence it is expected that the radial propagation of the flame across streamtubes is greater for counterswirl than for coswirl in zone 2.

Downstream of the recirculation region in zone 3, in addition to the mean velocities and the turbulence levels, variations in local equivalence ratio become increasingly important. Mixing between the outer air flow and the central jet dilutes the mixture at the edges of the central jet. Thus as the flame propagates radially toward the interjet layer it encounters in a time mean sense progressively weaker mixtures and ultimately the mixture is so weak that the flame is extinguished. Under counterswirl as opposed to coswirl, turbulence generation in the interjet mixing layer is large due to shear in the tangential velocity and there is less turbulence suppression by interactions between density gradients and swirl. Thus dilution of the central stream is more rapid in counterswirl, and the flames are shorter extending only to about $x/D_0 = 1.5$. With coswirl the opposite is true and dilution is much slower and the flame correspondingly much longer, extending beyond the exit of the test section. It is evident that for coswirl radial flame propagation occurs throughout zone 3. However, propagation across streamtubes is slow due to the high mean velocities present which cause the flame to lie nearly parallel to the stream surface. Thus the contribution of zone 3 to the overall efficiency is higher in coswirl than counterswirl but the difference is not in proportion to the additional apparent reaction zone volume.

Thus overall combustion efficiency is determined by the summation of effects of different flow and combustion characteristics in the different regions of the test section. For instance, it is seen that in zone 2 more fuel is likely to be burned in the counterswirl cases than in the coswirl cases, while the converse is true in zone 3. It so happens that in our study the amounts of fuels burned in the three zones add up to approximately the same amount for all the outer swirl conditions studied resulting in a similar efficiency in all cases. This apparent insensitivity of efficiency to outer swirl is the

result of a fortuitous balance of the various factors and is not an inherent characteristic of the combustor. Even a slightly different set of operating conditions is likely to alter this delicate balance making the efficiency sensitive to outer swirl. The results of Yetter [19] show an appreciable increase in efficiency in going from counter- to coswirl. Yetter [19] had a slightly larger inner swirl number, and in photographs of the flames in his study the central recirculation zone appears larger and the radial propagation of the flame in the coswirl cases is seen to be greater than in our study, resulting in higher efficiencies. The combustor appears to be very sensitive to small changes in operating conditions, the inner swirl in particular.[1] Relatively small changes in conditions can lead to large relative changes between the different factors affecting combustion efficiency, and therefore accurate predictions of combustion efficiency are difficult to make. The important conclusion to be drawn from these measurements is that combustion efficiency depends on a number of factors all of which must be accounted for in any model or correlation which would be used to predict combustion efficiency.

The proposed combustion model can also explain the great similarity between the data for methane and for propane firing. Methane lacks a carbon–carbon bond, and its ignition characteristics are quite different from those of other hydrocarbons. Because of these differences many investigators believe that propane rather than methane should be used in combustion studies requiring gaseous fuels because it is chemically more representative of practical hydrocarbon fuels. In our measurements we see no differences between the fuels.

The hypothesis of a thin instantaneous flame sheet type reaction zone implies that the time scales of reaction are much smaller than the turbulent time scales and that turbulent transport is the dominant factor in determining the propagation speed of the flame. Dandekar and Gouldin [34] report turbulent flame speed data for lean methane–air and propane–air mixtures for different turbulent flows. They find nearly identical flame speeds for identical turbulence conditions, mean velocity, and mixture strength for the two fuels. Thus the mechanism of combustion proposed here with its thin flame picture predicts little difference between methane and propane firings for combustion efficiency and other integral characteristics. Important differences in the instantaneous structure of the two flames may exist, but they do not affect the gross characteristics of combustor operation. The same conclusion can be extended to other combustors in which reactions occur in thin sheets and turbulence plays a dominant role. Justification for the extension is provided by the fact that though the configuration of the combustor in [34] (a premixed, nonswirling, rod-stabilized combustor) is quite different from the combustor in the present study, the conclusion with regard to fuel substitution between propane and methane is the same because of reasons mentioned above.

The oxidation of CO and formation of NO_2 proceed slowly compared to fuel breakup reactions. Hence, amounts of CO and NO_2 in the exhaust relative to the amounts of CO_2 and NO_x respectively are determined by the extent of mixing and quenching in zone 3. The high temperatures in the central core and the reduced quenching due to the poor mixing across the combustor in the coswirl cases allow the rapid conversion of CO to CO_2 in the central core. Hence the ratio of CO/CO_2 on the centerline and the overall ratio $[\overline{CO}]/[\overline{CO_2}]$ are lower for coswirl (Fig. 7, Table 2) than for counterswirl (Fig. 8). Note that the major cause of low efficiency is the quenching of fuel reactions and not the quenching of CO oxidation. The large fractions of NO_2/NO_x in the counterswirl cases (Fig. 10, Table 2) are a result of the increased quenching of the hydrocarbon oxidation reactions in zone 3 promoting the formation of excessive HO_2 which oxidizes NO to NO_2.

[1] Exploratory measurements performed by us showed that minor adjustments of the butterfly valve controlling the inner swirl causes changes in the mean temperature on the centerline at the exit of the order of 150 K. This experiment, done for the moderate coswirl case, supports the conclusion that combustor efficiency is very sensitive to inner swirl.

Summary and Conclusions

The results reported in this paper in combination with results from other studies with the swirl combustor lead to the following major conclusions.

The exhaust from the combustion of propane is free from lower hydrocarbons such as ethane, ethylene, and methane. There is no difference in observed properties for propane and methane firing; the use of either of the fuels results in nearly the same exit temperature and velocity profiles and the same efficiency for a given operating condition.

Practically all the combustion occurs in the region close to the combustor inlet (zones 1 and 2) in a thin, turbulent flame sheet. Turbulent mixing in the combustor is enhanced in going from coswirl to counterswirl due to increased shear and reduced tangential velocity levels. Large fractions of CO/CO_2 and NO_2/NO_x are found at the exit as a result of quenching in zone 3 due to mixing and dilution from the outer air, especially in the counterswirl cases. The NO_x levels in the exhaust are low as a result of lean premixed combustion.

Combustion efficiencies in the present study are low and constant with varying outer swirl. A mechanism for combustor operation is proposed which suggests explanations for the constant efficiencies observed in the present study as well as the increases in efficiency in going from counter- to coswirl observed by Yetter [19]. Important processes and flow characteristics considered significant to determining efficiency are identified and discussed. Combustion efficiency depends on the extent of lateral flame propagation across mean flow streamtubes which in turn depends on many factors. The interplay of all these factors on flame processes and combustion efficiency can be quite complex and will be difficult to predict in a combustion model. We expect that the efficiencies of other premixed, prevaporized combustors are similarly dependent on a number of interrelated processes equally difficult to model.

It is evident that combustor operation is very sensitive to even small changes in the inner swirl number. As a practical matter, such sensitivity is undesirable in practical devices. It is therefore necessary to study, for varying outer swirl conditions, the effect of changes in inner swirl on the characteristics determining efficiency in an effort to develop modified designs with high combustion efficiency which are devoid of extreme sensitivity to small changes in operating conditions.

Regarding the experimental aspects of this study, a novel chromatographic column arrangement was used to separate successfully and rapidly combustion products of propane, oxygen, nitrogen, and light hydrocarbons up to propane in less than fifteen minutes. *In situ* calibration of the pressure probe was necessary to correct for turbulence effects in velocity measurements. The use of laminar probe calibration data to make turbulent flow measurements with a pneumatic probe should be used only as a last resort and the data should be interpreted with care.

Acknowledgments

This work was supported in part by the NASA Lewis Research Center, Cleveland, Ohio, Grant NSG-3019. Dr. C.J. Marek was the technical monitor.

References

1 Syred, N., and Beer, J. M., "Combustion in Swirling Flows: A Review," *Combustion and Flame*, Vol. 23, 1974.

2 Lilley, D. G., "Swirl Flows in Combustion: A Review," *AIAA Journal*, Vol. 15, 1977, p. 1063.

3 Syred, N., Chigier, N. A., and Beer, J. M., "Flame Stabilization in Recirculation Zones of Jets with Swirl," Thirteenth Symposium (International) on Combustion, Combustion Institute, Pittsburgh, PA, 1971.

4 Kerr, N. M., and Fraser, D., *Journal of Institute of Fuel*, Vol. 38, 1965, p. 519.

5 Martin, D. J., Gouldin, F. C., and Yetter, R. A., "Preliminary Evaluation of Vortex Breakdown Stabilized Combustor," College of Engineering, Energy Program Report EPR-75-9, Cornell University, Ithaca, NY, Nov. 1975.

6 Yetter, R. A., and Gouldin, F. C., "Exhaust Gas Emissions of a Vortex Breakdown Stabilized Combustor," College of Engineering, Energy Program Report EPR-77-3, Cornell University, Ithaca, NY, 1977.

7 Beer, J. M., and Chigier, N. A., *Combustion Aerodynamics*, Applied Science Publishers, London, 1972.

8 Hall, M. G., "Vortex Breakdown," *Annual Review of Fluid Mechanics*, Vol. 4, 1972, p. 195.

9 Leibovich, S., "The Structure of Vortex Breakdown," *Annual Review of Fluid Mechanics*, Vol. 10, 1978, p. 221.

10 Faler, J. H., and Leibovich, S., "Disrupted States of Vortex Flow and Vortex Breakdown," *Physics of Fluids*, Vol. 20, 1977, p. 1385.

11 Fenimore, C. P., "The Ratio NO_2/NO in Fuel-Lean Flames," *Combustion and Flame*, Vol. 25, 1975, p. 85.

12 Anderson, L. B., Meyer, J. W., and McLean, W. J., "Turbojet Exhaust Reactions in Stratospheric Flight," *AIAA Journal*, Vol. 12, 1974, p. 56.

13 Fristrom, R. M., and Westenberg, A. A., *Flame Structure*, McGraw-Hill, New York, 1965.

14 Fenimore, C. P., and Moore, J., "Quenched Carbon Monoxide in Fuel-Lean Flame Gas," *Combustion and Flame*, Vol. 22, 1974, p. 343.

15 Rudy, R. A., and Reck, G. M., "Advanced Combustion Techniques for Controlling NO_x Emissions of High Altitude Cruise Aircraft," NASA TM-73473, 1976.

16 Chen, J. Y., McLean, W. J., and Gouldin, F. C., "The Oxidation of NO to NO_2 During Combustion Quenching Processes," Paper No. 79-17, presented at the Western States Section/ The Combustion Institute, Spring Combustion Meeting, Brigham Young University, Provo, UT, Apr. 1979.

17 Lefebvre, A., "Pollution Control in Continuous Combustion Systems," Fifteenth Symposium (International) on Combustion, The Combustion Institute, Pittsburgh, PA, 1974.

18 Oven, M. J., Gouldin, F. C., and McLean, W. J., "Temperature and Species Concentration Measurements in a Swirl-Stabilized Combustor," Seventeenth Symposium (International) on Combustion, The Combustion Institute, Pittsburgh, PA, 1978.

19 Yetter, R. A., "Experimental Study of a Vortex Breakdown Stabilized Combustor: Analysis of Exhaust Emissions and Combustion Efficiency," M.S. thesis, Cornell University, Ithaca, NY, 1981.

20 Patterson, D. J., and Henein, N. A., "Emissions From Combustion Engines and Their Control," Ann Arbor Science Publishers, Inc., 1973.

21 Homan, H. S., "An Experimental Study of Reciprocating Internal Combustion Engines Operated on Hydrogen," Ph.D. thesis, Cornell University, Ithaca, NY, 1978.

22 Oven, M. J., "Temperature and Species Concentration Measurements in a Swirl-Stabilized Combustor," M.S. thesis, Cornell University, Ithaca, NY, 1979.

23 Sigsby, J. E., Black, F. M., Bellar, T. A., and Klosterman, D. L., "Chemiluminescent Method for Analysis of Nitrogen Compounds in Mobile Source Emissions (NO, NO_2, NH_3)," *Environmental Science and Technology*, Vol. 7, 1973.

24 Schlichting, H., *Boundary Layer Theory*, McGraw-Hill, 1966.

25 Bilger, R. W., "Probe Measurements in Turbulent Combustion," *Combustion Measurements*, ed. R. Goulard, Academic Press, New York, 1976, p. 333.

26 Bryer, D. W., and Pankhurst, R. C., "Pressure Probe Methods for Determining Wind Speed and Flow Direction," Her Majesty's Stationery Office, London, 1971.

27 Gouldin, F. C., Depsky, J. S., and Lee, S. L., "Velocity Field Characteristics of a Swirling Flow Combustor," Paper presented at the AIAA 21st Aerospace Sciences Meeting, No. 83-0314, Reno, NV, Jan. 1983.

28 Depsky, J. S., "Laser Velocimetry Measurements in a Methane-Fueled Swirl Combustor," M.S. thesis, Cornell University, Ithaca, NY, 1982.

29 Prothero, A., "Computing With Thermochemical Data," *Combustion and Flame*, Vol. 13, 1969, p. 399.

30 Beyler, C. L., and Gouldin, F. C., "Flame Structure in a Swirl-Stabilized Combustor Inferred by Radiant Emission Measurements," Eighteenth Symposium (International) on Combustion, The Combustion Institute, Pittsburgh, PA, 1980.

31 Anand, M. S., "Exhaust Gas Measurements in a Propane Fueled Swirl-Stabilized Combustor," M.S. thesis, Cornell University, Ithaca, NY, 1982.

32 Allen, J. D., "Probe Sampling of Oxides of Nitrogen From Flames," *Combustion and Flame*, Vol. 24, No. 1, 1975.

33 Moreau, P., and Borghi, R., "Experimental and Theoretical Studies of Nitrogen Oxide Production in a Turbulent Premixed Flame," *Journal of Energy*, Vol. 5, No. 3, 1981.

34 Dandekar, K. V., and Gouldin, F. C., "Temperature and Velocity Measurements in Premixed Turbulent Flames," *AIAA Journal*, Vol. 20, No. 5, 1982.

Influence of Gas Turbine Combustor Design and Operating Parameters on Effectiveness of NO_x Suppression by Injected Steam or Water

G. L. Touchton
Engineer.
General Electric Company,
Schenectady, NY 12345

Steam or water injection has become the state-of-the-art abatement technique for NO_x, with steam strongly preferred for combined-cycle application. In combined-cycle plants, the degradation of the plant efficiency due to steam injection into the gas turbine combustor provides a powerful incentive for minimizing this flow over the entire plant operating map. This paper presents the results of extensive tests carried out on a variety of gas turbine combustor designs. Both test stand and field test data are presented. The usual fuel in the tests is methane; however, some data are presented for combustion of No. 2 distillate oil and intermediate Btu gas fuel. Similarly, the usual inert injected is steam, but some water injection data are included for comparison. The results support the conclusions: 1. Steam and water injection suppress NO_x exclusively through thermal mechanisms, i.e., by lowering the peak flame temperature. 2. Design changes have little effect on NO_x suppression effectiveness of steam or water in jet-stirred or swirl-mixed combustors. 3. Primary zone injection of steam in methane-fueled, jet-stirred combustors is equally effective whether the steam enters with an air stream or with the fuel stream. 4. Water-to-fuel ratio corrected to equivalent energy content correlates NO_x suppression effectiveness for turbulent diffusion flame combustors.

Introduction

The regulatory environment for gas turbine emissions has grown more complex in recent years. In the United States, limitations on the magnitude of emissions have been stable but the range of operating conditions over which the regulations are applied has broadened. In the Japanese market, pressure on the magnitude has been extreme and virtually all operational states of the gas turbine (including startup) are regulated. Further, in the U.S. cogeneration market and the Japanese market, the trend is toward efficient base-loaded, combined-cycle installations.

Steam or water injection has become the industry standard for meeting NO_x regulatory limits in the U.S. and overseas markets. Domestic regulations can be met, in general, with this mode of abatement alone, but Japanese standards can be achieved only through a combination of steam/water injection and exhaust denitrification.

In the U.S. the most stringent requirements are the California cogeneration market where levels of 45-50 ppm actual NO_x may be required. Achieving these levels requires water-to-fuel ratios in the range of 0.8 to 1.0. In Japan, total plant exhaust NO_x levels below 5 ppm may be mandated.

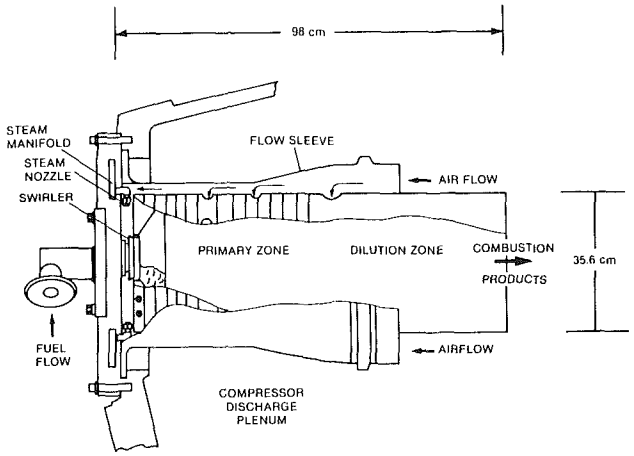

Fig. 1 Standard GE heavy-duty combustion system

Although extremely effective, the use of steam/water injection has the following disadvantages:

1 Plant heat rate is degraded

2 Parts life is lessened due to increased combustor pressure pulsations

Contributed by the Gas Turbine Division and presented at the Joint Power Generation Conference, Toronto, Ontario, Canada, September 30-October 4, 1984. Manuscript received by the Gas Turbine Division June 5, 1984. Paper No. 84-JPGC-GT-3.

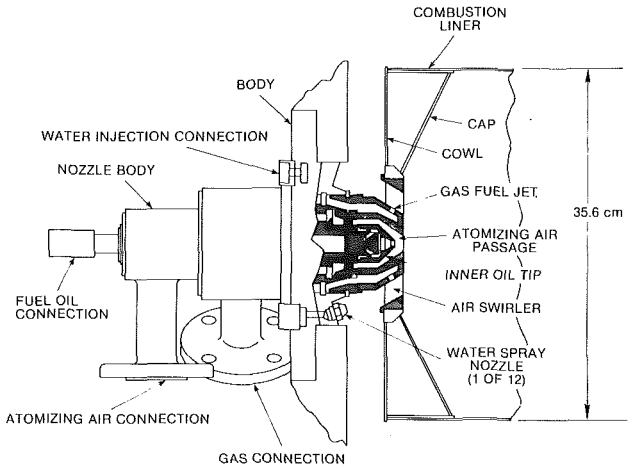

Fig. 2 Water injection fuel nozzle

3 Water treatment costs are an economic penalty
4 System complexity is increased
5 NO_x control steam/water is lost from the cycle

Obviously, there are strong incentives to minimize the amount of steam/water injected, consistent with achieving the abatement goals, i.e., to maximize the effectiveness.

This paper describes the results of a study undertaken to maximize the effectiveness of steam in abating NO_x. Modification of the injection mode or injection location in a standard combustion system was the first line of investigation. The second line of investigation was to characterize steam effectiveness in combustors of different designs. In particular, designs which had significantly different "effective" equivalence ratios and/or mixing schemes were investigated. After the study is described, results comparing steam with water injection in combustors of the same design are presented, and the effect of fuel type on steam/water effectiveness – again in combustors of the same design – is discussed. The surprisingly weak dependence on injection mode and design is noted. The thermal nature of steam versus water injection effectiveness and fuel composition is discussed. Finally, these results are compared with others found in the literature and assessed in light of simple models.

Conventional Combustors

The combustor chosen for this investigation was the combustion system for the GE MS7001E and MS9001E gas turbines. Both of these are single-shaft, constant-speed generator drive units. The latter is a scaled version of the former for 50 Hz power generation. By employing 14 combustors in the MS9000 versus 10 in the MS7000, essentially identical combustor inlet conditions are maintained. The combustion system is shown schematically in Fig. 1. Steam is injected radially inward through eight simple jet nozzles toward the swirler. However, some of the steam probably enters through the metering holes in the cowl and cooling louvers in the cap. The primary zone of this combustor is stirred by jets entering through the main combustion holes and stabilized by the swirler concentric with the fuel nozzle. In the standard nozzle, gas fuel enters the combustor through jets between the swirler vanes so that at least some of the steam contacts the gas fuel well before combustion is initiated. The standard water injection fuel nozzle is shown in Fig. 2. It is very similar to steam injection in that most of the water enters through the swirler, but some may enter through the cap/cowl.

The R_{NO_x} ratio (NO_x with steam injection divided by unbated NO_x) when burning methane for this system is shown in Fig. 3 for a variety of fuel-to-air ratios and inlet temperatures. For comparison, R_{NO_x} derived for a simple kinetic model, assuming the Zeldovich mechanism [1] and equilibrium atomic oxygen, is also plotted in Fig. 3. As expected, the practical abatement is much less than the theoretical. The explanation for this disparity was thought to be straightforward, with the major factors being:

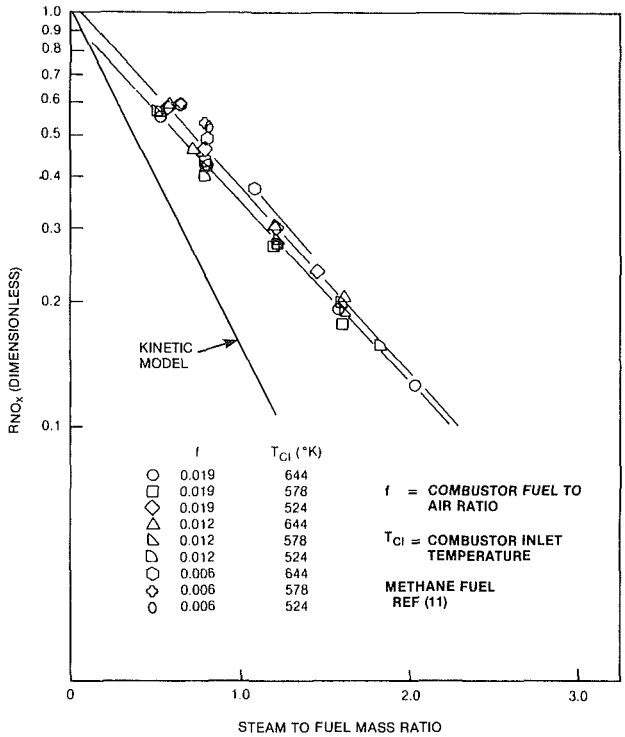

Fig. 3 R_{NO_x} for conventional combustion system – steam injection

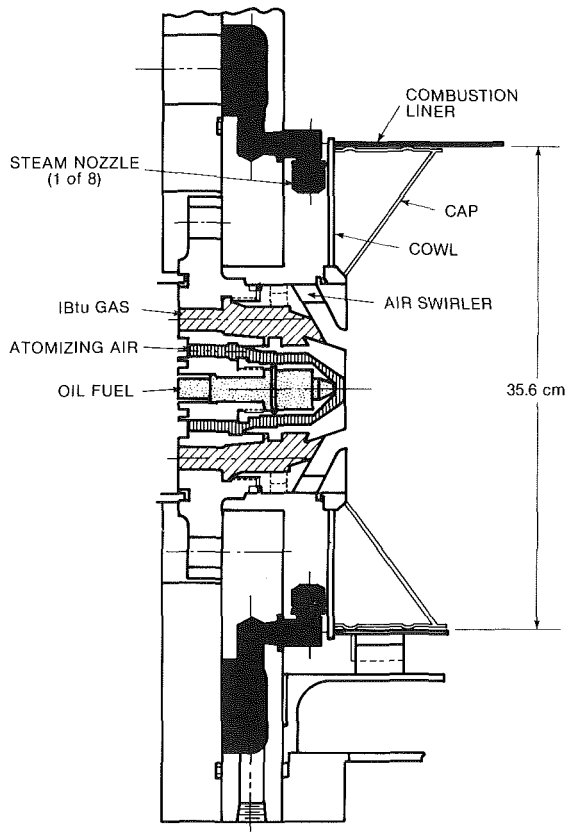

Fig. 4 Schematic of intermediate Btu gas fuel nozzle

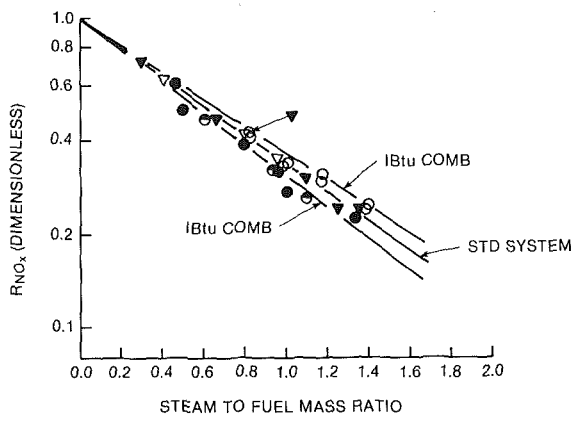

NOTES:
1. STANDARD STEAM INJECTION—OPEN SYMBOLS
2. STEAM AND FUEL MIXTURE—FILLED SYMBOLS
3. STEAM AND FUEL INTERLEAVED—HALF FILLED SYMBOLS
4. METHANE FUEL
5. RIG TEST RESULTS — HIGH LOAD

LEGEND:
—○—○— IBtu COMBUSTOR
—▽—▽— STD COMBUSTOR

Fig. 5 R_{NO_x} for standard versus IBtu combustor

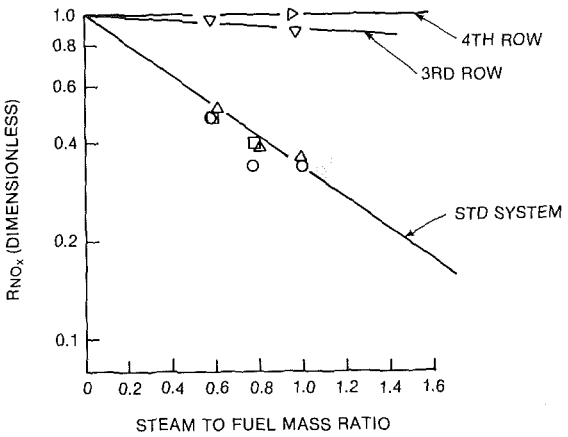

NOTES:
1. METHANE FUEL
2. LOW PRESSURE

LEGEND:
—○—○— HEAD END INJ.
—□—□— MIXED STEAM/FUEL
—△—△— 1ST ROW COMB. HOLES
—▽—▽— 3RD ROW COMB. HOLES
—▷—▷— 4TH ROW COMB. HOLES

Fig. 6 Steam effectiveness for scaled combustor

1 Gross bypassing of the flame by steam

2 Insufficient and/or unequal mixing of the steam and fuel prior to combustion

3 Steam wastage due to cooling very lean portions of the flame which produced insignificant NO_x

Mixing steam with fuel was the simplest suggestion for eliminating bypassing and ensuring complete mixing. Also, if the view that each fuel and air parcel must pass through stoichiometric in a diffusion flame were strictly true, then wastage due to cooling lean areas would be eliminated as well. Results which strongly supported all of these conclusions had been reported by Krockow [2]. Therefore, a system for mixing steam and fuel upstream of the fuel nozzle was constructed and installed. A fuel nozzle designed for greater volume flow of a wet intermediate Btu (IBtu) gas was chosen for testing. This nozzle is shown schematically in Fig. 4, and is described in detail by Savelli and Touchton [3]. Air enters through a radial swirler and is mixed with the fuel and steam mixture prior to entering the combustor. Because of the geometry, more swirler air is admitted than with the standard design, and some aspiration of air by the fuel and steam mixture takes place. The IBtu fuel nozzle is also designed to be used with a standard combustion liner (or sleeve) and to accommodate standard "head end" steam injection.

Far from agreeing with the kinetic predictions, the results of testing with this fuel nozzle were so surprising that a standard fuel nozzle was modified to accept the greater flow rate, and the test points were repeated with this hardware. Finally, a test was run using the IBtu nozzle with steam injected through gas passages and methane injected through the oil atomizing air passages. The idea here was to "blanket" or interleave the air/steam/fuel so that the fuel was forced to diffuse through the steam to the oxidant. This approach had been suggested by Heberling [4].

R_{NO_x} values for the conventional and IBtu fuel nozzle tests are shown in Fig. 5. The salient feature of this plot is the lack of any dramatic improvement in steam effectiveness from mixing with the fuel or interleaving. The mixed or interleaved effectiveness is improved by approximately 16 percent at a steam-to-fuel ratio of 1:1 with respect to the IBtu nozzle with standard steam injection. Compared to the standard combustion system the reduction at the same injection ratio is only 7 percent. Also, it is clear from these plots that there is no significant abatement difference between head end steam injection and mixed steam and fuel for the conventional system. These results show conclusively that the disparity between the kinetic model and practical results is not due to lack of mixing between steam and fuel. These results also suggest that the primary combustion zone is – at the macroscale – well mixed. However, the resuls of Tumanovskii [5] indicated that an optimum split of injected steam between combustion air holes and head end swirler might exist. Further tests were done to explore this avenue.

A series of tests utilizing a scaled version of the standard combustor was run to further investigate its primary zone characteristics. The combustor was scaled aerodynamically by maintaining the same relative flow splits. Geometrically, it was scaled on an equal length-to-diameter basis. The diameter was reduced to 20.3 cm from 35.6 cm. The fuel nozzle used was designed for a 25.4-cm-dia combustor so its scaling was fairly close. The tests were run in a rig which has been described in detail [6]. Most tests were run at reduced pressure for economy, but a check verified that a $p^{1/2}$ dependence was followed. The uncontrolled NO_x emissions for the scaled combustor compared well with mean results for the full-sized combustor.

Steam was injected into this combustor in four different locations in an attempt to introduce it into the flame at different temporal stages in the combustion. First, it was injected through the swirler (head end), contacting the fuel prior to initiation of combustion. Then it was introduced into the first, third, and fourth primary zone holes, which are located 0.38, 0.63, and 0.81 combustor diameters, respectively, downstream from the cowl plate. The objective was to introduce the steam in successively later stages of the postflame zone, where it was felt an optimum might be reached at a time of peak NO_x production. The R_{NO_x} results from this investigation are compared in Fig. 6 with the previous full-scale results. The agreement is good with the exception of one data point for head end injection. Most striking is the relative effectiveness of steam injected via the primary combustion holes. Far from reaching an optimum, the effectiveness of steam injected into the first row of holes is equal to that of the conventional system, while effectiveness is essentially zero for injection via the third and fourth row of holes. These scaled results also confirm that head end and mixed steam ef-

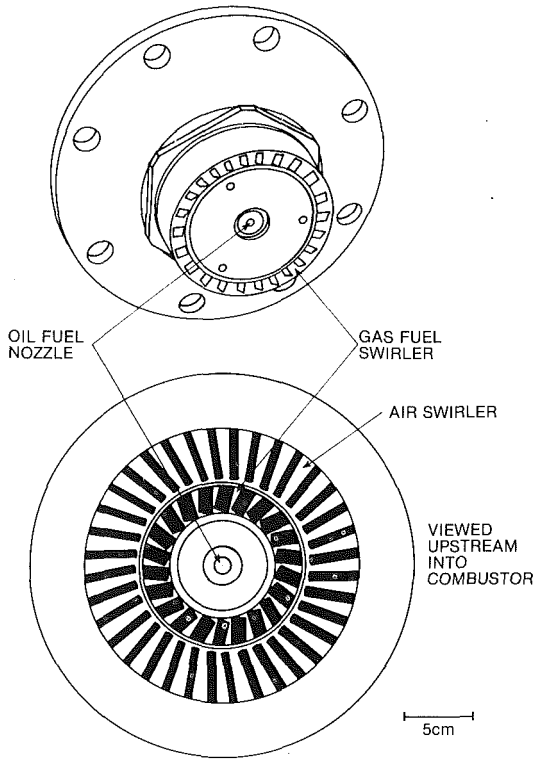

Fig. 7 Low-Btu fuel nozzle/cap cowl

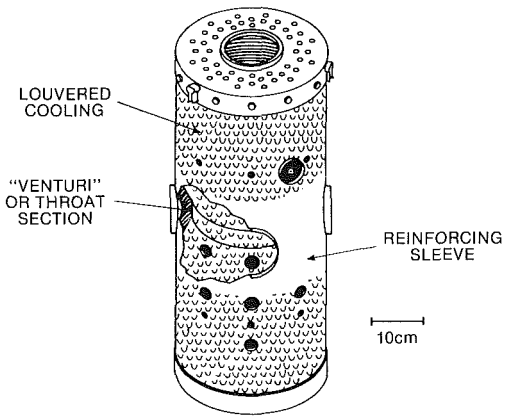

Fig. 8 Rich-lean combustor

fectiveness are essentially equivalent and further show that primary zone injection through the first row of air holes is equivalent to both. This equivalence clearly proves that the primary zone may be considered well mixed insofar as NO_x production is concerned.

Design Influences on Steam Injection Effectiveness

Design influences, in the context of the present paper, are those factors which change the gross equivalence ratio of the combustor and/or the gross mixing in the combustor. Of course, these design features are intended to change the small-scale characteristics of the flame. One speaks of "leaning the reaction out," "mixing times short compared to ignition," "quick quench," and the like. However, it is a universal observation that such statements are more easily uttered than effected. Therefore, in choosing candidates for screening, the major criterion was that some difference in NO_x production characteristics had been exhibited by the combustion system. This ensured that the effective combustor parameters had been altered.

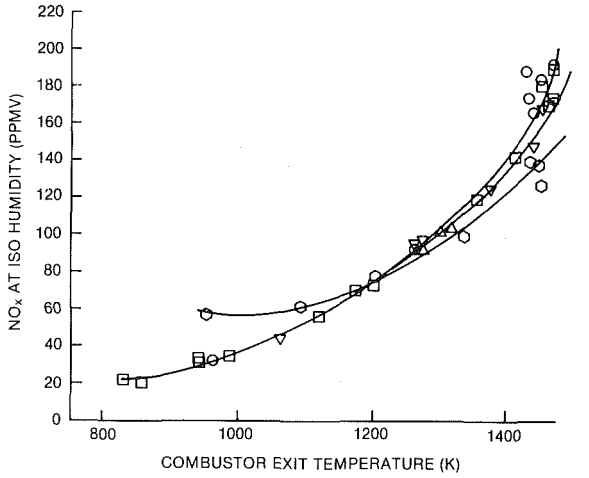

Fig. 9 Uncontrolled NO_x emissions

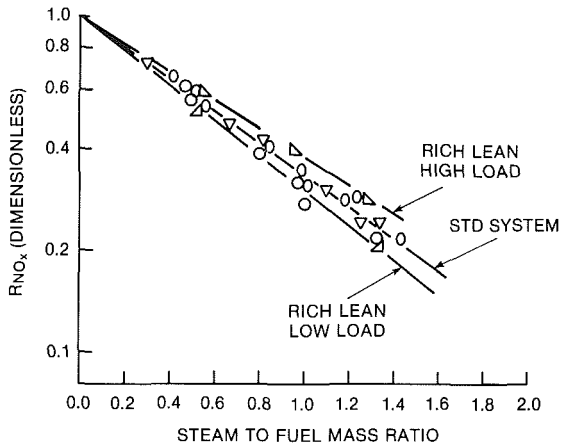

Fig. 10 R_{NO_x} for low-Btu and rich-lean combustors

Full Scale Testing of Alternate Designs

The two designs chosen for full-scale testing were a fuel nozzle and cap/cowl design developed for a low-energy gas fuel (low Btu) [7] and a rich-lean combustor. Both of these combustion systems had shown NO_x reductions in earlier testing, indicating some change in the actual flame characteristics. The low-Btu fuel nozzle and cap/cowl are shown in Fig. 7. The pertinent features are the use of counterswirling fuel and air streams and an air swirler with 1.8 times the effective area of the standard swirler. It should be noted that the low Btu nozzle was designed for application to a com-

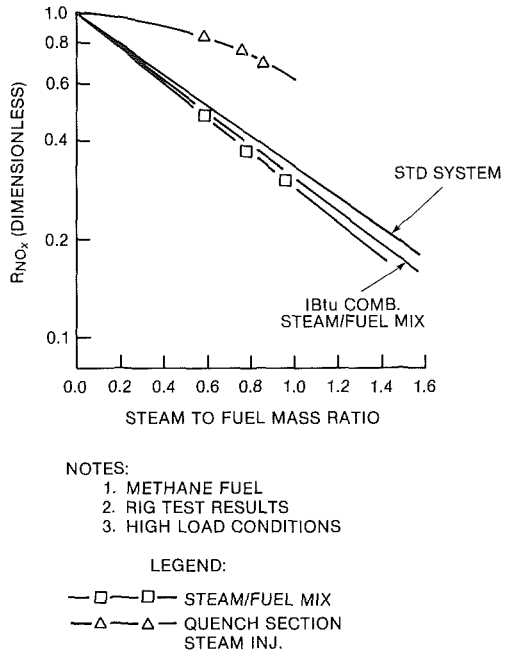

Fig. 11 R_{NO_x} for small-scale rich-lean combustor

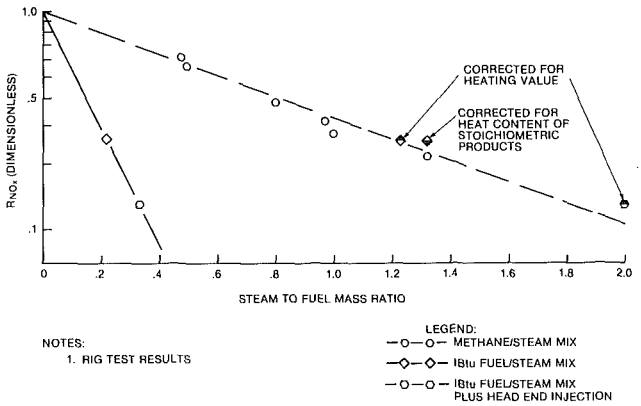

Fig. 12 R_{NO_x} for steam injection by fuel type

Table 1 IBtu test fuel properties

Composition (Volume Percent)		
Constituent	Dry Gas	Wet Gas
N_2	0.6	0.48
CO_2	15.7	12.56
CO	46.5	37.20
H_2	37.2	29.76
H_2O	0.0	20.00
Physical Properties		
Temperature	339	478
Lower Heating Value (mJ/m^3)	9.37	7.44
(mJ/kg)	10.6	8.7
Adiabatic Stoichiometric Flame Temperature (K)	2469	2341

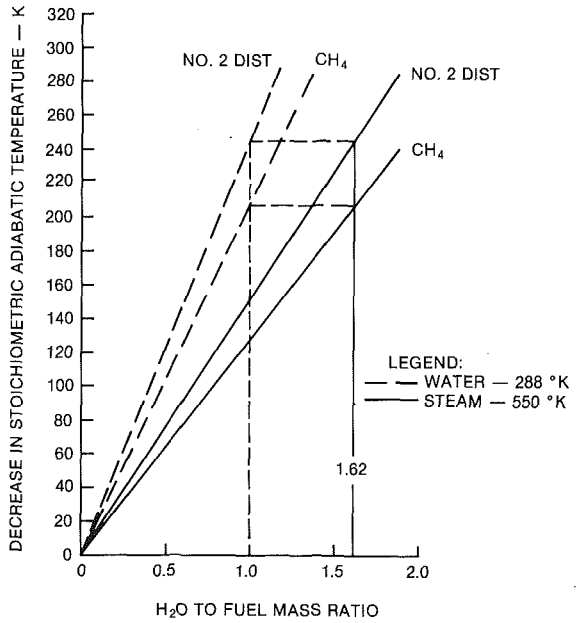

Fig. 13 Flame temperature reduction versus steam or water injection

bustor 25.4 cm in diameter. It was fitted to the 35.6-cm-dia standard combustor via a transition section. The only modification to the fuel nozzle was restricting the fuel swirler area. The rich-lean design shown in Fig. 8 was originally developed for No. 2 distillate. The combustor incorporates a rich first stage, a high-velocity throat, and a lean second stage. The object is to prevent combustion at stoichiometric conditions and, therefore, reduce NO_x production. It was used without modification to burn methane fuel in this program. Figure 9 shows the uncontrolled NO_x emissions for these two designs compared to the mean values for the standard system.

The emissions of the low-Btu fuel nozzle are lower than those of the standard system for high temperatures, while the rich-lean combustor exhibits lower emissions at high temperatures and higher emissions at low temperatures. The R_{NO_x} plots for the low-Btu nozzle and the rich-lean system (Fig. 10) show that the low-Btu system for steam/fuel mixture has essentially the same effectiveness as the standard. The rich-lean system shows a weak interaction with combustor equivalence ratio. The high-load condition (high fuel flow) effectiveness is inferior to the conventional system. At low load conditions the effectiveness is improved, but the improvement is more than offset by the higher emissions. The end result is an increase in steam required for a given NO_x level across the load range.

Reduced Scale Testing of Alternate Designs

A reduced scale, rich-lean combustor originally designed for MS7000 baseload inlet conditions (Concept 2-5 of [6]) was tested for steam injection effectiveness. Its R_{NO_x} values are shown in Fig. 11. An interesting feature of this test was the injection of steam into the quench section. The results indicate that a significant amount of NO_x is being formed in the first stage in spite of its overall rich equivalence ratio. This is probably due to the diffusion (rather than premixed) nature of the flame in the first stage. Therefore, these results suggest that a successful rich-lean concept would need to incorporate a prevaporize/premix section. The effectiveness of steam/fuel mixing is essentially equivalent to that of the IBtu combustor for high load conditions.

Fuel Composition Influence on Steam Injection Effectiveness

Figure 12 shows R_{NO_x} steam injection values of the IBtu nozzle for methane, and the IBtu test fuel (Table 1). The open symbols are plotted against steam-to-dry fuel mass ratio. The

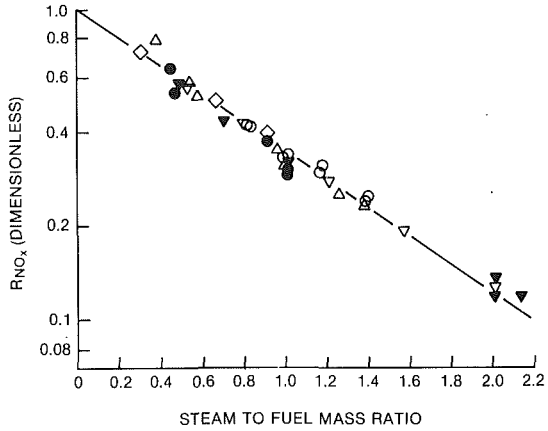

NOTES:
1. NAT. GAS OR METHANE — OPEN SYMBOLS
   NO. 2 DISTILLATE — FILLED SYMBOLS
2. STANDARD HEAD END INJECTION

LEGEND:
◇ FIELD TEST GE 33MW GAS TURBINE
△ FIELD TEST STD COMBUSTOR
▽ RIG TEST STD COMBUSTOR
○ RIG TEST IBtu COMBUSTOR

Fig. 14 R_{NO_x} for methane versus distillate

symbols half filled above are plotted against steam divided by mass of dry fuel for heat release equivalent to methane. The symbol half filled below is plotted against steam divided by the mass of dry fuel stoichiometric products with a heat content equal to methane stoichiometric products. The two methods of correction agree closely, and the corrected points agree (to within experimental error) with the R_{NO_x} results for a methane steam mixture. Thus, for conventional diffusion flame combustors operating on gaseous fuels within the range of steam-to-fuel ratios practical for NO_x control, the effect of the fuel type may be taken into account simply by considering the energy content of the dry fuel or, what amounts to the same thing, the energy content of the stoichiometric products. Since the heating value of methane is 18–20 percent greater than No. 2 distillate we expect that an 18–20 percent greater steam-to-fuel ratio for methane would be needed to produce an equivalent NO_x reduction. Another way to see this is to note that Fig. 13 shows that an 18 percent greater steam or water-to-fuel ratio is needed for methane to produce equal flame temperature reduction.

Figure 14 shows that, in practice, natural gas and No. 2 distillate have essentially the same effectiveness as a function of steam-to-fuel ratio. Therefore, it is clear that injector geometry, droplet burning, mixing, and the like influence the NO_x abatement seen with liquid fuel. An investigation of these influences is beyond the scope of the present study, but some data from the literature are discussed below. We expect that all but the very fine details of NO_x abatement by steam/water injection will be explained by considering the thermal effects of the injectant upon the stoichiometric products of the combustion. Thus, more intimate mixing of No. 2 distillate and the injectant should result in up to 18 percent greater effectiveness.

Water Versus Steam Injection Effectiveness

Simple thermal arguments predict that the steam required for a given reduction in flame temperature – and therefore NO_x – should be a constant times the water required. Figure 13 shows this ratio to be approximately 1.62. In Fig. 15, R_{NO_x} values for steam and water injection have been plotted against equivalent water-to-fuel ratio, computed using the 1.62 factor. Note that for clarity, only R_{NO_x} values for baseload or

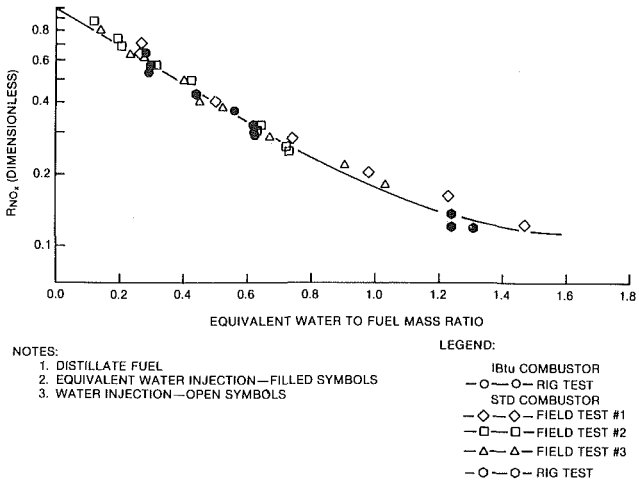

NOTES:
1. DISTILLATE FUEL
2. EQUIVALENT WATER INJECTION—FILLED SYMBOLS
3. WATER INJECTION—OPEN SYMBOLS

LEGEND:
IBtu COMBUSTOR
—○—○— RIG TEST
STD COMBUSTOR
—◇—◇— FIELD TEST #1
—□—□— FIELD TEST #2
—△—△— FIELD TEST #3
—○—○— RIG TEST

Fig. 15 R_{NO_x} versus equivalent water-to-fuel ratio

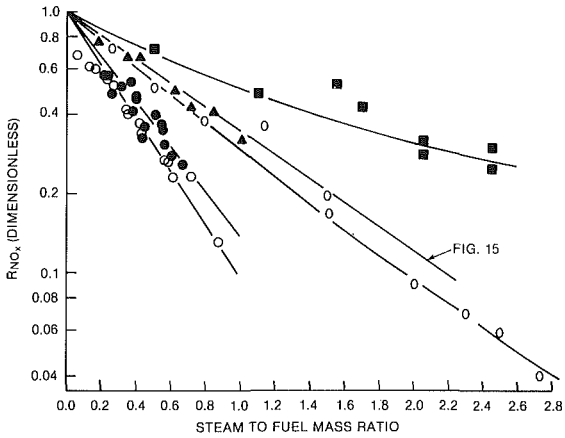

NOTES:
1. NATURAL GAS OPEN SYMBOLS
   NO. 2 DISTILLATE FILLED SYMBOLS
2. KWU AND LM5000 PREMIXED STEAM AND FUEL
3. KWU OIL DATA STEAM ATOMIZATION

LEGEND:
—△—△— BST COMB. RIG TEST (REF. 13)
—○—○— *KWU SILO COMB. FIELD TEST (REF. 2,9)*
—□—□— GT-100 USSR RIG TEST (REF. 8)
—0—0— GE LM5000 RIG TEST (REF. 10)

Fig. 16 Injection steam effectiveness – literature values

greater combustor exit temperatures have been plotted. The correlation using equivalent water-to-fuel ratio is excellent, confirming the thermal nature of the abatement process.

Comparison With Other Research

Steam injection results from the present study are compared in Fig. 16 with those obtained in tests of heavy-duty and aero-derivative industrial gas turbines. The BST results are for a can-type combustion system and agree with the present study. Slightly greater effectiveness is shown by the LM5000. This effect is probably due to the higher inlet temperatures and pressures of this engine. The high-pressure combustor of the GT100 shows very low effectiveness (although greater than that of water injection), as shown in Fig. 17. This may be explained by the low combustion efficiency [8]. The KWU silo combustor results show: (1) much greater abatement for equivalent steam-to-fuel levels; and (2) close agreement with calculations from simple kinetic models. These results are attributed by Krockow to the method of steam injection, which is steam/fuel mixing [2, 9]. As the present study and the work of Bahr and Lyon [10] clearly show, mixing the steam

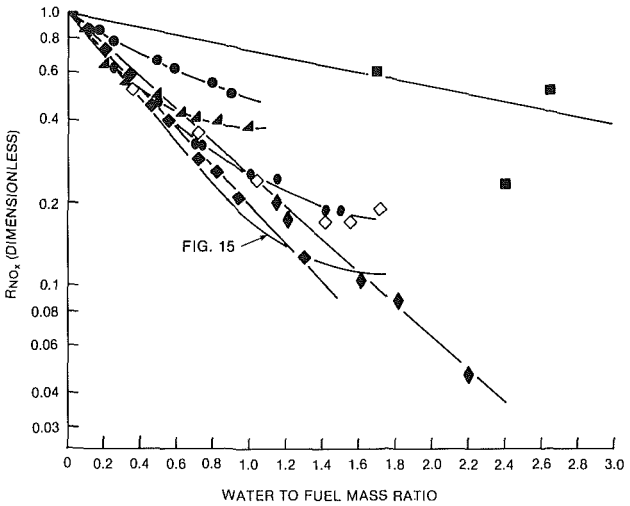

NOTES:
1. NATURAL GAS UNFILLED SYMBOLS
2. NO. 2 DIST. OF EQUIV. FILLED SYMBOLS
3. TYPE 11 DATA SWIRLER INJECTION
4. W35 MW DATA ATOMIZING AIR INJECTION

LEGEND:
—◇—◇— W35 MW (REF. 15)
—◊—◊— BBC TYPE 11 FIELD TEST (REF. 14)
—□—□— GT-100-RIG TEST (REF. 8)
GTE-150-RIG TEST (REF. 5)
—o—o— COMBUSTION HOLE INJECTION
—⊿—⊿— SWIRLER INJECTION
—o—o— COMB. HOLE & SWIRLER INJ.

Fig. 17 Water injection effectiveness – literature values

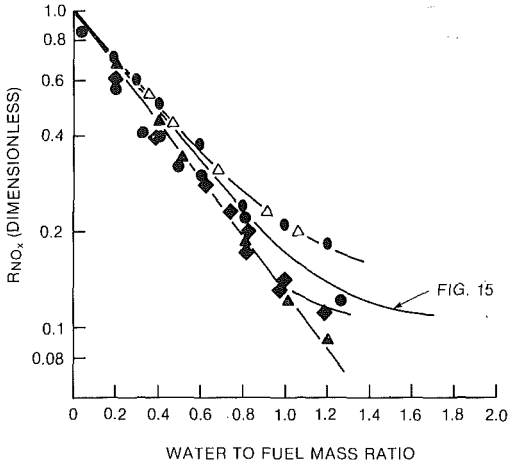

NOTES:
1. DIESEL — FILLED SYMBOLS
2. CH_4 — OPEN SYMBOLS

LEGEND:
GE-LM2500 (REF. 10)
—△—△— RIG TEST — DUAL FUEL NOZZLE
—o—o— RIG TEST — "UPSTREAM" INJ.
—o—o— RIG TEST — WATER/FUEL MIX
—◇—◇— ENGINE TEST — WATER/FUEL MIX

Fig. 18 Water injection effectiveness – aero derivative

and fuel does not result in agreement with kinetic calculations for jet-stirred combustors. However, the degree of abatement observed with steam/fuel mixing in jet-stirred combustors is consistent with that calculated from measured sensitivity to stoichiometric flame temperature variation [11, 12]. This implies that the deviation from kinetic predictions shown by the jet-stirred combustors is due to inadequate model assumptions. Assuming equilibrium atomic oxygen concentration and disregarding prompt NO_x are especially suspect.

Figures 17 and 18 compare the water-injected R_{NO_x} results from the present work with results from heavy-duty gas turbine combustors and aero-derivative gas turbines respectively. The heavy-duty combustor data fall into two broad groups: the GT100 data and all else. The GT100 data demonstrate that design may exhibit a strong negative influence on water injection effectiveness. In this case (as noted above) the water injection effectiveness is lower than that of steam. The GTE-150 data show that, even if the primary zone cannot be considered well mixed, an optimum injection mode can be found. When only the combustion hole plus swirler injection data for the GTE-150 are considered, the second data set groups quite closely – especially at water-to-fuel ratios less than 1.2. This is in spite of the range of test conditions, fuel, and designs. A final observation is that all the multiple can combustors exhibit less than exponential effectiveness for water-to-fuel ratios greater than 1.0, although the close contact between water and liquid fuel for the W35MW delays this upturn. Water is injected through the atomizing air passages, which are used for atomization at start-up only. The large single combustor of the BBC-11 shows no upturn and is exponential to a residual NO_x of approximately 14 percent of the original.

LM2500 R_{NO_x} results are compared with the present work in Fig. 18. In general the effectiveness is better for the LM2500 than the standard GE heavy-duty combustor. This is probably due in part to the higher combustor inlet temperature and pressure. Note that for this combustor R_{NO_x} is sensitive to fuel nozzle details. The dual fuel nozzle methane and diesel results agree fairly well with the thermal arguments – that is, about 15 percent more water is needed for natural gas to reach the same abatement. Another observation is that effectiveness for diesel increases as water and fuel are more intimately contacted prior to combustion. As is the case for steam injection, the data agree reasonably well with the present study.

In summary, the most outstanding feature of the steam and water injection from the literature is the narrow range of effectivness seen for many different designs and test conditions for water-to-fuel ratios up to 1.0. This result is true for both distillate and natural gas fuel. The R_{NO_x} values give only one part of the picture and caution must be exercised when comparing different designs for which the unabated NO_x values differ widely. The water-to-fuel ratio necessary to achieve a given *level* of NO_x provides a more practical figure of merit for applications, but does not give as much insight into the processes as the R_{NO_x} plot.

Summary and Conclusions

The detailed discussion of the paper may be summarized as follows:

1 Steam or water injection suppresses NO_x formation by depressing peak flame temperatures. Other effects such as altered mixing are negligible. Further, the greater effectiveness of water over steam injection is explained by the latent heat of vaporization of water.

2 The combustor primary zone of jet-stirred, swirl-stabilized combustors, such as the production designs shown above, is "well stirred" in a macroscopic sense in that steam entering with the air or fuel is equally effective in reducing NO_x. This is consistent with the "two-zone" model of Vulis [16].

3 Gross combustor parameters such as swirl, overall equivalence ratio, inlet temperature, etc., are observed to weakly influence NO_x abatement effectiveness consistent with the stoichiometric diffusion flame picture.

4 The postflame model with an effective equivalence ratio for NO_x formation near stoichiometric explains the ob-

servation that abatement by steam or water injection is almost entirely a function of the chemistry of the flame. Differences in abatement for different gaseous fuels are quantitatively accounted for. Oil fuel data show some deviation from this picture, but the deviation diminishes when the oil and water are mixed prior to injection into the combustor.

The above arguments support the conclusion that the combustor with superior unabated NO_x performance will exhibit superior injected NO_x performance. Thus, there is no advantage to be gained by attempting to design a combustor optimized for steam or water injection. The exception to this is that water injection effectiveness can be increased by more intimate admixture with oil fuel.

Thus, a broadly consistent picture of the mechanisms of NO_x formation and abatement by steam or water injection in diffusion flame combustors emerges. Flame temperature and the postflame zone model of combustion are the central unifying themes. The theorist will insist that the arguments presented are ad hoc; interesting effects such as increased NO_x abatement effectiveness with better oil/water admixture are beyond the scope: and a number of constraints such as adequate stirring and high efficiency must be satisfied. The practicing designer will note that trends are well explained within a design family and, therefore, test results may be interpolated or extrapolated. As for the constraints, they are satisfied by any well-designed combustion system.

References

1 Zeldovich, J., "The Oxidation of Nitrogen in Combustion and Explosions," *Acta Physicochimica, U.S.S.R.*, Vol. 21, 1946, pp. 577–628.

2 Krockow, W., "Burner Development for Large Industrial Gas Turbine Combustors," Paper No. GT 16, 14th CIMAC Cong., Helsinki, 1981.

3 Savelli, J. F., and Touchton, G. L., "Design and Development of a Combustion System for Intermediate Energy Coal Gas Fuel," to be published.

4 Heberling, P., General Electric Corporate Research and Development Center, Schenectady, NY, unpublished.

5 Tumanovskii, A. G., and Tul'skii, V.F., "Influence of Water Injection on the Formation of Nitrogen Oxides at the Outlet of the Combustion Chamber With Series Introduction of Air in the Combustion Zone," *Thermal Engineering*, Vol. 29, No. 6, 1982.

6 Cutrone, M. B., et al., "Low NO_x Heavy Fuel Combustor Concept Program—Phase 1 Final Report," NASA Report No. CR-165449, 1981.

7 Beebe, K., GE Gas Turbine Div., Schenectady, NY, unpublished.

8 Krugov, V. B., et al., "The Results of an Experimental Investigation Into Lowering the Emission of Nitrogen Oxides by Spraying Steam or Water Into the Combustion Zone," *Thermal Engineering*, Vol. 26, No. 11, 1979.

9 Krockow, W., and Schabbehard, H., "Alternate Fuels: Burner Concepts and Emission Characteristics of a Silo Combustor," ASME Paper No. 82-GT-29.

10 Bahr, D. W., and Lyon, T. F., "NO_x Abatement via Water Injection in Aircraft Derivative Turbine Engines," ASME Paper No. 84-GT-103.

11 Touchton, G. L., "An Experimentally Verified NO_x Prediction Algorithm Incorporating the Effects of Steam Injection," ASME JOURNAL OF ENGINEERING FOR GAS TURBINES AND POWER, Vol. 106, No. 4, Oct. 1984, pp. 833–843.

12 Lewis, G. D., "Prediction of NO_x Emissions," ASME Paper No. 81-GT-119, 1981.

13 Koch, H., "Investigations and Measures for the Reduction of Gas Turbine Emissions," *Sulzer Tech. Rev.*, No. 2, 1974, pp. 61–67.

14 Hanson, K. A., and Felix, P. C., "Emissions Characteristics of a Gas Turbine Combustor for High Nitrogen Content Fuels," Paper No. 75-PWR-28, presented at the ASME-IEEE Joint Power Conference, Portland, Sept. 1975.

15 Hung, W. S. Y., "Accurate Method of Predicting the Effect of Humidity or Injected Water on NO_x Emissions From Industrial Gas Turbines," ASME Paper No. 74-WA/GT-6, presented at ASME Winter Annual Meeting, New York, NY, 1974.

16 Vulis, L. A., *Thermal Regimes of Combustion*, translated by M. D. Friedman, McGraw-Hill, New York, 1961, pp. 89–106.

Utility Combustion Turbine Evaluation of Coal Liquid Fuels

M. J. Ambrose
Senior Engineer.
Westinghouse Electric Corporation,
Annapolis, MD[1]
Mem. ASME

R. F. Costello
Engineer.
Philadelphia Electric Company,
Philadelphia, PA

H. Schreiber
Project Manager.
Electric Power Research Institute,
Palo Alto, CA

A comprehensive field test was performed to evaluate the suitability of H-Coal middle distillate and full-range Exxon Donor Solvent (EDS) coal-derived liquids (CDLs) as utility combustion turbine fuels. A Westinghouse W251AA 26 MW combustion turbine operated by the Philadelphia Electric Company was the test engine. No. 2 petroleum distillate fuel was also fired to establish baseline data. This program was sponsored by the Electric Power Research Institute. Site modifications included a temporary CDL storage and fuel transfer system, water storage and injection equipment, an instrumented combustor, engine and emissions instrumentation and data acquisition systems, and industrial hygiene facilities required for the proper handling of the CDLs. The overall results of testing were positive for using such CDL fuels in combustion turbines for power generation. With the exception of higher combustor metal temperatures with the CDLs, and persistent fuel filter plugging with the EDS fuel (which occurred even with increased fuel temperature and filter size), the engine operated satisfactorily during approximately 80 hr of total running over the standard range of load and water injection conditions.

Introduction

In response to the disruption of petroleum fuel supplies and severe pricing disturbances in the 1970's, a significant effort to develop the capability to produce synthetic liquid fuels was undertaken by private industry and the federal government. A number of pilot plant operations produced various synthetic liquids from coal and oil shale in sufficient quantity to permit performing field tests to evaluate their suitability in full-scale utility power generation equipment. An earlier study [1] described such tests including two that were performed on combustion turbines firing methanol [2] and hydrotreated shale oil [3].

This paper describes tests performed burning H-Coal and Exxon Donor Solvent (EDS) coal liquids in a Westinghouse W251AA 26 MW utility combustion turbine at the Richmond Generating Station of Philadelphia Electric Company (PECO). The program was sponsored by the Electric Power Research Institute (EPRI), and was a logical extension of an earlier combustion laboratory evaluation of coal-derived and synthetic fuels [4].

Engine performance characteristics evaluated included heat rate, effect of water injection on emissions and performance, flame stability and dynamic pressure fluctuations, combustor liner metal temperatures, and observations of hot section components. The results of these tests were planned to shed light not only on the mechanical performance of the engine, including combustor dynamic response using these fuels, but also on the environmental and industrial hygiene factors to be addressed if these fuels are to be used commercially by utilities. No. 2 petroleum distillate fuel was run on the same engine configuration to establish baseline data. During this test program, H-Coal was burned for approximately 60 hr and EDS for approximately 20 hr.

The fuels tested were:

- No. 2 Distillate Fuel, with and without Smoke Reduction Additive (SRAD), provided by PECO
- H-Coal Middle Distillate, provided by EPRI
- Full range EDS, provided by EPRI

Laboratory fuel analyses were performed for each fuel prior to its being fired in the test engine. Typical properties of the as-fired fuels are listed in Table 1.

Test Preparations

CDL Fuel Storage and Transfer System. Four 6000-gal stainless steel fuel tank trucks were cleaned and manifolded on-site as a CDL day-tank storage system. These were insulated tankers with internal heating coils to which a portable steam generator was connected. The CDL tank manifold was connected via a low-pressure fuel supply piping system to the engine. A parallel filter arrangment enabled circulation (and heating) of CDL within the manifolded tank trucks while the engine was running on No. 2 distillate. The engine fuel bypass that normally returns fuel to storage was modified to recirculate back through a fin fan cooler into the high-pressure pump inlet to avoid contaminating either the station fuel or the CDL day-tank storage during fuel transfer. Engine transfer to and from CDL test fuel operation was made while at steady engine load, usually minimum load or 1/3 of base load. Fuel system flushing capability was built into the system, to enable purging any CDL test fuel from the fuel lines into a waste tank following an engine trip-out while operating on CDL. The CDL fuel and water injection systems

[1] Work performed at Concordville, PA

Contributed by the Gas Turbine Division and presented at the Joint Power Generation Conference, Toronto, Ontario, Canada, September 30-October 4, 1984. Manuscript received by the Gas Turbine Division June 18, 1984. Paper No. 84-JPGC-GT-13.

Table 1 Typical analyses of as-fired test fuels

Fuel		No. 2 distillate baseline fuel		H-Coal CDL	EDS CDL
Test date	Analytical procedure (ASTM-D)	with additive 11/9/82	untreated 11/17/82	12/6/82	3/8/83
Physical and chemical properties					
H.H.V. Btu/lb	240	19,296[3]	19,113	18,114[3]	18,270
SSU viscosity/°F	445	41/65	42/65	38/70	53/72
SSU viscosity/°F	445	35/100	36.5/100	34.5/100	42/100
SSU viscosity/°F	445	32/150	32.5/150	32.5/125	38/120
Specific gravity/°F	1298	0.860/65	0.851/65	0.9295/60	0.963/60
Specific gravity/°F	1298	0.847/100	0.840/100	0.9170/100	0.947/100
Specific gravity/°F	1298	0.836/150	0.827/150	0.8930/150	0.940/120
Flash point °F	92	200	195	205	225
Fire point °F	92	205	200	220	243
Distillation °F IBP	86	360	360	395	370
5% Vol.	86	–	–	–	400
10%	86	420	420	420	410
20%	86	440	450	420	450
30%	86	460	480	425	475
40%	86	480	500	430	495
50%	86	500	520	440	520
60%	86	520	540	440	560
70%	86	540	560	450	590
80%	86	570	580	460	635
90%	86	600	610	475	620[1]
95%	86	–	–	–	–
EP	86	660	660	510	450[1]
Residue %	86	<0.5	<0.5	<0.5	3.0
Elemental analysis wt%					
Carbon	–[2]	87.28	86.74	86.43	88.53
Hydrogen	–	12.63	13.25	10.36	10.16
Nitrogen	–	0.03	0.02	0.41	0.20
Oxygen	–	0.63	0.69	2.66	0.79
Sulfur	129	0.034	0.027	0.114	0.04
Sediment/Water	1796	0.10	<0.05	<0.05	0.40
Water	95	N.D.	N.D.	N.D.	N.D.
Trace metals, ppm wt					
Ash	482	38.0	<0.5	44.0	4.0
Sodium	2188	0.040	0.020	0.044	<0.02
Potassium	2188	2.0	N.D.	0.024	<0.02
Vanadium	2787	0.60	0.20	0.80	<0.25
Calcium	2188	0.05	N.D.	0.08	0.06
Lead	2188	0.50	0.060	0.160	N.D.
Zinc	2188	0.044	0.012	0.028	0.02
Cadmium	2188	N.D.	N.D.	N.D.	N.D.
Nickel	2188	<0.010	N.D.	N.D.	N.D.
Iron	2188	15.00	0.50	20.00	2.5
Manganese	2188	8.40	0.070	0.28	N.D.
Magnesium	2188	0.035	0.010	0.020	0.035
Copper	2188	0.080	N.D.	<0.020	N.D.
Chromium	2188	<0.050	<0.050	<0.050	N.D.

HHV = Higher heating value; SSU - Saybolt seconds universal; N.D. = not detected
(1) Cracked residue indicating decomposition during distillation
(2) C-H-N-O elemental analyzer (P-E Model 240)
(3) HHV analysis repeated due to ~600 Btu/lb sample-to-sample spread in data from first analysis

used for the test program were similar to earlier field test arrangements used to evaluate emissions and fuels [5, 6].

Water Injection System. A water injection system for nitrogen oxide (NO_x) emissions control was temporarily installed on the test engine. It was controlled manually and interlocked with the engine controls to terminate water flow if the engine tripped. Three 6000-gal stainless steel insulated tank trucks with internal heating coils were manifolded into a day-tank water storage system. Plant condensate was used as injection water.

Combustion System. A standard combustor was instrumented with 39 metal temperature thermocouples throughout its primary and secondary regions, and with two high-response pressure transducers and three accelerometers. A back-up combustor was also instrumented to minimize turnaround time if a failure of the first combustor were to occur. Two sets of fuel oil nozzle tips and atomizing air caps were flow calibrated, and one of the oil tips was tested for spray pattern and angle.

Exhaust Stack Sampling System. Six probe mounting exhaust port flanges and an access scaffold were installed on the engine exhaust silencer to enable mounting sampling probes for both gaseous and particulate emissions in each of the straight gas paths in the exhaust. Inlet sampling probes were mounted on the screen upstream of the compressor scroll and sampling lines were run to outside samplers.

PECO prepared the test site, including procurement and installation of test equipment, instrumentation and controls required, and furnishing the utilities needed by the emissions and data acquisition trailers. Figure 1 is a plot plan of the test site support equipment.

Data acquisition and monitoring systems were installed to collect the test data and monitor the engine test operations. A Westinghouse data acquisition trailer was positioned adjacent to the test engine to collect a wide range of engine performance test parameters, as well as signals from the special instrumentation installed on the test combustor. The trailer was also used as the engine test control station, with voice communications available to the PECO data acquisition van, the Westinghouse environmental test trailer, the stack

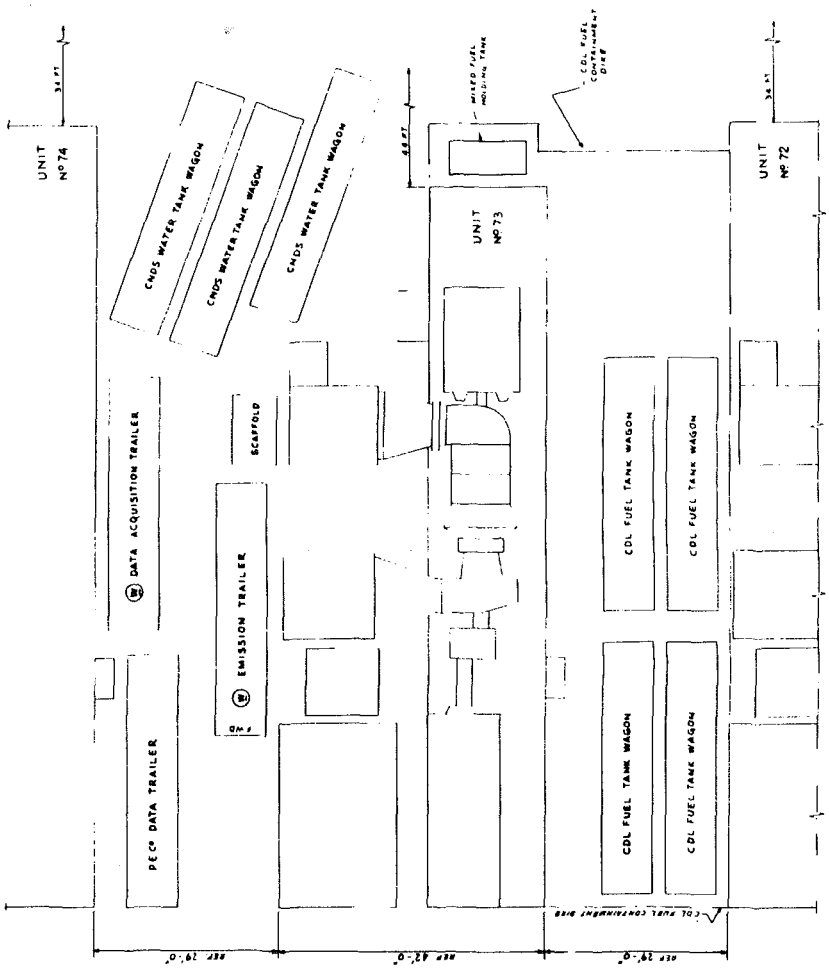

Fig. 1 Test engine (Unit No. 73) plot plan with test trailers and tank wagons

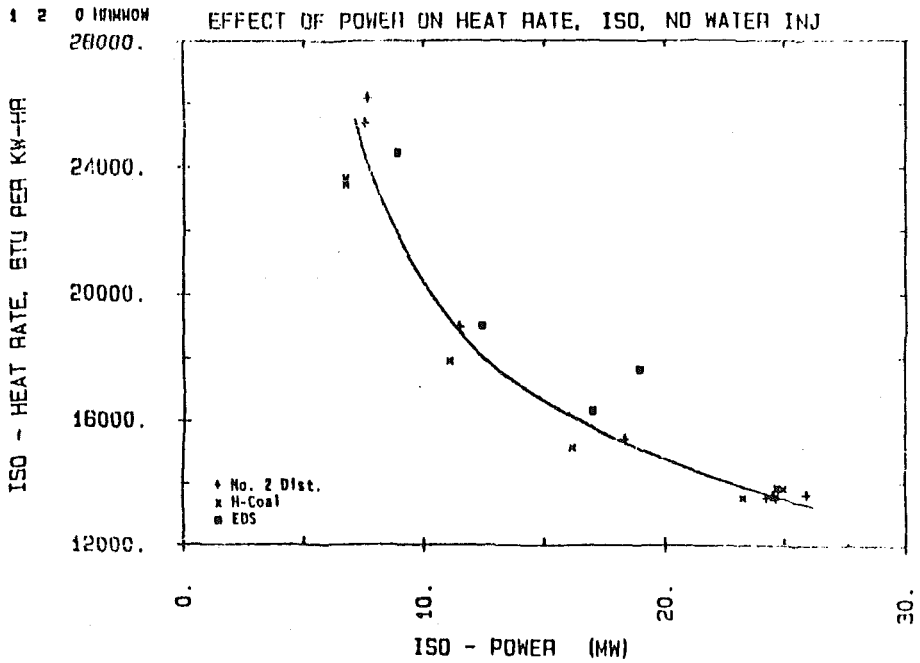

Fig. 2 The variation of heat rate performance with output power (normalized to ISO): no water injection

sampling station, and the CDL fuel transfer valve station. A PECO data acquisition van was spotted next to and connected with the Westinghouse data trailer to share monitoring of selected data channels.

Table 2 W251AA base load ISO performance (no water injection)

Test fuel	No. 2 distillate baseline fuel	H-Coal CDL	EDS CDL
(Hydrogen/carbon) ratio	0.1447	0.1223	0.1148
Power (kW)	25,400	24,821	24,576
Heat rate (Btu/kWh)	13,722	13,869	13,613
ΔkW (CDL-No. 2 baseline)	–	−579 kW (−2.3%)	−824 kW (−3.25%)
ΔHR (CDL-No. 2 baseline)	–	+147 Btu/kWh (+1.07%)	−109 Btu/kWh (−0.8%)

Table 3 W251AA base load ISO performance with maximum water injection (normalized to 1.22 W/F)

Test fuel	No. 2 distillate baseline fuel	H-Coal CDL	EDS CDL
W/F ratio	1.22	1.22 (1.105)*	1.22 (1.06)*
Power (kW)	26,267	25,343 (25,112)*	27,457 (27,110)*
Heat rate (Btu/kWh)	14,256	15,134 (15,099)*	14,474 (14,427)*
ΔkW (CDL-No. 2 baseline)	–	−924 kW (−3.5%)	+1190 kW (+4.5%)
ΔHR (CDL-No. 2 baseline)	–	+878 Btu/kWh (+6.2%)	+218 Btu/kWh (+1.5%)

*Denotes "as-tested" values

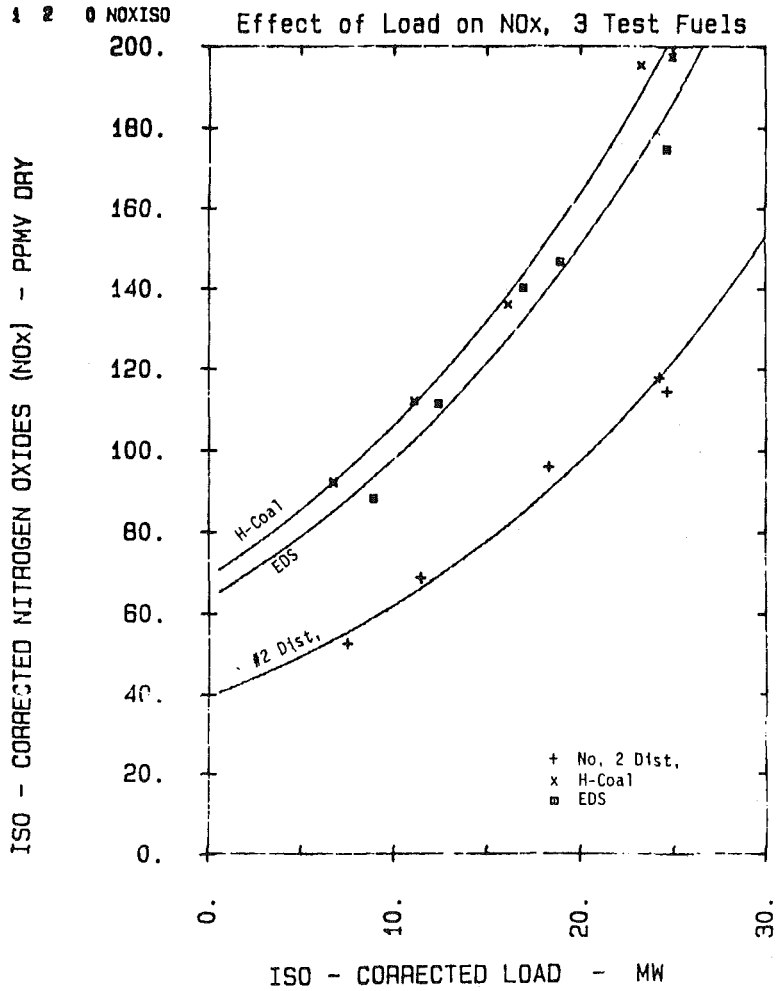

Fig. 3 Effect of load on NO_x (corrected to ISO conditions): no water injection

A Westinghouse environmental test trailer was located adjacent to the engine exhaust stack and contained the on-line gas analyzers used to monitor emissions and to guide the emissions control set point when water injection was used. This trailer also contained the physical chemistry laboratory to perform particulate and fuel analyses throughout the test program.

The final data station was the engine control room con-

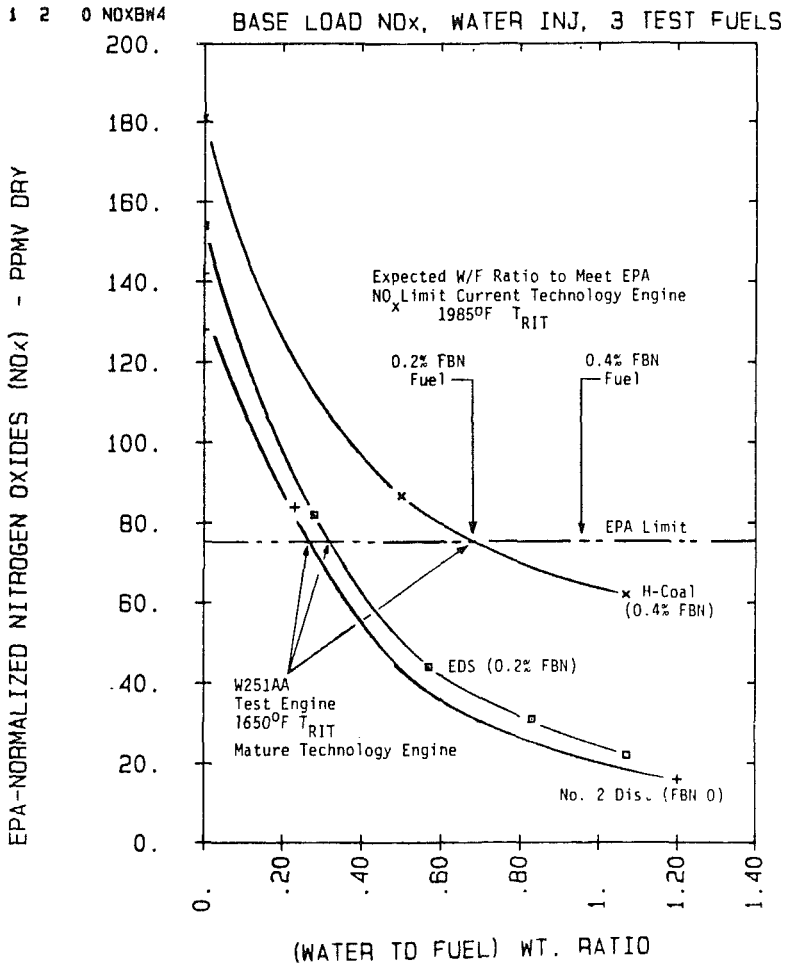

Fig. 4 Effect of water injection on base load NO_x: EPA normalized

taining the P-50 control computer which also displayed pertinent engine operational data.

In addition to operating the engine and the test support systems, PECO also made available industrial hygiene facilities (showers, lockers, eating area, protective gear, and coveralls as required for the proper handling of the test fuels), and provided for test site air monitoring.

Before the start of the test program, the unit was cleaned per standard procedures. Engine tests were then performed for each test fuel (No. 2 distillate baseline fuel, H-Coal, and EDS CDLs) over the range of 30 to 100 percent base load, both without water injection and with water injection up to approximately 1.2 water/fuel (W/F) weight ratio.

Engine Test Results

The overall results of engine testing with the two CDLs indicate that it is feasible to operate utility combustion turbines with these fuels, although some design modifications to deal with the tendency to higher combustor metal temperatures and suspended fuel solids may be required.

The engine power and heat rate showed essentially little difference for the CDLs compared to the baseline fuel. Table 2 shows the comparison of the base load performance at ISO conditions for all three test fuels without water injection. The power with CDL fuels is 2 to 3 percent less than, and the heat rate varies from 1 percent lower than, to 1 percent higher than, that with the No. 2 distillate baseline fuel. These differences are attributed to:

- Measurement test uncertainties and data scatter
- Fuels with lower H/C (hydrogen/carbon) ratio produce

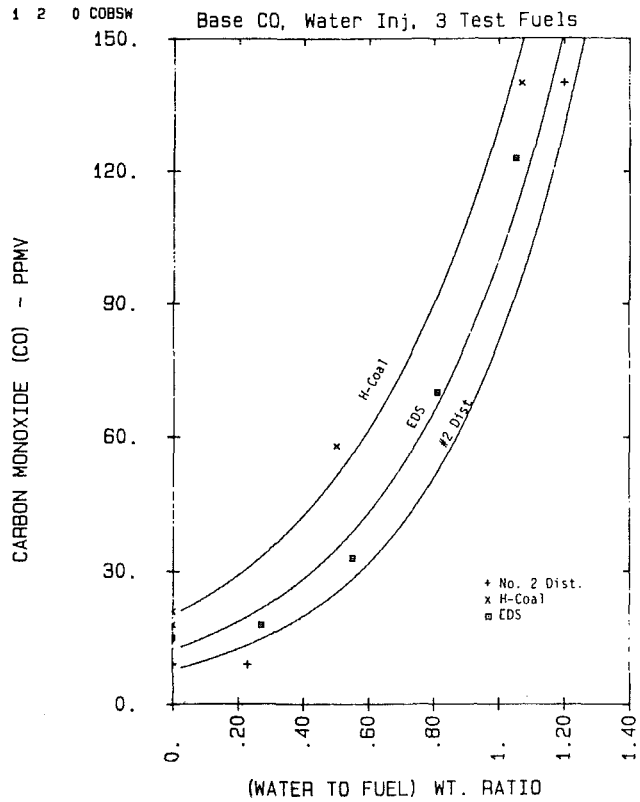

Fig. 5 Effect of water injection on carbon monoxide at base load

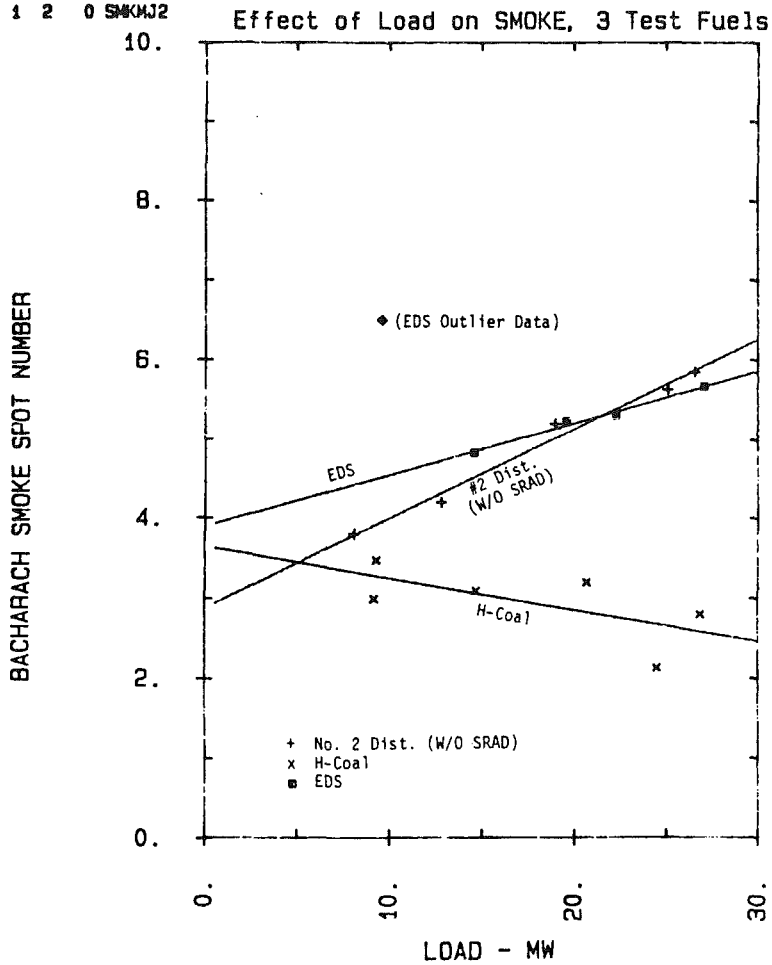

Fig. 6 Effect of load on smoke without water injection

slightly lower power, since the slightly lower exhaust water vapor content reduces the specific heat of the exhaust products expanding through the turbine

The variation of engine performance with load, normalized to ISO conditions, is shown in Fig. 2 for each test fuel without water injection. The normal trend of higher heat rate with lower power output occurs for all fuels.

Table 3 shows the base load ISO performance with normalized maximum water injection. The differences in the power and heat rate with the three test fuels are considered to be in a range attributable to measurement uncertainties and data scatter. The lower power for the H-Coal testing is due to having been at the engine fuel system flow limit, reached while testing with the high water injection rate at low ambient temperature. This limitation was not a result of firing H-Coal.

There was no measurable degradation in engine air flow during the approximately 80 hr of total CDL running time despite the appearance of a thin reddish-brown deposit on the engine hot parts after firing the H-Coal fuel. Due to the short duration of the test, it is not known whether this deposit may have increased in thickness to a point where engine performance might have been significantly affected.

The emissions signatures of the two CDL fuels were as expected. The fuel-bound nitrogen (FBN) in the CDLs contributed to higher levels of exhaust NO_x than were obtained with the baseline No. 2 distillate fuel, both without and with water injection as shown in Figs. 3 and 4, respectively.

As shown in Fig. 4, compliance with the Environmental Protection Agency (EPA) NO_x limit [7] of 75 ppmv for new

Table 4 Net particulate loadings (lb/hr): three test fuels

Fuel type	(W/F) ratio	Net particulate loadings
No. 2 Distillate	0	3.72
Baseline (SRAD)[a]	1.24	4.95
H-Coal CDL[a]	0	5.07
H-Coal CDL[a]	1.14	7.13
EDS CDL[b] (150°F, 50 μ fuel filters)	0	9.76
	~1.07	13.15

[a] Replicate sample
[b] No replicate samples

combustion turbines of this type could be achieved with approximately 0.28 (W/F) for No. 2 distillate, 0.33 (W/F) for EDS, and 0.65 (W/F) for H-Coal CDL. Calculations for higher temperature engines currently offered commercially indicate that (W/F) of approximately 0.7 would be required to meet the EPA NO_x limit with the EDS and approximately 0.95 with the H-Coal.

There was no significant effect of CDL fuel operation on emissions of carbon monoxide (CO) and unburned hydrocarbons (UHC). With high water injection rates for NO_x emissions reductions well below EPA requirements, the exhaust concentrations of CO increased notably at all test conditions for all three fuels. Figure 5 illustrates this effect at base load operations.

Compared with untreated No. 2 distillate fuel, Bacharach smoke number was lower with the H-Coal fuel and higher

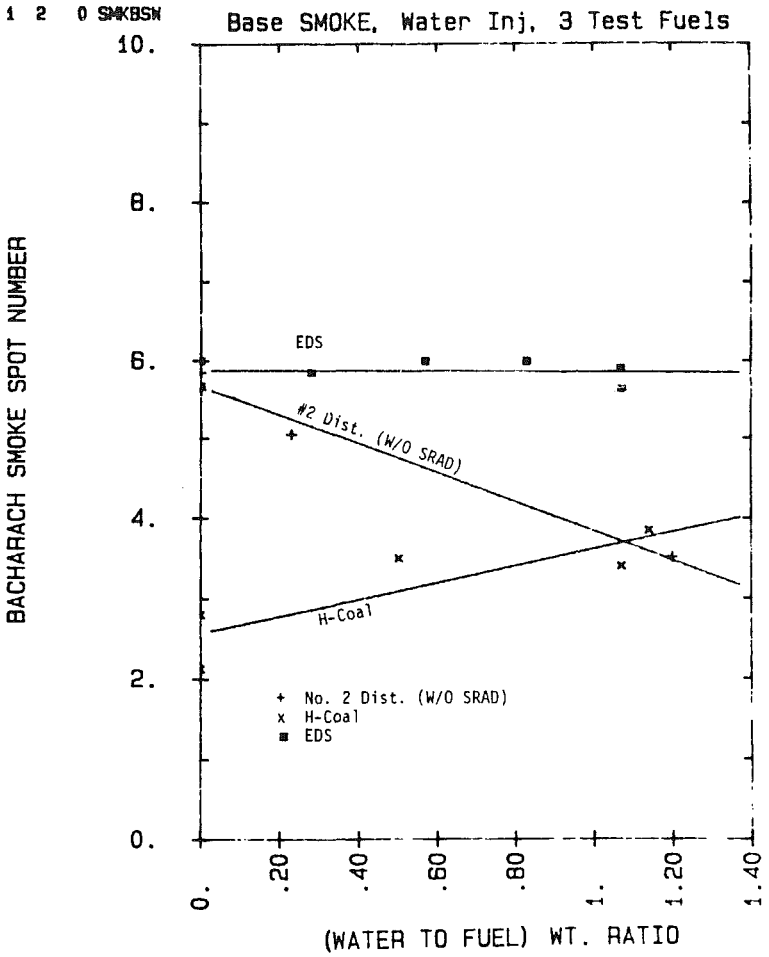

Fig. 7 Effect of water injection on smoke at base load

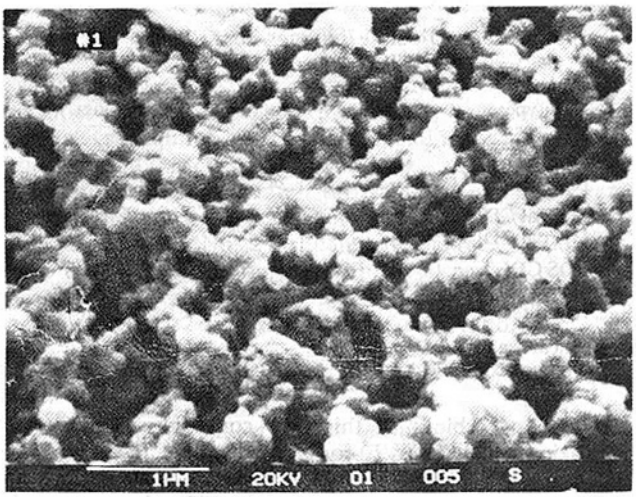

Fig. 8 Fine equiaxed particles from no. 2 distillate test

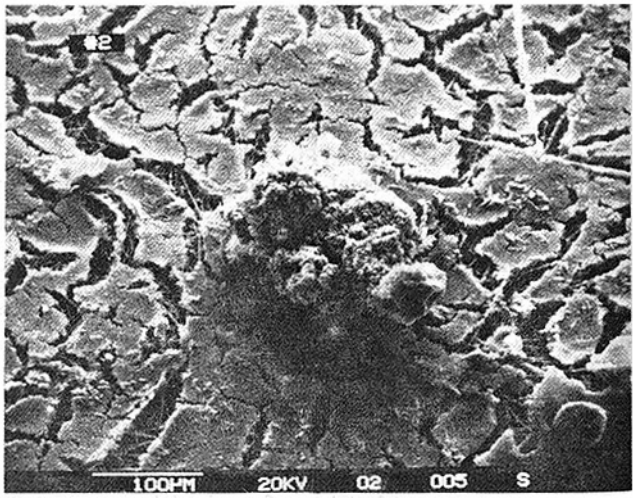

Fig. 9 A large clump of platelet particles in a distillate-fired sample

with EDS as shown in Figs. 6 and 7. The test fuel effects on exhaust smoke were somewhat varied, due to differences in the iron component of the fuel ash. The normal PECO No. 2 distillate fuel was treated with a smoke-reduction additive (SRAD) containing iron which produced a low smoke level at base load (Bacharach No. 0.7-0.8) regardless of water injection.

As shown in Fig. 6, the H-Coal smoke levels without water injection are much lower than those of untreated No. 2 distillate. It is believed this is due to a significant amount of iron in the H-Coal fuel ash. The high EDS smoke at 30 percent load may be associated with the higher distillation fractions found in this test fuel. Water injection for NO_x emissions control at base load affected the smoke level for all three test fuels differently as shown in Fig. 7. With increasing (W/F) smoke decreases for untreated No. 2 distillate fuel as expected; however, H-Coal smoke increases with (W/F) and EDS smoke is insensitive to water injection.

Total particulate loading at base load increased somewhat with the CDL fuels. As shown in Table 4, the net (exhaust

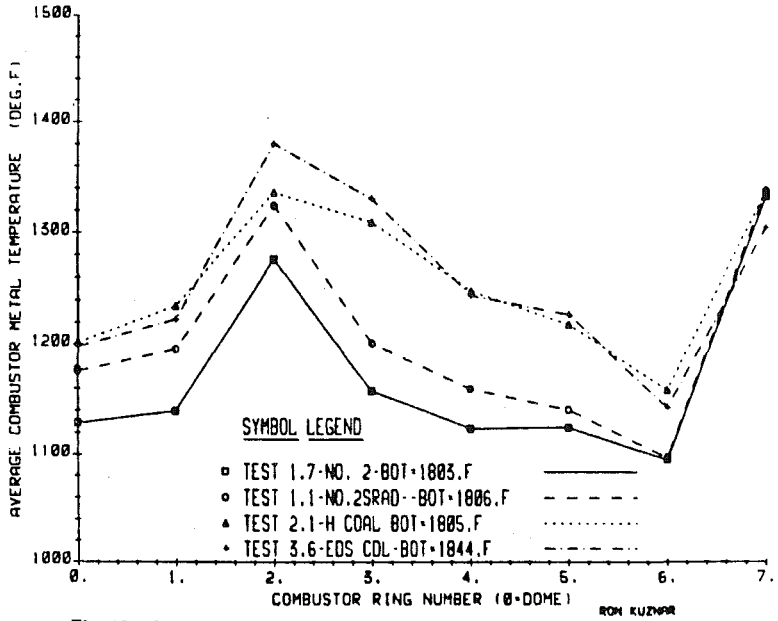

Fig. 10 Average combustor metal temperature versus location at base load operation: no water injection

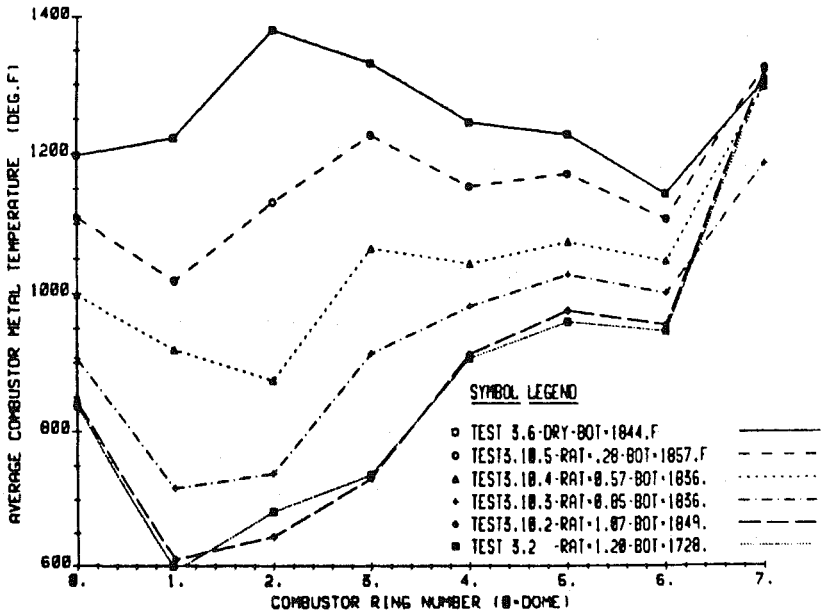

Fig. 11 EDS CDL; average combustor metal temperature versus location at base load: with and without water injection

minus inlet) particulate loadings ranged from 3.72 to 9.76 lb/hr without water injection ("dry"), and from 4.95 to 13.15 lb/hr when maximum injection water was used. The net particulate loadings were least for the No. 2 distillate baseline fuel that contained the smoke reduction additive and the highest for the EDS fuel. For all three test fuels, the net particulate loadings with maximum water injection increased above the "dry" loadings by approximately 1.1–1.2 lb/hr for both the No. 2 distillate (SRAD) and the H-Coal, and approximately triple that increment (3.4 lb/hr) for the EDS. Since the baseline distillate (with SRAD) and the H-Coal fuels had approximately the same level of iron (15-20 ppmwt), the difference in the particulate loadings for these two test fuels is believed to be due to their different hydrocarbon compositions. The much larger difference in particulate loadings between the H-Coal and EDS fuels is probably due to the heavier distillation ends in the EDS fuel, which smoked more.

Polycyclic organic emissions of concern from industrial hygiene considerations (polycyclic aromatic hydrocarbons (PAH), benzo-α-pyrenes (BAP), phenols, and formaldehyde) were sampled utilizing organic sorbent material (XAD-2 resin) in a series arrangement (two tubes in-line) inserted between a standard particulate collection prefilter and the water impinger/flowmeter assembly. These samples were analyzed by high performance liquid chromatography (HPLC), mass spectroscopy (MS), and differential pulse polarography. Concentrations were one-thousandth to one-millionth of the total particulate samples for both CDLs, with the analysis techniques straining the limits of detectability for many of the samples. The particles were submicron (0.12-0.21 μ) carbon spheroids for all three test fuels, and are typical of those shown in Fig. 8 for the No. 2 distillate fuel with additive.

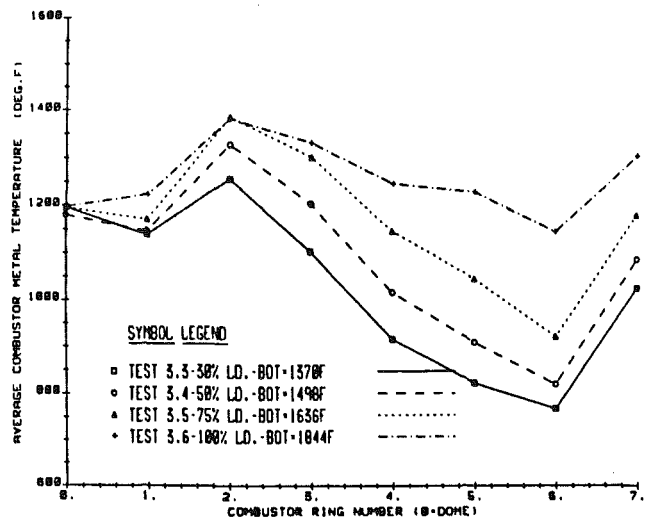

Fig. 12 EDS CDL; average combustor metal temperature versus location for various load points: no water injection

There was some evidence of larger iron platelets typical of that shown in Fig. 9 when the fuel contained significant amounts of iron (No. 2 distillate (SRAD) and H-Coal).

Combustor wall temperatures at baseload displayed the expected effects. Primary section (Rings 1-5) metal temperature increased with the lower-hydrogen and CDL fuels as shown in Fig. 10, and decreased with water injection as illustrated in Fig. 11 for EDS testing. Metal temperatures in the secondary section (rings 6, 7) tended to follow the combustor outlet temperature for all fuels regardless of water injection. This is illustrated in Fig. 12 for EDS testing without water injection. No metal temperatures exceeded the engine shutdown criteria for local hot spots or high average ring temperature levels. The higher combustor wall temperature, produced by the coal liquids, can reduce combustor life below present levels. To maintain the present life, wall temperatures would have to be reduced to those obtained during operation on No. 2 distillate untreated fuel. This could be achieved by increasing the film cooling air in the first two rings of the combustor. An alternative to modifying the film cooling could be an increase in the inspection frequency of the combustors as presently configured.

The combustor dynamic responses were monitored over the engine load and water injection range for each fuel. Most of the pressure fluctuations recorded during the test program were of such a small level that they caused no significant excitation to the combustor system, as illustrated in Fig. 13 for No. 2 distillate fuel. The singular exception to this was one broad-banded (150 Hz wide) pressure fluctuation, with a center frequency that varied from 1600 Hz to 1700 Hz. This provided high mechanical response on No. 2 distillate only, without water injection, only at 75 percent load shown in Fig. 14. Even though this atypical mechanical response was considered high (being nominally zero at all other test conditions), the frequency was high enough to be discounted as a possible source of mechanical distress, such as cracking, although it could cause fretting on contacting surfaces.

The pressure fluctuations caused by the compressor discharge are an order of magnitude larger than those generated by the combustor system, and sufficiently broad banded to excite the fourth ring mode to relatively high responses; but this has not caused any mechanical failures to date, and is not considered a threat to mechanical integrity.

The CDL fuels did show slightly higher levels of vibration and pressure fluctuations than the No. 2 distillate, but CDL and No. 2 distillate evolved the same basic patterns. Water injection sufficient to satisfy EPA NO_x requirements lowered vibratory responses for both CDL fuel and No. 2 distillate.

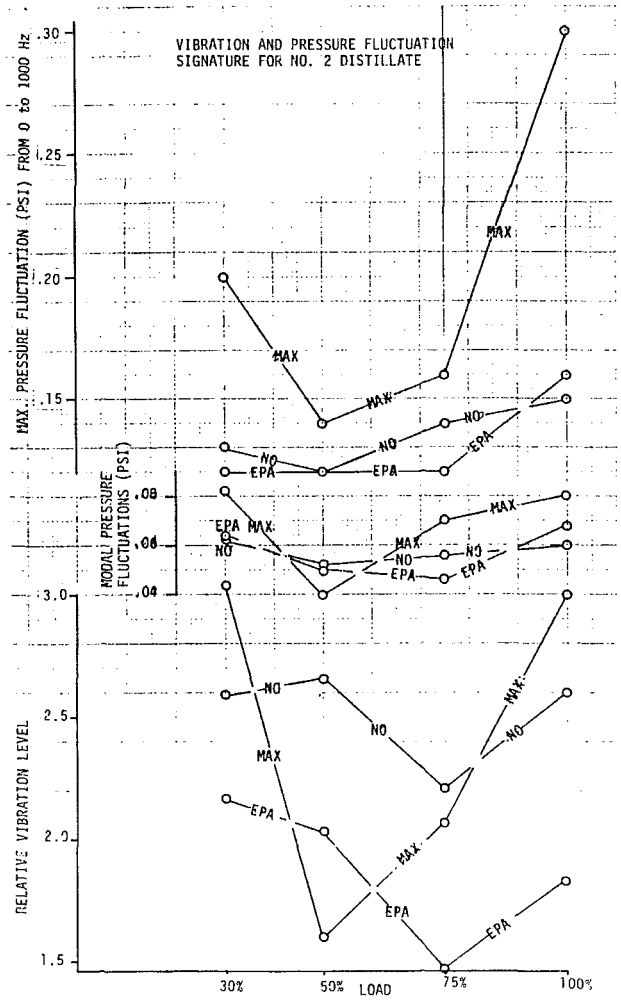

Fig. 13 Vibration and pressure fluctuation signature for No. 2 distillate fuel: with and without water injection

The high (W/F) ratio (1.2) showed higher vibratory levels at 30 and 100 percent load than the nonwater-injected case, but at 50 percent load was much lower than the nonwater-injected case. It is concluded that the CDL fuels analyzed show no greater risk to this combustor system from a mechanical vibratory standpoint than the No. 2 distillate fuel tested.

The engine fuel system had no difficulty handling the H-Coal fuel throughout 7 operational days. Fuel transfers and engine loading were uneventful. After completion of the 4 test days to execute the parametric test plan, the balance of the H-Coal test fuel was used to extend base load operational time as much as possible, accumulating about 60 total fired hours with this fuel.

Problems were experienced with the EDS test fuel, due to its high end point. High and low-pressure fuel filter plugging occurred persistently, both without and with heating of the fuel oil to 90°F. The fuel system was modified to incorporate 50 μ filters (versus the standard 5 μ), the fuel piping and filters heat traced and insulated, and the fuel heated to 135°F in an effort to minimize filter plugging within the mechanical and thermal constraints of the installed pumping and flow dividing systems. Filter plugging continued after these modifications, but at a sufficiently slow rate to obtain engine test data at all the planned test points. It was necessary to truncate some of the data collection and replication to minimize operating time on EDS fuel.

Immediately prior to the initial start of testing, all engine combustors were inspected, and calibrated nozzle assemblies installed. During re-inspection of these hot section parts immediately after the H-Coal tests, some minor deterioration

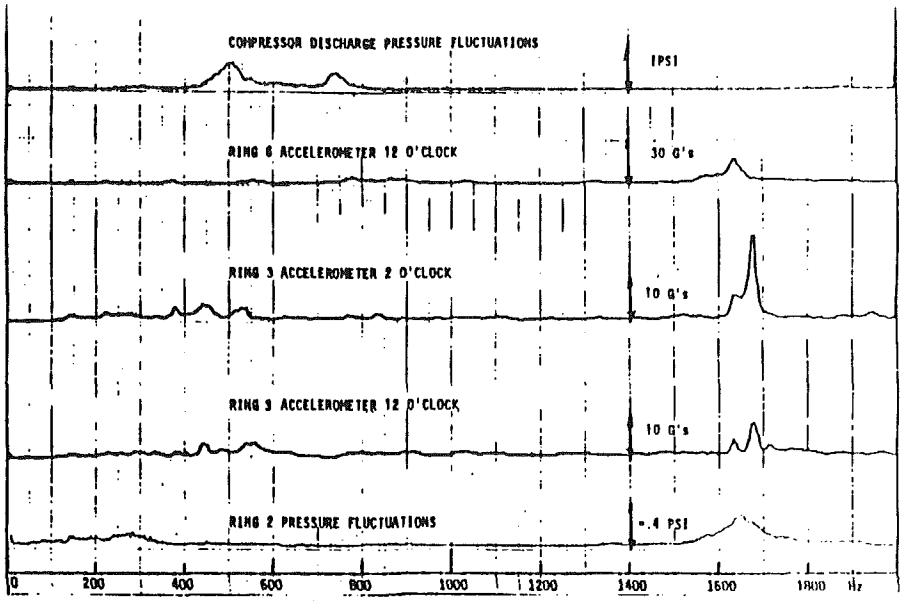

Fig. 14 No. 2 distillate fuel, 75 percent load, no water injection (note atypical responses at 1600 to 1700 Hz which were otherwise zero)

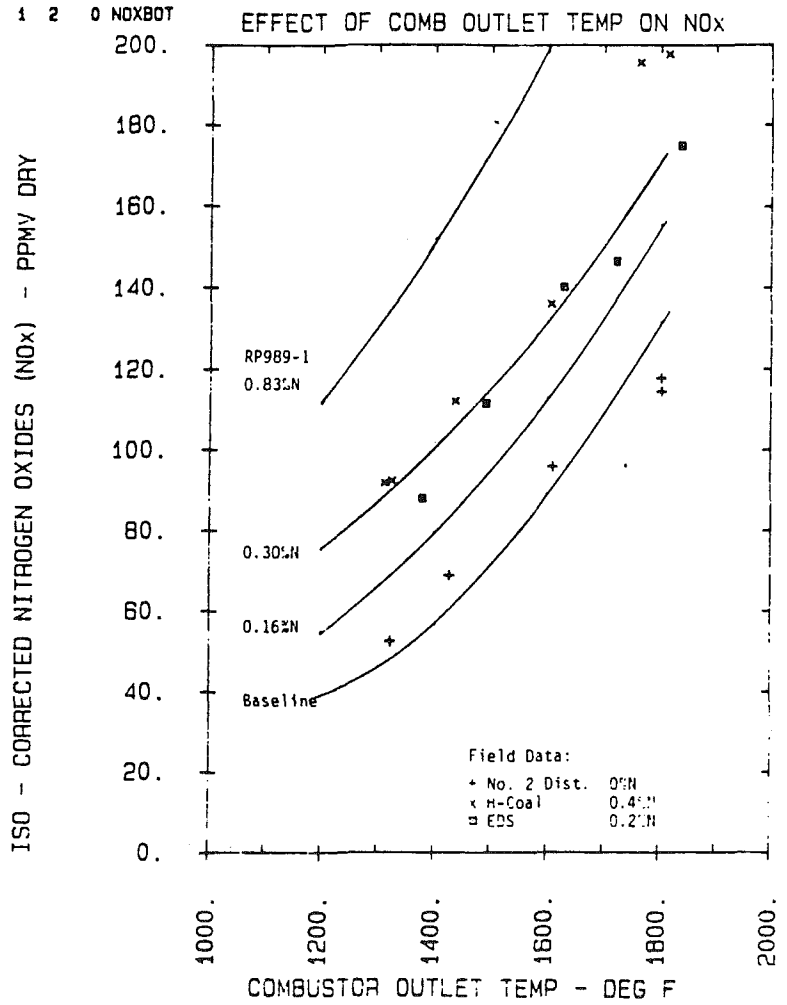

Fig. 15 Comparison of laboratory and engine NO_x emissions for varying levels of fuel-bound nitrogen: no water injection

of combustor spot welds was observed, mostly within the inspection allowance. Deposits were found in some atomizing air swirl caps and cleaning was required with a standard ultrasonic solvent bath. A very hard, thin reddish-brown deposit was seen on the flame-side surfaces of the combustors and transitions, and a softer deposit of similar color on the

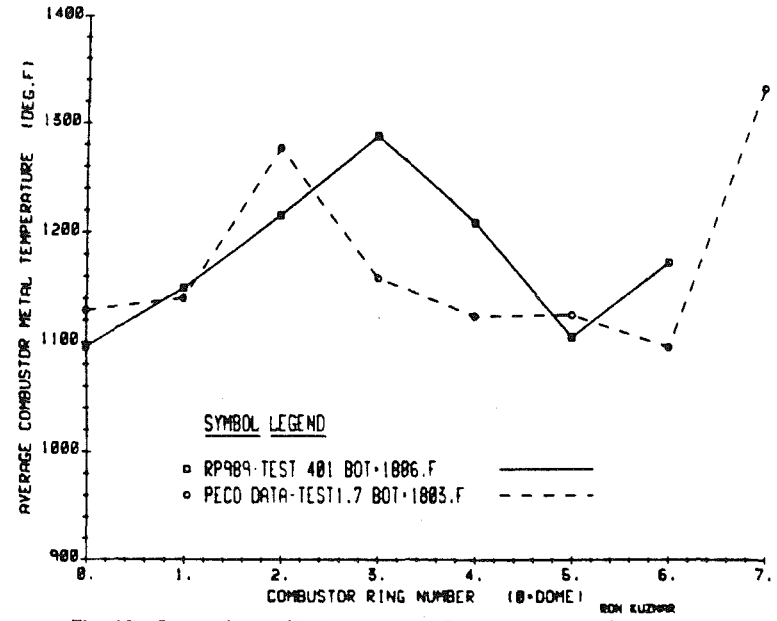

Fig. 16 Comparison of laboratory and PECO testing; average combustor metal temperature versus location; No. 2 distillate baseline fuel

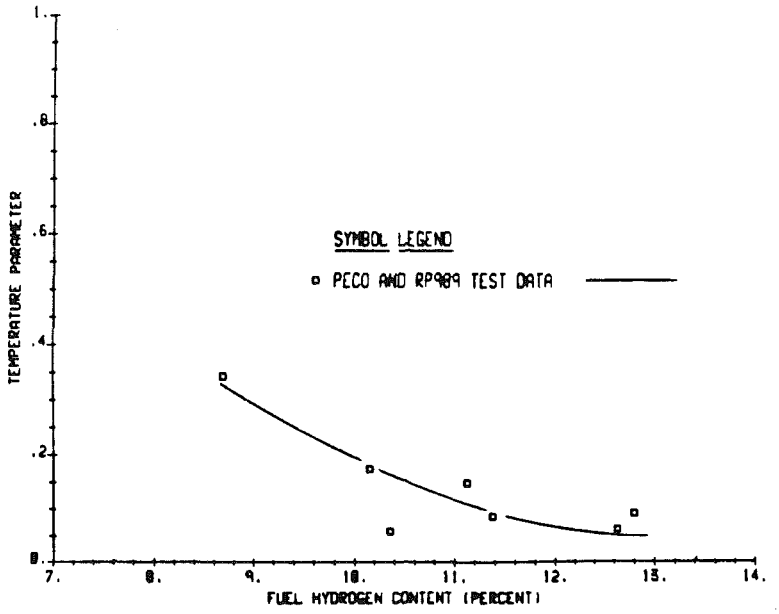

Fig. 17 Laboratory and PECO testing data; temperature parameter versus fuel hydrogen for the maximum test point BOT: range 1805°F to 1939°F

first row stator vanes. Deposit samples, thought to be primarily iron compounds from the H-Coal fuel, were collected for future analysis and correlation with fuel and engine operating conditions.

During and after the EDS runs with both 5 and 50 μ fuel filters, the engine experienced several starting failures due to dirty nozzle assemblies. The atomizing air caps required cleaning after each day's operation with EDS. Hot gas path deposits similar to those described above were observed after 20 hr cumulative operation on the fuel; samples were collected for future analysis.

Comparison of Field and Earlier Laboratory Results

NO_x and FBN Conversion. The engine NO_x emissions without water injection are superimposed on the laboratory NO_x trend curves [4] in Fig. 15. Good agreement for both the combustor outlet temperature and fuel-bound nitrogen effects is obtained. The 0.2 percent N and 0.4 percent N curves from the engine test results bracket the 0.3 percent N curve from the laboratory data.

With H-Coal, the engine FBN conversion values to NO_x for the "dry" base load conditions (no water injection) are in the 40 to 50 percent range. This is in reasonably good agreement with the previous laboratory conversion data. For the EDS fuel, there is notably higher FBN conversion with no water injection, ranging 70 to 90 percent. No simple explanation was found for this, although two possible factors may be contributing. First, it is not known what the thermal NO_x would have been if EDS contained no FBN; the thermal NO_x from No. 2 distillate is assumed. Second, the NO_x curve for the EDS without water injection is disproportionately close to the curve for the H-Coal (Fig. 3). Since the H-Coal contained 0.4 percent FBN and the EDS only 0.2 percent FBN, it would

be expected that for equal thermal NO_x from each fuel, the curves would be equally spaced relative to the distillate baseline. However, an unusually higher amount of NO_x was formed and measured during EDS testing. Perhaps this was due to high boiling fractions in the EDS, which in some way contributed to extending the NO_x-forming process in the flame zone. Another possibility is the difference in the other constituents found in the fuel analysis.

Combustor Wall Temperature. The combustion, dilution, and cooling air admission geometry of the combustors used in the laboratory test program and the PECO field tests is essentially the same. The primary difference between the two combustor configurations that may influence the wall temperatures is the fuel oil nozzle spray tip. A 250 gpm/50 deg[1] nozzle was used in the laboratory testing and 185 gpm/70 deg nozzles were utilized in the test engine.

The 70 deg nozzle tends to produce a wide short flame compared to the narrow longer flame resulting from the 50 deg spray angle. The wider 70 deg spray angle also tends to produce higher gas temperatures near the wall. Both of these aspects influence the heat transfer process from the combustion gases to the wall. Figure 16 compares the average combustor metal temperature versus location for both the laboratory and PECO test data for the No. 2 distillate baseline fuel. The temperature difference between the two combustors is less than 100°F. The differences in the fuel nozzles shift the peak primary zone metal temperature (1280°F) from ring 2 in the PECO test to ring 3 in the laboratory.

A dimensionless temperature parameter

$$TP = \frac{(T_{x\max} - T_{cx}) - (T_{2\max}) - (T_{2\max} - T_{c2})}{(T_{2\max} - T_{c2})}$$

where

$T_{x\max}$ = maximum combustor metal temperature for fuel x

T_{cx} = combustor inlet temperature for fuel x

$T_{2\max}$ and T_{c2} = same as above for the No. 2 distillate baseline fuel

has been used in other studies [8] including the laboratory program [4], to correlate the metal temperature obtained for a fuel (x) with a hydrogen content less than the baseline No. 2 distillate.

Figure 17 is a plot of the temperature parameter versus fuel hydrogen content at the maximum test point (burner outlet temperatures 1805°F to 1939°F) for both test programs. For design considerations, this point is the most meaningful, since the peak temperatures occur at base load operation. As shown, a second order curve fit showing good correlation is obtained.

Summary

H-Coal middle distillate and full-range Exxon Donor Solvent (EDS) CDLs have been successfully fired in a 26 MW utility combustion turbine. Higher combustor metal temperatures were observed with the CDLs, and persistent fuel filter plugging occurred with the EDS fuel.

The engine power output and heat rate performance characteristics were essentially unaffected. The emissions signatures of the two CDL fuels were as expected. Their fuel-bound nitrogen contributed to higher levels of exhaust nitrogen oxides than obtained with the baseline fuel. There was no significant effect of CDL fuel on emissions of CO and UHC. With high water injection rates CO increased for all fuels. Compared with baseline fuel, smoke was lower with the H-Coal fuel and higher with EDS. Total particulate loading (in the parts per million by weight range) increased somewhat with the CDLs. Particles were submicron carbon spheroids for all fuels. Emissions of PAH, BAP, and other polycyclic organic material were one-thousandth to one-millionth of the total particulate samples for both CDLs.

The combustor dynamic responses indicated no significant effect of operation with the CDL fuels. Combustor wall temperatures displayed the expected effects. Primary section metal temperature increased with the CDL fuels because of the brighter flame associated with decreased hydrogen content and decreased with water injection. Metal temperatures in the secondary section tended to follow the combustor outlet temperature for all fuels regardless of water injection. Good correlation of a dimensionless metal temperature parameter with fuel hydrogen content was obtained.

With the one exception of unexpectedly high FBN conversion for EDS, the emissions and combustor metal temperature results of this field test compared well with earlier laboratory test results for similar fuels. Extended operation with CDLs could require either increased cooling in the combustor primary zone, or an increased inspection frequency using present combustors.

Acknowledgments

The following individuals deserve recognition for their contribution to the preparation and conduct of this engine fuels test program:

From Westinghouse Electric Corporation: G. L. Carlson, R. E. Davis, C. A. Jersey, R. J. Kuznar, E. S. Obidinski, V. A. Ogale, and P. W. Pillsbury.

From Philadelphia Electric Company: P. J. Clelland, E. Spey, K. Smith, and M. Scanlan.

References

1 Lebowitz, H. E., and Schreiber, H., "Use of Synthetic Liquid Fuels for Power Generation," *Proceedings of the American Power Conference*, Vol. 44, 1982.

2 "Test and Evaluation of Methanol in a Gas Turbine System, RP988-1," EPRI AP1712, Electric Power Research Institute, Palo Alto, CA, Feb. 1981.

3 "Evaluation of Shale Oil as a Utility Gas Turbine Fuel--Final Report (RP1691-2)," EPRI AP1975, Electric Power Research Institute, Palo Alto, CA, Aug. 1981.

4 "Gas Turbine Combustor Performance on Synthetic Fuels, RP989-1," Electric Power Research Institute Report, AP-1623, Final Report, Vols. 1 and 2.

5 Carl, D. E., Obidinski, E. S., and Jersey, C. A., "Exhaust Emissions From a 25-MW Gas Turbine Firing Heavy and Light Distillate Fuel Oils and Natural Gas," ASME Paper No. 75-GT-68.

6 Ambrose, M. J., and Obidinski, E. S., "Recent Field Tests for Control of Exhaust Emissions From a 35-MW Gas Turbine," ASME Paper No. 72-JPG-GT-2.

7 Environmental Protection Agency, 40 CFR Part 60- "Standards of Performance for New Stationary Sources, Subpart GG, Standards of Performance for Stationary Gas Turbines," Federal Register Vol. 44, No. 176, Sept. 10, 1979.

8 "Advanced Cooled Combustor Development, RP1319-7," Electric Power Research Institute Report, AP-3104, Final Report.

[1] gpm flow number: gallons per minute at 100 psi ΔP

A. S. Abbas

F. C. Lockwood

Mechanical Engineering Department,
Imperial College of Science and Technology,
London, England

The Prediction of Several Residual Oil Flames

This paper describes the application of a general computational procedure to predict four residual oil trials conducted at the International Flame Research Foundation. These trials were conducted in an attempt to isolate scaling criteria based on conventional similarity arguments. However, it is here demonstrated that, after a single preliminary calibration limited to one of the model constants, very acceptable and detailed predictions can be obtained using the present method for all of the trials.

1 Introduction: Background and Present Objectives

Interest in oil fuels has been somewhat overshadowed by the growing interest in coal. All the same, new fields of oil and oil-bearing sands and rocks continue to be discovered and the advantages of oil are such that a considerable research effort has been aimed at the economic derivation of oil from coal. At the time of writing, the world oil recovery rate is substantially in excess of the usage rate. It seems that interest in oil firing will be maintained in the medium to long term.

Recently [1, 2] work was undertaken jointly by the International Flame Research Foundation and the United Kingdom Central Electricity Generating Board with a view to determining scaling criteria for oil-fired furnaces which would be of value to design engineers. Because many of the significant and complex processes obey markedly different scaling laws it was found extremely difficult to establish helpful rules; a simple criterion based on mean residence time was suggested as offering partial assistance.

The present authors felt that it would be of great interest to attempt to scale with the aid of a modern computer prediction procedure. The previous applications to oil firing of these procedure have been few [3, 4, 5] and all have been for light oil fuels. The additional complications of modeling residual oil firing are so extensive that we felt there was no realistic possibility in the absence of prior experience of obtaining decent "blind" predictions of the trials of [1, 2]. Instead we decided to "tune" the procedure to the data of one of the trials, the C3-flame, and to evaluate its accuracy when applied to the other trials without altering any of the model constants. If the evaluation proved successful then the prediction method would constitute a valuable weapon in the design engineer's armory.

The work of this paper is confined to the O-18/19 trials at the Flame Foundation [1] designated flames C3, D1, and D3 in the No. 1 furnace and flame E4 in the smaller No. 2 furnace. For reasons of computer economy it is conventional to model these furnaces as if they were axisymmetric. The loss of accuracy from this approximation appears to be small [6], and this is probably also true for the O-18/19 trials where the furnace was shortened by a partition. There is no other reason for doing this, and indeed fully three-dimensional computations of the Foundation's No. 1 furnace have been made [7]. The geometry of the CEGB furnace is such that it cannot be reasonably approximated by a two-dimensional simulation; work is in progress on a fully three-dimensional treatment.

2 The Prediction Method

2.1 The Numerical Solution Procedure. This has been previously described in [8]. The approach is based on original proposals of Migdal and Agosta [9]. Representative droplet flights are tracked through the prevailing gas field calculated in our case with the aid of a conventional TEACH-type code [10]. The influence of the droplets on the gas field is accounted for by source terms appended to the gas phase conservation equations prior to a recalculation of the gas field. New flights and interactions are determined for the recalculated gas field and the whole process is repeated until convergence is achieved.

2.2 The Spray Model. The momentum conservation equations for the axial, radial, and circumferential directions, ignoring gravitational effects, may be written

$$\frac{du_p}{dt} = \frac{3\rho_g}{4\rho_p D_p} C_D(u_g - u_p)|\mathbf{V}_g - \mathbf{V}_p|$$

$$\frac{dV_p}{dt} = \frac{3\rho_g}{4\rho_p D_p} C_D(v_g - v_p)|\mathbf{V}_g - \mathbf{V}_p| + \frac{w_p}{r_p} \quad (1)$$

$$\frac{dw_p}{dt} = \frac{3\rho_g}{4\rho_p D_p} C_D(w_g - w_p)|\mathbf{V}_g - \mathbf{V}_p| - \frac{v_p w_p}{r_p}$$

Williams (11) has cited the following recommendations for the drag coefficient C_D which are an across the board resumé of many experiments involving, it should be admitted, more volatile liquids than the present residual oil fuel

$$\begin{aligned} 0 < \mathrm{Re}_p < 80 \quad & C_D = 27\mathrm{Re}_p^{-0.84} \\ 80 < \mathrm{Re}_p < 10^4 \quad & C_D = 0.271\mathrm{Re}_p^{0.217} \\ \mathrm{Re}_p > 10^4 \quad & C_D = 2.0 \end{aligned} \quad (2)$$

Contributed by the Power Division for publication in the JOURNAL OF ENGINEERING FOR GAS TURBINES AND POWER. Manuscript received by the Power Division April 1984.

where Re_p is the droplet Reynolds number defined as $\mathrm{Re}_p = \rho_g |\mathbf{V}_g - \mathbf{V}_p| D_p/\mu$. The position of the particle is found from

$$\frac{dx_p}{dt} = u_p$$
$$\frac{dr_p}{dt} = v_p \tag{3}$$

The rate of droplet diameter diminution is given by

$$\frac{dD_p}{dt} = -\frac{4KgC}{\rho_p C_{p,g} D_p} \ln(1+B) \tag{4a}$$

where B is the transfer number

$$B \equiv \frac{c_p}{L}(T_g - T_{\mathrm{sat}}) \tag{4b}$$

and C is an empirical correction factor [12] to account for the effect of convection on the evaporation rate

$$C = \frac{1 + 0.278(\mathrm{Re}_p^{1/2}\mathrm{Pr}^{1/3})}{(1 + 1.237/\mathrm{Re}_p\mathrm{Pr}^{4/3})^{1/2}} \tag{4c}$$

The rate of change of droplet temperature is computed from

$$\frac{dT_p}{dt} = \frac{6Kg\mathrm{Nu}}{\rho_p C_{p,p} D_p^2}(T_g - T_p) - \frac{3L}{C_{p,p} D_p}\frac{dD_p}{dt} \tag{5}$$

The values of the Nusselt number have been obtained from Chigier and Yule [13]. Mean values of all the fuel properties have been taken from Cooper [14].

There will be some turbulence dispersion of the droplets although because of their high initial momenta and short vaporization times its effect is probably not very large. This phenomenon is much in need of detailed research. Our treatment of it is necessarily very approximate [8]. We express equations (1) in vectorial form by

$$\frac{d\mathbf{V}_p}{dt} = \mathbf{F}_D + \mathbf{F}_{\mathrm{TD}} \tag{6}$$

where $\mathbf{F}_D$ denotes the drag force per unit mass and represents the existing right-hand-side of equation (1). $\mathbf{F}_{\mathrm{TD}}$ represents the additional force on the particle due to turbulence. A corresponding diffusion velocity may be defined

$$\mathbf{V}_{\mathrm{TD}} = \tau_D \mathbf{F}_{\mathrm{TD}} \tag{7}$$

where $\tau_D \equiv (4/3\rho_p D_p^2)/(C_D \mathrm{Re}_p \mu)$ is the conventional particle dynamic relaxation time. The velocity is related to the particle concentration gradient by a simple Boussinesq relation

$$\mathbf{V}_{\mathrm{TD}} = -\frac{\rho_g}{\rho_p}\Gamma_{\mathrm{eff},p}\nabla m_p \tag{8}$$

The effective particle diffusion coefficient $\Gamma_{\mathrm{eff},p}$ is presumed to be related to the gas turbulence exchange coefficient $\nu_{\mathrm{eff}} = C_\mu k^2/\epsilon$ by:

$$\frac{\Gamma_{\mathrm{eff},p}}{\nu_{\mathrm{eff},g}} = 1 + \psi \tag{9}$$

where $\psi = \tau_D/\lambda$, and $\lambda \equiv (2/3)k\nu_{\mathrm{eff},g}$ is the gaseous turbulence integral time scale. This suggests that particles in the present size range tend to be flung out of the carrier gas vortices.

Because the majority of the droplets will experience only a cool air deficient atmosphere for the bulk of their lifetimes the possibility of combustion of individual droplets is excluded. All the combustion occurs in the gaseous phase and is handled in a conventional manner (see [15] for example).

2.2 The Radiation Model. A "four-flux" radiation model was considered sufficiently accurate for the present purposes. Since any properly conceived example would give comparable results, we have chosen the one of [16]. The equations have the usual diffusion form; that for the radial direction is

$$\frac{1}{r}\frac{\partial}{\partial r}\left(\frac{1}{k_{a,n}}\frac{\partial(rR_{r,n})}{\partial r}\right)$$
$$= k_{a,n}\left(\frac{8}{3}R_r - \frac{4}{3}R_{x,n}\right) - \frac{4}{3}k_{a,n}a_{g,n}\sigma T^4 \tag{10a}$$

while for the axial direction we have

$$\frac{\partial}{\partial x}\left(\frac{1}{k_{a,n}}\frac{\partial R_{y,n}}{\partial x}\right)$$
$$= k_{a,n}\left(-\frac{4}{3}R_{r,n} + \frac{8}{3}R_{x,n}\right) - \frac{4}{3}k_{a,n}a_{g,n}\sigma T^4 \tag{10b}$$

where R_x and R_r are linear combinations of the coefficients of a four-term Taylor series which is presumed to represent the spatial variation of radiation intensity at a specified combustor location. These equations are supplemented by the boundary relations which, for example, in the case of the radial wall is

$$\epsilon_w R_{r,n} + \frac{2}{3k_{a,n}r}\left(\frac{\partial(rR_{r,n})}{\partial r}\right)(2 - \epsilon_w) = \epsilon_w a_{g,n}\sigma T_w^4 \tag{10c}$$

The wall emissivities and temperature were known. The total reaction source term to be appended to the enthalpy equation at each control volume in the total energy balance is determined from

$$S_{\mathrm{rad}} = \sum_n \frac{16}{9}k_{a,n}[-(R_{r,n} + R_{x,n}) + 2a_{g,n}\sigma T^4] \tag{10d}$$

The $k_{a,n}$ are the grey gas absorption coefficients pertaining

Nomenclature

C_D = drag coefficient
C_p = specific heat at constant pressure
D = burner diameter
D_p = droplet diameter
k = kinetic energy of turbulence
K = thermal conductivity
L = latent heat of vaporization
m_d = droplet mass
$\tilde{m}_f, \tilde{m}_{O_2}, \tilde{m}_s$ = mass fraction of fuel vapor, oxygen, and soot
m_p = droplet mass fraction
n = band number
Nu = Nusselt number
Pr = Prandtl number
r = radial coordinate
Re = Reynolds number
S_f, S_s = stoichiometric oxygen/fuel and oxygen/soot ratios
t = time
T = temperature
$\mathbf{V}$ = total velocity vector
u, v, w = time-averaged velocity components
x = axial coordinate
Γ = diffusion coefficient
ϵ = dissipation rate of turbulence
μ = viscosity
ρ = density
σ = Stefan–Boltzmann constant

Subscripts

eff = effective
g = gas
i = inlet and initial
o = outlet
p = droplet
sat = saturation
TD = turbulent diffusion

to the grey bands of the model of [17] in which the nongrey nonluminous combustion products are represented by a hypothetical mixture of a few grey gases plus a clear gas. The $a_{g,n}$ are functions of temperature and represent the fractional total black body emissive power of each of these assumed participating gases. We have used the recommendations of Truelove [18] for k_n and $a_{g,n}$.

The sizes and optical properties of the soot particles are elusive quantities, depending on the fuel type, burner design, and firing conditions. Fortunately since residual oil engineering flames are normally not far from the optically thick limit it is not necessary to know these properties with great precision. Again, we have employed the recommendations of Truelove based on furnace data. He presumes reasonably and conventionally that the soot absorption coefficient is a linear function of the volumetric mass concentration. Its behavior is not quite grey and this is accommodated by discretizing the soot absorption coefficient such that it is uniform within each of the bands of the grey-plus-clear-gas model.

2.3 Soot Formation Model. The fraction of the total carbon content of the fuel which converts to soot is too small to influence significantly the overall heat release distribution. Rather soot is of concern because its presence greatly augments the radiation heat transfer and because it is a pollutant. Most reasonably operated and maintained modern burners ensure complete combustion of soot (although the relatively large-scale coke particles of residual oil combustion products constitute a problem, but this is a distinct phenomenon not considered here). So the primary function of our soot model will be the good characterizing of the optical properties of the flame.

As mentioned the soot content of residual oil flames is so great that those of industrial dimensions approach the black body limits. As a consequence the accurate prediction of the local soot concentration is not a prerequisite for the good calculation of the radiation transfer. This is indeed fortunate since the mechanisms of soot formation are far from being established even in the simplest laboratory flames [19].

We choose to simulate soot production by a simple global expression similar to that used by Khan and Greeves (20)

$$P_{s_+} = C_f p_{fu} \phi^n \exp(-E/T_g) \tag{12}$$

C_f is a function which would ideally depend on an easily definable fuel property such as the C/H ratio. Here we have simply tuned it to the C3-flame data of [1] and the value of 0.84 is appropriate. The fuel partial pressure p_{fu} and the equivalence ratio ϕ are intended to accommodate the known influences of these quantities. Although the work of [20] was performed in connection with diesel engines we have assigned their values of 3 and 40200/$\Re$ to n and E. Soot production is essentially zero for ϕ less than that corresponding to the incipient sooting limit [21]. The value of ϕ corresponding to the incipient sooting limit is assumed to be 2. Soot formation occurs for fuel rich mixtures [21]. The soot production term p_{s_+} ultimately tends to small values as ϕ increases. We set p_{s_+} equal to zero for ϕ equal to $\phi_{\max}$ defined as the value of ϕ at which p_{s_+} is less than 1 percent of its maximum value.

The calculated mixed mean mixture fraction is not appropriate for the calculation of soot since soot is produced in the immediate vicinity of the droplet. Indeed early calculations showed that the calculated mean mixture fraction was almost everywhere less than that corresponding to the lower sooting limit assigned to ϕ. The near droplet mixture fraction was characterized with reference to a variety of expressions which can be found in the literature. The calculated soot concentrations were insensitive to these possibilities to the extent that it was found sufficient to presume a linear variation of mixture fraction between an

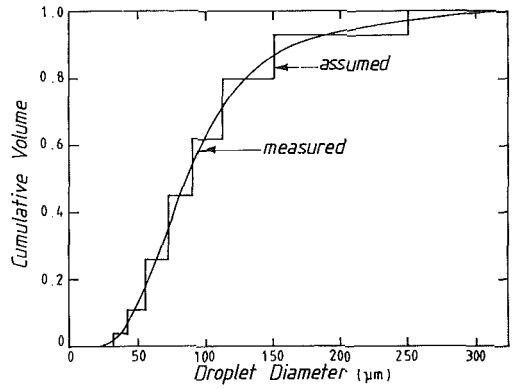

Fig. 1 Discretization of the droplet size distribution of the eight-hole, Y-jet, twin fluid atomizer

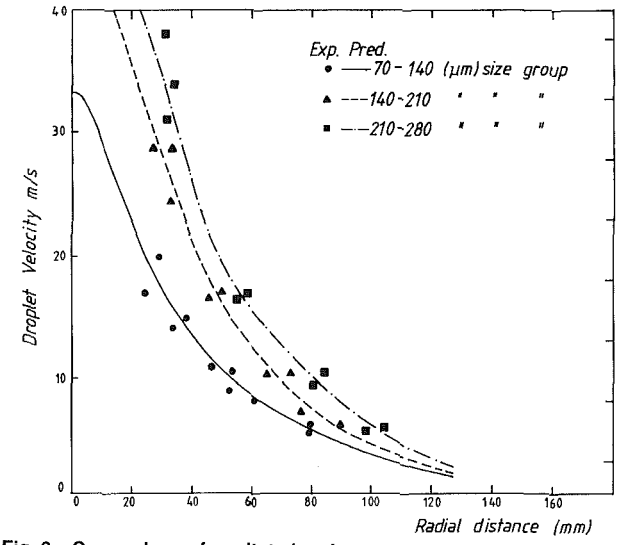

Fig. 2 Comparison of predicted and measured droplet velocities, 0.69 m downstream

assumed value of unity at the droplet surface and the far field mean value $\bar{f}$. A satisfactory near droplet mean value is then simply $\bar{f}_d = (1+\bar{f})/2$. The effect of the number of droplets in a cell on the calculated value of $\bar{f}_d$ has been approximated by multiplying $\bar{f}_d$ by the ratio of the number of droplets in the cell in question to the total number of droplets injected into the combustion space. The value of $\bar{f}_d$ calculated for each cell is in any case nearly the same regardless of the number of droplets in the cell. This is due to the fact that $\bar{f}$ is often much smaller than unity.

The conservation equation for $\bar{f}$ is

$$\frac{\partial}{\partial x}(\rho u \bar{f}) + \frac{1}{r}\frac{\partial}{\partial r}(r\rho v \bar{f}) = \frac{\partial}{\partial x}\left|\Gamma_{\text{eff}}\frac{\partial \bar{f}}{\partial x}\right| + \frac{1}{r}\frac{\partial}{\partial r}\left|r\Gamma_{\text{eff}}\frac{\partial \bar{f}}{\partial r}\right| + S_d \tag{13}$$

It is of interest in presenting this equation to draw attention to the source term S_d which is a consequence of the droplet vaporization

$$S_d = \left(\frac{1-\phi_a}{\phi_f - \phi_a}\right)\sum_{L=1}^{N}(\dot{m}_{d_i} - \dot{m}_{d_o})_L \tag{14}$$

where $\phi_a \equiv m_{0_{2,i}}/S_f$, $\phi_f \equiv \bar{m}_{f,i}$, and N is the number of droplet sizes.

In one sense the determination of the soot burning rate poses a much less demanding modeling problem since the particle sizes are so small that near-particle diffusion cannot possibly be controlling; rather, the combustion rate will be

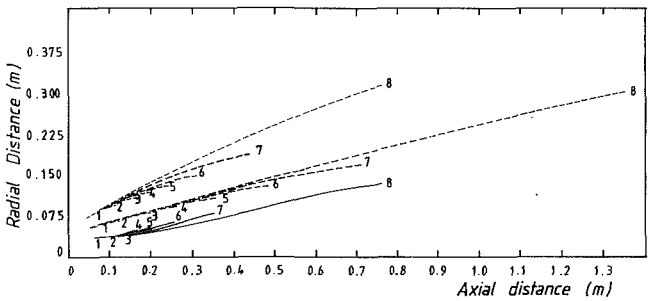

Fig. 3(a) Predicted droplet trajectories from three ports of the assumed six inlet ports; initial diameters: 1) 32, 2) 42, 3) 55, 4) 72, 5) 90, 6) 112, 7) 150, 8) 250 μm, C3 flame

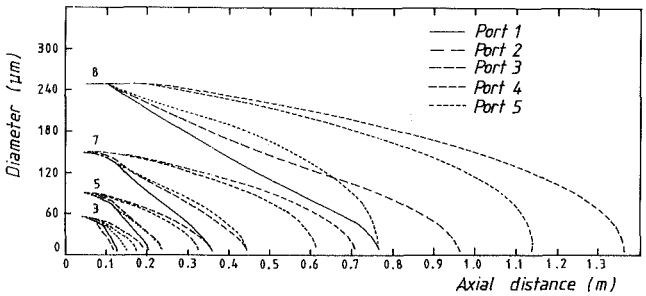

Fig. 3(b) Predicted droplet size variations for four of the assumed initial droplet sizes injected from the six inlet ports, C3 flame

controlled by the rate of mixing of the particle-bearing vortices with adjacent oxygen-bearing material. A simple, and appropriate for our purpose, method of rate has been proposed by Magnussen and Hjertager [22]. Following conventional turbulence concepts [23], they presume that the turbulence decay or mixing rate is proportional to the magnitude of the time mean soot concentration $\bar{m}_s$, and the time scale of the large-scale turbulence motion ϵ/k. Their expression for the soot consumption rate is

$$P_s = A\bar{m}_s(\epsilon/k) \tag{12a}$$

where A is a model constant assigned the value 4 based on numerical experimentation. This relation will not be satisfactory in regions where the reaction rate is limited by oxygen deficiency in which case Magnussen and Hjertager propose

$$P_s = A\left(\frac{\bar{m}_{O_2}}{\bar{m}_s S_s + \bar{m}_f S_f}\right)\bar{m}_s\left(\frac{\epsilon}{k}\right) \tag{12b}$$

The alternative giving the smallest reaction rate is used.

distribution was assumed to prevail at 0.1 m, the chosen starting station for the spray calculations.

Next computations were performed, using a parabolic code and commencing at the orifice exit plane, of the development of the fuel plus air jet. Mixed mean property values were used. These provided an estimate of the streamline directions at the 0.1-m station. Six locations or "ports" for droplet injection were selected across the width of the jet. Injection velocities were then guessed and parabolic calculations were made between the 0.1-m and 0.69-m stations and the predicted and measured velocities at the latter were compared. The guesses were adjusted to give the best agreement. The result is displayed in Fig. 2. Given all of the difficulties of this process the agreement is considered to be quite satisfying. All the calculations presented herein are commenced from the 0.1-m station using the starting conditions so determined.

3 Results of Calculations of the IFRF Flames

The conditions of four IFRF trials that have been predicted are summarized in the following table. Full details are provided by Payne and Salvi [1].

Trial No.	Flame No.	Burner diameter (m)	Flame throughout (MW)	Combustion air flow (kg/hr)	Fuel mass flow (kg/hr)
0-18 Furnace No. I	C3	0.232	2.31	2746	189
	D1	0.150	2.31	2746	189
	D3	0.150	0.93	1093	76.1
0-19 Furnace No. II	E4	0.150	0.58	685	47.5

2.4 Initial Conditions. An ideal treatment of the spray necessitates commencing calculations within the body of the atomizer. This approach was considered overly elaborate for our purposes and instead we decided to attempt to ascertain suitable starting conditions by reference to photographic data on the velocities and size distributions collected by Sargeant and Jones [24] for one hole of the eight-hole, Y-jet, twin fluid atomizer used in the burners of the IFRF tests. The data from these tedious experiments were limited and the fitting exercise which will now be outlined represents our attempt to optimize their use.

Figure 1 shows the measured droplet size distribution averaged over the width of the spray 0.69 m downstream of the atomizer injection orifice. This was discretized into eight uniform diameter ranges as shown. The fuel streaming from the atomizer hole breaks up into a spray about 0.1 m downstream. It was assumed, with reasonable justification, that the amount of fluid vaporized between this and the 0.69-m station was negligible and the 0.69-m droplet size

Figure 3 shows predictions of the droplet trajectories and diameters for the C3 flame. There are no measurements with which these results may be compared. Rather, they are presented to demonstrate the level of predicted detail and to reveal that at this level the results do conform with expectations.

Figure 4 shows temperature predictions for the C3 flame at three axial locations. It will be recalled that this was arbitrarily chosen as the reference flame for tuning the mathematical model. In the event however the only tuning which was done was on the constant C_f of the soot generation model. The droplet model parameters are those stated in Section 2.1, drawn from independent sources, while the turbulence model constants are the same as those used for previous gas phase calculations (e.g., [15]). The need to simulate well the soot concentration is demonstrated by the very large effect (Fig. 4) of neglecting the heat transfer, which is mainly by thermal radiation, on the temperature field.

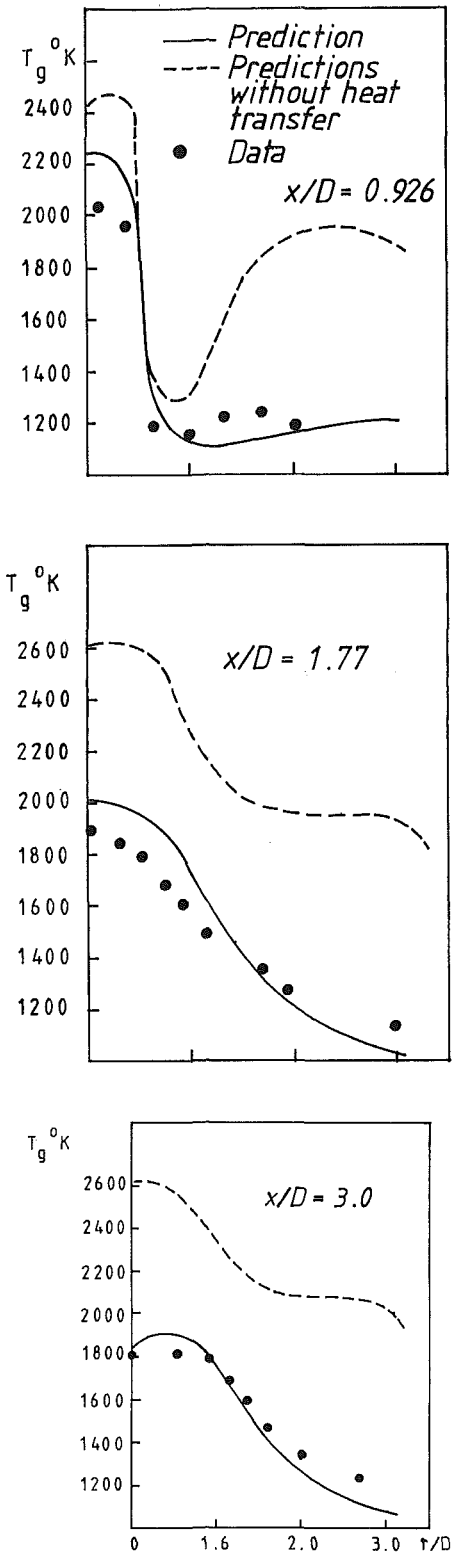

Fig. 4 Comparison of predicted and measured temperature profiles, C3 flame

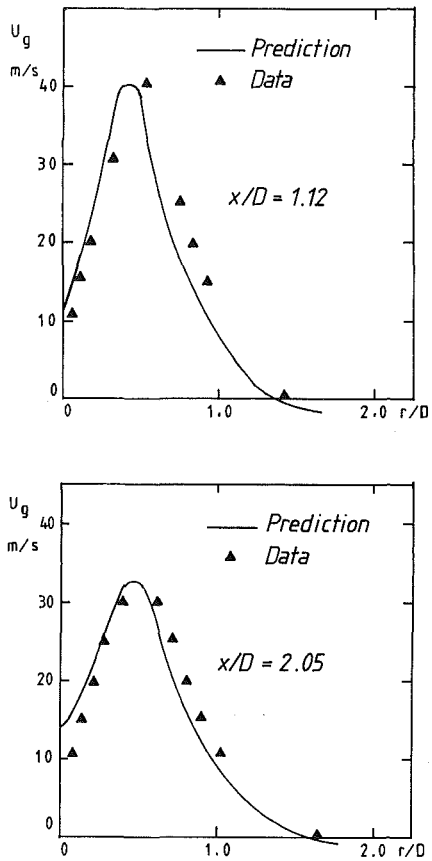

Fig. 5 Comparison of predicted and measured velocity profiles, C3 flame

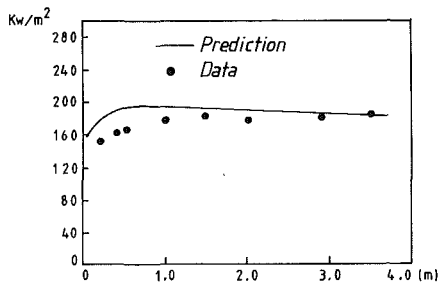

Fig. 6 Comparison of predicted and measured radiating incident wall radiation flux, C3 flame

Sample axial velocity profiles are shown in Fig. 5 and the wall heat transfer is presented in Fig. 6, all for the C3 flame. The quality of the velocity predictions is surprisingly good, broadly equal to that which can be expected for inert recirculating flows using present-day turbulence models. The prediction of the radiation flux incident on the outer walls is shown in Fig. 6 compared with the experimental values obtained with an ellipsoidal radiometer. Again these results are entirely satisfactory; the small overprediction near the burner will receive further comment in connection with the other trials.

Lastly, for the C3 flame, contours of the degree of oxidation (local mass of O_2 consumed/amount required for complete local combustion) and of soot concentration are shown in Fig. 7. This form of comparison tends to accentuate the discrepancies. It is our opinion that, given the detailed nature of the information being predicted, these comparisons are quite rewarding. A general comment about all of the C3 flame predictions is that the near burner discrepancies which are revealed are all consistent with overprediction of the spray evaporation rate implying that some reconsideration of the droplet model is demanded which is consistent with the low volatility of residual oils.

Representative predictions for the remaining flames, D1, D3, and E4, are portrayed in Figs. 8–15. They are barely distinguishable in quality from those of the base case C3 flame. The incident wall radiation fluxes (Fig. 14) are again overpredicted near the burner. The fact that the data do not

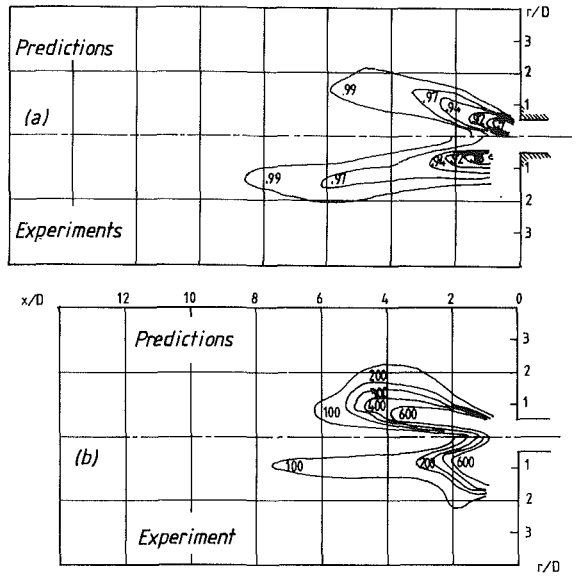

Fig. 7 Comparison of predicted and measured contours of: (*a*) degree of oxidation, (*b*) soot concentration (mg/nm^3), C3 flame

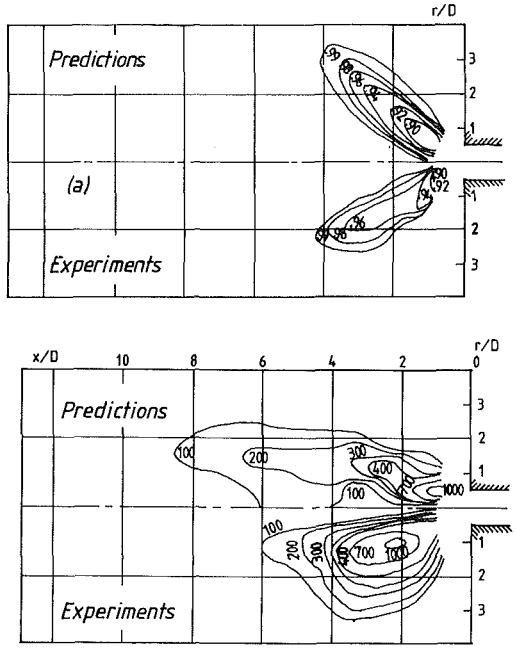

Fig. 9 Comparison of predicted and measured contours of (a) degree of oxidation, (*b*) soot concentration (mg/nm^3), E4 flame

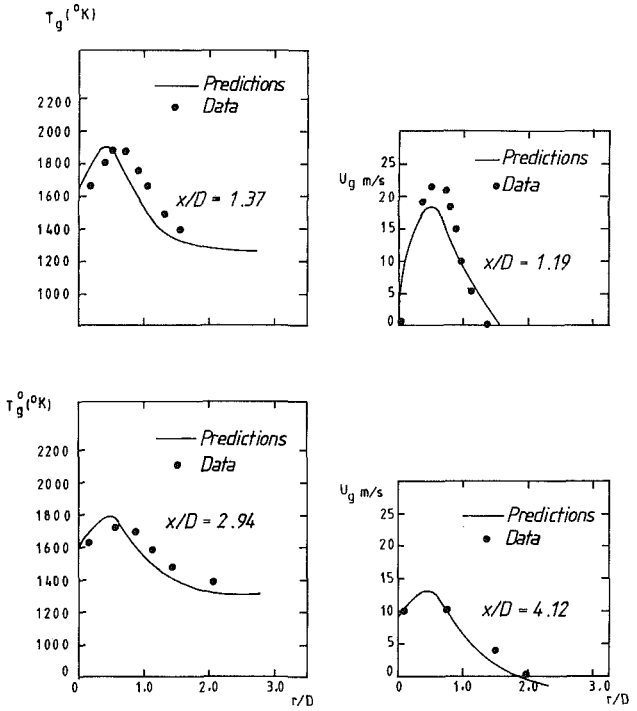

Fig. 8 Comparison of predicted and measured temperature and velocity profiles, E4 flame

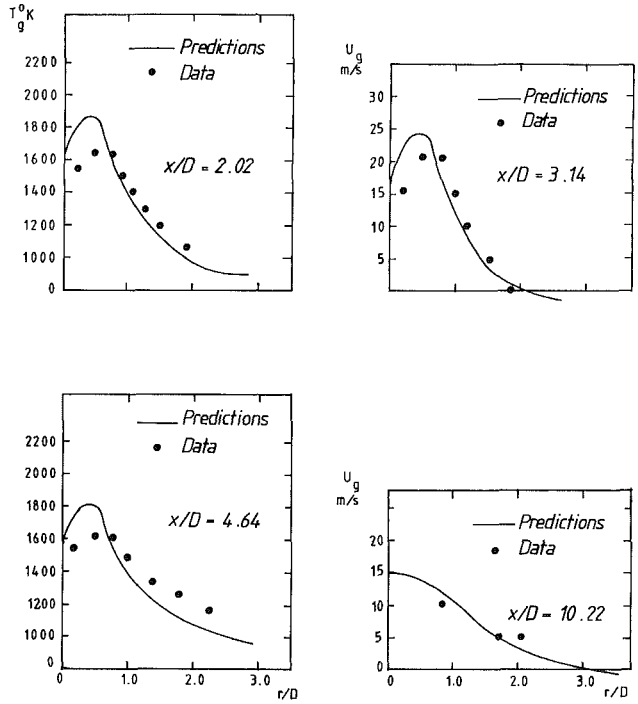

Fig. 10 Comparison of predicted and measured temperature and velocity profiles, D1 flame

reveal a peak in the near burner region for any of the flames is a little surprising. There is, however, not very great reason to doubt the accuracy of the radiometer measurements and it seems logical to ascribe again the discrepancy to an over-prediction of the evaporation rate tending to shift the flame base nearer to the burner. Indeed, photographs of the flames reveal that they did stabilize a little downstream of the predicted locations. Also, it is not unlikely that the four-flux radiation treatment could cause a noticeable predictive error. A recent radiation method [25] now makes it possible to obtain an exact solution of the radiation transfer for economic cost and this will be done at the earliest opportunity.

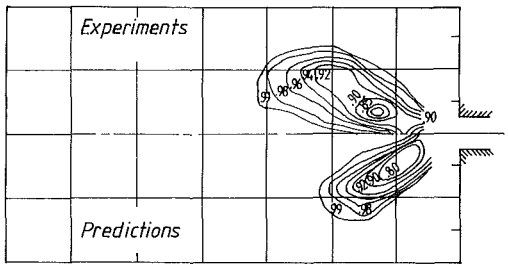

Fig. 11 Comparison of predicted and measured degree of oxidation contours, D3 flame

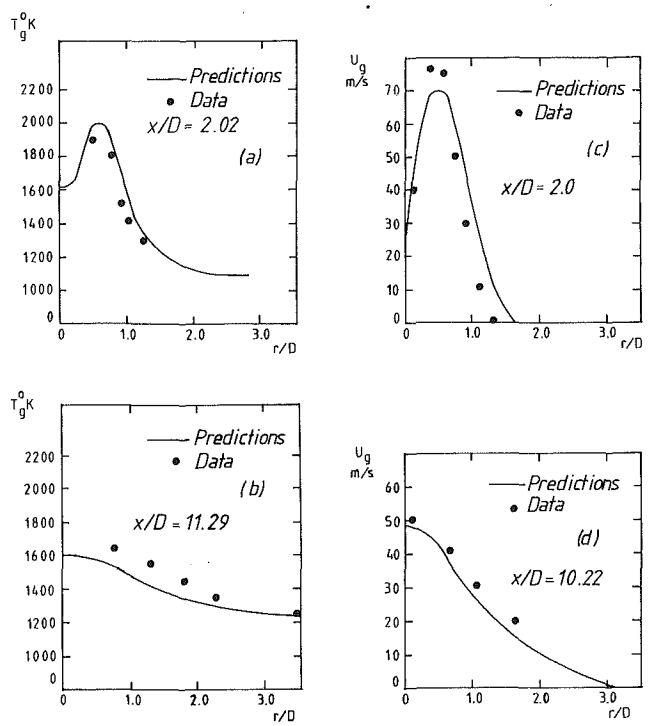

Fig. 12 Comparison of predicted and measured temperature and velocity profiles, D3 flame

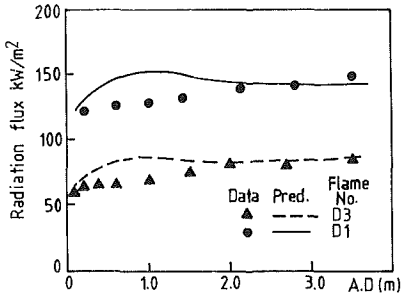

Fig. 14 Comparison of predicted and measured incident wall radiation fluxes for the D1 and D3 flames

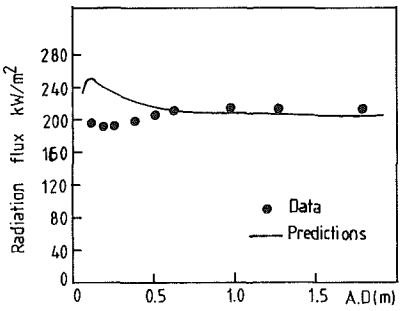

Fig. 15 Comparison of predicted and measured incident wall radiation fluxes for the E4 flame

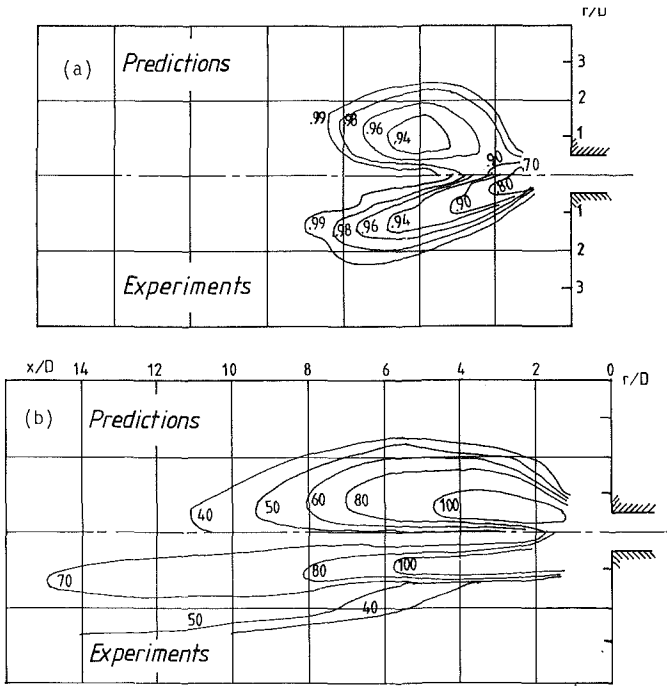

Fig. 13 Comparison of predicted and measured contours of: (a) degree of oxidation, (b) soot concentration (mg/nm^3), D1 flame

4 Concluding Commentary

The quality of the predictions of the flames is certainly sufficient to be of definite interest to the furnace designer. Their generality is certainly in excess of that which conventional similarity arguments are able to provide. At the outset we felt that, given the complexity of residual oil firing and our previous lack of experience in this area, we would have to do considerable tuning against the reference C3 flame. In fact, the existing physical laws describing the behavior of droplets and sprays have proved largely adequate for our purposes as have previously established values for the turbulence model constants. It has only been necessary to make a once and for all calibration of one of the soot production parameters. There will certainly be those who will criticize the simplicity of the soot production treatment, but we have found it suitable for our purposes, and we would point to the evidence of Glassman [26] which suggests domination of this process by a conventional Arrhenius temperature dependency.

The initial conditions for the spray calculations represent a principal source of uncertainty in any general application of the method. We were very fortunate to have the guiding data of [24]. Prior calculations could be initiated within the atomizer, and indeed the authors understand that some work on these lines has been performed 27. This plus improvement of the droplet behavior laws for residual oil fuels represent particularly useful as well as substantial avenues for research. Our own immediate goal is however to extend the present study to encompass the CEGB experiments [2] on a substantially larger and fully three-dimensional furnace. This work is in progress.

Acknowledgments

The authors wish to thank the United Kingdom Science Research Council for its financial support of the work of this paper under Grant No. GR/A55653.

References

1 Salvi, G., and Payne, R., "Investigation Into the Scaling of Combustion Systems: A Report on the O-18 and O-19 Trials Carried out Piecemeal in the Period from Dec. 1978 to June 1980," IFRF report, Feb. 1981.

2 Matthews, K. J., and Chappell, P. J., "Flame Scaling Trials: 33.6 MW Flame Results," CEGB, MM/Comb/TH113, June 1978.

3 El Banhawy, Y., and Whitelaw, J. H., "Assessment of an Approach to the Calculation of the Flow Properties of Spray-Flames," AGARD Conf. No. 275, 1979.

4 Gosman, A. D., and Ioannides, E., "Aspect of Computer Simulation of Liquid-Fuelled Combustor," AIAA Paper No. 81-0323, 1981.

5 Jones, W. P., and McGuirk, J. J., "A Comparison of Two Droplet

Models for Gas Turbine Combustion Chamber Flows," 5th Int. Symposium on Airbreathing Engines, Feb. 1981.

6 Gosman, A. D., and Lockwood, F. C., "Incorporation of a Flux Model for Radiation Into a Finite-Difference Procedure for Furnace Calculations," 14th Symposium (Int.) on Combustion, The Combustion Institute, 1973, pp. 661-671.

7 Abou Ellail, M. M. M., Gosman, A. D., Lockwood, F. C., and Megahed, I. E. A., "Description and Validation of a Three-Dimensional Procedure for Combustion Chamber Flows," *AIAA J. Energy*, Apr. 1978; also in: *Progress in Astronautics and Aeronautics*, Vol. 58, Turbulent Combustion, ed. L. A. Kennedy, AIAA, 1977.

8 Abbas, A. S., Koussa, S. S., and Lockwood, F. C., "The Prediction of Particle Laden Gas Flows," Imperial College, Mech. Eng. Dept., Fluid Section Report FS/80/1, Eighteenth Symposium (Int.) on Combustion, Combustion Institute, 1980.

9 Migdal, D., and Agosta, V. D., "A Source Flow Model for Continuous Gas-Particle Flow," *J. Applied Mechanics*, Vol. 34, No. 4, 1967, p. 860.

10 Gosman, A. D., and Ideriah, F. J. K., "TEACH-T: A General Computer Program for Two-Dimensional, Turbulent, Recirculating Flows," Imperial College, Mech. Eng. Dept. Report, 1976.

11 Williams, A., "Combustion of Droplets of Liquid Fuels; A Review," *Combustion and Flame*, Vol. 21, 1976, pp. 1-31.

12 Faeth, G. M., and Lazar, R. S., "Fuel Droplet Burning Rates in a Combustion Gas Environment," *AIAA J.*, Vol. 9, No. 11, 1971, pp. 2165-2171.

13 Chigier, N. A., and Yule, A. J., "Vaporization of Droplets in High Temperature Gas Stream; Physical Chemistry and Hydrodynamic," LEVICH Birthday Conf., Oxford, 1977.

14 Cooper, S., "Approximate Analysis of the Factors Influencing Combustion Rates in an Oil Spray Flame," CEGB, MM/Comb/TH267, 1981.

15 Gosman, A. D., Lockwood, F. C., and Salooja, A. P., "The Prediction of Cylindrical Furnaces Gaseous Fueled With Premixed and Diffusion Burners," *17th Symposium (Int.) on Combustion*, 1978, p. 747.

16 DeMarco, A. G., and Lockwood, F. C., "A New Flux Model for the Calculation of Radiation in Furnaces," *Italian Flame Days*, La rivista dei combustibili, Vol. 29, 1975, p. 184.

17 Hottel, H. C., and Sarofilm, A. F., "Radiative Transfer," McGraw-Hill, New York, 1967.

18 Truelove, J. S., "A Mixed Grey Gas Model for Flame Radiation," Report No. AERE-R-8794, AERE, Harwell, 1976.

19 Wagner, H. G., "Soot Formation in Combustion," 17th Symposium (Int.) on Combustion, Combustion Institute, 1978.

20 Khan, I. M., and Greeves, G., "A Method for Calculating the Formation and Combustion of Soot in Diesel Engines," *Heat Transfer in Flames*, ed. N. H. Afgan and J. M. Beer, Scripta, 1974.

21 Glassman, I., "Phenomenological Models of Soot Processes in Combustion Systems," Report No. 1450, Dept. of Mech. and Aero. Engineering, Princeton University, 1979.

22 Magnussen, B. F., Hjertager, B. H., Olsen, J. G., and Bhadvri, D., "Effects of Turbulent Structure and Local Concentrations on Soot Formation and Combustion in C_2H_2 Diffusion Flames," 17th Symposium (Int.) on Combustion, The Combustion Institute, 1978.

23 Tennekes, H., and Lumley, J. C., "A First Course in Turbulence," MIT Press, 1973.

24 Sarjeant, M., and Jones, A. R., "The Selection of Y-Jet Atomizers for Flame Scaling Trials," CEGB, Job No. TH326.

25 Lockwood, F. C., and Shah, N. G., "A New Radiation Solution Method for Incorporation, in General Combustion Prediction Procedures," *Proceedings of 18th Symposium (International) on Combustion*, The Combustion Institute, 1981.

26 Glassman, I., and Yaccarino, P., "The Temperature Effect in Sooting Diffusion Flames," *Proceedings of 18th Symposium (International) on Combustion*, The Combustion Institute, 1981.

27 Tranié, L. A., and Toussaint, M., "Liquid Fuels Atomization and Energy Saving," International Flame Research Foundation, Doc. nr. F17/ba/28, 1981.

Methanol as a Soot Reducer in a Turbulent Swirling Burner

A. J. Izquierdo
Intevep S. A. (R&D Center of Venezuelan Oil Industry), Department of Petroleum Products, Venezuela

D. P. Hoult
Massachusetts Institute of Technology, Department of Mechanical Engineering, Cambridge, MA 02139

The combined effect of using methanol as a fuel additive together with a prototype multifuel injector has been evaluated with regard to soot formation in a tubular laboratory burner with a turbulent swirl stabilized diffusion flame. Kerosene, ERBS fuel, and Blending Stock with approximately 14, 12.8, and 10.3 weight percent of hydrogen, respectively, were characterized in terms of soot loading at the axial positions $Z/D = 2.5$ *and 4.0 and normalized radius* $r/R = \pm 0.67$. *Mixtures of ERBS fuel and Blending Stock with 15 and 7.5 weight percent of methanol were also characterized in the same way. Measurements with the plain fuels showed a drastic reduction in soot formation, on the order to 150-fold decrease, due to the new injector design. Further reductions by a factor of 2 and 1.5 were accomplished with mixtures of 15 and 7.5 weight percent of methanol, respectively.*

Introduction

Projections of available world-wide petroleum resources anticipate a reduction in fuel hydrogen content [1]. Aircraft fuels in 1950 averaged about 7 weight percent aromatics; today the level is approaching 20 weight percent. Synthetic fuels from coal are expected to be less expensive to refine if allowed to exhibit greatly increased aromatic contents [2]; as aromatic content increases, hydrogen content decreases due to the ring structure of the former. Some studies [3,4] have predicted a combustor life reduction of over 60 percent if the hydrogen content in military aircraft fuels drops from the current 14.5 to 12.0 weight percent.

These impacts of reduced fuel hydrogen content arise because of increased rates of carbon particle formation (soot). The deposition of soot particles on parts of the combustion chamber can change the air and/or the fuel distribution inside the burner and therefore change the combustion pattern. If deposits spall, they can lead to significant mechanical erosion of the turbine blades downstream. Increased soot within the combustor also increases the radiation heat transfer to the combustor walls reducing hot part durability (a 25 K increase in temperature at a critical region of a turbine blade can result in a fourfold decrease in blade life [1]).

The effect of soot emissions on health has not been well established; although gas turbine particulates may be stated nontoxic [5], the current studies of diesel particulates as carcinogens should be extended to gas turbine engines.

Fuel properties, injector design, combustor inlet conditions, and gas turbine combustor design are all known to affect soot emissions in continuous combustion. Although the details of the formation and oxidation processes are poorly understood, the influence of macroscopic system parameters on the amount of soot formed has been well investigated for different systems.

Contributed by the Gas Turbine Division and presented at the Joint Power Generation Conference, Toronto, Ontario, Canada, September 30–October 4, 1984. Manuscript received by the Gas Turbine Division June 5, 1984. Paper No. 84-JPGC-GT-2.

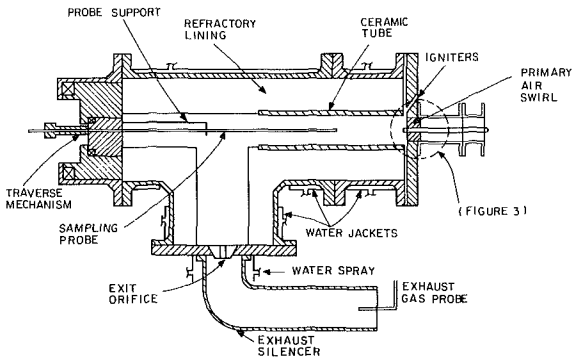

Fig. 1 Schematic of the high pressure burner

In situ measurements of soot formation in combustors [6, 7] have pointed out the importance of mixing and atomization in controlling soot formation in spray flames. Indeed, leaning out the primary zone by an appropriate air penetration jet scheme and/or by utilizing some type of air-blast atomization can make gas turbine combustors insensitive to small variations in hydrogen content, at least for petroleum-derived fuels [8].

The effect of pressure on soot formation has also been widely studied. Even though most agree that there is a direct proportionality between pressure and soot formation (soot loading increases with the cube of pressure [9]), there is some evidence that this proportionality does not continue indefinitely [10]. According to Mellor [8] the pressure dependence results in part from the chemistry of soot formation, the retardation of fuel evaporation due to increased boiling ranges, and the distribution of fuel in the front portion of the combustor.

Several investigators [1, 8, 10] report that the H/C ratio of the fuel correlates strongly with the formation of soot in the direction: more hydrogen, less soot. For fuel blends at the same H/C ratio but with different base fuels, the amount of soot produced can differ substantially [10]. The main purpose

Table 1 Chemical composition of the fuels tested

Fuel	Weight percent of C	Weight percent of H	Weight percent of O	Molecular weight	H/C ratio
Kerosene	86	14	–	200	1.95
ERBS	87.2	12.8	–	200	1.76
Blending stock	98.3	10.26	–	199.1	1.38
Methanol	37.38	12.57	50.17	32	4.01

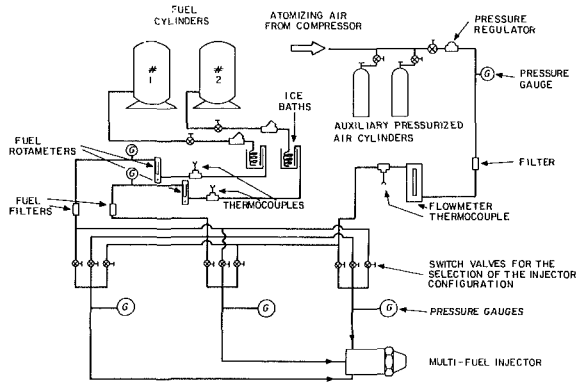

Fig. 2 Schematic of fuels and atomizing air supply systems

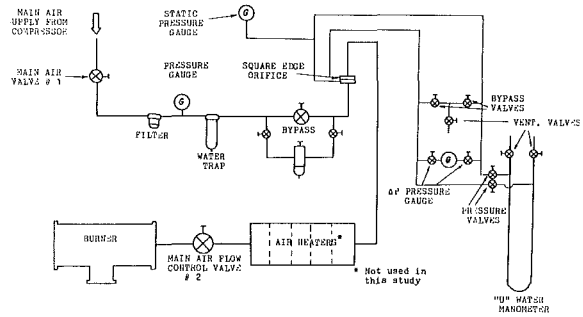

Fig. 3 Schematic of main air supply and measuring system

of this work is to assess the effects of methanol as a fuel extender in an experimental multiple fuel injector. The primary fuels considered were kerosene, ERBS, and blending stock, and methanol was used as secondary fuel. A summary of their chemical compositions is presented in Table 1. The soot formed using the three fuels mixed with methanol was investigated in a tubular burner with a swirl stabilizer diffusion flame. Saving in fuel costs by blending heavy fuels (in the range of ERBS fuel) with 7 to 10 weight percent of methanol may be achieved. A calculation is presented (section V) which suggests present cost savings on the order of 10 percent. This concept is feasible provided the performance of the blended fuel is identical to jet-grade kerosene. We show that the soot formation of the methanol mixtures is on the order that of kerosene.

Apparatus

The experimental facilities used in the present study consist of three main devices.

High Pressure Burner. This is a flame tube lined with ceramic of 10.2 cm i.d. set in refractory material which is water cooled outside of a steel jacket [11, 12, 13, 14] (see Fig. 1).

The front cover of the burner holds the fuel injector so that the tip of the injector is centered in 45 deg swirl vanes which creates a recirculating flow field, stabilizing the combustion process. The rear end of the burner is sealed by two eccentric

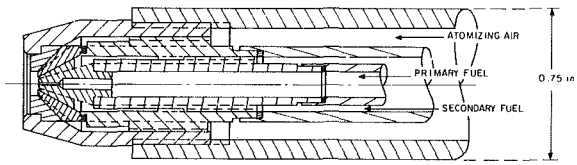

Fig. 4 Nozzle assembly

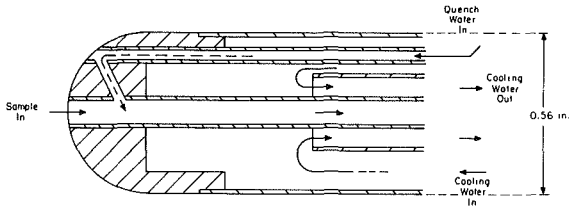

Fig. 5 Schematic of the sample probe

graphite bearings which hold the sampling probe. These bearings can be rotated to position the probe at any point inside the burner. The exhaust of the burner is a sonic orifice located in the bottom end of the burner. By changing the size of the sonic orifice, the mass flow rate and burner pressure can be controlled.

The fuels and atomizing air supply systems are shown in Fig. 2. In the present work, the primary fuel (fuel 1) is defined as the fuel used in higher percentages when using more than one fuel; therefore, fuel 1 refers to any of the fuels tested (kerosene, ERBS, or blending stock) and the secondary fuel (fuel 2) refers to methanol. The fuels are pumped into the injector by pressuring them with nitrogen in two fuel cylinders. The fuel flows are measured with rotometers, the air flow with a square edge orifice flow meter. The main air supply system and measuring devices are shown in Fig. 3. As it can be seen in Fig. 2, the primary fuel and atomizing air can be fed into the injector in any combination of the three fluids with the three passages of the injector by means of nine switch valves.

Multifuel Injector. A schematic of the multifuel injector used in this study is shown in Fig. 4.

It consists of three concentric passages identified as 1, 2, and 3 going from the outer to the inner passage (see Fig. 4). A complete description of the different components of the injector is in [15]. The injector was designed to handle three different fluids, usually two fuels and an atomizing air, and deliver them from the three concentric passages producing a fine spray with good atomizing characteristics (small particles and azimuthal symmetry).

Cold flow tests with this injector [5] showed that methanol can be mixed with fuels which in normal conditions are immiscible through the strong shearing action of the injector. The spray pattern was found to be very dependent on the injector's configuration. The configuration that showed best performance in the hot flow runs has the atomizing air in the outer passage, the primary fuel in the innermost passage, and the secondary fuel in the intermediate passage.

Sample Probe Rig. The sample probe is the device used to collect the soot and the combustion gases from any position inside the combustion chamber of the burner (see Fig. 5). The probe is located in the desired position Z/D and r/R by sliding it back and forth and rotating the eccentric back bearing of the burner. The sample probe used has the same features and configuration as those used in [11, 12, 14].

A small amount of water is fed into the inner tube near the probe's tip to quench reactions in the sample being collected and flush soot down the probe. The sample probe rig shown in Fig. 6 directs the sample (a mixture of soot, gas, and water) to either the soot measuring device, the gas analysis cart, or the

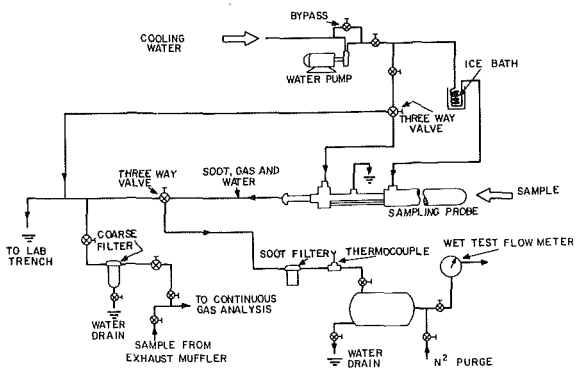

Fig. 6 Schematic of the sample probe rig

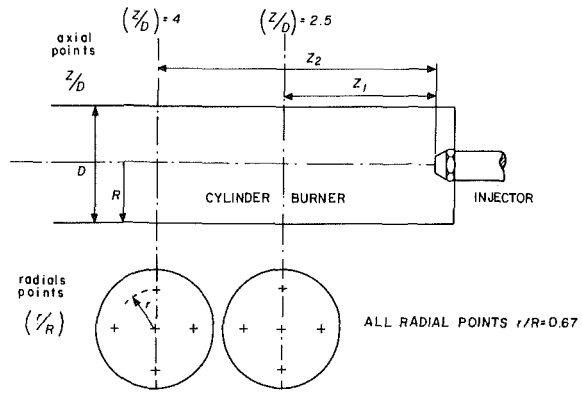

Fig. 7 Measuring points along the axial and radial axis

laboratory exhaust trench. When soot is being measured, the mixture is passed through a fiberglass filter previously extracted in methylene chloride, dried, and weighed. Then water is separated in a tank and the volume of the gas contained in the sample is measured on a wet test flow meter. During the gas composition measurement, most of the sample mixture is driven to the laboratory trench and a small portion is passed through a coarse filter that separates the soot particles and excess water. Then it is passed through a gas analyzer which measures the composition of the gas phase of the combustion products, i.e., CO, CO_2, O_2, HC, and NO_x. These measurements were used to calculate the local equivalence ratio at the point of sampling by assuming a water-gas equilibrium constant of 3.5 [16].

Experiments

The similarity between the combustion pattern of each fuel considered has to be established in order to compare their soot loading tendencies. The radial and azimuthal distribution of soot and equivalence ratio vary according to the hardward characteristics (injector design, burner type, etc.). For a given system configuration they may be a function of the fuel being used [6, 10, 12, 13]. This last dependency was explored for each one of the three fuels by taking measurements of soot loading and normalized equivalence ratios along the axis of the burner ($Z/D=4.0$ and 2.5) and across the horizontal and vertical diameters at $r/R=\pm 0.67$ for each axial position. Figure 7 shows schematically the locations where measurements were made. Next, soot loading as a function of H/C ratio was determined. Kerosene, ERBS fuel, and Blending Stock have 14, 12.8, and 10.6 weight percent of hydrocarbon, respectively (1.95, 1.76, 1.44 H/C ratios) (see Figs. 10 and 11).

In order to see if the addition of methanol changed the combustion pattern previously evaluated for each fuel, ERBS mixed with 15 weight percent of methanol was characterized

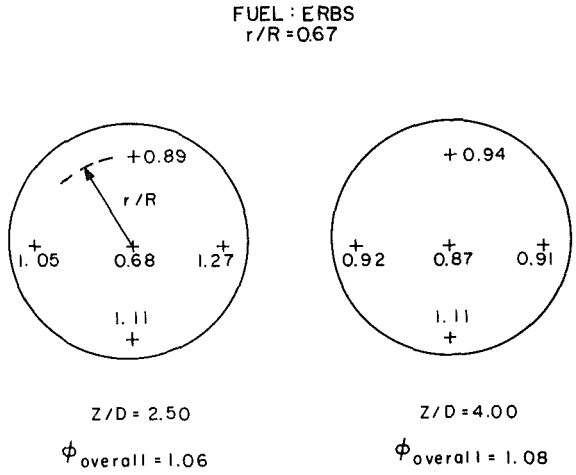

Fig. 8 Normalized equivalence ratio map for ERBS fuel

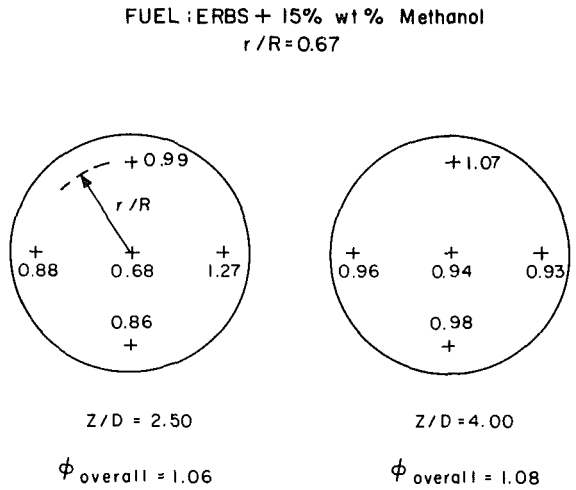

Fig. 9 Normalized equivalence ratio map for ERBS fuel mixed with 15 weight percent methanol

in terms of soot formation and equivalence ratio distribution at $Z/D=2.5$ and 4 and $r/R=\pm 0.67$. These results, shown in Figs. 8 and 9, illustrate the similar combustion pattern of the methanol mixtures and the plain fuels. Therefore, the measuring points established for the fuels alone are also representative points for the methanol mixtures.

Experimental Results

There is a lean region near the center line for small Z/D. This result is the opposite from what was observed by Gallagher [12] using another type of injector (two-fuel dual-orifice nozzle) which did not have the atomizing air.

This characteristic was not predicted by the cold tests (Korakianitis [15]). Apparently, the high angular momentum imparted to the fuel by the swirling air (the swirl number in the present test was in the order of 0.71), not present in the cold flow rig, changes the combustion process (see [17, 18]).

The equivalence ratio maps show that all the points have a normalized equivalence ratio close to 1, even for $Z/D=2.5$.

As expected, the uniformity of the normalized equivalence ratios increases with Z/D. Due to the early completion of the burning process, only slight differences were found between the distributions at $Z/D=2.5$ and $Z/D=4$.

The soot distribution is not as uniform as the distribution of equivalence ratios. This nonuniformity is more evident at $Z/D=2.5$ where the outer contour has very high soot loadings in comparison to the center line level. This is less evident at

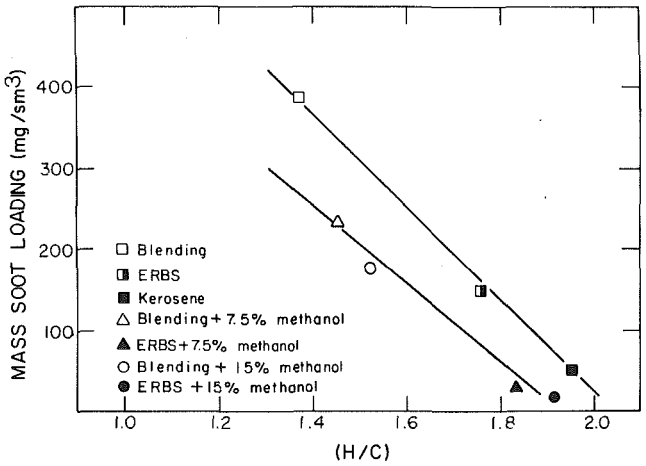

Fig. 10 Mass soot loading versus H/C ratio: 190 psi atomizing air pressure drop with the methanol mixtures

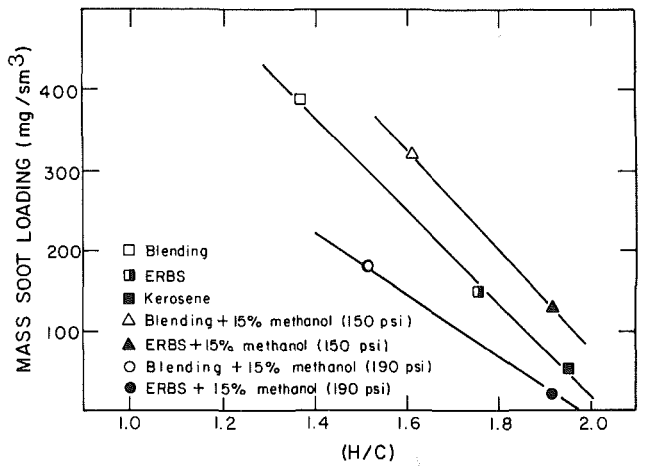

Fig. 11 Mass soot loading versus H/C ratio

$Z/D = 4.0$. A representative value of the soot concentration at a given Z/D is a weighed average of the local soot loadings measured at a cross section. At $Z/D = 4$ the soot formation is slightly higher than at $Z/D = 2.5$ for the three fuels tested. Gallagher, Hoover, and Hoult [10, 12, 13] have reported maximum values of soot formation around $Z/D = 2.5$ using different injectors. Figure 10 shows the current soot levels found for the blending stock, ERBS fuel and kerosene as a function of the H/C ratio. The overall equivalence ratio for these measurements was approximately 1.1, the burner pressure 45 psig, and the probe position $Z/D = 4$. These plots make evident the strong correlation betwen soot loading and H/C ratio. The general trend, higher soot levels for low hydrogen content fuels, reported in the literature is also observed here. These results indicate that in going from a fuel of about 14 weight percent hydrogen (e.g., kerosene) to one of about 10.3 weight percent hydrogen (e.g., Blending Stock) the soot loading increases by a factor of seven. The results reported by Hoover, Hoult, and Ekchian [10, 13] indicate a factor of approximately six of increasing soot loading for the same range of hydrogen percentage.

The soot levels found in the present study are remarkably lower, approximately by a factor of 22, compared to Hoover's results; furthermore, if corrections are made to compare them on the same stoichiometric basis, using the correlation for equivalence ratio and soot loading reported in [19] (the present tests were conducted with a richer equivalence ratio), the difference is on the order of a 150-fold decrease.

Table 2 Reference fuel prices

Price structure	Fuel type	cents per US gallon c/gallon
USA (bulk domestic prices)* 1982	Jet-grade kerosene	110
	Light fuel	96
	Methanol	48
Venezuelan (internal market prices)**	Jet-grade kerosene	18
	Light fuel	7
	Methanol	78

*Platt's-oil Price, Handbook and Oilmanac, 59th Edition, 1982 prices
**Intevep S.A. (private communications)

Figure 10 shows the soot levels found for the Blending Stock mixed with 15 weight percent of methanol and ERBS fuel mixed with 15 weight percent of methanol. The soot reduction obtained with the methanol mixtures is lower by over a factor of two. In this set of tests, the atomizing air pressure drop across the injector was adjusted (approximately to a 190 psi) so that the pressure drop in the primary fuel channel could reach the same value that it has when operating the injector with the heavy fuel alone (approximately 27 psi).

Mixtures of Blending Stock and ERBS fuel with 7.5 weight percent of methanol were also evaluated. In this case, the reduction in soot formation was a factor of 1.5. This last result indicates that the effect of the methanol addition and the one caused by the injector operating characteristics over soot loading cannot be readily quantified separately, and that the use of even small quantities of methanol together with the proper injector configuration lead to a significant soot reduction.

Figure 11 shows the results of the 15 weight percent methanol mixtures but this time run with the same atomizing air pressure drop as the one used with the heavy fuel alone (approximately 150 psi) and hence, a lower pressure drop in the heavy fuel channel. The soot reduction this time, due to the use of methanol, was on the order of 15 percent.

Conclusions and Discussion

1 Broadly speaking, there are two effects which arise in soot formation with heavy fuels. One is the fuel effect, which over the range of fuels considered is approximately a five to sixfold decrease in soot formation. The second effect is the injector design and configuration which is 30 times larger than the fuel effect. In the present study, this latter effect was a 150-fold decrease when compared to Hoover's result [13].

2 Methanol can be mixed with fuels which in normal conditions are immiscible, through the shear mechanism of a multichannel injector [15]. This result should be contrasted with other methods [20] which form microemulsions of alcohol, water, fuel, and then use a conventional injection.

3 The addition of 15 weight percent of methanol with either Blending Stock or ERBS fuel reduced the soot formation by a factor of two when operating the injector with the pressure drops of the atomizing air, primary fuel, and secondary fuel adjusted to 190, 27, and 6 psi, respectively. Mixtures of 7.5 weight percent of methanol reduced the soot loading by a factor of 1.5 when operating under these conditions.

The role of the injector design is of paramount importance when considering the use of alternate hydrocarbon fuels. The improvement of the combustion process achieved by the utilization of a properly designed multifuel injector allows burning of heavy fuels with small percentages of methanol in

a cleaner way. This scenario may be particularly attractive to countries with significant production of heavy crude oils (e.g., Venezuela) or with significant production of methanol (e.g., Brazil) or in countries with synthetic fuel production.

If one considers the actual international and domestic fuel prices (see Table 2 for cost data), it is possible to blend heavy fuels (in the range of the ERBS fuel) with 7 to 10 percent of methanol (the levels required to reduce the soot formation to that of the kerosene) with about a 10 to 15 percent savings in the cost of the fuel compared to jet-grade kerosene prices.

Acknowledgments

The work presented herein was supported in part by NASA, contract #NCC 3-15, and by INTEVEP, S.A.

References

1 Blazowski, W. S., "Future Jet Fuel Combustion Problems and Requirements," *Prog. Energy Combust. Sci.*, Vol. 4, pp. 177–199.

2 Odgers, J., and Fortier, P., Report #J.0.91, Laval University, 1980.

3 Gleason, C. C., Oller, T. L., Shayeson, M. W., and Bahr, D. W., AFAPL-TR-79=2015, 1979.

4 Gleason, C. C., Oller, T. L., Shayeson, M. W., and Bahr, D. W., AFAPL-TR-79=2018, 1979.

5 Durrant, T., SAE Paper No. 680347, 1968.

6 Sahmsavari, K., "Measurement of Soot in a Turbulent Diffusion Flame," M.S. thesis, Mechanical Engineering Dept., MIT, 1976.

9 McFarlane, J. J., Holderness, F. H., and Whitcher, F. S. E., *Comb. and Flame*, Vol. 8, 1964.

8 Mellor, A. M., in: *Particulate Carbon: Formation During Combustion*, D. C. Siegla and G. W. Smith, eds., Plenum Press, New York, 1981.

9 McFarlane, J. J., Holderness, and F. H., Whitcher, F. S. E., *Comb. and Flame*, Vol. 8, 1964.

10 Hoult, D. P., and Ekchian, A., "Soot Formation in a Turbulent Swirl Stabilized Laboratory Combustor," ASME JOURNAL OF ENGINEERING FOR POWER, Vol. 103, No. 1, Jan. 1981, pp. 49–53.

11 Gatowski, J. A., "Soot Studies in a High Pressure Turbulent Burner," M.S. thesis, Mechanical Engineering Dept., MIT, 1981.

12 Gallagher, M. L., "An Evaluation of Methanol as a Fuel Additive to Reduce Particulates in High Pressure Combustion," M.S. thesis, MIT, 1982.

13 Hoover, J. A., "Soot Production in a Turbulent Diffusion Flame: Turbulent Scaling and Fuel Composition Effects," M.S. thesis, Mechanical Engineering Dept., MIT, 1978.

14 Izquierdo, A., "Methanol as a Fuel Extender for Gas Turbine Combustors," M.S. thesis, Mechanical Engineering Dept., MIT, 1983.

15 Korakianitis, T. P., "Design of a Multi-Fuel Injector," M.S. thesis, Naval Architecture and Marine Engineering Dept., MIT, 1982.

16 Spindt, R. S., "Air-Fuel Ratios from Exhaust Gas Analysis," SAE Paper No. 650507.

17 Syred, N., and Beer, J. M., "Combustion in Swirling Flows: A Review," *Combustion and Flame*, Vol. 23, pp. 143–201, 1974; M.S. thesis, Naval Architecture and Marine Engineering Dept., MIT, 1982.

18 Komiyama, K., "The Effects of Fuel Injector Characteristics on Fuel–Air Mixing in a Burner," M.S. thesis, Mechanical Engineering Dept., MIT, 1975.

19 Irani, B., "Effects of Reynolds Number and Mixing on Soot Production in a Turbulent Diffusion Flame," M.S. thesis, Mechanical Engineering Dept., MIT, 1977.

20 Naegeli, D. W., and Moses, C. A., "Fuel Microemulsions for Jet Engine Smoke Reduction," ASME JOURNAL OF ENGINEERING FOR POWER, Vol. 105, 1983, pp. 18–23.

APPENDIX

H/C Ratio Calculation for the Methanol/Fuel Blends

First calculate the empirical formula of each fuel:

Fuel 1: CN1 HM1 OP1

Fuel 2: CN2 HM2 OP2

For each fuel N, M and P can be calculated by:

percent N; by weight C	percent M; by weight H	percent P; by weight O
Molecular weight of carbon	Molecular weight of hydrogen	Molecular weight of oxygen

N, M and P may need to be multiplied by a factor in order to give the right molecular weight of the fuel.

The H/C ratios of fuel 1 and fuel 2 are M1/N1 and M2/N2, respectively.

Second, calculate the empirical formula of the mixed fuel

Mixed fuel: $CX\,HY\,OZ$

where

$X = 1/\text{TOTMOL}\ (((\text{F1})(\text{N1})/(100)(\text{MWF1}))\cdot ((\text{F2})(\text{N2})/(100)(\text{MWF2})))$

$Y = 1/\text{TOTMOL}\ (((\text{F1})(\text{M1})/(100)(\text{MWF1}))\cdot ((\text{F2})(\text{M2})/(100)(\text{MWF2})))$

$Z = 1/TOTMOL\ (((F1)(P1)/(100)(MWF1)))\cdot ((\text{F2})(\text{P2})/(100)(\text{MWF2})))$

F1 and F2 are the percentages by weight of fuel 1 and fuel 2, respectively.

MWF1 and MWF2 are the molecular weight of fuel 1 and 2 calculated using N, M, and P of their respective empirical formulas determined above.

TOTMOL:

$$\frac{\text{F1}}{100\ \text{MWF1}} \cdot \frac{\text{F2}}{100\ \text{MWF2}}$$

Finally, the mixed fuel H/C ratio is Y/X.

Application of Reburning for NO_x Control to a Firetube Package Boiler

J. A. Mulholland
Acurex Corporation,
Research Triangle Park, NC 27709

W. S. Lanier
U.S. Environmental Protection Agency,
Industrial Environmental
Research Laboratory,
Research Triangle Park, NC 27711

A 730 kW (2.5×10^6 Btu/hr) firetube package boiler was used to demonstrate the application of reburning for NO_x emission control. An overall reduction of 50 percent from an uncontrolled NO_x emission of 200 ppm was realized by diverting 15 percent of the total boiler load to a natural-gas-fired second stage burner. Tests indicate that the overall reaction order of destruction with respect to initial NO_x is greater than one; thus, larger reductions can be expected from reburning applications to systems with higher initial NO_x. Rich zone stoichiometry has been identified as the dominant process variable. Primary zone stoichiometry and rich zone residence time are parameters that can be adjusted to maximize NO_x reduction. Reburning applied to firetube package boilers requires minimal facility modification. Natural gas would appear to be an ideal reburning fuel as nitrogen in the reburning fuel has been shown to inhibit NO_x reduction.

Introduction

Nitrogen oxides (NO_x) emitted from stationary combustion sources have been identified as significant contributors to the degradation of air quality. Modification of the conventional combustion process to reduce NO_x formation in flames by reducing peak temperatures and maximizing fuel-rich resistance times has proven to be a commercially viable method of controlling NO_x emissions [1]. However, when combustion process modification is impractical or insufficient to meet an emission level requirement, it may be necessary to reduce NO_x from the products of combustion. Reburning, a term coined by Wendt et al. [2] to describe the process of NO_x reduction by injection of a secondary fuel stream, represents an in-furnace NO_x control technology that destroys NO_x formed in the primary combustion flame. Laboratory studies utilizing both flat-flame burners [2] and tubular reactors [3] provided initial evidence of NO_x reduction via hydrocarbon radicals.

In the burning of a hydrocarbon fuel in air, NO_x is formed either from molecular nitrogen (N_2) in the combustion air or from fuel-bound nitrogen. Equilibrium calculations indicating thermodynamically favored speciation at specified temperature, pressure, and elemental constituency predict exceptionally low total fixed nitrogen (non-N_2 nitrogenous species) concentrations under fuel-rich conditions [4]. In fuel-lean flames, equilibrium NO_x values are extremely temperature sensitive. At typical flame temperatures, equilibrium NO_x levels can exceed 1000 ppm, whereas at typical boiler stack temperatures, equilibrium NO_x concentrations are well below 1 ppm. However, because the kinetics which dictate the speed at which equilibrium is approached are slow, actual NO_x emission levels vary enormously from equilibrium predictions.

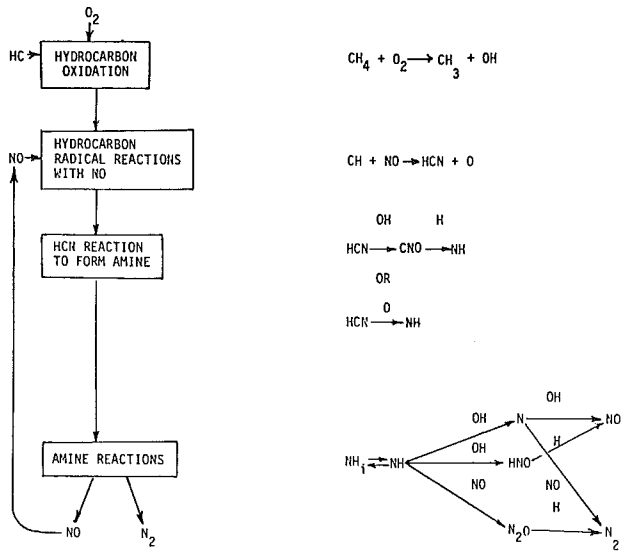

Fig. 1 Chemical mechanism for NO_x destruction by hydrocarbons

There are two key factors associated with the reburning process. First, injection of secondary fuel creates a fuel-rich environment where the chemical driving force is shifted toward N_2 formation rather than oxidation to NO_x. The second key factor is that formation of hydrocarbon radicals from the secondary fuel provides a rapid chemical reaction pathway for approaching the equilibrium state. Figure 1 (taken from [4]) describes the overall chemical mechanism for NO_x destruction by secondary hydrocarbon injection. The key steps include initial nitric oxide (NO) destruction by

Contributed by the Air Pollution Control Division and presented at the Joint Power Generation Conference, Toronto, Ontario, Canada, September 30–October 4, 1984. Manuscript received by the Air Pollution Control Division August 4, 1984.

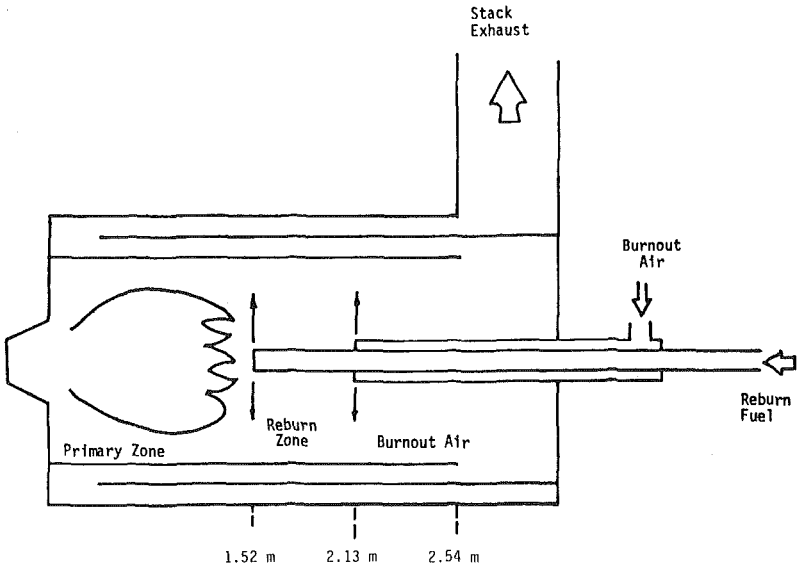

Fig. 2 North American boiler

reaction with the methylidyne radical (CH) to form hydrogen cyanide (HCN). Subsequent reactions lead to ammonia (or NH_i radicals) and eventually to the formation of N_2. Any fixed nitrogen species which exit the fuel-rich zone are partially converted to NO_x upon final air addition.

Though the basic concepts associated with reburning chemistry are not new, development of the technology has occurred only recently. In 1981, investigators for Mitsubishi Heavy Industries (MHI) reported that application of the reburning technology MACT (Mitsubishi Advanced Combustion Technology) to full-scale boilers resulted in NO_x reductions of 50 percent, roughly independent of fuel type and initial burner NO_x production [5]. Based on MHI claims, the United States Environmental Protection Agency (EPA), the Electric Power Research Institute (EPRI), and the Gas Research Institute (GRI) have initiated a multiscale research and development program to better understand the chemical and physical processes associated with reburning.

As a part of this program, the EPA is conducting in-house studies to investigate the application of reburning to firetube package boilers. Tests performed on a pilot scale package boiler simulator (PBS) equipped with a low-NO_x research burner have entailed extensive modification of boiler hardware and boiler operating conditions to provide fundamental insight into the chemistry and physics of natural gas reburning (as reported in [6]). A series of experiments was then performed on a commercial firetube package boiler to determine the representativeness of results obtained from the PBS tests and to assess the practicality of an actual retrofit application. These application tests are the subject of this paper.

Experimental Approach

In a conventional boiler, fuel and combustion air are introduced coaxially through a burner (or burner set) located on the front firing face. With reburning, portions of the fuel and combustion air are diverted from the main burner(s) for injection into the boiler at selected downstream locations. In this way, the boiler radiant section is divided stoichiometrically into three zones: a fuel-lean primary zone, a fuel-rich reburning zone, and a fuel-lean burnout zone.

A North American scotch-type package boiler was used for reburning application tests. The three-pass boiler, 0.61 m (2 ft) in internal diameter and 3.0 m (10 ft) long, has a continuous service rating of 1089 kg (2400 lb) of steam per hour. The North American swirl burner is capable of firing gas, light oil, and heavy oil and has a maximum rating of 733 kW (2.5×10^6 Btu/hr). The mechanical linkage for automatic control of air/fuel ratio with variation in load was disconnected from the burner and replaced with a manual adjustment that permitted independent control of primary flame excess air at any desired load.

Reburning fuel and burnout air are injected into the boiler through a boom assembly inserted from the rear of the boiler down the firetube centerline. The boiler endplate, which provides access for maintenance, was modified with a 9.0-cm (3.5 in.) opening to allow for boom assembly insertion. The assembly consists of two telescoping booms, allowing for independent variation in the location of secondary fuel injection and the rich zone length. The inner boom provides for radial injection of secondary natural gas plumbed directly from a 1.36-MPa (5 psi) supply line, and the outer concentric boom provides for radial addition of compressed air to complete combustion. Each boom is constructed of 304 stainless steel and is water cooled. Figure 2 presents a schematic of the facility with the reburning booms installed at nominal locations.

For this test series a No. 2 distillate oil and a No. 5 heavy oil were fired in the primary burner. Ammonia-doped and undoped natural gas was used as the reburning fuel to vary fuel nitrogen content. Total boiler load was held constant during the reburning tests, requiring that, as secondary load increased, main burner load decreased. Testing consisted of measuring stack exhaust emissions (O_2, CO_2, CO, and NO) for several single-parameter variation test series. The NO_x monitor used was a TECO Model 10A chemiluminescence analyzer.

Results and Discussion

As discussed in the following paragraphs, baseline (without reburning) and parametric tests were conducted to characterize reburning applied to a commercial firetube package boiler. Overall reburning NO_x reductions of 50 percent and more were achieved with the optimization of a variety of process parameters, as discussed in the example that concludes this discussion.

Baseline Tests. Baseline testing consisted of measuring the exhaust NO_x emission, centerline temperature profile, and visible flame length as a function of main burner firing rate for both distillate and heavy fuel oils. Exhaust NO_x con-

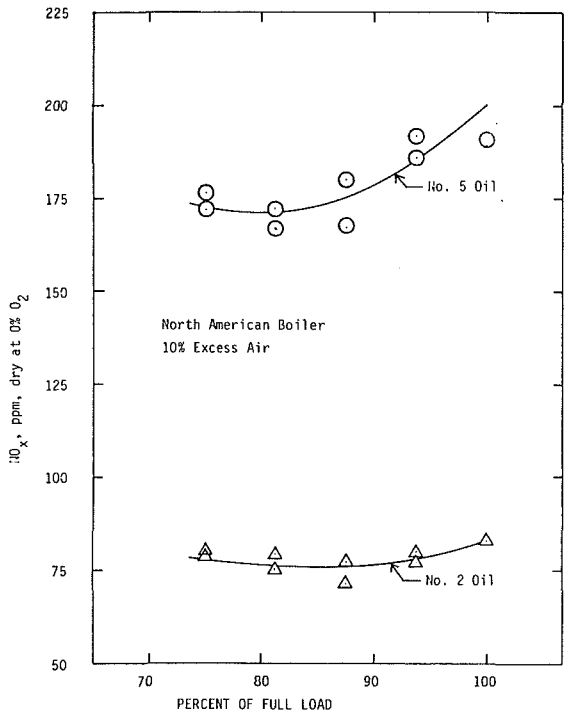

Fig. 3 Exhaust NO_x versus primary burner firing rate

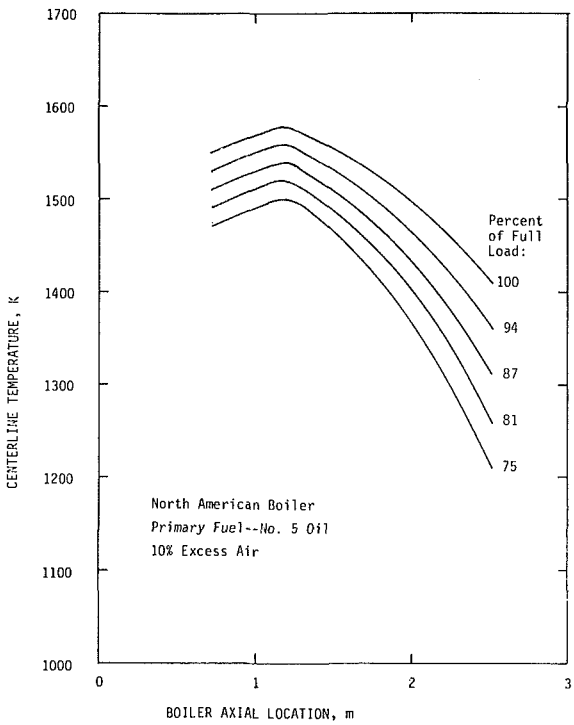

Fig. 4 Centerline temperature profiles for No. 5 fuel oil firing

centration, measured on a dry basis and corrected to zero percent O_2, is presented in Fig. 3 as a function of the percent of full load. The full-load NO_x emission level for the distillate oil (containing 0.01 percent nitrogen) is approximately 85 ppm; for the heavy fuel oil (containing 0.14 percent nitrogen) the full load emission is 200 ppm. From Fig. 3 it is observed that exhaust NO_x emissions decrease between 5 and 10 percent as primary load is dropped. This is characteristic of many applications where burner derating results in reduced flame zone mixing intensities and, hence, reduced NO_x.

With a practical burner, there is no well-defined flame shape. Primary flame length fluctuations of up to 0.5 m (1.6 ft) were observed. The average flame length decreased noticeably with decreasing load, from 2.5 m (8.2 ft) at full load to 1.5 m (4.9 ft) at 75 percent of full load. The reduced primary flame length allows for secondary fuel injection near the end of the visible flame with sufficient boiler length remaining for reburning. Figure 4 presents axial temperature profiles as measured on the boiler centerline for the heavy fuel oil. Temperatures were measured with a suction pyrometer at 25 cm (10 in.) intervals, with profiles recorded at five different firing rates. At the nominal secondary fuel injection point the centerline baseline temperature is about 1500 K (2290°F). Tests on the research boiler simulator indicate that, at this temperature, oil reburning leads to soot deposition on the water-cooled booms and on the boiler walls. Reburning in thermal environments less than 1600 K (2420°F) should be restricted to gaseous fuels.

Based on baseline tests, nominal operating conditions were defined. Heavy fuel oil was chosen as the nominal primary fuel because it provides an initial NO_x level comparable to the nominal primary NO_x concentration used in PBS testing. A nominal secondary fuel injection location of 1.52 m (60 in.) was defined based on flame length and temperature measurements. The final air injection location was selected to be 2.13 m (84 in.), providing a rich zone bulk residence time of approximately 200 ms.

Reburning Tests. Single-parameter variation tests were conducted on the major reburning process variables, including stoichiometry, initial NO_x, reburn fuel nitrogen, and residence time. Baseline tests (without reburning) were conducted prior to and at the conclusion of each test series to define primary zone effluent composition.

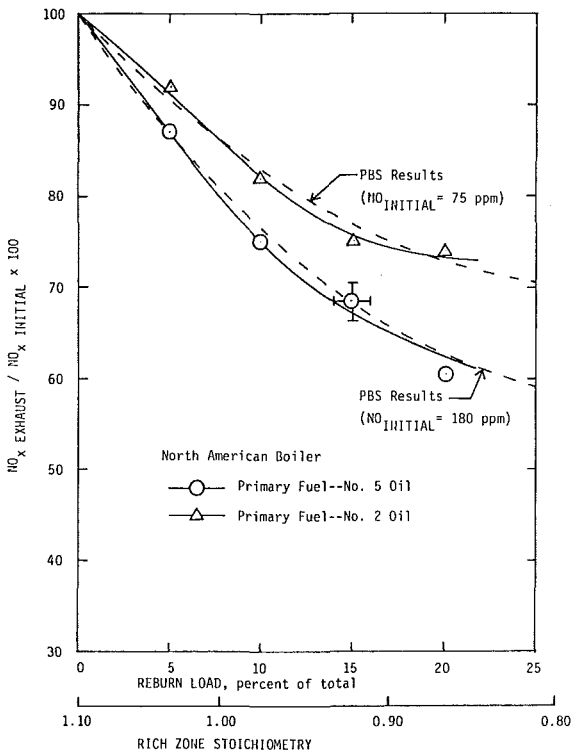

Fig. 5 Natural gas reburning

Initial NO and Rich Zone Stoichiometry. Figure 5 presents plots of reburn efficiency versus rich zone stoichiometry when firing No. 2 and No. 5 fuel oils in the main burner. The fraction of total boiler load contributed by the secondary fuel is shown as an alternate abscissa. Reburn efficiency is defined as the ratio of the exhaust NO emission with reburning to the

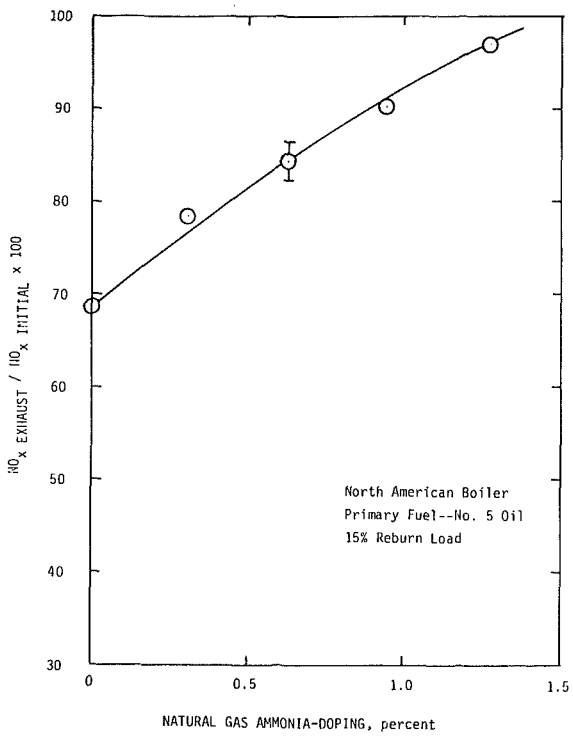

Fig. 6 Reburn efficiency versus amount of NH_3 doping of secondary fuel

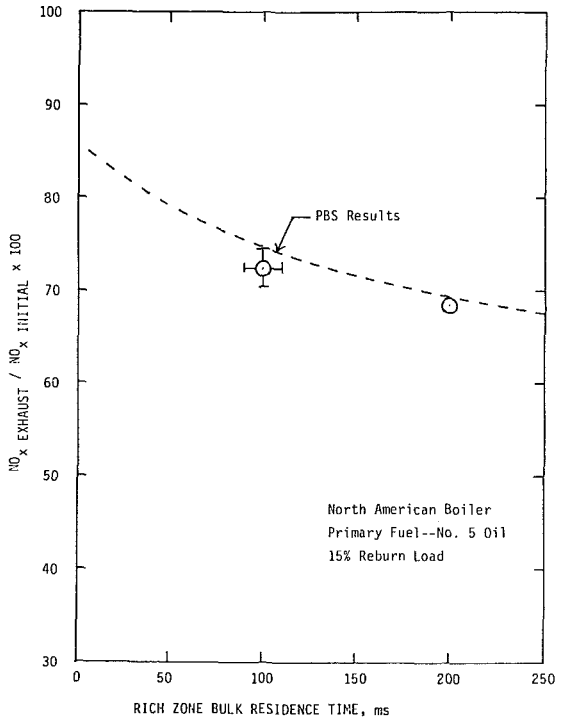

Fig. 7 Reburn efficiency versus rich zone residence time

primary NO_x emission *at the reduced primary load*. When compared to data obtained from PBS reburning tests under similar conditions, agreement is observed within the indicated data uncertainty bands.

Tests have been performed wherein the secondary fuel injection patterns were varied. Included were trials where the secondary fuel was (1) injected radially outward from the centerline boom assembly, (2) injected circumferentially near the firetube wall, and (3) injected in a manner to achieve a

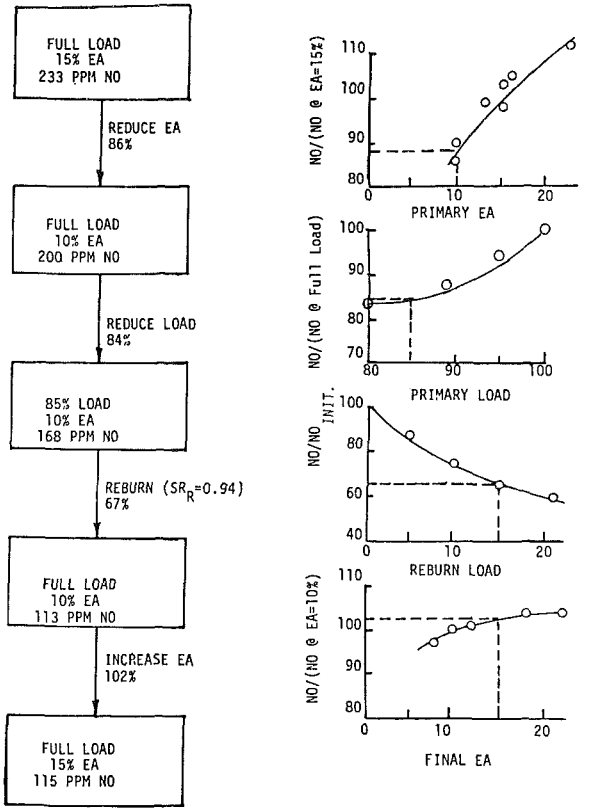

Fig. 8 Reburning application example on the North American boiler

spatially uniform distribution of stoichiometry. For this broad variation in mode of secondary fuel addition, there was essentially no variation in the extent of NO_x emission reduction by reburning [6]. This observation, which requires experimental verification to be extrapolated to other boiler types, significantly simplifies the design of reburning retrofit hardware for the firetube package boiler class. As rich zone stoichiometry decreases, two factors contribute to improved NO reduction. First, the availability of more hydrocarbon radicals results in increased destruction of primary NO. Second, a larger portion of the fuel is consumed in an environment not conducive to NO formation. Thus, the low-NO_x secondary burner heat release "dilutes" the relatively high NO_x primary burner effluent. This dilution component is strongly coupled to the destruction component of NO_x reduction and cannot be straightforwardly isolated.

Clearly, initial NO_x concentration influences the degree of NO_x reduction under a given set of reburning conditions. North American boiler tests yielded significantly smaller reductions for the low initial NO_x condition than for the high initial NO_x condition. For the distillate primary fuel condition (initial NO_x of 80 ppm), with 20 percent of the total load used for reburning, primary NO_x is reduced by about 20 percent; for the heavy fuel oil condition (initial NO_x of 180 ppm), a 40 percent reduction is realized under the same conditions. From results of PBS testing where initial NO_x concentrations were varied from 50 to 500 ppm, reaction orders with respect to NO_x between 1.5 and 1.6 were calculated for rich zone stoichiometries between 1.0 and 0.8. This contradicts the first-order reduction claims of the MHI investigators [5]. It is concluded here that, for low initial NO_x values (less than 200 ppm), other process parameters besides rich zone stoichiometry must be optimized to achieve 50 percent NO_x reductions.

Reburn Fuel Nitrogen. When ammonia is doped into the secondary natural gas stream, NO reductions are decreased

sharply. Figure 6 shows this data trend for ammonia doping of up to 1 percent. Though not directly comparable to fuels containing nitrogen (doping with a cyano compound like hydrogen cyanide would more closely model fuel-bound nitrogen evolution, but would also present increased safety hazards), these tests indicate that fuel nitrogen is an important factor in the reburning mechanism.

Rich Zone Residence Time. Reburn zone length was varied from 0.3 to 0.6 m (1 to 2 ft) by shifting the location of the final air injection. Injecting the final air beyond 2.13 m (84 in.) resulted in burnout zone residence times too short to achieve sufficient fuel burnout prior to thermal quenching, resulting in high CO stack emissions. Figure 7 shows that the limited residence time data obtained agree well with PBS results under similar test conditions. Detailed measurements in the PBS facility indicate that the characteristic kinetic time necessary for the rich zone species to approach an equilibrium is 50 ms. For a bulk residence time of 200 ms, the highest velocity rich zone streamtube has a rich zone residence time of 50 ms. Geometrically similar to the PBS facility, it is suggested that a rich zone bulk residence time of approximately 200 ms represents a near-optimum reburn zone length in the North American boiler.

Example. To put the above factors into perspective, an example is presented to show how reburning might be applied to achieve a significant level of NO_x emission reduction. This example is presented schematically as Fig. 8. The initial condition selected is full-load operation firing No. 5 fuel oil at 15 percent excess air. The NO_x emission level at that condition is 233 ppm. The first step is to reduce the primary flame excess air from 15 to 10 percent. This reduces the exhaust NO_x emission level to 200 ppm. Next, the boiler load is reduced by 15 percent, holding excess air constant at 10 percent. This reduces the NO_x emission level to 168 ppm. Thirdly, secondary flow of natural gas and final air is initiated to return the boiler to full load with a stack excess air of 10 percent. Accomplishing the third step sets the fuel-rich zone stoichiometry at 0.94. This causes the exhaust NO_x emission level to drop to 113 ppm. To return the overall excess air to 15 percent, the final air flow rate is increased, causing the exhaust NO_x emission level to increase to 115 ppm.

In this example, overall NO_x reduction via reburning is achieved by means of primary load reduction, primary excess air reduction, and the destruction and dilution effects of staged fuel combustion. The example illustrates a net 50 percent reduction in NO_x achievable by reburning, precisely the reduction claimed by Mitsubishi in [5]. It is noted that the 50 percent NO_x reduction is achieved by diverting only 15 percent of the main burner load and that larger emission reductions are possible. This should result from further process optimization.

Summary

The results from the reburning application tests are summarized in the following two conclusions:

- NO_x reductions of 50 percent and greater are achievable with the application of reburning to firetube package boilers.
- Retrofit modifications for natural gas reburning require minimal cost and effort.

The input/output demonstration tests provide little insight into the chemistry and physics of reburning, but do verify results obtained from the fundamental PBS tests. Future testing will focus on the application of oil burning to firetube package boilers.

Acknowledgments

This work was funded by EPA's Industrial Environmental Research Laboratory at Research Triangle Park, NC. The authors wish to express their appreciation for the technical discussions with R. E. Hall of EPA and the experimental support provided by E. E. Stephenson of Acurex Corporation and by N. L. Butts and R. W. Lowans of EPA's IERL-RTP.

References

1 Lim, K. J., et al., "Environmental Assessment of Utility Boiler Combustion Modification NO_x Controls: Vol. 1. Technical Results," EPA-600/7-80-075 (NTIS PB80-220957), Apr. 1980.

2 Wendt, J. O. L., Sterling, C. V., and Matovich, M. A., "Reduction of Sulfur Trioxide and Nitrogen Oxides by Secondary Fuel Injection," *Fourteenth Symposium (International) on Combustion*, The Combustion Institute, 1973, p. 897.

3 Myerson, A., "Reduction of NO_x by Hydrocarbons," *Fifteenth Symposium (International) on Combustion*, The Combustion Institute, 1975.

4 Chen, S. L., et al., "NO_x Reduction by Reburning With Gas and Coal—Bench Scale Studies," *Proceedings of the 1982 Joint Symposium on Stationary Combustion NO_x Control*, Vol. 1, Utility Boiler Applications, EPRI Report No. CS-3182, July 1983.

5 Takahashi, Y., et al., "Development of 'MACT' In-Furnace NO_x Removal Process for Steam Generators," *Proceedings of the 1982 Joint Symposium on Stationary Combustion NO_x Control*, Vol. 1, Utility Boiler Applications, EPRI Report No. CS-3182, July 1983.

6 Lanier, W. S., "An Investigation of Chemical and Mixing Phenomena Associated With Reburning Applied to Firetube Package Boilers," Ph.D. dissertation, University of Virginia, May 1984.

Fuel-Composition Effects on High-Temperature Corrosion in Industrial/Commercial Boilers and Furnaces: a Review

J. Bellan
Jet Propulsion Laboratory,
California Institute of Technology,
Pasadena, CA 91109

S. Elghobashi
University of California,
Irvine, CA 92717

In this review, literature relevant to the problems of deposits and corrosion in industrial/commercial furnaces and boilers is analyzed, and the facts are synthesized into a picture that addresses corrosion problems expected with the use of unconventional fuels. Corrosion is found to depend greatly on the phenomena occurring during the combustion of fuel-oil sprays introduced into the furnace. In a first step, the drops that form the spray heat up and evaporate in a way that closely resembles a batch distillation process. Eventually, ignition and combustion occur with the subsequent change of the liquid fuel drops into carbonaceous, porous, sphere-like particles called cenospheres. In a second step, these cenospheres burn and the products of this combustion step determine the majority of the deposits on metal surfaces. This observation is very important since nonvolatile, noncombustible, corrosive trace compounds existing in the initial fuel-oil drop will have a much higher concentration in the cenosphere than in the original fuel. Accordingly, it is recommended that the theoretical and experimental study of oil spray combustion, cenosphere formation, and cenosphere combustion in a cloud of cenospheres receive a very high priority. Corrosion by gases is found to be unimportant. Deposits are found to be much more corrosive when in liquid form, although corrosion by solid deposits is by no means negligible. As a result, it is suggested in the study that corrosion on highly polished metal surfaces should be studied in order to evaluate the potential of this method of inhibiting deposition and thus hindering corrosion. Recent advances in the theory of deposition from combustion gases are also outlined in this study. The literature survey shows that the main corrosion-causing fuel constituents present in unconventional fuels are sulfur, alkali, vanadium, carbon and carbon monoxide, iron, and chloride. It is found that sometimes one of these compounds might act as a catalyst in corrosive reactions initiated by another compound, and therefore great care must be taken to identify the corrosion-causing compound in the deposits on metal surfaces. It is also found that in some cases a corrosive compound will inhibit the corrosive action of another corrosive compound. It is recommended that such situations be studied further so as to investigate the possibility of an optimum concentration of two such corrosive compounds that would minimize metal wastage. The problem of performing meaningful corrosion experiments is also addressed in this report and specific recommendations are made to achieve this goal. Finally, the effects of additives and the furnace operating conditions are discussed, and potential problems with both additives and new operating conditions are mentioned. The recommendations at the end of this study present a comprehensive set of areas to be investigated in order to better understand and be able to mitigate corrosion problems associated with unconventional fuels. High-priority experimental and theoretical studies are also outlined.

I Introduction

Corrosion is defined as the spontaneous oxidation of metals which is detrimental to industrial practice [1] thereby reducing the service life of the metals. Thus "corrosion" is more of an engineering than a scientific term, since it tends to mean "harmful oxidation." A similar definition of corrosion is: the effect of unwanted chemical reactions on metals [2]. These processes are all governed by the thermodynamic instabilities experienced by the metals during service [1]. From the in-

Contributed by the Gas Turbine Division for publication in the JOURNAL OF ENGINEERING FOR GAS TURBINES AND POWER. Manuscript received by the Gas Turbine Division, August 1984.

dustrial point of view, corrosion is associated with the removal of material from a metal surface.

Corrosion costs the power industry in the U.S.A. about $6.3 billion/year [3], a significant percentage of the GNP. Estimates of a few years ago done by the Corrosion and Deposits Committee of the ASME showed that the direct out-of-pocket cost of remedying the effects of external corrosion caused by deposits in boiler furnaces was $10 M/year [4]. Additionally, the loss of availability of the system during an unscheduled maintenance service can cost about $40,000/day for a 500-MW unit [4]. This points to the fact that solving corrosion problems is an important consideration in the running of a profitable operation.

For this reason, corrosion from combustion products has been studied for many years and there is already an extensive compilation of literature abstracts available [5]. The work done so far has made an important contribution in identifying the specific problems of corrosion in various environments; however, much more needs to be done before a significant impact on the problem is made.

However, from the point of view of using unconventional fuels, such as gas and liquids derived from coal, tar sand, and shale, very few data are available since the utilization of these fuels is projected only for the future and the specifications for these fuels are only presently being defined. Therefore, the only way to foresee corrosion problems associated with unconventional fuels is to analyze the probable composition of the fuels, identify the important chemical compounds, and research the literature for information about corrosion problems associated with these compounds in environments similar to those existing in industrial and commercial boilers and furnaces.

Other literature associated with corrosion of utility-type furnaces or turbines is also sometimes relevant. This is because the difference between the industrial and commercial furnaces and the utility furnaces is mainly in the residence time of the fuel; since the residence time is associated with the distance from the injector, certain valuable information may be transferable from one situation to another. In general, corrosion problems in turbines are different from those in boilers because in furnaces, much dirtier fuels (i.e., fuels that contain a larger amount of impurities than the fuels presently used) can be used, and the combustion temperature and pressure are lower; however, some laboratory experiments performed for turbines might have a bearing on corrosion in industrial and commercial furnaces and boilers.

Similarly, literature on coal-fired furnaces is also relevant, despite the fact that this report considers only gas and liquid fired furnaces and boilers. Since the fuels with broader specifications derived from coal, tar sand, and shale will have a higher percentage of carbon than the presently used fuels, they are expected to show some of the corrosion behaviors identified in coal-fired furnaces.

The purpose of this study is to analyze the above-described literature and to synthesize the facts into a picture that will address the corrosion problems expected with the use of unconventional fuels.

Three major factors are involved in the deposition of particulates and the subsequent corrosion of the underlying metal surfaces:

1. the temperature of the metal and the gas stream
2. the composition of substances in contact with the metal surfaces and the nature of the surfaces themselves
3. aerodynamic considerations involving gas and particle velocity and the size of the deposited particles

There is a consensus that gas phase high-temperature corrosion in oil-fired boilers is not an important factor. Severe problems are ecountered only when a liquid phase is present [3, 6]. Also, not all corrosion products that deposit

Table 1 Melting points of some oil-ash constituents [13]

Compounds	Melting Point, °K
Aluminum oxide, Al_2O_3	2072
Aluminum sulfate, $Al_2(SO_4)_3$	1044*
Calcium oxide, CaO	2845
Calcium sulfate, $CaSO_4$	1722
Ferric oxide, Fe_2O_3	1839
Ferric sulfate, $Fe_2(SO_4)_3$	753*
Nickel oxide, NiO	2364
Nickel sulfate, $NiSO_4$	1114*
Silicon dioxide, SiO_2	1994
Sodium sulfate, Na_2SO_4	1158
Sodium bisulfate, $NaHSO_4$	522*
Sodium pyrosulfate, $Na_2S_2O_7$	672*
Sodium ferric sulfate, $Na_3Fe(SO_4)_3$	811
Vanadium trioxide, V_2O_3	2244
Vanadium tetroxide, V_2O_4	2244
Vanadium pentoxide, V_2O_5	964
Sodium metavanadate, $Na_2O \cdot V_2O_5 (NaVO_3)$	903
Sodium pyrovanadate, $2Na_2O \cdot V_2O_5$	914
Sodium orthovanadate, $3Na_2O \cdot V_2O_5$	1122
Sodium vanadylvanadates,	
$Na_2O \cdot V_2O_4 \cdot V_2O_5$	900
$5Na_2O \cdot V_2O_4 \cdot 11V_2O_5$	808

*Decomposes at a temperature around the melting point.

are undesirable, since some films formed through this process can actually improve heat transfer [3]. Some investigators have found that the choice between corrosion and the formation of a protective film is decided by the free-energy criterion (the reaction preferred will be that which leads to the state of lowest energy) if the changes are slow [7]. When changes are rapid, an activation-energy criterion appears to be decisive [7].

There are eight types of corrosion, all of which can occur in industrial furnaces: galvanic, uniform, crevice, pitting, erosion, dealloying, intergranular, and stress. Corrosion is caused by impurities and trace metals existing in the fuel and it is accelerated by catalysis of trace materials in the presence of other compounds formed during combustion (e.g., sodium and potassium with sulfates [8], and vanadium with sodium oxides [9]). Additionally, there is evidence that the content of heavy metal (e.g., vanadium) is also important due to the potential to catalyze soot formation [10]. In return, soot seems to catalyze corrosion, concentrating the sulfur attack on the material [11].

For these reasons, when corrosion is investigated, two important aspects seem to emerge: (1) deposition of substances originally existing in the fuel or formed during combustion, and (2) corrosion of the metals by those deposits. Accordingly, this report is subdivided in two main parts dealing with deposits and corrosion respectively. In the part discussing deposits, the compounds that deposit are briefly identified and reference is made to existing deposition theories and work in progress. In the part discussing corrosion, the chemical composition of the deposits is described in more detail so as to identify the several paths that may lead to corrosion. Additionally, the effect of chemical composition, additives, and operating conditions is discussed in relationship to broad-specification fuels. Experimental techniques and corrosion theories are discussed as well. Finally recommendations are made on what needs to be done to mitigate the problem of high-temperature corrosion in

Table 2 Characteristics of deposition over the spectrum of particle sizes [15]

Size	Deposition Mechanism	Typical Characteristics
vapors ($3\times10^{-4} \leq d_p \geq 10^{-3}$ μm	Fick diffusion	dp less than mainstream temperature
	eddy diffusion	low deposition efficiency
	Soret diffusion	weak thermophoretic (Soret) effect
		dep. rate plateau at T_w well below dp
subcritical (ca. $10^{-3} \leq d_p <$ 10 μm)	Brownian diffusion	lowest deposition (collection efficiency)
	eddy diffusion	large thermophoretic effect; rate more linear in $T_\infty - T_w$
	thermophoresis	apparent dp equal to mainstream T
		inertial "enrichment" effects below threshold for inertial impaction
supercritical (ca. $d_p >$10μm)	eddy impaction	no apparent dp
	inertial impaction	highest deposition efficiency ($\leq$ 100%)
		no thermophoretic effect rate insensitive to $T_\infty - T_w$

industrial/commercial furnaces and boilers using broad-specification fuels.

II Formation of Deposits During Combustion of Petroleum Oils

(*A*) **Background.** The constituents in the original crude oil which form deposits during the combustion process go through the refining process practically unchanged. Residual oil (main fuel used in steam-generating plants) usually has an ash content of 0.1 percent (ash here refers to the deposit-forming constituents). Nevertheless, this small amount of ash can be the cause of serious deposit and corrosion problems in furnaces.

Ash-forming constituents in the crude oil are introduced [12]:

(*a*) by the animal and vegetable matter from which the oil was formed;

(*b*) from contact of the oil with underground rock structure and brines; and

(*c*) during production, storage, and handling.

Sodium and *vanadium* are the most significant elements in petroleum oils because they can form complex compounds having low melting points (522–964K) as shown in Table 1. Tube-metal temperatures (800–866K) encountered in furnace and superheater tube banks of many oil-fired boilers [12, 13] exceed the melting temperature of many of the compounds. However, because of its complex chemical composition, fuel-oil ash seldom has a single melting point, but rather melts over a wide range of temperatures.

During combustion, the organic vanadium compounds in the oil thermally decompose and oxidize in the gas stream to V_2O_3 and V_2O_5. Although complete oxidation may not occur and there may be some dissociation, a large part of the vanadium originally present in the oil exists as a vapor phase, V_2O_5, in the flue gas.

The sodium, usually present as NaCl in the oil [13], vaporizes and reacts with sulfur oxides either in the gas stream or after deposition on tube surfaces. Subsequently, reactions take place between the vanadium and sodium compounds with the formation of complex vanadates having melting points lower than those of the parent compounds, for example:

$$Na_2SO_4 + V_2O_5 \longrightarrow 2NaVO_3 + SO_3$$

melting points 1158K 964K 902K

Excess vanadium or sodium in the ash deposit (above the necessary quantity for the formation of sodium vanadates) may be present as V_2O_5 and Na_2SO_4.

The *sulfur* in the oil is progressively released during combustion and is promptly oxidized to sulfur dioxide (SO_2). A small amount of sulfur dioxide is further oxidized to SO_3 by atomic oxygen present in the flame zone. Also catalytic oxidation of SO_2 to SO_3 may occur [13] as flue gases pass over vanadium-rich deposits.

Recent experiments by Jackson [14] indicate that the rate of deposition of oil ash and additive components onto convection tubes is such as to progressively deplete the flue gases of inorganic material during passage through the boiler. Thus, the upstream tubes receive more material and though much of this exfoliates from at least the high-temperature superheater during operation, experience shows that the net amount of deposit is greater at the gas inlet, where gas temperatures are higher. Of the order of 1/3 of the ash is retained in the boiler as deposits [14], the rest being discharged as fine dust in the flue gas or as coarse dust and deposit debris in the collecting hoppers, whether sootblowing is practiced or not. The greater thickness of deposit on the superheater inlet tubes reduces heat transfer and results in the outer portions of the deposits achieving temperatures close to

those of the flue gas. This in turn accelerates differentiation of the deposit constituents, leading to high concentrations of the more volatile and corrosive sodium and vanadium compounds close to the tube metal. It also allows the outer parts of the deposit to act as catalyst for the oxidation of SO_2 to SO_3; the greater bulk of the deposits allows better transfer of material between gas and deposits.

In the absence of significant proportions of magnesium, sodium appears to deposit on high-temperature surfaces according to convective mass transfer theory. Diffusion of vapor of sodium hydroxide or sulfate through the boundary layers appears to dominate.

Addition of magnesium to the fuel, at a proportion of three to five times (by mass) the sodium, increases the deposition rate of sodium, by a factor of two to three. This could be explained by depression of the vapor pressure of sodium compounds in the particulate solids arriving at the superheater.

An ash particle that is in a sticky, semimolten state at the tube surface temperature may adhere to the tube if it is brought into contact by the gas flow over the tube. Even a dry ash particle may adhere due to mutual attraction or surface roughness. Such an initial deposit layer will be at a higher temperature than that of the tube surface because of its relatively low thermal conductivity. This increased temperature promotes the formation of adherent deposits. Thus, fouling will continue until the deposit-surface temperature reaches a level at which all of the ash in the gas stream is in a molten state so that the surface is merely washed by the liquid without freezing and continued buildup.

In experimental furnaces it has been found that the initial rate of ash buildup was greatest when the sodium–vanadium ratio in the fuel oil was 1: 6, but an equilibrium thickness of deposit (1/8 to 1/4 in. thick) was reached in approximately 100 hr of operation. When the fuel oil contained more refractory constituents such as silica, alumina, and iron oxide in addition to sodium and vanadium, an equilibrium condition was not reached and the tube banks ultimately plugged with ash deposits. However, these ash deposits were less dense, i.e., more friable than the glassy slags encountered with a 1:6 sodium–vanadium fuel oil. Both the rate of ash buildup and the ultimate thickness of the deposits are also influenced by physical factors such as the velocity and temperature of the flue gases and particularly the tube-metal temperature. Geometry effects seem to be negligible [11].

In predicting the behavior of a residual oil insofar as slagging and tube-bank fouling are concerned, several fuel variables are considered including (1) ash content, (2) ash analysis, particularly the sodium and vanadium levels and the concentration of major constituents, (3) melting and freezing temperatures of the ash, and (4) the total sulfur content of the oil. Applying this information in boiler design at the present time is largely a matter of experience.

(B) Recent Advances in the Theory of Deposition From Combustion Gases

Mechanisms of Mass Transport. Rosner [15] classified the deposition mechanisms of combustion products for a typical pulverized-coal furnace situation according to the particle size and depending on whether the dew point (dp) of the products is less or greater than the mainstream temperature. Table 2 shows such classification.

Rosner's classification indicates that *vapor* transport is associated with: a dew point (dp) *less* than the mainstream temperature, above which deposition does not occur; low deposition efficiency (η) and low sensitivity to boundary layer temperature difference (ΔT_{BL}).

Small particle capture is characterized by an apparent dp equal to the mainstream temperature, even lower η values than those for smaller particles, and a spatial dependence similar to that for vapor capture but with increased sensitivity to ΔT_{BL}.

In contrast to the above two regimes, the large size (inertially dominated) capture is associated with: the absence of an apparent "dew point"; η values which can approach 100 percent for "sticky" collisions, preferential deposition on "windward" or "pressure" surfaces, and insensitivity of deposition rate to $(\Delta T)_{BL}$ except via the sticking coefficient.

Prediction of Deposition Rates of Small Particles. Rosner [15] proposed a model for predicting the deposition rates for vapors and small particles which have negligible inertial effects. The model neglects chemical reaction, condensation and coagulation *within* the thin mass transfer boundary layer adjacent to the deposition surface. Since small particles participating in the deposition process are often present in only trace amounts, for each such species, or particle size class, i, present in local mass fraction m_i, the diffusion mass flux J_i'' can be written as

$$J_i'' = -D_i \delta (\text{grad } m_i + \alpha_{T,i} m_i \text{ grad ln } T) \tag{1}$$

where D_i is the Fick or Brownian diffusion coefficient and $\alpha_{T,i}$ is the dimensionless thermal (Soret) diffusion coefficient.

Inertial Effects on Particle Deposition. Inertial effects on particle deposition are significant in the case of larger particles which are unable to "side-step" walls or obstacles. Predictions of the deposition rate are based generally on trajectory analysis. Existing work shows [16] that deposition (by impact) becomes impossible below a critical value of Stokes number

$$S = \frac{\delta_p d_p^2 U}{18 \mu L} \tag{2}$$

where δ_p, d_p are particle density and diameter; U is the gas stream velocity and μ is its viscosity; L is a characteristic dimension of the target. Impaction rates at higher than critical values of Stokes number are geometry and Stokes-value dependent. These rates are usually expressed as impaction efficiencies defined as the fraction of the mainstream particle mass flow rate through the projected area of the target which actually strikes the target.

Israel and Rosner [17] have recently found that inertial effects strongly influence local deposition rates even *well below* the critical value of Stokes number.

A detailed description of the mechanisms of deposition has also been published [18].

III Corrosion Problems in Furnaces and Boilers

In this section, the impact of fuel flexibility on corrosion in furnaces and boilers will be addressed; as it was mentioned in the Introduction, this is the second of two aspects of the general problem of corrosion in furnaces and boilers.

There is a basic difficulty in separating the effects of one fuel compound compared with another because many compounds are found together in deposits on metal surfaces, and some trace compounds act as catalysts in the reaction of other compounds. Therefore, great care must be taken in differentially analyzing experimental results in order to identify the compound causing corrosion under certain conditions. This brings up the problem of the difficulty in performing relevant corrosion experiments.

***(A)* Corrosion Experiments.** There are basically three ways of obtaining information on corrosion: (1) recording what happens in a real furnace, (2) setting up a moderately large experimental combustor operated under more closely controlled conditions than is possible for an operating boiler, and (3) setting up a small-scale laboratory experiment. The most useful results as far as relevance to fundamental information on corrosion processes occurring in furnaces and boilers are

Table 3 Vanadium, nickel, and sodium content of residual fuel oils (parts per million by weight) [13]

Source of Crude Oil	Vanadium	Nickel	Sodium
Africa			
1	5.5	5	22
2	1	5	--
Middle East			
3	7	--	1
4	173	51	--
5	47	10	8
United States			
6	13	--	350
7	6	2.5	120
8	11	--	84
Venezuela			
9	--	6	480
10	57	13	72
11	380	60	70
12	113	21	49
13	93	--	38

Table 4 Representative residual fuel analysis [23]

	Conventional high sulfur	Intermediate sulfur	Low sulfur
Sulfur, %	2.2	0.96	0.50
Carbon, %	86.25	87.11	87.94
Hydrogen, %	11.03	11.23	11.75
Nitrogen, %	0.41	0.26	0.16
API gravity	17.3	21.5	24.7
Vis. SS @ 38°C (100°F)	3138	586	225
Con carbon, %	12.51	5.64	2.43
Hexane insoluble, %	10.33	4.72	2.25
Ash, %	0.08	0.04	0.02
Trace metals, ppm			
Vanadium	350	155	70
Nickel	41	20	10
Sodium	25	10	<5
Iron	13	9	<5

Table 5 Sulfur content in fractions of Kuwait crude oil [13]

Fraction	Distillation Range, °K	Total Sulfur % by Weight
Crude oil	--	2.55
Gasoline	324-396	0.05
Light naphtha	398-422	0.05
Heavy naphtha	426-470	0.11
Kerosine	480-511	0.45
Light gas oil	520-542	0.85
Heavy gas oil	554-579	1.15
Residual oil	582-771	3.70

Source, Article by F.E. Hixon, Shell Refining and Marketing Co., Ltd., Chemistry and Industry, March 26, 1955, page 333.

obtained from the second type of setup [4]. This is because even though field testing is simple, it has the drawback of generally not having the gas phase well enough characterized in terms of composition and temperatures [19]; also, results can be obtained only after very long operation times. On the other hand, small-scale laboratory experiments, although necessary, have the drawback of generally not being able to reproduce the dynamic variations of temperature and composition, especially the short time temperature fluc-

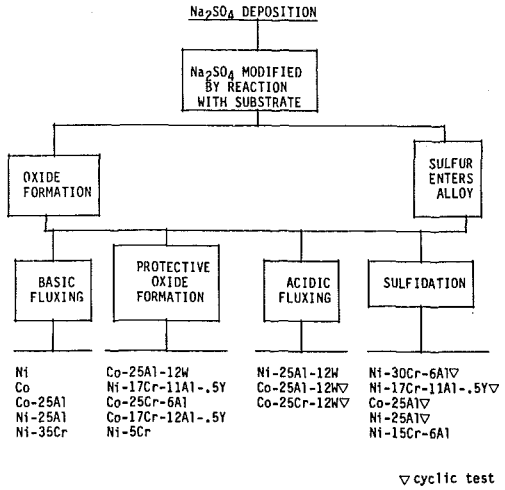

Depending on its composition, an alloy may form a protective or a non-protective oxide scale. Non-protective scales may form as a result of basic fluxing, acid fluxing, or formation of sulfides within the alloy (sulfidation).

Fig. 1 Schematic diagram illustrating the processes which can occur after Na_2SO_4 deposited on a neutral or alloy [22]

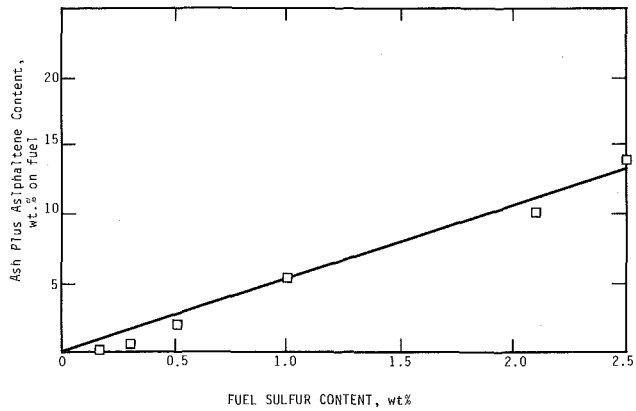

Fig. 2 Sulfur level versus fuel asphaltene ash content [23]

tuations, occurring in a real furnace [20, 21]. For this reason, when setting up a small-scale experiment, great care should be given to the thought of how to reproduce in a small time scale what happens in a long time scale in a real furnace. In particular, corrosion testing must be standardized [19], so that the material is exposed to a cyclic variation reproducing the situation in an operating furnace.

The standardization of experiments has the additional advantage of allowing the unification of various hot-corrosion theories. The importance of using the same materials and the same test conditions is illustrated by the fact that catastrophic oxidation rates are usually one to two orders of magnitude greater than normal oxidation rates, whereas accelerated oxidation rates are only one to two times greater than normal oxidation rates [22]. For example, Fig. 1 shows different processes which may occur after sodium sulfate deposits, depending upon the conditions. In order to properly reproduce conditions in a real furnace, a cyclic laboratory corrosion test with a semicontinuous Na_2SO_4 deposition is needed.

(*B*) Fuel Composition. To appreciate the future corrosion problems associated with unconventional fuels, one should consider ash composition of both fuel oil and coal, since some unconventional fuels will be derived from coal.

(1) Fuel-Oil Ash. The ash content of residual fuel oil is usually below 0.2 percent; however even this small quantity of

Table 6 Typical range of major constituents in residual fuel oil leading to corrosion and deposits [4]

Constituent	In residual fuel oil (ppm)	In oil ash (%)
Vanadium	0-500 as V	0.40 as V_2O_5
Sodium	2-300 as Na	0.1-30 as Na_2O
Sulfur	1000-40,000 as S	0.1-40 as SO_3

Table 7 Usual range of ash composition in American coals [4]

Component	Percentage
SiO_2	20-60
Al_2O_3	10-35
TiO_2	0.5-2.5
Fe_2O_3	5-35
CaO	1-20
MgO	0.3-4
Na_2O+K_2O	1-4
SO_3	0.1-12

Table 8 Composition of coal ash (typical analysis) [24]

PERCENT	COAL ASH
SiO_2	36.5
Fe_2O_3	26.8
SO_3	5.9
Al_2O_3	19.2
CaO	5.5
MgO	0.8
Na_2O	1.2
K_2O	2.5

ash can produce catastrophic high-temperature corrosion in boilers. The elements most responsible for this are vanadium, sodium, and sulfur [13]. In general, the ash content increases with the asphaltic constituents—the insoluble hexane present in the fuel. Table 3 shows the variation of the quantities of vanadium, nickel, and sodium according to the source of crude oil, while Table 4 shows how the sulfur content (as well as other constituents) can change according to the residual fuel. Most of the metallic compounds, as well as a considerable part of the sulfur compounds, are concentrated in the distillation residues, as shown in Table 5. In fact, there seems to be almost a linear variation of the ash plus asphaltene content versus the sulfur content of the fuel, as illustrated in Fig. 2.

The reasons that such small quantities of impurities in the original fuel oil can cause severe corrosion problems is that the deposits in fact contain much higher concentrations of these compounds, as shown in Table 6, due to the way in which ash is released during combustion. Typically, the atomized fuel oil burns in two stages [13]. First, the volatile compounds are evaporated and burned, leaving behind a porous coke residue, the cenosphere. The hexane-insoluble material is considered to be the precursor of the cenosphere [23]. In the second phase, the fuel is the cenosphere which now contains a much higher percentage of impurities by weight than the original fuel. Release of ash from the cenosphere is associated with the rate of oxidation of the carbon which is the main constituent of the cenosphere. This in turn depends upon the porosity of the cenosphere, the surrounding temperature and oxygen available, which are functions of the density of cenospheres in the volume in which they burn.

Table 9 Elemental composition of several fuels [25]*

ELEMENTAL COMPOSITION	SRC-II MD	SRC-II HD*	NO. 2 FUEL OIL	NO. 6 FUEL OIL
C (WT %)	84.59	88.98	86.4	87.2
H	8.84	7.64	13.3	11.96
N	0.85	1.03	0	0.46
S	0.20	0.39	0.3	0.47
O	5.43	1.9	0	0.86
ASH	0.002	0.058	0.001	0.008

Table 10 Trace elements in shale oil and solvent refined coal compared to coal and residual fuel oil [26]

Element	Shale Oil	Coal	SRC	Residual Fuel Oil
Fe (10^{-4}kg/kg)	5.35	17300	68	4.6
Co (10^{-9}kg/kg)	96.3	3700	310	320
Zn (10^{-9}kg/kg)	73.0	-	-	1000
Cu (10^{-9}kg/kg)	-	-	-	-
Cr (10^{-9}kg/kg)	21.9	14000	2680	70
Se (10^{-9}kg/kg)	252	1530	148	90
As (10^{-9}kg/kg)	15600	13600	1390	55
Sb (10^{-9}kg/kg)	4.38	500	74	4
Cs (10^{-9}kg/kg)		890	23	-
Rb (10^{-9}kg/kg)		22400	570	-
Sc (10^{-9}kg/kg)		2800	130	2
Eu (10^{-9}kg/kg)		292	13	2
Br (10^{-9}kg/kg)	9.3	3510	3950	220
Hg (10^{-9}kg/kg)	75.0	56	25	4.0*
Cl (10^{-6}kg/kg)	-	260	160	40
Ni (10^{-6}kg/kg)	0.88	20.0	2.7	12.5*
V (10^{-6}kg/kg)	-	30.1	4.63	87
Na (10^{-6}kg/kg)	1.0	148	9.55	33
Ti (10^{-6}kg/kg)	-	530	465	-
S (%)	-	4.34	0.74	0.32*

*Values for Canadian Residual Fuel Oil

(2) *Coal Ash.* Inherent mineral matter in U.S. coal seldom exceeds 2 percent by weight [4], and it is composed of the elements that were originally present in the plants yielding the coal. Extraneous mineral matter in the coal results from sedimentation processes and from inorganic solids left by water that passed through the sediments [4]. Tables 7 and 8 show compositions of coal ash. The information in these tables is relevant here only from a qualitative point of view, since it is not expected that unconventional fuels extracted from coal will produce the same amounts of ash constituents. In fact, some detailed data on SRC-II fuels [25] presented in Table 9 show that the ash content varies greatly with the distillate and sometimes compares with that of fuel oil. Table 10 additionally shows a comparison of trace elements of various broad-specification fuels. Since no other information exists for future dirtier fuels extracted from coal, the present review will necessarily have to be much more speculative on this subject.

For future fuels extracted from shale and tar, information on ash deposits is also not available. Therefore, the assumption will be made that, similar to the coal-extracted fuels, the

Table 11 Forms of sulfur in American coals [6]

Forms of Sulfur, percent			Total Sulfur,
Pyritic	Organic	Sulfate	percent
0.19	0.57	0.02	0.78
0.39	0.57	0.03	0.99
0.56	0.65	0.01	1.22
0.73	0.74	0.05	1.52
0.87	1.26	0.03	2.16
1.61	0.86	0.04	2.51
1.76	1.85	0.06	3.67
2.17	1.80	0.04	4.01

carbon content will be greater for these new fuels and most of the ash constituents will be those shown in Table 10.

(3) *Effects of Various Fuel Constituents.* (*a*) *Sulfur.* Generally, the amount of sulfur in residual fuel is about twice that of the crude oil from which it comes, although this depends upon the refining practices [6]. Some investigators [6] consider that of sulfur, vanadium, and the alkalies, sulfur is the major offender in corrosion and it is involved most frequently because it exists in both oil and coal. Also, compounds of sulfur with iron, oxygen [4], and alkali are the worst offenders in the wastage of metals and frequently in the accumulation of deposits.

Tables 4, 5, and 11 show respectively the sulfur content of oils and coals.

SO_3 is considered a major factor in corrosion [4]. During combustion, pyrites are dissociated thermally and with the organic sulfur in the coal, react with O_2, forming mostly SO_2 and SO_3. These react with sodium and potassium oxides (Na_2O and K_2O) formed in the high-temperature flame to form sodium or potassium sulfates. These sulfates are low-temperature melting materials which deposit on tubes, attract other ash particles, and eventually build up thick deposits on tubes. Alkali sulfates and SO_3 react to form complex sulfates which melt at about 900K in a high-SO_3 (about 1000 ppm) atmosphere.

It is interesting to point out that the large SO_3 concentration needed for the formation of alkali iron trisulfates does not exist in the bulk gas stream, but only near the surface of the metal [24]. Experiments have confirmed that beneath deposits where gas velocities are low, approaching stagnation, the SO_3 concentration can be 30 times or more greater than in the bulk, rapidly moving gas stream. Thus, enough SO_3 is easily available for the reactions forming the corrosive trisulfates on metal surfaces. These reactions forming trisulfates will also be discussed in the next section.

(*b*) *Alkali Metals.* Alkali metals such as sodium and potassium have a detrimental influence when present in fuel [8], whereas alkaline earth compounds such as Ca and Mg can have a beneficial influence [8]. The concern is here concentrated on the corrosive alkali. The influence of Ca and Mg will be discussed in the section presenting the effect of additives. Sodium and potassium are volatilized at high temperature from the mineral matter, forming Na_2O and K_2O. They react with sulfur oxides to form low-melting-point materials which deposit on tubes and attract other ash particles, thus building up deposits [8].

The vapor pressure of K_2O is much higher than that of Na_2O (i.e, K_2O is much more volatile than Na_2O), and thus although coals in the U.S.A. have about equal proportions of K and Na on a molar basis, deposits formed by condensation generally contain considerably more K_2O than Na_2O [6]. Potassium-rich sulfates are much more corrosive than sodium

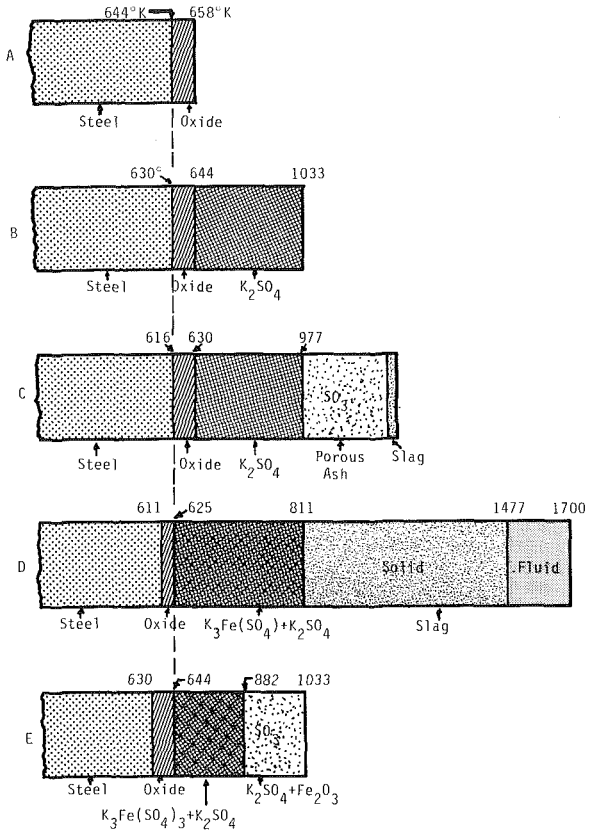

Fig. 3 Mechanism of corrosion of wall tubes by sulfate deposits [30]

sulfates [27]. According to recent findings [24], the total sodium content of coals is less important than the ratio of potentially volatilizable potassium to sodium in the boiler flame. Potassium might originate in coal flames from silicate coal minerals containing potassium [27]. The release of potassium results from an exchange reaction whereby potassium in the silicates is partly replaced by sodium, and up to 40 percent of potassium can be transferred into the vapor phase. This potassium is converted to sulfate and together with sodium sulfate can form a corrosive medium of low-melting sulfates for dissolution of protective oxide layers on boiler tube steels [27]. Alkali sulfates have also been implicated as the cementing agent that bonds the initial deposit to the tubes [28]. The reason for this is that alkali sulfates form melts on the metal surface which can support electrochemical corrosion of the metal [3].

Sodium causes most trouble when it is present as a chloride because it is readily volatilized when the fuel oil is burned [6]. For example Na_2SO_4 can be formed by reaction between NaCl and sulfur oxides [9]. Basic studies [29] show that when sodium is introduced as oxalate and sulfur introduced as SO_2 into premixed hydrocarbon-air flames at levels corresponding to those found in combustion gases from certain coals, they form deposits consisting essentially of Na_2CO_3, Na_2SO_3, and Na_2SO_4, all in solid phase. In rich flames, Na_2CO_3 is the main compound, whereas in lean ones Na_2SO_4 predominates. At intermediate stoichiometries, Na_2SO_3 is the main compound.

Figure 3 shows a postulated scheme for the corrosion mechanism of alkali sulfates.

An interesting observation has been that small amounts of lithium (0.5–1.0 percent) exist in "enamel" deposits of more corroded tubes; enamel results from the reactions of alkali-metal sulfates with SO_3 and Fe_2O_3 [30]. The role of lithium as a catalyst has not yet been established.

Small amounts of lithium compounds have also been found

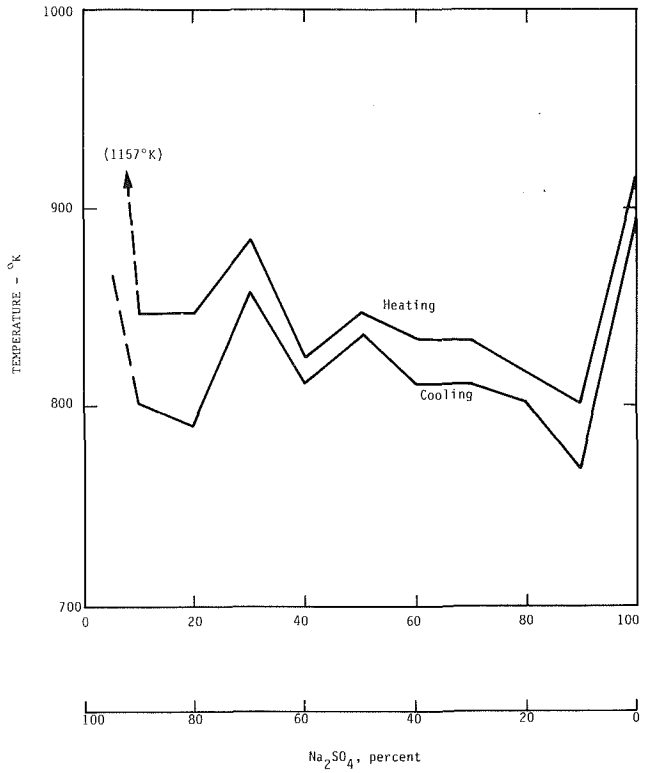

Fig. 4 Melting points in system V_2O_5-Na_2SO_4 [6]

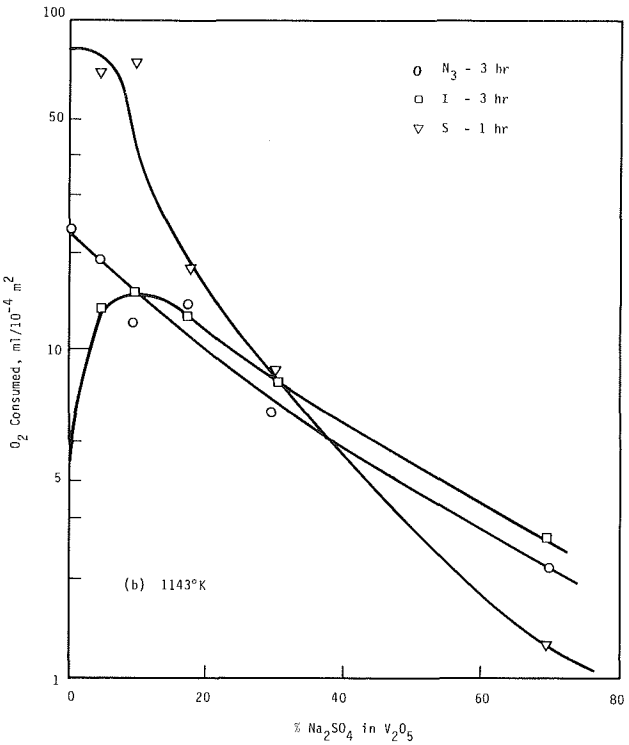

Fig. 5(*b*) Percent consumption versus log oxygen consumption at 1143K for alloys N_3, I, and S exposed respectively for 3 hr, 3 hr, and 1 hr to the corrosive mixture [32]

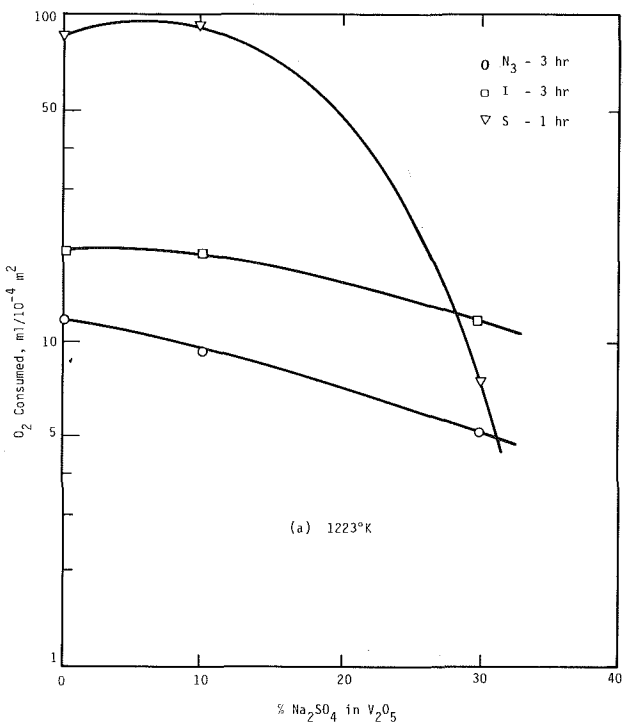

Fig. 5(*a*) Percent consumption versus log oxygen consumption at 1223K for alloys N_3, I, and S exposed respectively for 3 hr, 3 hr, and 1 hr to the corrosive mixture [32]

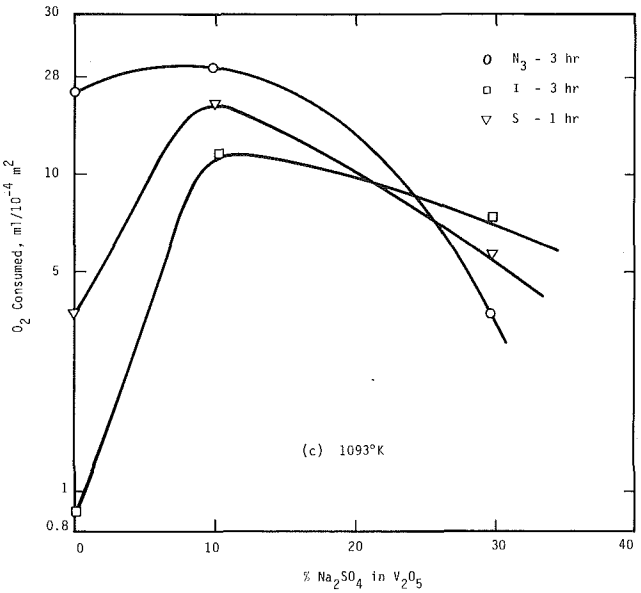

Fig. 5(*c*) Percent consumption versus log oxygen consumption at 1093K for alloys N_3, I, and S exposed respectively for 3 hr, 3 hr, and 1 hr to the corrosive mixture [32]

in boiler furnace deposits of alkali iron trisulfates, mainly $K_3Fe(SO_4)_3$ and $Na_3Fe(SO_4)_3$ [4]. Alkali iron trisulfates are formed by reaction of SO_3 with Fe_2O_3 and either K_2SO_4 or Na_2SO_4, or with mixed alkali sulfates. As has been discussed previously, the amount of SO_3 needed for this reaction largely exceeds the amount of SO_3 formed in the flame. It has been postulated, and subsequently proved [31] that the additional SO_3 needed for this reaction is formed through heterogeneous catalysis.

At present, two possible mechanisms for metal wastage involving alkali iron trisulfates have been postulated [4] in terms of competitive scale or film forming and destroying; both of these mechanisms might take place, but it has not yet been established which one predominates under certain conditions.

(*c*) *Vanadium.* Vanadium is an impurity of lower cost fuel oils [9] and it is not found in coal. As it was previously explained, even though a fuel droplet might contain less than 1

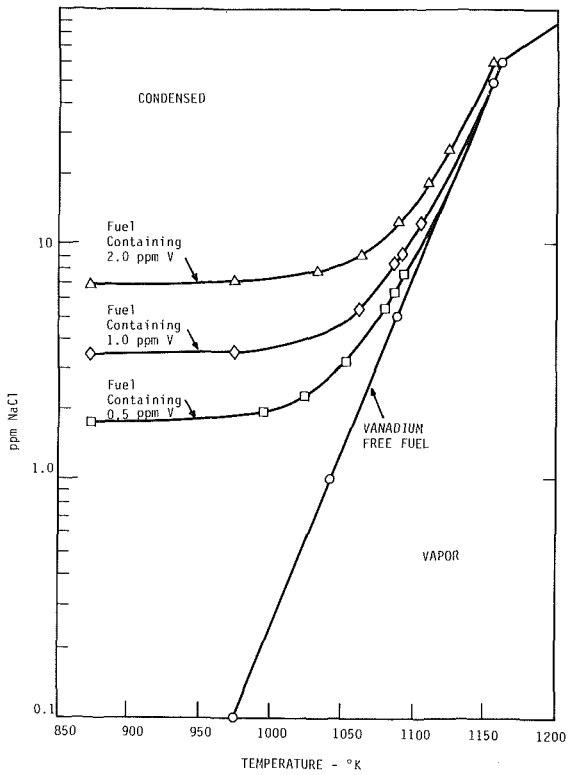

Fig. 6 Effect of V_2O_5 on dewpoint of Na_2SO_4 [9]

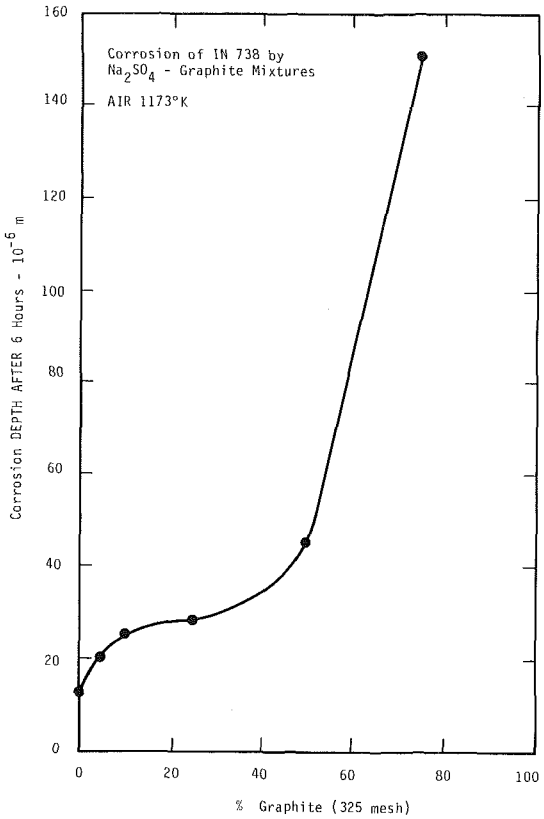

Fig. 7 Effect of graphite additions to Na_2SO_4-induced corrosion of IN 738 alloy: corrosion penetration depth (microns) after 6 hr in air at 1173K versus graphite concentration in salt mixture [33]

ppm V, the char yielded by its combustion could contain more than 500 ppm V, because of distillation processes occurring during evaporation and combustion [9].

During combustion of low-grade distillates and residual fuels, vanadium present in the fuel is oxidized to V_2O_5, which in liquid form (melting point 963K) markedly increases the rate of metal oxidation [9].

Traces of vanadium also increase the severity of sulfidation problems [9]. For example, condensed V_2O_5 and condensed Na_2SO_4 may react to form eutectic mixtures which are highly corrosive. Figure 4 shows that the melting point of almost any proportional combination of V_2O_5 and Na_2SO_4 is below 870K and thus prone to cause corrosion in furnaces. Furthermore, Fig. 5 shows how these mixtures affect corrosion at various temperatures. There seems to be a threshold beyond which the addition of Na_2SO_4 (for example) decreases the corrosivity of V_2O_5. It is thought that Na_2SO_4 in small amounts increases oxidation by controlling the fluidity of the molten slag at lower temperatures, but acts as a diluent at high concentrations and temperatures [32].

Vanadium may also present a problem when the fuel containing it is burned in air that contains small amounts of sea salt. This is because NaCl can react with both V_2O_5 and SO_2 in the gaseous phase forming sodium vanadates. Gaseous sodium vanadates slightly increase the rate of oxidation of superalloys, whereas condensed $NaVO_3$ increase the rate of oxidation by more than an order of magnitude [9]. The effect of V_2O_5 on the dewpoint of Na_2SO_4 in the presence of NaCl is shown in Fig. 6.

There is not yet a consensus on how vanadium compounds lead to metal wastage, although three mechanisms have been proposed [4]. However, it is generally agreed that a liquid film speeds up the corrosion rate and thus the problem will be more severe when the vanadate has a melting point lower than the temperature of the metal substrate [4]. The degree of attack is controlled by:

1. the extent of the corrosive vanadium compounds at the metal/oxide interface, and
2. the diffusion rate of O_2 to the metal oxide interface.

The main corrosive constituents are either free vanadium pentoxide or sodium vanadate, the former being the more aggressive [32].

It is to be pointed out that the nature of the oxide growth at the material surface is very important because it may alter scale porosity, thus hindering rapid diffusion of O_2 to the oxide/metal interface [32]. An interesting situation is that of the nickel base alloys that have a low oxidation rate due to the formation of $Ni_3(VO_4)_2$. This oxide, which has a relatively high melting point and stability and also a relatively low porosity, plugs the pores of the metal/oxide interface making it unavailable to further oxidation and thus hinders corrosion.

(*d*) *Carbon and CO.* Sooty deposits containing carbon might result from several phenomena occurring in the combustion zone of a furnace. These are incomplete mixing of the two phases yielding carbonized uncombustible fuel drops or solid carbon particles, uncombusted gaseous hydrocarbons which decompose catalytically on hot alloy surfaces, thermal cracking of high molecular weight fuel constituents, and incomplete mixing in the gas stream. As a result, hard, dense carbon layers that are only slowly oxidized by the combustion gases might form, and these would obviously persist for a long time [33].

Carbon deposition enhances hot corrosion in various ways. First, solid carbon reduces sodium sulfate (Na_2SO_4) condensate to corrosive sulfide (Na_2S) as shown in Fig. 7. It was shown that this reduction is much more readily accomplished in the presence of solid carbon than in a gaseous methane atmosphere [33], for example. However, even low gas phase concentrations of hydrocarbons, such as methane, result in accelerated hot corrosion of nickel-base alloys by SO_2 and condensed Na_2SO_4. The reduction of Na_2SO_4 to Na_2S depends upon the temperature, the particle size, and structure of the carbon deposit [33]. These last two points are illustrated in Figs. 8 and 9. Figure 10 shows that for a given type of carbon deposit, the effect on hot-corrosion rates

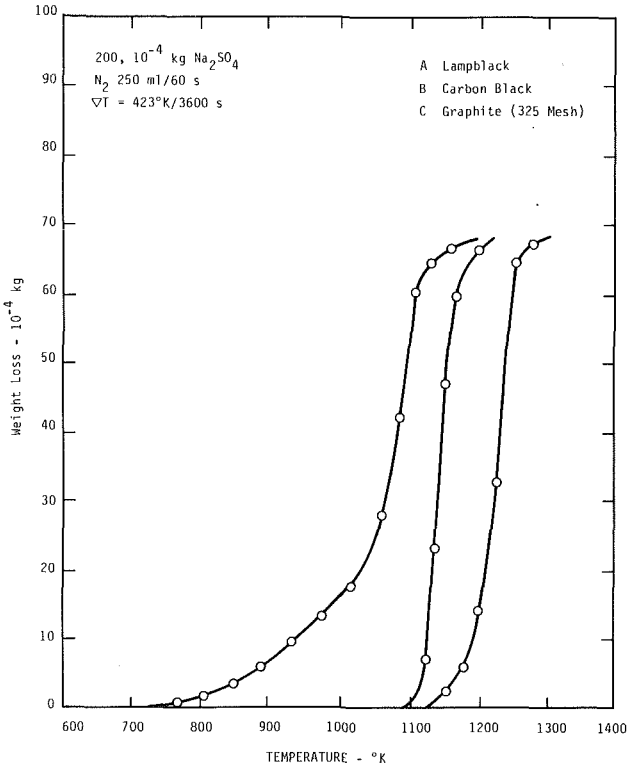

Fig. 8 Reaction of Na_2SO_4 with three different types of carbon: weight loss of salt versus temperature for (*A*) Na_2SO_4 + 25wt percent lampblack, (*B*) Na_2SO_4 + 50wt percent carbon black, (*C*) $NaSO_4$ + 50wt percent graphite (325 mesh) [33]

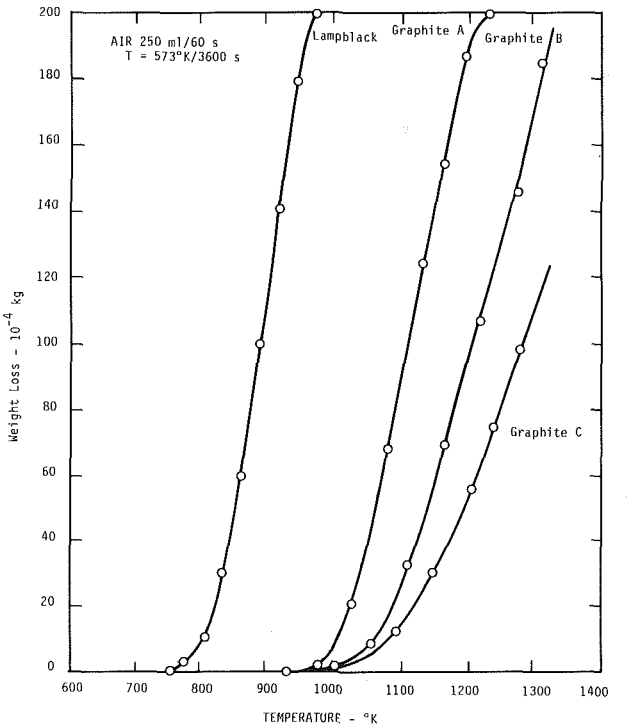

Fig. 9 Oxidation behavior of carbons in flowing air: weight loss versus temperature for lampblack, 1 micron graphite (*A*), 325 mesh (75 micron) graphite (*B*), and 1-2 mm flake graphite (*C*); 200 mg samples [33]

increases with increased weight fraction of carbon in the sodium sulfate-carbon condensate. It was also found that for a given type of carbon additive, such as graphite, the accelerating effect on hot-corrosion rates attained a maximum with intermediate size range particles, and it was inferred that

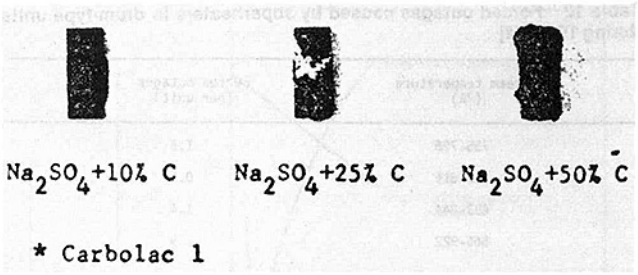

Fig. 10 Effect of increasing concentrations of lampblack on Na_2SO_4-induced corrosion of IN 738: appearance of alloy coupons after 6 hr in salt-carbon mixture at 1173K in air [33]

this presumably occurred because very fine cristallites are oxidized rapidly and coarse flakes are relatively unreactive toward sodium sulfate [33].

In general, it was found that carbon enhances sulfur activity and that the effects persist for long periods, even when the overall gaseous environment is intensely oxidizing [33].

The effect of solid carbon is dependent not only upon the combustion process, but also upon the composition of the alloy used as wall material. Generally, increased Cr and Al content gives increased corrosion resistance, although Al additives seem to be less effective than Cr in combating the combined effect of C and Na_2SO_4. With high initial concentrations of carbon, alloys having even high Al content were shown to be severely corroded [33]. Also, alloys that are resistant to corrosion by Na_2SO_4 due to their high Cr content became vulnerable to corrosion once a small amount of carbon is deposited [33].

Carbonaceous deposits from the combustion of crude oil, residual fuels, and coal tar have been proved to have an even more detrimental effect on hot corrosion than pure carbon. These deposits contain a volatile tarry constituent which readily reduces sodium sulfate to sulfide, thereby producing intense sulfidation conditions [33].

A general type of catastrophic metal deterioration that is observed in presence of carbonaceous gases at elevated temperatures has been termed "metal dusting" [34]. The gaseous phases are normally carbonizing and contain CO, CO_2, hydrocarbons, and often H_2O and H_2, and the temperature is about 700K-1100K. The product is a dense powder composed of graphite mixed with metal, metal carbides, and metal oxides. Most of the alloys containing iron, nickel, cobalt, and chromium are subject to the attack. Some studies [35] indicate the dominant role of Cr and its affinity for carbon resulting in severe carbonization and deterioration of surface layers of chromium-containing alloys.

It appears from various studies that carbon monoxide is the major compound involved in deterioration by metal dusting [34]. It was also found that oxygen and water influence the nature and amount of metal dusting by forming a themodynamically stable oxide on the metal surface and thus deterring further reactivity [34]. Sulfur was found to be an inhibitor of metal dusting through its reaction on iron-base materials to increase the stability of Fe_3C and poison adsorption sites for CO [34].

In general, it was found that metal dusting proceeds through several steps [34]:

1. Absorption of CO
2. Carbon formation through $2CO \rightarrow CO_2 + C$. This reaction is usually promoted by a catalyst metal or metal oxide [37].
3. Absorption of carbon into the surface by diffusion which is then rate controlling
4. Building up of carbon in the solid solution and the appearance of carbon on dislocations and subgrain boundaries

Table 12 Forced outages caused by superheaters in drum-type units during 1964[a] [4]

Steam temperature (°K)	Forced outages (per unit)
755-786	1.5
811-816	0.6
833-844	1.4
866-922	1.9

[a]Data from Edison Institute

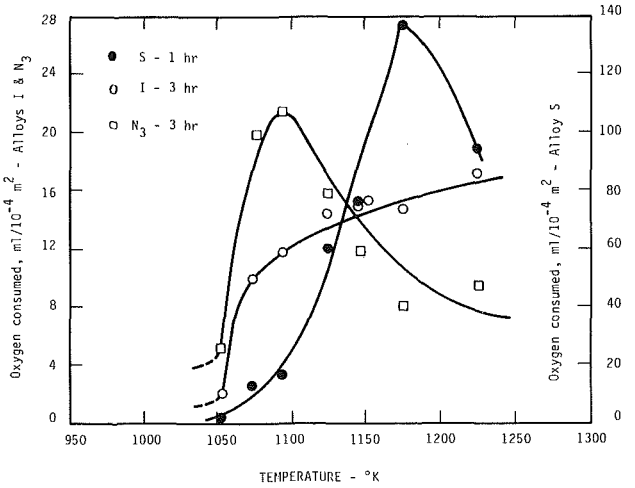

Fig. 11 Effect of temperature on oxygen consumption in 90 perecnt vanadium pentoxide plus 10 percent sodium sulfate mixture [32]

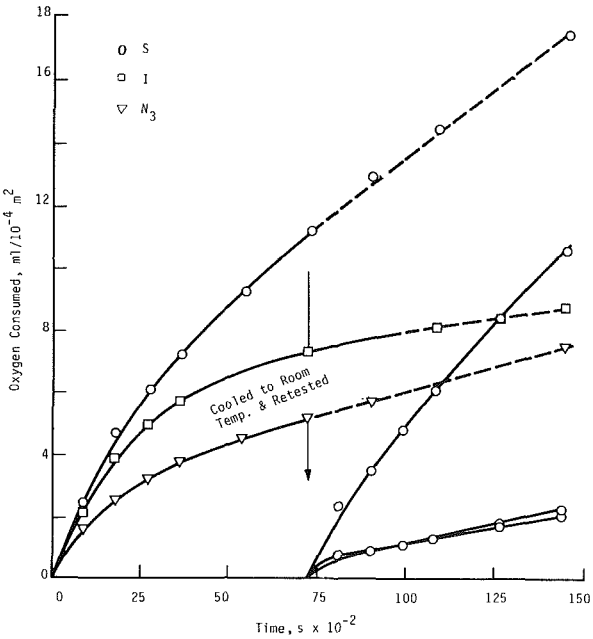

Fig. 12 Effect of intermediate cooling on corrosion of alloys S, I, and N_3 in 70 percent vanadium pentoxide plus 30 percent sodium sulfate mixture at 1143K [32]

5. Precipitation of cementite in areas of higher carbon concentrations
6. Growth of cementite without other forms of carbide formation
7. Once the critical concentration of cementite is reached in the matrix, the cementite decomposes, thus regenerating carbon and iron and initiating the precipitation of subcarbides.
8. At this point the deterioration of the base metal occurs by the continued precipitation of graphite with the growth of the above-cited decomposition products.

Carbon monoxide was found to be involved in other aspects of corrosion besides metal dusting. For example, corrosion of Ni-Cr alloys in the presence of CO was observed in some studies [37]. Others [38] have observed corrosion in gases obtained from the combustion of methane in an oxidizing atmosphere at temperatures of 760-1170K; the atmosphere thus obtained was shown to be composed of carbon monoxide, hydrogen, and finely divided graphite carbon. Carbon also may have been responsible for corrosion in this case. Finally, it was found [39] that as the ratio CO_2/CO in the flue gases decreases, the rate of corrosion increases.

(*e*) *Iron.* Iron and sulfur exist in coal in the form of pyrites; these oxidize slowly to Fe_2O_3 and Fe_3O_4 and the sulfur thus evolved combines with oxygen to form SO_2 and SO_3. Furthermore, presence of iron oxide was found to be necessary for the catalytic oxidation of SO_2 to SO_3 [8].

Iron content was found to correlate with corrosion rate [8] and in fact Fe_2O_3 and sulfur were found to correlate in the same way with metal loss [8].

(*f*) *Chloride.* Large amounts of chloride (greater than 0.3 percent) in fuel coal have been shown to lead to increased fireside metal wastage [40]. Furthermore, chlorine in coal has been found to be an accelerating agent in corrosive processes in a wide range of temperatures [41]; this is particularly so if sulfates are also present [41].

(*g*) *Effects of Additives.* The effects of additives are important in this context from the point of view of hindering the influence of certain corrosion-promoting compounds forming during combustion in furnaces.

Presently, the main reason for using additives in furnaces and boilers are (6):

1. to minimize catalytic formation of SO_3 on hot surfaces
2. to prevent formation of corrosive substances on heat receiving surfaces
3. to decrease the sintering tendency of high-temperature deposits.

Additivies have drawbacks because they are expensive due to the fact that generally a large amount must be added to modify deposits. To the initial cost of the material, the cost of handling it must be added, thus further increasing the expense. The present low-cost additives are lime and magnesium [6], and their effects are well characterized.

Magnesium might act either by neutralizing SO_3 through the formation of $MgSO_4$ or by covering the metal with a layer of MgO to prevent catalytic formation of large amounts of SO_3 [4].

Calcium is also used sometimes; however, there are some indications that accumulation of large deposits of $CaSO_4$ on surfaces may pose new problems [4].

(*h*) *Effects of Operating Conditions.* Similarly to the additives, the operating conditions influence combustion and thus may promote or hinder the formation of certain compounds involved in corrosion.

Generally, the parameters that can be controlled in the furnace are the temperature and the amount of air that mixes with the fuel.

Table 12 shows how temperature can greatly influence corrosion. More precisely, a threshold temperature was observed for some alloys beyond which corrosion became

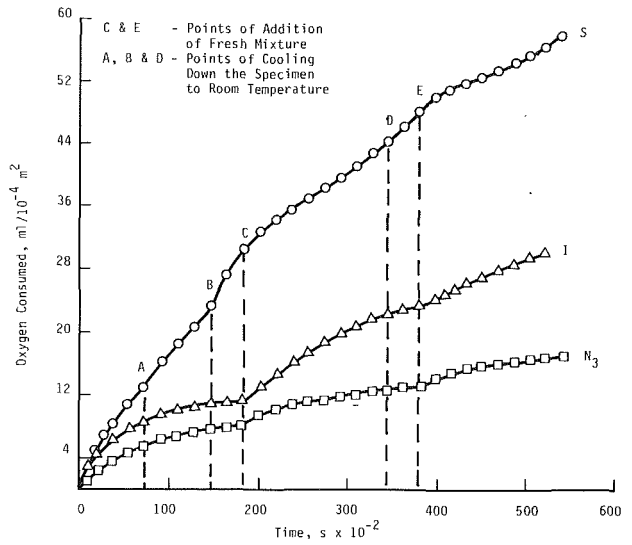

Fig. 13 Effect of replenishing the ash mixture on the corrosion rates of alloys S, I, and N_3 in a mixture of 70 percent vanadium pentoxide alloys 30 percent sodium sulfate at 1143K [32]

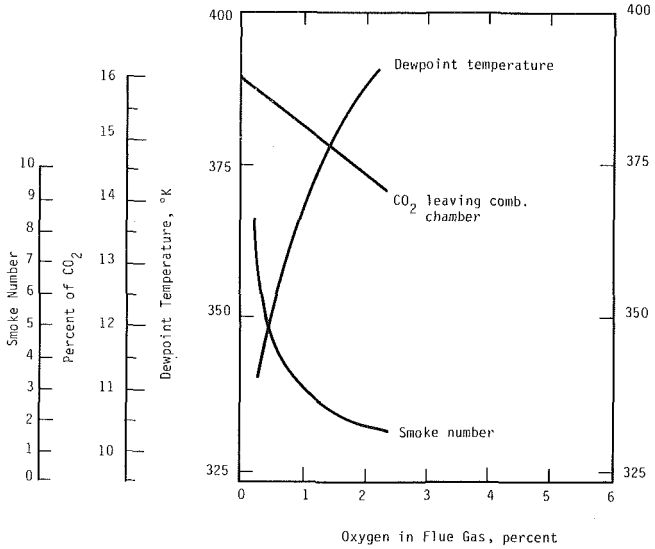

Fig. 14 Variations in performance characteristics of boiler furnaces with low excess air [6]

very high [32]; this temperature was a function of the alloy and slag composition. Figure 11 shows how temperature affects metal wastage.

There is a consensus that two important conditions that determine material corrosion in high temperature are: sudden changes in temperature and continuous buildup of fuel ash [32]. Figure 12 illustrates how temperature transients affect corrosion, while Fig. 13 shows how the addition of fresh mixture further increases the rate of attack of the alloys during a temperature transient.

Experiments and field results have demonstrated that it is beneficial to run oil-fired furnaces with low excess air because this has the advantage of eliminating formation of both V_2O_5 and SO_3 [4]. Instead of V_2O_5, other vanadium compounds such as V_2O_3 and V_2O_4 are formed, and these compounds have melting points much higher than V_2O_5, thus being less objectionable as corrosive compounds. Additionally, low excess air operation has a beneficial effect on the emission of acid smuts [6]. There seems to be a consensus that by operating at low excess air, corrosion problems can be about eliminated when burning residual fuel oil [4]. (However, the present state-of-the-art knowledge does not permit the burning of pulverized coal with so little excess oxygen [6] and thus it is projected that this method might not be applicable to unconventional fuels extracted from coal.) In fact, as little as 0.2 percent excess air was successfully used in oil-fired boilers with favorable results in eliminating corrosion [4].

The main drawback to this method of controlling corrosion is that the fuel-air ratio must be precisely controlled in all parts of the combustion system so as to prevent the promotion of fuel-rich zones which are the sites of thermal cracking hydrocarbon reactions yielding smoke. This point is illustrated in Fig. 14 where it is seen that the smoke number increases as oxygen in the flue gas decreases. Another drawback to low excess air is that a loss of efficiency of the furnace might result due to increased possibility of incomplete combustion. Despite these drawbacks, low excess air is presently considered one of the most promising methods of controlling both high-temperature and low-temperature corrosion in boilers and furnaces [13]. Figure 15 shows the effect of low excess air on low-temperature corrosion.

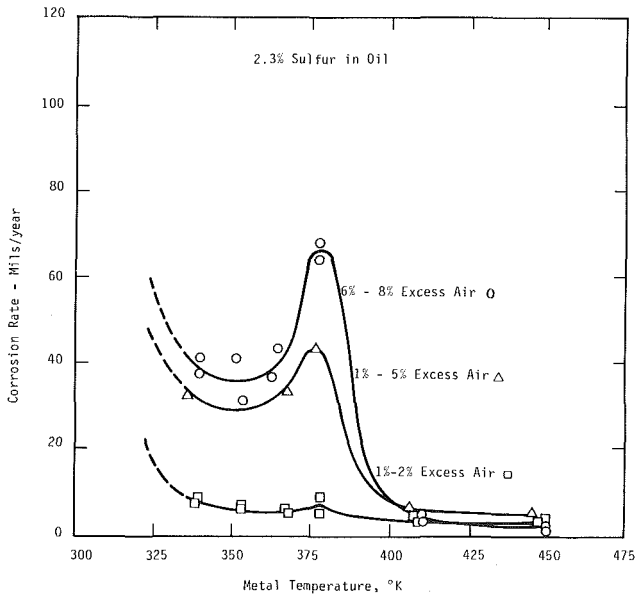

Fig. 15 Effect of excess air on low-temperature corrosion in carbon steel [13]

IV Recommendations

As a result of this study, several areas have been identified where there is a need for further investigations in order to achieve a better understanding of the deposition and corrosion processes occurring during combustion of heavy and residual oils in industrial/commercial furnaces and boilers. Specific areas recommended for further research are:

1. Behavior of nondilute oil sprays to determine conditions where carbonization of unburned liquid-fuel droplets occurs, leading to carbon deposits.
2. Formation and burning of cenospheres during combustion of heavy and residual oil sprays. These cenospheres have been identified by some investigators [42] as the building blocks of deposits of ash in boilers. A mechanism which has been experimentally corroborated has been proposed to show the involvement of cenospheres in furnace fouling [42].
3. Study of the chemical kinetics of hydrocarbons containing trace metals in order to determine the role that these play in corrosion reactions.

4. Corrosion of highly polished metal surfaces to determine their potential in mitigating corrosion. Highly polished metal surfaces would have a very low probability for sticking of deposits and this would hinder the first step toward corrosion.

5. Formation of protective films on metal surfaces.

6. Breaking of one of the chain processes leading from deposition to corrosion. For example, it has been shown in this review that metal dusting proceeds in eight steps to corrosion; the suggestion here is that one of these steps might be hindered and thus stop the chain from being completed.

7. Inhibition by some corrosive compounds of corrosion processes related to another corrosive compound. Such an example is inhibition by sulfur of corrosion by carbon. The suggestion is made here that it might be possible to find an optimum sulfur concentration that would be low enough so that it would not present corrosion problems, and yet inhibit carbon corrosion. In this manner, both sulfur and carbon corrosion would be controlled.

8. Investigation of the catalytic effects of trace metals in corrosion processes. For example, small quantities of lithium have been found in many deposits that resulted in corrosion; however, its role in this process has not yet been determined. It might be possible to find that other trace metals have similar properties.

9. Detailed documentation of the quantitative information existing on various corrosion processes. It is remarkable to notice that it is still impossible to find well-characterized quantitative information on corrosion by a certain compound under a variety of conditions. A compilation in tabular form of quantitative information already existing would show what the further investigation needs are.

10. Standardization of experimental procedures so as to make necessary the taking of a variety of important data before an experiment is considered successfully performed and completed. Such data would be used to complete the tabular documentation suggested above.

It appears important at this point to develop a well-conceived program to fulfill some of the research needs mentioned above. Such a program might contain two kinds of experiments:

1. Medium-size corrosion experiments carefully designed so as to reproduce the environment and fuel effects in an operating furnace. In particular, it is important to reproduce residence times, temperature levels, temperature transients, and the cyclic deposition of materials. Well-instrumented and careful measurements should be made of the composition of the combustion gases and temperatures, and of the composition of the deposits on the metal surface.

2. Small-scale laboratory experiments should be made in order to determine the chemical kinetic paths of the corrosion and corrosion-promoting reactions.

Theoretical investigations that appear to have a very high priority are those identified in items 1 and 2 of the Recommendations.

Acknowledgments

This work was performed by the Jet Propulsion Laboratory, California Institute of Technology, and was sponsored by the U. S. Department of Energy through an agreement with the National Aeronautics and Space Administration (DOE Interagency Agreement No. DE-AI01-81CS66001: NASA Task No. RE-152, Amendment 308).

The work was done for the Energy Conversion and Utilization Technologies Division, Mr. Marvin Gunn, Jr., Program Manager, U. S. Department of Energy.

References

1 Skorchelletti, V. V., *Theory of Metal Corrosion*, Keter Publishing House, Jerusalem, 1976.

2 Whitaker, R., "Corrosion," *EPRI Journal*, Sept. 1981, pp. 7-13.

3 Lister, D. H., "Corrosion Products in Power Generating Systems," in: *Fouling of Heat Transfer Equipment*, ed. E. F. C. Somersales and J. G. Knudsen, Hemisphere, Washington, D.C., 1981, pp. 135-200.

4 Reid, W. T., "Corrosion and Deposits in Combustion Systems," in: *Combustion Technology: Some Modern Developments*, ed. H. B. Palmer and J. H. Beer, Academic Press, 1974, pp. 35-59.

5 *Corrosion and Deposits From Combustion Gases*, Battelle Memorial Institute, 1970.

6 Reid, W. T., *External Corrosion and Deposits. Boilers and Gas Turbines*, Fuel and Energy Science Series, ed. J. M. Beer, American Elsevier, New York, 1971.

7 Evans, U. R., "Factors Deciding Between Corrosion and Protective Film Formation," *First International Conference on Metallic Corrosion*, Butterworths, 1962, pp. 3-9.

8 Borio, R. W., and Hensel, R. P., "Coal-Ash Composition as Related to High-Temperature Fireside Corrosion and Sulfur-Oxides Emission Control," ASME JOURNAL OF ENGINEERING FOR POWER, Vol. 94, 1972, pp. 142-148.

9 Bornstein, N. A., Decrescente, M. A., and Roth, H. A., "Interaction Between Vanadium in Gas Turbine Fuels and Sulfidation Attack," *Corrosion—NACE*, Vol. 28, No. 7, 1972, pp. 264-268.

10 Kramlich, J. C., Samuelsen, G. S., and Seeker, W. R., "Carbonaceous Particulate Formation From Synthetic Fuel Droplets," presented at the Fall Meeting of the Western States Section, The Combustion Institute, Arizona State Univ., Tempe, AZ, Oct. 19, 1981.

11 Marner, W. J., and Webb, R. L. (eds.), "Workshop on an Assessment of Gas-Side Fouling in Fossil Fuel Exhaust Environments," JPL Publication P2-67, DOE/ID-1213-1.

12 Miller, P. D., Slunder, C. J., Krause, H. H., and Fink, F. W., "Control of Corrosion and Deposits in Stationary Boilers Residual Fuel Oil," Tech. Report, Battelle Memorial Institute, Columbus, OH, 1963.

13 "Fuel-Ash Effects and Boiler Design and Operation, " in: *Steam, Its Generation and Use*, Babcock & Wilcox, 1972, pp. 15-21, 15-26.

14 Jackson, P. J., "Deposition of Inorganic Material in Oil-Fired Boilers," *Proceedings of the International Conference on Ash Deposits and Corrosion From Impurities in Combustion Gases*, ed. R. W. Bryers, Hemisphere, 1978.

15 Rosner, D. E., "Recent Advances in the Theory of Deposition From Combustion Gases," in: "Experimental Studies of Salt/Ash Deposition Rates From Combustion Products Using Optical Techniques," *Proc. Int. Conf. on Experimental Research Into Fouling and Slagging Due to Impurities in Combustion Gases*, ed. R. Bryers (in press).

16 Friedlander, S. K., *Smoke, Dust and Haze—Fundamentals of Aerosol Behavior*, Wiley, New York, 1977.

17 Israel, R., and Rosner, D. E., "Use of a Generalized Stokes Number to Correlate the Aerodynamic Capture Efficiency of Non-Stokesian Particles From a Compressible Gas Flow to Collectors of Different Geometry," *J. Aerosol Sci.*, Vol. 2, No. 1, 1983, pp. 45-51.

18 Stearns, C. A., Kohl, F. J., and Rosner, D. E., "Combustion System Processes Leading to Corrosive Deposits," DOE/NASA/2593-27, NASA TM-81752, Mar. 1981.

19 Wiederholt, W., "Laboratory Corrosion Testing," *First International Conference on Metallic Corrosion*, Butterworths, 1962, pp. 694-700.

20 Dils, R. R., and Follansbee, P. S., "Dynamic Oxidation and Corrosion in Power Generating Units," *Corrosion*, Vol. 33, No. 11, 1977, pp. 385-405.

21 Kane, R. H., "Characterization of High Temperature Gaseous Environments," *Corrosion—NACE*, Vol. 36, No. 3, 1980, pp. 112-118.

22 Goebel, J. A., Felten, E. J., and Pettit, F. S., "Concerning the Need for Unification of Hot Corrosion Theories for the Degradation of Materials in Gas Turbine," *Corrosion Problems in Energy Conversion and Generation*, ed. C. S. Tedmon, Jr., 1974, pp. 102-117.

23 Goldstein, H. L., and Siegmund, C. W., "Influence of Heavy Fuel Oil Composition and Boiler Combustion Conditions on Particulate Emissions," *Environmental Science and Technology*, Vol. 10, 1976, pp. 1109-1114.

24 Reese, J. T., Jonakin, J., and Koopman, J. G., "How Coal Properties Relate to Corrosion of High-Temperature Boiler Surfaces," *Proceedings of the American Power Conference*, Vol. XXIII, 1961, pp. 391-399.

25 *Solvent Refined Coal (SRC) Process*, Pittsburgh and Midway Coal Corp., DOE/FE-496-109 through -496-176, Oct. 1975-Feb. 1980, and COE/ET/10104, Sept. 1980.

26 Filby, R. H., Shah, K. R., and Yaglamair, F., "The Nature of Metals in Petroleum Fuels and Coal-Derived Synfuels," *Ash, Deposits and Corrosion Due to Impurities in Combustion Gases*, ed. R. Bryers, Hemisphere; and McGraw-Hill, 1977.

27 Raask, E., "Flame Imprinted Characteristics of Ash Relevant to Boiler Slagging, Corrosion, and Erosion," ASME JOURNAL OF ENGINEERING FOR POWER, Vol. 104, 1982, pp. 858-866.

28 Wilson, J. S., and Redifer, M. W., "Equilibrium Composition of Simulated Coal Combustion Products: Relationship to Fireside Corrosion and Ash Fouling," ASME JOURNAL OF ENGINEERING FOR POWER, Vol. 96, 1974, pp. 145-152.

29 Durie, R. A., Milne, J. W., and Smith, M. Y., "The Deposition of Salts From Hydrocarbon Flames Containing Sodium and Sulfur Species," *Combustion and Flame*, Vol. 30, 1974, pp. 221-230.

30 Corey, R. C., Gragowski, H. A., and Cross, B. J., "External Corrosion of Furnace-Wall Tubes—III. Further Data on Sulphate Deposits and the Significance of Iron Sulphide Deposits," *Trans. ASME*, 1949, pp. 951-962.

31 Cain, C., Jr., and Nelson, W., "Corrosion of Superheaters and Reheaters of Pulverized-Coal-Fired Boilers, II," ASME JOURNAL OF ENGINEERING FOR POWER, Vol. 83, 1961, p. 468.

32 Lahiri, A. K., Thilakan, H. R., and Banerjee, T., "Oil-Ash Corrosion of Alloy Steels at High Temperature," *Proceedings of the 4th International Conference on Metallic Corrosion*, ed. N. E. Hamner, NACE, 1969, pp. 264-270.

33 McKee, D. W., and Romeo, G., "The Effects of Carbon Deposition on Hot Corrosion," in: *Corrosion Problems in Energy Conversion and Generation*, ed. C. S. Tedmon, Jr., 1974, pp. 118-137.

34 Hochman, R. F., "Basic Studies of Metal Deterioration ("Metal Dusting") in Carbonaceous Environments at Elevated Temperatures," *Proceedings of the 4th International Conference on Metallic Corrosion*, ed. N. E. Hamner, NACE, 1969, pp. 258-263.

25 Lefrancois, P. A., and Hoyt, W. B., "Chemical Thermodynamics of High Temperature Reactions in Metal Dusting Corrosion," *Corrosion*, Vol. 19, 1963, pp. 360t-368t.

36 Hoyt, W. B., and Caughey, R. H., "High Temperature Metal Deterioration in Atmospheres Containing Carbon-Monoxide and Hydrogen," *Corrosion*, Vol. 15, 1959, pp. 21-24.

37 Hopkinson, B. E., and Copson, H. R., "Internal Carburization and Oxidation of Nickel-Chromium Alloys in Carbon Monoxide Type Atmosphere," *Corrosion*, Vol. 16, 1960, pp. 100-104.

38 Eberle, F., and Wylie, R. D., "Attack on Metals by Synthesis Gas from Methane-Oxygen Combustion," *Corrosion*, Vol. 15, 1959, pp. 16-20.

39 Merrick, R. D., "High Temperature Furnace Corrosion of Type 309 Alloy Steel," *Corrosion*, Vol. 16, 1960, pp. 134-136.

40 Plumley, A. L., and Roczniak, W. R., "Naturally Occurring High-Chloride Coal and Superheater Corrosion—A Laboratory Study," ASME JOURNAL OF ENGINEERING FOR POWER, Vol. 104, 1982, pp. 874-884.

41 Miller, P. D., Krause, H. H., Zupan, J., and Boyd, W. K., "Corrosive Effects of Various Salt Mixtures Under Combustion Gas Atmosphere," *Corrosion—NACE*, Vol. 28, No. 6, 1972, pp. 222-225.

42 Wynnyckyj, J. R., and Rhodes, E., "Mechanisms of Furnace Fouling," *Heat Exchangers—Theory and Practice*, 14th ICHMT Symp., ed. J. Taborek and G. F. Hewitt, Dubrovnick, 1981.

Multifuel Gas Turbine Propulsion for Naval Ships: Gas Turbine Cycles Implementing a Rotating Gasifier

F. Bander
Lecturer, Turbomachinery,
Laboratory of Marine Engineering,
Royal Netherlands Naval College,
Den Helder, The Netherlands

The purpose of this paper is to investigate the possibilities of implementing a rotating gasifier to convert aero-derived gas turbines into multifuel ship propulsion units, thereby combining the advantages of lightweight and compact gas turbines with the multifuel characteristics of a rotating gasifier. Problems (and possible solutions) to be discussed are: (i) aerodynamic interaction between gas turbine and gasifier; (ii) attaining maximum energy productivity together with ease of control; (iii) corrosion and/or erosion of gas turbine components.

Introduction

In search of ways to combust low-grade fuels in gas turbines, a rotating gasifier is currently being developed in the Netherlands [1, 11].

As pointed out in the paper by LTCDR Prins [11], combining such an energy converter with gas turbines is an interesting way of attaining a multifuel ship propulsion system.

The gasifier – in which either coal or fuel oil is gasified on a rotating packed bed of suitable material – is capable of producing a hot, low-joule product gas, free of sulphur, heavy metals and alkali-metals and containing virtually no solids. At the gasification temperature of 900°C, the ash does not sinter or clincker, and in the reducing atmosphere the alkali—and heavy—metal compounds in the bed material or coal remain in the solid state.

The use of dolomite as bed material or injected in the oil, ensures maximum sulphur retention during gasification. The high rotational speed of the basket in which the packed bed is retained creates a centrifugal force field (as experienced by the bed material) equivalent to 2500g, thereby retaining all but the smallest particles (> 5 μm) in the bed and achieving a particle concentration in the product gas of less than 30 ppm. [1]. A full description of the gasifier system is presented in the paper by LTCDR Prins [11].

As in most technical developments, where problems are solved, other problems arise. In this case, the main problems, mostly relative to straightforward marine gas turbine propulsion, are:

- A more complicated propulsion system, which, aside from the normal technical/constructional problems, is mainly a control and matching problem.
- The predicted lack of corrosive and/or erosive elements in the turbine gas stream has to be proven.
- When gasifying oil, the waterborne alkali metals will have to be removed beforehand (washing and centrifuging).

A brief description of some possible combinations of the TRG with existing and design study gas turbines shows the way to three fundamental configurations. An estimate of the energy productivity of these configurations is made, control aspects are reviewed and corrosion, erosion, and deposit problems are discussed.

Possible Combinations of the TRG With Gas Turbines

As the paper by LTCDR Prins [11] argues, two ways of enhancing the future of gas turbines in naval propulsion are:

1 Implementing a fuel conversion device, such as the rotaitng gasifier described

2 Choosing a gas turbine cycle that has a better energy productivity than the now-popular simple cycle, without becoming too bulky and/or complicated.

1 When considering ways to combine the TRG with gas turbines, a principal choice arises between separate and integrated gasification. This choice is largely governed by considerations of aerodynamic matching between the components of the gas turbine. In the design of conventional gas turbines, the separate components (compressor(s), combustor, turbine(s)) are thermodynamically, aerodynamically and, where applicable, mechanically matched. In these gas turbines, the fuel/air ratio is in the order of 1.5–2 percent (when using recuperation even lower) and, as a similar percentage of compressed air is bled off for cooling and sealing purposes, the turbine gas flow is approximately equal to the compressor air flow.

If, however, the fuel is first gasified separately with air and steam and then combusted in the gas turbine (Fig. 1), the

Contributed by the Gas Turbine Division of THE AMERICAN SOCIETY OF MECHANICAL ENGINEERS and presented at the 29th International Gas Turbine Conference and Exhibit, Amsterdam, The Netherlands, June 4-7, 1984. Manuscript received at ASME Headquarters January 26, 1984. Paper No. 84-GT-265.

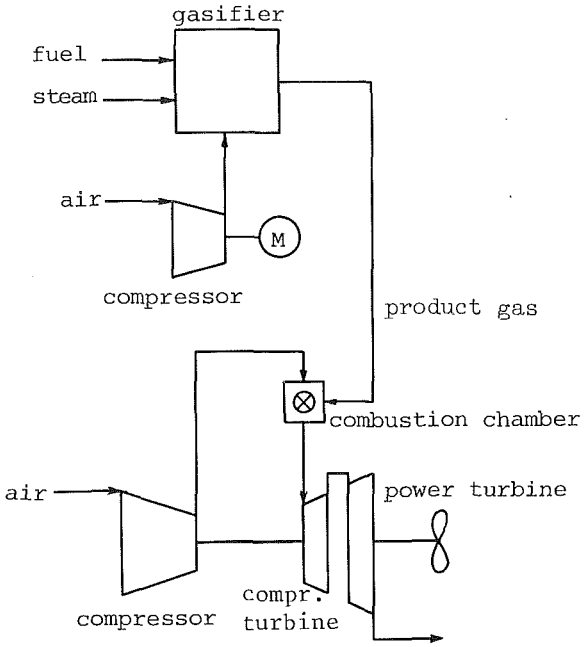

Fig. 1 Separate gasification and gas turbine cycle

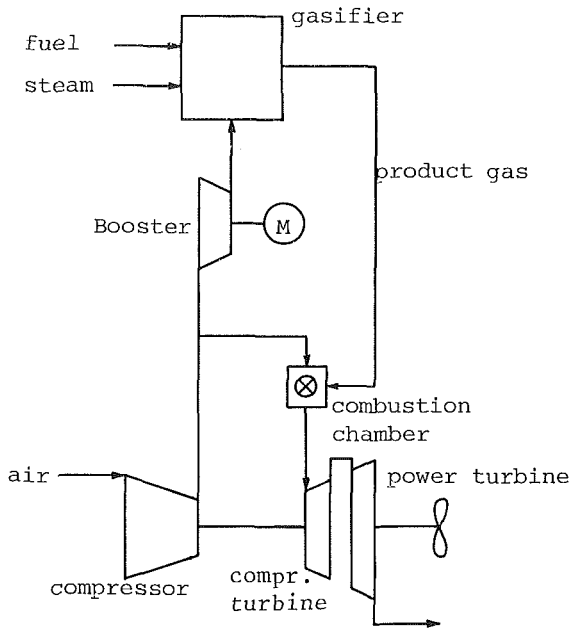

Fig. 2 Integrated gas turbine gasifier cycle

result is a relatively large mass flow of fuel gas added to the compressor air flow, leading to a higher mass flow through the turbines (up to 10 percent extra) [9, 12]. Thus, if a standard gas turbine is combined with a *separate* gasifier, the larger turbine flow will change the position of the (matched) running line of the gas turbine, usually shown in the compressor characteristic, Fig. 3.

As has been reported [9, 12] the running line will move towards, and probably pass the surge limit of the compressor(s), thus making this an impossible combination unless redesign of one or more components is considered. This not being the case, as has been stated in the introduction, the remaining option is an *integrated* gasifier, shown in Fig. 2, which has been described by LTCDR Prins [11].

2 The next step is the choice of cycles or combinations of cycles that offer good energy productivity, without becoming too bulky and/or complicated. The thermal efficiency of the simple gas turbine cycle is relatively low for two fundamental reasons.

(*i*) A large amount of energy is lost with the combustion gas exiting the gas turbine. This is a result of the high turbine inlet temperature in combination with modest pressure ratios, and the large amount of excess air inherent to the gas turbine cycle. Ways to diminish the energy lost in the exhaust gas are principally twofold:

(*a*) Use part of this thermal energy to preheat the compressed air before combustion (internal recuperation)[1]

(*b*) Extract thermal energy for use in a bottoming cycle (external recuperation)

(*ii*) In all gas turbine cycles the power needed for compression amounts to 50–70 percent of the total power developed, so that every way of minimizing the amount needed leads to a substantial increase in net power output. Efficiency, however, may or may not increase, as less compression power means lower air temperature to the combustor requiring more heat input to attain a specified turbine inlet temperature.

The compression power for a given pressure ratio is thermodynamically minimized by implementing isothermal compression as opposed to adiabatic compression. However, this poses technical problems, but a substantial reduction in compression power can still be realized by cooling the compressed air at some stage in the compression process. This

[1] Although not standardized, recuperation refers to stationary, fixed wall heat exchangers, while regeneration applies to rotary heat exchangers.

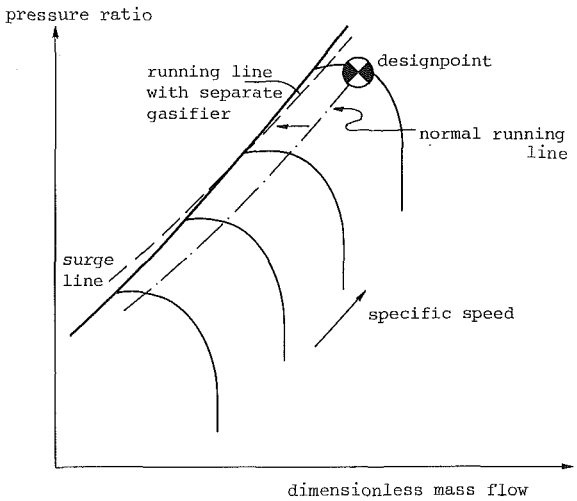

Fig. 3 Compressor characteristics, including gas turbine running line

Nomenclature

g = acceleration of gravity: 9.81 (m/s^2)
HHV = higher heating value of fuel
M = electric motor
p = pressure (bar)
s.g. = density (kg/m^3 or kg/L)
T = absolute temperature (K)
TRG = Thomassen Rotating Gasifier
wt = weight
Φ = flow (kg/s or m^3/s)

Subscripts

c = compressor or compression
gg = gasifier gas
m = mass
mg = mass combustion gas
$\dot{m}gg$ = mass gasifier gas
t = turbine

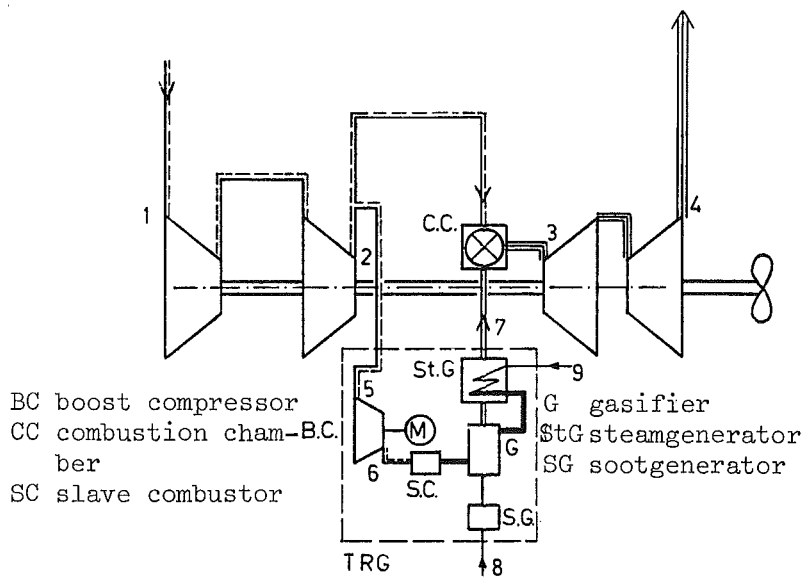

Fig. 4 Configuration 1, simple cycle with integrated TRG

point is designated "compression division point" in the following.

As compression cooling has two effects, i.e., increasing specific power and increasing fuel flow, the compression division point can be chosen to give maximum specific power or maximum thermal efficiency [18, 39]. As argued by Gasparović [39] and mentioned by Bowen [18], the optimum division point also depends on the cycle layout. When compression cooling is combined with internal recuperation, there is only a minor difference between the two optima, at approximately equal pressure ratios over both compressors. If, however, compression cooling is the only addition to the simple cycle, or when combined with external recuperation, the optimum division point for maximal thermal efficiency (being the more important criterion) is found at a low-pressure compression ratio.

As most twin-spool engines have more or less equal pressure ratios over both compressors, *efficient* compression cooling cannot be readily retrofitted to existing gas turbines unless internal recuperation is included as well.

Returning to internal recuperation, its application has mostly been confined to gas turbines of low pressure ratio, as its success is largely dependent on the temperature difference between the exhaust gas and the outlet compressor air. By adding compression cooling, this temperature difference is enlarged, thus rendering more energy recuperation possible. In this way, the overall pressure ratio has a less significant effect on cycle performance, although there will be an optimum ratio for a given cycle and turbine inlet temperature [18].

Bearing the foregoing arguments in mind, three propulsion systems combining TRG and gas turbines will be evaluated with respect to energy productivity. Taking a hypothetical second-generation aero-engine with fixed pressure ratio and turbine inlet temperature as reference, a first configuration includes only the integrated gasifier and the simple cycle aero-engine (Fig. 4).

A second configuration features integrated gasification, simple-cycle and add-on external recuperation (Fig. 5). As it is not readily possible to retrofit internal recuperation on an existing engine without aerodynamic adjustment of one or more mayor components (hp turbine, hp compressor), the third configuration combines the gasifier with an existing design of a low pressure ratio second generation heavy-duty gas turbine, with intercooling and internal recuperation (Fig. 6), having a thermal efficiency at 288 K of 44 percent [38].

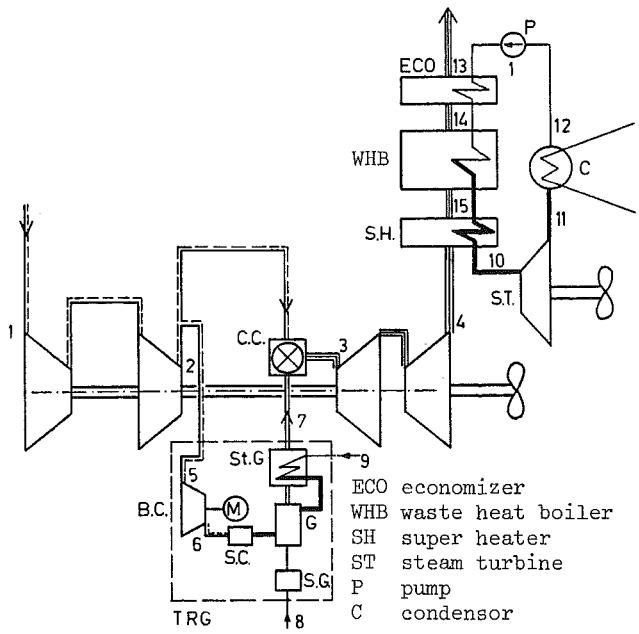

Fig. 5 Configuration 2, simple cycle with integrated TRG and external recuperation

Comparison of configuration 1 with the reference turbine will show the loss in efficiency brought about by the integrated gasifier.

Comparison of 1 and 2 will show the benefits of external recuperation. Configuration 3 gives an idea of the possibilities of compression cooling and internal recuperation and shows the feasibility of combining the TRG with an interesting gas turbine design.

Not mentioned hitherto is a factor of importance to *part-load* efficiency, e.g., variable inlet geometry [16, 17, 18], but as it can be implemented in any gas turbine cycle, it will not be evaluated in this paper.

It could be argued that use of internal or external recuperation leads to heavy, voluminous and more complicated machinery, and looking at state of the art technology this may be true.

On the other hand, there are signs of change. Recent articles [16, 17, 18] show a growing interest in recuperated gas turbines for naval propulsion and mention recuperator weights

of 10–20 tons (as opposed to heavy-duty recuperators weighing 60 tons!, for the same power). A leading navy has funded a feasibility study of retrofitting an existing second-generation aero-derived gas turbine, with intercooling and internal recuperation. And although the design used in configuration 3 represents modern heavy-duty technology more than aero-engine technology, there is no reason why aero-engine designers could not come up with similar performance for less machinery weight. (In fact, a mayor U.K. gas turbine manufacturer has just completed a study on the matter showing promising results.)

Energy Productivity and Part Load Characteristics

In order to demonstrate the thermodynamic and aerodynamic feasibility, preliminary calculations were made of the proposed systems.

Energy Productivity. The results of the preliminary design point calculations of the reference engines and the three systems considered are tabulated (Tables 2, 3). In calculating these results, the following points were observed:
Gas turbine calculations [13, 14]:

- No in- or outlet pressure losses, appropriate losses in various heat exchangers
- Polytropic and mechanical efficiencies comparable with a second-generation aero-engine-derived gas turbine were used (configurations 0, 1, and 2)
- To account for thermodynamic loss of compressor cooling flow, 5 percent extra compressor flow was calculated and treated as lost for expansion (configurations 0, 1, and 2)
- Combustor efficiency of 99 percent and a 5 percent combustor pressure drop were assumed
- In configuration 3, pressure drops, cooling flows and other losses were taken from the (proprietary) specifications of the reference gas turbine [16, 38]
- All configurations and reference gas turbines use the same fuel, specified in Table 1, and operate at 1 bar/25°C inlet conditions.

Steam turbine cycle:

- Steam pressure: 40 bar; steam temperature: 400°C; condensor pressure: 0.04 bar; pinch point temperature difference: 32°C; gasside pressure drop waste heat boiler: 0.1 bar

Gasifier [15]:

- The system boundary includes the slave combustor, the steam generator, the soot generator, and the product gas bleed line for simplification
- The gasifier efficiency—estimated to be 96 percent—is applied to the energy content of the product gas that would theoretically be produced and includes all losses inside the system boundary, as well as the power needed to drive the gasifier and the feedwater pump.
- As definite calculations of the gasifier have still to be completed, use has been made of a calculated value of the energy content of the product gas resulting from gasification at 14.8 bar, 900°C, and an absolute air/fuel ratio of 2.8, using 0.785 kg steam per kg oil. As gas composition and hence heating value are not very sensitive to pressure (see Control Aspects) this heating value was applied to the integrated gasifier system.

Table 1 presents the mayor parameters associated with the gasifier.

Configuration 1, Fig. 4, Table 2. Compared to the reference gas turbine, the extra energy losses in the integrated configuration originate from the gasification efficiency, the air boost compressor power and the lost heat of evaporation of the steam. The associated power losses amount to 1.3%, 1.1%, and 1.2% of fuel power respectively. The steam loss is structural, gasifier efficiency has been conservatively estimated and air boost compressor power depends heavily on the pressure level of the main cycle.

Any substantial increase in total efficiency will therefore have to be effected through the main gas turbine cycle. If for instance intercooling (with equal pressure ratio's over both compressors) is added to this configuration, thermal efficiency will rise to 31.5%, meaning that for this system the effects of intercooling and gasification on efficiency compensate each other.

Configuration 2, Fig. 5, Table 2. Compared to configuration 1, both net power and thermal efficiency have increased, albeit at the expense of a more complicated system. Part-load efficiency is also somewhat improved, and a

Table 1 Fuel specifications [15]

Residual oil	Product gas (4.581 kg/kg oil)	
C 85.4 % wt.	N_2 34.2 % vol.	air/fuel ratio: 2.8
H 11.4 % wt.	H_2O 5.6 % vol.	(0.225 of stoichiometric)
S 2.8 % wt.	CO_2 3.2 % vol.	
Ash 0.4 % wt.	CO 23.8 % vol.	steam/fuel ratio:
(HHV = 44431 kJ/kg	H_2 31.2 % vol.	0.785
	CH_4 2.0 % vol.	
Gasifier temperature		: 900°C
Gasification air/steam temperature		: ≥ 550°C
Steam pressure/temperature		: 33 bar/450°C
Product gas temperature		: 589°C

Table 2 Simple-cycle gas turbine

	configuration 0			configuration 1			configuration 2		
	reference gas turbine (13,14)			integrated TRG			integrated TRG + external recuperation		
position numbers see fig. 4 en 5	p bar	T K	Φ_m kg/s	p bar	T K	Φ_m kg/s	p bar	T K	Φ_m kg/s
1 air	1	298	63,36	1	298	63,36	1	298	63,36
2 air	18	750,5	60,34	18	750,5	60,34	18	750,5	60,34
3 comb. gas	17,1	1325	61,34	17,1	1325	62,44	17,1	1325	62,44
4 comb. gas	1	723,1	61,34	1	725	62,44	1,1	740	62,44
5 air	-	-	-	18	750,5	3,287	18	750,5	3,287
6 air	-	-	-	32,7	910,7	3,287	32,7	910,7	3,287
7 product gas	-	-	-	30,6	862	5,378	30,6	862	5,378
8 oil	1	423	1,0	1	423	1,174	1	423	1,174
9 water	-	-	-	1	298	0,922	1	298	0,922
10 steam	-	-	-	-	-	-	40	673	6,24
13 water/comb. gas	-	-	-	-	-	-	40/1	1/454	6,24/62,44
pressure losses (bar)									
slave combustor		-			0,8			0,8	
gasifier		-			1,0			1,0	
steam generator		-			0,3			0,3	
p_7/p_2		-			1,7			1,7	
waste heat boiler		-			-			0,1	
cycle efficiency (LHV)		31,47%			27,60%			37,09%	
power output, MW		13,390			13,561			12,336 + 5,89 = 18,226	

Table 3 Intercooled, internally recuperated cycle

see fig. 7	ref. gas turbine	integr. TRG	conf. 3 equiv. mass flow
cycle compression ratio	9	9	9
compressor mass flow [kg/s]	25	25	63,36
gasifier air flow [kg/s]	-	1,33	3,371
gasifier product gas flow [kg/s]	-	2,178	5,52
turbine gas flow (exit) [kg/s]	25,075	25,61	64,9
oil flow [kg/s]	0,41	0,475	1,204
water flow [kg/s]	-	0,393	0,945
turbine entry temp. [K]	1476	1476	1476
cycle efficiency (LHV)	43,34%	38,91%	38,97
power output MW	7,337	7,734	19,642

Table 4 Design point and idling condition for configuration 1

position numbers see fig. 5	design point p bar	design point T K	design point Φ_m kg/s	idling p bar	idling T K	idling Φ_m kg/s
1 air	1	298	63,30	1	298	18,31
2 air	18	750,5	60,34	3	448	17,49
3 comb. gas	17,1	1325	62,44	2,85	761	17,81
4 comb. gas	1	725	62,44	1	616	17,81
5 air	18	750,5	3,287	3	448	0,49
6 air	32,7	910,7	3,287	6,45	585	0,49
7 product gas	30,6	862	5,378	5,1	862	0,81
8 oil	1	423	1,174	1	423	0,17
9 water	1	298	0,922	1	298	0,14
pressure losses (bar)						
slave combustor	0,8			0,6		
gasifier	1,0			0,5		
steam generator	0,3			0,25		
p_7/p_2	1,7			1,7		

practical advantage is that external recuperation can easily be retrofitted, even in existing gas turbine ships.

Configuration 3, Fig. 6, Table 3. Table 3 contains the main parameters of the original design [16, 38], the same with TRG integrated, and a hypothetically scaled up version to be able to compare the three systems with respect to equal air flows. Note however that the TET is significantly higher, which is one of the reasons for the higher efficiency level. The relative decrease in efficiency due to the TRG is less than for configuration 1. In this configuration use of variable geometry power turbine nozzles is very effective in maintaining high efficiency at partload [17, 18].

A technical advantage of internal recuperation is the lower air temperature to the boost compressor. Another technical advantage of internal recuperation is that the air flow at compressor exit is led out of the axial flow path, facilitating extraction of the gasifier air flow.

As far as design point matching is concerned, the configurations all show a small increase in turbine flow (2 percent) due to integration of the gasifier, as well as a slight increase in the specific heat capacity of the combustion gas. In the case of a retrofit to an engine with a normally choked power turbine, both factors independently will lead to a slight increase in compressor speed, pressure ratio, and air mass flow. This increase will be correspondingly slight and will not necessarily diminish the surge margin of the compressor(s).

Part-Load Characteristics. To be able to estimate the control problems associated with running the system from no load to full load, a cycle calculation of configuration 1 at gas turbine idling condition was performed, at which point gasifier and gas turbine match quite well. The results of these calculations are summarized in Table 4 and used in Control Aspects.

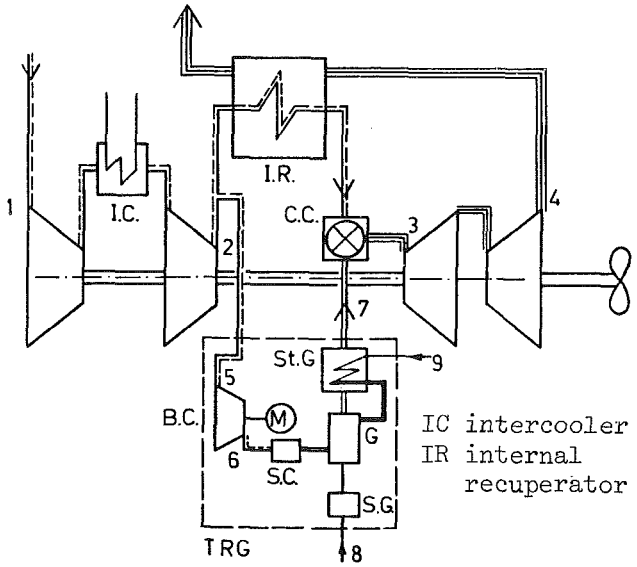

Fig. 6 Configuration 3, internally recuperated, intercooled cycle with integrated TRG

Part-load operation of the gas turbine is not significantly influenced by gasifier operation, although the air boost compressor power requirement decreases relative to gas turbine output. Part-load efficiency will therefore be primarily dictated by part-load performance of the gas turbine cycle.

Control Aspects

Control aspects can roughly be divided in two categories:

1 Steady-state and transient control of the installation from idling to full power, at the fastest possible rate.

2 Control aspects related to starting, stopping, emergency shutdown and other intentional or unintentional disruptions of normal operation

1 Operation of the Installation From Idling to Full Load. This part of the operation has two aspects:

(*a*) All components must be matched at every point over the load range

(*b*) Transition from one load to another must be achievable with a minimum of control effort and at an acceptable rate.

The overall control system must match gasifier performance to the inevitable variation of pressure and temperature level and varying flow requirements of the main gas turbine as a function of load, while the gasifier system as a whole has its own characteristics of pressure drop (variation), various interrelated flow requirements, etc. Predictable problem areas are the air boost compressor (which operates between a variable inlet temperature and pressure and a differently varying outlet pressure) and the gas boost compressor (which is dependent on the bed material circulation system). As a number of subsystems with specific constraints can be identified, control of these subsystems will be dealt with first, resulting in an overall control strategy.

As has been stated in Operating Characteristics, air/fuel and steam/fuel ratios in the *gasifier* can be held constant over the full range of control and thus the heating value and temperature of the product gas should be constant as well. The only other possible variable is the temperature of the incoming air/steam mixture, and it is the objective of the slave combustor to produce a constant temperature flow of gasification air/steam. In the integrated system, however,

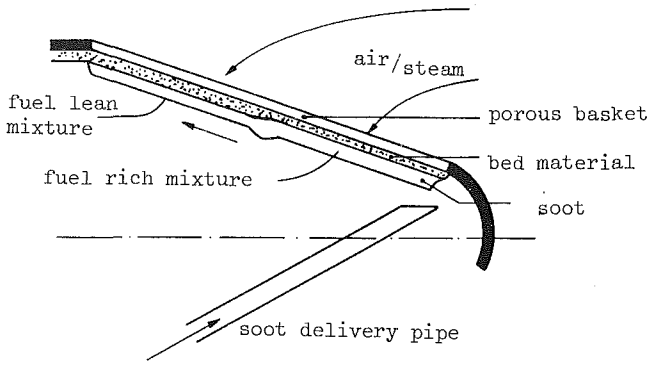

Fig. 7 Lean and rich zones halfway a load transient (more fuel)

gasifier pressure can change by a factor 6, and as pressure has a slight influence on gasification reactions and hence gas composition, the changes in product gas properties were calculated for a similar pressure change [19].

The results are: At constant temperature, heating value decreases by 5 percent and specific mass, molar weight, and Wobbe Index all change less than 5 percent. For the gasifier itself, this means that straightforward control of the fuel flow and slave control (easily automated) of air and steam flow will produce a direct proportional amount of fuel power to the gas turbine combustor.

In fluidized bed gasification, a temperature control flow (water, steam, or stack gas recycle [3, 10, 12]) is needed to control gasifier temperature, because gas-composition and heating value vary as a result of varying air/fuel ratio. Therefore, the described constant ratios in the TRG are of distinct advantage as no such extra flow is necessary. Rotational speed and total bed depth for a given fuel quality can be held constant.

For soot generated from residual oil, a residence time of 20–30 s, depending on soot particle size, is estimated (actually gasification time is estimated and equal residence time is the result). The rate at which the fuel flow can be changed will be dependent on this residence time as will be explained in the following. If the amount of soot deposited on the bed is changed, it will take the residence time before the whole bed area has received the new amount of fuel. Meanwhile the amount of gasification air/steam is being adjusted, and although the overall air- and steam/fuel ratios can be kept constant, at half the residence time (the air/steam flow having been adjusted halfway), there will be too little air/steam flowing through one-half of the bed, and too much through the other half, Fig. 7. The limit of fuel change rate is determined by the appearance of a local oxidizing zone in the fuel-lean bed area previously described. However, as fuel flow changes will be of a more gradual nature (e.g., ramp function), and taking into account the relatively short residence time, this limitation is not expected to be serious.

The *air boost compressor* aero- and thermodynamically takes a floating position between the main compressor and the gasifier, having a variable inlet pressure, as well as a variable pressure ratio and massflow. As the objective of the boost compressor is to overcome the flow restrictions imposed by slave combustor, soot generator, gasifier, steam generator and fuel nozzles of the main combustion chamber, the necessary pressure ratio will be dependent on the sum of these restrictions and on the discharge pressure of the main compressor.

The pressure ratio of the fuel nozzles can be evaluated as follows: If a (near-) sonic velocity through a convergent nozzle, constant over the load range, isentropic flow, constant gas composition and ideal gas behavior are assumed, a constant (over-) critical pressure ratio over the nozzles is required. The mass flow will be proportional to the inlet pressure of the product gas. Taking this pressure ratio as 1.7, the full-load gas inlet pressure will be 30.6 bar and idling inlet pressure 5.1 bar, giving a turndown ratio of 6, which is well matched to the fuel oil turndown ratio.

If the pressure drops over slave combustor, gasifier and steam generator are respectively 0.8, 1.0, and 0.3 bar at full load, and 0.6, 0.5, and 0.25 bar at idling, the pressure ratio of the air boost compressor can be calculated, resulting in a ratio of 1.817 at full load, and 2.150 at idling. As mass flow and dimensionless mass flow increase with load, the requirements of the system would seem to conflict with conventional turbocompressor running characteristics (Fig. 3). However, the required dimensionless mass flow turndown ratio is 1.44 and radial flow compressors, as used in turboblowers for diesel engines, are capable of passing such a dimensionless mass flow ratio at constant speed with a negative pressure ratio change [20, 21]. To be able to instantly change the air flow to the gasifier, without having to wait for the main compressor to speed up or slow down, a control valve in the discharge line of the air boost compressor is needed. If this valve is controlled directly by the fuel oil control system, the following strategy is feasible. More fuel needs more air, so the valve opening is increased, thereby lowering the pressure ratio of the boost compressor and thus more airflow is delivered by the boost compressor. When gas turbine reaction sets in the main compressor discharge pressure rises, but the back pressure at the entrance to the slave combustor rises less, so the boost compressor ratio decreases further. A control loop that relates p_6 to fuel flow or soot generator temperature overrules the initial control signal to the valve and closes it to allow the boost compressor to deliver the correct amount of air compatible with the fuel flow.

The *gas boost compressor* delivers a gas flow that is separated to perform three functions:

1 A small portion of the gas is combusted in the soot generator.

2 Part of the flow is combusted in the slave combustor to bring the gasification air/steam mixture to the required ignition temperature of the coal or soot.

3 The remaining portion is used as pneumatic transport medium for recirculation and make-up of bed material.

The amount of gas needed for combustion in the slave combustor depends mainly on the amount and temperature of the compressed air entering the slave combustor, and the gas mass flow is accordingly calculated to vary by a factor of 2.3 (see slave combustor). The gas pressure is not critical, and the gas-nozzle can be designed to operate at the pressure dictated by the requirements of the pneumatic transport system.

The amount of bed material recirculating is dictated by the requirement that the total bed mass remain constant over the load range (for a given fuel quality). In this way, gasifier speed can be held constant over load range. As total bed mass is the sum of fuel and bed material, the amount of bed material must be adapted inversely to the amount of fuel. There are several ways to achieve this and the gas mass flow and pressure requirements will depend on the method adopted.

(*a*) One solution is a *constant* circulating volume flow in which bed material can be added or removed as required. In this case a constant pressure ratio (over a convergent nozzle) is needed.

(*b*) Another possibility is to use *variation* of volumetric gas flow rate to transport more or less material per unit time to the bed. This requires a constant gas pressure before a velocity nozzle.

Considering option (*a*) above, this means a gas mass flow turndown ratio of 6 for the transport system, and for the gas boost compressor a mass flow turndown ratio of approximately 3.5 and a constant compression ratio of about 2. However if the dimensionless mass flow is calculated, the boost compressor must pass about *twice as much* dimensionless mass flow *at idling*, than at full load (at constant pressure ratio). This problem can be overcome by adopting a variable speed drive combined with a controllable pressure reducing valve in maximum reduction setting at idling. The power loss will be slight because of the small mass flow (40 g/s) and the low temperature level (400 K).

Aside from its role in the start-up sequence described later, the *slave combustor* is incorporated to guarantee a sufficiently high temperature of the air/steam gasification flow. Using the appropriate process parameters a first-order calculation shows that, although the temperature rise necessary at idling is about 300 K larger than at full power, the much larger air mass flow at full load requires 2.3 times more product gas to be combusted at full load, than at idling.

A straightforward control method is to throttle the gas flow to the slave combustor as a function of the combustor outlet temperature. This coincides well with the part load operation of the gas boost compressor.

The *steam generator* must raise the required amount of steam at constant pressure and temperature and if possible cool the product gas flow to a *constant* temperature over the load range. This seemingly formidable task is greatly relieved by the adoption of constant air/fuel and steam/fuel ratios, which lead to a constant air/steam ratio over the load range. Thus the energy balance over the generator reduces to a specific enthalpy balance (neglecting the influence of pressure fluctuations on the gas side) and a constant gas outlet temperature is assured. The steamflow (= waterflow) can be conventionally controlled by a return line over the feedpump or a direct flow control valve in the pump discharge line to the steam generator.

The amounts of air and product gas that are *combusted* in the *soot generator* are directly proportional to each other and to the oil flow entering the soot generator. As the pressure difference between the air boost compressor and the exit of the soot generator is equal to the (large) pressure drop over slave combustor and gasifier, (1.1 to 1.8 bar), it is possible to control air flow to the soot generator by a control valve in relation to fuel flow. A flow control valve in the product gas line to the burner functions on the same control input. Dolomite feed to the fuel/dolomite mixer is controlled parallel to the main fuel flow. Residence time in the soot generator is estimated to be between 10 and 50 milliseconds.

The *overall control strategy* has been more or less unfolded in the foregoing and what remains is a summary linked to ship propulsion control. In most cases, ship propulsion power is measured as – and controlled by – shaft revolutions. Any difference between measured and selected revolutions will be transformed into a control signal to the fuel system. Whether parallel signals are sent to gasifier air and steam systems, or slave signals – derived from fuel flow or product gas flow change – are used, will depend largely on the dynamic response times of the various subsystems.

To summarize the main points of control, a brief telegram style description follows of a power reduction:

1st control signal source: selected shaft rpm < measured rpm

1st actions:
- fuel and dolomite flow decrease, air and gas to burner of soot generator decrease
- air boost compressor discharge valve throttles, boost compressor ratio rises, less air to gasifier
- bed material circulation rate rises
- net water flow decreases.

1st results:
- product gas flow decreases
- TET decreases
- gas generator and power turbine rpm decrease
- gt compressor outlet pressure and temperature decrease, thus further increasing boost compressor ratio and decreasing air flow.

2nd control signal source: - air boost compressor discharge pressure (upstream of valve) decreases below control value related to fuel flow or gasifier temperature.

2nd actions: - discharge valve opens far enough for boost compressor to establish aerodynamic balance between main compressor discharge pressure and required airflow (as related to fuel flow or gasifier temperature).

Overall response times can be limited by one or more of the following factors.

- Thermal or mechanical inertias
- Large gas volumes
- Allowable fuel flow change rate
- Possible bed material change rate

Neither thermal nor mechanical inertia will pose a problem as the highest temperatures are constant over the load range and the components of the system are of low weight and volume, which also precludes large gas volumes. The allowable fuel flow change rate will be dictated by the transient local air-fuel ratios as pointed out, but given an average gasification (= residence) time for soot of 20–30 s, the maximum fuel flow change is estimated to take 1 to 3 min. The bed material recirculation system will be capable of changing the bed inventory in the same rate as the fuel flow is changed as the difference between maximum and minimum bed inventory is approximately 8 kg (being equal to the maximum change in fuel inventory) and a rate of change of 4 kg per minute is certainly feasible.

2. Control Aspects Related to Starting, Stopping, etc.

Start Procedure. The combustor of the gas turbine is equipped with dual fuel nozzles and is therefore started on a destillate fuel, with the gasifier system off-line. At gas turbine idling condition, air is bled through the air boost compressor, reduced to almost atmospheric pressure by the control valve, and passed through the gasifier and the steam generator to an atmospheric outlet. Distillate fuel is combusted in the slave combustor and the hot combustion gas raises steam in the steam generator. When sufficient steam is available to pressurize the gasifier seals, the slave combustor and gasifier are gradually pressurized by opening the air control valve and starting the air boost compressor.

The gasifier can now be started and by passing part of the combustion gas through the gas boost compressor line to the pneumatic conveyor, bed material circulation can be set up. Dolomite or other bed material can be added at this stage. If the residual oil has been heated sufficiently, compressed air and product gas can be fed to the soot generator, and ignited, producing a near stoichiometric combustion gas in which the fuel oil flow can now be partially gasified and converted to dry soot. When this soot reaches the gasifier bed, gasification commences.

The main gas flow is flared (without burning) to atmosphere while the gas boost line is purged with product gas. The slave combustor and soot generator can be switched to combustion of product gas. The last step is to shut off the flare and switch over to gas combustion in the gas turbine combustor. This procedure might require 15 to 30 min, but if necessary, it is of course possible to get *on load* on distillate fuel and change over when convenient as, aside from using a slight amount of bleed air from the compressor, the start of the gasifier is performed independently of the gas turbine.

Shutdown Procedure. To prevent blockage of fuel lines with residual oil, the first step is to switch over a distillate fuel to the soot generator. After shutdown of fuel flow, the gasifier airflow can be reduced via the control valve, and by keeping steam flow constant, a steam purge of the gasifier and product gas line is effected. At the same time, gas turbine combustion is changed to distillate fuel and the gas turbine can be shut down independently. If necessary, the slave combustor can be switched to distillate fuel and with the air boost compressor switched to atmospheric air intake, the gasifier can be kept at temperature or shut down at will. Before the gasifier is stopped, bed material circulation is terminated, allowing most of the bed material to leave the gasifier. Sealing steam is kept on until the gasifier is stationary.

The problem of a transient local oxidizing atmosphere in the gasifier during changes of fuel flow, as described under Gasifier Control, arises during start and stop sequences as well. A solution here is to overfuel (on start up) during a time equal to the residence time, thus making it impossible for all the soot to start *and complete* gasification in the same time. During shutdown the problem is solved by the steam purge, as described.

The need for an *emergency shutdown* can arise from faulty gasifier operation or faulty gas turbine operation. In the latter case the product gas is flared off so that the gas turbine can be stopped immediately, and the gasifier can be shut down at a normal rate, the air boost compressor taking in atmospheric air. If the problem stems from the gasifier, the procedure to be adopted will depend on the nature of the problem. In all events, the gas turbine can be instantly switched to distillate fuel, so that power output need not be lost.

Development has not yet reached a point where all possible gasifier upsets, let alone solutions to them, have been recognized. However, one possible major problem to be solved is evident; a crash stop of the rotating basket while containing a high fuel inventory can lead to a temperature overshoot that could melt the bed material and/or damage the gasifier structurally.

Corrosion, Erosion, Deposition

Although it is known that corrosion, erosion, and deposition are interdependent mechanisms, and positive synergisms have been demonstrated [12, 24], the scope of this paper only permits a brief first-order evaluation of each mechanism individually.

Corrosion. Problems: The main source of gas turbine corrosion are well documented [12, 25, 26, 27], as being sulphur, alkali metals, vanadium, lead, chlorine, and especially combinations of these elements, in the presence of oxygen at elevated temperatures. These elements originate from the air, the bed material, and for the most, but least predictably, from the fuel [35]. To set the scene, a "worst possible" fuel oil in the next decennia can be specified as follows [12, 28]:

- Specific mass : 0.99 kg/l
- Viscosity : 500–700 cSt (5000-7600 s RI)
- Sulphur : 5 percent (mass)
- Vanadium : 600 ppm (mass)
- Alkali metals : 500 ppm (mass)
- Ash content : 1–5 percent (mass)

Solutions: Sulphur retention is achieved in the soot generator by reaction of H_2S with dolomite, forming CaS and MgS (solid). As long as the dolomite is dispersed in a small enough size, the residence time in the soot generator is long enough to enable this reaction (0–40 milliseconds) to take place. The ratio of dolomite to fuel flow will determine the percentage of sulphur retained; 95 percent retention is regarded feasible. The CaS and MgS are deposited on the bed material with the soot and remain there while the soot reacts with the incoming air. Eventually the CaS and MgS leave the bed circulation system along with the ash, and can if necessary be transformed to $CaSO_4$ and $MgSO_4$ by oxidation (for instance in a small portion of the exit combustion gas) [3, 6].

As has been noted earlier, vanadium and other heavy metals (lead, etc.) in the fuel are expected to react with the dolomite and form compounds with high melting points. In the case of vanadium, the long established practice of doping the fuel oil with magnesium is imitated by coincidence in the proposed system by the introduction of dolomite in the fuel oil, so that vanadium retention is started in the soot generator and ends in the bed material. By relying on these mechanisms, it is assumed that the product gas is free of heavy metals [5, 12, 26, 28, 30, 31].

Alkali metals and chlorine are present in the fuel, the air, as well as in the dolomite (or other natural bed material). Of the alkali metals in the dolomite, it is well known [33, 34] that they are present in two forms: (*a*) as a solid in clay minerals; (*b*) as chlorides originating from the ground water. Experiments in gasifying conditions [7, 33, 34] have shown that, given time, the alkali chlorides will evaporate, while the remaining alkali metals are transformed to stable alkali silicates. In times ranging from 5 min to several hours 1 to 10 percent of alkali metals can volatilize [7, 33, 34].

In the case of the rotating gasifier and the soot generator, however, residence times—30 s and 50 milliseconds, respectively—are so short that it can be assumed that no significant amount of alkali metals will volatilize from the dolomite and/or the bed material. By far the greater part of alkali metals in the fuel originates from the groundwater and/or in a marine environment from seawater contamination. In both cases, they are in the form of chlorides, and when the oil is volatilized in the soot generator, these compounds will evaporate, rendering the chance of retaining these alkali metals in the gasifier bed material very slight. It will therefore be assumed that any alkali metal in the oil will be present in the product gas, and so, albeit diluted, in the combustion gas.

For this reason, if a fuel oil containing more than 20 ppm alkali metals is to be used, a fuel washing and centrifuging system will have to be installed [31, 32, 36]. A typical system has two stages of water wash and centrifuging, resulting in a cleaned oil containing 1 ppm (weight) or less of alkalimeter [36]. Requirements are: up to 5 percent fresh water if alkali content of fuel is 500 ppm, 0.02 percent emulsion-breaking fluid, fuel and water heating to 95°C. The effluent water contains from 50–500 ppm oil, which, if first stored in a settling tank, can be discharged within environmental limits at sea [36].

The high specific gravity of residual fuels can be a problem with respect to centrifuging; however, it has been demonstrated [28] that a difference in specific gravity of 0.01 kg/L is sufficient. If the maximum s.g. of 0.99 kg/L, together with the larger temperature effect on s.g. of oil and the fact that the water contains salt, are taken into account, the problem ceases to exist. It will thus be assumed that 1 ppm alkali metals or less is present in the fuel oil entering the gasifier system.

Evaluation of Possible Corrosive Contaminents in the Combustion Gas Entering the Turbine. By assuming the amounts in the ingoing flows of fuel, air, and steam estimating the amounts that are not retained in the bed material or elsewhere, and taking into regard the respective flow ratios, it is possible to calculate the expected amounts of contaminants. Assuming the cited "worst" oil specifications,

a salt content in the air after filtration of 0.05 ppm [12], a salt content in the oil after treatment of 1 ppm Na, and a sulphur retention capability of 95 percent, the calculations predict 0.06 ppm Cl^-, 0.03 ppm alkali, and 100 ppm SO_2 in the combustion gas. Compared with the current limits imposed on aeroderived gas turbines, as cited in [12], (150 ppm S, 0.025 ppm Na, 0–30 ppm Cl), these results are encouraging as they are certainly of the same order as—and in fact stay within—the limits. On one side caution is necessary, as experiments will still have to prove the foregoing assumptions to be valid. On the other hand, the development of turbine blade protective claddings is still progressing and shows promise of even better results in the future [12, 35].

Erosion And Deposition. The mechanisms of erosion and deposition are interrelated in that larger particles with high velocities cause erosion and small particles with lower velocities are deposited, with the intermediate particle size capable of both [12, 24].

Many known and unknown parameters influence the actual events, a major factor being the geometry of the engine, a fact that renders the outcome of small scale experiments of relative use [12]. Not only must the maximum allowable particle size (mostly designated by diameter, although mass also plays a role) be defined, the maximum concentration (ppm mass or volume) must be specified as well. The former is dictated by erosion mechanism, the latter by deposition. A literature study [12, 24] cites maximum particle size at 10 μm and maximum concentration as 25 ppm (mass), whereas a calculated estimate specifies no particles larger than 6 μm and a maximum concentration of 5 ppm (mass) [37].

As stated earlier, the only elutration occurs at the surface of the bed, thus drastically reducing the amount of particles entrained, compared to fluidized bed technology. A preliminary estimate shows that a mass concentration of *less than 30 ppm* is expected to leave the bed.

The maximum size of elutriated particles is dictated by the rotational speed and can thus be chosen to meet the turbine restrictions. In the proposed gasifier, only particles *smaller than 5 μm* will enter the turbine, which seems a tolerable size. And as the product gas is substantially diluted by the combustion air, less than 3 ppm is expected to enter the gas turbine.

Conclusions

- A highly innovative energy converter of excellent efficiency is in a decisive design stage. Although a number of technical problems still have to be solved, the basic principles are soundly established.
- Integration of the TRG with a second-generation, aeroderived or heavy-duty gas turbine is feasible, as no major matching or control problems arise and the combustion gas is clean enough to ensure a reasonable turbine life.
- As there is a 10–12 percent relative reduction in cycle efficiency, a high efficiency gas turbine cycle is recommended.
- When designing for a specific ship, machinery weight and volume being restricted, there would appear to be an overall choice between:

  - cruise and boost aero-engines, both integrated with TRG's
  - one or more engines of the same size with TRG integrated, and using compression cooling, internal recuperation and variable power turbine geometry.
  - In the case of a retrofit, external recuperation can more than off-set the efficiency loss caused by the gasifier.

Acknowledgments

The author is indebted to the inventor of the Thomassen Rotating Gasifier, ir. Alwie J. W. Oude Alink, without whose generous cooperation this paper could not have been written at all. The author also wishes to thank ir. Bud P. van Marle and others of Thomassen International for their assistance in supplying information needed to produce the paper. The cooperation with ir. Roel T. G. Prins has benefited us both.

References

1 Hendriks, R., Van Marle, B. P., Oude Alink, A. J. W., "Apparatus for the Gasification of Fuel," U.S. patent No. 4317658 d.d. 2 March 1982; also, Oude Alink, A. J. W., "Method and Installation for Preparing a Combustible Gas Mixture," Rep. South Africa patent No. 82/1390 d.d. 26 Jan. 1983.

2 Brown, T. D., "Coal Gasification—Combined Cycles for Electricity Production," *Progr. Energy Combust. Sci.*, Vol. 8, 1982, pp. 277–301.

3 Newby, R. A., et al., "Fluidized-Bed Oil Gasification for Clean Power Generation—Atmospheric and Pressurized Operation," *Proc. 3ICFBC*, Hueston Woods, 1973, pp. IV-5.

4 Johnes, G. L., et al., "Samengevatte teksten van de conferentie: Fluidized Bed," *Energie Spectrum*, Vol. 2, No. 5, May 1978, pp. 125–135.

5 Johnes, G. L., "Fluid Bed Gasification of Coal and Heavy Fuel Oil for Clean Power Generation," *Proc. of Conference Fluidized Combustion: Systems and Applications*, London 1980, pp. IB-5.

6 Ramsden, A. W., and Kowszun, Z., "Chemically Active Fluid-Bed Plant for Sulphur Removal During Gasification of Heavy Fuel Oil Phase 4," EPA-600/7-79-066, Feb. 1979.

7 Mulik, P. R., et. al., "High-Temperature Removal of Alkali and Particulates in Pressurized Gasification Systems," 26th Int. Gas Turbine Conference, Houston, 1981, Paper No. 81-GT-67.

8 Foster-Pegg, R. W., "The Integration of Gasification with Combined Cycle Power Plants," J.A.C.C. 1979, Denver AIChE paper, unnumbered.

9 Van Marle, B. P., Multifuel Scheepsvoortstuwing met Gasturbines, internal survey, July 1982, Thomassen International.

10 Kapteijn, P. K. A., "Fluidized Bed Energie Conversie R en D rapport," 79002 dl 1 en 2, RSV-concern, 1980.

11 Prins, R. T. G., "Multifuel Gas Turbine Propulsion System for Naval Ships. Part I: Logistic and Operational Rationale," ASME Paper No. 84-GT-207.

12 Bander, F., "Onderzoek naar de Toepasbaarheid van Wervelbed-Energie-omzetting in Kombinatie met Scheepsgasturbines," Afstudeeropdracht TH-Delft, 1982.

13 De Biasi, V., "Mid-1983 Delivery for Marine Spey Engines," Gas Turbine World, Mar. 1980.

14 General Electric, Product Information, 1983.

15 Oude Alink, A. J. W., "Thomassen Rotating Gasifier, Technical Description," June 1983.

16 McCoy, A. W., "Gas Turbine Propulsion Systems for Small Naval Ships," ASME Paper No. 80-GT-110, New Orleans, 1980.

17 McCoy, A. W., "Regenerative Gas Turbines for Naval Escorts Ships," ASME Paper No. 81-GT-115, Houston, 1981.

18 Bowen, T. L., Ness, J. C., "Regenerated Marine Gas Turbines, Part I: Cycle Selection and Performance Estimation," ASME Paper No. 82-GT-306, London 1982; also, Watts, J. W., and Bowen, T. L., "Regenerated Marine Gas Turbines, Part II: Regenerator Technology and Heat Exchanger Sizing," ASME Paper No. 82-GT-314, London, 1982.

19 Oude Alink, A. J. W., personal memorandum.

20 Hartley, J., "Turbocharging and Turbochargers," *Review of I Mech E. conference*, London, 1978; *Automotive Engineer*, June/July 1978.

21 Anon., "Turbocharging Progress by Holset," *Diesel Engineering*, Summer 1978.

22 Metcalfe, C. I., and Howard, J. R., "Combustion Experiments Within a Rotating Fluidized Bed," *Proc. 5 ICFBC*, Vol. III, Washington, 1977, pp. 275–286.

23 Levy, E. K., Norman, W. M., and Chen, J. C., "Centrifugal Fluidized Bed Combustion," *Proc. 5 ICFBC*, Vol. III, Washington, 1977, pp. 288–296.

24 Stringer, J., et. al., "Assessment of Hot Gas Clean-Up Systems and Turbine Erosion/Corrosion Problems in Pfbc Combined Cycle Systems," ASME Paper No. 79-GT-195, San Diego, 1979.

25 Condé, J. F. G., and McCreath, C. G., "The Control of Hot Corrosion in Marine Gas Turbines," ASME Paper No. 80-GT-126, New Orleands, 1980.

26 Bornstein, N. S., and De Crescente, M. A., "Deposition in Gas Turbine Engines," ASME Paper No. 81-GT-192, Houston, 1981.

27 McCarron, R. L., et al., "Turbine Materials Corrosion in the Coal Fired Combined Cycle," *Proc. 5 ICFBC*, Vol. III, pp. 714.

28 Bauer, W., "Die Zükunftigen flüssigen Brennstoffe für die Seeschiff-fahrt," Schiff & Hafen/Kommandobrücke, Heft 3/1980 32. Jahrgang.

29 Barker, D., and Beacham, B., "Development and Commercial Application of Liquid Fueled Fluidized Combustion," *Proc. Conf. Fluid-Combustion Systems and Applications*, London 1980, nr. I.A.-3.

30 Lunn, H. G., et. al., "Combustion of Residual Fuels in Fluidized Beds," *Proc. 3 ICFBC*, Hueston Woods 1973, pp. V-5.

31 Meyer, J. H., "Evaluation of the Impact on C.G.T. Operation When Converting to Crude Oil Fuel," ASME Paper No. 81-GT-207, Houston 1981.
32 Tomlinson, L. O., and Alff, R. K., "Economics of Heavy Fuels in Gas Turbines and Combined Cycles," ASME Paper No. 81-GT-45, Houston, 1981.
33 Keairns, D. L., et al., "Pressurized Fluid Bed Combustor Gascleaning Turbine Systems Integration," *Proc. 6 ICFBC*, Vol. II, Atlanta, 1980, pp. 270–282.
34 Mulik, P. R., Alvin, M. A., and Bachovchin, D. M., "Simultaneous High-Temperature Removal of Alkali and Particulates in a Pressurized Gasification System," 5th Quarterly Report DOE/MC/16372—5.
35 Wenglarz, R. A., Alvin, M. A., and Schneider, S. J., "Predictions of Combustion Turbine Performance in Pressurized Fluidized-Bed Combustion Power Plants," EPRI report CS-1845, May 1981.
36 Henke, R. T., Dreymann, S. S., and Hickey, J. W., "Liquid-fuel Treatment Systems," Gas Turbine Reference Library, GER-2484C, General Electric.
37 Menguturk, M., and Sverdrup, E. F., "Calculated Tolerance of a Large Electric Utility Gas Turbine to Erosion Damage by Coal Gas Ash Particles." *Erosion*: Prevention and Useful Applications, *ASTM*, STP 664, 1979, pp. 193–224.
38 Hendriks, R., and Levine, P., "Cycle Optimization for a 10.000 SHP High-Efficiency Gas Turbine System," ASME Paper No. 80-GT-157.
39 Gasparovic, N., "Some Considerations on Gas Turbine Cycles," Doctoral thesis, TH-Delft, 1971.

APPENDIX

Technical Description

The gasifier, as described in [11], can be built in three versions:

(*a*) for gasifying coal
(*b*) for gasifying coal with simultaneous retention
(*c*) for gasifying fuel oil with or without sulfur retention

Figure 8 shows the oil gasifier unit (*c*), which is the most interesting for marine – certainly naval – propulsion.

Referring to Fig. 8, the main components of the gasifier are the porous basket (13) and the gasifier housing (4). The conically shaped basket has a porous wall, the rounded cone being massive. The basket is attached to the hollow drive shaft (10) by the basket support (8) to which a cylindrical outlet ring (5) is bolted.

The cylindrical housing is split horizontally, bolted to the drive housing (15) on one end and closed off by a cover (3) in which the product gas discharge pipe (1) is situated. The gasifier housing further contains seals (9) around the drive shaft (10) through which the gasifying air/steam mixture is admitted to the porous basket. A particle collector (11) retains the bed material leaving the basket, which is led from the housing by the solid discharge pipe (12). A heat shield (14) limits the gasifier housing temperature. Not shown is an inlet pipe through which an inert material such as dolomite or another appropriate bed material is fed onto the inside of the basket, near its smallest radius.

As the packed bed gasifier will only accept dry fuel, a state-of-the-art soot generator is used to convert the fuel oil to a mixture of gas and soot. The soot generator consists of a housing (16) and oil (or gas) burner (19), oil feed points around the circumference of the housing (18), and a ceramic combustor lining (17).

Operation of the Gasifier

In the soot generator a small portion (4 percent) of the product gas is combusted, slightly over stoichiometric, producing a hot gas of 1500–1700°C, in which the fuel oil (containing fine dolomite particles) is partially gasified in air to produce dry soot and low-Joule gas. The gas transports the soot through the delivery pipe (2) onto the layer of bed material (6) that forms a packed bed against the inside of the porous basket. As described, the packed bed moves at uniform rate outward along the basket wall. Residence time of the layer and thus the soot is governed by the total mass of the bed + soot.

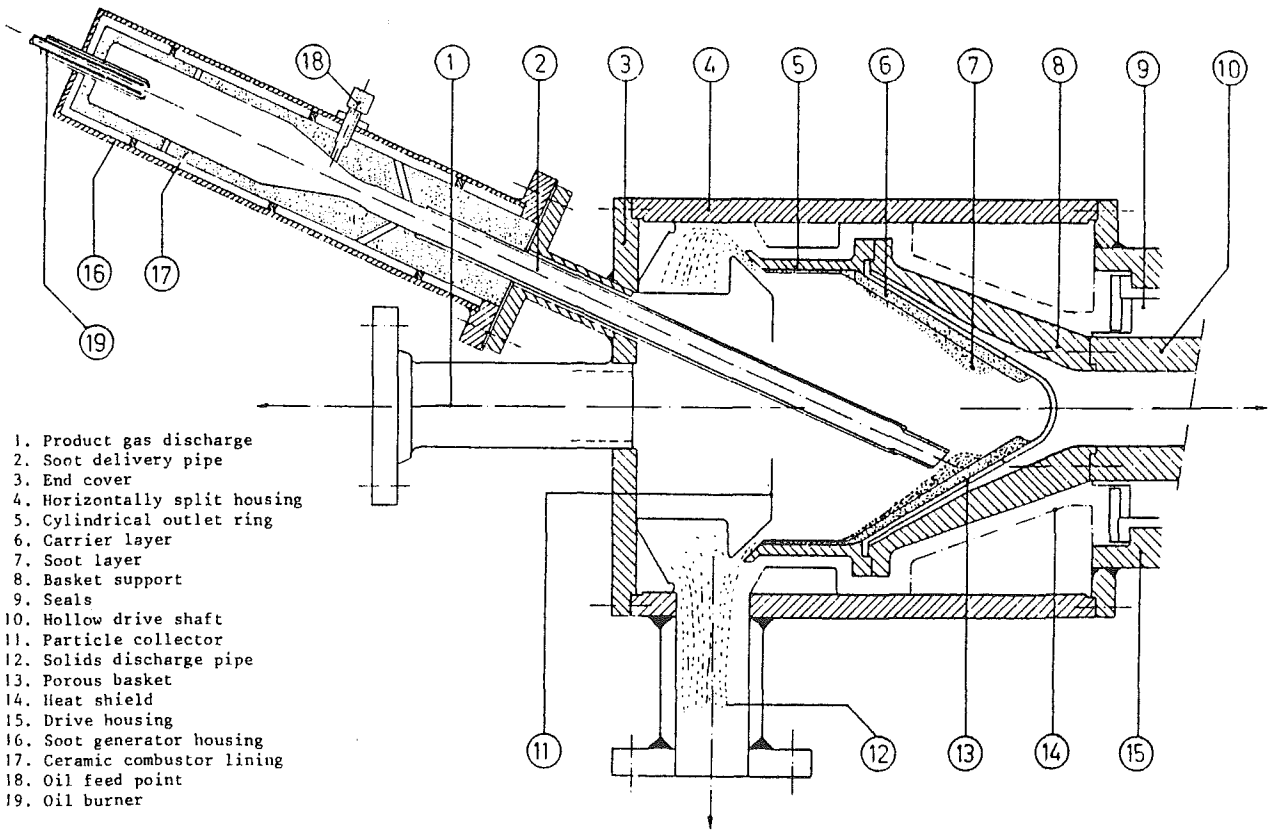

Fig. 8 Rotating gasifier for residual oil

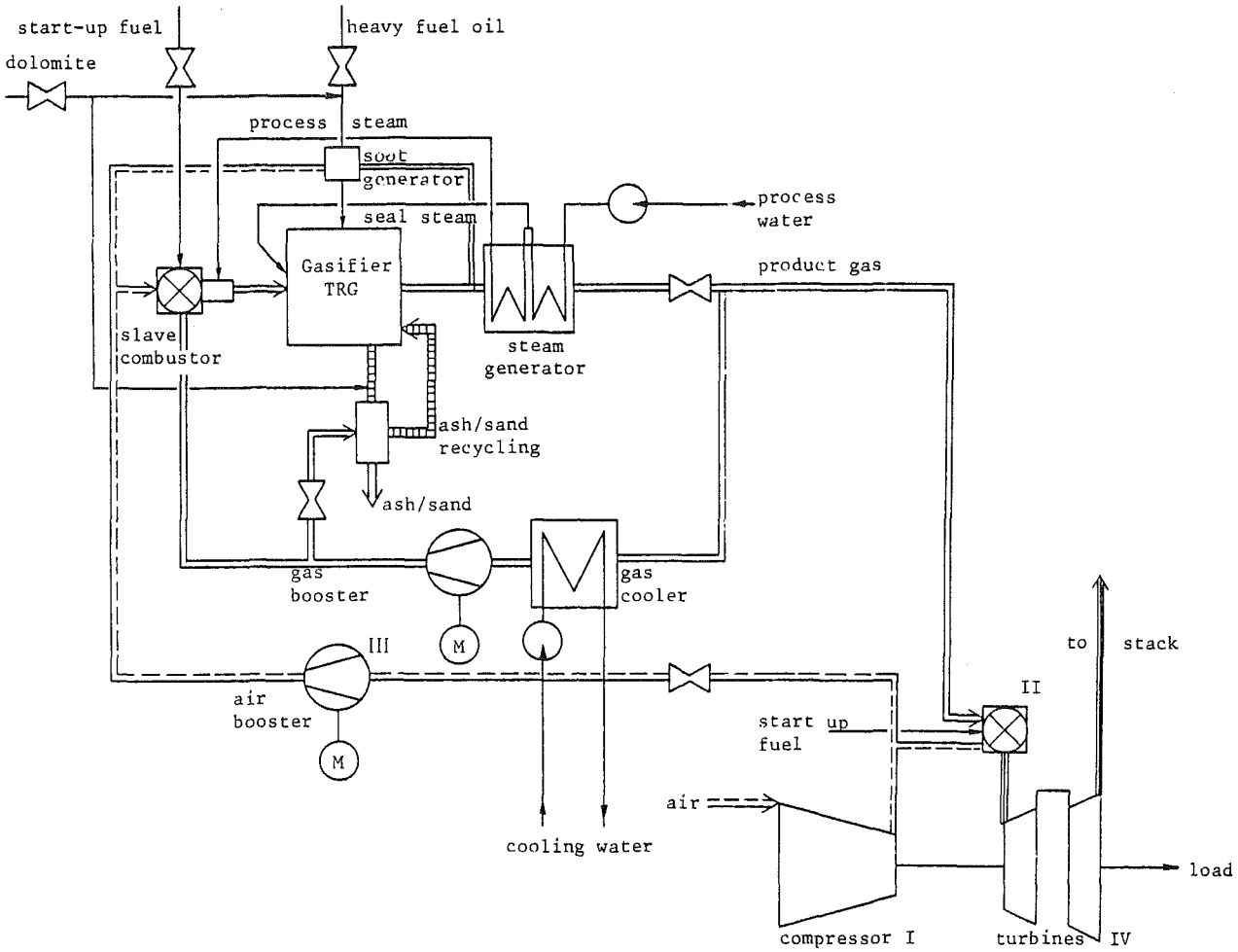

Fig. 9 Process scheme of an integrated gas turbine-gasifier propulsion unit

Compressed air (from a gas turbine compressor for instance) and steam enter the gasifier through the hollow drive shaft (10), flow through the porous basket, pass through the soot layer and, by reacting with the soot, produce a hot low-Joule product gas that leaves the gasifier via discharge pipe (1). At the end of the outer ring the bed material and any fuel ash "falls" out in the radial direction and is discharged from the gasifier housing.

Nearly all the bed material is recirculated to the bed via a pneumatic conveyer system, using product gas as transport medium. Re-entry is effected via the dolomite inlet pipe not shown.

Desulfurization is accomplished in the soot generator, the necessary dolomite having been mixed in the oil before it enters the generator. The dolomite, partially reacted to CaS and MgS, is carried by the produced gas through the delivery pipe (2) and deposited on the carrier layer, along with the soot where it remains to be carried off by the bed material (5). Combined with the gas turbine, the following process scheme is proposed (Fig. 9).

Part of the compressed air from the main compressor (I) is bled off from the main line to the combustor (II) and further compressed in air boost compressor (III). Part of this air flow is extracted and fed to the soot generator, as is the preheated (and dolomite-doped) fuel oil. The remainder of the compressed air flow enters the slave combustor, in which it is preheated by combustion of a small amount of product gas (the need for preheating depends on the compression rate and/or the use of internal recuperation). If process steam is needed it is added in the slave combustor. The resulting air/combustion gas/steam mixture at 550°C or more flows through the gasifier drive shaft into the gasifier. The pressure seals are steam fed and the bed material is recirculated by another small amount of product gas.

The product gas leaves the gasifier, and releases free heat to generate the necessary steam; this also has the advantage of cooling the product gas sufficiently to ease the constructional problems of transporting and controlling a combustible gas at high temperature. The main product gas flow is fed to the low-Joule combustor (II) and combusted in the main air stream from the compressor. The combustion gas expands through the compressor and power turbines (IV).

As noted, a small amount (3 percent) of product gas is extracted for preheating and pneumatic transport. This flow is cooled to atmospheric temperature and compressed in the gas boost compressor at a pressure ratio of approximately two. [Dolomite is mixed in the main fuel oil flow (which has been heated) and fed to the bed material circulation system as makeup.]

Fuel Effects on the TF30 Engine (Alternate Test Procedure)

P. A. Karpovich
Project Engineer.
Naval Air Propulsion Center,
Trenton, NJ

A. I. Masters
Project Engineer.
Pratt & Whitney Aircraft,
West Palm Beach, FL

The objective of the Alternate Test Procedure (ATP) is to develop the capability to qualify new fuels for Navy aircraft use with a minimum of testing. The effect of fuel composition and properties on engine performance and component life has been show to vary significantly from one engine configuration to another. The P&WA approach to the ATP has been to define fuel effects on the TF30 engine and then apply the methodology to other engines of interest to the Navy. Investigations of the TF30 conducted under the ATP Program and other Navy and Air Force Contracts have produced one of the most complete fuel effect characterizations available for any gas turbine engine. Major fuel effects which have been quantified are the relationships of lubricity to main fuel control reliability, viscosity and volatility to main burner and augmentor ignition limits, and hydrogen content to smoke and combustor life. The effects of fuel properties and composition on combustion efficiency and elastomeric seal life were found to be of secondary importance. Remaining uncertainties are the effects of fuel properties on turbine life and fuel nozzle fouling rate.

Introduction

While gas turbine fuel costs have been declining in recent months and world fuel supply has been abundant, the fuel shortages of 1973 and 1979 demonstrated how quickly this situation can change. Since any dramatic reduction in availability and increase in cost will likely be accompanied by an increase in world tension, it is imperative that the Defense Department have contingency plans to contend with such a situation. These plans must deal with anticipated pressure to relax fuel specifications to provide increased fuel availability and to allow temporary use of non-specification fuels in emergency situations.

Other more gradual changes in the petroleum supply picture are producing changes in the chemistry of gas turbine fuels and are likely to increase pressure to broaden jet fuel specifications. The light, high-quality American crudes, which made up much of our supply in the past, are rapidly being replaced by heavier crudes with increased aromatic content. Synthetic fuels derived from low hydrogen content crude sources such as shale, tar sands, and coal are beginning to come into use. Diminished gasoline consumption, utility conversion to coal, and increased use of diesel fuel are increasing competition for the middle distillate products from which kerosine base gas turbine fuels are obtained.

The Alternate Test Procedure (ATP) is the heart of the Navy's plan for responding to these changes. The objective of the ATP program is to develop a means of qualifying new fuels for Navy aircraft with a minimum of costly full-scale engine testing. The ATP data bank provides the information necessary to define performance or durability penalties associated with a particular fuel property change and thereby provides quantitative guidance as to the acceptability of any change to the jet fuel specifications. The ATP also provides an estimate of the problems and risks associated with the use of an out-of-specification fuel in an emergency situation.

Development of the Alternate Test Procedure

Phase I of the ATP was completed in December 1980 [1]. Under Phase I, the basic ATP model for prediction of fuel effects was developed, a study of refinery production trends was completed, and Phase II plans were prepared. The Phase I modeling effort concentrated on defining fuel effects in the TF30 engine and F-14 aircraft while generally outlining approaches that could be applied to other systems. The Phase I fuel effect predictions were based on existing TF30 data and extrapolation of fuel effect data from other engines; no new data were generated. The refinery study, conducted under subcontract to Suntech, Inc., suggested three fuel trends that could create pressure for fuel specification changes, i.e.:

- Increased aromatic content and associated reduction in hydrogen content and smoke point
- Reduced volatility and associated increases in viscosity and freeze point
- Reduced lubricity caused by hydroprocessing to limit aromatic concentration and increase the hydrogen content of highly aromatic crudes

Phase II centered around component testing to confirm and improve the ATP model with emphasis on the projected fuel trends and the potential problems that might be imposed [2]. Because the effect of fuel properties on engine operation was found to be much more significant than the effect of fuel properties on operation of other aircraft components, only engine effects were studied in Phase II. In addition to the

Contributed by the Gas Turbine Division and presented at the Joint Power Generation Conference, Toronto, Ontario, Canada, September 30-October 4, 1984. Manuscript received by the Gas Turbine Division June 5, 1984. Paper No. 84-JPGC-GT-1.

Table 1 TF30 fuel effect summary

Property	*Component*	*Effect Above Threshold*
Viscosity	Fuel Control	Reduced Groundstart, Reduced Response, Flow Errors
	Combustor	Reduced Ignition, Reduced Low-Power Efficiency, Increased Pattern Factor
	Turbine	Life Reduced by Combustor Pattern Factor
	Augmentor	Reduced Efficiency, Reduced Altitude Blowout Limits
10% Distillation Temp.	Combustor	Reduced Sea Level Ignition and Altitude Relight
	Augmentor	Reduced Ignition
90% Distillation Temp.	Combustor	Increased Pattern Factor, Reduced Low-Power Efficiency
	Turbine	Life Reduced by Combustor Pattern Factor
	Augmentor	Reduced Efficiency
Hydrogen Content	Combustor	Reduced Liner Life, Increased Smoke and Particulates
	Augmentor	Possible Reduced Life
Aromatic Content	Materials	Reduced Seal Life
Lubricity	Fuel Control and Hydraulic Pump	MFC Malfunction, Reduced Pump Life
Specific Gravity	Fuel Control	Incorrect Fuel Flow
Freeze Point	Fuel System	Fuel Starvation
Thermal Stability	Combustor	Fuel Nozzle Fouling and Nozzle Support Coking

component testing conducted under the Phase II contract, other data sources used to confirm the ATP model included combustor fuel effects test results from [3] and TF30-P-3 engine test results from [4].

Table 1 summarizes the fuel properties which were shown under Phase II to have the most significant impact on TF30 performance and life, the components affected, and the nature of the fuel effect. While the relative sensitivity of these effects may vary for other engines, it is believed the table provides a representative list of the fuel effects which should be evaluated in any gas turbine engine. The remainder of this paper presents an expansion of these effects in the TF30. For discussion purposes the fuel effects have been divided into those effects which occur while the fuel is in the liquid state, prior to atomization and vaporization, and those effects which are related to the combustion process.

Liquid Fuel Related Effects

The physical properties and chemical composition of liquid hydrocarbon fuels are known to affect the operation and life of certain fuel supply system mechanical components, the life and sealing capacity of some elastomeric materials, and the plugging or fouling tendency of parts with close tolerances exposed to high-temperature fuels. Specific areas of concern in the TF30 have been the effect of fuel lubricity on the main fuel control reliability and hydraulic pump life, the effect of fuel aromatic content on elastomeric seal life, and the effect of fuel thermal stability on fuel nozzle support manifold plugging and fuel nozzle fouling.

TF30-P-414 main fuel controls (MFC's) which incorporate a recent Microseal treatment engineering change show a wide

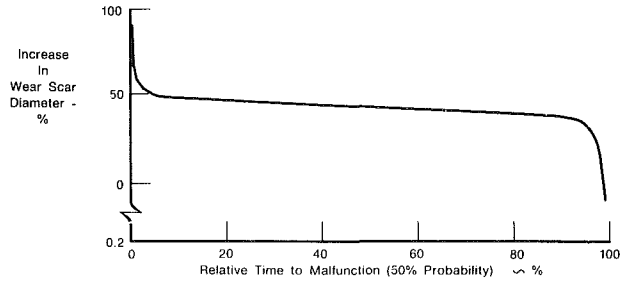

Fig. 1 Effect of lubricity on unmodified MFC malfunction rate

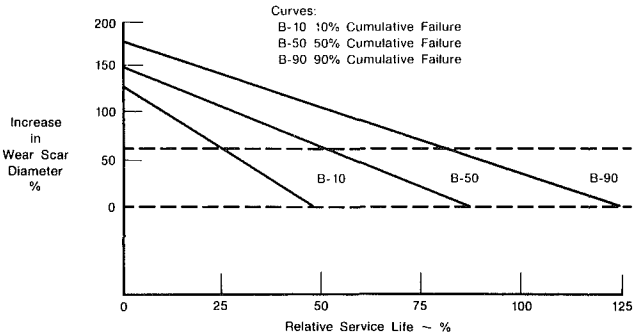

Fig. 2 Effect of fuel lubricity on unmodified hydraulic pump life

tolerance to fuels of poor lubricity. Original model MFC's without this engineering change have been found to malfunction when exposed to low-lubricity fuels. The failure mode is a random hang-up which occurs suddenly but is self-correcting when normal-lubricity fuel is reintroduced. Under ATP Phase II component tests were conducted to quantify this effect. As shown in Fig. 1, fuels whose ball-on-cylinder (BOCLE) wear scar diameter is less than a critical value have no effect on MFC operation while fuels with BOCLE wear scar diameters above this value are clearly unsuitable.

Low-lubricity fuel can produce excessive wear of the TF30-P-414 hydraulic pump. The effect of lubricity on the hydraulic pump service life based on limited field service data is illustrated in the chart shown in Fig. 2. An increase in the BOCLE wear scar diameter of 60 percent is estimated to reduce pump life by 50 percent.

Lubricity effects in the afterburner and exhaust nozzle control are similar to the MFC, although somewhat less sensitive. As with the MFC, incorporation of the microseal treatment greatly reduces the control sensitivity to changes in fuel lubricity.

The only TF30-P-414 component for which there are documented test results for varying viscosity fluids is the main fuel control. Test data are limited, but they show that increased viscosities can affect the ground starting capability. Figure 3 shows the relationship between viscosity and temperature for which normal accelerations could be obtained and also the limits for engine light-off with hung accelerations. Fuels falling below the normal accel threshold will result in degraded start performance; those below the engine light-off threshold are unsuitable for operation with the TF30. This correlation was developed assuming a strict dependence of starting characteristics on fuel viscosity, thus ignoring other ignition dependent fuel properties such as volatility and surface tension. This assumption is not completely realistic; however, the correlation does provide an indication of the effect of fuel viscosity on ground start capability.

Fuel viscosity may also affect the MFC in such a way as to impair air starting and control response but no data exist with which reliable correlations can be made. There are also no test

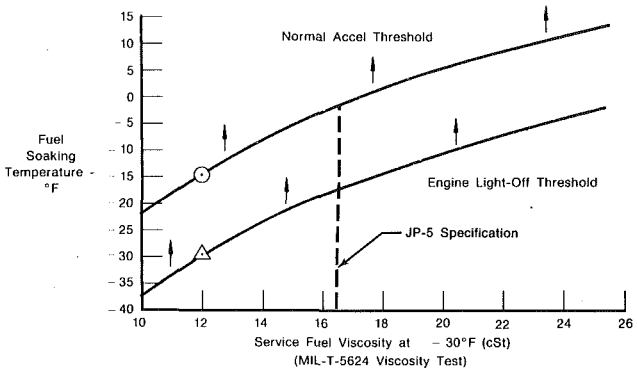

Fig. 3 Effect of fuel temperature on engine starting capability

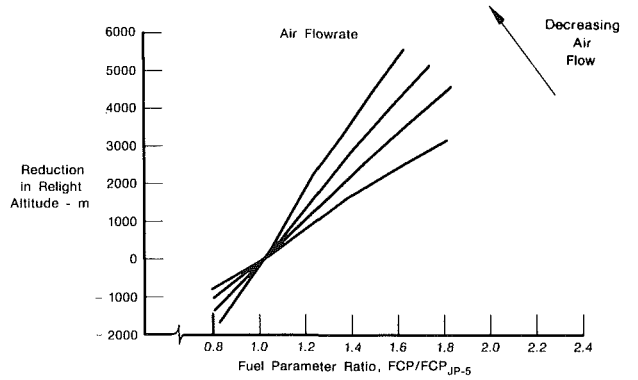

Fig. 4 Effect of fuel properties on relight altitude

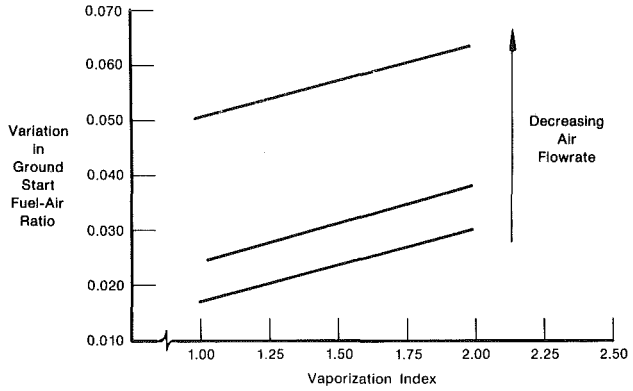

Fig. 5 Effect of fuel properties on ground start ignition limits

data defining afterburner and exhaust nozzle control performance with high-viscosity fuels or fuels at varying temperatures, but since this component is similar to the MFC in construction, reductions in response may result. As fuel is metered open loop in the afterburner fuel control, errors in fuel metering affecting steady-state performance may also develop if operated on high-viscosity fuels at low temperature.

Assessment of the effect of changes in specific gravity on the TF30 fuel systems indicates that its sensitivity is low. Pumps will be affected to the extent that pressure rise and horsepower are proportional to specific gravity. The controls are provided with adjustments to compensate for specific gravity changes within the nominal range of JP-4 and JP-5.

Increases in the freeze point of future fuels may have an impact on operation at low soak temperatures. Areas of concern when operating on partially frozen fuels are degraded pump performance and plugging and clogging of flow orifices and nonrelieving screens and filters. Increasing viscosity, which should accompany rising freeze point, will probably have a more severe impact on day-to-day performance. However, the high freezing point of marine diesel fuel (up to 270 K) will limit its use in emergency situations.

The applicability of materials used in the TF30 fuel system was generally found to be unaffected over the range of fuel properties and conditions likely to be encountered in Navy applications. Fluorocarbon and fluorosilicone O-rings should be unaffected by fuel system operation up to 40 volume percent aromatic content, the limit of the ATP Phase II data. Aromatic concentrations above 40 volume percent are considered to be very unlikely. High aromatic content can be quite detrimental to polysulfides and to Buna-N rubbers. Buna-N is found primarily in earlier engine designs and is not found in most models of the TF30. The only use of Buna-N in the TF30 is in the nonafterburning TF30-P-408 engine. Polysulfide sealants are not used in the TF30, but are used in low-pressure, low-temperature static application in the F-14 aircraft fuel system.

Fluorosilicone elastomers sometimes respond to cyclic changes in aromatic concentration and ring structure causing an alternating swelling and shrinkage which may produce leaks in some applications. Experimental laboratory studies conducted under ATP Phase II showed that this effect was magnified when the aromatics were primarily the low-molecular-weight compounds found primarily in JP-4. Thus this hysteresis effect is of concern primarily where JP-4-type fuel with widely varying aromatic concentration is used or where a highly aromatic JP-4 is interchanged with a kerosine base fuel such as JP-5 or JP-8.

The pumps and heat exchangers within the TF30 fuel supply system produce fuel temperatures up to 460 K at the fuel spray nozzle primary orifice. This maximum temperature is achieved at high altitude–low Mach number operation and at other operating points where the fuel temperature is reduced. Some blockage in the nozzle support manifold and distortion of the fuel nozzle spray pattern is found during engine hot section inspections. The frequency with which this problem is encountered appears to be directly tied to the length of time the engine is operated at high fuel inlet temperatures. For example, maintenance records show a much higher incidence of nozzle fouling in the TF30-P-414 used in the F-14 than in the TF30-P-3 and P-100 models used in the F-111. This is attributed to differences in mission requirements which result in the F-14 flying a much larger percentage of the time at high altitude–low Mach number flight points. Heated fuel bench testing has shown that the nozzle fouling rate correlates well with the jet fuel thermal oxidation test (JFTOT) breakpoint temperature, but a quantitative relationship has not yet been developed. Any significant decrease in fuel thermal stability as determined by the JFTOT breakpoint temperature is predicted to have a detrimental effect on this nozzle fouling rate.

Combustion Related Fuel Effects

Combustion related fuel effects fall into two categories: those that are dominated by fuel vaporization, e.g., ignition and combustion efficiency and those that are dominated by differences in the fuel chemical make-up, e.g., smoke generation and radiation. Two parameters have been developed to correlate vaporization related effects. The fuel characterization parameter FCP was developed from an ignition model formulated by Ballal and Lefebvre for ignition of a heterogeneous mixture in a flowing stream [5]. A similar expression, the vaporization index VI, was developed from a greatly simplified analysis of droplet vaporization [6].

Variations in altitude relight capability correlate very well with FCP. The FCP for the TF30 (and any other engine with a pressure atomizing nozzle) is

$$\text{FCP} = \frac{\rho_f \nu_f^{0.3} \sigma_f^{0.9} \Delta P^{-0.6}}{\ln (1+B)} \tag{1}$$

where

ρ_f = fuel density, kg/m
σ_f = fuel surface tension, N/m
ΔP = nozzle primary pressure drop, kPa
ν_f = fuel kinematic viscosity
B = Spalding mass transfer number based on 10 percent distillation temperature

The most predominant fuel properties in this relationship are viscosity and fuel volatility. Note that while surface tension and fuel density appear in the relationship with larger exponents than viscosity, the potential variation in these variables is small relative to viscosity; consequently, the potential effect is secondary. Nozzle pressure drop will remain essentially constant for a constant fuel flow rate. The correlation of changes in relight altitude with FCP is shown in Fig. 4. Note that the sensitivity of altitude capability to changes in FCP is also a function of combustor airflow and that the sensitivity increases as air flowrate diminishes. Thus the greatest fuel sensitivity occurs in the high-altitude–low Mach number region where ignition is most difficult.

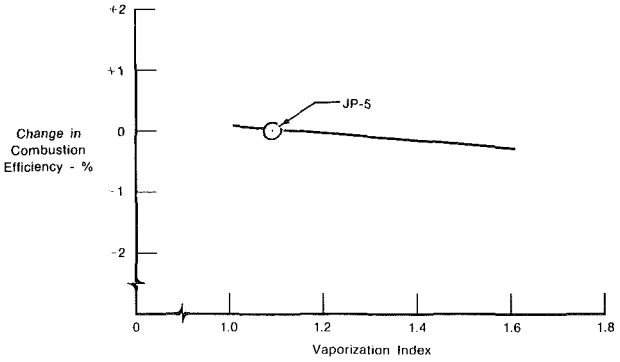

Fig. 6(*a*) Effect of fuel on combustion efficiency

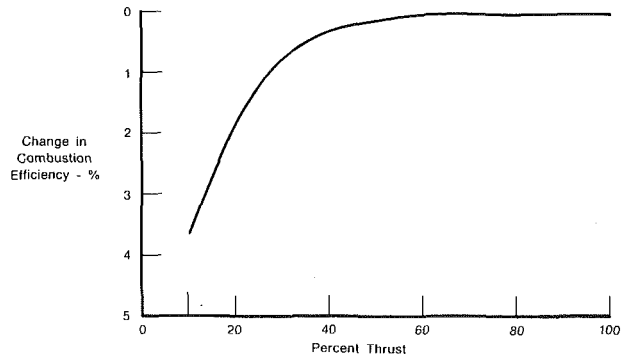

Fig. 6(*b*) Effect of thrust on combustion efficiency

The vaporization index is expressed as

$$\text{VI} = \frac{\delta (D_{32}/D_{32_{\text{JP}-5}})^2}{\ln (1+B)} \tag{2}$$

where

D_{32} = Sauter mean diameter (microns)
δ = fuel specific gravity

Figure 5 shows the correlation of ground start fuel–air ratio with VI and Fig. 6(*a*) shows the combustion efficiency correlation for sea level idle operation. At thrust levels above idle, combustion efficiency rapidly approaches 100 percent and fuel effects diminish as shown in Fig. 6(*b*). For thrust levels above idle the efficiency loss may be estimated by

$$L = (L_{Ref})(L_I/L_{RI}) \tag{3}$$

where

L = combustion efficiency loss
L_{Ref} = efficiency loss with JP-5 at the thrust of interest
L_I = efficiency loss at idle with the fuel of interest
L_{RI} = efficiency loss at idle with JP-5

Since the fuel-induced loss in combustion efficiency is only appreciable at low power levels where the effect on fuel consumption is minimal, efficiency losses are not a significant concern.

Combustor exhaust smoke and radiation correlate with fuel hydrogen content. The amount of smoke generated with JP-5 is a function of engine operating condition as shown in Fig. 7. The smoke number with another fuel may be related to the smoke number with JP-5 at the engine operating point of interest through the equation

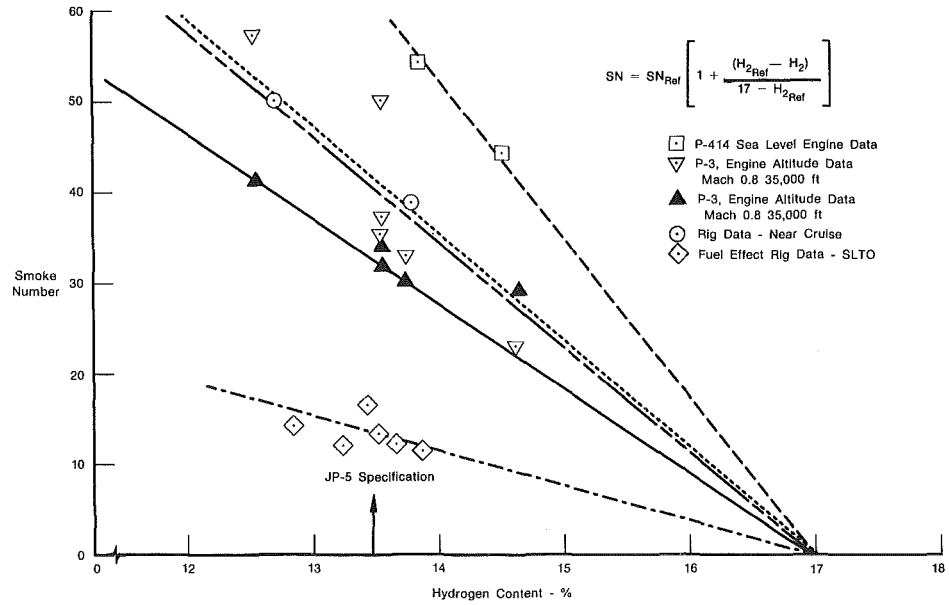

Fig. 7 Effect of hydrogen content on smoke

$$SN = SN_{Ref}\left[1 + \frac{(H_{2_{Ref}} - H_2)}{(17 - H_{2_{Ref}})}\right] \quad (4)$$

where

SN = smoke number
H_2 = hydrogen content, % by wt.
Ref = refers to baseline fuel value (usually JP-5)

The effects of vaporization rate and naphthalene content on smoke formation were also considered. It was concluded that their effect was small and their inclusion as separate variables did not statistically improve the hydrogen correlation [6].

Increased radiation will raise the combustor liner temperature, thereby reducing low-cycle-fatigue (LCF) life. The correlation of LCF life with fuel hydrogen content is given in Fig. 8. As indicated in the figure, a 1.0 percent reduction in hydrogen content will result in a 25 percent reduction in combustor liner life. The LCF life analysis is discussed in [3].

Within reasonable limits turbine efficiency will not be affected by fuel property variations. Turbine durability is affected by the fuel through measurable changes within the combustor. The combustor characteristics which affect the TF30 are pattern factor and radiation. Pattern factor and radiation effects are felt by the turbine first-stage vanes but do not impact the turbine blades or higher-stage vanes. Since the first-stage vanes are the life limiting area in the TF30 turbine, any reduction in first-stage vane life will seriously impact TF30 maintenance cost.

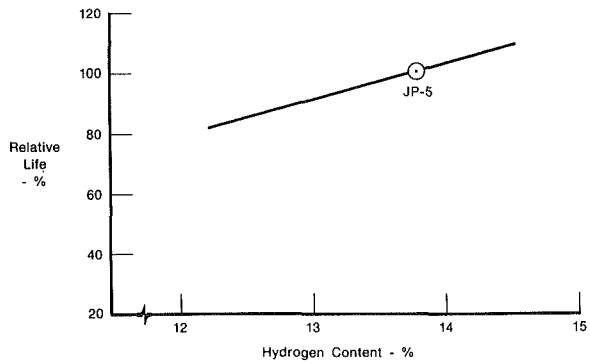

Fig. 8 Effect of hydrogen content on combustor liner life

The effect of fuel property changes on pattern factor has been measured in TF30 combustor rig tests. The applicability of these data to full engine operation is open to question, but assuming the correlation is directly applicable the effect on turbine life is significant. Figure 9 shows the combined effects of fuel properties on TF30 first vane life. The fuel physical properties, i.e., viscosity, volatility, and density, may be used to calculate the vaporization index which directly determines combustor pattern factor. Radiation effects are accounted for by the lines of constant hydrogen content. By matching the fuel vaporization index to the fuel hydrogen content the turbine life with the fuel of interest is indicated.

Sector rig testing conducted under ATP Phase II provided quantitative data for prediction of TF30-P-414 augmentor combustion efficiency, ignition limits, and blow-out limits. Correlation of the data showed a surprising increase in combustion efficiency with reduced volatility fuels, i.e.

$$\eta = \eta_{Ref} + (0.749/\Delta T_{10} - 0.3\Delta T_{90})\, f/a + 0.0267(\Delta T_{10}) + 0.165(\Delta T_{90}) \quad (5)$$

where

ΔT_{10} = $(T_f - T_{ref})$ at the 10 percent recovery temperature
ΔT_{90} = $(T_F - T_{ref})$ at the 90 percent recovery temperature
f/a = overall fuel–air ratio
η = combustion efficiency
Ref = reference fuel, typically JP-5

The altitude ignition capability of the augmentor correlates well with vaporization index as shown in Fig. 10. A significant reduction in ignition capability was found with the more viscous, less volatile fuels. The magnitude of the efficiency increase and loss in ignition capability may have been exaggerated by the nature of the sector rig tests, but the trends are believed to be correct, at least as they apply to the TF30-P-414. Of the two effects, the loss in ignition capability is anticipated to be the more significant.

No data have yet been obtained on the effect of fuel differences on the TF30-P-414 augmentor liner temperature.

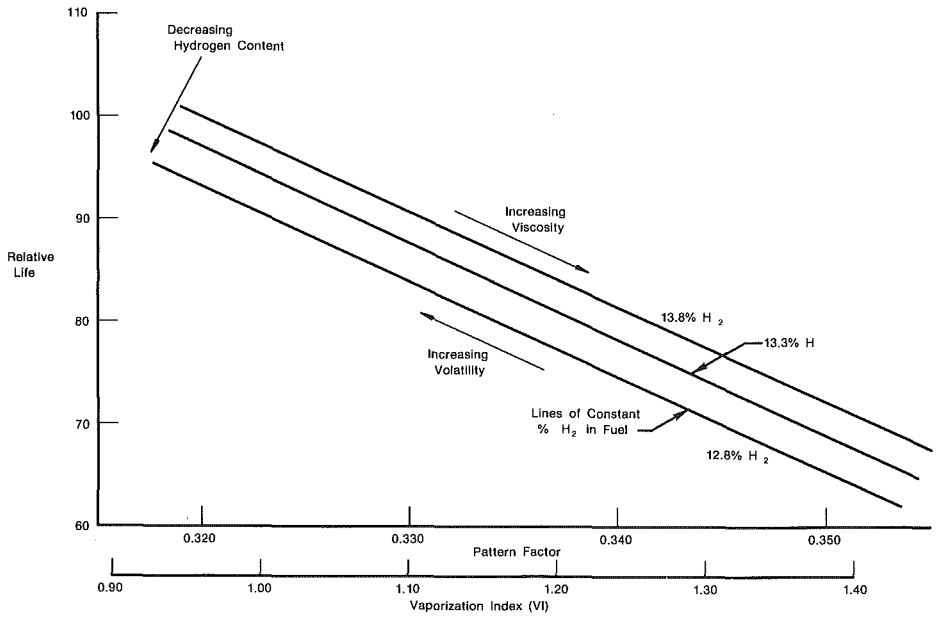

Fig. 9 Fuel effect on turbine (first-vane) life

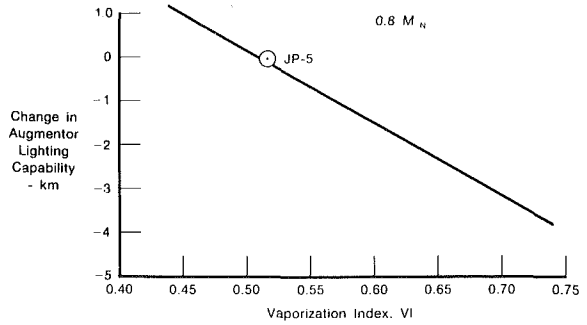

Fig. 10 Effect of fuel on augmentor ignition (rig data with electric ignitor)

Data for the TF30-P-3 from [4] indicate that liner temperature may show a slight sensitivity to fuel hydrogen content, but the data cannot be directly applied to the TF30-P-414. It is anticipated that the effect of fuel hydrogen content on augmentor liner life will be similar to, but less severe than, the effect on mainburner life.

Conclusions

Evaluations of the TF30 conducted under the ATP and other U.S. Navy and Air Force sponsored programs provide one of the most complete fuel characterizations available for any gas turbine engine. Most of the important fuel effects have now been examined and quantitative correlations developed; however, a few uncertainties remain. The current status may be summarized as follows:

1 The most critical fuel related safety problem (aside from serious fuel contamination) is possible hang-up in unmodified main fuel controls caused by use of low-lubricity fuel. It is of particular concern that fuel lubricity is not part of current gas turbine fuel specifications and is not usually measured.

2 Use of fuels with higher viscosity and lower volatility than specification JP-5 will result in reduced mainburner ignition, start transient, and altitude relight capability. The reduced capability is primarily of concern for low-temperature operation.

3 Reduced fuel hydrogen content will cause increased smoke and reduced combustor and turbine life.

4 Use of broadened specification fuels including fuels with aromatic concentrations up to 40 volume percent should not affect the life or suitability of elastomeric seals in the TF30 as long as the flashpoint is limited to above 333 K (60°C).

5 The effect of fuel properties on combustion efficiency is of secondary importance.

6 Reduced fuel thermal stability is likely to cause excessive fuel injector fouling, but more data are necessary to quantify the effect.

7 If current predictions based on combustor rig data are correct, increased viscosity and reduced volatility can seriously reduce turbine life. Such a reduction would be the most important single fuel effect on engine maintenance and life cycle cost. The effect of fuel property variations on pattern factor and the resulting impact on turbine life is the most important unanswered question relative to TF30 fuel effects.

8 Use of fuels with higher viscosity and lower volatility than specification JP-5 will result in reduced augmentor ignition limits. Other augmentor fuel effects are probably minor.

Acknowledgments

The technical contributions of G. W. Beal, T. B. Biddle, P. A. Warner, C. F. Weiss, and S. A. Mosier of Pratt & Whitney Aircraft, and the advice and support of C. J. Nowack, L. Grabel, and G. Speck of the Naval Air Propulsion Center are greatly appreciated.

References

1 Herrin, J. R., Longnecker, K. O., and Biddle, T. B., "Alternate Test Procedure for Navy Aircraft Fuels—Phase I," NAPC-PE-63C, Jan. 1982.

2 Masters, A. I., et al., "Alternate Test Procedures for Navy Aircraft Fuels—Phase II," Final Report, Contract N00140-80-C-0269, to be published.

3 Beal, G. W., "Effect of Fuel Composition on Navy Aircraft Engine Hot Section Components," NAPC-PE-74C, May 1983.

4 Russell, P. L., "Fuel Character Effects on USAF Gas Turbine Engine Afterburners, Part II—TF30 Afterburners," Final Report Contract F33615-81-C-2406, to be published.

5 Ballal, D. R., and Lefebvre, A. H., "Ignition and Flame Quenching of Flowing Heterogeneous Fuel-Air Mixtures," *Combustion and Flame*, Vol. 35, 1979, pp. 155-168.

6 Ernst, R. C., and Andreadis, D., "Fuel Effects on Gas Turbine Engine Combustion," AFWAL-TF-83-2048, June 1983.

Rotating Stall Caused by Pressure Surface Flow Separation on Centrifugal Fan Blades

S. Madhavan
American Davidson—Sturtevant Division
Hyde Park, MA

T. Wright[1]
Westinghouse Fluid Systems Laboratory,
West Lafayette, IN

A rotating stall associated with massive flow separation on the pressure surface (p-stall) of a centrifugal fan blade is identified. The stall cell rotates in the same sense as the rotation of the impeller. The frequency of pressure pulsation is greater than the running frequency and approaches 4/3 the running frequency. It is proposed that the mechanism of p-stall propagation is similar to that of the classical rotating stall caused by flow separation on the suction surface (s-stall). However, it is emphasized that the cause of p-stall is different from s-stall and any corrective treatment applied should take its nature into consideration. In the present work, pressure surface stall was induced by prerotating the inlet flow using inlet guide vanes and operating the fan against a low system resistance. Heuristic models are proposed for the inception and propagation of p-stall, and computational predictions of the flow fields, along with experimental results, are presented to support the model.

Introduction

Rotating stall in turbomachinery has been widely discussed in the literature and its behavior documented by experiments [1-4]. Its occurrence has been identified in both axial and centrifugal pumping machines. Although the majority of the literature is related to stall in compressors, the behavior of stall is similar in fans. However, high-specific-speed centrifugal fans are characterized by geometric features which differ considerably from compressors. Blade leading edges are usually straight across the blade span (parallel to the fan axis), wide relative to other machines, and not twisted. The ratio of the fan inlet radius and the minimum radius of curvature of the end wall comprised by sideplate and inlet cone is usually rather large so that the radial component of the inflow velocity can vary strongly across the blade span. Both of these factors lead to unusually large variations in velocity and incidence distributions across a blade leading edge, both at design flow rate and particularly at higher or lower flows. Because of the potentially large variations, it should be expected that leading edge incidence effects leading to blade stall occurrences will cover a wider range of behavior in a centrifugal fan than would be observed in pumps or compressors.

Classical rotating stall is always associated with flows well below the design flow rate. While models detailing the phenomena are available [1, 2], the concept of rotating stall inception and sustenance is discussed here for completeness.

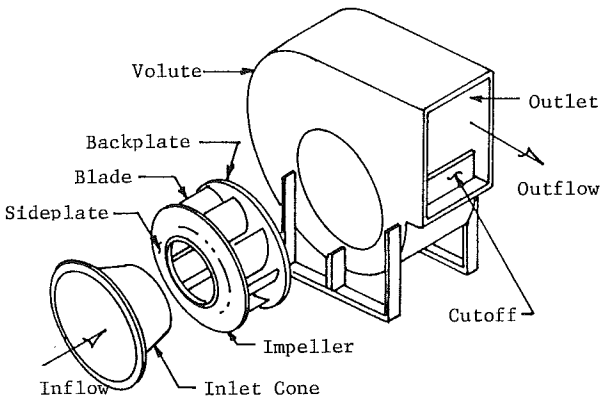

Fig. 1 Centrifugal fan components

Figure 1 shows the configuration of a centrifugal fan with its various components. Figure 2 shows the front and side view of a typical backwardly curved, airfoil-bladed centrifugal fan impeller. As seen in Fig. 3, W_1 is the relative flow with respect to the blade leading edge, and V_{r_1} is the radial component of the inflow vector. At some flow below ϕ_{des}, β_{1f} is less than β_1, blade leading edge incidence (α) increases, and finally causes stall in a blade passage. The restricted flow passage in this channel causes a rearrangement of the entering flow field in the neighboring passages. In the forward passage, the entering flow vector V_1 rotates in a prespin sense, relieving the approach to stall, while V_1 in the following passage undergoes a rotation in a contraspin sense causing β_{1f} to decrease and thereby stalling that passage. By this argument, it can be seen that a stall cell consisting of one or more blade passages is created. It is also evident that this stall cell will rotate relative to the blade row in a sense opposite to that of the impeller.

[1]Currently with Department of Mechanical Engineering, University of Alabama at Birmingham.

Contributed by the Gas Turbine Division of THE AMERICAN SOCIETY OF MECHANICAL ENGINEERS and presented at the 29th International Gas Turbine Conference and Exhibit, Amsterdam, The Netherlands, June 4-7, 1984. Manuscript received at ASME Headquarters, December 19, 1983. Paper No. 84-GT-35.

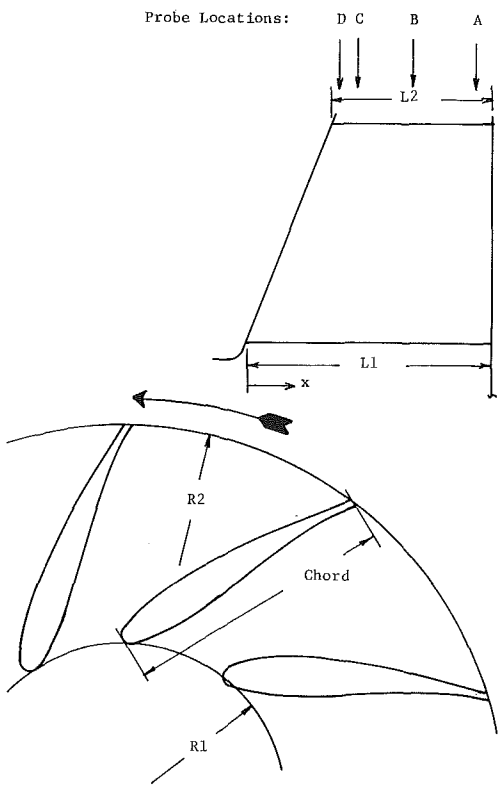

Fig. 2 Fan/blade geometry

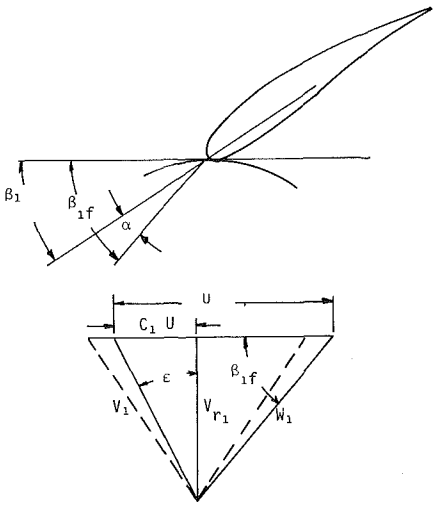

Fig. 3 Inlet velocity vector diagrams

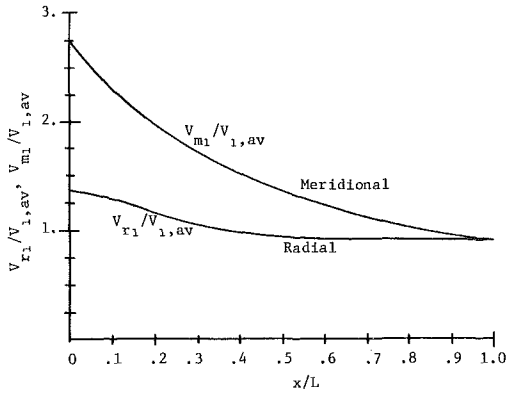

Fig. 4 Nondimensionalized radial and meridional component of inlet velocity at blade leading edge for Design 1 at $\phi = 0.2017$ based on quasi-three-dimensional analysis [9]

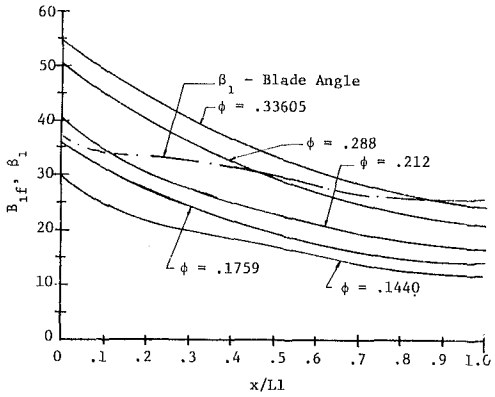

Fig. 5 Flow angle and blade angle distribution at leading edge for Design 1 based on quasi-three-dimensional analysis [9]

The stall speed in the stationary reference, $\omega_s = \omega_{stall}$, lies between 0.75 ω and 0.67 ω, tending toward 2/3 ω [4, 5]. For the purpose of clarity, this type of stall is referred to as rotating suction stall, or s-stall.

It is now proposed that under conditions where $\beta_{1f} >> \beta_1$ such that α approaches α_{stall} on the pressure surface, stall of a blade passage occurs. In this case, however, the prespun inlet flow vector V_1 in the forward passage stalls that blade passage while stall inception in the contraspun following passage is suppressed (excessive negative incidence is relieved). The stall cell in this situation moves forward and, again, may consist of one or several blade passages. If this stall should occur, the stall speed referred to a stationary reference frame will be $\omega_s = \omega + \omega_{stall}$, where ω_{stall} is the stall cell speed relative to the rotating impeller. Since the inception of a forward rotating stall depends on stall of the pressure surface, for clarity it will be referred to as rotating pressure stall, or p-stall. Prior ex-

Nomenclature

A = fan reference area, $\pi D^2/4$
C_1 = slip factor for induced tangential velocity
D = fan diameter
$L1$ = width (axial) of blade leading edge
$L2$ = width (axial) of blade trailing edge
P = pressure
Δp = pressure rise
$\delta\bar{p}$ = normalized rms pressure fluctuation in stall
Q = volume flow rate
$R1$ = radius to blade leading edge
$R2$ = radius to blade trailing edge
U = peripheral speed
V = absolute velocity
W = relative velocity
x = axial distance from sideplate along leading edge
α = flow incidence angle
β = blade or relative velocity angle, Fig. 3
ϵ = inlet velocity swirl angle relative to axial direction
ω = rotational speed
ϕ = flow coefficient, $Q/(U_2 A)$
Ψ = pressure rise coefficient, $\Delta p/(\frac{1}{2}\rho U_2^2)$
ρ = air density

Subscripts

av = average
des = design point, zero average incidence at blade leading edge
f = flow related
m = meridional direction
p-stall = pressure surface stall
r = radial direction
s = stall
s-stall = suction surface stall
1 = leading edge, i.d.
2 = trailing edge, o.d.

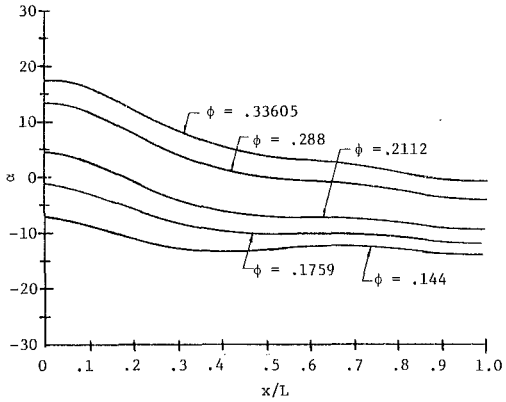

Fig. 6 Incidence angle distribution at blade leading edge of Design 1 based on quasi-three-dimensional analysis [9]

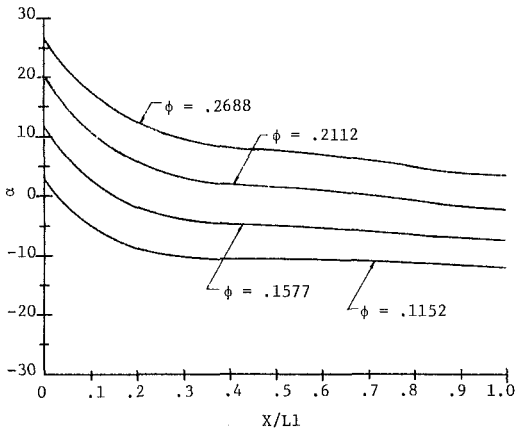

Fig. 7 Incidence angle distribution at blade leading edge of Design 2 based on quasi-three-dimensional analysis [9]

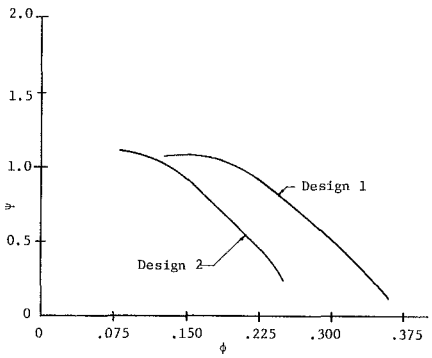

Fig. 8 Ψ versus ϕ for both designs (experimental results)

perience with pumps [6] pulsating at very high flow rates seems to support this concept.

In order to achieve the condition of large negative incidence that will support p-stall, it is clear that ϕ must be larger than ϕ_{des}, in general. For positively cambered blades, this stall need not be precipitous (see [7]) and may occur at values of α much higher than that for $\alpha_{s\text{-}stall}$. Indeed, values of β_{1f} large enough for stall may occur only by the compounding effect of increased preswirl (Fig. 3). That is, one case where conditions are right for forward rotating stall is where ϕ is larger than ϕ_{des} and preswirl is positive, for example when inlet guide vanes are turned down.

In the case of rotating suction stall, the operating conditions are clearly outside the design bounds. Such is not necessarily the case where p-stall is expected. The blading itself is designed to operate satisfactorily in this regime. Since

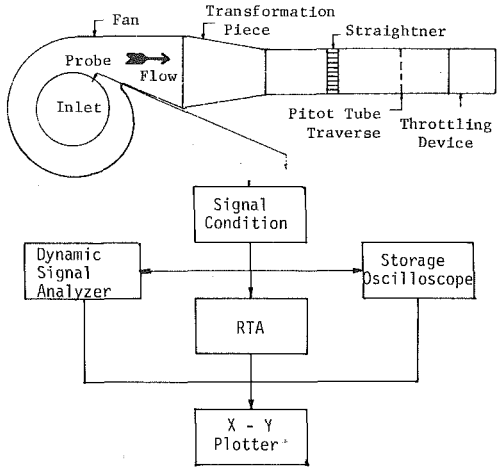

Fig. 9(*a*) Test setup and instrumentation block diagram

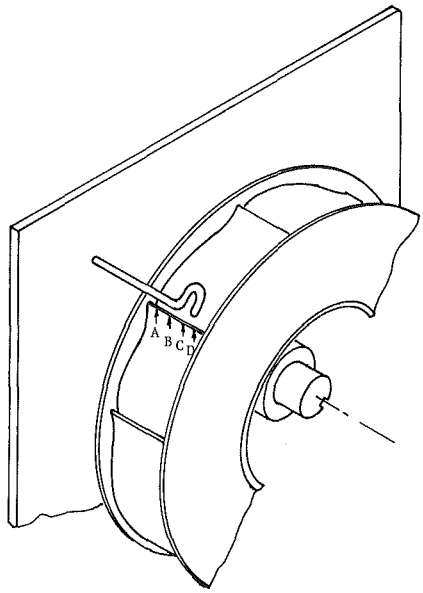

Fig. 9(*b*) Probe orientation

turning vanes are usually a primary control device, the flow field even under turned-down conditions is expected to fall within stall limits. It is suggested that typical fans will generally undergo severe p-stall only in the presence of a strong supporting influence such as precessing inlet vortex. The preswirling flow through the converging section of an inlet provides proper conditions for vortex precession [8]. Precession of the vortex allows the vortex centerline to deviate from the fan centerline and move radially into the blade row leading edge. The swirl velocity in the precessing vortex aggravates the situation of excessive β_{1f} in the sideplate region of the blade row, assisting in stall inception. Once stall in a blade passage is achieved, the stall cell propagates forward in the same direction as the precessing vortex.

To test this hypothesis, two fan designs were considered. The flow field in each design was calculated using a quasi-three-dimensional computational scheme [9, 10] for turbomachinery flows. To get experimental verification, these fans were operated at various inlet vane settings and throttle settings to cover the majority of their performance maps. During operation the flow output of the impeller was monitored in time and frequency domain. The results of both phases of the investigation are reported here. The two fans are referred to in this work as Design 1 and 2. While most of the

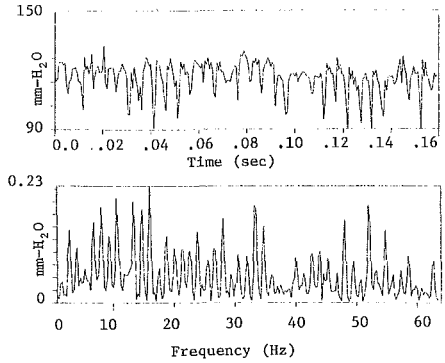

Fig. 10 Time and frequency scan of impeller exit flow for Design 1 at $\phi = 0.288$ at location B

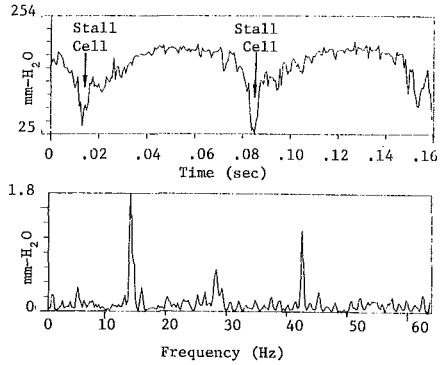

Fig. 11(*a*) Time and frequency scan of impeller exit flow of Design 1 at $\phi = 0.144$ at location A

discussion is presented for Design 1, results for Design 2 are also included as supportive evidence.

Analysis

The entire flow field within the impeller was resolved using the numerical approach. The area of interest in the present model is around the leading edge of the rotating blade row.

In the context of Figs. 2 and 3, an average value for the radial inflow velocity V_{r1} may be calculated by

$$V_{1,\text{av}} = \frac{Q}{2\pi(R1)(L1)}$$

The meridional and radial velocity normalized on $V_{1,\text{av}}$ is presented as a function of the leading edge length measured from the sideplate in Fig. 4. A family of curves for various values of ϕ covering the operating range of the fan is included in all plots. The blade leading edge angle, measured in the meridional plane, is presented in Fig. 5, along with the actual flow angle β_{1f}. The difference between the blade angle and flow angle, the incidence angle, is presented in Fig. 6. It is noted that the numerical model does not take into account any prerotation of the inlet velocity due to viscous effects and that the swirl entering the impeller is zero. The incidence angle results for Design 2 are included in Fig. 7. Plots of Ψ versus ϕ for both the fans are included in Fig. 8.

The incidence angle distribution suggests that for ϕ larger than ϕ_{des}, there is a change in sign with the incidence being positive in the vicinity of the sideplate and dropping to a negative value near the backplate. It is also reasonable to expect that the actual inlet flow is prerotated due to viscous effects and will tend to shift the family of curves in Figs. 6 and 7 to a more positive position. Experimental evidence of this skew in incidence angle may be deduced from measured blade pressure profiles [11].

The condition of high incidence at the sideplate side of the leading edge is made worse by the addition of any prerotation to the inlet flow by use of inlet guide vanes. Consider the inlet condition as represented by Fig. 3.

$$\beta_{1f} \cong \tan(\beta_{1f}) = \frac{V_1 \cos(\epsilon)}{U_1 - V_1 \sin(\epsilon)}$$

where fluid angle ϵ is the angle of the inlet flow vector, measured relative to the fan axis (positive in the turned-down direction), and V_1 is the vector sum of the axial and radial components of the inflow vector.

That β_{1f} increases with ϵ is evident, and it is seen that a positive shift of the family of incidence curves will occur. Furthermore, the effect of increased β_{1f} due to increased ϵ is skewed and greater near the sideplate since V_1 is greater there. $\partial\beta_{1f}/\partial\epsilon$ is given by

$$\frac{\partial\beta_{1f}}{\partial\epsilon} = \frac{V_1^2 - U_1 V_1 \sin(\epsilon)}{U_1^2 - 2U_1 V_1 \sin(\epsilon) + V_1^2 \sin^2\epsilon}$$

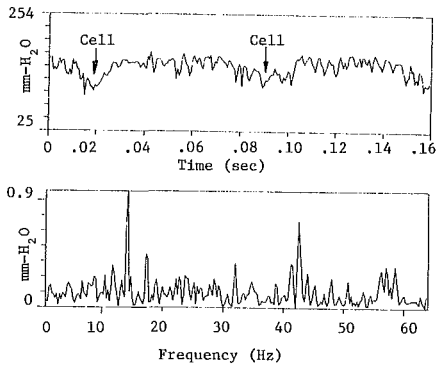

Fig. 11(*b*) Time and frequency scan of impeller exit flow for Design 1 at $\phi = 0.144$ at location B

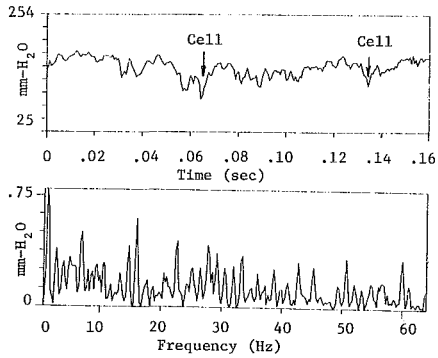

Fig. 11(*c*) Time and frequency scan of impeller exit flow for Design 1 at $\phi = 0.144$ at location C

For ϵ small (or in the limit as $\epsilon = 0$),

$$\frac{\partial\left(\frac{\partial\beta_{1f}}{\partial\epsilon}\right)}{\partial V_1} = \frac{2V_1}{U_1^2}$$

That is, as V_1 increases, $\partial\beta_{1f}/\partial\epsilon$ increases, causing a magnified effect near the sideplate.

The behavior of stall speed in relation to ϕ may be anticipated through examining the distribution of incidence angle at the leading edge. While positive ϵ causes α to increase, the turn-down also modulates the flow output, reducing V_{r1}. This causes an opposing trend which reduces β_{1f}. However, as shown above, β_{1f} increases more rapidly at the backplate compared to the sideplate based on modulation of the radial component of V_1, or ϕ, since V_{r1} is changing rapidly at the backplate, proportionately. That is, the influences of ϵ and V_{r1} may reinforce to yield a highly skewed incidence angle distribution. The result is strong negative (pressure side) incidence at the sideplate and strong positive

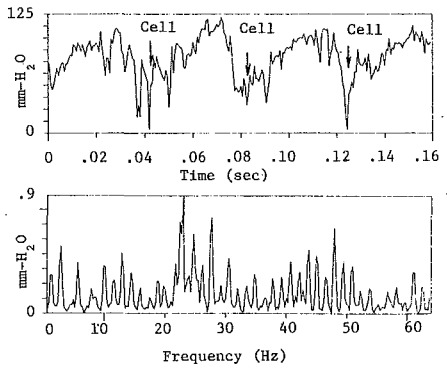

Fig. 12(*a*) Time and frequency scan of impeller exit flow at location A of Design 1 at $\phi = 0.24$ and inlet vane setting of 60 deg

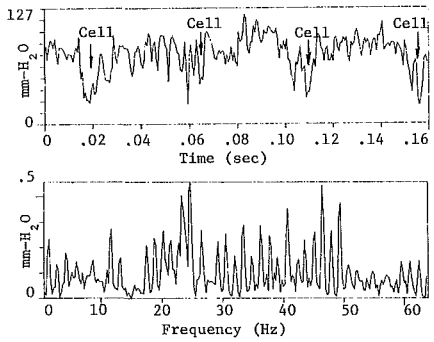

Fig. 12(*b*) Time and frequency scan of impeller exit flow at location B of Design 1 at $\phi = 0.24$ and inlet vane angle = 60 deg

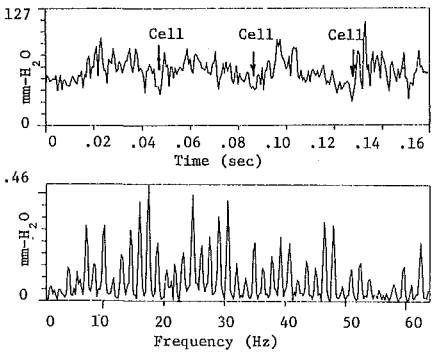

Fig. 12(*c*) Time and frequency scan of impeller exit flow at location C of Design 1 at $\phi = 0.24$ with inlet vane angle = 60 deg

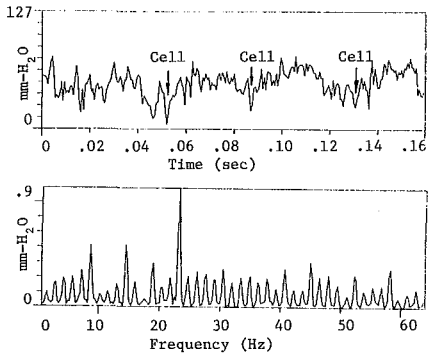

Fig. 12(*d*) Time and frequency scan of impeller exit flow at location D of Design 1 at $\phi = 0.24$ and inlet vane angle = 60 deg

(suction side) incidence at the backplate. Given such a condition due to positive ϵ and a typical V_{r1} distribution, reduction of ϕ will yield s-stall at the backplate; increasing ϕ will yield p-stall at the sideplate. It appears that overall stall cell speed and direction are governed by the combined effect of these two types of stall. Further, a balanced condition may

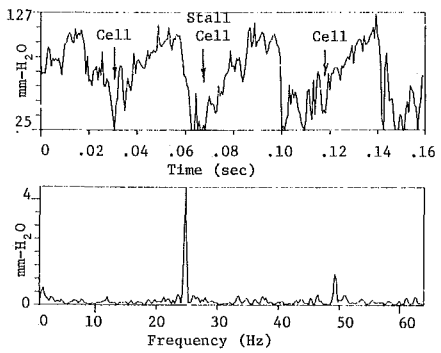

Fig. 13(*a*) Time and frequency scan of impeller exit flow at location A of Design 1 at $\phi = 0.24$, inlet vane angle = 60 deg and dummy shaft removed; shows forward rotating stall

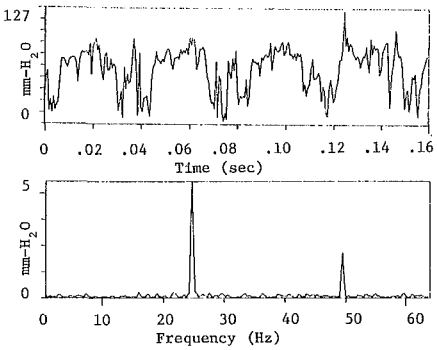

Fig. 13(*b*) Time and frequency scan of impeller exit flow at location B for Design 1 at $\phi = 0.24$, inlet vane angle = 60 deg, and dummy shaft removed

yield a stationary cell with respect to the impeller. Calculation shows that a uniform 10-deg prerotation imparted to the inlet flow of Design 1 will result in an increase of negative incidence angle at the sideplate of about 3.5 deg and about 0.5 deg at the backplate. The argument holds for the general class of fans under consideration here, including Design 2.

Excessive flow angles at the sideplate under the above conditions can cause a stall on the pressure surface. The inception of stall in such cases should be in the vicinity of the sideplate and could, on development, cover the entire blade channel. It is also recognized that for the designs under consideration, the backwardly curved blade and the generous leading edge geometry [11, 7, 12] mitigate the severity of p-stall.

Experiment

In order to introduce a positive preswirl into the inlet flow, a guide vane system was installed in each of the fans to be studied. While the vane designs differed in each case, performance in terms of imparting a swirl was comparable. Design flow rate for Design 1 was $\phi = 0.202$; for Design 2, the value is $\phi = 0.152$. More extensive design details are available [11].

The fans were set up with an outlet duct following the AMCA 210-74 code for laboratory testing of fans [13]. An additional probe implanted with a high-frequency-response pressure transducer was placed close to the trailing edge of the blades of the impeller. The probe used for Design 1 was a hooked impact tube (diameter = 9.5 mm) while an L-shaped impact tube housed the transducer for monitoring Design 2. The transducers were piezoresistive devices with a frequency range of 0–50 kHz and a flat response of 0–10 kHz. The signals from the transducers were fed into a digital storage scope, real time analyzer, and an X-Y plotter. In the detailed

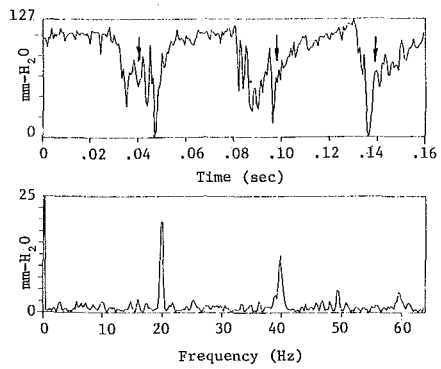

Fig. 14 Time and frequency scan of impeller exit flow at location A of Design 1 at $\phi = \phi_{des}$, inlet vane angle = 60 deg, and dummy shaft removed; shows a nonrotating stall, $\omega_s = \omega$

experiments run on Design 1, the signals were monitored by a dynamic signal analyzer.

The actual measurements were made by triggering a tachometer signal obtained from a fiber optic sensor monitoring the shaft. The signals were monitored for 0.16 s, or about three rotations of the impeller, and were also analyzed for frequency content. Since the rotating speed of the impeller was 1200 rpm (20 Hz), the range of interest in the frequency domain was limited from 0–64 Hz. In the time domain, data points were acquired at 1028 reading over a time window of 1/64 s.

The probes were used to monitor the exit flow from the impeller in real time. The probes were placed at a distance of 0.06 D from the trailing edge of the blade. Since they were not designed to resolve the flow directions, the turbulence and changes in direction within the blade wakes made it difficult to get meaningful data too close to the trailing edge without time averaging. For the purpose of studying stall, a considerable amount of qualitative information is lost by time averaging since the stall cell is moving relative to the wheel. The time-averaged data filter out the stall cell movement. To avoid this loss of information, the signal was monitored in time domain for a single scan. In the frequency domain the signal was averaged over 25 samples. The inability of the probes to track flow vectors exactly as a wake or stall cell passes the probe causes the pressure magnitude information gained to be somewhat qualitative.

Results

The experiment on Design 1 was run on two separate configurations. In the first case, a "dummy" shaft representing a typical arrangement 3 (center-hung wheel) [13] was installed. The presence of the shaft tends to stabilize the precession of the inlet vortex. In the second case, the shaft was removed.

During the course of the experiment, the fan was run at three separate throttle settings (system resistance) for various inlet vane angles. For each setting of the fan, the probe signal was measured in time and frequency domain at locations A, B, and C as shown in Fig. 9. A representative plot is shown in Fig. 10. The y axis represents pressure in mm of w. g. In this case the inlet total pressure is the same as the ambient atmospheric pressure.

From the discussion in the previous section, it is clear that the inlet flow matches the blade leading edge angle at the backplate for high flows ($\phi > \phi_{des}$) and at the sideplate for $\phi < \phi_{des}$. Figure 10 presents the flow for $\phi = 0.288$ for Design 1, at location B, as a typical example of unstalled off-design performance. The blade-to-blade flow is somewhat rough, but there are no significant spikes in the accompanying frequency domain.

At stall, $\phi = 0.144$ (Figs. 11*a–c*), the stall cells are clearly visible at section A with reduced magnitude at B and C as seen

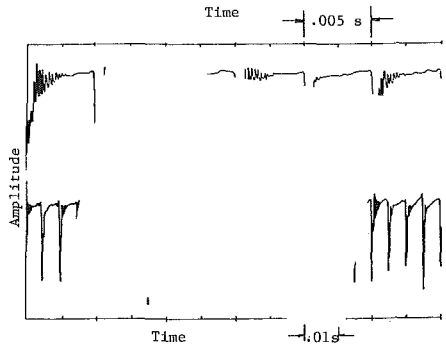

Fig. 15(*a*) Time scan of impeller exit flow, Design 2 at location B with $\phi = 0.1523$

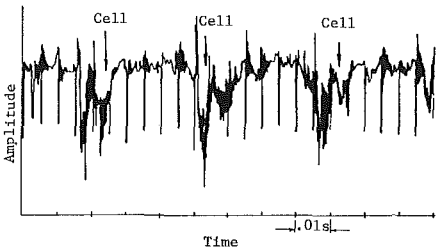

Fig. 15(*b*) Time scan of impeller exit flow, Design 2 at location B, with $\phi = 0.2112$ and vane angle set at 45 deg, showing a forward rotating stall

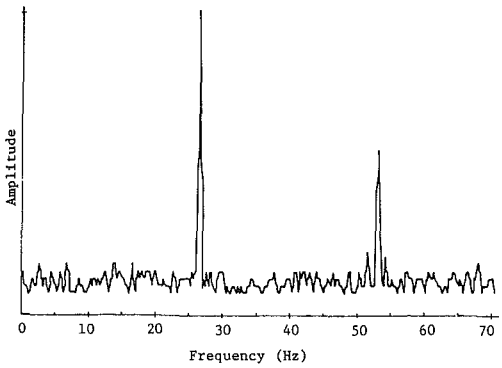

Fig. 15(c) Frequency spectrum of time trace shown in Fig. 15 (*b*)

in the figures. The magnitude of the stall, which occurred at 14.18 Hz, rapidly diminishes from A to C, suggesting that the total separation at the backplate side of the blade is the driving mechanism for s-stall. Second and third harmonics of the stall are also visible in Figs. 11(*a*) and 11(*b*). The time traces show a time lapse between cells of roughly 0.072 s. while a revolution of the fan requires 0.05 s. Clearly the cell is rotating more slowly than the fan itself.

At a 60-deg prespin vane setting, Figs. 12(*a*), 12(*b*), and 12(*c*) show evidence of a forward rotating stall. Figures 12(*a*) and 12(*b*) show multiple peaks in the vicinity of 23 to 27 Hz (1.15 – 1.35) times running frequency. A measurement taken closer to the sideplate (Fig. 12*d*) shows a single spike at 23 Hz. Here, the time lapse between cells is roughly 0.045 s. The behavior indicates a strong single cell rotating just slightly faster than the fan. (If the frequency were interpreted as signifying two cells, they would be rotating very slowly indeed.)

In the second configuration of Design 1, the shaft was removed. While the frequency is unchanged, the magnitude (see Figs. 13*a* and 13*b*) of pressure pulsation expressed as a percentage of local static pressure is substantially higher. The significant difference in these results supports the concept of the reinforcing effect of a precessing vortex. Visualization of

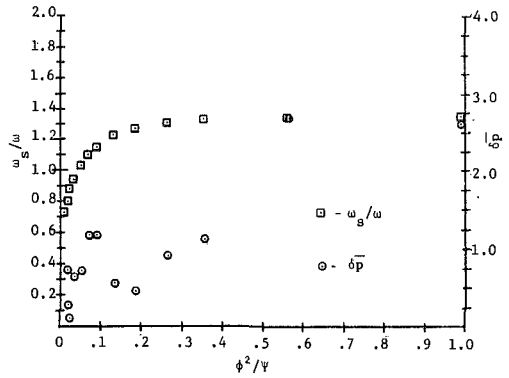

Fig. 16 Variation of stall frequency and magnitude over the operating range of Design 1 set at an inlet vane angle of 45 deg

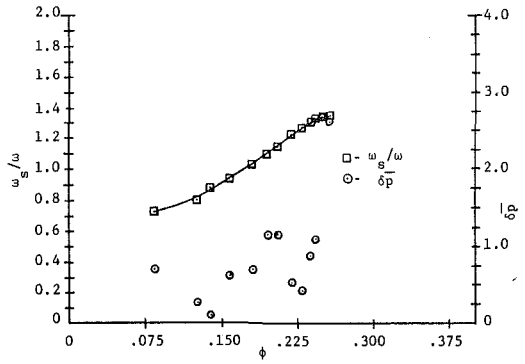

Fig. 17 Variation of stall frequency and magnitude for Design 1 at 45-deg vane setting expressed against ϕ

this flow with tufts lends support to the notion, showing motion of such a vortex and its penetration into the blade row.

In Fig. 14 the throttle was adjusted to operate the fan at its peak efficiency point for a 60-deg vane setting. The stall is evident (based on the magnitude of the 20 Hz spike, compared to that of Fig. 10), a ratio of $\cong$ 10:1, but the frequency is equal to the running frequency; that is, a very strong disturbance (a stall cell) exists, and is stationary with respect to the impeller.

Figure 15(*a*) shows a time trace of the approximate stagnation pressure for Design 2 at ϕ_{des} with the probe located at B. The fan was also run with the inlet vanes at 45 deg and a throttle setting corresponding to ϕ larger than ϕ_{des} at $\epsilon = 0$. The time trace shows the stall cells very clearly (Fig. 15*b*) and the frequency spectrum (Fig. 15*c*) indicates the major spectral component at 26.5 Hz or 1.33 ω.

From the results for Design 1, it is seen that the frequency or speed of stall varies with the system resistance. This variation appears to be continuous from about 1.3 ω to 0.7ω with increased system resistance. To check this continuous behavior, a series of tests were run at a fixed inlet vane angle of 45 deg for various throttle settings. These results, shown in Fig. 16, show continuous variation of the stall speed or frequency from an upper limit of approximately 1.35 ω at low system resistance ($\phi > \phi_{des}$) to 0.75 ω at high resistance ($\phi < \phi_{des}$). The stall frequency tends toward the limiting value of 0.67 ω as ϕ approaches zero. This continuous behavior in frequency is considered to be strong support for the concept of a single cell rotating either forward or backward relative to the fan itself. The same trend was observed for Design 2 [14]. Figure 16 shows ω_s/ω as a function of Φ^2/Ψ which represents the inverse of the parabolic system resistance curve or the inverse of the "diffusion" property of the impeller, Ψ/Φ^2 [15, 16]. (Note the stationary cell behavior $\omega_s/\omega = 1$.)

The magnitude of the pressure pulsation associated with stall is shown in Fig. 17. Here $\delta\bar{p}$ is the approximate rms magnitude normalized by the static pressure rise of the fan at a given flow rate ϕ. The curve shows a double minimum behavior, where the first minimum occurs at the value of ϕ yielding best efficiency at the 45-deg vane setting. The implication of the second minimum is not presently understood.

Conclusions

Evidence has been presented to support the contention that under certain conditions such as a preswirled inlet flow at a low system resistance, a forward rotating stall can be sustained in a centrifugal impeller. It has been shown that the frequency of stall can be made to vary continuously from the lowest system resistance to the fully developed s-stall condition.

The proposed model for p-stall inception seems to be supported by the experimental evidence. Stall inception under the conditions supporting p-stall appears to require a "seed" or "trigger" in the form of a precessing vortex or other significant disturbance in order to attain large amplitudes of pressure variation. Another potential seed is a highly nonaxisymmetric back pressure at the outlet of the impeller.

Since the results of this work indicate that the stall phenomenon in centrifugal fans is considerably more complex than was previously known, more study needs to be done to further categorize the complete range of behavior of rotating stalls. In particular, some means of visualizing the flow in the impeller or on-board total pressure or velocity probes located in each blade channel would help to clarify the existence of the single, forward-rotating stall cell.

References

1 Greitzer, E. M., "Surge and Rotating Stall in Axial Flow Compressors," ASME JOURNAL OF ENGINEERING FOR POWER, Vol. 98, No. 2, Apr. 1976, pp. 190-217.

2 O'Brien, W. F., Jr., Cousins, W. T., and Sexton, M. R., "Unsteady Pressure Measurements and Data Analysis Techniques in Axial-Flow Compressors," *Measurement Methods in Rotating Components of Turbomachinery*, ASME, New York, 1980, pp. 195-202.

3 Larguier, R., "Experimental Analysis Methods for Unsteady Flow in Turbomachinery," *Measurement Methods in Rotating Components of Turbomachinery*, ASME, New York, 1980, pp. 71-81.

4 Wormley, D. N., Rowell, D., and Goldschmied, F. R., "Air/Gas System Dynamics of Fossil Fuel Power Plants, Volume 5: System Excitation Sources," EPRI Research Report No. CS-1444, Vol. 5, Oct. 1981.

5 Goldschmied, F. R., Wormley, D. N., and Rowell, D., "Air/Gas System Dynamics of Fossil Fuel Power Plants, Volume 5: System Excitation Sources," EPRI Research Report No. CS-1444, Vol. 5, Oct. 1981.

6 Mackey, E., "Centrifugal Pump Hydraulic Instability," EPRI Research Report No. CS-1445, June 1980.

7 Emery, J. C., et al., "Systematic Two-Dimensional Cascade Tests of NACA 65-Series Compressor Blades at Low Speed," NACA TR-1368, 1958.

8 Batchelor, G. K., *Introduction to Fluid Dynamics*, Cambridge University Press, New York, 1977, pp. 543-567.

9 Novak, R. A., "A Computer Program for the Mean Streamsheet Design and Analysis of Turbomachinery," Dyna Tech R&D Company, Cambridge, MA, Mar. 1, 1980.

10 Novak, R. A., "Streamline Curvature Computing Procedures for Fluid Flow Problems," ASME JOURNAL OF ENGINEERING FOR POWER, Vol. 89, No. 4, Oct. 1967, pp. 478-490.

11 Wright, T., Tzou, K. T. S., Greaves, K. W., and Madhavan, S., "The Internal Flow Field and Overall Performance of a Centrifugal Fan Impeller—Experiment and Prediction," ASME Paper No. 82-JPGC-GT-16, Oct. 1982.

12 Wright, T., DiRe, J., and Madhavan, S., "Centrifugal Fan Performance With Distorted Inflows," ASME Paper No. 83-JPGC-GT-5, Sept. 1983.

13 AMCA 210-74/ASHRAE 51-75, *Laboratory Methods for Testing Fans for Rating*, AMCA/ASHRAE, 1975.

14 Pasquariello, J. W., Consultant, Cambridge, MA, private communications to S. Madhavan, Westinghouse Sturtevant Division, Aug. 1983.

15 Wright, T., "Axial Fan Performance with Blade-Base Clearance," ASME Paper No. 83-JPGC-GT-6, Sept. 1983.

16 Koch, C. C., "Stalling Pressure Rise Capability of Axial Flow Compressor Stages," ASME JOURNAL OF ENGINEERING FOR POWER, Vol. 103, No. 4, Oct. 1981, pp. 645-656.

Distorted Flow Field in Compressor Inlet Channels

P. Bry

P. Laval

G. Billet

Office National D'Etudes et de Recherches Aerospatiales, 92320 Chatillon, France

Solving the complex inlet-distortion related problems in turbojets or turbofans has become crucial to the successful development of new-generation engines. In order to curtail costs, reliable prediction methods, both analytical and numerical, must be developed and implemented. ONERA has been studying this problem for several years now. This paper reports on the preliminary numerical investigations of the three-dimensional flow field in the annular duct extending in front of a compressor with distorted inflow. The computational approach is a fully unsteady time-splitting, finite difference method solving the inviscid flow equations with nonuniform steady boundary conditions. Some analytical examples are presented and discussed. Matching of this three-dimensional computer code with models representing rotating or fixed blade rows is under way and will be reported on in a future contribution.

1. Introduction

The development of new generation fighter aircraft calls for careful design of propulsion systems and proper integration of the aircraft body, air intakes, engines and ejectors. This requires a lot of cooperative hard work on the part of both aircraft and engine manufacturers; one of the major problems facing the engine designers is that of predicting the response of turbomachines to inlet flow nonuniformities resulting from critical operation of the aircraft at the outer limits of the flight envelope or atmospheric turbulence or armament firing—just to name a few sources of distortion (for a more complete survey, see [1]). It is well known that these degraded inlet conditions can trigger engine instabilities. The axial flow compressor is particularly sensitive to inlet distortion and a compressor stall can lead to engine surge which must be avoided in any event. Considering the widespread occurrence of distorted flow and the detrimental and sometimes fatal effects it may have on engine operation—not to mention the general complexity of the problem—it is not surprising that a great deal of study has already been devoted to nonuniform flows in axial turbomachines. In particular, steady, circumferential inlet distortion has been extensively investigated as it can greatly effect compressor stall margins and performance. However, most of this theoretical work has been carried out under the assumption that the flow nonuniformities are small perturbations superposed on a uniform mean flow in such a way that the leading equations can be linearized, (see Plourde and Stenning [2], Erich [3], Fabri [4], Callahan and Stenning [5] and others for two or three-dimensional analyses).

There are, however, many instances where this type of approximation is no longer sufficient and the complete set of nonlinear equations must be considered. This is the case, for example, when the compressor operates close to the stall line at a high pressure ratio and reduced mass flow, in a region of the operating field where small perturbations can degenerate into large amplitude instabilities. Unfortunately, the ever-increasing demands for engine performance push the operating point further into this zone and make it necessary to analyse the problem on a nonlinear basis. This calls for numerical solutions.

The first attempts to solve the problem of nonlinear distorted inlet flows were made by Nagano and Takata [6] and Adamczyk and Carta [7], both of which were based on a two-dimensional approach. The flow outside of the blade rows is assumed inviscid and incompressible and is described by the classical unsteady flow equations which are integrated numerically. The solutions are matched at the blade row, using matching conditions obtained from an unsteady blade passage analysis based on an actuator disk model. Some interesting results have been obtained, showing the various kinds of response of the blade row as a function of the intensity of the distortion and of the position of the operating point in the characteristic field. Moreover some kind of propagative perturbation has been shown to appear under certain conditions usually associated with the occurrence of rotating stall. However, it may be somewhat optimistic to relate the theoretically obtained flow patterns to the more complex rotating stall bubbles in which strong three-dimensional effects and backflows have been observed experimentally [8].

More recently, Greitzer and Strand [9] have called attention to the behaviour of circumferentially nonuniform swirling flows that occur (*a*) in turbomachines once the flow has passed through one or more blade rows or (*b*) upstream of the first rotor as an effect of flow redistribution induced by the compressor. The combination of a strong swirl and nonuniformities induces three-dimensional effects which cannot be taken into account by the above-mentioned two-dimensional approaches. Kimzey (10) has developed a three-dimensional computer model based on a finite volume method. In this model, the blade rows are replaced by a force distribution which must be evaluated by comparison with experimental results.

Contributed by the Gas Turbine Division of THE AMERICAN SOCIETY OF MECHANICAL ENGINEERS and presented at the 27th International Gas Turbine Conference and Exhibit, London, England, April 18-22, 1982. Manuscript received at ASME Headquarters December 10, 1981. Paper No. 82-GT-125.

Whereas this approach takes into account the basic characteristics of the flow (three-dimensional, unsteady, compressible), the blade row model seems to rely too heavily on empirical data which is not always readily available in the compressor development process. Therefore, it appeared worthwhile to attempt to build a model that would require less data (a sort of generalization of the actuator disk approach used by Nagano and Takata and Adamczyk) and would be matched to the three-dimensional compressible outer flow that must be calculated numerically.

This paper reports on the first part of this project: it is devoted to the development of a three-dimensional computer code for compressible nonlinear unsteady and nonuniform inviscid flow. This numerical calculation will be used subsequently for the blade-free domain within the compressor. In a second step, the solutions obtained will be matched to the blade rows.

2. Three-Dimensional Effects in Nonuniform Swirling Flows

As pointed out by Greitzer and Strand, it appears necessary to take into account the three-dimensional nature of nonuniform swirling flows in theoretical analyses, in other words, to develop three-dimensional computer codes. This can best be demonstrated through visualization of the flow in a cylindrical annular channel downstream of an inlet guide vane with circumferentially nonuniform inflow. Such an experiment was carried out in the ONERA water tunnel [11].

The nonuniform flow is generated through a classical variable porosity distortion screen located upstream of the test section as presented in Fig. 1. A one-lobe, sinus-shaped, total pressure circumferential distribution is delivered. The axial nonuniform flow is then deflected through a high

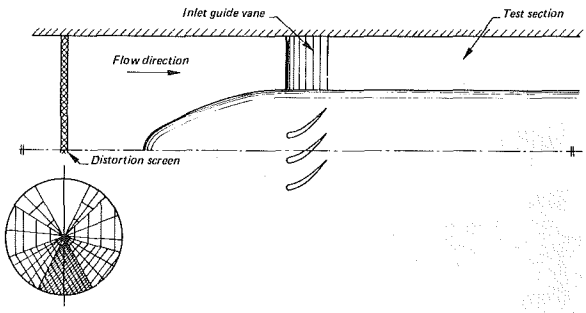

Fig. 1 Experimental setup for flow visualization

solidity inlet guide vane at a constant exit angle of approximately 50 deg. Flow is visualized downstream of the blade row at mid-radius using colored streaks.

Figure 2(*a*), obtained without inlet distortion, shows the expected wrapping of the streamlines on a surface coaxial to the channel walls: no three-dimensional effect is detected. Figures 2(*b*) and 2(*c*) have been obtained with inlet distortion and refer respectively to the picture of the high total pressure and low total pressure regions. It is obvious that some strong three-dimensional effects exist in both regions. In the high-pressure portion of the circumference, the streamlines are deflected toward the outer casing, while in the low pressure zone, the deflection occurs toward the inner casing. Furthermore, these effects do not seem to be negligible.

As shown by Grietzer and Strand [9], these radial displacements can be readily interpreted on the basis of simplified radial equilibrium considerations for a high solidity inlet guide vane (delivering a circumferentially uniform exit angle). With inlet distortion, a static pressure imbalance appears in the channel downstream of the row. This phenomenon is located at the boundaries between the high

Nomenclature

A_1-A_5 = coefficients of the compatibility equation along the negative slope C^- characteristic line in the inlet plane for subsonic operation

B_1-B_7 = coefficients of the compatibility equation along the positive slope C^+ characteristic line in the outlet plane for subsonic operation

E = total energy per unit volume

L = channel length

$\mathcal{L}_Z, \mathcal{L}_\Theta, \mathcal{L}_R$ = one-dimensional operators in the time splitting scheme

n = defines the physical time as a multiple of the time increment $t^n = n\Delta t$

p = static pressure

P_t = total pressure in the inlet plane

ΔP_t = amplitude of the inlet total pressure nonuniformity

P_{to} = undisturbed total pressure

$\mathcal{P}$ = Log p

r = radius and radial coordinate in the physical reference frame

$\tilde{r}$ = channel height

r^* = linear radial function of the inner and outer wall slopes

R = transformed radius and radial coordinate in the transformed reference frame

t = physical time

T_t = total temperature in the inlet plane

T_{to} = undisturbed total temperature

$\mathbf{V}$ = absolute velocity vector (V = velocity magnitude)

V_Z = axial velocity component

V_Θ = circumferential velocity component

V_R = radial velocity component

z = axial coordinate in the physical reference frame

Z = axial coordinate in the transformed reference frame

β = inlet tangential flow angle

γ = ratio of specific heats

θ = absolute circumferential angle and circumferential coordinate in the physical reference frame

Θ = circumferential coordinate in the transformed reference frame

Δt = time increment

ΔZ = mesh axial spacing

$\Delta\Theta$ = mesh circumferential spacing

ΔR = mesh radial spacing

ρ = density

φ = inlet radial flow angle

Subscripts

c = outer casing

h = hub

i = index identifying grid point axial location

j = index identifying grid point circumferential location

k = index identifying grid point radial location

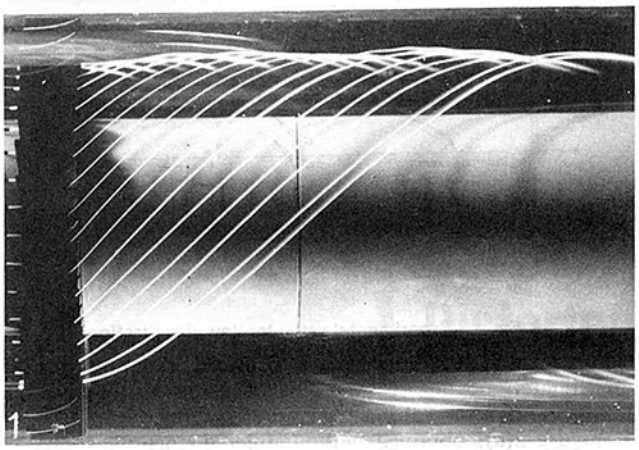

(a) Without inlet distorsion: no three-dimensional effect

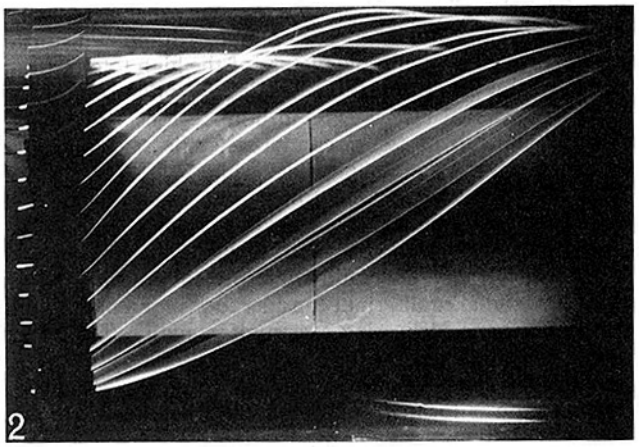

(b) With inlet distortion: high total pressure streamlines deflected towards outer casing

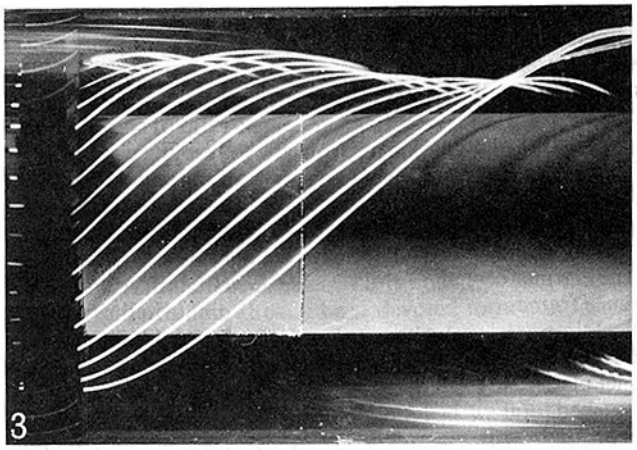

(c) With inlet distortion: low total pressure streamlines deflected towards inner casing

Fig. 2 Flow patterns downstream of an inlet guide vane

and the low total pressure regions. It results from the existence of a larger radial static pressure gradient in the high total pressure zone than in the low total pressure region. This pressure imbalance induces some mass flow redistribution at the interfaces between the regions. This, in turn, leads to radial flows within the two zones such as visualized in Fig. 2 and schematically described in Fig. 3.

The occurrence of such secondary flows makes it necessary to approach the theoretical problem of inlet distortion on a three-dimensional basis. The next section is devoted to the numerical method selected to solve this problem.

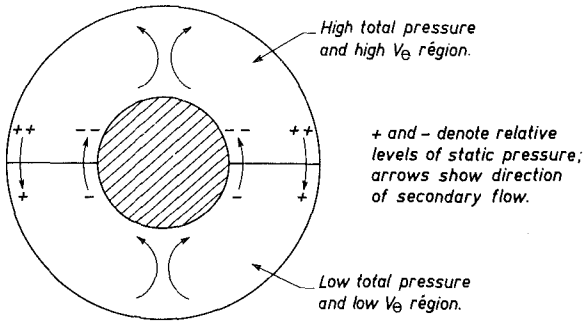

Fig. 3 Flow pattern due to static pressure imbalance (from reference [9]

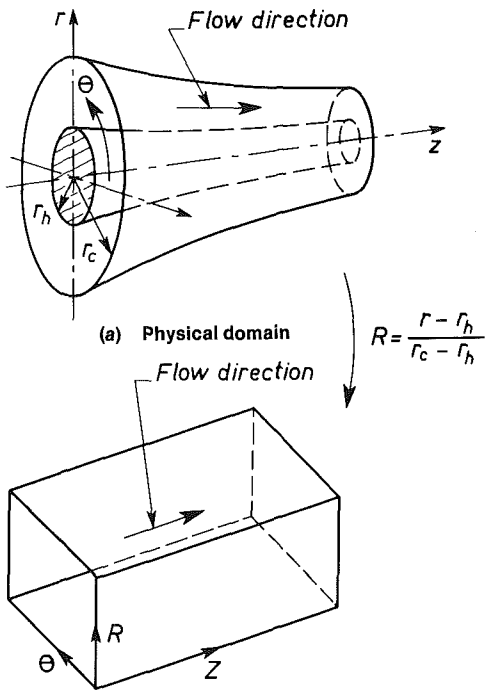

Fig. 4 Transformation of the physical domain

3. Numerical Approach

As mentioned above, the calculation presented herein is part of a larger project: the goal is to predict the response of a compressor to inlet flow nonuniformities and as a side product to study propagative perturbations at and relative to the blade rows such as those obtained in above-mentioned two-dimensional numerical analyses by Nagano-Takata, Adamczyk, and others. The basic approach selected here is quite similar to the ones proposed in the literature: the blade free channel flow is calculated numerically by integrating the classical time-dependent, three-dimensional flow equations and the blade rows are replaced by actuator disk models. Only the numerical calculation of the blade free channel under nonuniform boundary conditions is presented here; the matching of this three-dimensional computer code with the actuator disk model is still under way and will be reported on later.

The future application of the three-dimensional code to inlet distortion problems in compressors determined the general outline of the calculation. As shown in the previous section, three-dimensional flows have to be taken into consideration. Further, the occurrence of unsteady inlet conditions such as those encountered in high incidence maneuvers as well as the concern with the high back-pressure operation

of the compressor (where large amplitude propagative perturbations may appear) calls for a fully unsteady nonlinear numerical calculation. On the other hand, it was decided to restrict loss generation to the blade rows; the flow in the blade free channel is assumed invisicid.

The domain of interest is schematically presented in Fig. 4(*a*). It consists of the annular channel limited by the inner and outer casings of the turbomachine (radii r_h and r_c, respectively) and the inlet and outlet planes at abscissa $z=0$ and $z = L$, respectively. In a cylindrical coordinate reference frame (z, θ, r) relative to the channel and under the above-mentioned assumptions, the flow in the channel is described by the complete Euler's equations.

In order to simplify the numerical processing, the physical domain is transformed into a parallelepipedic calculation domain (such as presented in Fig. 4(*b*)) via a simple linear transformation

$$r \longrightarrow \mathrm{R} = \frac{r - r_h(z)}{r_c(z) - r_h(z)} \tag{1}$$

Applying this transformation to the basic system of Euler's equations written in conservation form leads to a similar system in the transformed reference frame $Z = z$, $\Theta = \theta$, R

$$\frac{\partial \mathrm{U}}{\partial t} + \frac{\partial \mathrm{F}}{\partial Z} + \frac{\partial \mathrm{G}}{\partial \Theta} + \frac{\partial \mathrm{H}}{\partial R} = 0 \tag{2}$$

with

$$\mathrm{U} = \begin{bmatrix} \mathrm{U}_1 \\ \mathrm{U}_2 \\ \mathrm{U}_3 \\ \mathrm{U}_4 \\ \mathrm{U}_5 \end{bmatrix} = \begin{bmatrix} \rho r \tilde{r} \\ \rho r \tilde{r} V_Z \\ \rho r \tilde{r} (V_R \sin\theta + V_\theta \cos\theta) \\ \rho r \tilde{r} (V_R \cos\theta - V_\theta \sin\theta) \\ r \tilde{r} E \end{bmatrix}$$

and

$$F = \begin{bmatrix} F_1 \\ F_2 \\ F_3 \\ F_4 \\ F_5 \end{bmatrix} = \begin{bmatrix} U_2 \\ U_2^2/U_1 + p r \tilde{r} \\ U_3 U_2/U_1 \\ U_4 U_2/U_1 \\ (U_5 + p r \tilde{r}) U_2/U_1 \end{bmatrix},$$

$$G = \begin{bmatrix} G_1 \\ G_2 \\ G_3 \\ G_4 \\ G_5 \end{bmatrix} = \begin{bmatrix} (U_3 \cos\theta - U_4 \sin\theta)/r \\ G_1 U_2/U_1 \\ G_1 U_3/U_1 + p \tilde{r} \cos\theta \\ G_1 U_4/U_1 - p \tilde{r} \sin\theta \\ (U_5 + p r \tilde{r}) G_1/U_1 \end{bmatrix}$$

$$H = \begin{bmatrix} H_1 \\ H_2 \\ H_3 \\ H_4 \\ H_5 \end{bmatrix} = \frac{1}{\tilde{r}} \begin{bmatrix} f - U_2 r^* \\ f U_2/U_1 - (U_2^2/U_1 + p r \tilde{r}) r^* \\ f U_3/U_1 + p r \tilde{r} \sin\theta - U_3 U_2 r^*/U_1 \\ f U_4/U_1 + p r \tilde{r} \cos\theta - U_4 U_2 r^*/U_1 \\ (U_5 + p r \tilde{r})(f - U_2 r^*)/U_1 \end{bmatrix}$$

$$f = U_3 \sin\theta + U_4 \cos\theta = \rho r \tilde{r} V_R$$

$\tilde{r}(Z)$ is the channel height, $\tilde{r}(Z) = r_c(Z) - r_h(Z)$. $r^*(Z)$ is a linear function of the slopes of the inner and outer walls ($tg\ \varphi_h(Z)$ and $tg\ \varphi\phi_c(Z)$, respectively) and is expressed as: $r^*(Z) = tg\ \varphi_h(Z) + R\ (tg\ \varphi_c(Z) - tg\ \varphi_h(Z))$. The radius r can be readily expressed as a function of R through equation (1), ρ is the density, p the static pressure, V_Z, V_θ, V_R the axial, tangential, and radial components of the velocity V, respectively, and E is the total energy-per-unit-volume which can be expressed for a perfect gas as: $E = p/(\gamma - 1) + 1/2\ \rho V^2$.

System (2) describes the nonuniform unsteady three-dimensional inviscid flow within the transformed calculation domain. This system can only be numerically integrated. It will be solved by using a finite difference time-marching method based on time-splitting. This approach is an extension (to three dimensions) of the one implemented in [12], [13], [14] for two-dimensional problems. The basic principles of the method are briefly presented below.

A constant-spacing orthogonal mesh is fitted to the calculation domain. We assume that the solution U_{ijk}^n of (2) has been obtained at instant $t^n = n\Delta t$ and at every grid point (ijk) of the domain where Δt is the time increment of the time-marching method and i, j, k refer to the axial, tangential, and radial position of the grid point within the mesh (spacings ΔZ, $\Delta\Theta$, ΔR).

Then, the simplest way of obtaining the solution U_{ijk}^{n+1} of (2), through splitting (component by component or disintegration method), at the previously defined locations in the mesh and at the next time increment can be conceptually summarized as follows:

$$t^n \longrightarrow t^{n+1/3}\ (U_{ijk}^n \longrightarrow U_{ijk}^{n+1/3})$$

$$\frac{1}{3}\frac{\partial U}{\partial t} + \frac{\partial F}{\partial Z} = 0 \tag{3a}$$

$$t^{n+1/3} \longrightarrow t^{n+2/3}\ (U_{ijk}^{n+1/3} \longrightarrow U_{ijk}^{n+2/3})$$

$$\frac{1}{3}\frac{\partial U}{\partial t} + \frac{\partial G}{\partial \Theta} = 0 \tag{3b}$$

$$t^{n+2/3} \longrightarrow t^{n+1}\ (U_{ijk}^{n+2/3} \longrightarrow U_{ijk}^{n+1})$$

$$\frac{1}{3}\frac{\partial U}{\partial t} + \frac{\partial H}{\partial R} = 0 \tag{3c}$$

The three-dimensional operator allowing the passage from u_{ijk}^n to U_{ijk}^{n+1} is split into three one-dimensional operators (one for each direction) which discretize one-dimensional systems in a fraction of the time increment (one-third of Δt in our case and for the sake of simplicity). Even though the solution obtained at the fractional time steps does not represent the physical situation, it has been shown that for a complete cycle (i.e., at instant t^n, n integer) the physical description of the flow is retained.

The three one-dimensional systems (3) are discretized in time according to the second-order finite difference procedure of McCormack [15] which can be written for equation (3*a*):

$$t^n \longrightarrow t^{n+1/3}$$

$$U_{ijk}^n \xrightarrow{\mathcal{L}_Z\left(\frac{\Delta t}{3}\right)} U_{ijk}^{n+1/3}$$

$$\times \begin{cases} \overline{U_{ijk}^{n+1/3}} = U_{ijk}^n - \dfrac{\Delta t}{\Delta Z}\,(F_{ijk}^n - F_{(i-1)jk}^n) \\ U_{ijk}^{n+1/3} = \dfrac{1}{2}\left[\overline{U_{ijk}^{n+1/3}} + U_{ijk}^n - \dfrac{\Delta t}{\Delta Z}\,(\overline{F_{(i+1)jk}^{n+1/3}} - \overline{F_{ijk}^{n+1/3}})\right] \end{cases} \tag{4}$$

and similar expressions for operators $\mathcal{L}_\Theta$ ($\Delta t/3$) and $\mathcal{L}_R$ ($\Delta t/3$) in the Θ and R directions, respectively.

The stability limit of these explicit one-dimensional schemes is given by the Courant-Friedrichs-Lewy criteria. The passage from U_{ijk}^n to U_{ijk}^{n+1} is obtained by applying the so-called resulting scheme which is defined as the product of the already mentioned one-dimensional schemes. The resulting scheme will be numerically stable as long as the three one-dimensional schemes are stable; in other words, the stability

limit of the resulting scheme will be of a one-dimensional nature; it is less restricting than one from a classical three-dimensional scheme. This allows larger time increments and shorter computing times to achieve convergence. This is one of the main advantages of the time-splitting method.

Finally, in order to retain the second-order accuracy of the McCormack scheme at the full time incements, a commutative product of one-dimensional operators must be applied [14].

$$U_{ijk}^{n} \xrightarrow{\mathcal{L}_Z\left(\frac{\Delta t}{3}\right)\mathcal{L}_\Theta\left(\frac{\Delta t}{3}\right)\mathcal{L}_R\left(\frac{\Delta t}{3}\right)\mathcal{L}_R\left(\frac{\Delta t}{3}\right)\mathcal{L}_\Theta\left(\frac{\Delta t}{3}\right)\mathcal{L}_Z\left(\frac{\Delta t}{3}\right)} U_{ijk}^{n+2} \tag{5}$$

In fact it can be shown that the solution of the resulting scheme approximates equation (2) with accuracy of the second order [14].

3.1 Boundary conditions. Three types of boundary conditions must be considered:

1 The simplest one is the so-called periodicity condition which is applied over the whole circumference and is implemented in a classical manner by rendering the solutions obtained in $\Theta = 0$ equal to those in $\Theta = 2\pi$.

2 On the hub and on the outer casing, the slip condition is applied

$$V_R / V_Z = tg\ \varphi_{h\,\text{or}\,c} \tag{6}$$

The flow field on the walls is first calculated by the integration of system (2). Operators $\mathcal{L}_Z$ and $\mathcal{L}_\Theta$ can be applied as in any R = constant plane. The situation is somewhat different for operator $\mathcal{L}_R$ in the radial direciton. The classical McCormack scheme cannot be applied since it would require grid points outside of the calculation domain. It is replaced by the second-order Kutler-Reinhardt-Warming scheme [16], which can be expressed on the hub ($R = 0$, $k = 0$) as follows:

$$\overline{U_{ij0}^{n+1}} = U_{ij0}^{n+2/3} - \frac{\Delta t}{\Delta R}\left(H_{ij1}^{n+2/3} - H_{ij0}^{n+2/3}\right)$$

$$U_{ij0}^{n+1} = \frac{1}{2}\left[U_{ij0}^{n+2/3} + \overline{U_{ij0}^{n+1}} - \frac{\Delta t}{\Delta R}\left(\overline{H_{ij1}^{n+1}} - \overline{H_{ij0}^{n+1}}\right)\right. \tag{7}$$

$$\left. + \frac{\Delta t}{\Delta R}\left(H_{ij2}^{n+2/3} - 2\,H_{ij1}^{n+2/3} + H_{ij0}^{n+2/3}\right)\right]$$

For the sake of simplicity, the slip condition is then implemented by allowing the velocity vector to align with the wall while retaining its magnitude. The velocity components are corrected accordingly.

The slip condition will be applied only at full time steps—as it is here alone that a physical description of the flow is obtained.

3 The boundary conditions at the inlet and outlet planes of the domain require a more thorough investigation. This is done by considering the physical domain of dependence of the grid points located on the boundaries such as defined by the characteristic lines in a (Z, t) plane of the one-dimensional system

$$\frac{\partial U}{\partial t} + \frac{\partial F}{\partial Z} + D = 0 \quad \text{with} \quad D = \frac{\partial G}{\partial \Theta} + \frac{\partial H}{\partial R}$$

Different cases can arise depending on the type of boundary (inlet versus outlet) and the axial velocity level (subsonic versus supersonic). This is best illustrated in Fig. 5.

For the inlet plane, if the axial component of the velocity is subsonic, only one piece of information is fed back from inside the computational domain along the negative slope C^- characteristic line: therefore, in addition to this piece of information, four quantities must be given for a complete defining of the inlet flow. This will always be the case for compressor applications.

For the outlet plane, two cases can be considered

1 Either the axial component of the velocity is subsonic as in the previous case—except that the piece of information is fed back from the outside and has to be independently provided for – or

2 The axial component of the velocity is supersonic like in sonic nozzles. Both cases have been considered, especially in light of the problems that have arisen from trying to define a downstream condition that would be consistent with the upstream distortion

At the inlet, the boundary condition requirements are fulfilled through:

- the total pressure P_t;

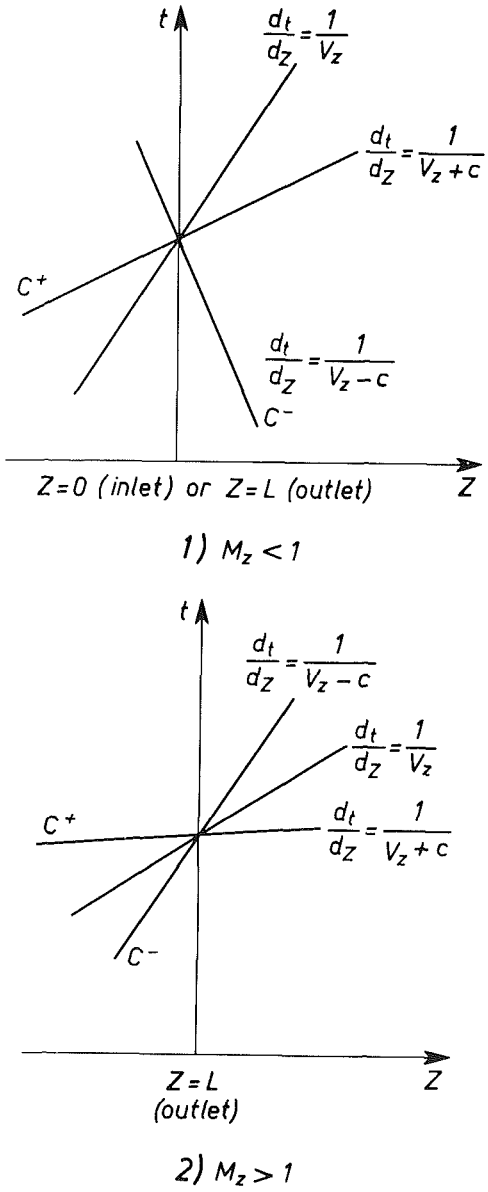

Fig. 5 Characteristic lines of system $\delta u/\delta t + A\,\delta u/\delta Z + B = 0$ in a (Z, t) plane

- the total temperature T_t;
- the direction of the velocity vector as defined by the angles between the axial direction and the projections of the velocity vector in a blade-to-blade plane (angle β) and a meridional plane (angle φ), respectively.

In the case of subsonic outlet axial velocity, the static pressure is given.

These boundary conditions have to be imposed at all grid points in the inlet (outlet) plane and can therefore be highly nonuniform both in space and in time.

The theoretical approach to the flow problem at the boundaries is based on the compatibility equations along the characteristic lines as derived from the method of characteristics. At the inlet plane, the only unknown is obtained though integration of the compatibility equation along the C^- characteristic line

$$\frac{\partial \mathcal{P}}{\partial t}+A_1\frac{\partial \mathcal{P}}{\partial Z}+A_2\frac{\partial V_Z}{\partial Z}+A_3\frac{\partial \mathcal{P}}{\partial R}+A_4\frac{\partial \mathcal{P}}{\partial \Theta}+A_5=0 \quad (8)$$

where $\mathcal{P} = \text{Log}\, p$ (p static pressure). The coefficient A_1 to A_5 are direct functions of the inlet conditions P_t, T_t, β and φ as well as the channel geometry. This equation is integrated using the previously-mentioned time-splitting method:

$$t^n \xrightarrow{l_Z\left(\frac{\Delta t}{3}\right)} t^{n+1/3} \qquad (\mathcal{P}^n_{ijk} \longrightarrow \mathcal{P}^{n+1/3}_{ijk})$$

$$\frac{1}{3}\frac{\partial \mathcal{P}}{\partial t}+A_1\frac{\partial \mathcal{P}}{\partial Z}+A_2\frac{\partial V_Z}{\partial Z}+A_3=0 \quad (9a)$$

$$t^{n+1/3} \xrightarrow{l\Theta\left(\frac{\Delta t}{3}\right)} t^{n+2/3} \qquad (\mathcal{P}^{n+1/3}_{ijk} \longrightarrow \mathcal{P}^{n+2/3}_{ijk})$$

$$\frac{1}{3}\frac{\partial \mathcal{P}}{\partial t}+A_4\frac{\partial \mathcal{P}}{\partial \Theta}=0 \quad (9b)$$

$$t^{n+2/3} \xrightarrow{l_R\left(\frac{\Delta t}{3}\right)} t^{n+1} \qquad (\mathcal{P}^{n+2/3}_{ijk} \longrightarrow \mathcal{P}^{n+1}_{ijk})$$

$$\frac{1}{3}\frac{\partial \mathcal{P}}{\partial t}+A_3\frac{\partial \mathcal{P}}{\partial R}=0 \quad (9c)$$

Equation (9a) is discretized using the Kutler-Reinhardt-Warming scheme for equations in nonconservation form, while equations (9b) and (9c) are dealt with by using the classical McCormack scheme—again for equations in nonconservation form (both schemes are given in the Appendix).

A quite similar approach is used in the outlet plane for the subsonic case. Except that here the characteristic lines considered are the positive slope C^+ characteristic line and the streamline. Four equations must be integrated: the compatibility equation along C^+ and three equations from the basic system (2)

$$\frac{\partial V_Z}{\partial t}+B_1\frac{\partial V_Z}{\partial Z}+B_2\frac{\partial P}{\partial Z}+B_3\frac{\partial V_Z}{\partial \Theta}+B_4\frac{\partial V_\Theta}{\partial \Theta}+B_5\frac{\partial V_Z}{\partial R}+B_6\frac{\partial V_R}{\partial R}+B_7=0 \quad (10)$$

$$\frac{\partial U_l}{\partial t}+\frac{\partial F_l}{\partial Z}+\frac{\partial G_l}{\partial \Theta}+\frac{\partial H_l}{\partial R}=0 \quad \text{for} \quad l=1,3,4$$

where U_l, E_l, G_l and H_l are defined in (2), and the coefficients B_1 to B_7 of the compatibility equation are functions of the static pressure (boundary condition) the velocity components and the channel geometry.

This system can be readily integrated by using the time-splitting method and the same numerical procedure as presented for the inlet plane. For the supersonic case, the basic system (2) is integrated up to the outlet plane. For the one-dimensional operator in the Z-direction, the McCormack scheme has to be replaced by the Kutler-Reinhardt-Warming scheme for grid points at the outlet.

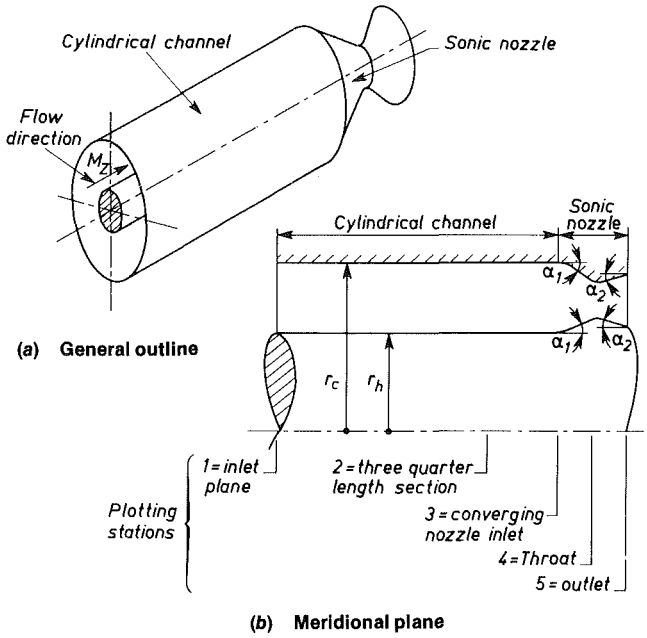

Fig. 6 Physical domain

3.2 Corner points. These are the points that belong both to the inner (outer) wall and to the inlet (outlet) plane.

The inlet plane requires no special consideration since the slip condition is directly dealt with by the inlet boundary conditions (angle φ).

At the outlet, a problem arises only when the axial component of the velocity is subsonic, because two conditions have to be verified at the corner grid points: the outlet static pressure boundary condition and the slip condition. As pointed out by the previously mentioned characteristic line analysis, this cannot be the case. Therefore, the slip condition has been dropped and a jet-like flow readjustment is thus allowed.

A classical smoothing technique [13], similar in nature to the introduction of an artificial viscosity term, is implemented to eliminate the numerically induced small oscillations that may occur during the calculation and retard convergence. Second-order accuracy is retained through adjustable parameters within the procedure.

4 Results

The above-described computing procedure has been applied to determine the flow in a cylindrical annular channel fitted downstream with a nozzle which is assumed to remain sonic regardless of the inflow conditions. As pointed out in the previous section, adding this nozzle eliminates the requirement for a downstream boundary condition. The geometry of the physical domain is given below and illustrated in Fig. 6.

Cylindrical channel

inner radius r_h	= 0.055 m
outer radius r_o	= 0.103 m
hub-to-tip ratio	= 0.534
length	= 0.24 m

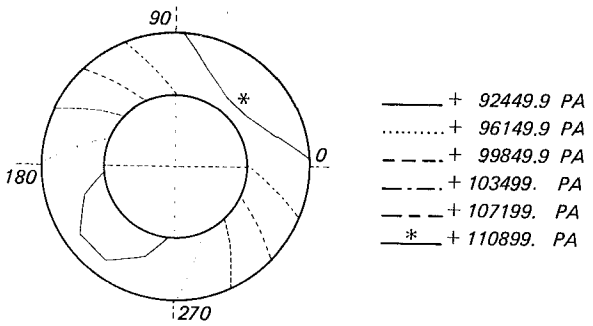

Fig. 7 Inlet total pressure distribution

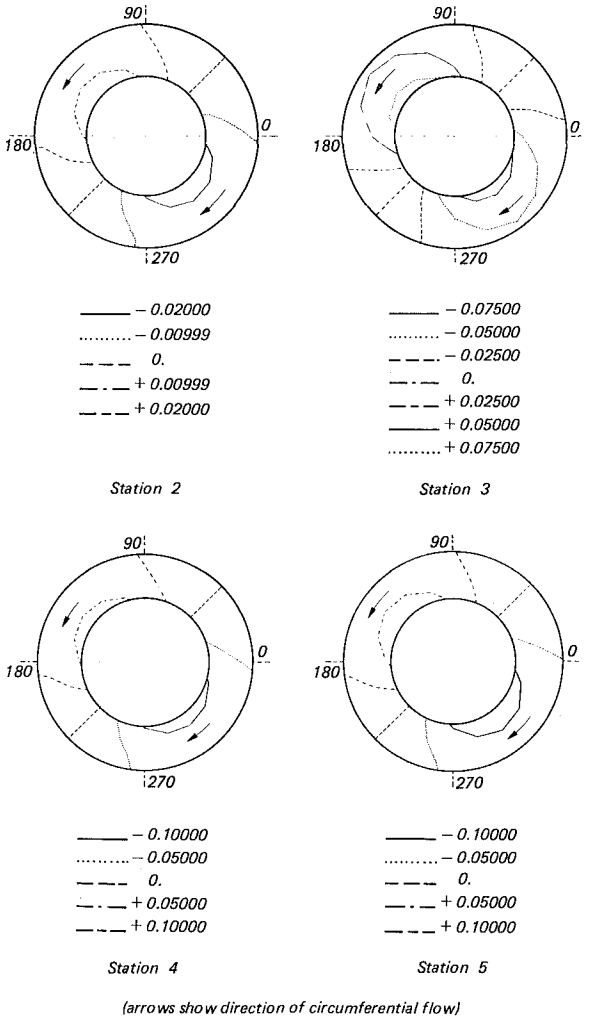

Fig. 8 Secondary swirl distribution along the channel for the no-swirl inlet condition (tangential Mach number)

Nozzle

slope angle of converging duct	$\alpha_1 = 10$ deg
slope angle of diverging duct	$\alpha_2 = 3$ deg
contraction ratio at the throat	= 0.8416
length	= 0.057 m

The throat is located at mid-length of the nozzle. The nozzle has been calculated on a one-dimensional basis to ensure sonic flow at the throat for an initial axial Mach number of 0.6 under uniform stagnation conditions at the inlet ($P_{to} = 1$ atm, $T_{to} = 300$ K).

A mesh with evenly distributed grid points in each direction

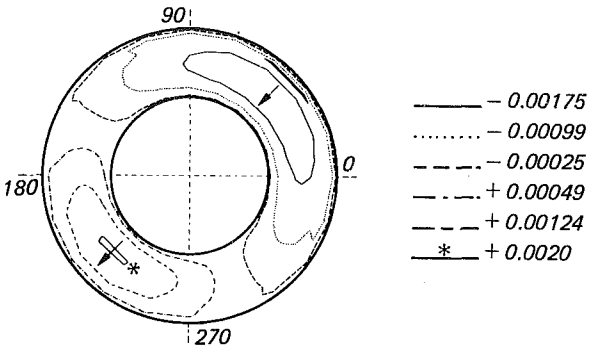

(arrows show direction of radial flow).

Fig. 9 Radial Mach number distribution at station 2 for the no-swirl inlet condition

is used for all calculations: 11 points are provided in the radial direction, 21 in the tangential direction; the number of points in the axial direction is restricted by the fast memory capacity of the ONERA CDC Cyber 750 digital computer. Practically speaking, 53 grid points could be provided for in the axial direction which brings the total number of grid points to 12243. Considering this fairly small number of points, it was expected that the results in the nozzle would be somewhat inaccurate. However, the main purpose of the nozzle being to disjoin the flow field from the downstream outer flow, this situation was not considered too detrimental.

A special procedure is used for the introduction of the boundary conditions at the inlet plane: first, the starting condition is given by the one-dimensional channel solution with uniform boundary conditions. Then, for a certain period of time which may extend over the first 40 time steps, the upstream boundary conditions are progressively modified according to a quasi-steady linear procedure bringing the uniform initial conditions to their required final expressions. For the computations presented here, only steady-state nonuniformities were considered.

Two distinct cases are presented here. They refer to the same nonuniform stagnation conditions (P_t, T_t) and correspond respectively to:

1 a non-swirling flow ($\beta = 0$ deg), and
2 a swirling flow ($\beta = 20$ deg) at the inlet.

The boundary conditions are summarized below

$$P_t(\theta,r) = \left(P_{to} + \rho V_{\theta_{ini}}^2 \log\frac{r}{r_h}\right)\left(1 + \frac{\Delta P_t}{P_{to}}\sin\left(\theta + \frac{\pi}{4}\right)\right)$$

$$T_t = T_{to} \quad = 300 \text{ k} = \text{constant} \qquad (11)$$

$$\varphi = 0 \text{ deg} \quad = \text{constant (slope angle of the flow)}$$

$$\beta = C_1 \quad = \text{constant (swirl angle)}$$

where $C_1 = 0$ deg for the no-swirl calculation and $C_1 = 20$ deg for the second test-case.

Further $P_{to} = 1$ atm and $\Delta P_t/P_{to} = 0.1$. This last value sets the level of distortion at approximately 50 percent of the dynamic pressure available at the starting axial Mach number of 0.6: this is a severe distortion level. The fairly complicated total pressure distribution was selected in order to detect the flow characteristics that might not appear with a simple circumferential nonuniformity. It was tailored to the swirling flow test-case in order to compensate for the effect of the static pressure radial gradient ($V_{\theta_{ini}}$ is the tangential component of the velocity of a one-dimensional 20 deg angle swirling flow with an axial Mach number of 0.6 under uniform stagnation conditions ($P_{to} = 1$ atm, $T_{to} = 300$ K)). The inlet total pressure nonuniform distribution is presented in Fig. 7. The asterisk makes the difference between two solid lines (as in Figs. 9, 11 and 12).

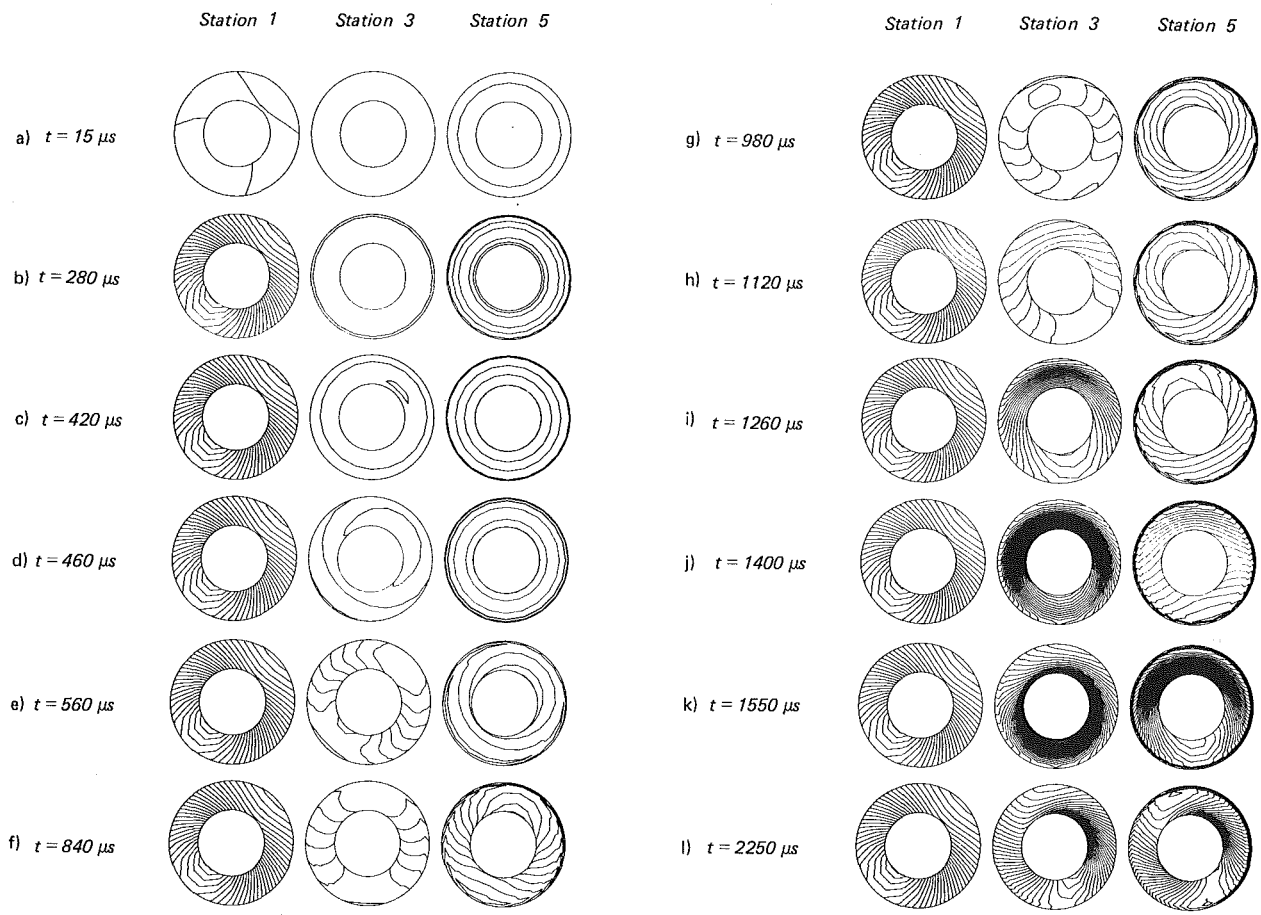

Fig. 10 Time-dependent total pressure distributions along the channel for swirling inlet flow (from initial to near convergence conditions)

4.1 Non-Swirling Inlet Flow. Three-dimensional computer codes yield a very large amount of theoretical results. The reduction of numerically obtained theoretical data is therefore a problem which must be addressed early on in the development process of the calculation. The procedure selected here is similar to the one used in classical inlet testing under nonuniform conditions. The constant level lines of the main flow characteristics (static/total pressure, total temperature, velocity components) are plotted in discrete radial planes perpendicular to the axis of the duct. We considered it sufficient to retain only five plotting locations along the channel as indicated in Fig. 6: the inlet plane, the three-quarter length plane in the cylindrical channel, the outlet of the cylindrical channel, the sonic nozzle throat and the nozzle outlet. We will refer to these as stations 1 to 5, respectively.

The most interesting results concern the secondary flows that appear in the duct. Figure 8 presents the distribution obtained for the tangential Mach number at stations 2 to 5 (the inlet plane distribution is not presented since the swirl angle is set equal to 0 deg at the inlet).

It can be seen that some flow redistribution occurs; it is probably induced by the nozzle which is assumed to remain sonic. Some flow is deflected from the high total pressure zone in the first quadrant of the circumference toward the low total pressure region located in the third quadrant. However, this process does not affect the symmetry of the charts; the global circulation conservation is therefore demonstrated.

The swirl components which appear in the channel on both sides of the 45 deg symmetry axis of the charts produce some radial flow within the high and low total pressure regions. This is linked directly to the continuity requirement. This can be seen in Fig. 9 which presents the radial Mach number distribution at station 2 in the cylindrical channel. Some radial flow toward the hub is observed in the high total pressure region while in the low total pressure zone radial flow is toward the outer casing.

4.2 Inlet Swirling Flows. The introduction of an inlet swirling component modifies radically the flow picture within the duct. The symmetry of the charts obtained in the preceeding case at the different axial locations in the channel disappears.

Figure 10 shows how the solution for the total pressure distribution is established in time in the cylindrical part of the duct: the graphs presented correspond to stations 1, 3, and 5. The unsteady process is illustrated from the uniform starting conditions to the (almost) final flow configuration. The starting procedure extends over the first 40 time steps and brings the inlet boundary conditions from their uniform initial values to the required distortion levels (Fig. 10(*b*)). The inlet nonuniformities being of a steady-state nature, no modification of the inlet total pressure distribution is observed beyond this stage throughout the remainder of the computation. The acoustic waves generated during the starting procedure propagate downstream at a velocity which is sonic relative to the flow; they cross station 3 after about 400 μs (physical time) which corresponds approximately to the time required by the Courant-Friedrichs-Lewy criteria to guarantee numerical stability. Station 5 is reached after 560 μs.

Now, the gradual rotation of the distribution and a lag between stations 3 and 5 can be seen. This rotation

corresponds to the progressive establishment of the radial equilibrium solution and is due to the three-dimensional acoustic wave interaction on the flow field. A very strong radial gradient appears within the channel. This is indicated by the strengthening of the constant level line density. This phenomenon can be detected at $t = 1400$ μs (Fig. 10 (*j*)) in station 3 and $t = 1550$ μs (Fig. 10(*k*)) in station 5. Careful study of the static pressure axial distribution shows that this radial gradient still corresponds to the establishment of the radial equilibrium solution. The decrease of the radial total pressure gradient indicated by the decrease in the constant level line density observed in Figs. 10(*k*) and 10(*l*) could be linked to the convection of the high total pressure fluid through the nozzle.

Figure 10(*l*) shows a flow configuration similar to the one obtained when the computation reaches convergence. The rotation angle of the total pressure distributions corresponds approximately to the inlet swirl angle. The rotation is more pronounced at the hub than at the tip.

Figure 11 depicts the radial Mach number distribution at station 2 in the cylindrical channel. Two distinct regions can be observed: like the high total pressure region, one is centered in the first quadrant and is characterized with a positive or toward the outer casing oriented radial velocity; like the low total pressure zone, the second one is centered in the third quadrant and is characterized with a negative or toward the inner casing oriented radial velocity. The interfaces between these two regions show no radial flow. Such a distribution corresponds to the trend indicated by the above-mentioned flow model introduced by Greitzer and Stand. However, while the towards the axis radial flow region seems to align well with the rotated low total pressure zone, some phase lag is observed between the high total pressure zone and the positive radial flow region. This may be traced back to the more complex static pressure distribution obtained in this case as compared to the one used for the model derivation. Because of the particular boundary conditions selected here, no real attempt was made to compare the numerically obtained results to the conclusions derived by Greitzer and Strand concerning certain features of distorted channel flows [9]. However, such a comparison could be very worthwhile.

4.3 Downstream Boundary Condition Problems. Fitting the channel with a sonic nozzle downstream is a very tempting numerical solution since the boundary condition requirement bcomes nonexistent and is therefore automatically fulfilled. This is the case as long as the nozzle remains sonic despite the inlet conditions. While this may be possible in many instances, particular inlet distortions can undoubtedly lead to unchoking of the nozzle. Besides, in a real compressor application, the choked nozzle is located far downstream at the first turbine stator throat beyond the combustor. Under these circumstances, adding a sonic nozzle at the downstream end of the compressor channel is not always a realistic procedure.

For all these reasons, it seemed worthwhile to consider the case of subsonic outlet velocity more carefully this allowed in the meanwhile, testing the program's so-called subsonic capability and its special previously-described outlet plane numerical treatment (compatibility equations).

For this purpose, the computational domain was reduced and only the cylindrical duct extending from the inlet plane to station 2 was considered. The inlet conditions as summarized in [11] (with inlet swirl) were retained. Furthermore, the static pressure distribution furnished by the previous calculation (with sonic nozzle) at station 2, considered as part of the original computational domain, was used as input for the downstream boundary condition with the cut-off domain.

Figure 12 shows a comparison of the total pressure distributions obtained at station 2 which is considered:

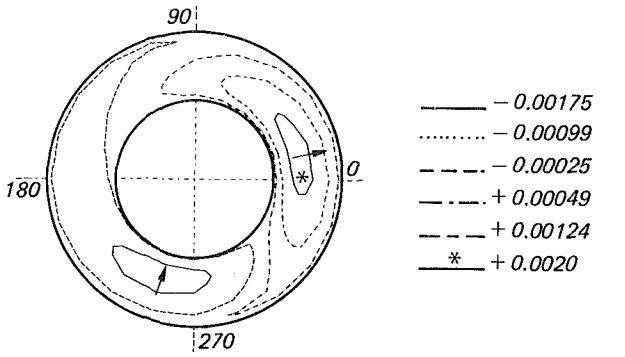

(arrows show direction of radial flow).

Fig. 11 Radial Mach number distribution at station 2 for inlet swirling flow

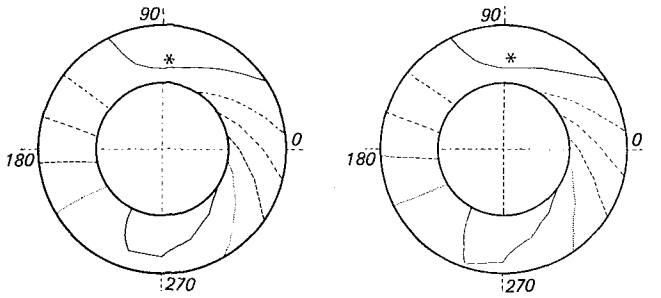

(a) Calculation with outlet sonic nozzle **(b) Fully subsonic channel calculation**

— + 92449.9 PA
..... + 96149.9 PA
– – – – + 99849.9 PA
— . — . + 103499. PA
— — — + 107199. PA
* + 110899. PA

Fig. 12 Comparison of the total pressure distribution at station 2

1 as an interior plane in the calculation with the sonic nozzle, and

2 as a boundary in the fully subsonic calculation.

Examination of the charts does not show some discrepancies between the two cases, but, generally speaking, the results can be considered very similar and satisfactory. Virtually, no difference has been found at other axial locations.

In the calculation presented here, the problem of defining the downstream static pressure condition was easily solved by using the previously calculated static pressure distribution at the plane where the computational domain was cut-off. This procedure guaranteed the consistency of the inlet distorted flow conditions and the downstream boundary condition. However, in most cases and especially at the compressor development stage, no information is available as to the downstream static pressure distribution.

Making the outlet static pressure uniform over the entire downstream boundary, as commonly done in two-dimensional analyses, proves impracticable in three-dimensional swirling flow because of the inconsistency between the radial equilibrium solution and this simple static pressure condition.

Given these circumstances, it seems that the only practical solution out of this deadlock – aside from the sonic nozzle – would be to follow Hedstrom's proposition [17]: to implement some kind of non-reflecting downstream boundary condition which allows bringing "downstream infinity" at a finite distance by cutting-off the back-flow of information from downstream.

5. Summary and Recommendations

A fully unsteady numerical method of solution for inviscid, sub and supersonic, nonuniform flow in a turbomachine channel has been developed. Particular attention has been devoted to the statement and method of implementation of upstream and downstream nonuniform boundary conditions. The solution algorithms employed at the interior and boundary points of the grid have been described.

Numerical test cases have been concluded to demonstrate the capabilities and limitations of the method. The results presented herein describe the flow-pattern in a channel fitted downstream with a sonic nozzle, the upstream nonuniformities imposed at the inlet plane being defined analytically. For a given set of nonuniform boundary conditions, the computation indicated fundamental differences in the secondary flow pattern depending on whether or not inlet swirl was considered. In the case of inlet swirl, the validity of the flow model introduced by Greitzer and Strand [9] was demonstrated. The problem of defining the downstream boundary condition for subsonic three-dimensional nonuniform outlet flow was briefly addressed. More effort will have to be devoted to this particular aspect of nonuniform, three-dimensional flow in turbomachines. Comparison with experimental data was not carried out because of the lack of reliable experiments. This should be amended in the future.

Matching of the three-dimensional calculation presented above with an actuator disk model is under way and will be reported on in a future contribution [18] [19].

References

1 Fuhs, A. E., "Introduction to Distortion Induced Engine Instability," *AGARD Lecture Series*, No. 72, Nov. 1974.

2 Plourde, G. A., and Stenning, A. H., "Attenuation of Circumferential Inlet Distortion in Multistage Axial Compressors," *Journal of Aircraft*, Vol. 5, No. 3, p. 236-242.

3 Erich, F., "Circumferential Flow Distortions in Axial Flow Turbomachinery," *Journal of Aeronautical Sciences*, Vol. 24, 1957, pp. 413-417.

4 Fabri, J., Growth of a Perturbation in an Axial Flow Compressor," ASME Paper No. 78-GT-30, 1978.

5 Callahan, G. M. and Stenning, A. H., "Attenuation of Inlet Flow Distortion Upstream of Axial Flow Compressors," *Journal of Aircraft*, Vol. 8, 1971, pp. 227-233.

6 Nagano, S. and Takata, H., "Non-Linear Analysis of Rotating Stall," Institute of Space and Aeronautical Science, University of Tokyo, Report No. 449, 1970.

7 Adamczyk, J. J. and Carta, F. O., "Unsteady Fluid Dynamic Response of an Axial Flow Compressor Stage with Distorted Inflow," Project SQUID Technical Report UARL-2-PU, 1973.

8 Day, I. J. and Cumpsty, N. A., "The Measurement and Interpretation of Flow within Rotating Stall Cells in Axial Compressors," Cambridge University, CUED/A - Turbo/TR - 90.

9 Greitzer, E. M. and Strand, T., "Asymmetric Swirling Flows in Turbomachine Annuli," ASME Paper No. 78-GT-109, 1978.

10 Kimzey, W. F., "An Analysis of the Influence of Some External Disturbances on the Aerodynamic Stability of Turbine Engine Axial Flow Fans and Compressors," *AEDC Technical Report* 77-80, August 1977.

11 Huard, J. and Werlé, H., "Influence d'une Distorsion Amont sur l'Ecoulement dans une Grille d'Aubes Annulaire Fixe," Entropie, No. 81, mai-juin 1978, pp. 15-20.

12 Laval, P., "Méthodes Instationnaires de Calcul des Effets d'Interaction de Paroi en Ecoulement Bidimensionnel Supercritique," *La Recherche Aérospatiale*, 1973-5, Translation ESRO TT-40, 1974, pp. 275-288.

13 Laval, P., "Calcul de l'Ecoulement Instationnaire Transsonique Autour d'un Profil Oscillant par une Méthode à Pas Fractionnaires," *Archives of Mechanics*, 28, 5-6, Warszawa, 1976, pp. 855-880.

14 Laval, P., "Schemas Explicites de Desintegration du Second Ordre pour la Résolution des Problèmes Hyperboliques Non-Linéaires: Théorie et Applications aux Ecoulements Transsoniques," ONERA Technical Note No. 1981-10 (English translation ESA-TT768, 1982).

15 McCormack, R. W., "The Effect of Viscosity in Hypervelocity Impact Cratering," *AIAA Paper* No. 69-354.

16 Kutler, P., Reinhardt, W. A., and Warming, R. F., "Numerical Computation of Multishocked, Three-Dimensional Supersonic Flow Fields with Real Gas Effects," *AIAA Paper* No. 72-702.

17 Hedstrom, G. W., "Nonreflecting Boundary Conditions for Nonlinear Hyperbolic Systems," *Journal of Computational Physics*, Vol. 30, 1979, pp. 222-237.

18 Billet, G., Laval, P., and Chevalier, P., "Response of an Axial Compressor to Distorted Inlet Flow," Conference on Computational Methods in Turbomachinery, Birmingham, Apr. 1984.

19 Billet, G., Laval, P., and Chevalier, P., "Numerical Simulation of the Response of an Axial Compressor to a Nonhomogeneous Inlet Flow," *La Recherche Aerospatiale*, 1985-3 (English translation ESA to appear).

APPENDIX

The Kutler-Reinhardt-Warning sheme for equation (9*a*) (in nonconservation form) yields:

$$\overline{\mathcal{P}^{n+1/3}_{1jk}} = \mathcal{P}^{n}_{1jk} - A_1 \frac{\Delta t}{\Delta Z}(\mathcal{P}^{n}_{2jk} - \mathcal{P}^{n}_{1jk}) - A_2 \frac{\Delta t}{\Delta Z}(V^{n}_{Z_{2jk}} - V^{n}_{Z_{1jk}}) - A_5 \Delta t$$

$$\mathcal{P}^{n+1/3}_{1jk} = \frac{1}{2}\left[\mathcal{P}^{n}_{1jk} + \overline{\mathcal{P}^{n+1/3}_{1jk}} - \bar{A}_1 \frac{\Delta t}{\Delta Z}(\overline{\mathcal{P}^{n+1/3}_{2jk}} - \overline{\mathcal{P}^{n+1/3}_{1jk}}) - \bar{A}_2 \frac{\Delta t}{\Delta Z}(\overline{V^{n+1/3}_{Z_{2jk}}} - \overline{V^{n+1/3}_{Z_{1jk}}}) + A_1 \frac{\Delta t}{\Delta Z}(\mathcal{P}^{n}_{3jk} - 2\mathcal{P}^{n}_{2jk} + \mathcal{P}^{n}_{1jk}) + A_2 \frac{\Delta t}{\Delta Z}(V^{n}_{Z_{3jk}} - 2\,V^{n}_{Z_{2jk}} + V^{n}_{Z_{1jk}}) - (A_5 + \bar{A}_5)\Delta t)\right]$$

where $\bar{A}_1$, $\bar{A}_2$, and $\bar{A}_5$ are evaluated at the predictor level.

The McCormack scheme for equation (9*b*) (in nonconservation form) can be expressed as:

$$\overline{\mathcal{P}^{n+2/3}_{1jk}} = \mathcal{P}^{n+1/3}_{1jk} - A_4 \frac{\Delta t}{\Delta \Theta}(\mathcal{P}^{n+1/3}_{1jk} - \mathcal{P}^{n+1/3}_{1(j-1)k})$$

$$\mathcal{P}^{n+2/3}_{1jk} = \frac{1}{2}\left[\mathcal{P}^{n+1/3}_{1jk} + \overline{\mathcal{P}^{n2/3}_{1jk}} - \bar{A}_4 \frac{\Delta t}{\Delta \Theta}(\overline{\mathcal{P}^{n+2/3}_{1(j+1)k}} - \overline{\mathcal{P}^{n+2/3}_{1jk}})\right].$$

Again, $\bar{A}_4$ is evaluated at the predictor level.

Ejector Performance Characteristics and Design Analysis of Jet Refrigeration System

B. J. Huang

C. B. Jiang

F. L. Hu

Department of Mechanical Engineering,
National Taiwan University,
Taipei, Taiwan, Rep. of China

Ejector performance characteristics and design analysis of jet refrigeration systems were studied. It was shown that choking phenomena in the secondary vapor play a very important role in ejector performance. Ejector choking, which is usually associated with a hypothesized effective area for the secondary vapor in the mixing zone, takes place when the ejector is operating at a back pressure below the critical value. The effective areas analyzed from the experiment were shown not to be constant but to vary with operating conditions. A performance map was constructed from the experimental results to show the ejector performance characteristics and from which the design analysis of jet refrigeration systems was carried out. Several important features of jet refrigeration system design are summarized in the present paper. Further analyses were also made to show the performance characteristics of jet refrigeration systems operating at off-design conditions.

Introduction

Air-conditioning and refrigeration equipment play very important roles in modern human life. The utilization of this equipment in homes, buildings, vehicles, and industries provides for living comfort and necessary means for industrial production. However, the large amount of energy consumed by this equipment consequently becomes a serious problem to be solved. Thus it is desirable to seek a new technique which can effectively and economically use heat such as solar, geothermal, or waste heat as an energy source to directly power air-conditioning and refrigeration equipment. Since a jet refrigeration system can operate at relatively low temperature, and has very stable performance characteristics, recent investigations have shown that it appears to be a favored choice for this purpose [1-8].

The design of jet refrigeration systems is similar to that of conventional vapor-compression systems except that the mechanical compressor is replaced by a thermal compressor, which is usually called an "ejector." Figure 1 is the schematic diagram of a typical jet refrigeration system. As heat is added to the generator, the refrigerant vapor at fairly high temperature and pressure, called primary or actuating vapor, is evolved and enters the ejector (see Fig. 2). By expansion through the nozzle inside the ejector, supersonic flow at low pressure is formed at the exit of the nozzle and has the secondary vapor entrained from the evaporator. The primary and the secondary vapors then mix with each other at the mixing section and enter the constant-area section where an aerodynamic shock is induced to create a major compression

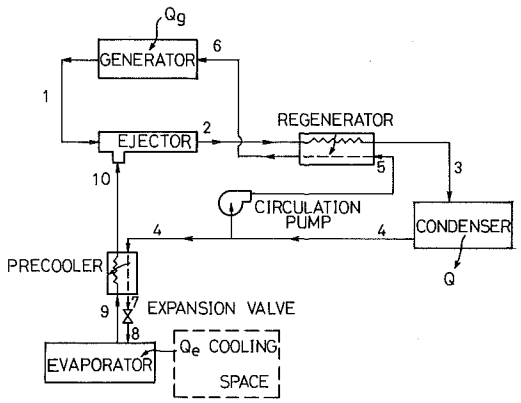

Fig. 1 Schematic diagram of jet refrigeration system

effect. Further compression of the mixed vapor to the back pressure of the ejector can be achieved as it passes through the subsonic diffuser section. By this process in the ejector, the refrigerant vapor which acts as the secondary vapor is compressed aerodynamically from the lower pressure at the evaporator to the higher presure at the condenser.

The inflow of the internal energy associated with the primary vapor serves as the energy input required for the compression operation. To obtain a cooling effect, a part of the refrigerant condensate in the condenser is allowed to expand in the evaporator to absorb heat from the environment. The rest is recirculated to the generator by a liquid circulation pump to complete a cycle. To increase the system efficiency, a regenerator and a precooler are usually added to the system. The thermodynamic cycle can be illustrated by the Mollier diagram as shown in Fig. 3.

Contributed by the Power Division for publication in the JOURNAL OF ENGINEERING FOR GAS TURBINES AND POWER. Manuscript received by the Power Division March 1984.

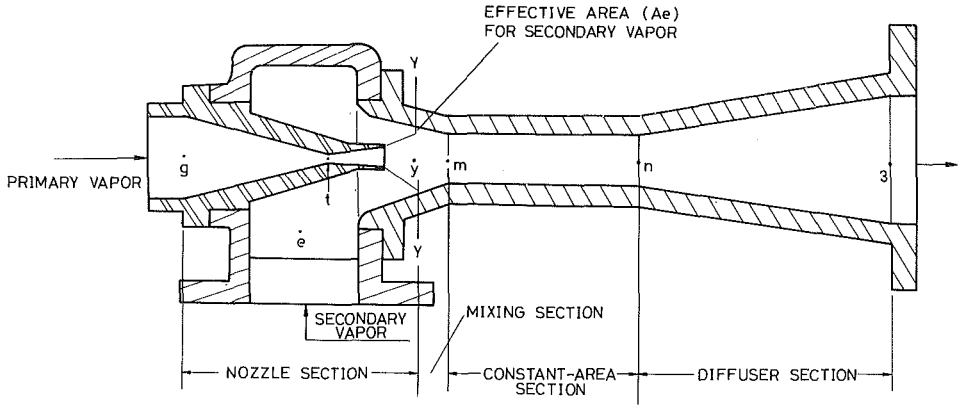

Fig. 2 Ejector design

The performance of a jet refrigeration system can be accurately calculated by use of the method of system analysis only when the performance characteristics of each component in the system are all clearly understood. In the present study, the ejector is the component which requires further study of its performance characteristics prior to the system analysis.

Performance Characteristics of Ejector

State of the Art. It is obvious that the ejector is the heart of the jet refrigeration system. The design of an ejector is, however, not a new technique. Ever since the ejector was invented early in this century, the steam jet refrigeration system has found wide applications in industrial processes, especially in large-scale plants. In recent years, research on jet refrigeration systems using Freon as the working fluid has become an interesting topic due to the growing awareness in the utilizing of low-grade energy. However, knowledge of the physical mechanisms of ejector performance is still limited.

Pioneer research work was carried out by Keenan, Neumann, and Lustwork [9, 10]. They first developed a 1-D ejector theory based on gas dynamics of ideal gas in conjunction with the principles of mass, momentum, and energy conservation and ignored heat and friction losses. Basically, the constant-pressure mixing process at the mixing section was assumed for the type of ejector as shown in Fig. 2. Several important features for ejector design based on Keenan and Neumann's theory and some other experiments were summarized later by Kroll [11].

Experimental studies for ejectors operating with various working fluids were also carried out by Work and Haedrich [12] and Holton [13]. They showed that for a fixed ejector the performance characteristics are very similar for working fluids with different molecular weights and at different operating temperatures [12–14].

Combining the theory developed by Keenan and Neumann [9, 10] and the experiment carried out by Work and Haedrich [12], Defrate and Hoerl [15] further developed a computer program to calculate the performance of an ejector working

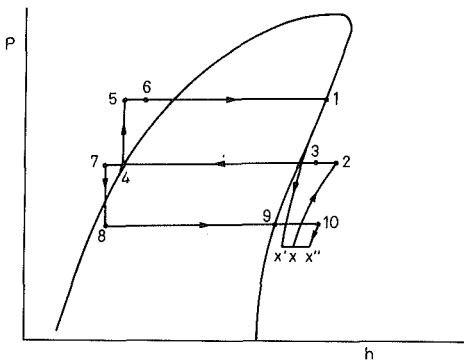

Fig. 3 Mollier diagram of jet refrigeration system

with ideal gases and including the effects of operating temperature and molecular weights of working fluids. Khoury, Heyman, and Resnick [16] later carried out an experiment using butane and hexane as the working fluids to measure the ejector performance and compare it with the theoretical calculation using Defrates' analysis [15]. It was shown that the experimental results did not agree very well with the theoretical calculations. Similar investigations were also carried out later by Emanuel [17] and Chen [18].

Following Elrod's analysis [19], which is similar to Keenans' approach, Chen [20] further theoretically designed a vapor jet air-conditioning system utilizing exhaust gas from automobile engines as the energy source but without any verification by field tests. Recently, Jeelani et al. [21, 22] summarized the aforementioned studies to develop some charts and monographs for practical design of air and steam ejectors. Investigations essentially by a similar approach were also carried out in the USSR [23–25] especially for ejectors operated by Freon fluids.

To eliminate analytical errors induced by the assumption of an ideal gas for ejectors operated by Freon fluids or steam, Stoecker [6] and Zeren, Holmes, and Jenkins [26] directly applied the thermodynamic properties of working fluid in the calculation of ejector performance. In both investigations, the

Nomenclature

A = area
h = enthalpy
m = mass flowrate
P = pressure
Q = rate of energy transfer
T = temperature
ω = entrainment ratio ($=m_s/m_p$)
W_{pump} = rate of energy consumed in pumping refrigerant

Subscripts

c = condenser
e = evaporator; effective value
g = generator
m = constant-area section
p = primary or actuating vapor
s = secondary or suction vapor
t = throat of actuating nozzle
x = nozzle exit
1, 2. . . = cycle locations

Superscript

* = critical conditions at condenser

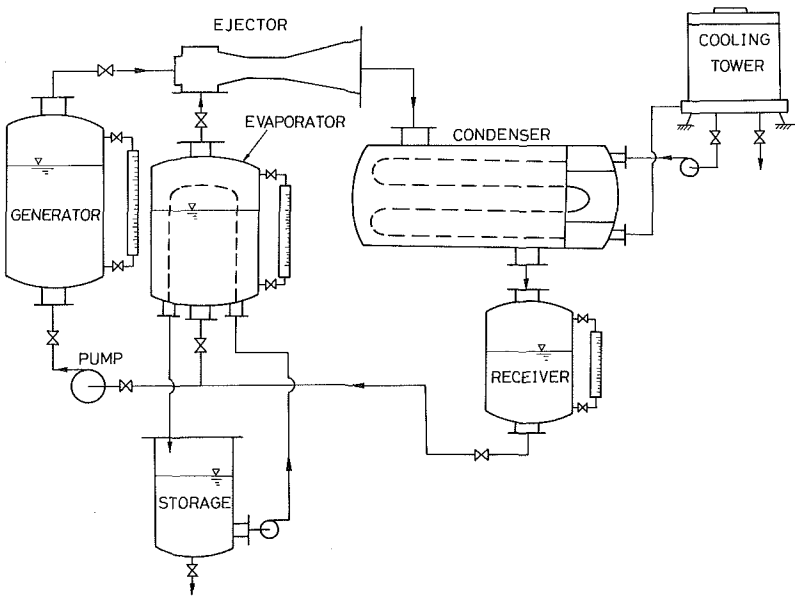

Fig. 4 Schematic diagram of ejector testing facilities

constant-pressure mixing in the mixing section of the ejector was assumed and the 1-D theory was applied. Zeren et al. [26] studied Freon-12 ejector and carried out a single sample design calculation, while Stoecker [6] developed a computer program to calculate the performance of steam ejector for a range of design parameters. According to their analysis, the entrainment ratio of the ejector will continue to increase when lowering the condenser pressure (i.e., back pressure) or raising the pressure of the actuating or primary stream. This obviously violates the fact that the ejector has long been known as a "constant-capacity device" observed from many experimental evidences [12, 20, 27–29] and field operations of jet refrigeration systems.

It had already been found that the choking phenomenon of the secondary stream takes place as the back pressure continues to lower. From this evidence, the phenomenon of constant capacity of ejectors can be well explained. However, little attention to the choking phenomenon in ejectors has been paid by researchers [6, 9–29, 33, 34] until recently.

Since the mixing process in the mixing section of the ejector is extremely complicated, it is still not well understood exactly how the primary and the secondary streams are mixed. Apparently, the constant-pressure mixing process as assumed by many investigators [9–26] is not exactly correct. Recently, Munday and Bagster [30–32] developed a semi-empirical ejector theory. They made a postulation that, after exhausting from the nozzle, the primary vapor fans out without mixing with the secondary vapor and forms a converging duct for the secondary vapor. This duct then acts as a converging nozzle such that the secondary vapor reaches sonic velocity at some cross section yy (see Fig. 2). After that, mixing of the two streams starts. The effective area A_e for the flow of secondary vapor thus can be hypothetically defined at location yy and determined from experiments. Following this concept and assuming that the effective area is constant and independent of operating conditions for an ejector, Munday et al. [32] computed the effective area A_e using the data collected from the field operation of full-scale plants and calculated the performance of the steam jet refrigeration system.

From Munday and Bagster's theory, the choking phenomenon in the secondary stream can be clearly explained. Moreover, it can be realized that the effective area as well as the ejector performance is closely related to the detailed geometric configuration of ejector interior, the operating conditions, and the primary vapor flow. The physical mechanism is so complicated that it is almost impossible at the present stage to develop a theoretical method to accurately predict the ejector performance. Therefore, an experimental analysis was carried out in the present study.

Testing Facility of Ejector. Freon-113 was selected as the working fluid in the present study since it has a low boiling point and is suitable for low-grade energy applications. The testing facility used is shown in Fig. 4.

Heat energy was directly transferred to the generator by four 2.5-kW electric heaters such that the Freon vapor (i.e., the primary vapor) was evolved at actuating pressure and entered the ejector. The electric heaters could be separately controlled, as were the heating rate, generator temperature and pressure. To eliminate the heat loss and retain thermal equilibrium, the connector between the generator and the ejector was carefully insulated so that the evolved vapor was approximately at saturated state. The generator was designed in a vertical cylinder shape, using glass for liquid level observation. Therefore, the flow rate of the primary vapor could be determined by measuring the drop of the liquid volume over a finite time interval in a steady operation. The volume of the liquid with respect to its level position in the generator was carefully calibrated using water prior to the experiment to ensure the accuracy of the measurement of flow rate to within ± 5 percent.

The flow rate of the entrained or secondary vapor was determined by measuring the drop of the liquid volume in the evaporation tank, which also served as the evaporator, over a finite time interval. Similar calibration procedures for the liquid volume as described above were also made for the evaporation tank. To generate secondary vapor for the ejector, five U-type heat exchanging tubes were immersed in the tank. By circulating warmer water through them, the evaporation process took place as a result of energy transfer from the circulated water to the liquid refrigerant in the tank. In addition, heat was added to the storage of the circulating water by an electric heater in order to maintain a constant temperature.

The control of the rate of energy transferred to the liquid refrigerant in the evaporator tank was difficult due to inevitable conduction heat leakage from the ejector to the evaporation tank along the connecting tube wall. The entrained vapor was therefore slightly superheated. The pressure of the entrained or secondary vapor was directly measured by

a mercury-type vacuum manometer which was installed in the tank and gave an uncertainty ± 0.003 bar (1 bar $= 10^5$ Pascal).

The back pressure of the ejector was controlled by adjusting the flowrate of cooling water through the condenser and also measured by a mercury-type vacuum manometer.

Since the tests could not be run continuously, a liquid receiver was installed beneath the condenser to receive the condensate during each test run. After a test run was completed, a circulation pump was used to pump the liquid Freon to the generator and the evaporator tank for another test run.

Table 1 Specifications of ejector being tested

Area ratio, A_m/A_t	34.0
Diverging angle at nozzle exit	6.3 deg
Diverging angle of diffuser	8.6 deg
Converging angle of constant-area section	17.4 deg
Length of constant-area section	130 mm
Length of diffuser	300 mm

Since some air seepage was inevitable during the charging of Freon fluid into the system, the testing procedure started with a trial run for several minutes which would flush and entrain the seeped air toward the condenser. Then partial evacuation of the condenser was performed with a vacuum pump so as to further reduce the inert gas inside the system. After this operation, the experiment could start. The time intervals taken for the flow-rate measurements were about 4 min for each test run, during which the temperature and pressure measurements were also made.

Performance Characteristics of Ejector. The specifications of the ejector used in the present test are shown in Table 1. Basically, the performance of an ejector can be represented by the entrainment ratio (ratio of flow rates of secondary to primary vapor) in terms of the pressures of primary and secondary vapors, and the back pressure (or condenser pressure). By fixing the actuating vapor pressure P_g

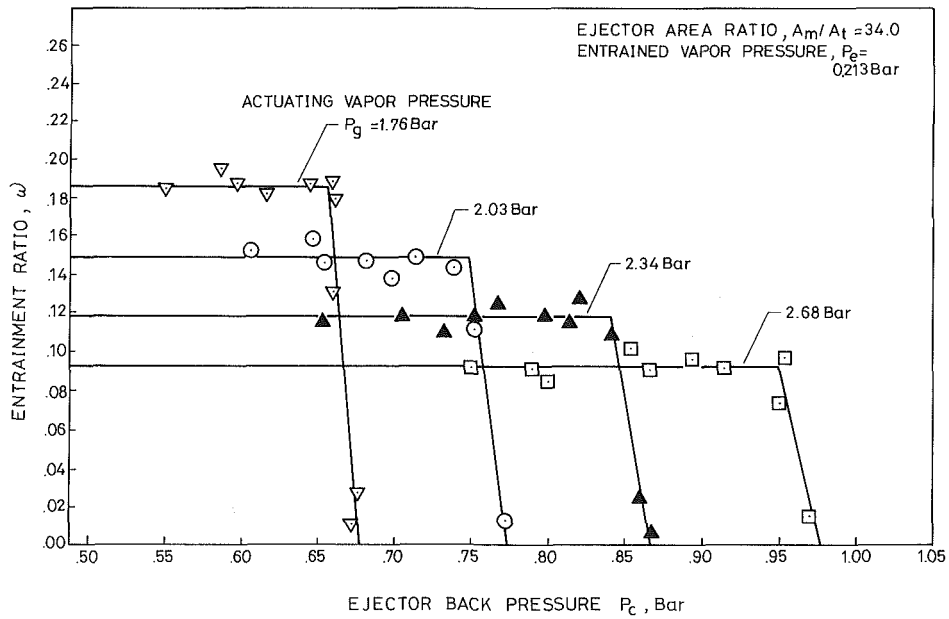

Fig. 5 Measured ejector entrainment ratios

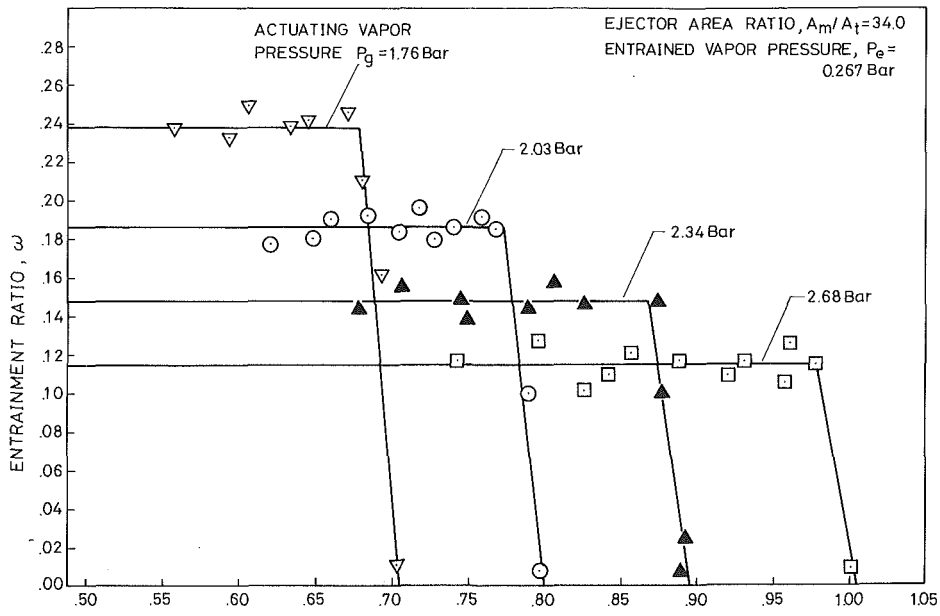

Fig. 6 Measured ejector entrainment ratios

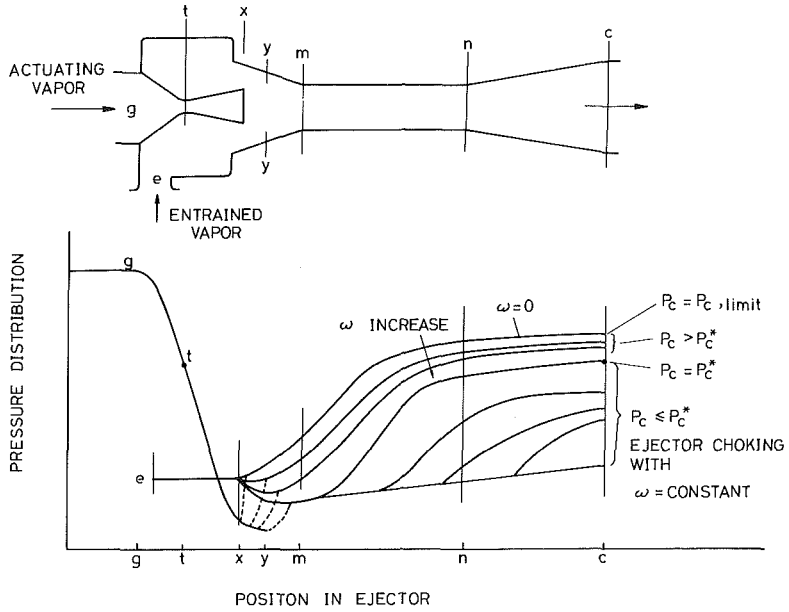

Fig. 7 Pressure variations inside the ejector

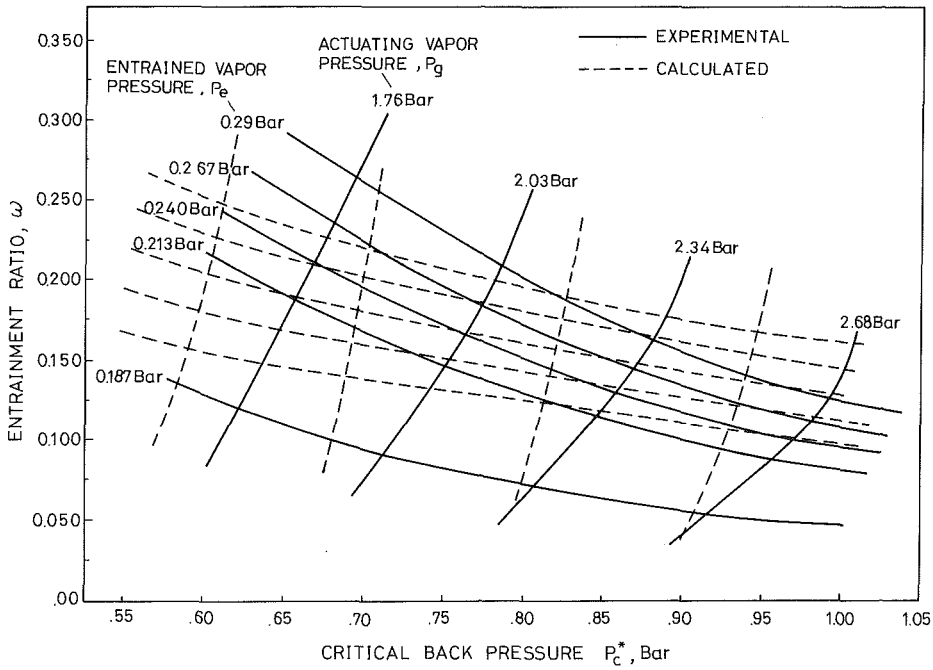

Fig. 8 Measured and calculated ejector performance map

and the entrained or secondary vapor pressure P_e, we measured the entrainment ratio of the ejector at various back or condenser pressures P_c.

Figures 5 and 6 show some of the testing results. From these, it can be seen that the entrainment ratio starts to build up and continues to increase quickly while lowering the back pressure from a limiting value $P_{c,\text{limit}}$. The entrainment ratio then remains constant as the back pressure continues to decrease to below a critical back pressure P_c^*. This is known as the choking phenomenon of ejectors. (Throughout this paper, choking of the ejector implies choking for the secondary vapor.) It is also shown in Figs. 5 and 6 that ejectors can be operated only below a limiting back pressure, which is dependent on the pressures of actuating and entrained vapors.

The choking phenomenon of ejectors was classified by Munday and Bagster [32] as upper and lower choking in accordance with the mixing and shock formation processes in the mixing section. In practice, shocks always occur somewhere in the ejector as long as the ejector functions normally. For ejectors at choking conditions, transverse shocks will appear in the passage of constant-area section as a result of the presence of a thick boundary layer. The secondary vapor will reach sonic velocity at some cross section *yy* (see Fig. 2) in the mixing section associated with a hypothesized effective area.

The shocks tend to move toward the mixing section as the back pressure of the ejector continues to increase. Further rise in back pressure beyond the critical back pressure will cause the shocks to penetrate into the mixing section and the entrainment ratio starts to decrease rapidly. At this point, choking of the secondary vapor disappears and mixing of the two streams associated with shock interactions in the mixing section is so severe that it is very difficult to clearly define an effective area for the secondary vapor. The flow of secondary vapor results from an adiabatic expansion or throttling process from the entrance to the mixing zone.

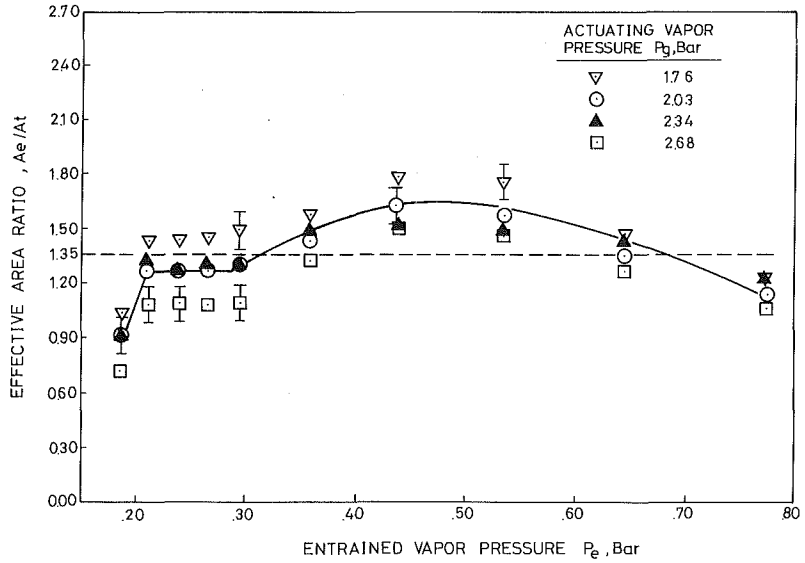

Fig. 9 Variations of effective area ratio

The effect of a rise in back pressure is transmitted upstream of the shock. As the back pressure is raised to the limiting back pressure, the shocks will finally pass through the mixing section and reach the exit of the actuating nozzle. At this location, the pressures of the two streams will be raised to the pressure of the entrained vapor P_e and the entrainment ratio drops to zero. This movement of shocks in ejector associated with the variations of back pressure can be qualitatively illustrated by the pressure distribution curves as shown in Fig. 7.

The pressure distributions or other properties in the ejector were not measured in the present test. However, the phenomena of shock movement in ejectors can be verified by the Schlieren photographs and the pressure distributions in ejectors which were observed by Keenan et al. [10]. The experimental results shown in [10] also indicate that the movement of shocks, as well as the entrainment ratio, is closely related to the area ratio of constant-area section to actuating nozzle throat, the length of constant-area section, the converging angle of the mixing section, the location of actuating nozzle, and even the surface roughness of the ejector.

If the back pressure is higher than the limiting value, negative entrainment, i.e., vapor reversely forced back to the evaporator, will occur. When the back pressure is too high, choking in the actuating nozzle will finally disappear and the ejector loses its function completely.

From Figs. 5 and 6, it also can be seen that the entrainment ratio increases with decreasing actuating vapor pressure P_g and increasing secondary vapor pressure P_e. Since ejectors are normally designed to be operated at choking conditions, the experimental data obtained at the critical back pressures could be used to construct an ejector performance map as shown in Fig. 8.

It can be seen from Fig. 8 that, at fixed secondary vapor pressure P_e, the entrainment ratio increases with decreasing actuating vapor pressure P_g, but the critical back pressure P_c^* also decreases. This indicates that the pressure of actuating vapor, either in design or in field operation, has to be selected or adjusted, according to the performance map, as close to the critical back pressure as possible in order to obtain highest efficiency.

Analysis of Effective Area. The effective areas for the secondary vapor at ejector choking conditions were computed by use of the experimental data and Munday and Bagster's method [32] in the present study. During the computation, thermodynamic properties of Freon-113 were directly read from a chart published by ASHRAE. For rapid computation on a computer, the thermodynamic chart was first fitted to a set of polynomial equations using the method of least squares. The results are shown in the Appendix.

Assuming that the friction and the heat loss in the ejector can be ignored and applying the conservations of mass, momentum, and energy to actuating nozzle, secondary flow channel, mixing zone, constant-area section, and diffuser, we can derive a set of governing equations and solve the entrainment ratio if a value of effective area A_e is given. Here, the secondary flow channel covers the region from the entrance of secondary vapor to the *yy* cross section where the effective area is defined. The mixing zone covers the region from the whole cross section at position *yy* to the entrance of constant-area section, the *mm* position as shown in Fig. 2.

Changing the value of effective area and repeating the computation until the calculated entrainment ratios and the experimental values were matched, the effective area was then determined. As discussed previously, the effective area is significant only at choking conditions. Therefore, only the entrainment ratios at choking conditions were taken to calculate the effective area. Since there were several data points at each choking condition to be matched in determining the effective area, the method of least squares was therefore employed to determine a best value. The final results are shown in Fig. 9. The associated standard deviations in the determination of the ratio of effective to throat areas were approximately at ± 0.1.

Figure 9 shows the ratio of effective area A_e to nozzle throat area A_t at various choking conditions. It can be seen that the effective area first increases then remains constant to a value of the secondary vapor pressure P_e at approximately 0.3 bar. It then increases and finally decreases as P_e continues to increase. This evidence indicates that the effective area of the secondary vapor at choking conditions is not just a constant for an ejector as Munday and Bagster presumed [32] but may vary with operating conditions.

As the mixing process is supersonic, the variations of effective area with the pressures of actuating and secondary vapors might result from the interactions between transverse shocks generated at the exit of actuating nozzle, ejector wall boundary, and secondary stream. If the secondary vapor is not at choking conditions, the effects of movement and penetrating of the transverse shocks from the constant-area section toward the mixing section will also be encountered. At this case, the effective area is also affected by the back

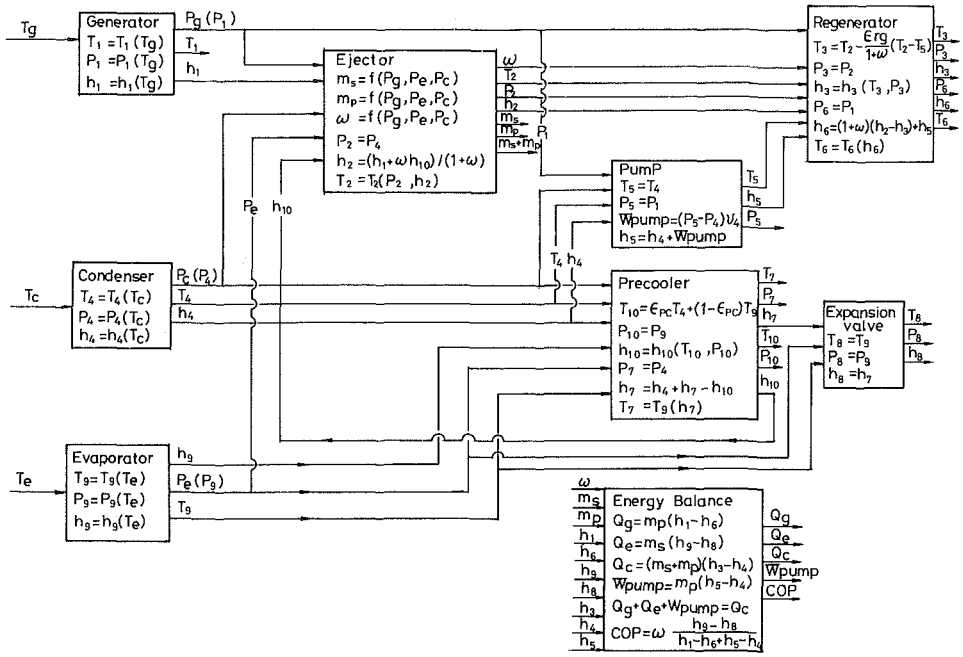

Fig. 10 Information-flow chart of system design analysis

pressure and is hardly realized. The detailed mechanisms may involve the effect of mixing of two streams associated with transition from subsonic to supersonic flow in the secondary vapor. The process is extremely complicated and thus needs further investigations. Figure 9 gives a mean value of 1.35 for the effective area ratio if it was assumed to be constant as Munday and Bagster cited [32]. By this mean value, the entrainment ratio of the ejector can be computed by use of the method in [26, 32] and the results are plotted as dotted curves in Fig. 8. It is seen that the computation for ejector performance using a constant effective area of the ejector leads to significant errors.

Design Analysis of Jet Refrigeration Systems

1 Analytical Procedures. The jet refrigeration system studied here is shown in Fig. 1. Freon-113 was selected as the working fluid because it has a low boiling point at moderate pressure. To facilitate the analysis, the following assumptions were made:

1. The system operates at steady state.
2. Pressure losses in all the components and the connecting pipes are negligible.
3. Heat losses to the ambient are negligible except for the components requiring energy exchange with the environment.
4. The exit of condenser is at saturated liquid state.
5. The fluid at the exits of evaporator and generator is at saturated vapor state.
6. The effectivenesses of precooler and regenerator are all at 0.80.
7. The temperature rise across the circulation pump is negligible.
8. The expansion through the expansion valve is a throttling process.

By making use of mass and energy balances to generator, ejector, regenerator, condenser, circulation pump, expansion valve, evaporator, and precooler, a set of system performance equations can be derived and solved for the thermodynamic states all over the system. The performance map of an ejector and the above assumptions were also used for the solution.

Prior to the analysis, the performance map of an ejector was first fitted to a set of equations using the technique of least squares in the following functional relations:

$$m_s = f(P_g,P_e,P_c)$$
$$m_p = f(P_g,P_e,P_c)$$
$$\omega = f(P_g,P_e,P_c)$$

where m_s and m_p are the mass flowrates of the secondary and the primary vapors respectively. In addition, to facilitate the analysis on a computer, the thermodynamic properties of Freon-113 were represented by a set of polynomial equations and directly used (see the Appendix).

The system performance calculation then proceeds by a sequential simulation process, following the information-flow diagram as shown in Fig. 10. The performance equations are all listed in the blocks. It can be shown that there are three independent design variables for the design of jet refrigeration systems, namely, temperatures at generator, condenser, and evaporator, i.e., T_g, T_c, and T_e. As these three variables are independently specified according to the conditions at which the system is to be operated, the system performance can be directly calculated. The efficiency of a jet refrigeration system can be represented by a coefficient of performance (COP) which can be derived as

$$\text{COP} = \frac{Q_e}{Q_g + W_{\text{pump}}} = \omega \frac{h_9 - h_8}{h_1 - h_6 + h_5 - h_4} \tag{1}$$

where Q_e, Q_g, and W_{pump} are the rates of energy transfer in evaporator, generator, and circulation pump, respectively, and expressed as

$$Q_g = m_p(h_1 - h_6) \tag{2}$$
$$Q_e = m_s(h_9 - h_8) \tag{3}$$
$$W_{\text{pump}} = m_p(h_5 - h_4). \tag{4}$$

2 System Design Analysis. The computations mentioned above were carried out on a PDP 11/44 digital computer. Figure 11 shows the variations of COP with temperatures of the generator, evaporator, and condenser. Since there is a critical back pressure (or condenser pressure) for the ejector, at fixed generator and evaporator temperatures COP will remain constant and move along a horizontal YZ line as shown in Fig. 11 (i.e., the system works at choking condition), when the condenser temperature is designed at any temperature below T_c^*, where T_c^* is the equilibrium temperature corresponding to the critical back pressure of ejector. Any

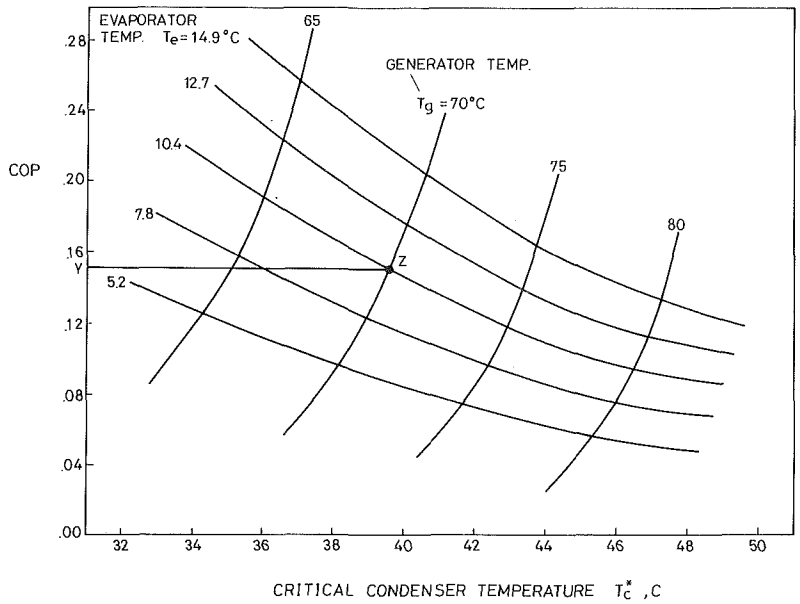

Fig. 11 Critical system design map – COP map

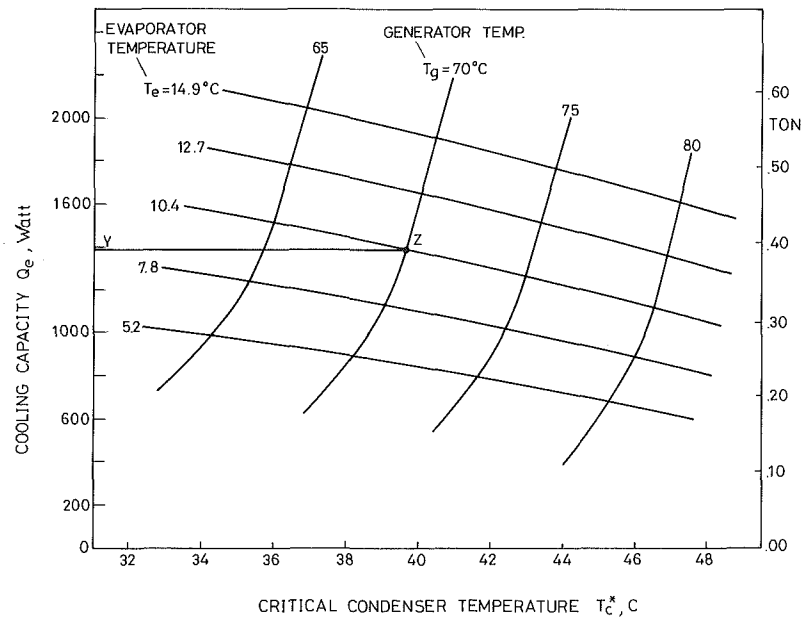

Fig. 12 Critical system design map – Q_e map

design with a condenser temperature above this critical value will cause a dramatic decrease in system COP. This means that the selection of condenser temperature in the design of jet refrigeration systems cannot be arbitrary but is restricted by the critical condenser temperatures, which are dependent on generator and evaporator temperatures as shown in Fig. 11.

It also can be seen from Fig. 11 that, at fixed evaporator temperature, COP increases with decreasing generator temperature, but the critical condenser temperature also decreases. Therefore, in designing a jet refrigeration system, the selection of a condenser temperature, which is related to type of cooling device to be used and local weather conditions, is very important. It is preferable to design the system at a condenser temperature as close to its critical value as possible in order to obtain better performance. In other words, Fig. 11 can be regarded as a critical system design map for jet refrigeration systems if the condenser temperature is designed at its critical value. In addition to the COP design map, the cooling capacity of the refrigeration system is calculated; its critical design map is shown in Fig. 12.

To illustrate the application of Figs. 11 and 12, a typical design example is given. In designing a system, the critical point Z should be located first in Figs. 11 and 12 based on given generator and evaporator temperatures and from which the critical condenser temperature is determined. Then, draw a horizontal line to the left from the critical point Z. The condenser temperature then should be designed in the range from Y to Z and the system COP is represented by the YZ line. For instance, assume that a jet refrigeration system is designed to be operated at 70°C generator temperature and 10.4°C evaporator temperature. So, the critical point Z can be located as shown in Fig. 11. At this point, the critical condenser temperature is 39.4°C. The system COP will be located on the horizontal YZ line and has a constant value of 0.15 as the condenser temperature operates at any value below 39.4°C. From Fig. 12, the cooling capacity is 1377 W.

An analysis was also carried out for systems without precooler and regenerator. It can be seen from Figs. 13 and 14 that COP and cooling capacity drop by about 20 percent if precooler and regenerator are not installed. Therefore, it is

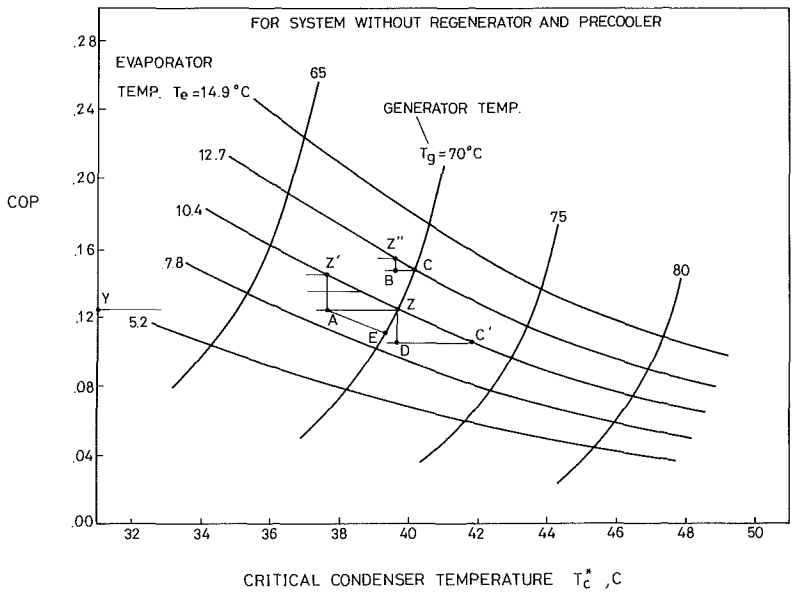

Fig. 13 COP design map for systems without regenerator and precooler

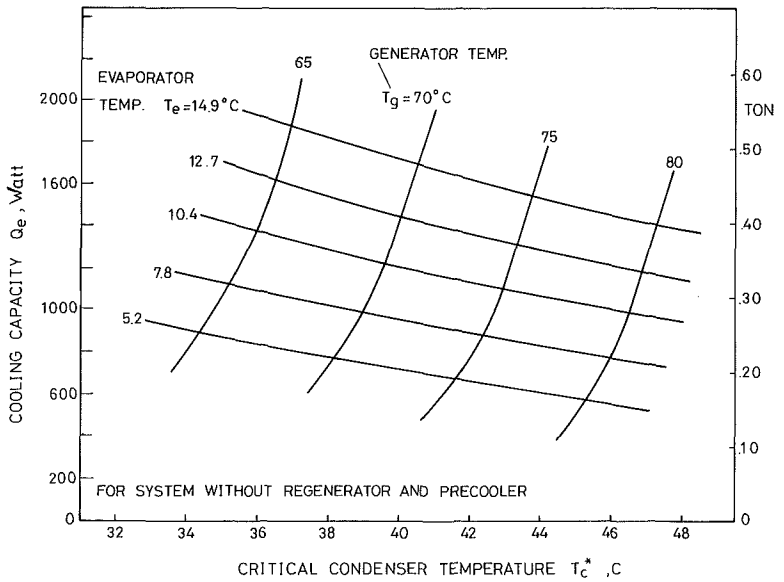

Fig. 14 Q_e design map for systems without regenerator and precooler

suggested to install the regenerator and precooler in jet refrigeration systems to improve the system COP.

3 Performance Characteristics for Systems Working at Off-Design Conditions. The development of the critical design maps for the jet refrigeration system (Figs. 11–14) is basically a process of system design analysis rather than a simulation. However, the design maps (Figs. 11 and 12) can be regarded as a result of system simulation if the effectiveness of the regenerator and precooler are assumed to remain approximately constant at their original design values during field operation. On the other hand, the temperatures of the generator, evaporator, and condenser are usually adjustable in practical applications. Therefore, Figs. 11 and 12 can be treated as an approximation of system simulation. For systems without regenerator and precooler, this precaution can be precluded. Thus, Figs. 11 and 12, or Figs. 13 and 14, can be used to predict the performance of a jet refrigeration system when it works at off-design conditions.

Assume that point Z is the critical point for a given generator and evaporator temperatures and the system design point is also located at the point Z as shown in Figs. 11–13. As the condenser temperature is lowered during operation due to variations of weather or other unexpected conditions, the operating point will be shifted to point A in the case of COP unchanged. (Hereinafter, we use Fig. 13 for the discussion.) At this position, if we still want the refrigeration system to be operated at the critical condition, the generator temperature should decrease by some amount (represented by the line segment AE as shown in Fig. 13) for the case of COP or cooling capacity unchanged, but consequently the evaporator temperature will be simultaneously lowered from the ZZ'-line to the AE-line. In other words, when the condenser temperature is lowered during operation, reducing the generator temperature can simultaneously decrease the cooling or refrigeration temperature for critical operating conditions but the system COP as well as the cooling capacity is not changed.

Next, we will discuss the case where we desire to keep the evaporator temperature unchanged. When the condenser temperature is lowered during operation, the generator

temperature should be lowered as well if we still want the system to work at the critical condition. In this circumstance, the system COP, as well as the cooling capacity, can increase to a higher value and the operating point will be shifted to a new critical point Z'.

It can be further seen from ejector performance that the points on the constant-T_e line represent critical conditions. For fixed evaporator temperature T_e, by drawing a horizontal line to the left from any point on the line segment ZZ', we can locate the subcritical operating point by intercepting the horizontal line with the line segment AZ'. For subcritical operations, the operating point will sit on the line segment AZ' and the generator temperature will be higher but the system COP will be lower than that for critical operation, for the cases of unchanged evaporator temperature.

It therefore can be seen that an optimum operating efficiency can be obtained by keeping the operating condition at critical points all the time. Figure 11 or 13 can be treated as a critical system operating map which can be fed into a computer or an automatic control system to automatically control the temperatures at generator, evaporator, and condenser in field operation so that the highest operating efficiency can be attained.

To consider the overload conditions, assume that the system is designed at a critical point, say at point Z in Figs. 11–13. At fixed generator and condenser temperatures, if the evaporator temperature increases due to overload operation so that the operating condition is shifted to point B which is in a subcritical region (with respect to its critical point C), then the system COP as well as the cooling capacity increases. Further an increase in COP or cooling capacity can be achieved if the generator temperature is also decreased. The maximum possible COP and cooling capacity can be obtained if the system is working at another critical condition (at the new critical point Z'' as shown in Fig. 13). In other words, the operating efficiency increases with increasing cooling load or at overload operation. This is a very interesting performance characteristic which takes place in jet refrigeration systems.

For systems designed at the critical point (for example, point Z in Fig. 11 or 13), at fixed condenser temperature, the system COP or cooling capacity will decrease with increasing generator temperature and the operating condition (point D in Fig. 13) will be in a subcritical region (with respect to its critical condition, point C'). This is attributed to the fact that the entrainment ratio of the ejector decreases with increasing generator temperature. Therefore, it is impossible to raise the system COP or cooling capacity by increasing generator temperature; this just wastes the heating energy added to the generator. This was also concluded by Munday and Bagster [32].

For systems designed at critical points according to the critical design maps (Figs. 11–14), any slight increase during operation in condenser temperature away from the designed value will cause a rapid drop in system COP and cooling capacity. Therefore, a safety factor should be considered in jet refrigeration system design.

Conclusions

Studies on the performance characteristics of an ejector were carried out in the present work. It was experimentally shown that the choking phenomena in the secondary or entrained vapor play a very important role in ejector performance. Ejector choking, usually associated with transverse shocks in the passage of constant-area section and an "effective area" for the secondary vapor in the mixing zone, takes place as the ejector operates at a back pressure below the critical value, which is dependent on the pressures of actuating and entrained vapors. The experimental data were used to construct an ejector performance map which is quite useful either in jet refrigeration system design or in optimum control of an ejector in field operation.

The experiment shows that for the secondary vapor at fixed inlet pressure, the ejector entrainment ratio increases with decreasing actuating vapor pressure, but the critical back pressure also decreases. The effective areas of the ejector which were calculated from the experimental results were shown not to be a constant as presumed by Munday and Bagster [32] but to vary with operating conditions. It was shown that the calculation of ejector performance by assuming a constant effective area leads to significant errors. Although the experiments were performed with Freon-113 refrigerant, the qualitative conclusions obtained in the present study can be applied to ejectors working with other refrigerants.

Based on the performance map determined from the present experiment, a design analysis of jet refrigeration system was carried out. It was found that there are three independent system design variables for jet refrigeration systems, namely, the temperatures of the generator, condenser, and evaporator. The analysis yielded a critical system design map from which a system design can be easily done. It was found from the design map that, at fixed evaporator temperature, the system COP as well as the cooling capacity increases with decreasing generator temperature, but the critical condenser temperature also decreases. It thus indicates that the design of condenser temperature which is related to a type of cooling device to be used and local weather conditions is an essential process in the design of jet refrigeration systems. It is preferable to design the system at a condenser temperature as close to its critical value as possible in order to obtain a better performance.

Performance characteristics for jet refrigeration systems working at off-design conditions were also analyzed in the present study. It was found from this analysis that the highest operating efficiency can be achieved if the refrigeration system was automatically adjusted so that it operates at critical conditions in line with the critical design map. Therefore, as the condenser temperature is lowered during field operation, reducing the generator temperature will increase the system COP as well as the cooling capacity, with the evaporator temperature fixed. On the other hand, the system COP will increase with decreasing generator temperature as the refrigeration system works at overload conditions (both cooling load and evaporator temperature increase). It is also noticeable that it is impossible to raise the system COP or cooling capacity by increasing the generator temperature, but just wasting the heating energy added to the generator. To achieve highest operating efficiency, it is better to design a jet refrigeration system at critical points with a design safety factor according to the critical design maps developed in the present study and to automatically control the temperatures of the generator, condenser, and evaporator in field operation such that the system always works at critical conditions.

Acknowledgments

This project was partially supported by the National Science Council of the Republic of China through Grant No. NSC71-0201-E002-17.

References

1 Martynowsky, W., "Use of waste heat for refrigeration," *Refrigeration Engineering*, Mar. 1954, p. 51.

2 Anderson, H., "Assessment of solar powered vapor jet A/C systems," *1975 ISES Conference Proceedings*, Los Angeles, CA, 1975, pp. 408–409.

3 Hamner, R. M., "An alternative source of cooling: The ejectors—Compression heat pump," *ASHRAE J.*, July 1980, pp. 62–66.

4 Chat, V. W., and Lansing, F. L., "Solar-powered Jet Refrigerator," *Mechanical Engineering*, Apr. 1980, pp. 64–65.

5 *ASHRAE Guide and Data Book Equipment*, Chap. 13, Steam-Jet Refrigeration Equipment, 1974, pp. 127–134.
6 Stoecker, W. F., "Refrigeration and Air-Conditioning," McGraw-Hill, 1958.
7 Havemeyer, H. R., "Do you know enough about steam jet refrigeration?" *Chemical Engineering*, Sept. 1948, pp. 102–106.
8 Jackson, D. H., "Steam jet ejector: Their uses and advantages," *Chemical Engineering Progress*, July 1976, pp. 77–79.
9 Keenan, J. H., and Neumann, E. P., "A simple air ejector," ASME *Journal of Applied Mechanics*, Vol. 64, 1942, pp. A75–78.
10 Keenan, J. H., Neumann, E. P., and Lustwerk, F., "An investigation of ejector design by analysis and experiment," ASME *Journal of Applied Mechanics*, Sept. 1950, pp. 299–309.
11 Kroll, A. E., "The design of jet pumps," *Chemical Engineering*, Vol. 1, No. 2, 1947, pp. 21–24.
12 Work, L. T., and Haedrich, V. W., "Performance of ejector as a function of the molecular weights of vapors," *Ind. and Eng. Chemistry*, Vol. 31, No. 4, 1939, p. 464–477.
13 Holton, W. C., "Effect of molecular weight of entrained fluid on the performance of steam-jet ejectors," *Trans. ASME*, Oct. 1951, pp. 905–910.
14 Holton, W. C., and Schulz, E. J., "Effect of temperature of entrained fluid on the performance of steam-jet ejectors," *Trans. ASME*, Oct. 1951, pp. 911–913.
15 Defrate, L. A., and Hoerl, A. E., "Optimum design of ejector using digital computers," *Chem. Eng. Progr. Symp.*, Ser. 55, No. 21, 1959, pp. 43–51.
16 Khoury, F., Heyman, M., and Resnick, W., "Performance characteristics of self-entrainment ejectors," *I&EC Process Design and Development*, Vol. 6, No. 3, 1967, pp. 293–302.
17 Emanuel, G., "Optimum design for a single-stage gaseous ejector," *AIAA J.*, Vol. 14, No. 9, 1976, pp. 1292–1296.
18 Chen, L. T., "On the design theory of constant-area-mixing type jet compressors," *J. Chinese Inst. of Eng.*, 1978, pp. 53–59.
19 Elrod, H. G., "The theory of ejectors," *J. Applied Mechanics*, 1945, pp. A170–174.
20 Chen, L. T., "A heat driven mobile refrigeration cycle analysis," *Energy Conversion*, Vol. 18, 1977, pp. 25–29.
21 Jeelani, S. A. K., Rajkumar, A., and Kasipathi Rao, K. V., "Designing air-jet ejectors," *Chem. Eng.*, Sept. 1978, pp. 135–136.
22 Jeelani, S. A. K., Kasipathi Rao, K. V., and Balasubramanian, G. R., "Designing steam-jet ejectors," *Chem. Eng.*, Apr. 1979, pp. 135–136.
23 Davletov, A., "Experimental study of a low-output Freon ejectors," *Izr. An. Turkm. USSR*, No. 1, 1963.
24 Kakabaev, A., and Davletov, A., "A Freon ejector solar collector," *Geliotekhnika*, Vol. 2, No. 5, 1966, pp. 42–48.
25 Zhadan, S., and Schetinina, N. A., "Selection of cycle design parameters for solar ejector Freon refrigeration machine," *Geliotekhnika*, Vol. 16, No. 1, 1980, p. 14.
26 Zeren, F., Holmes, R. E., and Jenkins, P. E., "Design of Freon jet pump for use in a solar cooling system," ASME Paper No. 78-WA/SOL-15, Aug. 1979.
27 Deled, R. V., Rose, R. E., and Dart, R. S., "An experimental investigation of the use of supersonic driving jet for ejector pumps," *Trans. ASME*, Apr. 1962, pp. 204–212.
28 Harris, L. S., and Ficher, A. S., "Characteristics of the steam-jet vacuum pump," *Trans. ASME*, Nov. 1964, pp. 358–364.
29 Balatchley, C. G., "Selection of air ejectors," *Chem. Eng. Progr.*, Vol. 57, No. 10, 1961, pp. 114–120, 144–150.
30 Munday, J. T., and Bagster, D. F., "Design and performance of a steam jet refrigeration system," *Conference on Thermal Fluids Inst. Eng. Australia*, Aug. 1974, pp. 57–61.
31 Munday, J. T., and Bagster, D. F., "The choking phenomena in ejector with particular reference to steam jet refrigeration," *Thermal Fluids Conference of Inst. of Eng. Australia*, Hobart, National Conference Publication, 1976, pp. 84–88.
32 Munday, J. T., and Bagster, D. F., "A new ejector theory applied to steam jet refrigeration," *Ind. Eng. Chem., Process Des. Dev.*, Vol. 16, No. 4, 1977, pp. 442–449.
33 Balasubramanian, M., "Combined engine cooling system and waste-heat-driven jet-vapor-compression automotive air-conditioning system," Ph.D. dissertation, University of Pennsylvania, 1975.
34 Zeren, F., "Freon-12 vapor compression jet pump solar cooling system," Ph.D. dissertation, Texas A&M University, Texas, 1982.
35 *Thermodynamic Properties of Refrigerants*, ASHRAE Inc., New York, 1969.

APPENDIX

The thermodynamic properties of R-113 can be fitted to a set of polynomial equations by using the data (which are all in English units) published by ASHRAE [35]. For convenience in the curve fitting, the English units were retained. That is, °F for temperature T, psia for pressure P, Btu/lbm for enthalpy h, and Btu/lbm R for entropy S in the following equations. One may convert results to SI units.

For saturated vapor state:

$$\begin{aligned} P(T) = {} & 1.00018 + 1.67794\times10^{-2}T \\ & + 5.7737\times10^{-4}T^2 - 6.04359\times10^{-8}T^3 \\ & + 2.63702\times10^{-8}T^4 - 6.23935\times10^{-11}T^5 \\ & + 8.5771\times10^{-14}T^6. \end{aligned} \quad (A1)$$

The maximum error of the above equation is 0.33 percent.

$$\begin{aligned} h(T) = {} & 78.3411 + 0.190907T - 1.53674\times10^{-3}T^2 \\ & + 2.4538\times10^{-5}T^3 - 1.97103\times10^{-7}T^4 \\ & + 7.77384\times10^{-10}T^5 - 1.19879\times10^{-12}T^6. \end{aligned} \quad (A2)$$

The maximum error of the above equation is 0.03 percent.

$$\begin{aligned} S(T) = {} & 0.171123 + 7.23768\times10^{-5}T \\ & - 2.24038\times10^{-6}T^2 + 3.98186\times10^{-8}T^3 \\ & - 3.14496\times10^{-10}T^4 + 1.21468\times10^{-12}T^5 \\ & - 1.84318\times10^{-15}T^6. \end{aligned} \quad (A3)$$

The maximum error of the above equation is 0.04 percent.

For saturated liquid state:

$$\begin{aligned} h(T) = {} & 7.80358 + 0.212589T - 1.9668\times10^{-4}T^2 \\ & + 3.08707\times10^{-6}T^3 - 1.49096\times10^{-8}T^4 \\ & + 3.24006\times10^{-11}T^5 - 1.89425\times10^{-14}T^6. \end{aligned} \quad (A4)$$

The maximum error of the above equation is 0.03 percent.

$$\begin{aligned} S(T) = {} & 1.81451\times10^{-2} + 4.28571\times10^{-4}T \\ & + 1.3096\times10^{-7}T^2 - 7.42969\times10^{-9}T^3 \\ & + 6.96948\times10^{-11}T^4 - 2.8667\times10^{-13}T^5 \\ & + 4.43105\times10^{-16}T^6. \end{aligned} \quad (A5)$$

The maximum error of the above equation is 0.13 percent.

For superheated state:

$$\begin{aligned} h(T,P) = {} & (79.4428 + 0.133485T + 1.25508\times10^{-4}T^2 \\ & - 1.47264\times10^{-7}T^3) + (-0.599669 \\ & + 8.76725\times10^{-3}T - 4.72337\times10^{-5}T^2 \\ & + 8.69309\times10^{-8}T^3)P \\ & + (0.141287 - 2.10871\times10^{-3}T \\ & + 1.05776\times10^{-5}T^2 - 1.77793\times10^{-8}T^3)P^2 \\ & + (-6.56184\times10^{-3} + 9.50394\times10^{-5}T \\ & - 4.5834\times10^{-7}T^2 + 7.36751\times10^{-10}T^3)P^3. \end{aligned} \quad (A6)$$

The maximum error of the above equation is 0.2 percent.

$$\begin{aligned} S(P,T) = {} & (0.173887 + 2.96756\times10^{-4}T \\ & - 2.30768\times10^{-7}T^2 + 3.74401\times10^{-10}T^3) \\ & + (-6.44247\times10^{-3} + 9.56305\times10^{-6}T \\ & + 1.10595\times10^{-8}T^2 - 1.04455\times10^{-10}T^3)P \\ & + (5.41147\times10^{-4} - 1.52274\times10^{-6}T \\ & - 5.81394\times10^{-10}T^2 \\ & + 1.32798\times10^{-11}T^3)P^2 \\ & + (-1.81134\times10^{-5} + 7.93386\times10^{-8}T \\ & - 8.09921\times10^{-11}T^2 \\ & - 3.44308\times10^{-13}T^3)P^3. \end{aligned} \quad (A7)$$

The maximum error of the above equation is 0.3 percent.

D. H. H. Quon
Research Scientist.

S. S. B. Wang
Research Scientist.

T. T. Chen
Research Scientist.

Mineral Processing Laboratory,
Mineral Sciences Laboratories,
CANMET,
Energy, Mines and
Resources Canada,
Ottawa, Canada

Viscosity Measurements of Slags From Western Canadian Coals

The flow characteristics of slags formed by burning of western Canadian coals were characterized by means of high-temperature viscosity measurements. The results show that there is a general linear relationship between viscosities and SiO_2/Al_2O_3, $SiO_2/(Al_2O_3+Fe_2O_3)$ mass ratios and base/acid ratio of the slags. It can be concluded that the viscosities of the slags are sensitive to compositional variation. Attempts were made to correlate the viscosities calculated by Watt and Fereday and Bomkamp's modified methods with the measured viscosities. The correlation is unsatisfactory. The computed viscosities are higher than the measured values.

Introduction

The Canadian Combustion Research Laboratory (CCRL) of CANMET has been actively involved in research on the performance of the Canadian coals in a pilot-scale boiler in collaboration with or on behalf of coal and utilities companies. The major objective of the work is to optimize conditions for achieving the best coal combustion in boilers. Ash fouling of the heat transfer surfaces is one of the most serious operating problems in burning low-grade coals. The ash deposits reduce the thermal efficiency and often lead to unscheduled shutdown of the boiler. Traditionally, the assessment of the slagging and fouling potential of the coals used in these pilot-scale experiments has been carried out using empirical indices based on the ash analyses of the raw coal, the analyses of the fireside deposits, and visual examination of the deposits produced in the boiler. These indices include the ash fusion temperatures, base-to-acid ratio, slagging factor, fouling indicators, sodium content of the ash, and calculated viscosity temperature of the ash based on chemical composition [1, 2]. Viscosity measurements of ash deposits conducted at CANMET show that the calculated viscosity is higher than the measured value by three to five times [3]. In order to understand the thermal behavior of the ash deposits, it is necessary to examine the temperature-viscosity relationship of the deposits in detail and to develop a model that can be used for predicting the conditions under which slagging occurs.

Materials. The boiler slags were produced by burning western Canadian coals in a pilot-scale boiler at CCRL in 1982 and 1983. In addition, a sample of each of bottom ash, fly ash, and lagoon ash was obtained from Saskatchewan Power Corporation Poplar generating station. Chemical analyses of the slags and the ashes and their thermal behavior are given in Tables 1 and 2 respectively.

Table 3 lists the samples and the types and origins of the parent coals. The slags were produced by burning high to medium volatile bituminous or subbituminous coals from Alberta and British Columbia. The Saskatchewan ash samples were derived from a lignite coal.

Characterization. Viscosity measurements were conducted for the slag and ash samples using a high-temperature rotational viscometer described in detail previously [3]. The rotating bob has a diameter of 21 mm and a height of 25 mm. The crucible for containing the melt has a capacity of 30 ml, with dimensions of 32 mm in diameter by 51 mm in height. The system was calibrated using Brookfield silicone standard fluids; the calibration procedure has been described elsewhere [3].

The as-received slag samples were ground to minus 150 μm and calcined at 1000°C to reduce volatiles. They were then pressed into disks, 1 cm high by 2 cm in diameter. The disks were packed into the molybdenum crucible for melting.

Results and Discussion

The viscosity versus temperature data for the slags measured are plotted in Fig. 1. In general, the viscosity is higher for the slags derived from medium volatile bituminous coals than for those derived from the subbituminous coals. The ashes derived from the lignite have the lowest viscosities.

Effect of Chemical Compositions on Viscosity. Previously, it was postulated that the viscosity of the slags is controlled to a great extent by the mass ratio of SiO_2/Al_2O_3 [3] and the results showed that the viscosity tends to increase with decreasing SiO_2/Al_2O_3 mass ratio.

The mass ratios SiO_2/Al_2O_3 for various slag samples were calculated and the results are given in Table 4. The viscosities at constant temperature for the different mass ratios of SiO_2/Al_2O_3 are plotted in Fig. 2. The results show that there is a general tendency for the viscosity to decrease with increasing SiO_2/Al_2O_3 mass ratio, which agrees with the previous postulation.

Contributed by the Power Division for publication in the JOURNAL OF ENGINEERING FOR GAS TURBINES AND POWER. Manuscript received by the Power Division July 1984.

Table 1 Chemical compositions of the slag samples

Sample number	SiO_2	Al_2O_3	TiO_2	Fe_2O_3	CaO	MgO	Na_2O	K_2O	P_2O_5	LOI
A448	67.58	20.32	0.47	3.49	4.16	1.17	0.87	0.31	0.28	0.5
A516	68.89	19.81	0.45	3.63	4.17	1.12	0.92	0.30	0.24	0.5
A317	63.30	20.02	0.32	4.58	5.43	1.19	2.56	1.61	0.48	0.5
A390	61.70	20.16	0.44	4.98	5.99	1.22	1.86	1.10	0.43	0.5
A538	67.57	22.12	0.70	3.93	2.58	0.90	1.26	0.33	0.34	0.5
A559	67.97	21.13	0.67	4.64	2.46	0.91	1.12	0.34	0.27	0.5
A601	61.76	26.97	1.17	3.92	2.29	0.75	0.71	0.84	0.03	0.5
A202	64.78	17.81	1.20	8.76	1.97	1.07	0.54	0.57	0.78	0.8
S1	44.72	24.25	0.66	4.48	13.78	3.75	2.49	1.38	0.43	0.7
S2	42.43	22.30	0.81	5.81	13.95	3.71	2.69	1.55	0.39	5.49

Table 2 Thermal behavior of the slag samples

Sample no.	Determined by ASTM technique							
	Under oxidizing condition, °C				Under reducing condition, °C			
	I	S	H	F	I	S	H	F
A448	1322	1407	1435	1455+	1310	1365	1404	1454
A516	1332	1366	1399	1455+	1310	1327	1363	1443
A317	1238	1298	1326	1355	1199	1255	1299	1343
A390	1232	1260	1316	1355	1198	1255	1293	1349
A538	1426	1455+			1404	1454+		
A559	1413	1454+			1382	1430	1454	
A601	1454+				1454+			
S2	1205	1225	1245	1305	1160	1195	1205	1280
A202								

+above temperature.

Table 3 Slag samples, origins, and types of coals from which they are derived

Sample no.	Rank of coal	Coal origin
A538	medium volatile bituminous	British Columbia
A601	medium volatile bituminous	Alberta
A202	medium volatile bituminous	British Columbia
A516	high volatile bituminous	Alberta
A390	subbituminous	Alberta
A317	subbituminous	Alberta
A448	high volatile bituminous	Alberta
S1	lignite (fly ash)	Southern Saskatchewan
S2	lignite (bottom ash)	Southern Saskatchewan

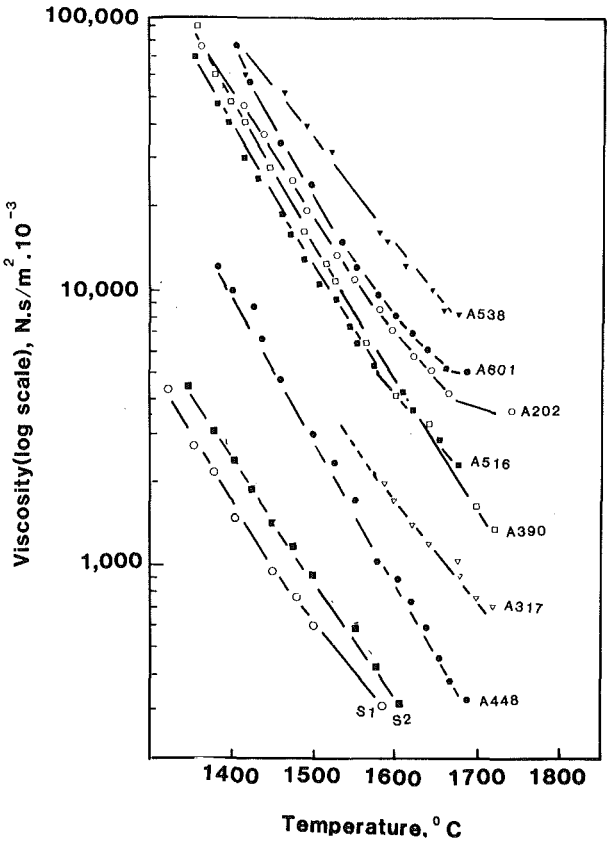

Fig. 1 Viscosity as a function of temperature for the slag samples

It is well known that in silicate melts, Si^{4+} is regarded as an acid cation and acts as a network former (in fourfold oxygen coordination), and basic cations such as Na^+, K^+, Ca^{2+}, Mg^{2+}, and Fe^{2+} act as network modifiers (in sixfold or higher coordination). Al^{3+} is amphoteric. As Fe^{3+} has the same charge and nearly the same ionic radius as Al^{3+} (0.051 nm versus 0.064 nm) and also exhibits isomorphic behavior with Al^{3+} in some crystalline solids, it might be expected to behave analogously with Al^{3+} in the molten slag. The mass ratios $SiO_2/(Al_2O_3 + Fe_2O_3)$ were calculated and are given in Table 4. The mass ratios of $SiO_2/(Al_2O_3 + Fe_2O_3)$ versus experimental viscosities at constant temperature are plotted in Fig. 3. The results show that there is a general linear relationship between the log viscosity and mass ratio of $SiO_2/(Al_2O_3 + Fe_2O_3)$ for four of the slag samples. The viscosity decreases at constant temperature with an increase in $SiO_2/(Al_2O_3 + Fe_2O_3)$ mass ratio.

Effect of Base/Acid Ratio on the Viscosity of Slags. The base-to-acid ratio (B/A) has been used extensively to predict the viscosities of metallurgical slags. This ratio is defined as follows:

$$B/A = (Fe_2O_3 + CaO + MgO + Na_2O + K_2O)/(SiO_2 + Al_2O_3 + TiO_2)$$

Table 4 Calculated SiO_2/Al_2O_3 and $SiO_2/(Al_2O_3 + Fe_2O_3)$ mass ratio for the slag samples

Sample no.	SiO_2/Al_2O_3	$SiO_2/(Al_2O_3 + Fe_2O_3)$
A448	3.32	2.48
A516	3.47	2.94
A317	3.16	2.57
A390	3.06	2.45
A538	3.05	2.59
A601	2.28	1.99
S2	1.90	1.51
S1	1.84	1.55

Table 5 Calculated base-to-acid ratio of the coal slags

Sample no.	Base to Acid ratio
A448	0.11
A516	0.12
A317	0.18
A390	0.18
A538	0.09
A601	0.09
S2	0.42
S1	0.37

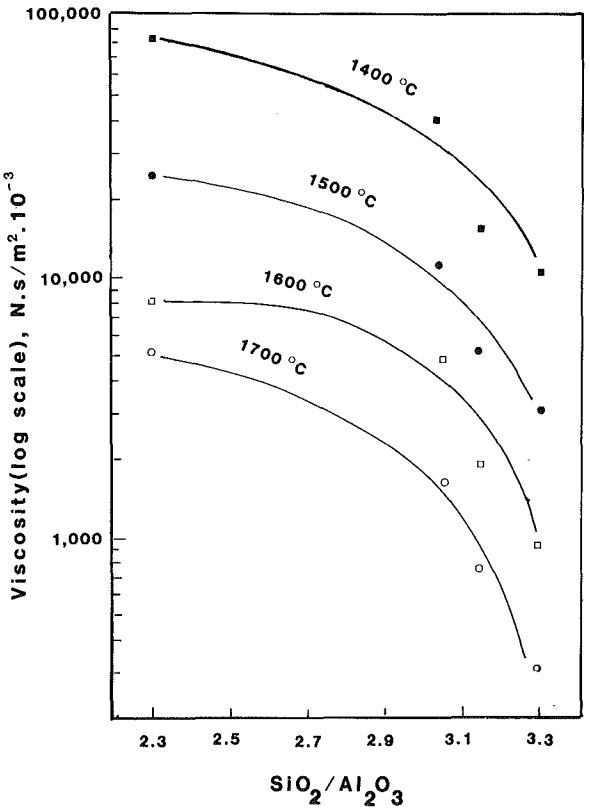

Fig. 2 Viscosity as a function of SiO_2/Al_2O_3 mass ratio at constant temperature

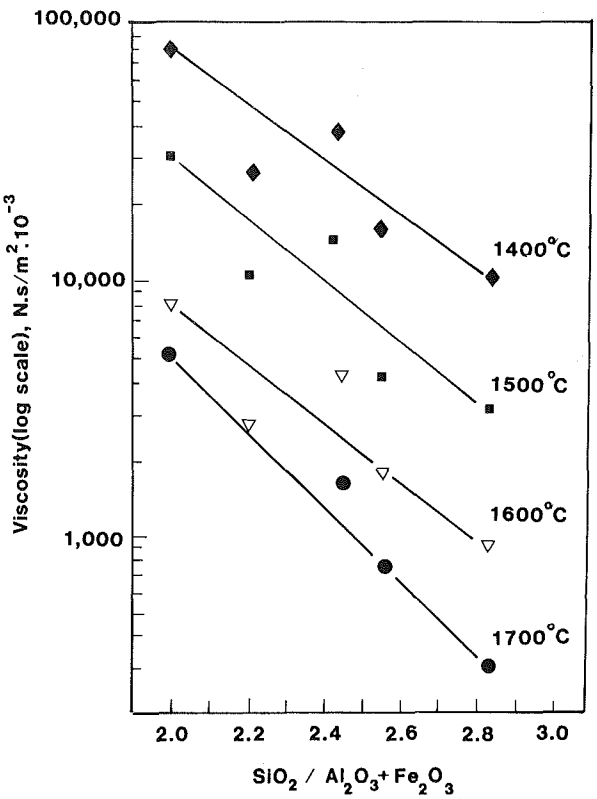

Fig. 3 Viscosity as a function of $SiO_2/(Al_2O_3 + Fe_2O_3)$ mass ratio at constant temperature

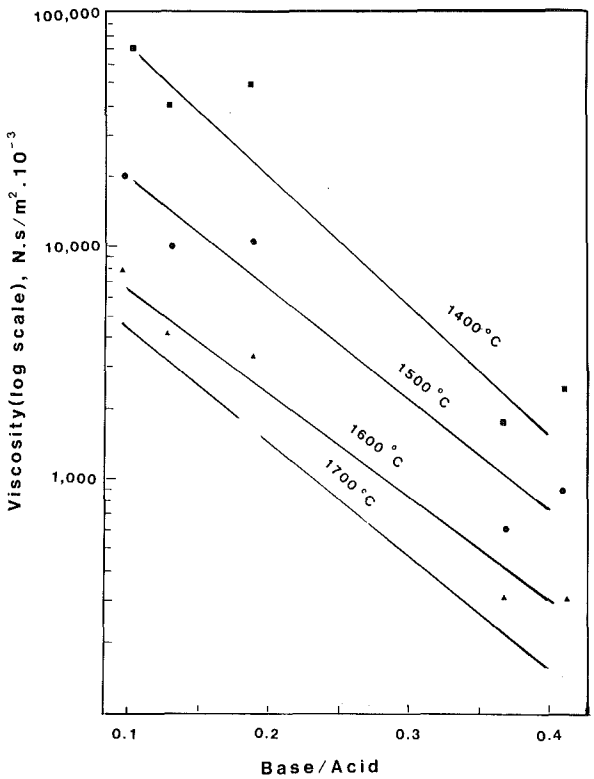

Fig. 4 Viscosity as a function of *B/A* ratio at constant temperature

where each oxide is expressed in weight percent of total slag. The *B/A* ratio was also used to predict the viscosity of the coal ash. It was reported that there is a general correlation between *B/A* ratio and the viscosity of the coal ash [1, 2] and that the viscosity decreases as the *B/A* ratio increases to 1. The *B/A* ratios of the slag samples were calculated and are given in Table 5. These ratios are plotted against measured viscosities at a constant temperature in Fig. 4. The results show that, for certain slag samples, viscosity and *B/A* ratio correlated reasonably well as indicated by the almost linear relationship between these two parameters.

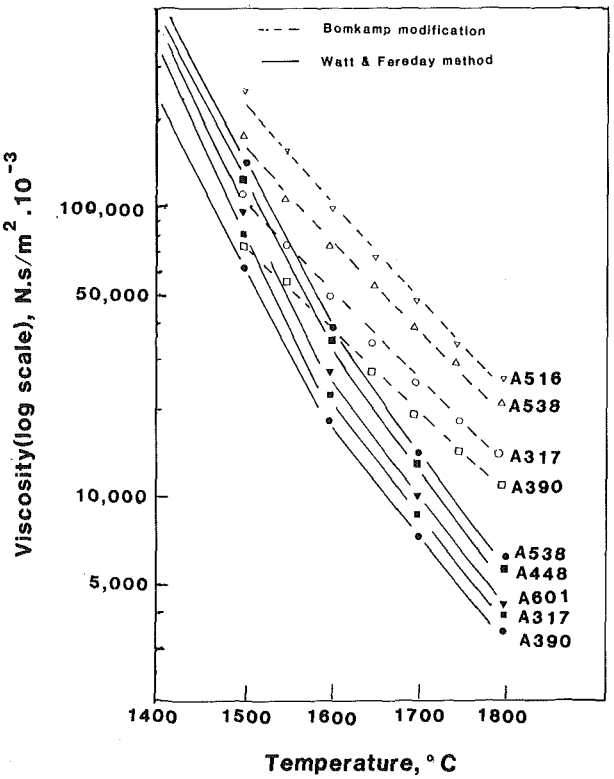

Fig. 5 Calculated viscosity-temperature relationship for the slag samples

Estimation of Viscosity of Slags. Based on experimental measurements on ashes of more than 100 British coals, Watt and Fereday proposed the following viscosity-temperature-chemical composition relationship [4].

$$\log \eta = \frac{10^7 M}{(T-150)^2} + C \tag{1}$$

where

η = viscosity in poises

T = temperature, °C

$M = 0.00835(SiO_2) + 0.00601(Al_2O_3) - 0.109$

$C = 0.0415(SiO_2) + 0.0192(Al_2O_3) + 0.0276(Fe_2O_3) + 0.016(CaO) - 3.92$

The oxides in parentheses are the concentrations of these oxides in the melt expressed in weight percent.

Using equation (1), the viscosities of the present slag samples were calculated and are compared with the measured viscosities of these slags in Fig. 5. The calculated viscosities are higher than the measured ones at any given temperature for most slag samples. Only for sample A601 do the calculated and the experimental values agree reasonably well. Similar disagreement between the calculated and experimental viscosity data was reported by others [5, 6]. To improve the accuracy of viscosity prediction, Bomkamp [6] modified the Watt and Fereday equation for calculating constants M and C to account for the MgO content. These two constants are:

$M = 0.0104291(SiO_2) + 0.0100297(Al_2O_3) - 0.296285$

$C = 0.0154148(SiO_2) - 0.0388047(Al_2O_3) - 0.0167264(Fe_3O_4) - 0.0089096(CaO) - 0.012932(MgO) + 1.04678$

Figure 5 gives the viscosities of four slag samples calculated according to the Bomkamp formula. The results show that the calculated viscosities are appreciably higher than those using the Watt and Fereday method.

Coal slag is a complex material, consisting primarily of silica, alumina, iron oxide, and lime. A minor change of the major constituents or of some of the minor constituents such as alkalies and alkali earths, and the variation of the oxidation state of the iron between the ferrous and ferric state would alter the fluid characteristics of the slag. It is not surprising that the calculated viscosities for a particular slag are in disagreement with the experimental values as these results are computed based on the major constituents present in the slag. A small difference in composition may have a great influence on the viscosity of the slag. In their study of the viscosity of coal ashes, Schobert et al. [5] reported a difference in temperature-viscosity relationship for two ash samples having similar chemical compositions. The two samples differed only by 0.6 mass percent in Na_2O, a minor constituent, and by no more than 2.0 mass percent in the major constituents silica, alumina, ferric oxide and calcium oxide. This indicates that minor changes in composition can significantly affect viscosity, and may explain in part why a precise prediction of viscosity based only on the major constituents in the slag sample is difficult.

Conclusions

The primary objective of this study was to provide direct support to determination of the cause of slagging in a pilot-scale coal-fired boiler using the viscosity measurement technique. At this stage of the work, several observations have emerged:

1 There is a fair correlation between viscosity versus SiO_2/Al_2O_3, $SiO_2/(Al_2O_3 + Fe_2O_3)$, and B/A mass ratios for certain slag samples. This indicates that the major constituents may be used in a qualitative way to predict the viscosity-temperature relationship of a slag.

2 Both Watt and Fereday's method and Bomkamp's modification used for viscosity-temperature calculation produce higher values than those determined experimentally.

Acknowledgments

The writers wish to express gratitude to R. Prokopuk and H. Whaley of the CCRL, CANMET, and D. Smith of the Saskatchewan Power Corporation for supplying the samples for this study. Thanks are also due to G. Lemieux of the Mineral Sciences Laboratories and E. Brouillard, a summer student from the University of Ottawa, for their assistance in the experimental work. We also wish to extend our thanks to L. C. Janke of the Coal Laboratory for providing the chemical analyses of the slags.

References

1 Brown, T. B., and Lee, G. K., "A Pilot Scale Combustion Evaluation of Tulameen Coal," *Division Report* ERP/ERL 79-7, CANMET, Energy, Mines and Resources Canada, 1979.

2 Winegartner, E. C., and Ubbens, A. A., "Understanding Coal Ash Quality Parameters," *Trans. AIME*, Vol. 204, 1976, p. 67.

3 Quon, D. H. H., Wang, S. S. B., and Chen, T. T., "Viscosity Measurements of Slags From Pulverized Coals in a Pilot-Scale Research Boiler," *Fuel*, Vol. 63, 1984, p. 939.

4 Watt, J. D., and Fereday, F., "The Flow Properties of Slags Formed From the Ashes of British Coals: Part 1: Viscosity of Homogeneous Liquid Slags in Relation to Slag Composition," *Journal of Institute of Fuel*, Vol. 42, 1969, p. 99.

5 Schobert, H. H., Diehl, E. K., and Streeter, R. C., "Current Studies in Coal Ash Slag Viscosity," *Proceedings of the Low-Rank Coal, Basic Coal Science Workshop*, Report #CONF-811268, U.S. Department of Energy, 1982.

6 Institute of Gas Technology, "Preparation of a Coal Conversion Systems Technical Data Book," *Energy and Development Administration Report* FE-1730-21, 1976.